

*membranes*

# Membranes for Water and Wastewater Treatment

---

Edited by

Asuncion Maria Hidalgo and Maria Dolores Murcia

Printed Edition of the Special Issue Published in *Membranes*

# **Membranes for Water and Wastewater Treatment**



# Membranes for Water and Wastewater Treatment

Editors

**Asuncion Maria Hidalgo**  
**Maria Dolores Murcia**

MDPI • Basel • Beijing • Wuhan • Barcelona • Belgrade • Manchester • Tokyo • Cluj • Tianjin



*Editors*

Asuncion Maria Hidalgo  
Chemical Engineering  
University of Murcia  
Murcia  
Spain

Maria Dolores Murcia  
Chemical Engineering  
University of Murcia  
Murcia  
Spain

*Editorial Office*

MDPI  
St. Alban-Anlage 66  
4052 Basel, Switzerland

This is a reprint of articles from the Special Issue published online in the open access journal *Membranes* (ISSN 2077-0375) (available at: [www.mdpi.com/journal/membranes/special\\_issues/water\\_wastewater](http://www.mdpi.com/journal/membranes/special_issues/water_wastewater)).

For citation purposes, cite each article independently as indicated on the article page online and as indicated below:

LastName, A.A.; LastName, B.B.; LastName, C.C. Article Title. <i>Journal Name</i> <b>Year</b> , <i>Volume Number</i> , Page Range.
--

**ISBN 978-3-0365-1989-0 (Hbk)**

**ISBN 978-3-0365-1988-3 (PDF)**

© 2021 by the authors. Articles in this book are Open Access and distributed under the Creative Commons Attribution (CC BY) license, which allows users to download, copy and build upon published articles, as long as the author and publisher are properly credited, which ensures maximum dissemination and a wider impact of our publications.

The book as a whole is distributed by MDPI under the terms and conditions of the Creative Commons license CC BY-NC-ND.

# Contents

<b>Preface to "Membranes for Water and Wastewater Treatment"</b> . . . . .	vii
<b>Asunción María Hidalgo and María Dolores Murcia</b> Membranes for Water and Wastewater Treatment Reprinted from: <i>Membranes</i> <b>2021</b> , <i>11</i> , 295, doi:10.3390/membranes11040295 . . . . .	1
<b>Humeyra B. Ulusoy Erol, Christa N. Hestekin and Jamie A. Hestekin</b> Effects of Resin Chemistries on the Selective Removal of Industrially Relevant Metal Ions Using Wafer-Enhanced Electrodeionization Reprinted from: <i>Membranes</i> <b>2021</b> , <i>11</i> , 45, doi:10.3390/membranes11010045 . . . . .	7
<b>Maria Beatriz Cristóvão, Solomon Tela, Andreia Filipa Silva, Micaela Oliveira, Andreia Bento-Silva, Maria Rosário Bronze, Maria Teresa Barreto Crespo, João Goulão Crespo, Mónica Nunes and Vanessa Jorge Pereira</b> Occurrence of Antibiotics, Antibiotic Resistance Genes and Viral Genomes in Wastewater Effluents and Their Treatment by a Pilot Scale Nanofiltration Unit Reprinted from: <i>Membranes</i> <b>2020</b> , <i>11</i> , 9, doi:10.3390/membranes11010009 . . . . .	23
<b>José R. Álvarez, F. Enrique Antón, Sonia Álvarez-García and Susana Luque</b> Treatment of Aqueous Effluents from Steel Manufacturing with High Thiocyanate Concentration by Reverse Osmosis Reprinted from: <i>Membranes</i> <b>2020</b> , <i>10</i> , 437, doi:10.3390/membranes10120437 . . . . .	39
<b>Gerardo León, Asunción María Hidalgo, Beatriz Miguel and María Amelia Guzmán</b> Pertraction of Co(II) through Novel Ultrasound Prepared Supported Liquid Membranes Containing D2EHPA. Optimization and Transport Parameters Reprinted from: <i>Membranes</i> <b>2020</b> , <i>10</i> , 436, doi:10.3390/membranes10120436 . . . . .	53
<b>Saiful Saiful, Maurisa Ajrina, Yusuf Wibisono and Marlina Marlina</b> Development of Chitosan/Starch-Based Forward Osmosis Water Filtration Bags for Emergency Water Supply Reprinted from: <i>Membranes</i> <b>2020</b> , <i>10</i> , 414, doi:10.3390/membranes10120414 . . . . .	65
<b>Asunción María Hidalgo, Gerardo León, María Gómez, María Dolores Murcia, Elisa Gómez and José Antonio Macario</b> Removal of Different Dye Solutions: A Comparison Study Using a Polyamide NF Membrane Reprinted from: <i>Membranes</i> <b>2020</b> , <i>10</i> , 408, doi:10.3390/membranes10120408 . . . . .	79
<b>Ryo-ichi Nakayama, Koki Katsumata, Yuta Niwa and Norikazu Namiki</b> Dependence of Water-Permeable Chitosan Membranes on Chitosan Molecular Weight and Alkali Treatment Reprinted from: <i>Membranes</i> <b>2020</b> , <i>10</i> , 351, doi:10.3390/membranes10110351 . . . . .	95
<b>Aldo Bottino, Gustavo Capannelli, Antonio Comite, Camilla Costa, Raffaella Firpo, Anna Jezowska and Marcello Pagliero</b> Treatment of Olive Mill Wastewater through Integrated Pressure-Driven Membrane Processes Reprinted from: <i>Membranes</i> <b>2020</b> , <i>10</i> , 334, doi:10.3390/membranes10110334 . . . . .	109

<b>Shamas Tabraiz, Burhan Shamurad, Evangelos Petropoulos, Alex Charlton, Obaidullah Mohiudin, Mohammad Danish Khan, Emeka Ekwenna and Paul Sallis</b> Diversity of Acyl Homoserine Lactone Molecules in Anaerobic Membrane Bioreactors Treating Sewage at Psychrophilic Temperatures Reprinted from: <i>Membranes</i> <b>2020</b> , <i>10</i> , 320, doi:10.3390/membranes10110320 . . . . .	<b>125</b>
<b>Krzysztof Mitko, Ewa Laskowska, Marian Turek, Piotr Dydo and Krzysztof Piotrowski</b> Scaling Risk Assessment in Nanofiltration of Mine Waters Reprinted from: <i>Membranes</i> <b>2020</b> , <i>10</i> , 288, doi:10.3390/membranes10100288 . . . . .	<b>143</b>
<b>Vitaliy I. Volkov, Alexander V. Chernyak, Daniil V. Golubenko, Vladimir A. Tverskoy, Georgiy A. Lochin, Ervena S. Odjigaeva and Andrey B. Yaroslavtsev</b> Hydration and Diffusion of H <sup>+</sup> , Li <sup>+</sup> , Na <sup>+</sup> , Cs <sup>+</sup> Ions in Cation-Exchange Membranes Based on Polyethylene- and Sulfonated-Grafted Polystyrene Studied by NMR Technique and Ionic Conductivity Measurements Reprinted from: <i>Membranes</i> <b>2020</b> , <i>10</i> , 272, doi:10.3390/membranes10100272 . . . . .	<b>161</b>
<b>Mariane Carolina Proner, Ingrid Ramalho Marques, Alan Ambrosi, Katia Rezzadori, Cristiane da Costa, Guilherme Zin, Marcus Vinícius Tres and Marco Di Luccio</b> Impact of MWCO and Dopamine/Polyethyleneimine Concentrations on Surface Properties and Filtration Performance of Modified Membranes Reprinted from: <i>Membranes</i> <b>2020</b> , <i>10</i> , 239, doi:10.3390/membranes10090239 . . . . .	<b>175</b>
<b>Agata Marecka-Migacz, Piotr Tomasz Mitkowski, Arkadiusz Nedzarek, Jacek Róžański and Waldemar Szaferski</b> Effect of pH on Total Volume Membrane Charge Density in the Nanofiltration of Aqueous Solutions of Nitrate Salts of Heavy Metals Reprinted from: <i>Membranes</i> <b>2020</b> , <i>10</i> , 235, doi:10.3390/membranes10090235 . . . . .	<b>193</b>
<b>Yi Ding, Zhansheng Guo, Zhenlin Liang, Xuguang Hou, Zhipeng Li, Dashuai Mu, Changzi Ge, Chunpeng Zhang and Chao Jin</b> Long-Term Investigation into the Membrane Fouling Behavior in Anaerobic Membrane Bioreactors for Municipal Wastewater Treatment Operated at Two Different Temperatures Reprinted from: <i>Membranes</i> <b>2020</b> , <i>10</i> , 231, doi:10.3390/membranes10090231 . . . . .	<b>213</b>
<b>Norhan Nady, Noha Salem, Ranya Amer, Ahmed El-Shazly, Sherif H. Kandil and Mohamed Salah El-Din Hassouna</b> Comparison between a Conventional Anti-Biofouling Compound and a Novel Modified Low-Fouling Polyethersulfone Ultrafiltration Membrane: Bacterial Anti-Attachment, Water Quality and Productivity Reprinted from: <i>Membranes</i> <b>2020</b> , <i>10</i> , 227, doi:10.3390/membranes10090227 . . . . .	<b>225</b>
<b>He Bai, Yakai Lin, Hongbin Qu, Jinglong Zhang, Xiaohong Zheng and Yuanhui Tang</b> Technical and Economic Evaluation of WWTP Renovation Based on Applying Ultrafiltration Membrane Reprinted from: <i>Membranes</i> <b>2020</b> , <i>10</i> , 180, doi:10.3390/membranes10080180 . . . . .	<b>247</b>
<b>Chengyi Zhang, Wen Zhang and Yuxin Wang</b> Diffusion Dialysis for Acid Recovery from Acidic Waste Solutions: Anion Exchange Membranes and Technology Integration Reprinted from: <i>Membranes</i> <b>2020</b> , <i>10</i> , 169, doi:10.3390/membranes10080169 . . . . .	<b>263</b>

<b>Mayko Rannany S. Sousa, Jaime Lora-García, María-Fernanda López-Pérez, Asunción Santafé-Moros and José M. Gozávez-Zafrilla</b> Operating Conditions Optimization via the Taguchi Method to Remove Colloidal Substances from Recycled Paper and Cardboard Production Wastewater Reprinted from: <i>Membranes</i> <b>2020</b> , <i>10</i> , 170, doi:10.3390/membranes10080170 . . . . .	<b>287</b>
<b>Hao Xu, Kang Xiao, Jinlan Yu, Bin Huang, Xiaomao Wang, Shuai Liang, Chunhai Wei, Xianghua Wen and Xia Huang</b> A Simple Method to Identify the Dominant Fouling Mechanisms during Membrane Filtration Based on Piecewise Multiple Linear Regression Reprinted from: <i>Membranes</i> <b>2020</b> , <i>10</i> , 171, doi:10.3390/membranes10080171 . . . . .	<b>309</b>
<b>Zongyao Zhou, Xiang Li, Digambar B. Shinde, Guan Sheng, Dongwei Lu, Peipei Li and Zhiping Lai</b> Tuning the Surface Structure of Polyamide Membranes Using Porous Carbon Nitride Nanoparticles for High-Performance Seawater Desalination Reprinted from: <i>Membranes</i> <b>2020</b> , <i>10</i> , 163, doi:10.3390/membranes10080163 . . . . .	<b>323</b>
<b>Bin Huang, Hangkun Gu, Kang Xiao, Fangshu Qu, Huarong Yu and Chunhai Wei</b> Fouling Mechanisms Analysis via Combined Fouling Models for Surface Water Ultrafiltration Process Reprinted from: <i>Membranes</i> <b>2020</b> , <i>10</i> , 149, doi:10.3390/membranes10070149 . . . . .	<b>335</b>
<b>Hongyi Han, Ruobin Dai and Zhiwei Wang</b> Fabrication of High-Performance Thin-Film Composite Nanofiltration Membrane by Dynamic Calcium-Carboxyl Intra-Bridging during Post-Treatment Reprinted from: <i>Membranes</i> <b>2020</b> , <i>10</i> , 137, doi:10.3390/membranes10070137 . . . . .	<b>347</b>
<b>Alibek Omir, Aliya Satayeva, Aigerim Chinakulova, Arailym Kamal, Jong Kim, Vassilis J. Inglezakis and Elizabeth Arkhangelsky</b> Behaviour of Aquaporin Forward Osmosis Flat Sheet Membranes during the Concentration of Calcium-Containing Liquids Reprinted from: <i>Membranes</i> <b>2020</b> , <i>10</i> , 108, doi:10.3390/membranes10050108 . . . . .	<b>361</b>





# Preface to “Membranes for Water and Wastewater Treatment”

Water is a vital element for life and the environment. The vast majority of water on the Earth’s surface (96%) is saline water in the oceans, and only a small volume of water has the right qualities to be consumed as drinking water. Water pollution has been documented as a contributor to a wide range of health problems. In recent years, the water quality levels have greatly deteriorated because of rapid social and economic development and because it is used as a “dump” for a wide range of pollutants.

Many technologies have been developed to remove these pollutants. Among the different available treatments, “membrane technology” is one of the most viable alternatives, as it achieves high removal yields and has low costs. For this reason, membrane separation processes play an important role in water and wastewater treatment. Different membrane processes, including microfiltration (MF), ultrafiltration (UF), nanofiltration (NF), reverse osmosis (RO), and forward osmosis (FO), have been used to treat water and wastewater. Besides these, membrane bioreactors (MBRs) have great potential for the treatment of municipal and industrial wastewater. In the last decade, new materials and fabrication processes have been developed to improve the performance of membrane synthesis and membrane-modification processes.

This Special Issue aims to cover recent developments and advances in all aspects of membrane and wastewater treatment, including membrane processes, combined processes (including one membrane step), modified membranes, new materials, and new technologies to reduce fouling and to improve the efficiency of enhanced processes.

This book aims to reach researchers and students in the membranes field who are interested in recent studies about membranes for water and wastewater treatment.

The authors acknowledge Mr. Ian Tu as the assistant editor in the first step of this Special Issue and Mrs. Jasmine Xu, who has invested a lot of time and effort into the development of this project.

**Asuncion Maria Hidalgo, Maria Dolores Murcia**  
*Editors*



# Membranes for Water and Wastewater Treatment

 Asunción María Hidalgo \* and María Dolores Murcia \*

Departamento de Ingeniería Química, Facultad de Química, Univesidad de Murcia, 30100 Murcia, Spain

\* Correspondence: ahidalgo@um.es (A.M.H.); md.murcia@um.es (M.D.M.)

Water is a vital element for life and the environment. Water pollution has been documented as a contributor to a wide range of health problems. In recent years, water quality levels have suffered a great deterioration because of rapid social and economic development and because it is used to “dump” a wide range of pollutants.

This Special Issue entitled “Membranes for Water and Wastewater Treatment” contains featured research papers dealing with recent developments and advances on all the aspects related to membrane for water and wastewater treatment: membrane processes, combined processes (including one membrane step), modified membranes, new materials, and the possibility to reduce fouling and improve the efficiency of enhanced processes.

The papers compiled in this Special Issue can be read as a response to the current needs and challenges in membrane development for water and wastewater treatment (Table 1). A total of 23 articles have been accepted; in total, 22 of them correspond to research articles in different fields, and one is a review paper.

**Table 1.** Summary of the detailed information of the publications in this Special Issue.

Numbers and Type of Articles	Fields	Industrial Process	Type of Membrane Process	Model	References
Review (1)	Diffusion dialysis	Acidic waste solution	Anion Exchange	-	[1]
		Antibiotics	NF	-	[2]
		Mine	NF	-	[3]
		Nitrate salts and heavy metals	NF	Donnan–Steric partitioning model	[4]
		Dyes	NF	Spiegler–Kedem–Katchalsky	[5]
		Steel	RO	Solution–Diffusion	[6]
		Olive mill	MF +RO	-	[7]
		Recycler paper and cardboard	UF	-	[8]
		Municipal wastewater	AnMBR	-	[9]
		Sewage	AnMBR	-	[10]



**Citation:** Hidalgo, A.M.; Murcia, M.D. Membranes for Water and Wastewater Treatment. *Membranes* **2021**, *11*, 295. <https://doi.org/10.3390/membranes11040295>

Received: 29 March 2021

Accepted: 9 April 2021

Published: 19 April 2021

**Publisher’s Note:** MDPI stays neutral with regard to jurisdictional claims in published maps and institutional affiliations.



**Copyright:** © 2021 by the authors. Licensee MDPI, Basel, Switzerland. This article is an open access article distributed under the terms and conditions of the Creative Commons Attribution (CC BY) license (<https://creativecommons.org/licenses/by/4.0/>).

**Table 1.** *Cont.*

Numbers and Type of Articles	Fields	Industrial Process	Type of Membrane Process	Model	References
			MF + UF	Semiempirical Multiple Linear Regression	[11]
		Surface water	UF	Combined models	[12]
		Aquaporin	FO	-	[13]
		Dopamine	UF	-	[14]
	Fouling	Ca <sup>2+</sup>	NF/RO	-	[15]
		Chitosan+alkali		-	[16]
		Chlorination pretreatment	UF	-	[17]
		Chitosan	FO	-	[18]
		Nanoparticles	RO	-	[19]
	Resins		Ion Exchange	-	[20,21]
	Liquid membrane		Liquid Membrane	-	[22]
	Economic study	WWT plant	UF	-	[23]

Half of the research articles correspond to concrete and practical applications of the use of membrane processes in different fields of the industry, with the aim of treating and conditioning water and wastewater. The studies reveal the treatment of industrial streams, mining, recycled paper industry, olive mill, urban wastewater, etc. Another important percentage of studies are related to the membrane modification processes with the aim of obtaining new materials with better performance in the separation processes, thus describing the use of membranes modified with chitosan, nanoparticles, and other organic compounds. This field also includes studies related to fouling and its modeling. Another field that is opening corresponds to the membranes of ion exchange resins and liquid membranes, and finally, the importance of the economic study to be able to predict the change of the membranes is also very interesting.

The revision paper carried out by Zhang et al. [1] about diffusion dialysis for acyl recovery from acidic waste solutions showed three important problems and directions for further improvements in anion exchange membranes (AEMs). The chemicals with high stability and alkalinity can be used as modifiers to prepare AEMs with improved acid recovery and stability. The materials with a size-sieving effect could be introduced into AEMs to enhance acid selectivity. Finally, the acidic functional groups, such as –COOH and –HSO<sub>3</sub>, have an excellent effect on the acid recovery of AEMs and could even overcome trade-off effects.

About 50% of the published works related to the applications in the field of the industry use nanofiltration membranes in the processes of separation and treatment of wastewater. Cristóvão et al. [2] tested the occurrence of the broad-spectrum fluoroquinolone antibiotics ciprofloxacin and levofloxacin in real wastewater effluents using a nanofiltration pilot-scale unit installed in the same sampling site of the WWTP. The results of a 24 h assay conducted at a constant pressure of 6 bar showed that the permeance was maintained and that a high removal of antibiotics, antibiotic resistance genes, and viral genomes can be expected with this treatment process.

In the treatment of mine water, one of the main problems is the risk of crystallization of sparingly soluble salts on the membrane surface (scaling). Mitko et al. [3] studied a series of batch-mode nanofiltration experiments of the mine waters performed in a dead-end Sterlitech® HP 4750X Stirred Cell. Based on the laboratory results, the concentration profiles of individual ions along the membrane length in a single-pass, industrial-scale nanofiltration (NF) unit was calculated, assuming the tanks-in-series flow model inside the membrane module. The dead-end experiments showed that the nanofiltration process may be safely operated even at 80% recovery of permeate.

The experiments carried by Marecka-Migacz et al. [4] using nanofiltration processes in the separation of aqueous solutions containing nitric salts of Zn, Cu, Fe, or Pb at various pH showed that it is possible to obtain the total volume membrane charge densities through mathematical modeling based on the Donnan–Steric partitioning model.

Hidalgo et al. [5] evaluated the performance of polyamide nanofiltration membrane on the removal of six different dyes. It has been proven that the chemical structure of the dyes has an important influence on the permeate fluxes and rejection coefficients obtained, these being the molecular volume and the length perpendicular to the maximum area the most relevant parameters.

The feasibility of reverse osmosis (RO) for treating coking wastewaters from a steel manufacturing plant, rich in ammonium thiocyanate was assessed by Álvarez et al. [6]. DOW FILMTECTM SW30 membrane performance with synthetic and real thiocyanate-containing solutions was established at the laboratory and (onsite) pilot plant scale. No short-term fouling was observed, and the data followed the known solution–diffusion model and the film theory.

Bottino et al. [7] used the integrated pressure-driven membrane processes for the treatment of olive mill wastewater (OMW). They consist of a first stage (microfiltration, MF) in which a porous multichannel ceramic membrane retains suspended materials and produces a clarified permeate for a second stage (reverse osmosis (RO)) in order to separate (and concentrate) dissolved substances from water, thus allowing the concentration of valuable products and produce water with low salinity, chemical oxygen demand (COD), and phytotoxicity.

Sousa et al. [8] investigated the optimization of the ultrafiltration (UF) process to remove colloidal substances from a paper mill's treated effluent. The effects of four operating parameters in a UF system (transmembrane pressure (TMP), cross-flow velocity (CFV), temperature and molecular weight cutoff (MWCO)) on the average permeate flux ( $J_v$ ), organic matter chemical oxygen demand (COD) rejection rate, and the cumulative flux decline (SFD) was investigated by robust experimental design using the Taguchi method. The results demonstrate the validity of the approach of using the Taguchi method and utility concept to obtain the optimal membrane conditions for the wastewater treatment using a reduced number of experiments.

Membrane bioreactors (MBRs) have a great potential for the treatment of municipal and industrial wastewater. The papers published in this Special Issue showed the relevance of the characterization of the activated sludge and the study of the fouling phenomena. Ding et al. [9] found that the membrane fouling rate of the anaerobic membrane bioreactor (AnMBR) at 25 °C was more severe than that at 35 °C. The membrane fouling trends were not consistent with the change in the concentration of soluble microbial product (SMP). On the other hand, Tabraiz et al. [10] investigated the status of acyl-homoserine lactone (AHL) in the sludge and biofilm of conventional AnMBR and the upflow anaerobic membrane bioreactor (UAnMBR), as well as in the sludge of a UASB reactor, all treating real sewage. Specifically, the work focuses on the relationship between the microbial community profile and the AHL detected in these membrane/sludge-based anaerobic systems, especially when they operate under extreme conditions (i.e., low temperatures). According to the authors, the molecules C10-HSL, C4-HSL, 3-oxo-C4-HSL, and C8-HSL are the main AHL present in anaerobic reactors (with or without membranes); these molecules require special

attention in future work to further understand their role in biofilm formation/fouling and granulation.

In addition, other studies carried out show the need to model fouling phenomena and determine the mechanisms that influence these processes. Xu et al. [11] propose a semi-empirical multiple linear regression model to describe flux decline, incorporating the five fouling mechanisms (the first and second kinds of standard blocking, complete blocking, intermediate blocking, and cake filtration) based on the additivity of the permeate volume contributed by different coexisting mechanisms. On the other hand, Huang et al. [12] investigated the membrane fouling mechanism based on that combined models could provide theoretical supports to prevent and control UF fouling for surface water treatment.

The scaling and performance of flat sheet aquaporin FO membranes in the presence of calcium salts were examined by Omir et al. [13]. These authors found that the amount of sodium chloride (NaCl), saturation index, cross-flow velocity, and flow regime all play an important role in the scaling of aquaporin FO flat sheet membranes.

In the last decade, new materials and fabrication processes have been developed to improve performance in membrane synthesis and membrane-modification processes. The study conducted by Proner et al. [14] about modifying commercial ultrafiltration membranes to induce antifouling characteristics shows the relevance of investigating parameters such as the influence of membrane pore size and the polymer concentration used in modifying the solution. Other works show that it is possible to modify a thin-film composite nanofiltration membrane using a novel and facile method based on introducing  $\text{Ca}^{2+}$  in the heat posttreatment. Hand et al. investigated the introduction of  $\text{Ca}^{2+}$  induced in situ  $\text{Ca}^{2+}$ -carboxyl intra-bridging, leading to the embedment of  $\text{Ca}^{2+}$  in the polyamide (PA) layer [15].

Zhou et al. [16] reported the use of a porous carbon nitride ( $\text{C}_3\text{N}_4$ ) nanoparticle to potentially improve both the water flux and salt rejection of the state-of-the-art polyamide (PA) thin-film composite (TFC) membranes. Benefitting from the positive effects of  $\text{C}_3\text{N}_4$ , a more hydrophilic, more crumpled thin-film nanocomposite (TFN) membrane with a larger surface area and an increased cross-linking degree of PA layer was achieved.

Nady et al. [17] compared the efficiency of a conventional chlorination pretreatment with a novel modified low-fouling polyethersulfone (PES) ultrafiltration (UF) membrane in terms of bacteria attachment and membrane biofouling reduction. The results showed that the filtration of pretreated, inoculated seawater using the modified PES UF membrane without the prechlorination step maintained the highest initial flux ( $3.27 \pm 0.13 \text{ m}^3 \cdot \text{m}^{-2} \cdot \text{h}^{-1}$ ) in the membrane, as well as having one and a half times higher water productivity than the unmodified membrane.

The use of chitosan as a cross-linked agent to obtain new membranes has been reported in this Special Issue. Saiful et al. [18] developed a forward osmosis (FO) membrane from a mixture of chitosan and *Dioscorea hispida* starch, which was cross-linked using glutaraldehyde. The cross-linked chitosan/starch membrane was revealed to have high mechanical properties with an asymmetric structure. On the other hand, Nakayama et al. [19] prepared chitosan membranes by the casting method combined with alkali treatment. The molecular weight of chitosan and the alkali treatment influenced the water content and water permeability of the chitosan membranes. The water content increased as the NaOH concentration was increased from 1 to 5 mol/L. The water permeation flux of chitosan membranes with three different molecular weights increased linearly with the operating pressure and was highest for the membrane formed from chitosan with the lowest molecular weight. Membranes with a lower water content had a higher water flux.

Among the advances in membrane preparation and modification, exchange ionic resins and liquid membranes have obtained special attention. Volkov et al. [20] investigated the cation-exchange membranes based on cross-linked sulfonated polystyrene (PS) grafted on polyethylene with an ion-exchange capacity of 2.5 mg-eq/g, while Erol et al. [21] reported the performance comparison of four commonly used cation exchange resins (Amberlite IR120  $\text{Na}^+$ , Amberlite IRP 69, Dowex MAC 3  $\text{H}^+$ , and Amberlite CG 50) and

their influence on the current efficiency and selectivity for the removal of cations from a highly concentrated salt stream. The current efficiencies were high for all the resin types studied. Results also revealed that weak cation exchange resins favor the transport of the monovalent ion ( $\text{Na}^+$ ), while strong cation exchange resins either had no strong preference or preferred to transport the divalent ions ( $\text{Ca}^{2+}$  and  $\text{Mg}^{2+}$ ).

León et al. [22] studied the pertraction of Co(II) through novel supported liquid membranes prepared by ultrasound, using bis-2-ethylhexyl phosphoric acid as the carrier, sulfuric acid as stripping agent, and a counter-transport mechanism.

Finally, the economic study is very important to evaluate the effectiveness of applied processes. Bai et al. [23] studied the economic performance of the renovation via the net present value (NPV) method. The result reveals that the NPV of the renovation of the WWTP within the 20-year life cycle is CNY 72.51 million, and the overall investment cost can be recovered within the fourth year after the reoperation of the plant.

**Funding:** This research received no external funding.

**Conflicts of Interest:** The authors declare no conflict of interest.

## References

- Zhang, C.; Zhang, W.; Wang, Y. Diffusion dialysis for acid recovery from acidic waste solutions: Anion exchange membranes and technology integration. *Membranes* **2020**, *10*, 169. [[CrossRef](#)]
- Cristóvão, M.B.; Tela, S.; Silva, A.F.; Oliveira, M.; Bento-Silva, A.; Bronze, M.R.; Crespo, M.T.B.; Crespo, J.G.; Nunes, M.; Pereira, V.J. Occurrence of antibiotics, antibiotic resistance genes and viral genomes in wastewater effluents and their treatment by a pilot scale nanofiltration unit. *Membranes* **2021**, *11*, 9. [[CrossRef](#)]
- Mitko, K.; Laskowska, E.; Turek, M.; Dydo, P.; Piotrowski, K. Scaling risk assessment in nanofiltration of mine waters. *Membranes* **2020**, *10*, 288. [[CrossRef](#)]
- Marecka-Migacz, A.; Mitkowski, P.T.; Nędzarek, A.; Rózański, J.; Szaferki, W. Effect of pH on total volume membrane charge density in the nanofiltration of aqueous solutions of nitrate salts of heavy metals. *Membranes* **2020**, *10*, 235. [[CrossRef](#)]
- Hidalgo, A.M.; León, G.; Gómez, M.; Murcia, M.D.; Gómez, E.; Macario, J.A. Removal of different dye solutions: A comparison study using a polyamide NF membrane. *Membranes* **2020**, *10*, 408. [[CrossRef](#)]
- Álvarez, J.R.; Antón, F.E.; Álvarez-García, S.; Luque, S. Treatment of aqueous effluents from steel manufacturing with high thiocyanate concentration by reverse osmosis. *Membranes* **2020**, *10*, 437. [[CrossRef](#)]
- Bottino, A.; Capannelli, G.; Comite, A.; Costa, C.; Firpo, R.; Jezowska, A.; Pagliero, M. Treatment of olive mill wastewater through integrated pressure-driven membrane processes. *Membranes* **2020**, *10*, 334. [[CrossRef](#)] [[PubMed](#)]
- Sousa, M.R.S.; Lora-García, J.; López-Pérez, M.-F.; Santafé-Moros, A.; Gozávez-Zafrilla, J.M. Operating conditions optimization via the taguchi method to remove colloidal substances from recycled paper and cardboard production wastewater. *Membranes* **2020**, *10*, 170. [[CrossRef](#)] [[PubMed](#)]
- Ding, Y.; Guo, Z.; Liang, Z.; Hou, X.; Li, Z.; Mu, D.; Ge, C.; Zhang, C.; Jin, C. Long-term investigation into the membrane fouling behavior in anaerobic membrane bioreactors for municipal wastewater treatment operated at two different temperatures. *Membranes* **2020**, *10*, 231. [[CrossRef](#)] [[PubMed](#)]
- Tabraiz, S.; Shamurad, B.; Petropoulos, E.; Charlton, A.; Mohiudin, O.; Danish Khan, M.; Ekwenna, E.; Sallis, P. Diversity of acyl homoserine lactone molecules in anaerobic membrane bioreactors treating sewage at psychrophilic temperatures. *Membranes* **2020**, *10*, 320. [[CrossRef](#)] [[PubMed](#)]
- Xu, H.; Xiao, K.; Yu, J.; Huang, B.; Wang, X.; Liang, S.; Wei, C.; Wen, X.; Huang, X. A simple method to identify the dominant fouling mechanisms during membrane filtration based on piecewise multiple linear regression. *Membranes* **2020**, *10*, 171. [[CrossRef](#)] [[PubMed](#)]
- Huang, B.; Gu, H.; Xiao, K.; Qu, F.; Yu, H.; Wei, C. Fouling mechanisms analysis via combined fouling models for surface water ultrafiltration process. *Membranes* **2020**, *10*, 149. [[CrossRef](#)]
- Omir, A.; Satayeva, A.; Chinakulova, A.; Kamal, A.; Kim, J.; Inglezakis, V.J.; Arkhangelsky, E. Behaviour of aquaporin forward osmosis flat sheet membranes during the concentration of calcium-containing liquids. *Membranes* **2020**, *10*, 108. [[CrossRef](#)]
- Proner, M.C.; Ramalho Marques, I.; Ambrosi, A.; Rezzadori, K.; da Costa, C.; Zin, G.; Tres, M.V.; Di Luccio, M. Impact of MWCO and dopamine/polyethyleneimine concentrations on surface properties and filtration performance of modified membranes. *Membranes* **2020**, *10*, 239. [[CrossRef](#)]
- Han, H.; Dai, R.; Wang, Z. Fabrication of high-performance thin-film composite nanofiltration membrane by dynamic calcium-carboxyl intra-bridging during post-treatment. *Membranes* **2020**, *10*, 137. [[CrossRef](#)]
- Zhou, Z.; Li, X.; Shinde, D.B.; Sheng, G.; Lu, D.; Li, P.; Lai, Z. Tuning the surface structure of polyamide membranes using porous carbon nitride nanoparticles for high-performance seawater Desalination. *Membranes* **2020**, *10*, 163. [[CrossRef](#)]



17. Nady, N.; Salem, N.; Amer, R.; El-Shazly, A.; Kandil, S.H.; Hassouna, M.S.E.-D. Comparison between a conventional anti-biofouling compound and a novel modified low-fouling polyethersulfone ultrafiltration membrane: Bacterial anti-attachment, water quality and productivity. *Membranes* **2020**, *10*, 227. [[CrossRef](#)]
18. Saiful, S.; Ajrina, M.; Wibisono, Y.; Marlina, M. Development of chitosan/starch-based forward osmosis water filtration bags for emergency water supply. *Membranes* **2020**, *10*, 414. [[CrossRef](#)]
19. Nakayama, R.-i.; Katsumata, K.; Niwa, Y.; Namiki, N. Dependence of water-permeable chitosan membranes on chitosan molecular weight and alkali treatment. *Membranes* **2020**, *10*, 351. [[CrossRef](#)] [[PubMed](#)]
20. Volkov, V.I.; Chernyak, A.V.; Golubenko, D.V.; Tverskoy, V.A.; Lochin, G.A.; Odjigaeva, E.S.; Yaroslavtsev, A.B. Hydration and diffusion of H<sup>+</sup>, Li<sup>+</sup>, Na<sup>+</sup>, Cs<sup>+</sup> ions in cation-exchange membranes based on polyethylene- and sulfonated-grafted polystyrene studied by NMR technique and Ionic conductivity Measurements. *Membranes* **2020**, *10*, 272. [[CrossRef](#)] [[PubMed](#)]
21. Ulusoy Erol, H.B.; Hestekin, C.N.; Hestekin, J.A. Effects of resin chemistries on the selective removal of industrially relevant metal ions using wafer-enhanced electrodeionization. *Membranes* **2021**, *11*, 45. [[CrossRef](#)] [[PubMed](#)]
22. León, G.; Hidalgo, A.M.; Miguel, B.; Guzmán, M.A. Pertraction of Co(II) through novel ultrasound prepared supported liquid membranes containing D2EHFA. Optimization and transport parameters. *Membranes* **2020**, *10*, 436. [[CrossRef](#)] [[PubMed](#)]
23. Bai, H.; Lin, Y.; Qu, H.; Zhang, J.; Zheng, X.; Tang, Y. Technical and economic evaluation of WWTP renovation based on applying ultrafiltration membrane. *Membranes* **2020**, *10*, 180. [[CrossRef](#)] [[PubMed](#)]

Article

# Effects of Resin Chemistries on the Selective Removal of Industrially Relevant Metal Ions Using Wafer-Enhanced Electrodeionization

Humeyra B. Ulusoy Erol , Christa N. Hestekin and Jamie A. Hestekin \*

Ralph E. Martin Department of Chemical Engineering, University of Arkansas, Fayetteville, AR 72701, USA; hbulusoy@uark.edu (H.B.U.E.); chesteki@uark.edu (C.N.H.)

\* Correspondence: jhesteki@uark.edu; Tel.: +1-479-575-3492

**Abstract:** Wafer-enhanced electrodeionization (WE-EDI) is an electrically driven separations technology that occurs under the influence of an applied electric field and heavily depends on ion exchange resin chemistry. Unlike filtration processes, WE-EDI can be used to selectively remove ions even from high concentration systems. Because every excess ion transported increases the operating costs, the selective separation offered by WE-EDI can provide a more energy-efficient and cost-effective process, especially for highly concentrated salt solutions. This work reports the performance comparison of four commonly used cation exchange resins (Amberlite IR120 Na<sup>+</sup>, Amberlite IRP 69, Dowex MAC 3 H<sup>+</sup>, and Amberlite CG 50) and their influence on the current efficiency and selectivity for the removal of cations from a highly concentrated salt stream. The current efficiencies were high for all the resin types studied. Results also revealed that weak cation exchange resins favor the transport of the monovalent ion (Na<sup>+</sup>) while strong cation exchange resins either had no strong preference or preferred to transport the divalent ions (Ca<sup>2+</sup> and Mg<sup>2+</sup>). Moreover, the strong cation exchange resins in powder form generally performed better in wafers than those in the bead form for the selective removal of divalent ions (selectivity > 1). To further understand the impact of particle size, resins in the bead form were ground into a powder. After grinding the strong cation resins displayed similar behavior (more consistent current efficiency and preference for transporting divalent ions) to the strong cation resins in powder form. This indicates the importance of resin size in the performance of wafers.

**Keywords:** selective separation; ion-exchange resin; wafer-enhanced electrodeionization; desalination



**Citation:** Ulusoy Erol, H.B.; Hestekin, C.N.; Hestekin, J.A. Effects of Resin Chemistries on the Selective Removal of Industrially Relevant Metal Ions Using Wafer-Enhanced Electrodeionization. *Membranes* **2021**, *11*, 45. <https://doi.org/10.3390/membranes11010045>

Received: 28 November 2020

Accepted: 7 January 2021

Published: 9 January 2021

**Publisher's Note:** MDPI stays neutral with regard to jurisdictional claims in published maps and institutional affiliations.



**Copyright:** © 2021 by the authors. Licensee MDPI, Basel, Switzerland. This article is an open access article distributed under the terms and conditions of the Creative Commons Attribution (CC BY) license (<https://creativecommons.org/licenses/by/4.0/>).

## 1. Introduction

The increase in population and industrial development has triggered physical and economic water scarcity. For instance, in various industries such as the semiconductor, pharmaceutical, power, and hydraulic fracturing industries, an average facility can use 2 to 4 million gallons of water per day [1]. Specifically, the consumption of large volumes of fresh water and the generation of highly contaminated wastewater has drawn negative attention from both the public and environmental groups. Besides this attention, excessive freshwater use can create hardships for industries, households, farmers, and wildlife [2]. Hydraulic fracturing, commonly known as fracking, is used to release natural gas and oil and also uses large amounts of water in its production [3,4]. Produced wastewater contains a high concentration of dissolved solids which often exceeds 50,000 parts per million (ppm) and is about 2–6 times higher than seawater concentration [5]. The fracking wastewater contains divalent cations (such as calcium and magnesium) and monovalent ions (such as sodium and potassium) as well as other anions, chemicals, and bacteria [6].

Due to the high concentration of dissolved solids, fracking wastewater can threaten the environment and alter the health of agriculture, aquatic life, and humans. Considering

the health threats, fracking water cannot be discharged into freshwater streams or treated at municipal wastewater treatment plants. Currently, there are several ways to dispose of fracking wastewater with the cost ranging from \$1 to \$10 per barrel [7]. In addition, logistics and water hauling can increase the water management costs when the disposal outlet is not nearby, and it may increase the cost of disposal to \$94 per barrel per hour of transport [7].

Hence, there is a need for on-site wastewater treatment to minimize the freshwater use and damaging effects of fracking wastewater. If the wastewater can be reused or reduced, then the expenses from transportation and disposal can be decreased or eliminated. Membrane-based technologies have become a remedy for the removal of particulates, ionic, gaseous, and organic impurities from aqueous streams without the use of hazardous chemicals due to their reliability and cost-effectiveness. Wastewater treatment technologies using membranes appear to be the more practical and feasible strategies to overcome one of the primary issues the world faces; the shortage of freshwater supplies and degradation of water quality [8]. Membrane technologies also have essential advantages such as the simplicity of operation, high flexibility and stability [9], low energy requirements [10], high economic compatibility [11], and easy control of operations and scale-up under a broad array of operating conditions and good compatibility between different integrated membrane system operations [12].

Electrodeionization (EDI) is a hybrid technology that is based on electrodialysis (ED), which employs electrical current and semi-impermeable membranes, and ion exchange (IE) that contains ion exchange resins [13] to overcome the disadvantages of both technologies such as concentration polarization, chemical regeneration [14], and excessive power utilization at low ion concentrations [15–17]. EDI can be operated in both continuous and batch modes and does not require a separate step to regenerate resins. Furthermore, EDI can work with low concentration streams with a lower power requirement compared to ED [15,16,18].

Even though there are major advantages of EDI over ED and ion exchange processes, there are also several disadvantages of EDI. The ion exchange resins are inserted into a pair of anionic- and cationic-exchange membranes loosely. This loose resin structure complicates sealing between compartments and leads to leakage of ions from one compartment to another due to convection instead of diffusion [19,20]. Another disadvantage of loose resins in EDI systems is the uneven distribution of flow within the channels which decreases the separation efficiency [20–23]. Previous studies have found ways to eliminate leakage issues by using spiral-wound configurations [24] or the channeling problem by immobilizing the resin using magnetic fields [25]. Each method was able to eliminate only one of the disadvantages of conventional EDI. Therefore, there was a need for a new system specifically designed to overcome both disadvantages. As a result, an integrated approach, wafer-enhanced electrodeionization (WE-EDI), was proposed by Arora et al. [26].

The wafer-enhanced electrodeionization (WE-EDI) is one of the methods that enable on-site wastewater treatments and maintenance, and removal of hardness causing ions and metals [26,27]. In WE-EDI, the loose ion exchange resin structure of conventional EDI is replaced by a wafer inserted between the two membranes as the spacer. The wafer is a mixture of immobilized cation- and anion-exchange resins using a polymer as a binding agent. Compared to conventional EDI, WE-EDI can be easily built and run more efficiently, and it prevents uneven flow distribution and leakage of ions between the compartments simultaneously [28]. Because there is less leakage, WE-EDI can be used for more selective separations such as the removal of acidic impurities from corn stove hydrolysate liquor, CO<sub>2</sub> capture, and purification of organic acids [26,29].

Besides treating wastewater for the removal of impurities, there is a need for an efficient and economical process of ion-selective separation. In wastewater treatment processes, not every ion has the same priority to be removed. Depending on the application, the user may need a selective removal of an ion relative to the remaining ions in the system. Also, because every ion transported that does not need to be transported increases the operating costs, there is a need for ion selectivity to create an energy-efficient and cost-

effective process. Ion selectivity in WE-EDI processes heavily depends on ion exchange resin chemistry [23]. However, there are no studies that show the effect of commonly used resins (Amberlite IR 120 Na<sup>+</sup>, Amberlite IRP 69, Amberlite CG 50, and Dowex MAC 3 H<sup>+</sup>) on the ion selectivity and current efficiency in systems with a high salt concentration to the best of our knowledge. Amberlite IR 120 Na<sup>+</sup> and Amberlite IRP 69 are strong cation exchange resins whereas Amberlite CG 50 and Dowex MAC 3 H<sup>+</sup> are weak cation exchange resins. These resins are widely used in applications of conventional EDI and ion exchange chromatography such as metal removal [30–32], water softening [33,34], drug delivery [35], and enzyme immobilization and purification [36,37]. While these four resins have been commonly used in applications requiring ion transport at low salt concentrations, this study explores their use for selective and energy-efficient removal of ions in a highly concentrated system using wafer-enhanced electrodeionization (WE-EDI). The unique wafers used in WE-EDI enhance the effects of transport by diffusion. Therefore, the effect of resin size in resins with the same chemistry was also evaluated.

## 2. Materials and Methods

### 2.1. Chemicals

Cationic exchange resins (Amberlite IR 120 Na<sup>+</sup>, Amberlite IRP 69, Dowex MAC 3 H<sup>+</sup>, and Amberlite CG 50), anionic exchange resin (Amberlite IRA-400 Cl<sup>-</sup>), sucrose, low-density polyethylene, sodium chloride, magnesium chloride, and calcium chloride were purchased from VWR International. The technical specifications of each resin are shown in Table 1. Neosepta food-grade anionic and cationic exchange membranes (AMX and CMX, respectively) were purchased from Ameridia Innovative Solutions, Inc. (Somerset, NJ, USA)

**Table 1.** Cation exchange resins and their properties.

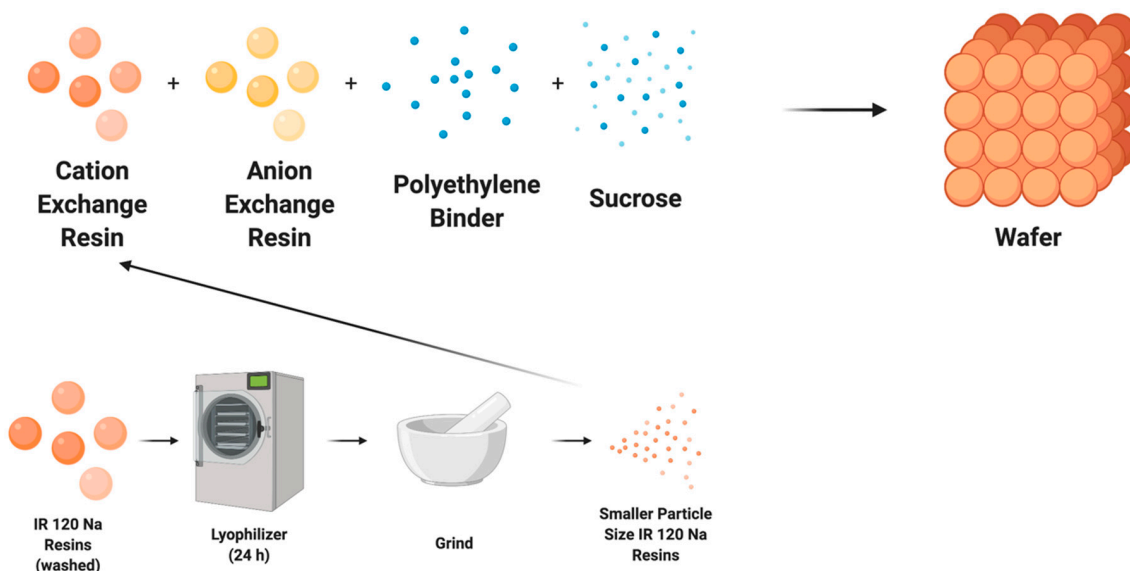
Name	Functional Group	Matrix	Particle Size (Mesh) *	Exchange Capacity (eq/L)
Amberlite IR120 Na <sup>+</sup>	Sulfonic Acid	Styrene-divinylbenzene (gel)	16–50 mesh (0.297 to 1.19 mm)	≥2.0
Amberlite IRP 69	Sulfonic Acid	Crosslinked styrene-divinylbenzene	100–200 mesh (0.074 to 0.149 mm)	5
Dowex MAC 3 H <sup>+</sup>	Carboxylic Acid	Polyacrylic-divinylbenzene (gel)	16–50 mesh (0.297 to 1.19 mm)	3.8
Amberlite CG 50	Carboxylic Acid	Methacrylic (macroporous)	100–200 mesh (0.074 to 0.149 mm)	3.5

\*: Mesh is a measurement for the particle size that is used to determine the particle size distribution of a granular material. Particle size conversion (mesh to mm) was determined from [38].

### 2.2. Wafer Composition, Fabrication, and System Setup

The wafer recipe has been previously published [23], but briefly consists of anion and cation exchange resins, polymer, and sucrose (Figure 1). The cationic exchange resins used were Amberlite IR 120 Na<sup>+</sup>, Amberlite IRP 69, Dowex MAC 3 H<sup>+</sup>, and Amberlite CG 50. The first two are strong cationic exchange resins and the latter two are weak cationic exchange resins. The anion exchange resin bead was Amberlite IRA 400 Cl<sup>-</sup>. Polyethylene (500 micron-low density) and sucrose were used to bind the resins and create porosity, respectively. The ratios of cation exchange resin, anionic resin, polymer, and sucrose in the mixture were 23:23:10:15, respectively. The mixture then was uniformly combined using a FlackTeck Inc (Landrum, SC, USA). SpeedMixer™ (model: DAC 150 SP) at a rate of 300 rpm for 5 s. The combined mixture for the wafer was cast in a steel mold and placed in a Carver press (model 3851-0) heated to 250 °F at 10,000 psi for ninety min. This process was followed by a 20-min cooling period via pressurized air treatment. The wafer was pre-soaked in deionized (DI) water for 24-h to create porosity. The thickness of the final product was 2 mm. The wafer was then cut to size to fit within the WE-EDI cell.

Membranes used in the WE-EDI system were Neosepta food-grade AMX and CMX membranes and were conditioned in the dilute (feed) solution (described in the next section) 24 h prior to the experiments. WE-EDI was performed within a Micro Flow Cell (ElectroCell North America, Inc.). The MicroFlow Cell was tightened to 25 in-lbs across all bolts to ensure even flow throughout the system and prevent leakage. The cations tested for selective separation were  $\text{Na}^+$ ,  $\text{Ca}^{2+}$ , and  $\text{Mg}^{2+}$  and the counter ion for all cations was  $\text{Cl}^-$ .



**Figure 1.** Illustration of typical wafer fabrication and particle size reduction (grinding) of ion exchange resins for wafer fabrication.

### 2.3. Size Reduction for IR 120 Na

To compare the effects of resin size on the system performance, the size of the IR 120  $\text{Na}^+$  resins was reduced (Figure 1). The IR 120  $\text{Na}^+$  resins were first washed with deionized water and then dried using a freeze dryer (Labconco FreeZone Plus 12 Liter #7960044, Kansas City, MO, USA). Dried resins were ground using a mortar and pestle and passed through sieves to get resin particles of less than 0.149 mm (100 mesh). Ground resins were then made into a wafer using the same recipe given in Section 2.2.

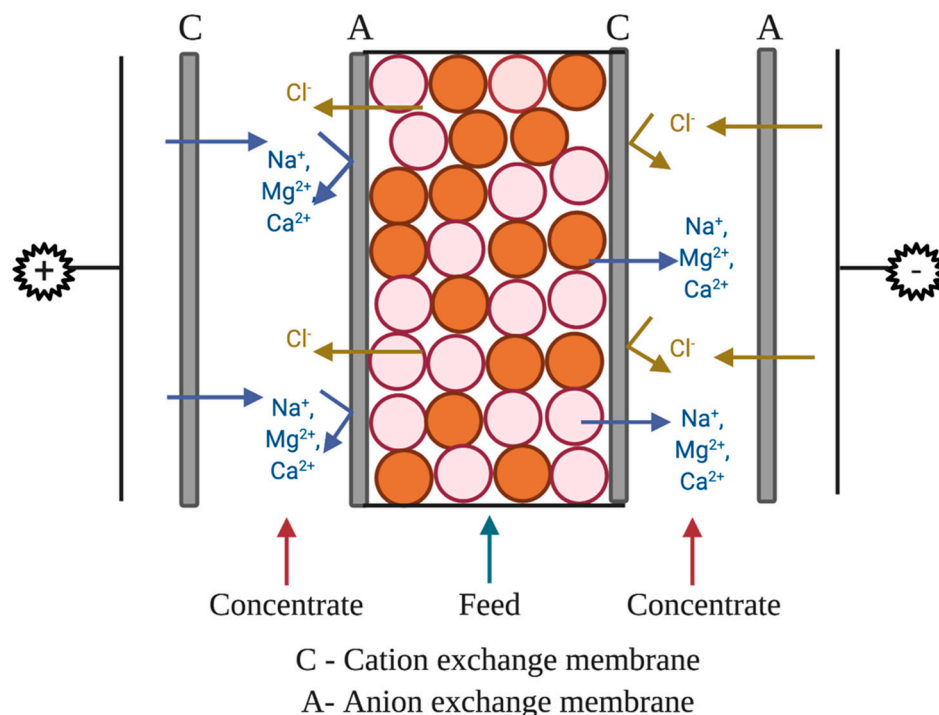
### 2.4. Particle Image Analysis

Both the original IR 120  $\text{Na}^+$  and the ground IR 120  $\text{Na}^+$  resins were examined with an optical microscope. The calibration and particle size detection were completed with ImageJ image processing tool [39].

### 2.5. WE-EDI Chamber Setup and Sample Collection

The setup (Figure 2) for ion removal used four separate solutions of equal volume. The concentrate solution was 300 mL of 2% wt (20 g/L in DI water) sodium chloride solution. The two rinse chamber solutions were 300 mL of 0.3 M (42.6 g/L in DI water) sodium sulfate ( $\text{Na}_2\text{SO}_4$ ). The feed (dilute) was 50,000 ppm sodium (126.8 g of  $\text{NaCl}$ /L in DI water), 1000 ppm of calcium (2.7 g of  $\text{CaCl}_2$ /L in DI water), and 1000 ppm of magnesium (3.9 g of  $\text{MgCl}_2$ /L in DI water). The dilute (feed) stream is the solution from which ions are being diluted (i.e., transported out of or removed).

All experiments were performed in a continuous mode with recycling. A constant current of 0.2 Amps was used for all experiments. Experiments were run for 8 h, with samples collected at the initial (0-h), 2-h, 4-h, and 8-h marks. To determine the concentration of individual ions, ion chromatography (Dionex™ ICS-6000 Standard Bore and Microbore HPIC™ Systems, Thermo Scientific, Waltham, MA, USA) was used because of its speed, precision, and sensitivity.



**Figure 2.** Illustration for wafer-enhanced electrodeionization (EDI) setup.

2.6. Statistical Analysis

Statistical differences in the data were determined using an unpaired *t*-test in GraphPad QuickCalcs (GraphPad Software Inc., San Diego, CA, USA). Values were considered to have a statistically significant difference if the *p*-value was less than 0.05.

2.7. FTIR-ATR Spectroscopy

The changes to the chemistry of the resin in the wafer were identified using Fourier Transform Infrared—Attenuated Total Reflection (FTIR-ATR) Spectroscopy (Perkin Elmer LR64912C, Waltham, MA, USA). The individual peaks were evaluated in terms of wavenumber and intensity.

3. Results and Discussion

3.1. Current Efficiency

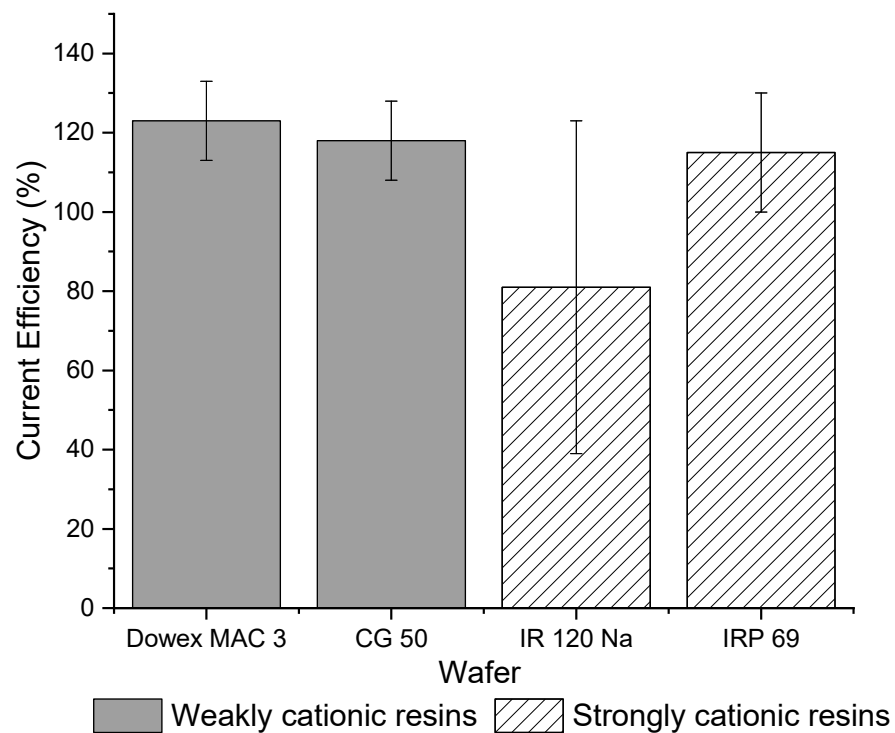
The current efficiency ( $\eta$ ) for the WE-EDI system indicates how efficiently a particular ion is being transferred across the membranes and the wafer due to the electrical field applied to the system. It is defined as:

$$\eta = \frac{zFV(C_i - C_f)}{tIM_w} \times 100\%, \tag{1}$$

where *z* is the ionic valence of the ion (2 for calcium and magnesium, and 1 for sodium), *F* is Faraday’s constant, *V* is the volume of the feed chamber, *C<sub>i</sub>* is the initial concentration of the ion in the feed chamber, *C<sub>f</sub>* is the final concentration of the ion in the feed chamber, *t* is the total operation time, *I* is the current, and *M<sub>w</sub>* is the molecular weight of the ion.

Figure 3 shows that the total current efficiency is similar between weak cation exchange and strong cation exchange wafers. The total current efficiency for each strong cation exchange resin wafer was close to 100% and for each weak cation, resin wafer was over 100%. While current efficiencies should be below 100%, other studies have previously reported efficiencies greater than 100%. Pan et al., showed that current efficiency increased in resin wafer EDI as the ion concentration in the dilute stream increased [20]. Luo and Wu [40] observed that the overall current efficiency of their system was greater than 100%

at high concentrations. Lopez and Hestekin [29] reported that high ion diffusion during the experiment coupled with ion transport due to potential gradients can cause greater than 100% current efficiency. Another reason why these current efficiencies may exceed 100% is that the concentration of the solution in the dilute chamber is higher than in the concentrate chamber and therefore the electrically driven transport is being assisted by the concentration gradient. In this study, the strong cation exchange IRP 69 resin wafer had a current efficiency that was more consistently approximately 100% whereas the IR 120 Na<sup>+</sup> wafer showed a lot of variabilities, which makes it less desirable for the selective removal of ions. In terms of the weak cation exchange resin wafers, both resin wafers showed similar average values and smaller variability in their current efficiencies.



**Figure 3.** Overall current efficiencies for strong (IR 120 Na<sup>+</sup> and IRP 69) and weak cation exchange wafers (Dowex MAC 3 H<sup>+</sup> and CG 50).

### 3.2. Selectivity

Selectivity is a measure of the removal rate of one ion compared to another. Selectivity was determined using the separation coefficient ( $\alpha$ ) and was calculated using the following equation:

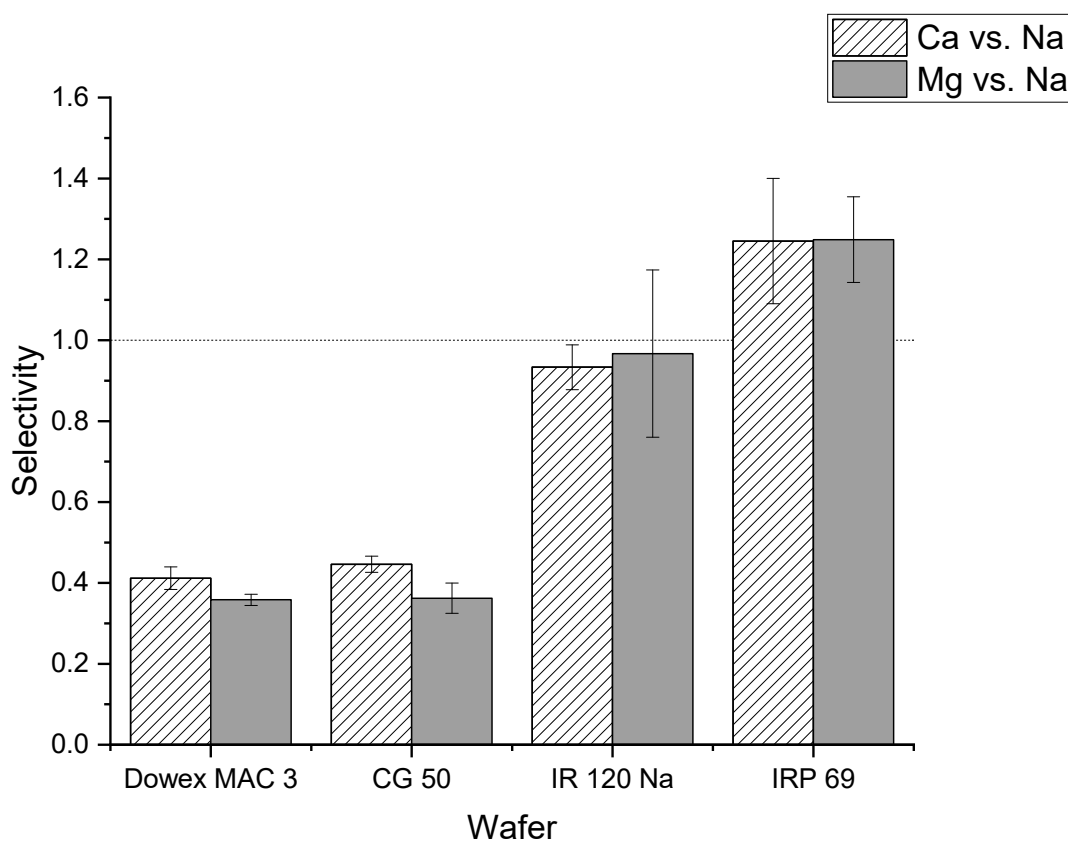
$$\alpha = \frac{(C_i^f - C_i^s) / C_i^s}{(C_j^f - C_j^s) / C_j^s}, \tag{2}$$

where  $C_i^f$  is the final concentration of ion  $i$  (calcium or magnesium ion),  $C_i^s$  is the starting concentration of ion  $i$ ,  $C_j^f$  is the final concentration of ion  $j$  (sodium ion), and  $C_j^s$  is the starting concentration of ion  $j$ . If  $\alpha$  is greater than one, it indicates the preferential transport of ion  $i$ . If  $\alpha$  is less than one, then it indicates the preferential transport of ion  $j$ .

Figure 4 shows the selectivity values for calcium and magnesium relative to sodium for strong and weak cation exchange resin wafers. The selectivity of calcium to sodium was greater than one for the IRP 69 resin wafer (strong cation exchange) which indicated that calcium ions were preferentially transported compared to sodium ions. In the IR 120 Na<sup>+</sup> resin (strong cation exchange), the selectivity for calcium relative to sodium was close to one which indicated that there was not a strong preference for the transport of sodium or calcium ions. The statistical analysis showed that there was a statistically significant

difference between IR 120 Na<sup>+</sup> and IRP 69 resins for calcium selectivity ( $p < 0.02$ ). In Dowex MAC 3 H<sup>+</sup> and CG 50 (weak cation exchange resin wafers), the selectivity values for calcium relative to sodium were less than one which indicated that both resin wafers prefer to transport sodium ions over calcium ions. Our statistical analysis showed no difference between Dowex MAC 3 H<sup>+</sup> and CG 50 resin wafers for calcium removal ( $p > 0.2$ ).

A similar situation was observed for the selectivity of magnesium relative to sodium. The IRP 69 demonstrated a selectivity greater than one, indicating that magnesium was preferentially transported over sodium. For IR 120 Na<sup>+</sup> resin, the selectivity was at or below one indicating that there was no preference for the transport of magnesium. However, statistical analysis showed that the difference between IR 120 Na<sup>+</sup> and IRP 69 resin for magnesium selectivity was not significant ( $p > 0.15$ ). In the weak cation exchange resin wafers formed from Dowex MAC 3 H<sup>+</sup> and CG 50, the selectivity values were less than one which indicated that both resin wafers preferred to transport sodium ions over magnesium ions. The statistical analysis showed no difference between Dowex MAC 3 H<sup>+</sup> and CG 50 resin wafers for magnesium removal ( $p > 0.8$ ).



**Figure 4.** Comparison of selectivity values of calcium and magnesium relative to sodium for different strong cation exchange (IR 120 Na<sup>+</sup> and IRP 69) and weak cation exchange (Dowex MAC 3 H<sup>+</sup> and CG 50) resin wafers.

It is well established that resins with sulfonic acid groups have a higher affinity for divalent ions than resins with carboxylic acid functional groups [41,42]. For the Amberlite IR 120 Na<sup>+</sup> sulfonic acid resin, it has been previously reported that the order of selectivity is Ca<sup>2+</sup> > Mg<sup>2+</sup> > Na<sup>+</sup> [41]. Weak cation exchange resins, on the other hand, have more affinity towards monovalent ions. Specifically, the carboxyl group exhibits a very high affinity towards H<sup>+</sup> which may result in its lower affinity for other ions [42]. Alternatively, the sulfonic acid group has a higher affinity for Ca<sup>2+</sup> and Mg<sup>2+</sup> and a low affinity for Na<sup>+</sup> and H<sup>+</sup> [42].

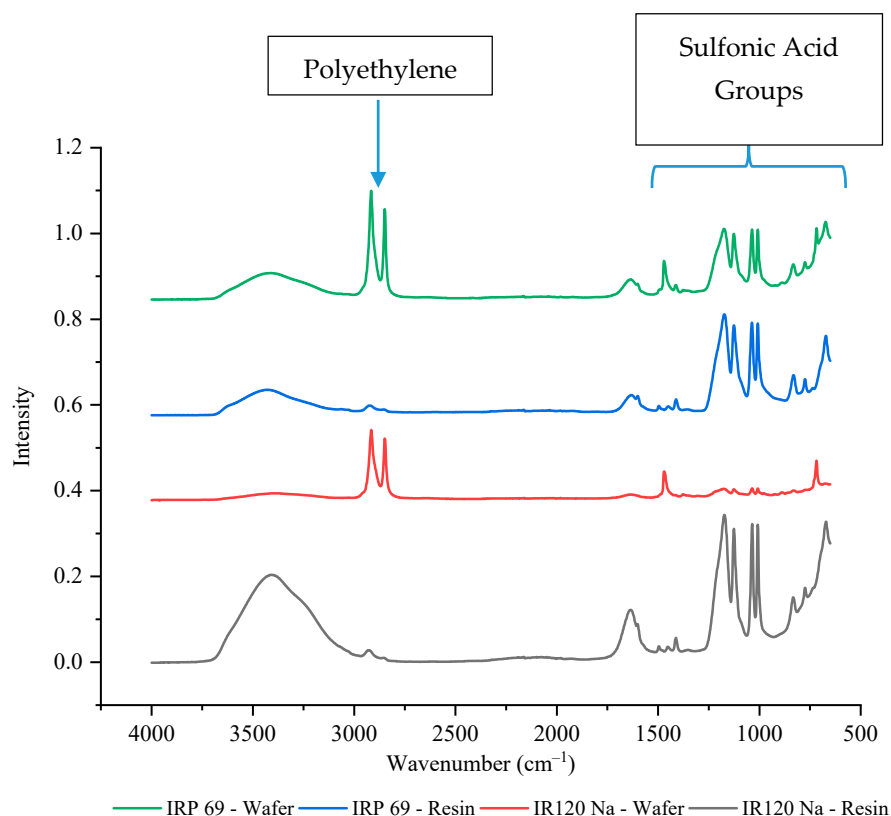
A study by Zhang and Chen used EDI to separate ions in groundwater using Amberlite resins with sulfonic acid functional groups and their data indicated that there was no



significant preference for divalent over monovalent ions [43]. However, it is important to note that they used different resins, had more types of ions present, and their system was at a much lower ion concentration. Another study using WE-EDI to remove ions from fracking water found that sulfonic acid resins (Amberlite 120 Na<sup>+</sup>) tended to have a preference for divalent cations more than carboxylic acid resins (Dowex MAC 3 H<sup>+</sup>) [44].

### 3.3. FTIR-ATR Spectroscopy Analysis

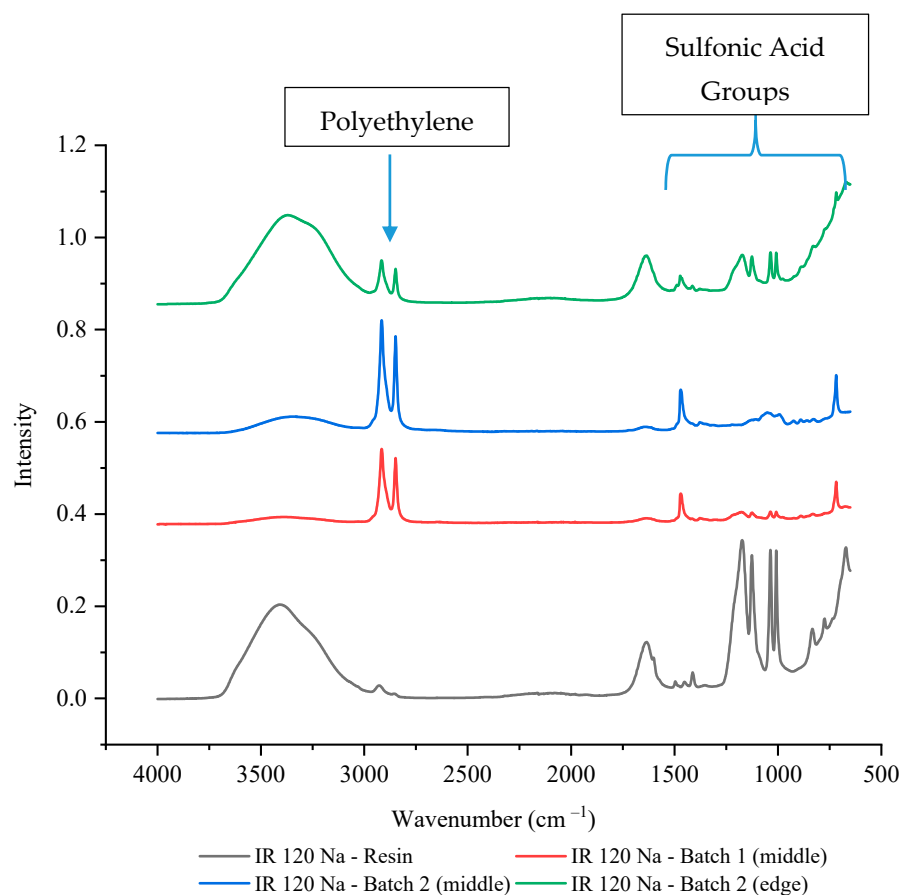
The IR 120 Na<sup>+</sup> and IRP 69 resins have the same functional group of sulfonic acid which makes the resins strong cation exchangers. Since both resins had the same functional group, it was expected that their current efficiencies and selectivity values would be similar. However, it was observed that the IRP 69 wafer had a current efficiency that was consistently around 100% whereas IR 120 Na<sup>+</sup> had a lower average value as well as a lot of variability, which made it less desirable for the selective removal of ions. Since these resins have the same chemistry, perhaps the difference in their performance was due to a variation in the accessibility of the active site. To better understand their differences, FTIR-ATR was performed. As shown in Figure 5, four peaks were observed between 1000 cm<sup>-1</sup> and 1200 cm<sup>-1</sup> that correspond to sulfonic acid functional groups. The peaks between 1030 to 1200 cm<sup>-1</sup> have been previously reported to correspond to the symmetric and asymmetric stretching vibration of the  $-SO_3^-$  group of sulfonic acid [45]. The peaks at ~1000 cm<sup>-1</sup> have been typically associated with an S-O stretch. While these groups were clearly present in IRP 69 wafer, their intensity was much lower in IR 120 Na<sup>+</sup> wafer which indicated a significant decrease of the sulfur content and exposure of  $-SO_3^-$  groups. Specifically, in the IR 120 Na<sup>+</sup> wafer, the intensity of the sulfonic acid peaks was around 10% of the resin's value while for IRP 69 wafer the peaks were 65–70% of the resin's value (exact values are provided in Supplementary Table S1). This could indicate that polyethylene is covering the IR 120 Na<sup>+</sup> resin's larger bead form and thereby decreasing the availability of the sulfonic acid functional groups. This may explain the high variability seen in the current efficiency and selectivity of the IR 120 Na<sup>+</sup> wafer.



**Figure 5.** The FTIR-ATR spectrum of strong cation exchange resins and wafers including these resins.

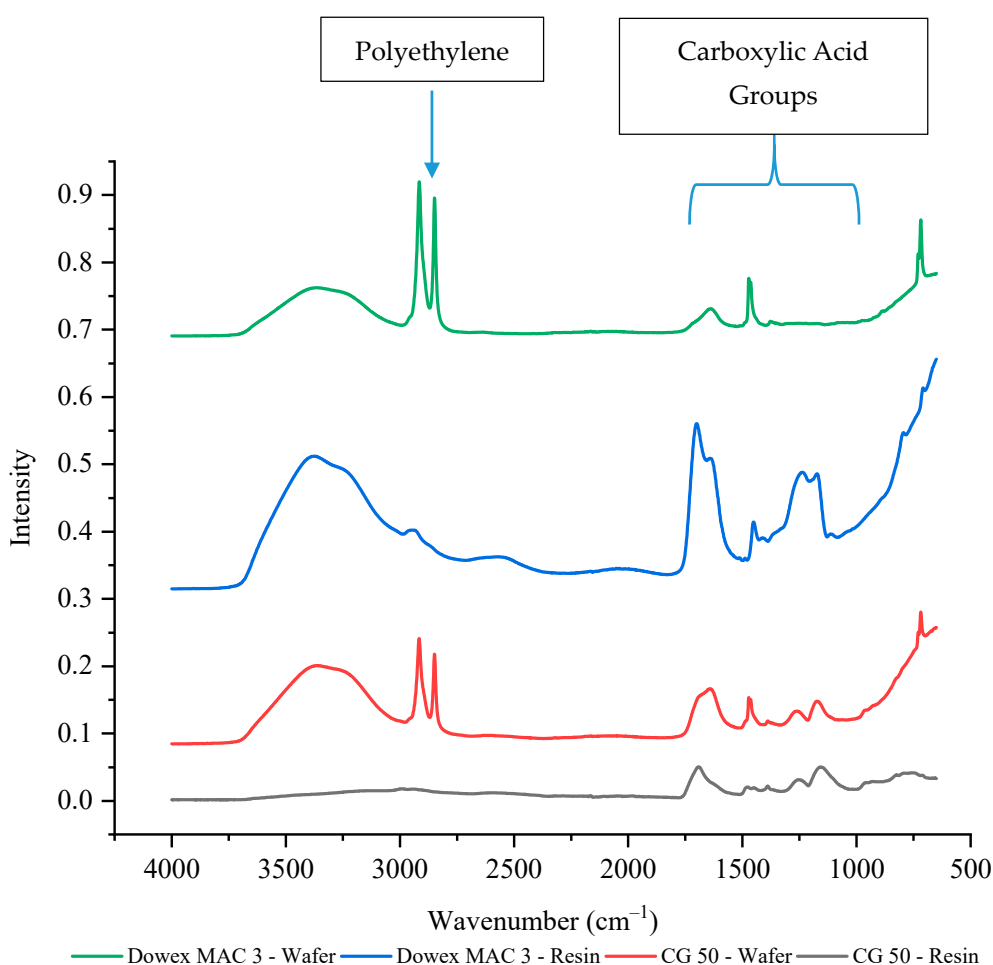
To verify that this was not the result of a single batch issue or due to analysis placement, another batch of IR 120 Na<sup>+</sup> wafer was made and multiple locations were tested using FTIR-ATR. Figure 6 shows that the second batch of IR 120 Na<sup>+</sup> wafer also had lower intensities of sulfonic acid functional groups compared to the IR 120 Na<sup>+</sup> resin, especially in the middle of the wafer (~10% of the resin's value). While the edge of the wafer showed decreased intensity of the sulfonic acid functional groups compared to the resin, it was higher than the middle of the wafer with a value that was between 30–35% of the resin's value (see Supplementary Table S1 for exact values). This could be due to the resin bead being more exposed at the edge of the wafer than it can be in the middle of the wafer. This finding supports the theory that the availability of the sulfonic acid functional groups of IR 120 Na<sup>+</sup> have decreased availability possibility due to being covered by the polyethylene binding polymer.

A recent study by Palakkal et al. using SEM observed that polyethylene was partially covering their cation exchange resin (Purolite PFC100E) which had sulfonic acid functional groups and was a similar size to the Amberlite IR 120 Na<sup>+</sup> resins at around 0.3 to 0.5 mm [28]. When they used an ionomer binder rather than polyethylene, they observed significantly less coverage of their cation exchange resin. Another possible reason for the difference between the intensity of the sulfonic acid functional groups between the resin and wafer could be due to thermal degradation during the wafer making process. However, a study by Singare et al. showed that during FTIR analysis the sulfonic acid group peaks for Amberlite 120 were present at a significant intensity up to 200 °C (392 °F) while they disappear at around 400 °C (752 °F) [46]. This is well above the wafer making temperature of 250 °F, which further supports the idea that the reduction is due to interactions with the binding polymer.



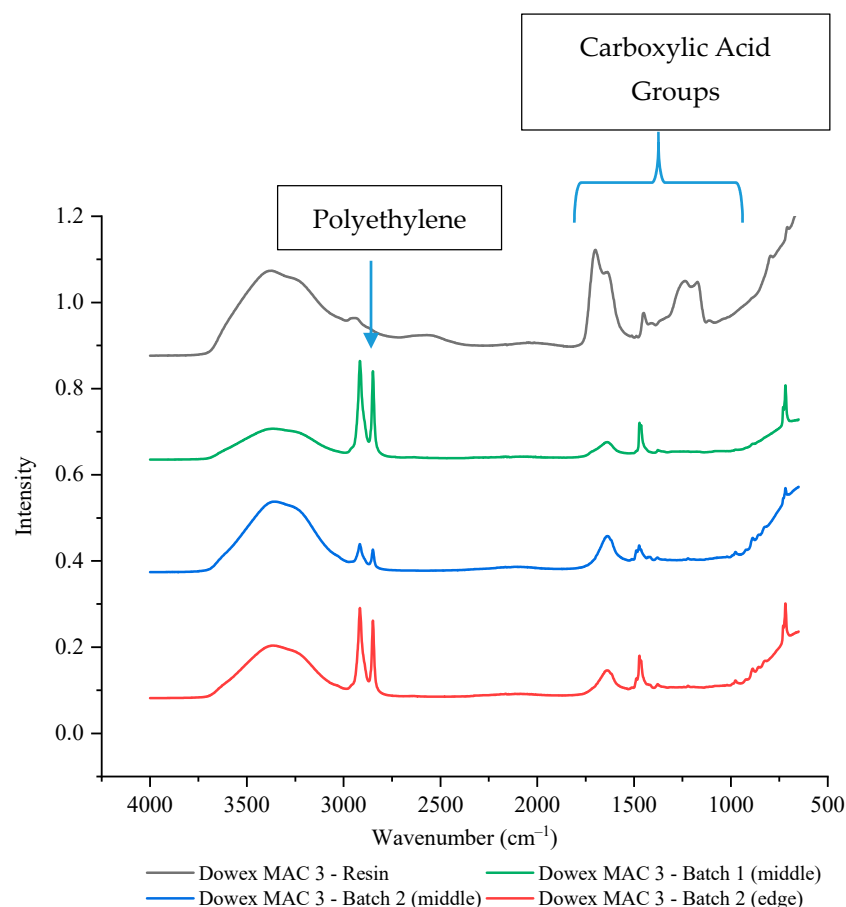
**Figure 6.** The FTIR-ATR spectrum of IR 120 Na<sup>+</sup> resin alone and in two different wafers.

The weak cation exchange resins both have carboxylic acid functional groups which should have a peak between  $1760$  to  $1690\text{ cm}^{-1}$  for the C=O stretch and a peak between  $1320$  to  $1210\text{ cm}^{-1}$  for the C–O stretch [47]. Unlike the strong cation exchange resin wafers, the current efficiencies and selectivity values were similar between the two weak cation exchange resin wafers. However, the size of the cation exchange resins was also different between the Dowex MAC 3 H<sup>+</sup> (bead form) and the CG 50 (powder form). As shown in Figure 7, the intensity of the carboxylic acid functional groups for powdered CG 50 resin was only about 20% of the intensity of the Dowex MAC 3 H<sup>+</sup> bead resin. Once incorporated into a wafer, the Dowex MAC 3 H<sup>+</sup> wafer had around 10% of the peak intensity of the resin alone (exact values are provided in Supplementary Table S2). For the CG 50 (powder) wafer, the wafer peak intensities were actually around 40–50% higher than the resin alone. As the CG 50 resin intensities were so much lower than the Dowex MAC 3 H<sup>+</sup>, it is possible that interference from other groups present in the wafer (from the polyethylene or anion exchange resin) led to the higher intensities.



**Figure 7.** The FTIR-ATR spectrum of weak cation exchange resins and wafers formed using these resins.

To confirm that the bead resins led to less availability of the function groups, two different batches and multiple wafer positions of Dowex MAC 3 H<sup>+</sup> resin wafers were tested by FTIR-ATR. In both batches, the intensity of the carboxylic acid functional groups was significantly reduced at both the edge and the middle with intensity values of around 10–18% of the resin alone (Figure 8, Supplementary Table S2). It is interesting to note that this reduction did not appear to have any effect on the performance of the Dowex MAC 3 H<sup>+</sup> resin wafer unlike what was observed with the strong cation exchange resin bead (IR 120 Na<sup>+</sup>).



**Figure 8.** The FTIR-ATR spectrum of Dowex MAC 3 H<sup>+</sup> resin alone and in two different wafers.

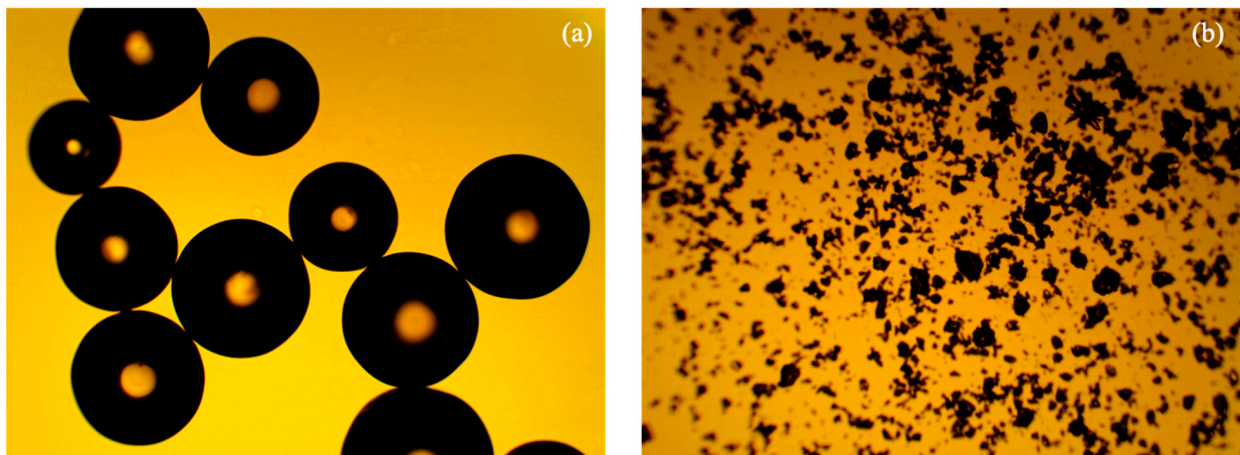
The difference might be explained by how the functional groups interact with the polyethylene. Sulfonic acid functional groups tend to attach to polyethylene. This behavior can be positive for membrane processes as it has been reported to increase ion transport [48] and lower fouling [49]. However, this attachment may be decreasing the availability of sulfonic acid functional groups in the wafer and thereby, decreasing the efficiency and the performance of the resin wafer for the removal of ions from high concentration wastewaters.

### 3.4. Performance Comparison of the Powdered and Bead Form IR 120 Na<sup>+</sup>

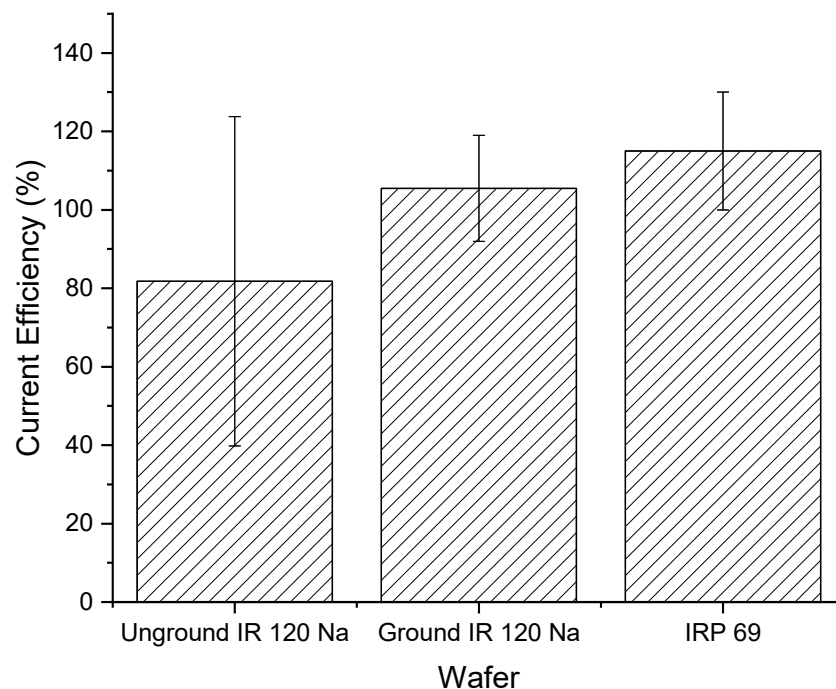
The interaction of polyethylene with the sulfonic acid groups does not fully explain the difference in performance between the two strong cation exchange resins. Therefore, we decided to evaluate if decreasing the particle size of the IR 120 Na<sup>+</sup> resin would increase its performance when incorporated in a wafer. Using the same method outlined in Section 2.3, a new batch of wafers were produced from ground IR 120 Na<sup>+</sup> resins.

Figure 9 clearly shows the particle size difference between the original IR 120 Na<sup>+</sup> resin and the ground IR 120 Na<sup>+</sup> resin. The original IR 120 Na<sup>+</sup> resin had a particle diameter of  $536 \pm 65 \mu\text{m}$  (N = 8) and the ground IR 120 Na<sup>+</sup> resin had a particle diameter of  $30 \pm 20 \mu\text{m}$  (N = 1101).

Figure 10 shows the ground IR 120 Na<sup>+</sup> wafer had a higher and less variable current efficiency compared to the unground IR 120 Na<sup>+</sup> wafer. In addition, the ground IR 120 Na<sup>+</sup> wafer looked similar in performance to the powdered IRP 69 resin wafer. However, it is important to note that all the current efficiency values were statistically the same ( $p > 0.4$ ).

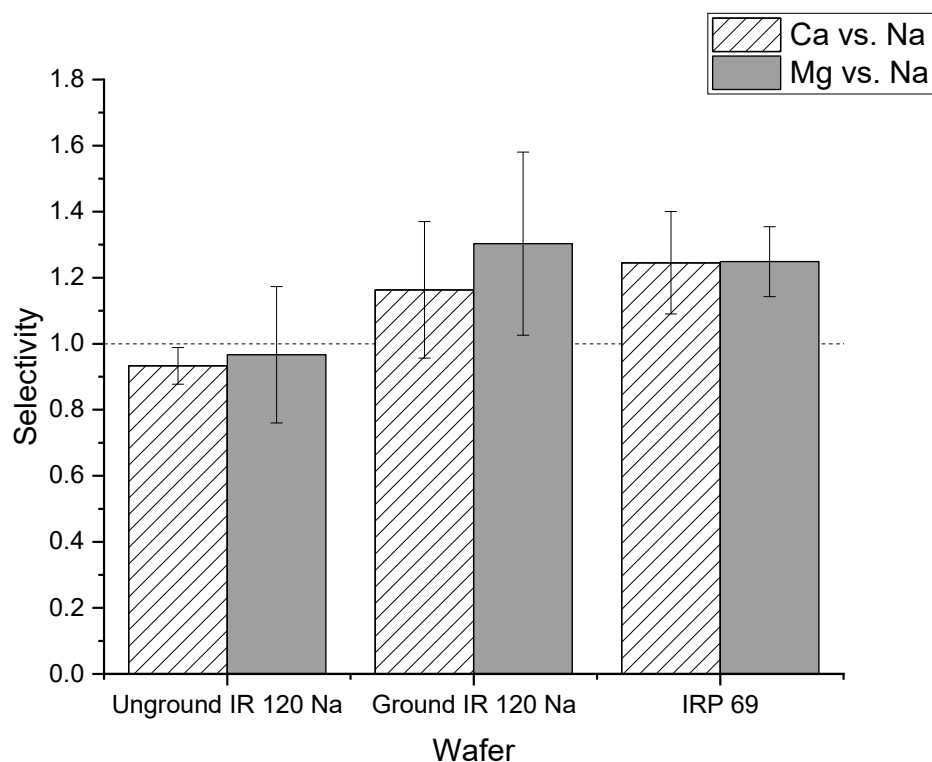


**Figure 9.** Optical microscopy images of (a) unground IR 120 Na<sup>+</sup> resin and (b) ground IR 120 Na<sup>+</sup> resin.



**Figure 10.** Current efficiencies for unground bead form IR 120 Na<sup>+</sup> and ground IR 120 Na<sup>+</sup>.

In addition to current efficiency, the cation selectivity of the two different forms of the IR 120 Na<sup>+</sup> resin in wafers were compared. As shown in Figure 11, the average selectivity of calcium to sodium of ground IR 120 Na<sup>+</sup> wafer was greater than one which indicated that the ground IR 120 Na<sup>+</sup> wafer preferentially transported calcium ions over sodium. For the unground IR 120 Na<sup>+</sup> resin, the selectivity was close to one which indicated that there was not a strong preference for the transport of sodium or calcium ions. However, statistical analysis showed that the difference between the wafer produced from ground versus unground IR 120 Na<sup>+</sup> for calcium selectivity was not significant ( $p > 0.05$ ). A similar situation was observed for the selectivity of magnesium over sodium. While the ground IR 120 Na<sup>+</sup> demonstrated selectivity for magnesium over sodium which the unground did not, their values were statistically the same ( $p > 0.1$ ) When compared to the powder resin IRP 69, the selectivity of ground IR 120 Na<sup>+</sup> resin wafers were statistically the same ( $p > 0.05$ ) for both calcium to sodium and magnesium to sodium. Overall, significantly better performance was produced by wafers composed of the ground IR 120 Na<sup>+</sup> resin compared to its bead form which indicates the importance of strong cation exchange resin size when being used in an electrodeionization wafer.



**Figure 11.** The selectivity of the unground IR 120 Na<sup>+</sup> and the ground IR 120 Na<sup>+</sup>.

#### 4. Conclusions

Four different cation exchange resins were tested for their performance in electrodeionization wafers for the removal of monovalent and divalent cations. Wafers made from weak cation exchange resins and strong cation exchange resins showed similar current efficiencies, although they showed differences in their degree of variability. Based on the selectivity values, weak cation exchange resins seemed to favor the transport of the monovalent ion (sodium), while strong cation exchange resins either had no preference or a preference for the divalent ions (calcium and magnesium), which are usually the more valuable ions in wastewaters.

In addition, the strong cation exchange resins in powder form generally performed better in wafers for the selective removal of divalent ions. This could be due to a more homogeneous mixing with the other wafer materials or it could be due to differences in how it interacts with the polyethylene binding polymer during the formation of wafers. Specifically, wafers formed from IRP 69 strong cation exchange resin in powder form gave the most promising results for the removal of divalent ions.

The positive impact of powder form was also verified by testing two different forms (ground vs. unground) of the same strong cation exchange resin for their performance in electrodeionization wafers for the removal of monovalent and divalent ions. The resin in powder form from the grinding process showed higher overall current efficiencies compared to the unground form (bead) of the resin. Based on the selectivity values, the ground resin seemed to favor the transport of divalent ions (calcium and magnesium) that are more valuable, while the unground resin did not show any preference for either monovalent or divalent ions.

**Supplementary Materials:** The following are available online at <https://www.mdpi.com/2077-0375/11/1/45/s1>, Table S1: FTIR sulfonic acid functional group peak intensity values for strong cation exchange resins alone and incorporated into wafers, Table S2: FTIR carboxylic acid functional group peak intensity values for weak cation exchange resins alone and incorporated into wafers.

**Author Contributions:** Conceptualization, H.B.U.E.; methodology, H.B.U.E.; validation, H.B.U.E.; formal analysis, H.B.U.E.; writing—original draft preparation, H.B.U.E.; writing—review and editing, H.B.U.E., C.N.H., and J.A.H.; visualization, H.B.U.E.; supervision, C.N.H. and J.A.H.; project administration, C.N.H. and J.A.H.; funding acquisition, C.N.H. and J.A.H. All authors have read and agreed to the published version of the manuscript.

**Funding:** Funding for this work was provided by the National Science Foundation Industry/University Cooperative Research Center for Membrane Science, Engineering and Technology (IIP 1361809 and IIP 1822101) and the University of Arkansas.

**Institutional Review Board Statement:** Not applicable.

**Informed Consent Statement:** Not applicable.

**Data Availability Statement:** Data is contained within the article or supplementary material.

**Acknowledgments:** Authors thank Erik Pollock of Biological Sciences at the University of Arkansas for his help with the ion chromatography and John P. Moore II for his help with particle image analysis.

**Conflicts of Interest:** The authors declare no conflict of interest.

## References

1. Risk, C.W. 8 Things You Should Know about Water & Semiconductors. 11 July 2013. Available online: <http://www.chinawaterrisk.org/resources/analysis-reviews/8-things-you-should-know-about-water-and-semiconductors/> (accessed on 30 October 2019).
2. Armstrong, D. Measurement of Ultra-Pure Water in the Semiconductor Industry. 1 January 2008. Available online: <https://www.watertechonline.com/home/article/14171506/measurement-of-ultrapure-water-in-the-semiconductor-industry> (accessed on 21 September 2020).
3. Denchak, M. Fracking 101. 19 April 2019. Available online: <https://www.nrdc.org/stories/fracking-101> (accessed on 2 June 2020).
4. Greenpeace, Fracking's Environmental Impacts: Water. Available online: <https://www.greenpeace.org/usa/global-warming/issues/fracking/environmental-impacts-water/> (accessed on 2 June 2020).
5. Nicot, J.P.; Scanlon, B.R.; Reedy, R.C.; Costley, R.A. Costley, Source and fate of hydraulic fracturing water in the Barnett shale: A historical perspective. *Environ. Sci. Technol.* **2014**, *48*, 2464–2471. [CrossRef] [PubMed]
6. Kausley, S.B.; Malhotra, C.P.; Pandit, A.B. Treatment and reuse of shale gas wastewater: Electrocoagulation system for enhanced removal of organic contamination and scale causing divalent cations. *J. Water Process Eng.* **2017**, *16*, 149–162. [CrossRef]
7. Saltworks, Frack & Shale Produced Water Management, Treatment Costs, & Options. 25 October 2019. Available online: <https://www.saltworkstech.com/articles/frac-shale-produced-water-management-treatment-costs-and-options/> (accessed on 7 June 2020).
8. Strathmann, H. *Ion Exchange Membrane Separation Processes*, 1st ed.; Elsevier: Amsterdam, The Netherlands, 2004; Volume 9, p. 360.
9. Drioli, E.; di Profio, G.; Fontananova, E. Membrane separations for process intensification and sustainable growth. *Fluid Part Sep. J.* **2004**, *16*, 1–18.
10. Drioli, E.; Romano, M. Progress and New Perspectives on Integrated Membrane Operations for Sustainable Industrial Growth. *Ind. Eng. Chem. Res.* **2001**, *40*, 1277–1300. [CrossRef]
11. Buonomenna, M.G.; Golemme, G.; Perrotta, E. Membrane Operations for Industrial Applications. In *Advances in Chemical Engineering*; InTechOpen: London, UK, 2012; pp. 543–562.
12. Lopez, A.M.; Demydov, D.; Rogers, B.; Cleous, H.; Tran, L.; Smith, C.; Williams, M.; Schmelzle, J.; Hestekin, J.A. Economic comparison of pressure driven membrane processes to electrically driven processes for use in hydraulic fracturing. *Sep. Sci. Technol.* **2017**, *53*, 767–776. [CrossRef]
13. Glueckauf, E. Electrodeionization through a packed bed. *Br. Chem. Eng.* **1959**, *4*, 646–651.
14. Houldsworth, D.W. Demineralization of whey by means of ion exchange and electro dialysis. *Int. J. Dairy Technol.* **2007**, *30*, 143–156. [CrossRef]
15. Ganzi, G.C.; Egozy, Y.; Guiffreda, A.J. Deionization-high-purity water by electrodeionization performance of the ion-pure continuous deionization system. *Ultrapure Water* **1987**, *4*, 43–50.
16. Ganzi, G.C.; Jha, A.D.; Dimasco, F.; Wood, J.H. Electrodeionization theory and practice of continuous electrodeion-ization. *Ultrapure Water* **1997**, *14*, 64–69.
17. Ganzi, G.C.; Wood, J.H.; Griffin, C.S. Water purification and recycling using the CDI process. *Environ. Prog.* **1992**, *11*, 49–53. [CrossRef]
18. Lopez, A.M.; Williams, M.; Paiva, M.; Demydov, D.; Do, T.D.; Fairey, J.L.; Lin, Y.J.; Hestekin, J.A. Potential of elec-trodialytic techniques in brackish desalination and recovery of industrial process water for reuse. *Desalination* **2017**, *409*, 108–114. [CrossRef]
19. Meyer, N.; Parker, W.J.; van Geel, P.J.; Adiga, M. Development of an electrodeionization process for removal of nitrate from drinking water. Part 2: Multi-species testing. *Desalination* **2005**, *175*, 167–177. [CrossRef]

20. Pan, S.Y.; Snyder, S.W.; Ma, H.W.; Lin, Y.J.; Chiang, P.C. Development of a resin wafer electrodeionization process for impaired water desalination with high energy efficiency and productivity. *ACS Sustain. Chem. Eng.* **2017**, *5*, 2942–2948. [[CrossRef](#)]
21. Vu, H.T.; Koshchuh, W.; Kulbe, K.D.; Kromus, S.; Krotscheck, C.; Novaldin, S. Desalination of high salt content mixture by two-stage electro dialysis as the first step of separating valuable substances from grass silage. *Desalination* **2004**, *162*, 343–353.
22. Zheng, X.Y.; Pan, S.Y.; Tseng, P.C.; Zheng, H.L.; Chiang, P.C. Optimization of resin wafer electrodeionization for brackish water desalination. *Sep. Purif. Technol.* **2018**, *194*, 346–354. [[CrossRef](#)]
23. Ho, T.; Kurup, A.; Davis, T.; Hestekin, J. Wafer Chemistry and properties for ion removal by wafer enhanced electro-deionization. *Sep. Sci. Technol.* **2010**, *45*, 433–446. [[CrossRef](#)]
24. Menzal, T.; Beusshausen, S. Deionization improvements of semiconductor water treatment using spiral-wound EDI. *Ultrapure Water* **2006**, *23*, 31–35.
25. Lacher, C.; Franzreb, M.; Holl, W.H. Improving the efficiency of electrodeionization by means of magnetic ion exchange resins. *Powerpl. Chem.* **2004**, *6*, 465–471.
26. Arora, M.B.; Hestekin, J.A.; Snyder, S.W.; Martin, E.J.S.; Lin, Y.J.; Donnelly, M.I.; Millard, C.S. The separative bioreactor: A continuous separation process for the simultaneous production and direct capture of organic acids. *Sep. Sci. Technol.* **2007**, *42*, 2519–2538. [[CrossRef](#)]
27. Arora, M.; Hestekin, J.; Lin, Y.; Martin, E.S.; Snyder, S. Porous Solid Ion Exchange Wafer for Immobilizing Biomolecules. U.S. Patent 7,306,934 B2, 11 December 2007.
28. Palakkal, V.M.; Valentino, L.; Lei, Q.; Kole, S.; Lin, Y.K.; Arges, C.G. Advancing electrodeionization with conductive ionomer binders that immobilize ion-exchange resin particles into porous wafer substrates. *npj Clean Water* **2020**, *3*, 5. [[CrossRef](#)]
29. Lopez, A.M.; Hestekin, J.A. Improved organic acid purification through wafer enhanced electrodeionization utilizing ionic liquids. *J. Membr. Sci.* **2015**, *493*, 200–205. [[CrossRef](#)]
30. Franco, P.E.; Veit, M.T.; Borba, C.E.; Gonçalves, G.d.; Fagundes-Klen, M.R.; Bergamasco, R.; da Silva, E.A.; Suzaki, P.Y.R. Nickel(II) and zinc(II) removal using Amberlite IR-120 resin: Ion exchange equilibrium and kinetics. *Chem. Eng. J.* **2013**, *221*, 426–435. [[CrossRef](#)]
31. Borba, E.; Santos, G.H.F.; Silva, E.A. Mathematical modeling of a ternary Cu–Zn–Na ion exchange system in a fixed-bed column using Amberlite IR 120. *Chem. Eng. J.* **2012**, *189*, 49–56. [[CrossRef](#)]
32. Fernández-González, R.; Martín-Lara, M.A.; Blázquez, G.; Tenorio, G.; Calero, M. Hydrolyzed olive cake as novel adsorbent for copper removal from fertilizer industry wastewater. *J. Clean. Prod.* **2020**, *268*, 121935. [[CrossRef](#)]
33. Gomelya, M.; Hrabitchenko, V.; Trokhymenko, A.; Shabliy, T. Research into ion exchange softening of highly mineralized waters. *East. Eur. J. Enterp. Technol.* **2016**, *4*, 4–9.
34. Hosseini, M.S.; Sarab, A.R.R. Cr(III)/Cr(VI) speciation in water samples by extractive separation using Amberlite CG-50 and final determination by FAAS. *Int. J. Environ. Anal. Chem.* **2007**, *85*, 375–385. [[CrossRef](#)]
35. Alayoubi, A.; Daihom, B.; Adhikari, H.; Mishra, S.R.; Helms, R.; Almoazen, H. Development of A Taste Masked Oral Suspension of Clindamycin HCl Using Ion exchange Resin Amberlite IRP 69 for Use in Pediatrics. *Drug Dev. Ind. Pharm.* **2016**, *46*, 1579–1589. [[CrossRef](#)]
36. Al-Shams, J.K.K.; Hussein, M.A.K.; Alhakeim, H.K. Activity and stability of urease enzyme immobilized on Amberlite resin. *Ovidius Univ. Ann. Chem.* **2020**, *31*. [[CrossRef](#)]
37. Swoboda, B.E.P.; Massey, V. Purification and Properties of the Glucose Oxidase from *Aspergillus niger*. *J. Biol. Chem.* **1965**, *240*, 2209–2215. [[CrossRef](#)]
38. Aldrich, S. Particle Size Conversion Table. Available online: <https://www.sigmaaldrich.com/chemistry/stockroom-reagents/learning-center/technical-library/particle-size-conversion.html> (accessed on 17 September 2020).
39. Rasband, W. *ImageJ*; U.S. National Institutes of Health: Bethesda, MD, USA, 1997.
40. Luo, G.S.; Wu, F.Y. Concentration of formic acid solution by electro-electrodialysis. *Sep. Sci. Technol.* **2000**, *35*, 2485–2496. [[CrossRef](#)]
41. Ion Exchange. Approximate Selectivity Scales—Cation Exchange Resins. 16 October 2012. Available online: [http://dardel.info/IX/other\\_info/selectivity\\_c.html](http://dardel.info/IX/other_info/selectivity_c.html) (accessed on 28 December 2020).
42. Kunin, R.; Barry, R.E. Carboxylic, weak acid type, cation exchange resin. *Ind. Eng. Chem.* **1949**, *41*, 1269–1272. [[CrossRef](#)]
43. Zhang, Z.; Chen, A. Simultaneous removal of nitrate and hardness ions from groundwater using electrodeionization. *Sep. Purif. Technol.* **2016**, *164*, 107–113. [[CrossRef](#)]
44. Rogers, B. Electrodeionization Versus electro dialysis: A Clean-Up of Produced Water in Hydraulic Fracturing. Master’s Thesis, University of Arkansas, Fayetteville, AR, USA, August 2016. Available online: [http://scholarworks.uark.edu/etd/1692?utm\\_source=scholarworks.uark.edu%2Fetd%2F1692&utm\\_medium=PDF&utm\\_campaign=PDFCoverPages](http://scholarworks.uark.edu/etd/1692?utm_source=scholarworks.uark.edu%2Fetd%2F1692&utm_medium=PDF&utm_campaign=PDFCoverPages) (accessed on 3 January 2021).
45. Lazar, L.; Bandrabur, B.; Tataru-Färmus, R.-E.; Drobotă, M.; Bulgariu, L.; Gutt, G. FTIR analysis of ion exchange resins with application in permanent hard water softening. *Environ. Eng. Manag. J.* **2014**, *13*, 2145–2152. [[CrossRef](#)]
46. Singare, P.U.; Lokhande, R.S.; Madyal, R.S. Thermal degradation studies of some strongly acidic cation exchange resins. *Open J. Phys. Chem.* **2011**, *1*, 45–54. [[CrossRef](#)]
47. Smith, B.C. The C=O bond, part III: Carboxylic acids. *Spectroscopy* **2017**, *33*, 14–20.



48. Trigg, E.B.; Gaines, T.W.; Maréchal, M.; Moed, D.E.; Rannou, P.; Wagener, K.B.; Stevens, M.J.; Winey, K.I. Self-assembled highly ordered acid layers in precisely sulfonated polyethylene produce efficient proton transport. *Nat. Mater.* **2018**, *17*, 725–731. [[CrossRef](#)] [[PubMed](#)]
49. Alghunaim, A.; Newby, B.M.Z. Cross-linked polystyrene sulfonic acid and polyethylene glycol as a low-fouling material. *Colloids Surf. B Biointerfaces* **2016**, *140*, 514–522. [[CrossRef](#)]



## Article

# Occurrence of Antibiotics, Antibiotic Resistance Genes and Viral Genomes in Wastewater Effluents and Their Treatment by a Pilot Scale Nanofiltration Unit

Maria Beatriz Cristóvão<sup>1,2</sup>, Solomon Tela<sup>1,2</sup>, Andreia Filipa Silva<sup>1,3</sup> , Micaela Oliveira<sup>1,3</sup>, Andreia Bento-Silva<sup>4</sup> , Maria Rosário Bronze<sup>1,3,4</sup> , Maria Teresa Barreto Crespo<sup>1,3</sup>, João Goulão Crespo<sup>2</sup>, Mónica Nunes<sup>1,3</sup> and Vanessa Jorge Pereira<sup>1,3,\*</sup>

<sup>1</sup> iBET, Instituto de Biologia Experimental e Tecnológica, Apartado 12, 2781-901 Oeiras, Portugal; b.cristovao@ibet.pt (M.B.C.); solomon.tela@ibet.pt (S.T.); andreiasilva@ibet.pt (A.F.S.); micaelaoliveira@ibet.pt (M.O.); mrbronz@ff.ulisboa.pt (M.R.B.); tcrespo@ibet.pt (M.T.B.C.); mnunes@ibet.pt (M.N.)

<sup>2</sup> LAQV-REQUIMTE, Department of Chemistry, Faculdade de Ciências e Tecnologia, Universidade Nova de Lisboa, 2829-516 Caparica, Portugal; jgc@fct.unl.pt

<sup>3</sup> Instituto de Tecnologia Química e Biológica António Xavier, Universidade Nova de Lisboa, Av. da República, 2780-157 Oeiras, Portugal

<sup>4</sup> Faculdade de Farmácia, Universidade de Lisboa, 1649-003 Lisboa, Portugal; abentosilva@ff.ulisboa.pt

\* Correspondence: vanessap@ibet.pt



**Citation:** Cristóvão, M.B.; Tela, S.; Silva, A.F.; Oliveira, M.; Bento-Silva, A.; Bronze, M.R.; Crespo, M.T.B.; Crespo, J.G.; Nunes, M.; Pereira, V.J. Occurrence of Antibiotics, Antibiotic Resistance Genes and Viral Genomes in Wastewater Effluents and Their Treatment by a Pilot Scale Nanofiltration Unit. *Membranes* **2021**, *11*, 9.

<https://dx.doi.org/10.3390/membranes11010009>

Received: 25 November 2020

Accepted: 16 December 2020

Published: 23 December 2020

**Publisher's Note:** MDPI stays neutral with regard to jurisdictional claims in published maps and institutional affiliations.



**Copyright:** © 2020 by the authors. Licensee MDPI, Basel, Switzerland. This article is an open access article distributed under the terms and conditions of the Creative Commons Attribution (CC BY) license (<https://creativecommons.org/licenses/by/4.0/>).

**Abstract:** Broad-spectrum fluoroquinolone antibiotics (ciprofloxacin and levofloxacin), carbapenem and fluoroquinolone resistance genes, as well as viral genomes, were detected in grab samples of wastewater effluents. Passive samplers, which are simpler and easier to use and provide information about the concentrations and combination of contaminants present in a certain fluid matrix over time, proved to be extremely promising devices to monitor the presence of the target antibiotics in wastewater effluents. Nanofiltration was tested with a pilot-scale unit installed at a domestic wastewater treatment facility, using a Desal 5DK membrane operated at a constant transmembrane pressure of 6 bar and 70% recovery rate. In a 24 h experimental assay, the variation of the membrane permeance was low (6.3%). High rejections of the target contaminants from the wastewater effluent were obtained by the pilot-scale treatment. Hence, nanofiltration using the Desal 5DK membrane is considered to be a promising treatment to cope with chemical and biological contaminants present in wastewater effluents.

**Keywords:** antibiotics; antibiotic resistance genes; viral genomes; wastewater effluents; occurrence; pilot-scale treatment; nanofiltration

## 1. Introduction

Population growth, urbanization, industrialization, agricultural expansion and climate change globally intensified massive freshwater consumption [1]. This, in turn, increases wastewater production, which, if not effectively treated, can pose a pollution risk to the ecosystem and human health due to the presence of contaminants (e.g., pharmaceutically active compounds and pathogenic microorganisms such as antibiotic-resistant bacteria and viruses) in the discharged effluents.

Regarding pharmaceutically active compounds, special interest should be given to antibiotics since this group of drugs is widely consumed [2], persists in wastewater and drinking water treatment [3], and facilitates the development of antibiotic-resistant bacteria and antibiotic resistance genes, which can cause deleterious human health effects [4,5].

According to a recent report from the United Nations interagency coordinating group on antimicrobial resistance, at least 700,000 people die each year due to drug-resistant diseases [2]. The same report estimates that these diseases could force up to 24 million

people into extreme poverty by 2030, cause 10 million deaths per year by 2050 and damage the economy as devastatingly as the 2008–2009 global financial crisis [2]. Although treating many diseases in animals and humans relies on the use of effective antibiotics, it is extremely urgent to control their use.

A growing number of studies have focused on the occurrence of antibiotics in the aquatic environment, and several antibiotics have been detected in hospital effluents, wastewater effluents and surface waters [3,4]. Particular attention should be given to broad-spectrum antibiotics like quinolones and carbapenems that have a high potential for resistance development [5]. Following this, according to the European Commission implementing decision 2018/840, some antibiotics such as ciprofloxacin (a fluoroquinolone) have been included in the watch list of substances for Union-wide monitoring. This decision is in alignment with the European one health action plan against antimicrobial resistance, which encourages the use of this watch list to improve the worldwide knowledge of antimicrobials occurrence in the environment [6]. Predictions based on structures and physicochemical properties indicated that ciprofloxacin and levofloxacin are expected to be present in wastewater effluents to a greater extent compared to carbapenems due to their low biodegradability [7]. Loos et al. analyzed 156 polar organic chemical contaminants (including a large number of antibiotics) in effluents from 90 European wastewater treatment plants (WWTPs) and found out that ciprofloxacin was among the most frequently detected contaminants, with a frequency of detection around 90% [8]. Some studies have also already reported the occurrence of antibiotic-resistant bacteria and genes in wastewater effluents and in the receiving water bodies [9,10].

Additionally, other pathogenic agents, like viruses, can also persist in raw wastewater and treated wastewater as well as in the receiving water bodies [11]. One of the main sources of viral pathogens in wastewater is the human fecal matter from infected persons [12–14] that can shed  $10^5$  to  $10^{12}$  viral particles per gram of fecal matter [15]. Besides human pathogenic viruses, waterborne viruses that originate from food production, animal husbandry, seasonal surface runoff and other sources are also present in wastewater [16]. The abundance and diversity of pathogenic viruses in wastewater have been shown to reflect the pattern of infection in the human population [11,17]. Adenovirus (AdV), rotavirus (RoV), hepatitis A virus (HAV), and other enteric viruses, such as noroviruses (NoV), coxsackievirus, echovirus, reovirus and astrovirus, are some of the principal human pathogens viruses transmissible via water media.

Hence, there is an urgent need for the development of effective treatment solutions as an alternative to the conventional wastewater treatment processes to avoid the release of these contaminants in the aquatic environment. In this way, membrane filtration processes such as nanofiltration and reverse osmosis could be considered a promising solution for the treatment of effluents with several emerging contaminants like antibiotics, antibiotic resistance genes and viruses. Nanofiltration membranes may be used to produce high-quality wastewater effluents in a more sustainable way than reverse osmosis membranes due to their lower energy consumption and higher throughput. Indeed, laboratory-scale studies conducted on the removal of antibiotics, antibiotic resistance genes, and viruses (both enveloped and non-enveloped) based on nanofiltration technology have demonstrated promising results (e.g., [18–20]).

This work focused on testing the occurrence of the broad-spectrum fluoroquinolone antibiotics ciprofloxacin and levofloxacin in real wastewater effluents. Grab samples were collected during different sampling dates throughout a year. The use of passive samplers was also evaluated for the detection of these two compounds by determining a time-weighted average concentration and comparing it with the results obtained from the grab samples. Additionally, antibiotic resistance genes and pathogenic viral genomes were also quantified in the same wastewater effluent. Finally, the removal of these contaminants was addressed using a nanofiltration pilot-scale unit installed in the same sampling site of the WWTP.

## 2. Materials and Methods

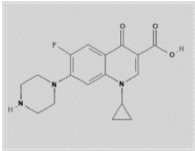
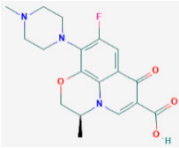
### 2.1. Occurrence Study

In this study, the occurrence of the target antibiotics, antibiotic resistance genes, as well as viral genomes, were analyzed in wastewater samples. All the wastewater samples were collected after the biological treatment and prior to the disinfection step at a wastewater treatment utility. The average pH value of the wastewater samples collected during a year was  $7.1 \pm 0.1$ . For each target contaminant, different protocols were followed, which are detailed on the following sections.

#### 2.1.1. Antibiotics

Regarding the antibiotics, ciprofloxacin and levofloxacin were selected as target drugs in this study. Both target drugs are broad-spectrum antibiotics with different structures, and their physicochemical properties are represented in Table 1.

**Table 1.** Main physicochemical properties of ciprofloxacin and levofloxacin.

Compound	Structure	Molecular Formula	Molecular Weight (Da)	Log $K_{ow}$ <sup>a</sup>
Ciprofloxacin		$C_{17}H_{18}FN_3O_3$	331.3	0.28
Levofloxacin		$C_{18}H_{20}FN_3O_4$	361.4	-0.39

<sup>a</sup> Pubchem-NIH database-<https://pubchem.ncbi.nlm.nih.gov/ accessed August 2020>.

### Sampling Campaign

Since antibiotics are expected to be present in the aquatic environment at trace concentration levels (often  $\mu\text{g}\cdot\text{L}^{-1}$  or  $\text{ng}\cdot\text{L}^{-1}$ ), solid-phase extraction is commonly used to preconcentrate the samples. However, these conventional procedures are usually costly and time-consuming. As an alternative, the use of effective passive samplers that provide real information about the concentrations of different contaminants and their combinations present in different matrices over time was also tested since these samplers may constitute a much more accurate approach than relying on intermittent grab samples that may misrepresent average concentrations due to short-term temporal variability. In this study, the two sampling approaches (grab and passive sampling) were, therefore, performed for the detection of the target antibiotics.

In the first sampling approach, wastewater effluent samples were collected on different dates during a year (from October 2018 until December 2019). These samples were stored in glass bottles, transported to the laboratory and kept at  $4\text{ }^\circ\text{C}$  under dark conditions. All wastewater effluent samples were filtered with  $1.2\text{ }\mu\text{m}$  filters (GE Healthcare, Amersham, UK) and  $0.45\text{ }\mu\text{m}$  polyamide membrane filters (Filter-Lab, Barcelona, Spain) to avoid the clogging of the solid phase extraction cartridges used during the concentration step.

In addition, the potential use of polar organic chemical integrative samplers (POCIS) for the detection of ciprofloxacin and levofloxacin was assessed. For this, a canister containing duplicate POCIS was deployed in the same sampling site previously described, with a rope at two m-depth, during three different days of a week (from 9 a.m. until 6 p.m.). In parallel, grab wastewater samples were collected on the same days in the morning and afternoon periods. After their collection, all POCIS were kept in an aluminum foil bag, transported to the laboratory and kept at  $-20\text{ }^\circ\text{C}$  until extraction. Moreover, two

POCIS were used as a field blank, and none of the target contaminants were detected on their extracts.

#### Solid Phase Extraction Procedures

All grab samples were subjected to a sample concentration procedure using a stationary phase (Oasis HLB cartridges 200 mg, six cc; Waters, Milford, MA, USA) previously optimized for the detection of anticancer drugs [21]. Briefly, 500 mL of sample were loaded into the cartridge at a flow rate of  $5 \text{ mL}\cdot\text{min}^{-1}$  under vacuum, after which the cartridge was rinsed with 3 mL of laboratory grade water and then dried for approximately one hour. Methanol (Carlo Erba reagents, Barcelona, Spain) was then used to elute the compounds from the cartridge. Finally, the extracted sample was concentrated with a gentle nitrogen stream until a final volume of 500  $\mu\text{L}$  was achieved. All samples were stored at  $-20^\circ\text{C}$ , filtered and were further analyzed by UPLC-MS/MS. Following this procedure, the percent recovery of each target antibiotic spiked in the same wastewater effluent was  $21 \pm 5\%$  and  $49 \pm 1\%$ , for ciprofloxacin and levofloxacin, respectively. These recovery values were considered to correct the measured concentrations of the target antibiotics in the wastewater effluent.

Regarding the passive samplers, Pharmaceutical-POCIS (ExposMeter, AB, Tavejsjö, Sweden) that contain 200 mg of OASIS HLB sorbent comprised between two microporous polyethersulfone membranes were used. The extraction procedure consisted of simpler and less time-consuming steps. First, each POCIS was clean with laboratory-grade water, and then the sorbent was gently transferred into an empty 6 mL SPE cartridge and placed between two polyethylene frits (Supelco, Bellefonte, PA, USA). After, 6 mL of methanol was used to elute the target compounds from the cartridges and the obtained extract was dried with a gentle stream of nitrogen until a final volume of 500  $\mu\text{L}$  was achieved. All the samples were stored at  $-20^\circ\text{C}$  until further analysis.

After the UPLC analysis, the mass of analyte accumulated in each POCIS was determined and, since it was assumed that POCIS were deployed during their linear uptake regime, Equation (1) was used to estimate the time-weighted average concentrations:

$$M_s = R_s C_{TWA} t \quad (1)$$

where  $M_s$  is the amount of analyte accumulated in the sorbent (ng),  $R_s$  is the sampling rate ( $\text{L}\cdot\text{day}^{-1}$ ),  $C_{TWA}$  ( $\text{ng}\cdot\text{L}^{-1}$ ) is the time-weighted average concentration, and  $t$  is the time of deployment (days).

For the determination of the time-weighted average concentrations, the sampling rate, i.e., the volume of water cleared per unit of time for a given compound, must be estimated. In this study, the sampling rate obtained by Bailly et al. for ofloxacin (an isomer of levofloxacin) was assumed to be the same for ciprofloxacin and levofloxacin ( $0.1 \text{ L}\cdot\text{day}^{-1}$ ) [22]. This sampling rate has already been used by Ory et al. to estimate the concentration of ciprofloxacin in an hospital effluent [23].

#### Analysis by Liquid Chromatography with Tandem Mass Spectrometry

The analyses were performed on a Waters® Acquity™ ultra-high-performance LC. The separation was performed after injection of a 10  $\mu\text{L}$  sample on a reversed-phase column (HPLC/UPLC Mediterranean Sea 18;  $2.2 \mu\text{m}$   $100 \times 2.1 \text{ mm}$ ) at  $35^\circ\text{C}$ . The mobile phase consisted of 0.1% (*v/v*) formic acid in Milli-Q water (A) and 0.1% (*v/v*) formic acid in acetonitrile (B) with a flow rate of  $0.30 \text{ mL}\cdot\text{min}^{-1}$ . Tandem mass spectrometry (MS/MS) detection was performed on an Acquity™ triple quadrupole (Waters®, Dublin, Ireland) using an electrospray ionization source operating at  $130^\circ\text{C}$  and applying a capillary voltage of 2.2 kV. The compounds were ionized in positive ion mode (ESI+). Analytical conditions and collision energies were optimized for each compound. All analyses were performed in multiple reaction monitoring (MRM) mode in order to achieve a higher selectivity and sensitivity. Two transitions were used in order to identify and quantify the antibiotics in the different samples. The MS/MS conditions optimized for each target antibiotic are presented

in Table 2 and the gradient conditions optimized for the separation of the compounds are depicted in Table 3. High purity nitrogen (N<sub>2</sub>) was used both as drying gas and as a nebulizing gas. Ultra-high purity argon (Ar) was used as collision gas. MassLynx software (version 4.1; Waters<sup>®</sup>, Dublin, Ireland) was used to control the system, for data acquisition and processing.

**Table 2.** Optimization of tandem mass spectrometry (MS/MS) ion transitions and other parameters for detection of the target antibiotics.

Compound.	Ciprofloxacin	Levofloxacin
Retention time (min)	6.72	6.49
Precursor ion [M + H] <sup>+</sup>	332	362
Source potential (V)	50	50
Collision Energy (eV)	20	20
MRM1 transition	332 > 288	362 > 318
MRM2 transition	332 > 314	362 > 261

**Table 3.** Gradient conditions of mobile phases used in UPLC-MS/MS analysis.

Time (min)	0	1	7	8	8.10	10	10.10	20
% A	100	95	80	80	10	10	100	100
% B	0	5	20	20	90	90	0	0

A—0.1% (v/v) formic acid in Milli-Q water, B—0.1% (v/v) formic acid in acetonitrile.

Before analysis by UPLC-MS/MS all samples as well as the calibration standards were filtered with 0.2 µm filters (GE Healthcare, Amersham, UK).

Selectivity, linearity (range 5 to 500 µg·L<sup>-1</sup>), precision and accuracy of the analytical method were determined for the target antibiotics, ciprofloxacin (Sigma Aldrich, Saint Louis, MO, USA) and levofloxacin (Sigma Aldrich, Saint Louis, MO, USA). The results obtained are presented in the Supporting Information section and discussed as proposed in the EU Commission Decision 2002/657/EC according to the following criteria: (i) the retention time of the compound in the real sample must not vary more than ±2.5% from the retention times corresponding to the calibration standards, (ii) the MRM1/MRM2 ratio for target compounds in samples do not deviate more than 20–30% when comparing with the same values obtained for the calibration standards, and (iii) the signal/noise ratio must be higher than 10.

### 2.1.2. Antibiotic Resistance Genes

#### DNA Extraction

The water samples were primarily filtered in triplicate through 0.45 µm pore-size polyethersulfone filters (Pall Corporation, New York, NY, USA) and the resulting filtrates were again filtered through 0.22 µm pore-size polyethersulfone filters (Pall Corporation, New York, NY, USA). Filtration volumes were defined by clogging of the filters as a measure of the same amount of retained biomass. After filtration, the DNA was extracted from each of the two filters per sample following the standard protocol from the DNeasy PowerWater Kit (Qiagen, Hilden, Germany), being recovered in 50 µL elution buffer. At the end, the DNA extracted from both related filters was mixed. DNA concentrations and purity were measured using a NanoDrop 1000 spectrophotometer (Thermo Fisher Scientific, Waltham, MA, USA) and stored at 4 °C for further use.

#### Detection and Quantification of the Target Resistance Genes by TaqMan Multiplex qPCR

According to their importance in terms of clinical relevance and global distribution, five carbapenem-*bla*<sub>KPC</sub>, *bla*<sub>OXA-48</sub>, *bla*<sub>NDM</sub>, *bla*<sub>IMP</sub> and *bla*<sub>VIM</sub>- and three (fluoro)quinolone-

*qnrA*, *qnrB* and *qnrS*- resistance genes were chosen to be detected and quantified by three TaqMan multiplex qPCR assays previously developed and optimized [24].

The quantification of the target carbapenem (*bla*) and (fluoro)quinolone (*qnr*) resistance genes, as well as of the 16S rRNA gene, was conducted in triplicate on a LightCycler 96 real-time PCR system (Roche, Basel, Switzerland) using the following program: DNA denaturation/polymerase activation at 95 °C for 5 min; 40 cycles of amplification at 95 °C for 10 s and 60 °C for 30 s. Information about the mix reactions of each TaqMan qPCR was detailed by Oliveira et al. [24].

### 2.1.3. Viruses

#### Concentration of Viral Particles from the Water Samples

Viral particles concentration was made by organic flocculation with skimmed milk, based on a procedure previously described [25]. Flocculants were allowed to sediment for 8 h, and centrifuged at  $8000 \times g$  for 40 min. The pelleted viral concentrate was suspended in 8 mL phosphate buffer (1:2 (*v/v*) mixture of 0.2 M  $\text{Na}_2\text{HPO}_4$  and 0.2 M  $\text{NaH}_2\text{PO}_4$ ), and the viral concentrate was stored at  $-80$  °C until viral nucleic acids extraction.

#### Viral DNA and RNA Extraction and cDNA Preparation

Nucleic acids were extracted from 140  $\mu\text{L}$ -portions of the respective viral concentrate using the QIAamp Viral RNA minikit (Qiagen, Valencia, CA, USA), following the manufacturer's instructions. Nucleic acids were dissolved in 40  $\mu\text{L}$  of RNase free elution buffer (AVE), and the concentration and purity of the obtained extracts determined using a NanoDrop 1000 spectrophotometer. Total RNA was converted to cDNA in a final volume of 20  $\mu\text{L}$  with the NZY First-Strand cDNA synthesis kit (NZYTech, Lisboa, Portugal) according to the manufacturer's instructions. The nucleic acids were stored at  $-80$  °C until further use.

#### Detection and Quantification of the Viral Genomes by TaqMan Multiplex qPCR

Multiplex qPCRs protocols for the simultaneous detection of viral genomes of HAV, NoV GI and GII and HEV (MqPCR 1) and adenovirus and polyomavirus (MqPCR2) were previously developed and optimized (data not showed). The MqPCR 1 reaction was carried out in a total volume of 20  $\mu\text{L}$  using SensiFAST™ Probe No-ROX amplification mix (Bioline, London, UK). The concentrations of HAV, NoV GI and GII, and HEV for forward and reverse primers were 100 nM and 400 nM, respectively, and for the probes were 100 nM for NoV GII, HAV and HEV, and 250 nM for HEV. Regarding the MqPCR2 the concentrations of the forward and reverse primers were 300 nM and for each probe (AdV, PyV) were 100 nM. The MqPCR 1 temperature profile was: 5 min at 95 °C as hot start, and 40 cycles of 15 s at 95 °C for denaturation, 1 min at 60 °C for annealing, and 1 min at 65 °C for extension. For the MqPCR2 the temperature profile was: 5 min at 95 °C as hot start, and 40 cycles of 10 s at 95 °C for denaturation and 30 s at 60 °C for annealing. Thermal cycling, fluorescent data collection, and data analysis were performed in a LightCycler 96 real-time PCR system (Roche), according to the manufacturer's instructions.

### 2.2. Nanofiltration Experimental Assay

The efficiency of a nanofiltration system for the retention of the target antibiotics, antibiotic resistance genes as well as viral genomes was assessed by conducting an experimental assay in the same sampling site where the occurrence samples were collected. A nanofiltration pilot unit was placed after the biological treatment and, consequently, the viability of using nanofiltration as tertiary treatment in a wastewater treatment plant was assessed.

A submersed pump was constantly collecting the effluent from the biological treatment into a 1  $\text{m}^3$  tank, which was then connected to the pilot unit. The pilot unit comprised one feed pump, one pressurization pump as well as one recirculation pump, which ensured a recirculation of  $900 \text{ L}\cdot\text{h}^{-1}$ . Additionally, two pre-filters (70  $\mu\text{m}$  and 30  $\mu\text{m}$ ) were located at

the entrance of the pilot unit to protect the membrane. The membrane used consisted of a spiral wound Desal 5DK module (model DK4040F30, Suez membranes, Lenntech, Delfgauw, The Netherlands), with an active membrane surface area of 7.9 m<sup>2</sup>. The Desal 5DK membrane is a thin film composite membrane with polysulfone support layer and is negatively charged at neutral pH. Prior to the experimental assay, the permeance of the membrane was measured with tap water and the obtained value was 3.5 L·h<sup>-1</sup>·m<sup>-2</sup>·bar<sup>-1</sup> (20 °C).

The operation of the pilot unit has been optimized in a previous study conducted with the same effluent and several assays were conducted under controlled permeate flux (12.7 L·m<sup>-2</sup>·h<sup>-1</sup>, 15.2 L·m<sup>-2</sup>·h<sup>-1</sup>, 19.0 L·m<sup>-2</sup>·h<sup>-1</sup> and 25.3 L·m<sup>-2</sup>·h<sup>-1</sup>) or controlled transmembrane pressure conditions (5 bar and 6 bar) and different recovery rates (feed flow of water converted into treated flow of water (permeate); approximately 20%, 30%, 40%, 70% and 80%) to determine the operating conditions that would minimize fouling resistance, would maximize the production of treated water and rejection of anticancer compounds [26]. The best operating conditions for this wastewater effluent were found at a controlled pressure difference of 6 bar and using a recovery rate of approximately 70%. Hence, a 24 h experimental assay was performed using the same conditions.

All samples from feed, permeate and retentate were analyzed for the target antibiotics, antibiotic resistance genes and viral genomes, following the protocols described in the above section.

The apparent rejection of each target contaminant was calculated using Equation (2):

$$\text{Rejection (\%)} = \left(1 - \frac{C_p}{C_f}\right) \times 100 \quad (2)$$

where  $C_p$  is the concentration of the target contaminant in the permeate side and  $C_f$  is the concentration of the target contaminant in the feed.

### 3. Results and Discussion

#### 3.1. Occurrence of the Target Contaminants

##### 3.1.1. Antibiotics

The occurrence of ciprofloxacin and levofloxacin in the wastewater effluent was evaluated from October 2018 until December 2019. Figure 1 represents the concentration of the target antibiotics obtained from grab wastewater effluent samples.

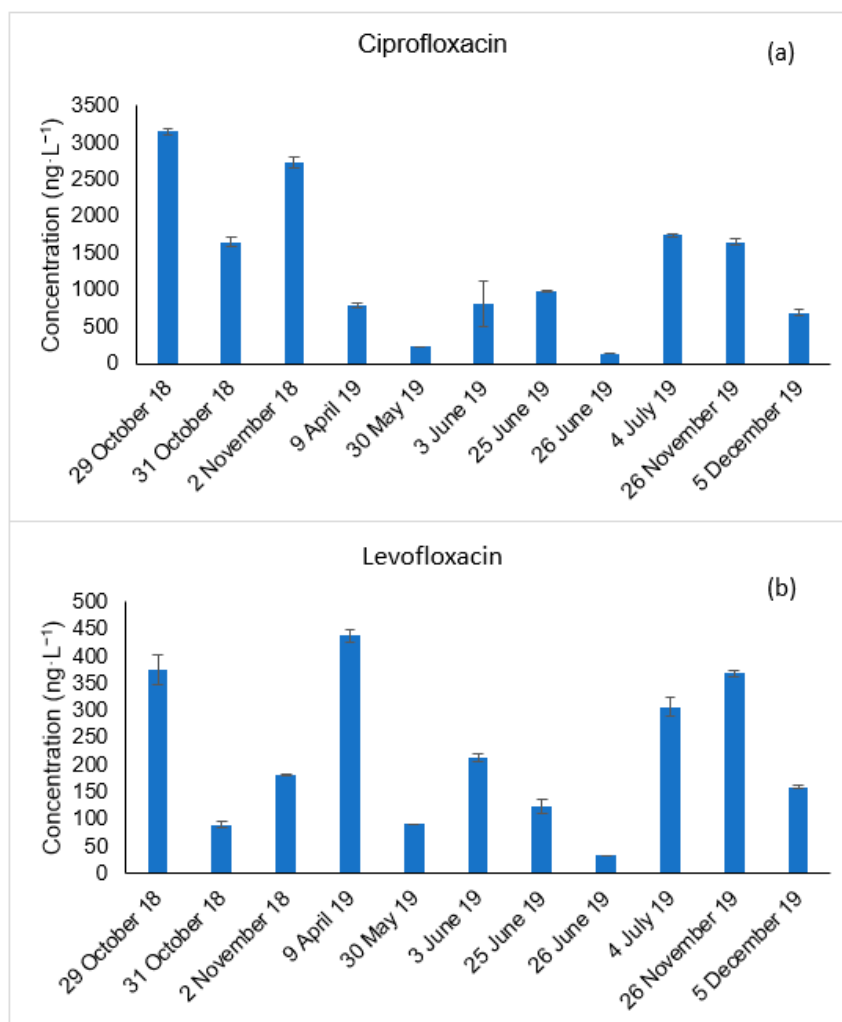
As represented in Figure 1, both target antibiotics were detected in all the collected samples and their concentration did not vary much between the different seasons of the year, which could be expected since these broad spectrum antibiotics are used to treat a wide variety of bacterial infections.

Regarding ciprofloxacin (Figure 1a), its concentration ranged between 135 and 3150 ng·L<sup>-1</sup>. The lowest measured concentration was on 26 June 2019, whereas the highest concentration was obtained on 29 October 2018. Similar occurrence values have been reported in the literature. For example, Verlicchi et al. detected ciprofloxacin in several wastewater effluent samples collected from a WWTP located in the Northern of Italy with average concentrations of 630 ng·L<sup>-1</sup> [27]. In addition, Rossmann et al. detected ciprofloxacin at 920 ng·L<sup>-1</sup> in a wastewater effluent from a WWTP located in Germany [28].

In the same way, levofloxacin (Figure 1b) was detected in all the wastewater samples in concentrations ranging from 34 ng·L<sup>-1</sup> to 438 ng·L<sup>-1</sup>. The minimum and maximum concentrations were recorded on 26 June 2019 and 9 April 2019, respectively. These values are also in agreement with others already reported in the literature. For example, levofloxacin has been detected in wastewater effluents of two WWTPs located in Slovakia at concentrations up to 58 ng·L<sup>-1</sup>. In addition, Rossmann et al. detected levofloxacin in concentrations up to 836 ng·L<sup>-1</sup> [28].

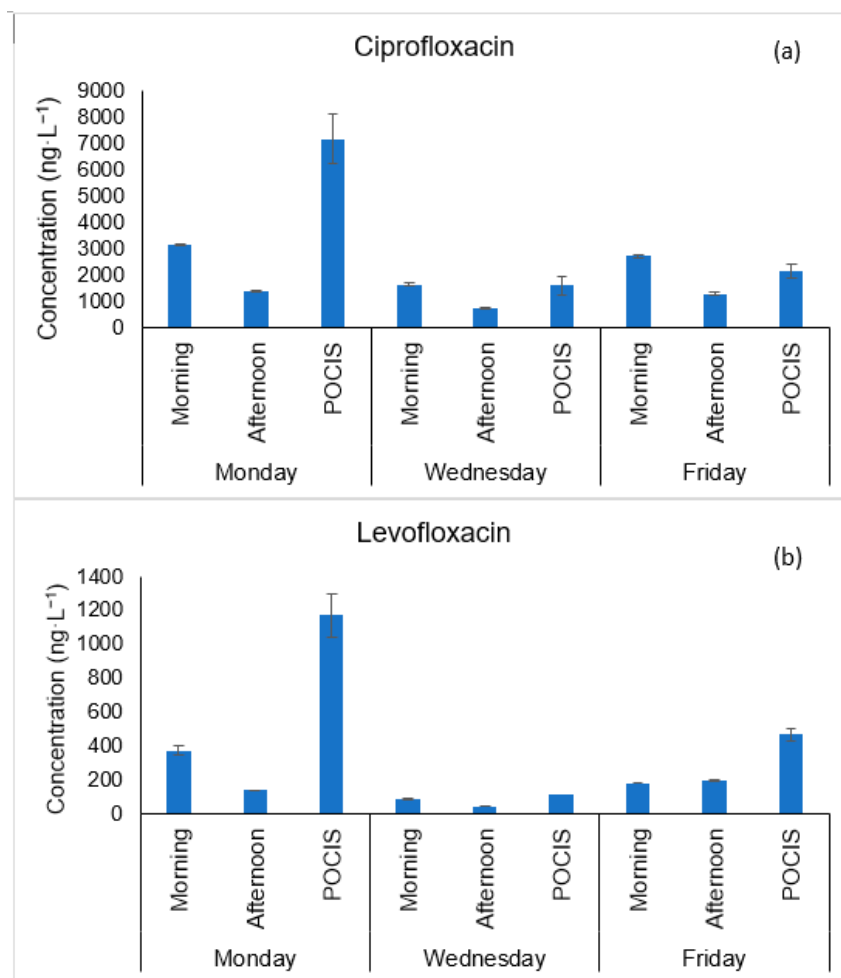


In addition, the potential use of the pharmaceutical-POCIS for the detection of the target antibiotics was assessed. For this, POCIS were deployed on the week of 29 October 2018–2 November 2018, on Monday, Wednesday and Friday from 9 a.m. until 6 p.m. The time-weighted average concentrations, estimated for each compound assuming a sampling rate of  $0.1 \text{ L}\cdot\text{day}^{-1}$  and using Equation (1), are represented in Figure 2.



**Figure 1.** Occurrence of ciprofloxacin (a) and levofloxacin (b) in a wastewater effluent at different periods of a year.

As represented in Figure 2, a good agreement was found between the time-weighted average concentrations obtained from the POCIS deployed on Wednesday and Friday with the concentrations obtained from the grab samples collected on these days in the morning and afternoon period. For example, on Wednesday, the estimated  $C_{\text{TWA}}$  value for ciprofloxacin was  $1611 \text{ ng}\cdot\text{L}^{-1}$  and according to grab samples, on this day its concentration ranged from  $752$  to  $1655 \text{ ng}\cdot\text{L}^{-1}$ . In the same way, the  $C_{\text{TWA}}$  value estimated for levofloxacin was  $118 \text{ ng}\cdot\text{L}^{-1}$  and the concentration estimated from the grab samples ranged from  $45$  to  $90 \text{ ng}\cdot\text{L}^{-1}$ . On the other hand, the results obtained on Monday for both antibiotics with the POCIS are much higher than the results obtained with the grab samples showing us that the grab sampling events may have missed higher occurrence levels of these two compounds in other periods of the day.



**Figure 2.** Concentration of ciprofloxacin (a) and levofloxacin (b) obtained from grab effluent samples collected on 29 October 2018 (Monday), 31 October 2018 (Wednesday) and 2 November 2018 (Friday) in the morning and afternoon period, as well as time-weighted average concentrations of each target compound obtained from polar organic chemical integrative samplers (POCIS), deployed on these days.

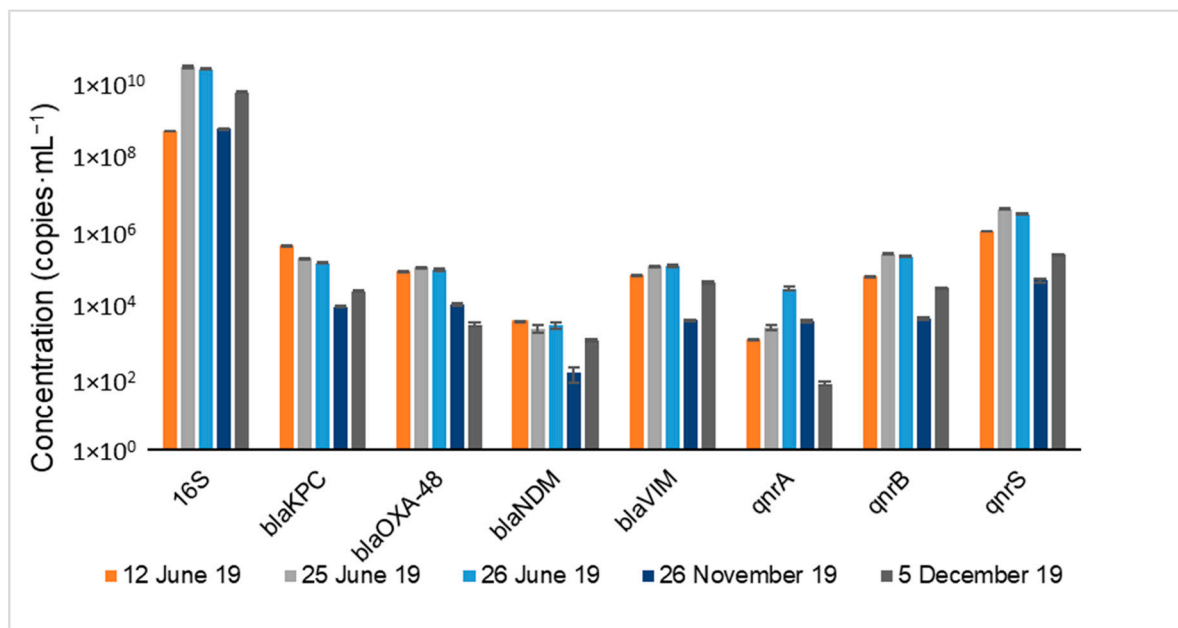
Future work should test the uptake profile of different chemical contaminants by exposing the samplers to wastewater effluents over several days so that more reliable sampling rates could be determined, since the calibration would be performed in situ.

Nevertheless, POCIS proved to be efficient in qualitatively and quantitatively monitoring the presence of ciprofloxacin and levofloxacin in wastewater effluents since both antibiotics were detected in all the POCIS extracts. For this reason, POCIS can be a useful tool for a first screening of the problem and it brings several advantages since it is simpler and less time-consuming when compared to the traditional grab samples.

Finally, the occurrence of both target antibiotics proves that, in some plants, conventional wastewater treatment may not guarantee their complete removal.

### 3.1.2. Occurrence of Antibiotic Resistance Genes and Viral Genomes

The occurrence of carbapenem (*bla*<sub>KPC</sub>, *bla*<sub>OXA-48</sub>, *bla*<sub>NDM</sub>, *bla*<sub>IMP</sub> and *bla*<sub>VIM</sub>) and (fluoro)quinolone (*qnrA*, *qnrB* and *qnrS*) resistance genes in the wastewater effluent at different days is represented in Figure 3. 16S rRNA gene is also represented in Figure 3 since its quantification was performed to assess the bacterial abundance on different days.



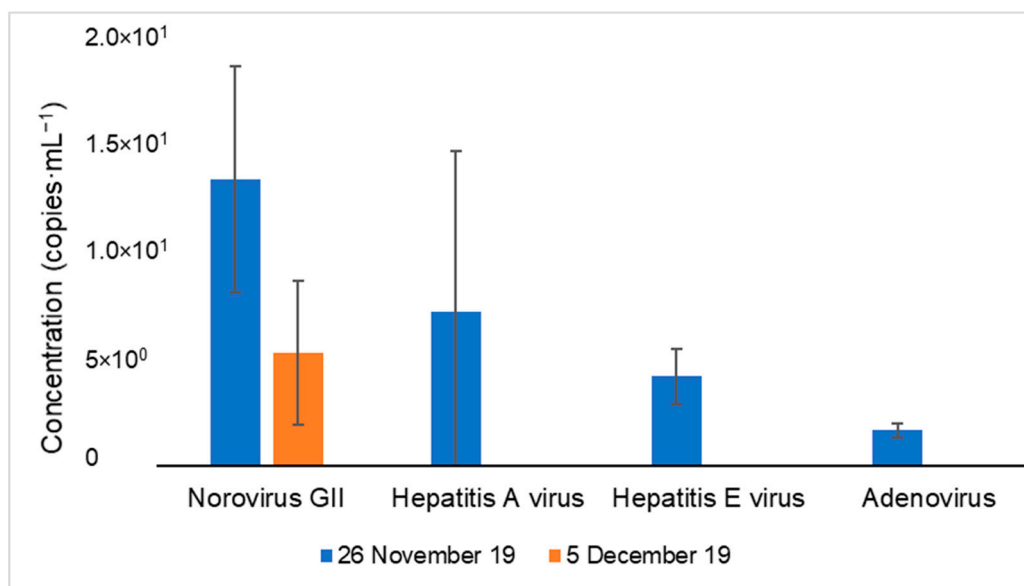
**Figure 3.** Occurrence of carbapenem (*bla<sub>KPC</sub>*, *bla<sub>OXA-48</sub>*, *bla<sub>NDM</sub>* and *bla<sub>VIM</sub>*) and (fluoro)quinolone (*qnrA*, *qnrB* and *qnrS*) resistance genes in wastewater effluent at different days. The data for *bla<sub>IMP</sub>* is not represented since it was lower than the detection limit in all the samples (1 copy·mL<sup>-1</sup>).

Regarding the studied antibiotic resistance genes, all the target carbapenem and fluoro(quinolone) resistance genes (*bla<sub>KPC</sub>*, *bla<sub>OXA-48</sub>*, *bla<sub>NDM</sub>*, *bla<sub>VIM</sub>*, *qnrA*, *qnrB* and *qnrS*) except *bla<sub>IMP</sub>* were detected in all the sampling days. The lowest concentration obtained was for the *qnrA* gene (59.5 copies·mL<sup>-1</sup>) on 5 December, and the highest concentration was for the *qnrS* ( $2.85 \times 10^6$  copies·mL<sup>-1</sup>) gene on 25 June.

The high concentrations of carbapenem resistance genes present in the effluents reflect the increasing resistance in the microbial community towards this group of last-line antibiotics. Other studies recently published have reported the presence of carbapenem and (fluoro)quinolone resistance genes in the wastewater treatment processes of different European WWTPs [9,10,29], showing that most of these genes are present at higher concentrations in WWTPs of Southern Europe rather than in those of Northern Europe [29]. This is in line with the concentrations of carbapenem and (fluoro)quinolone resistance genes found in this study. This can be explained by the differences at the level of the antibiotic consumption pattern between Northern and Southern European countries, and possibly by the warmer waters of Southern Europe, which may be another favorable factor for the bacterial growth, including the bacteria-harboring resistance genes, being this a major driver of antibiotic resistance in the environment [29].

Regarding the target viral genomes, their detection was only possible on 26 November and 5 December 2019, and their concentration is represented in Figure 4.

Low concentration of the viral genomes NoV GII, HAV, HEV and adenovirus were detected, being the NoV GII genome the only one present on both days. Additionally, NoV GI and Polyomavirus genomes were not detected in any of the sampling days. The absence of these viral genomes in the collected samples does not necessarily mean that these genomes are not present in the effluents; it could be due to the detection limit of the multiplex qPCR protocols (1 copy of the genome·L<sup>-1</sup>).



**Figure 4.** Occurrence of different types of viral genomes (norovirus GII, hepatitis A virus, hepatitis E virus and adenovirus) in wastewater effluent on two different days.

Consistent results have also been reported by Teixeira et al. 2020 [28] in a WWTP where NoV GI and NoV GII genomes were detected in the effluent after the secondary treatment, with an average concentration of  $10^5$  genome copies·L<sup>-1</sup>, and in the effluent after the tertiary treatment, with concentrations of  $10^4$  genome copies·L<sup>-1</sup>. In addition, La Rosa et al. 2010, detected NoVGI/GII genomes in the influents and effluents of five WWTPs from Italy, with a higher prevalence of NoV GI, one of the most predominant type on the human population [30].

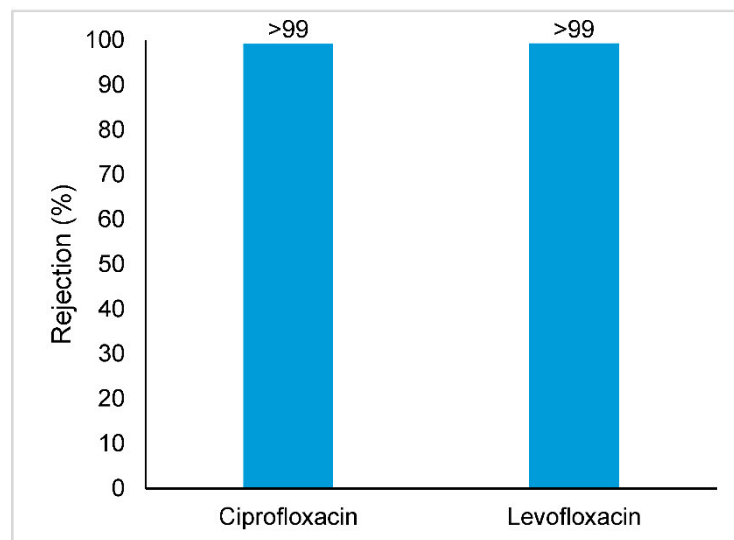
For HEV, Portugal is considered endemic for this virus [31,32], which is mainly present in pigs [33,34]. Thus, its release into the aquatic environment is expected, and consequently, its presence in the wastewater samples. Although in this study HEV genome was present at low concentrations, in another study from Matos et al. [34], the HEV genome was also detected but only in the influent samples of two Portuguese WWTPs. These authors did not indicate the HEV concentrations since their main goal was to perform molecular characterization of the virus. Similar results were obtained in a Spanish study [35], which detected HEV genomes only in the influent samples of four WWTPs, with average concentrations of  $10^3$  genome copies·L<sup>-1</sup>. Additionally, a study from de-Beyer et al. revealed the presence of the HEV genomes in the effluent samples of several German WWTPs, with an average concentration of  $10^3$  genome copies·L<sup>-1</sup> [36].

### 3.2. Efficiency of Nanofiltration for the Removal of the Target Contaminants

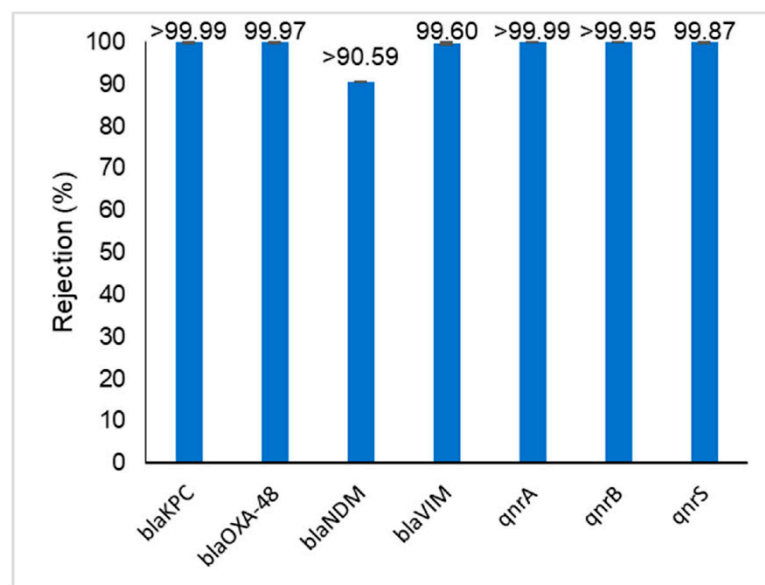
The efficiency of a nanofiltration pilot-scale unit using the Desal 5DK membrane to remove the target antibiotics, antibiotic resistance genes and viral genomes from the wastewater effluent was evaluated.

Based on previously optimized conditions, the pilot unit was operated at a controlled pressure difference of 6 bar and an average recovery rate of 70% [26]. During the 24 h of in situ experiments, the permeance did not change much with an average normalized value (20 °C) of  $2.8 \text{ L}\cdot\text{h}^{-1}\cdot\text{m}^{-2}\cdot\text{bar}^{-1}$  and a coefficient of variation of 6.3%. The membrane could therefore be operated using these conditions for significantly longer times before washing events are needed.

The rejections obtained for the target antibiotics, antibiotic resistance genes and viral genomes are represented in Figures 5–7, respectively.

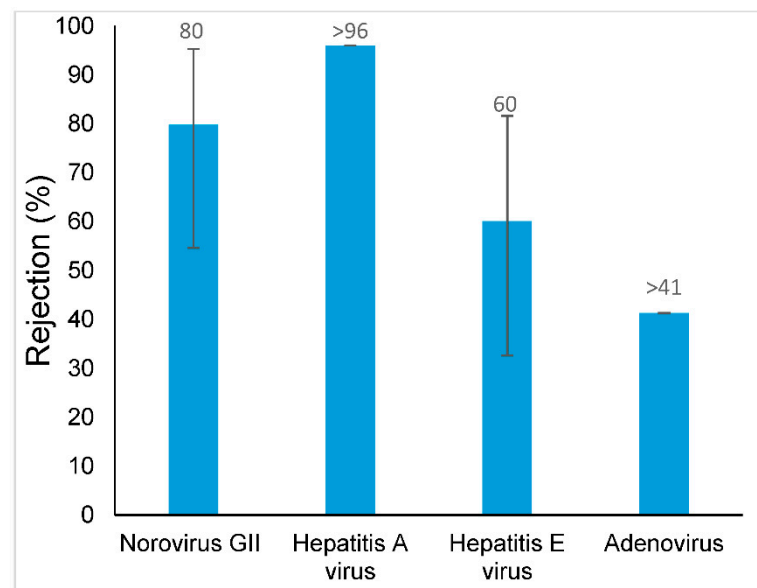


**Figure 5.** Removal of the target antibiotics from wastewater effluent using a Desal 5DK nanofiltration membrane; When the symbol “>” is used, it means that the compound was not detected in the permeate sample (below detection limit).



**Figure 6.** Removal of the target carbapenem (bla) and (fluoro)quinolone (qnr) resistance genes from wastewater effluent using a Desal 5DK membrane. When the symbol “>” is used, it means that this resistance gene was not detected in the permeate sample (below detection limit).

As illustrated in Figure 5, high rejections were obtained for ciprofloxacin and levofloxacin. Both target antibiotics were not detected in the permeate samples. The percent rejection values were therefore calculated considering the lowest point measured in the calibration curve with a signal-to-noise ratio higher than 10. Taking into account the concentration factor and the recovery from the solid phase extraction procedure, that will correspond to a concentration of  $24 \text{ ng}\cdot\text{L}^{-1}$  for ciprofloxacin and  $10 \text{ ng}\cdot\text{L}^{-1}$  for levofloxacin in the permeate samples. It can be assured that the rejection was higher than 99% for both target compounds.



**Figure 7.** Removal of the target viral genomes from wastewater effluent using a Desal 5 DK membrane; When the symbol “>” is used, it means that this viral genome was not detected in the permeate sample (below detection limit).

As it is well known, different mechanisms may be involved in the rejection of solutes by a nanofiltration membrane, such as size exclusion, electrostatic interactions and hydrophobic interactions. Based on the molecular weight and characteristics of both target antibiotics (Table 1) compared to the molecular weight cutoff of the membrane used, their rejection is expected to be mainly governed by size exclusion.

Dolar et al. reported rejections of ciprofloxacin in Milli-Q water higher than 99% when using an NF 270 and NF90 membrane, which are similar to the rejection values obtained with the Desal 5DK membrane used in this work, processing real wastewater after biological treatment [19].

As represented in Figure 6, the carbapenem resistance genes *bla<sub>NDM</sub>* and *bla<sub>KPC</sub>* as well the fluoroquinolones resistance genes *qnrA* and *qnrB*, were not detected in the permeate samples. The percent rejection values were therefore calculated considering the detection limit of 1 copy·mL<sup>-1</sup>. Regarding the other target resistance genes, even though high rejections were obtained, it was possible to detect them on the permeate samples, at levels ranging from 3.2 ± 3.1 copies·mL<sup>-1</sup> (*bla<sub>OXA-48</sub>*) to 58.2 ± 3.5 copies·mL<sup>-1</sup> (*qnrS*). Considering that this WWTP facility has the particularity of being in a closed environment, these low concentrations of some ARG could be due to the dissemination of aerosols near the sampling points of the pilot-scale unit.

The effective retention of the target carbapenem and fluoroquinolone resistance genes reported in this study agrees with results obtained by other authors. Slipko et al. showed that ultrafiltration, nanofiltration and reverse osmosis membranes could retain more than 99.8% of free DNA (pure plasmid and linear fragments of different sizes) [20]. Size exclusion was reported as the main retention mechanism. Lan et al. reported that nanofiltration and reverse osmosis treatment processes were extremely effective in retaining sulfonamide and tetracycline resistance genes (4.98–9.52 logs removal compared to raw sewage) [37]. The higher levels of rejection reported can be explained due to the extremely high levels of the sulfonamide and tetracycline resistance genes present in the raw sewage sampled by the authors (swine wastewater treatment). Lu et al. reported that a combination of microfiltration and reverse osmosis filtration processes could be used to effectively remove tetracycline, sulfonamide, macrolide and quinolone resistance genes from wastewater effluents [38]. Gros et al. studied the fate of pharmaceuticals and antibiotic resistance genes in a full-scale on-farm livestock waste treatment plant and reported that even though the

reverse osmosis permeates had low levels of pharmaceuticals, antibiotic resistance genes copy numbers were still detected [39].

Figure 7 shows that the viral genomes from hepatitis A virus and Adenovirus genomes were not detected in the permeate samples, and consequently, their rejections were calculated assuming the detection limit of the method (1 genome copy·L<sup>-1</sup>).

Even though it was not expected that viral particles/viral fragments of the genome would pass through the nanofiltration membrane, Norovirus GII and hepatitis E viral genomes were detected in the permeate samples at levels lower than 4.3 genome copies·L<sup>-1</sup>. According to Van der Bruggen [40], viruses might not be completely removed by driven membrane processes due to the potential presence of “abnormally large” pores, which may lead to the leakage of viruses. Additionally, as mentioned above, the pilot-scale treatment process was operated in a real wastewater treatment plant where aeration facilities can generate and diffuse bioaerosols containing chemicals and microorganisms including viruses that are typically non-waterborne [41,42], being impossible to guarantee a sterile environment, and thus, contamination of the permeate samples cannot be ruled out.

It is important to note that the molecular techniques used in this study only provide estimates of the presence and abundance of the viral genomes in a sample, not measuring the viral infectivity. For a complete assessment of the presence of viruses in treated wastewater effluents, their presence, viability and potential infectivity should also be addressed by cell-line cultures studies.

Similar results were also obtained by Gimenez et al. 2009 where adenovirus and polyomavirus genomes were detected in some permeate samples collected in a drinking-water treatment plant after nanofiltration and reverse osmosis treatment. However, these samples did not show infectivity in the cell culture assays [39].

Overall, high removal of most target contaminants was achieved and thus, nanofiltration with a Desal 5DK membrane has the potential to be used as a tertiary treatment in a wastewater treatment facility and guarantee higher water quality. Nevertheless, long term assays should be conducted to study if adsorption of the target contaminants on the membrane is significant and guarantee there is no breakthrough of the compounds after several days of operation. Furthermore, if membrane filtration is applied, retentate treatment should be addressed, for example, by direct photolysis or advanced oxidation processes.

#### 4. Conclusions

The fluoroquinolone antibiotics ciprofloxacin and levofloxacin, as well as several carbapenem and fluoroquinolone resistance genes, were detected in grab sampling events conducted throughout a year. When daily samples collected in grab events and using passive samplers were compared, the pharmaceutical polar organic chemical integrative samplers were found to be an extremely promising alternative to grab samples since their use avoids the most time-consuming steps of the solid phase extraction procedure. The occurrence of different types of viral genomes from Norovirus GII, hepatitis A virus, hepatitis E virus and adenovirus was also reported in one of the sampling events using the same wastewater effluent.

Nanofiltration using a Desal 5DK membrane was tested at pilot-scale to remove antibiotics, antibiotic resistance genes and viral genomes detected at occurrence levels in real wastewater effluent. The results of a 24 h assay conducted at a constant pressure of 6 bar showed that the permeance was maintained and that a high removal of antibiotics, antibiotic resistance genes and viral genomes can be expected with this treatment process. The use of nanofiltration as a tertiary treatment is, therefore, a promising solution to increase the quality of the wastewater effluents produced.

**Author Contributions:** Conceptualization, V.J.P., M.N. and J.G.C.; methodology, M.B.C., S.T., A.F.S., M.O., A.B.-S., M.R.B., M.T.B.C., J.G.C., M.N., V.J.P.; formal analysis, M.B.C., S.T., A.F.S., M.O., A.B.-S.; writing—original draft preparation, M.B.C., S.T., M.N., V.J.P.; writing—review and editing, M.B.C., S.T., A.F.S., M.O., A.B.-S., M.R.B., M.T.B.C., J.G.C., M.N., V.J.P.; supervision, V.J.P., M.N., M.R.B., M.T.B.C. and J.G.C. All authors have read and agreed to the published version of the manuscript.

**Funding:** This research was funded by Fundação para a Ciência e a Tecnologia through the project PTDC/CTA-AMB/29586/2017. We also acknowledge the financial support from Fundação para a Ciência e Tecnologia and Portugal 2020 to the Portuguese Mass Spectrometry Network (LISBOA-01-0145-FEDER-402-022125). iNOVA4Health-UIDB/04462/2020, a program financially supported by Fundação para a Ciência e Tecnologia/Ministério da Educação e Ciência, through national funds, is gratefully acknowledged. Associate Laboratory for Green Chemistry-LAQV, which is financed by national funds from FCT/MCTES (UID/QUI/50006/2019), is gratefully acknowledged. Funding from INTERFACE Program, through the Innovation, Technology and Circular Economy Fund (FITEC), is gratefully acknowledged.

**Conflicts of Interest:** The authors declare no conflict of interest.

## References

- Zhang, Y.; Shen, Y. Wastewater irrigation: Past, present, and future. *Wires Water* **2019**, *6*, 1234. [CrossRef]
- United Nations Interagency Coordinating Group on Antimicrobial Resistance. *No Time to Wait: Securing the Future from Drug-Resistant Infections, Report to the Secretary-General of the United Nations*; WHO: Geneva, Switzerland, 2019.
- Watkinson, A.J.; Murby, E.J.; Kolpin, D.W.; Costanzo, S.D. The occurrence of antibiotics in an urban watershed: From wastewater to drinking water. *Sci. Total Environ.* **2008**, *407*, 2711–2723. [CrossRef]
- Dinh, Q.; Moreau-guigon, E.; Labadie, P.; Alliot, F.; Teil, M.; Blanchard, M.; Eurin, J.; Chevreuil, M. Fate of antibiotics from hospital and domestic sources in a sewage network. *Sci. Total Environ.* **2017**, *575*, 758–766. [CrossRef]
- Yewale, V.N. Antimicrobial resistance—A ticking bomb. *Indian Pediatr.* **2014**, *51*, 171–172. [CrossRef]
- European Commission. *A European One Health Action Plan against Antimicrobial Resistance (AMR)*; European Commission: Brussels, Belgium, COM (2017) 339 Final; Available online: <https://eur-lex.europa.eu/legal-content/EN/TXT/?uri=CELEX%3A52017DC0339> (accessed on 23 December 2020).
- Tela, S.H. Occurrence of Antibiotics in Wastewater Effluents and Their Treatment by a Pilot Scale Nanofiltration Unit. Master's Thesis, Faculdade de Ciências e Tecnologia, Universidade Nova de Lisboa, Caparica, Portugal, 2020.
- Loos, R.; Carvalho, R.; António, D.C.; Comero, S.; Locoro, G.; Tavazzi, S.; Paracchini, B.; Ghiani, M.; Lettieri, T.; Blaha, L.; et al. EU-wide monitoring survey on emerging polar organic contaminants in wastewater treatment plant effluents. *Water Res.* **2013**, *7*, 6475–6487. [CrossRef] [PubMed]
- Auguet, O.; Pijuan, M.; Borrego, C.M.; Rodriguez-mozaz, S.; Triadó-margarit, X.; Varela, S.; Giustina, D.; Gutierrez, O. Sewers as potential reservoirs of antibiotic resistance. *Sci. Total Environ.* **2017**, *605*, 1047–1054. [CrossRef] [PubMed]
- Cacace, D.; Fatta-kassinos, D.; Manaia, C.M.; Cytryn, E.; Kreuzinger, N.; Rizzo, L.; Karaolia, P.; Schwartz, T.; Alexander, J.; Merlin, C.; et al. Antibiotic resistance genes in treated wastewater and in the receiving water bodies: A pan-European survey of urban settings. *Water Res.* **2019**, *162*, 320–330. [CrossRef] [PubMed]
- Fumian, T.M.; Fioretti, J.M.; Lun, J.H.; Ingrid, A.L.; White, P.A.; Miagostovich, M.P. Detection of norovirus epidemic genotypes in raw sewage using next generation sequencing. *Environ. Int.* **2019**, *123*, 282–291. [CrossRef] [PubMed]
- Gerba, C.P.; Betancourt, W.Q.; Kitajima, M. How much reduction of virus is needed for recycled water: A continuous changing need for assessment? *Water Res.* **2017**, *108*, 25–31. [CrossRef] [PubMed]
- Hellmér, M.; Paxéus, N.; Magnus, L.; Enache, L.; Arnholm, B.; Johansson, A.; Bergström, T. Detection of Pathogenic Viruses in Sewage Provided Early Warnings of Hepatitis A Virus and Norovirus Outbreaks. *Appl. Environ. Microbiol.* **2014**, *80*, 6771–6781. [CrossRef]
- Symonds, E.M.; Griffin, D.W.; Breitbart, M. Eukaryotic Viruses in Wastewater Samples from the United States. *Appl. Environ. Microbiol.* **2009**, *75*, 1402–1409. [CrossRef] [PubMed]
- Gerba, C.P. Assessment of Enteric Pathogen Shedding by Bathers during Recreational Activity and its Impact on Water Quality Assessment of Enteric Pathogen Shedding by Bathers during Recreational Activity and its Impact on Water Quality. *Quant. Microbiol.* **2000**, *2*, 55–68. [CrossRef]
- Corsi, S.R.; Borchardt, M.A.; Spencer, S.K.; Hughes, P.E.; Baldwin, A.K. Human and bovine viruses in the Milwaukee River watershed: Hydrologically relevant representation and relations with environmental variables. *Sci. Total Environ.* **2014**, *490*, 849–860. [CrossRef] [PubMed]
- Montazeri, N.; Goettert, D.; Achberger, E.C.; Johnson, C.N.; Prinyawiwatkul, W.; Janes, M.E. Pathogenic Enteric Viruses and Microbial Indicators during Secondary Treatment of Municipal Wastewater. *Appl. Environ. Microbiol.* **2015**, *81*, 6436–6445. [CrossRef] [PubMed]
- Urase, T.; Yamamoto, K.; Ohgaki, S. Effect of pore structure of membranes and module configuration on virus retention. *J. Membr. Sci.* **1996**, *115*, 21–29. [CrossRef]
- Dolar, D.; Vukovi, A.; Asperger, D.; Kosuti, K. Effect of water matrices on removal of veterinary pharmaceuticals by nanofiltration and reverse osmosis membranes. *J. Environ. Sci.* **2011**, *23*, 1299–1307. [CrossRef]
- Slipko, K.; Reif, D.; Markus, W.; Hufnagl, P.; Krampe, J.; Kreuzinger, N. Removal of extracellular free DNA and antibiotic resistance genes from water and wastewater by membranes ranging from micro filtration to reverse osmosis. *Water Res.* **2019**, *164*, 114916. [CrossRef]



21. Cristóvão, M.B.; Bento-Silva, A.; Bronze, M.R.; Crespo, J.G.; Pereira, V.J. Detection of anticancer drugs in wastewater effluents: Grab versus passive sampling. 2020; submitted manuscript.
22. Bailly, E.; Levi, Y.; Karolak, S. Calibration and field evaluation of polar organic chemical integrative sampler (POCIS) for monitoring pharmaceuticals in hospital wastewater. *Environ. Pollut.* **2013**, *174*, 100–105. [[CrossRef](#)]
23. Ory, J.; Bricheux, G.; Togola, A.; Bonnet, J.L.; Donnadiou-bernard, F.; Nakusi, L.; Forestier, C.; Traore, O. Ciprofloxacin residue and antibiotic-resistant biofilm bacteria in hospital effluent. *Environ. Pollut.* **2016**, *214*, 635–645. [[CrossRef](#)]
24. Oliveira, M.; Nunes, M.; Crespo, M.T.B.; Silva, A.F. The environmental contribution to the dissemination of carbapenem and (fluoro) quinolone resistance genes by discharged and reused wastewater effluents: The role of cellular and extracellular DNA. *Water Res.* **2020**, *182*, 116011. [[CrossRef](#)]
25. Cantalupo, P.G.; Calgua, B.; Zhao, G.; Hundesa, A.; Wier, A.D.; Katz, J.P.; Grabe, M.; Hendrix, R.W.; Girones, R.; Wang, D.; et al. Raw Sewage Harbors Diverse Viral Populations. *mBio* **2011**, *2*, 1–11. [[CrossRef](#)] [[PubMed](#)]
26. Cristóvão, M.B.; Bernardo, J.; Bento-Silva, A.; Bronze, M.R.; Crespo, J.G.; Pereira, V.J. Treatment of anticancer drugs in a real wastewater effluent using nanofiltration: A pilot scale study. 2020; submitted manuscript.
27. Verlicchi, P.; Al Aukidy, M.; Jelic, A.; Petrovi, M.; Barceló, D. Comparison of measured and predicted concentrations of selected pharmaceuticals in wastewater and surface water: A case study of a catchment area in the Po Valley (Italy). *Sci. Total Environ.* **2014**, *471*, 844–854. [[CrossRef](#)] [[PubMed](#)]
28. Rossmann, J.; Schubert, S.; Gurke, R.; Oertel, R.; Kirch, W. Simultaneous determination of most prescribed antibiotics in multiple urban wastewater by SPE-LC-MS/MS Simultaneous determination of most prescribed antibiotics in multiple urban wastewater by SPE-LC-MS/MS. *J. Chromatogr. B* **2014**, *969*, 162–170. [[CrossRef](#)] [[PubMed](#)]
29. Pärnänen, K.M.M.; Narciso-da-rocha, C.; Kneis, D.; Berendonk, T.U.; Cacace, D.; Do, T.T.; Elpers, C.; Fatta-kassinos, D.; Henriques, I.; Jaeger, T.; et al. Giustina, Antibiotic resistance in European wastewater treatment plants mirrors the pattern of clinical antibiotic resistance prevalence. *Sci. Adv.* **2019**, *5*, 9124. [[CrossRef](#)] [[PubMed](#)]
30. La Rosa, G.; Pourshaban, M.; Iaconelli, M.; Muscillo, M. Quantitative real-time PCR of enteric viruses in influent and effluent samples from wastewater treatment plants in Italy. *Ann. Ist. Super. Sanità* **2010**, *46*, 266–273.
31. Nascimento, M.S.J.; Pereira, S.S.; Teixeira, J.; Abreu-silva, J. A nationwide serosurvey of hepatitis E virus antibodies in the general population of Portugal. *Eur. J. Public Health* **2017**, *28*, 720–724. [[CrossRef](#)]
32. Oliveira, R.; Mesquita, J.R.; Pereira, S.; Abreu-Silva, J.; Teixeira, J.; Nascimento, M.S.J. Seroprevalence of Hepatitis E Virus Antibodies in Portuguese Children. *Pediatr. Infect. Dis. J.* **2017**, *37*, 623–626. [[CrossRef](#)]
33. Berto, A.; Backer, J.A.; Mesquita, J.R.; Nascimento, M.S.J.; Banks, M.; Martelli, F.; Ostanello, F.; Angeloni, G.; Di Bartolo, I.; Ruggeri, F.M.; et al. Prevalence and transmission of hepatitis E virus in domestic swine populations in different European countries. *BMC Res. Notes* **2012**, *5*, 190. [[CrossRef](#)]
34. Mesquita, J.R.; Oliveira, R.M.S.; Coelho, C.; Nascimento, M.S.J. Hepatitis E Virus in Sylvatic and Captive Wild Boar from Portugal. *Transbound. Emerg. Dis.* **2016**, *63*, 574–578. [[CrossRef](#)]
35. Cuevas-ferrando, E.; Randazzo, W.; Pérez-cataluña, A. HEV Occurrence in Waste and Drinking Water Treatment Plants. *Front. Microbiol.* **2020**, *10*, 2937. [[CrossRef](#)]
36. Beyer, S.; Szwedzyk, R.; Gnirss, R.; John, R.; Christoph, H. Detection and Characterization of Hepatitis E Virus Genotype 3 in Wastewater and Urban Surface Waters in Germany. *Food Environ. Virol.* **2020**, *12*, 137–147. [[CrossRef](#)] [[PubMed](#)]
37. Lan, L.; Kong, X.; Sun, H.; Li, C.; Liu, D. High removal efficiency of antibiotic resistance genes in swine wastewater via nanofiltration and reverse osmosis processes. *J. Environ. Manag.* **2019**, *231*, 439–445. [[CrossRef](#)] [[PubMed](#)]
38. Lu, J.; Zhang, Y.; Wu, J.; Wang, J.; Cai, Y. Fate of antibiotic resistance genes in reclaimed water reuse system with integrated membrane process. *J. Hazard. Mater.* **2020**, *382*, 1–10. [[CrossRef](#)] [[PubMed](#)]
39. Gros, M.; Marti, E.; Luis, J.; Boy-roura, M.; Busquets, A.; Colón, J.; Sánchez-melsió, A.; Lekunberri, I.; Borrego, C.M.; Ponsá, S.; et al. Fate of pharmaceuticals and antibiotic resistance genes in a full-scale on-farm livestock waste treatment plant. *J. Hazard. Mater.* **2019**, *378*, 120716. [[CrossRef](#)]
40. Van der Bruggen, B.; Vandecasteele, C. Removal of pollutants from surface water and groundwater by nanofiltration: Overview of possible applications in the drinking water industry. *Environ. Pollut.* **2003**, *122*, 435–445. [[CrossRef](#)]
41. Pasalari, H.; Ataei-pirkooh, A.; Aminikhah, M.; Jonidi, A. Assessment of airborne enteric viruses emitted from wastewater treatment plant: Atmospheric dispersion model, quantitative microbial risk assessment, disease burden. *Environ. Pollut.* **2019**, *253*, 464–473. [[CrossRef](#)]
42. Wang, H.; Kjellberg, I.; Sikora, P.; Rydberg, H.; Lindh, M. Hepatitis E virus genotype 3 strains and a plethora of other viruses detected in raw and still in tap water. *Water Res.* **2020**, *168*, 115141. [[CrossRef](#)]

Article

# Treatment of Aqueous Effluents from Steel Manufacturing with High Thiocyanate Concentration by Reverse Osmosis

José R. Álvarez, F. Enrique Antón, Sonia Álvarez-García  and Susana Luque 

Department of Chemical and Environmental Engineering, University of Oviedo, 33071 Oviedo, Spain; jras@uniovi.es (J.R.Á.); feantonr@gmail.com (F.E.A.); alvarezsonia@uniovi.es (S.Á.-G.)

\* Correspondence: sluque@uniovi.es

Received: 16 November 2020; Accepted: 14 December 2020; Published: 18 December 2020



**Abstract:** The feasibility of reverse osmosis (RO) for treating coking wastewaters from a steel manufacturing plant, rich in ammonium thiocyanate was assessed. DOW FILMTEC™ SW30 membrane performance with synthetic and real thiocyanate-containing solutions was established at the laboratory and (onsite) pilot plant scale. No short-term fouling was observed, and the data followed the known solution-diffusion model and the film theory. Those models, together with non-steady state mass balances, were used in simulations that aided to design a full scale two-stage RO plant for thiocyanate separation.

**Keywords:** reverse osmosis; modeling; thiocyanate; wastewater treatment; process design

## 1. Introduction

As part of the steel manufacturing plant, the coke gas generated during the destructive distillation of coal is commonly washed with water at the coke oven exit and is then distributed to several facilities of the steel factory. The condensation of several compounds as the gas temperature decreases requires the use of purge pits placed along the pipe network. This generates an aqueous effluent, designated as coke wastewater in this study, which has to be treated before its definitive disposal. Coke wastewater is expected to contain the same pollutants than a typical refractory industrial wastewater (i.e., those used to quench the coke as it comes out of the blast furnaces or those employed during the cooling and cleaning of the gases), but at different concentrations. These residual streams contain cyanide, thiocyanate, high-strength ammonia, phenolic compounds, heterocyclic nitrogenous compounds and polynuclear aromatics compounds [1,2]. As the biological treatment has become the most reliable option to remove these pollutants, the steel factory has its own wastewater treatment plant in order to provide meaningful control over the detoxification and purification of the coke wastewater. Unfortunately, due to the refractory and inhibitory contaminants present in coking wastewater, the biological treatments are not sufficient.

Coke wastewaters with more than 400 mg/L of thiocyanate cause serious problems in the biological reactor. Phenols and free cyanide seriously inhibit various biological reactions, especially the nitrification reaction [3]. Thus, the biological treatment of the coke wastewater is not as easy as that of domestic wastewaters. To solve these problems, a large amount of  $\text{NH}_4\text{SCN}$  degradation processes are described in the literature, both chemical [4–6] and biological, using the anaerobic and anoxic denitrifiers process previously to the aerobic reactor [1,3,7–9]. However, since  $\text{NH}_4\text{SCN}$  is a salt with several industrial applications: antibiotic fermentations in pharmaceuticals, metal electroplating, flotation agent in metal industries, stabilizer and accelerator in photography, adjuvant in printing, finishing accelerator in fixing baths in textile industries, as a raw material for the production of

herbicides and rustproofing compositions, as a water tracer in oil fields [10] and its recovery is presented as a more interesting alternative.

The developed techniques for recovering thiocyanates can be classified in five groups: solvent extraction, distillation, gel filtration, membrane separation and, in recent years, electrochemical treatment methods [11–13]. Selective extraction is based on the difference of solubility, using a polar organic solvent that selectively extracts thiocyanate ions, but it requires high energy input for the subsequent recovery of the solvents. Distillation under pressure is a good alternative for obtaining a pure product but also needs a great amount of energy and generates gaseous thiocyanate, which is highly toxic. Gel filtration uses a polymer gel for separation, but it is expensive, slow and inefficient for large volumes. Electrochemical methods such as electro oxidation, electrocoagulation and electroflotation have been reported for the treatment of various wastewaters, and they have various benefits including simple equipment, easy operation, shortened retention time, rapid-settling and decreased amount of precipitate or sludge [14]. Nevertheless, these electrochemical methods are usually applied to the wastewater already biologically pretreated. On the other hand, membrane-based processes can safely separate thiocyanates from a large amount of wastewater with low energy consumption, which makes them suitable for addressing the  $\text{NH}_4\text{SCN}$  recovery.

Reverse osmosis (RO), forward osmosis (FO) and nanofiltration (NF) have been applied to wastewater from desulfuration of coke oven gas containing  $\text{NH}_4\text{SCN}$  [11,12], water from the ammonia-N liquor tank of a coke-making plant in India [15] and to an aqueous process stream from acrylic fiber industries containing  $\text{NaSCN}$  [13,16], respectively. RO has also been used to remove cyanides and ammonium salts, though at concentrations lower than those included in this study [17]. Additionally, when two thiocyanate salts are present, NF and/or RO membranes can be employed not only for recovering them, but also for separating one salt from another [18,19]. Recently, polymer inclusion membranes (PIM) have been also proposed as an appropriate method for cleaning-up of thiocyanate from gold mine waters [20]. Jin et al. (2013) reported a pilot-scale system based in the combined use of a membrane bioreactor as a pretreatment followed by the NF-RO system to treat coking wastewater reduced thiocyanate concentration to a level suitable for industrial reuse [21].

In the present work, several samples of the coke condensates taken from a steel factory were analyzed and found that  $\text{NH}_4\text{SCN}$  was the most important contaminant.

The experimental part focuses on assessing the performance of a RO commercial membrane with synthetic aqueous solutions of  $\text{NH}_4\text{SCN}$  and real wastewaters. Based on those experimental results, an appropriate mathematical model of the RO process is to be developed and used in the design of a full-scale RO plant. This RO plant design must treat a condensate flow rate of  $50 \text{ m}^3/\text{day}$  and produce a permeate with a low thiocyanate content, eligible for the biological wastewater treatment and a highly concentrated  $\text{NH}_4\text{SCN}$  solution, which can be used as raw material for several applications.

## 2. Materials and Methods

### 2.1. Experimental Equipment and Procedure

There are a variety of RO membranes available in the market, although each type is particularly suited to certain applications. From a preliminary screening (results not shown), a polymeric membrane from DOW FILMTEC™ (Edina, MN, USA) was selected: SW30. A spiral wound module of 2.5" (diameter) and 40" length was used for laboratory-scale experiments. Larger spiral modules (4"-40") were used for the pilot unit tests. Table 1 shows the specifications for both module types. The same modules were used throughout the whole study. No damage was observed, so no replacing was needed.

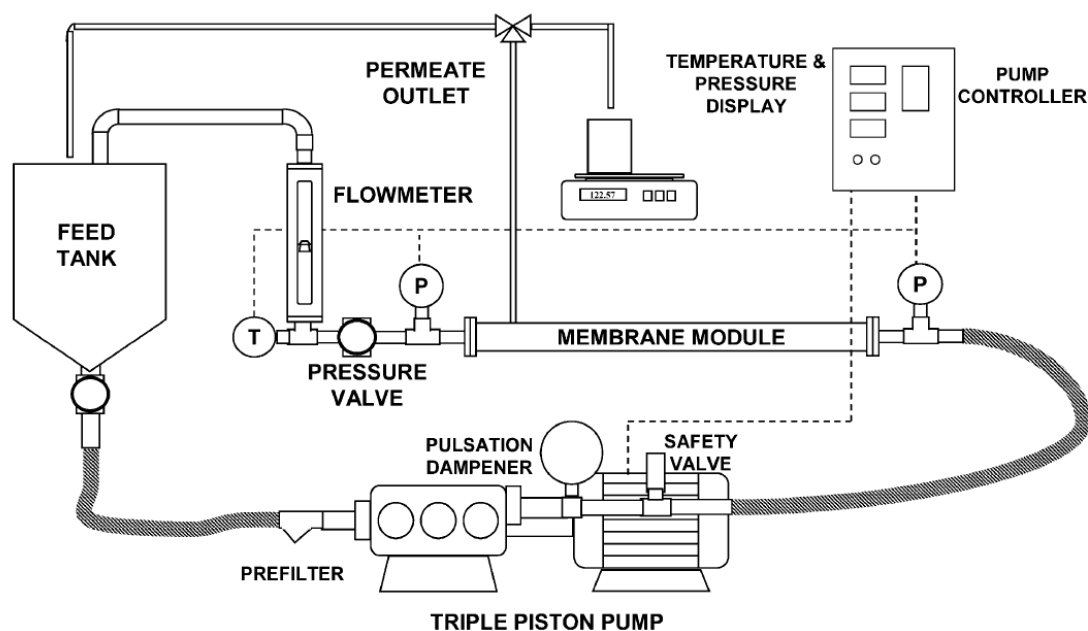
Figure 1 shows a diagram of the equipment used to perform laboratory experiments. It consists of a small filtration unit fed from a 100 L tank by a positive-displacement pump. Pressure transducers are placed before and after the module to monitor the pressure in the feed and retentate. Permeate is

open to atmosphere. A needle valve is placed after the membrane module to vary the applied pressure. Temperature is monitored using a Pt100 thermoresistance (WIKA, Kingenberg, Germany).

**Table 1.** Membrane specifications (according to the manufacturer).

Membrane Module	Nominal Active Surface Area (m <sup>2</sup> )	Maximum Feed Flow Rate (m <sup>3</sup> /h)	Stabilized Salt Rejection <sup>1</sup> (%)
SW30-2540	2.8	1.4	99.4
SW30-4040	7.4	3.6	99.4

<sup>1</sup> Measured at 32,000 mg/L NaCl, 55 bar, 25 °C and 8% recovery.



**Figure 1.** Experimental setup.

Although the condensates do not contain suspended solids, they do have a large number of suspended tar droplets. Tar is insoluble in most solvents and, thus, it is difficult to clean. It can deposit on equipment and at the inlet of the membrane modules, clogging them. Therefore, basic water filter cartridges (50 and 5 microns) were employed for its removal.

Pressure effect experiments were carried out at the total recycle, that is, retentate and permeate were recycled to the feed tank. Concentration experiments were carried out at constant pressure removing continuously the permeate.

The permeate flux through the membrane ( $J$ ) was calculated using the following equation:

$$J = \frac{M}{A_m \cdot \rho \cdot t} \tag{1}$$

where  $M$  is the permeate mass collected,  $\rho$  its density,  $A_m$  the membrane area and  $t$  the permeation time.

Membrane separation performance was assessed by means of retention (also called rejection), defined as:

$$\text{Retention (\%)} = \left(1 - \frac{c_P}{c_F}\right) \cdot 100 \tag{2}$$

where  $c_P$  and  $c_F$  are the concentrations in the permeate and in the feed, respectively.

The effect of pressure was assessed by conducting an experiment with increasing feed pressure from 10 up to 50 bar, in 10 bar intervals at constant temperature (25, 35 or 45 °C). In the concentration mode experiments, a constant temperature of 25 °C and a pressure of 50 bar were used. Results were

analyzed using the solution-diffusion model [22] and the classic film theory [23], with the following mathematical expressions for the overall permeate flux and for the solute flux, respectively:

$$J = A(\Delta P - \Delta\pi) \quad (3)$$

$$J = k \ln \frac{c_m - c_P}{c_B - c_P} \quad (4)$$

$$J_S = B (c_B - c_P) \quad (5)$$

where,

$J$ : Overall permeate flux (L/m<sup>2</sup> h).

$J_S$ : Solute flux,  $J_S = J \cdot c_P$ , (g/m<sup>2</sup> h).

$k$ : Mass transfer coefficient (L/m<sup>2</sup> h).

$c_m$ : Solute concentration on the membrane surface (g/L).

$c_B$ : Bulk solute concentration in the retentate (g/L).

$c_P$ : Solute concentration in the permeate (g/L).

$A$ : Solvent (water) membrane permeability (L/m<sup>2</sup> h bar).

$B$ : Solute membrane permeability (L/m<sup>2</sup> h).

In the data analysis presented, the solute is the thiocyanate ion. Equation (4) can be simplified when high retention membranes are used in reverse osmosis processes. As concentration in the permeate is generally much lower than that in the retentate, it can be neglected and when  $c_m$  is constant, according to the film theory:

$$J = const - k \ln(c_B) \quad (6)$$

Water permeability was checked before and after each run by checking tap water flux at five transmembrane pressures (from 10 to 50 bar). The osmotic pressure was negligible and the permeability was calculated as the slope,  $A$ , following Equation (3). The difference in water permeability was used as a way to estimate fouling.

Experiments were done also at the industrial site in the vicinity of one of the purge pits, using the same apparatus shown in Figure 1, but equipped with two commercial 4" RO membrane modules, with an overall filtration area of 15 m<sup>2</sup> (a six-fold increase from laboratory-scale). The two modules were placed in series, and a water-cooled shell and tube heat exchanger was also located after the modules for improving the temperature control.

Additionally, two 1 m<sup>3</sup> tanks were used as intermediate storage for the condensate feed to the module and to collect the permeate, respectively. The apparatus was also equipped with two auxiliary centrifugal pumps. One of them was used to pump the condensates out of the purge pit into the first 1 m<sup>3</sup> feed tank, and the other one was placed between the 100 L tank and the in-line prefilters, before the main high pressure pump, to overcome the prefiltration pressure drop and avoid cavitation at the suction of the high pressure pump.

The water filter cartridges used in the laboratory tests gave poor performance in the industrial installation, so they were replaced by in-line filters, with self-cleaning capability: A Rotorflush RF Series filters, capable of removing suspended solids above 50 microns, allowed maintaining constant flow rates with little maintenance.

Pilot testing lasted one month. It was not run continuously, but in daily 8–10 h shifts, because of the nature of the condensates collection (they were also drawn daily).

## 2.2. Analytical Methods

Samples were analyzed as follows:

- pH and conductivity were determined by a potentiometric method, using a Mettler Toledo Seven Multi Dual pH (Columbus, OH, USA) and conductivity meter.

- Chemical oxygen demand (COD) was determined by refluxing a sample in strongly acid solution with a known excess of potassium dichromate and then measuring the absorbance of the mixture at a wavelength of 620 nm with a HACH DR/2010 spectrophotometer (HACH Co, Loveland, CO, USA) [24].
- Phenolic compounds were characterized by their absorbance at 280 nm [25], with a T80 ultraviolet/visible (UV/VIS) spectrophotometer (PG Instruments Ltd., Leicestershire, UK)
- Total cyanide, free cyanide and weak acid dissociable cyanide concentrations were determined with the same T80 UV/VIS spectrophotometer at 300 nm after the reaction of HCN with chloramine-T, and the addition of a pyridine-barbituric acid agent. The hydrogen cyanide is generated by the alkaline distillation [24] or of ultraviolet radiation [26] on the sample.
- The thiocyanate ion was analyzed by their reaction with  $\text{Fe}(\text{NO}_3)_3 \cdot 9\text{H}_2\text{O}$  at low pH, because it forms an intense red color, suitable for colorimetric determination by a PG Instruments Ltd. T80 UV/VIS spectrometer at 460 nm [24].
- The concentration of ammonium was obtained through a potentiometric method, with a selective electrode (Mettler Toledo Type 15 223 3000 Ammonium Electrode) (Columbus, OH, USA) and an Ag/AgCl reference electrode (Mettler Toledo Type 373-90-WTE-ISE-S7) (Columbus, OH, USA) [27].
- $\text{SCN}^-$  and  $\text{NH}_4^+$  were also measured through ion-exchange chromatography, together other anions such as  $\text{SO}_4^{2-}$ ,  $\text{NO}_3^-$  and  $\text{Cl}^-$ . A Metrohm Ion Chromatograph 850 Professional IC (Metrohm AG, Herisau, Switzerland) was used, equipped with a Metrosep A Supp 5–100 column for anions, a Metrosep C 3–250/4.0 column for cations and a conductivimeter as a detector.
- Heavy metals and other atomic elements were evaluated by inductively coupled plasma (ICP) in an Agilent 7500 ICP-MS (mass spectrometer) device (Agilent, Santa Clara, CA, USA).

### 3. Results

#### 3.1. Analysis of the Samples

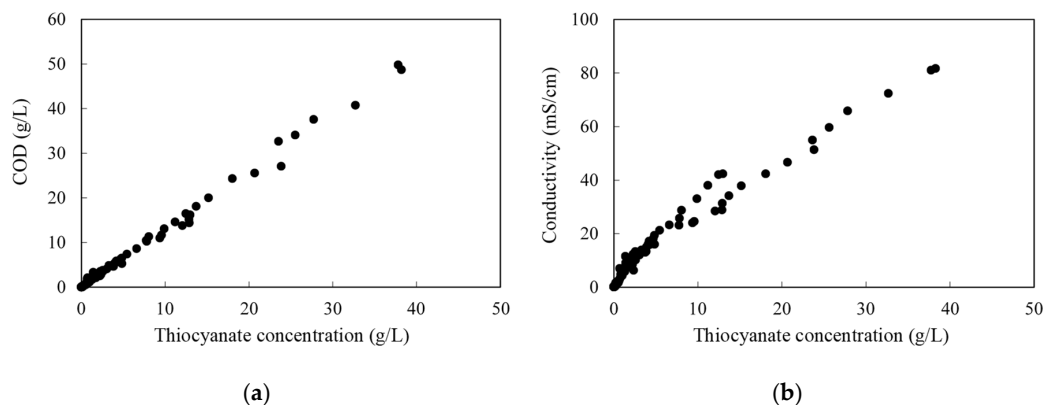
Several samples of the condensates were taken from the purge pits during four months, and then, analyzed. Over the first three months, 150 L of the actual condensates were collected weekly, shipped, and used for the lab-scale experiments. Pilot plant experiments were carried out onsite for a month and daily samples were also analyzed. The maxima and minima values of the studied parameters are given in Table 2. The major constituent in the coke wastewaters of this steel company is ammonium thiocyanate. Typical values for thiocyanate ions were between 1 and 3 g/L. Cyanide concentrations have not been included because they were always under the detection limit, 1 mg/L.

**Table 2.** Analyses of condensates collected during the sampling period.

Parameter/Element	Minimum	Maximum	Element	Minimum	Maximum
pH	8.6	9.1	Ca (mg/L)	0.6	3.5
Conductivity (mS/cm)	4.8	14.6	K (mg/L)	0.6	2.7
COD (g/L)	0.6	3.2	Si (mg/L)	0.0	2.1
$\text{SCN}^-$ (g/L)	0.2	9.0	Br (mg/L)	0.1	0.6
$\text{NH}_4^+$ (g/L)	1.0	12.9	I (mg/L)	0.0	0.2
Phenols (measured as absorbance at 280 nm)	1.16	3.55	Sr (mg/L)	0.0	0.1
$\text{SO}_4^{2-}$ (mg/L)	130	1007	Al (mg/L)	0.0	0.2
$\text{Cl}^-$ (mg/L)	6	50	Cu (mg/L)	0.0	5.0
$\text{NO}_3^-$ (mg/L)	12	60	Zn (mg/L)	0.0	0.1
Fe (mg/L)	12	30	As (mg/L)	0.0	0.1
Mg (mg/L)	0.9	13.6	B (mg/L)	0.0	0.2
Na (mg/L)	1.3	6.6	Ba (mg/L)	0.0	0.5
			Ge (mg/L)	0.0	0.3

Both thiocyanate and phenols can be oxidized, thus contributing to the COD load, but after an examination of the compiled data, it was concluded that the phenolic effect was rather limited,

being the most of the COD associated with the thiocyanate concentration (an almost linear relation between thiocyanate content and COD can be seen in Figure 2a). During these experiments, it was also observed that the conductivity was mainly influenced by the thiocyanate concentration (Figure 2b). This was useful for designing the experimental work, as conductivity is an easy parameter to follow.

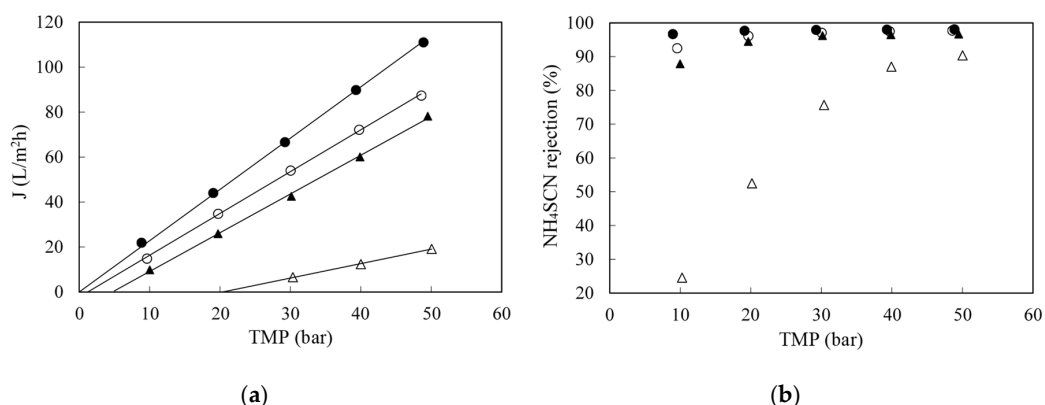


**Figure 2.** Chemical oxygen demand (COD; (a)) and conductivity at 25 °C (b) as a function of the thiocyanate concentration.

Ammonium thiocyanate is highly soluble in water (over 1.5 kg/L), and at high concentrations (above 300 g/L) conductivity does not behave proportionally to concentration (this was experimentally checked). This behavior was also found in concentrated sodium thiocyanate solutions [28]. However, the latter exhibits a maximum in conductivity that was not found in this work for the ammonium salt.

### 3.2. Effect of Operating Variables with Synthetic Solutions

The effect of pressure on RO of synthetic  $\text{NH}_4\text{SCN}$  solutions between 1 and 50 g/L in the temperature range 25–45 °C was evaluated in the total recycle mode. Figure 3a shows the effect of pressure at 25 °C. As the concentration increased, the permeate flow decreased, since polarization and osmotic pressure increased. The former resulted in a lower slope, while the latter implies that more pressure had to be applied in order obtain flux through the membrane. For a given concentration, as the transmembrane pressure increased, the permeate flux also increased. No membrane fouling was seen, as water permeability before and after each experiment was the same.



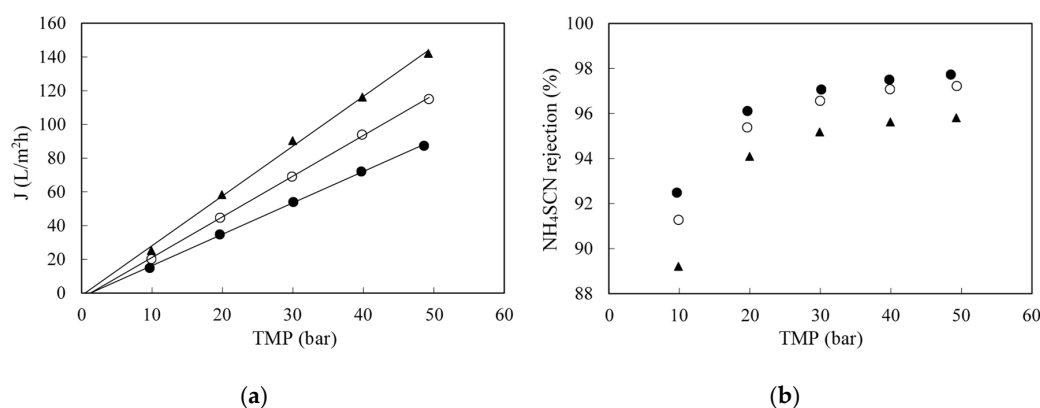
**Figure 3.** Effect of concentration on permeate flux (a) and on  $\text{NH}_4\text{SCN}$  retention (b) when filtering synthetic solutions of ammonium thiocyanate at 25 °C with the SW30-2540 RO membrane. (●): 1 g/L; (○): 5 g/L; (▲): 10 g/L and (△): 50 g/L.

As concentration increased, salt rejection also decreased, as it can be seen in Figure 3b. This is the result of a decreased water flux, as shown in Figure 3a together with an increase in solute diffusion,

owing to the larger concentration difference across the membrane (the latter is the driving force for diffusional transport). Therefore, the thiocyanate concentration plays a very important role in the filtration process. As it increases, it actually influences negatively the performance of the process, decreasing the filtration rate and salt rejection.

The experimental osmotic pressures computed from the linear regression of the data shown in Figure 3 were compared with those calculated by the Morse (a modified Van't Hoff) equation [29], assuming that  $\text{NH}_4\text{SCN}$  was fully dissociated. The Morse equation gave values higher than the experimentally determined ones at any condition. That is an indication that the salt is not entirely dissociated.

The effect of the temperature on permeate flux can be seen in Figure 4a. Within the concentration range studied, the higher the temperature, the higher the permeate flux. It can be explained by the reduced viscosity, which reduced the resistance of water transport through the membrane and higher membrane permeability. However, as temperature increased, ammonium thiocyanate retention decreased (Figure 4b). This is again inherent to the nature of the separation process, in which the solute transport through the membrane is a function of the solute solubility and diffusion coefficient in the membrane. Both solubility and diffusivity increased exponentially with temperature, so the solute permeability (the product of solubility and diffusivity) increased to a much larger extent than the water flux (associated with viscosity). The result was the observed reduced retention.



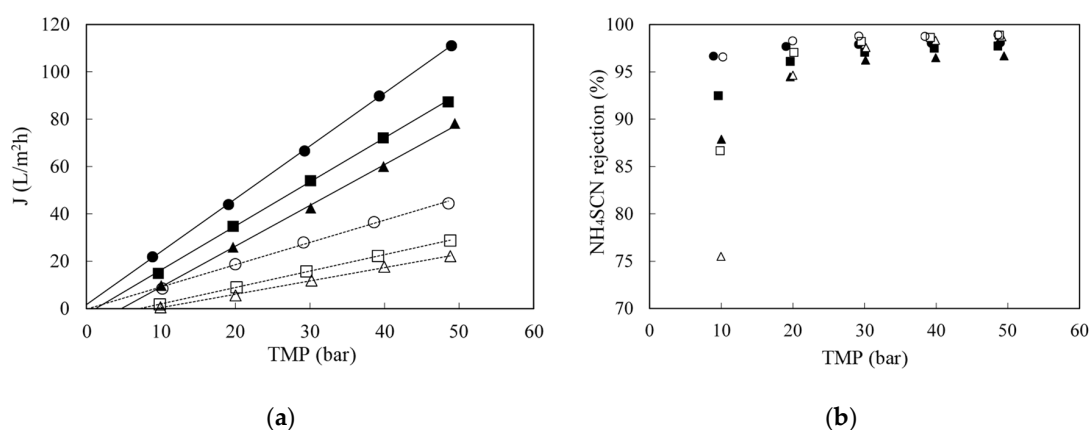
**Figure 4.** Effect of temperature on permeate flux (a) and on  $\text{NH}_4\text{SCN}$  retention (b) when filtering a 5 g/L  $\text{NH}_4\text{SCN}$  synthetic solutions with the SW30-2540 RO membrane. (●): 25 °C; (○): 35 °C and (▲): 45 °C.

### 3.3. Effect of the Transmembrane Pressure with Real Wastewaters

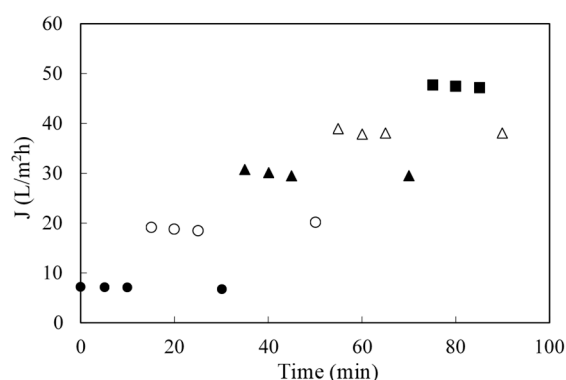
The fluxes obtained with the real coking wastewaters were lower (Figure 5a) than those obtained with synthetic solutions, but they followed the same trends with respect to pressure and feed concentration. However, rejections were similar at and above 20 bar, as shown in Figure 5b. A minimum pressure of 20 bar is required for ensuring rejections above 90%. The results shown are an extract of those performed with the weekly samples.

To account for fouling, water permeability was measured before and after each filtration. No significant change was observed and no chemical cleaning was needed. The same RO module was used for all experiments. To further analyze fouling, a hysteresis experiment was also carried out, following the evolution of flux with time at each transmembrane pressure (TMP) was monitored as shown in Figure 6. An operating pressure was selected and the permeate flux was measured for over a period of time (normally flux declines with time, so data was collected until stable flux was reached); then, the pressure was increased to achieve a new stable permeate flux and, before proceeding to the higher next pressure it was decreased to its previous value to account for irreversible fouling owing to increased pressure [30].





**Figure 5.** Effect of concentration on permeate flux (a) and on NH<sub>4</sub>SCN retention (b) when synthetic solutions (S) and real coke gas condensates (R) are filtered at 25 °C with the SW30-2540 RO membrane. (●): S-1 g/L; (○): R-0.8 g/L; (■): S-5 g/L; (□): R-4 g/L; (▲): S-10.0 g/L and (△): R-9.0 g/L.

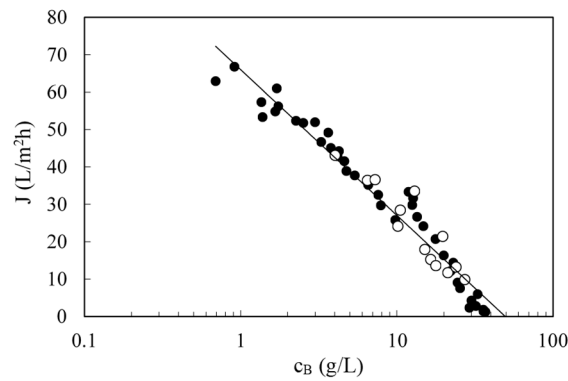


**Figure 6.** Effect of transmembrane pressure (TMP) on flux stability at 25 °C. Membrane SW30-2540 and NH<sub>4</sub>SCN concentration around 1 g/L. TMP were (●): 10 bar; (○): 20 bar; (▲): 30 bar; (△): 40 bar; and (■): 50 bar.

Since the flux remained stable and there was no decrease in water permeability, it can be concluded that there was no significant (short-term) fouling observed. Flux decline with respect to water flux was, thus, associated with the reversible phenomena, i.e., polarization. The ammonia content and high pH of the condensates, together with a lack of organic matter and scaling inorganic salts were believed to be the main reason for flux stability. This very positive result marked the industrial viability of the RO treatment, since membrane fouling (and the subsequent flux decayed with time) is a key challenge and obstacle for applying membrane technologies to industrial processes [31]. However, for a full-scale plant it is recommended to install—as backup—a clean-in-place unit, for eventual rinsing, cleaning or maintenance of the RO plant.

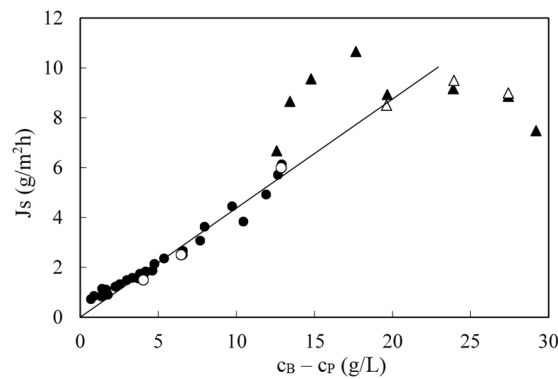
### 3.4. Effect of Feed Concentration with Real Wastewaters

Due to the variations in the initial concentration (in the weekly samples and in the daily condensates fed to the pilot unit), fluxes also differed from day to day at the same pressure. When all data were plotted together, flux decreased with concentration (Figure 7). Laboratory (black circles) and pilot scale (open circles) results followed the same trend. Flux follows a logarithmic dependence with concentration, as film theory predicts (Equation (4)). The constant term in Equation (6) and the mass transfer coefficient can be calculated from the fitting line, being 66.0 L/m<sup>2</sup> h and 16.9 L/m<sup>2</sup> h, respectively.



**Figure 7.** Permeate flux as a function of retentate concentration for several runs. Data collected at 50 bar and 25 °C. Filled circles are data obtained in the laboratory and empty circles are data obtained in onsite pilot tests at the steel factory. Solid line is the fitting to Equation (6).

To calculate the solute permeability, a plot of the solute flux vs. the concentration difference between the retentate and permeate is required as shown in Figure 8. This figure, again, includes data from multiple runs. The slope of the straight line was  $B$  (0.438 L/m<sup>2</sup> h) according to Equation (5) of the solution-diffusion model. At higher concentrations, towards the end of the batch concentration runs, implying lower volumes in the feed tank, temperature was more difficult to control and there was more data scattering (shown as triangles). Those values were not included in the regression.



**Figure 8.** Solute flux through the membrane as a function of the difference between retentate and permeate concentrations for several runs. Data collected at 50 bar and 25 °C (circles) and at various temperatures (triangles). Filled and empty symbols have the same meaning that in Figure 7. Solid line is the fitting of circles to Equation (4).

The initial assumption that permeate concentration was negligible seems reasonable only at low feed concentrations. When retentate concentration rose, solute flux through the membrane also increased leading to a rise in permeate concentration, which could reach non-negligible values. Therefore, for the complete validation of the model, a batch concentration operation was simulated using non-steady mass balances and the transport equations, and compared with experimental data. Firstly, it was taken into account that only the permeate stream left the process. Thus, the overall and solute non-steady mass balances can be written as follows:

$$\frac{dV}{dt} = -J A_m \tag{7}$$

$$\frac{d(V \cdot c)}{dt} = -J A_m c_P \tag{8}$$

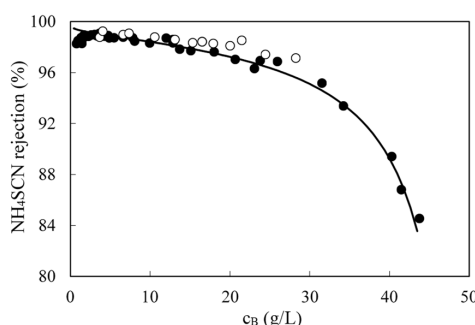
where  $V$  is the volume of the feed/retentate remaining in the tank at a given time,  $c$  the thiocyanate concentration in the feed tank at the same given time and  $A_m$  the membrane surface area. Developing Equation (8) and substituting Equation (7) in it results in the following expression:

$$\frac{dc}{dV} = -\frac{(c - c_P)}{V} \tag{9}$$

Combining Equations (5) and (6), and considering that the solute and solvent flux are related by the solute concentration in the permeate,  $J_s = J.c_P$ , the resulting expression is as follows:

$$c_{Pi} = \frac{B c_i}{B + const - k \ln(c_i)} \tag{10}$$

The numerical integration of Equation (9) along with Equation (10) with the experimentally determined values of  $B$ ,  $const$  and  $k$ , allowed the mathematical description of the complete RO process. As it can be seen in Figure 9, the proposed transport model fit successfully the experimental results over the whole concentration range. Therefore, this model will be used for the design of the full-scale RO plant.



**Figure 9.** Influence of SCN-concentration on the membrane rejection of this ion. Filled circles are data obtained in the laboratory, empty symbols are experiments done in the steel factory and the solid line is the model prediction.

### 3.5. Design of a RO Plant for Continuous Operation

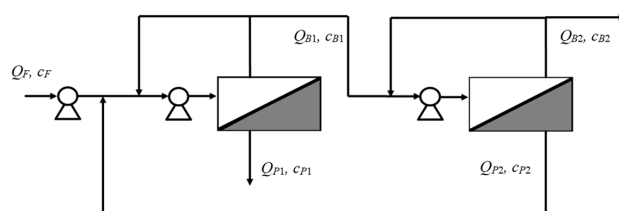
Based on the experimental results and the model, a full scale RO plant was designed. The plant must treat a condensate flow rate of 50 m<sup>3</sup>/day and produce a permeate with a low thiocyanate content, eligible for the biological wastewater treatment and a retentate concentrated in NH<sub>4</sub>SCN. The RO plant design began with the easiest assembly, a single stage. The operation mode chosen for the system was fed and bled (a part of the retentate stream is recycled to the stage input) since it allows working in the best hydrodynamics conditions. Based on the aforementioned limited capability of the biological digestion to treat thiocyanate, the target maximum permeate concentration was set at 300 mg/L (0.3 g/L).

Initial values needed for solving the corresponding model equations were the feed flow rate and feed concentration. The feed flow rate was set at 50 m<sup>3</sup>/day. As thiocyanate concentrations falls typically in the range 1–3 g/L, but at times the concentration may spike to 9 g/L, those three values were chosen for calculating different case studies. The membrane area and water recovery (ratio between permeate flow and feed flow) were varied and the resulting permeate concentrations calculated. In order to achieve high recovery, upstream concentration has to increase. One stage was unable to meet the maximum allowed permeate concentration when the concentration was above 10 g/L.

To overcome this restriction, which is inherent to the lack of flexibility of a single stage design, a two-stage RO process with internal recycle was then proposed. The first stage treats the condensates, and produces a permeate stream, which always meets the concentration restrictions for reuse or biological treatment. The second stage allows the concentration of thiocyanate in the retentate stream

to a greater extent, while yielding a permeate stream, exceeding the 0.3 g/L, that is internally recycled to the front end of the RO process.

The operating mode of each stage continues to be fed and bled. Thus, the retentate stream of each stage is recycled back at the beginning of each stage respectively to allow proper hydrodynamics conditions as shown in Figure 10.



**Figure 10.** The two-stage reverse osmosis process working in the feed and bleed mode with internal recycle.

The design equations used, in addition to the solution-diffusion and film theory expressions given in Equations (4) and (10), are the overall and solute mass balances for the two stage process:

$$Q_F = Q_{B2} + Q_{P1} \tag{11}$$

$$Q_F c_F = Q_{B2} c_{B2} + Q_{P1} c_{P1}, \tag{12}$$

and the balances around the recycled permeate stream and first stage:

$$Q_{B1} + Q_{P1} = Q_F + Q_{P2} \tag{13}$$

$$Q_{B1} c_{B1} + Q_{P1} c_{P1} = Q_F c_F + Q_{P2} c_{P2} \tag{14}$$

where  $Q$  denotes flowrate,  $c$  denotes concentration at the stream locations indicated in Figure 10.

The required membrane area,  $A_m$ , for each stage  $j$ , can be calculated from the ratio of permeate flowrate and permeate flux:

$$A_{mj} = \frac{Q_{Pj}}{J_j} \tag{15}$$

In order to solve the above set of equations, it was necessary to define the feed flow rate, feed concentration (1, 3 or 9 g/L) and two more parameters, one for each stage, respectively. For the first one, permeate concentration was specified (0.3 g/L). For the second one, permeate concentration was also selected and matched to be the same as the fresh condensate feed entering the first stage, although other options are possible for this second variable (i.e., a given thiocyanate concentration in the final retentate to facilitate further processing). The optimization criterion was to minimize the total membrane area (as the sum of the areas of stage 1 and 2,  $A_{m1}$  and  $A_{m2}$ ).

After the corresponding calculations, it was found that  $A_{m1}$  and  $A_{m2}$  were 50 and 41 m<sup>2</sup>, respectively. For this design, Table 3 indicates volumetric flowrates and concentrations for different feed concentrations. The designed plant would be able to treat condensates in within the studied (1–9 g/L) thiocyanate feed concentrations always meeting the design constrains by adjusting the recovery. In practice, this can be easily automated with an in-line conductivity sensor.

**Table 3.** Volumetric flowrate in L/h (thiocyanate concentration in g/L) for the selected two-stage reverse osmosis process design.

$Q_F (c_F)$	$Q_{P1} (c_{P1})$	$Q_{B1} (c_{B1})$	$Q_{P2} (c_{P2})$	$Q_{B2} (c_{B2})$
2083 (1.0)	2007 (0.050)	525 (4.6)	449 (1.0)	76 (26.0)
2083 (3.0)	1750 (0.078)	1025 (6.3)	691 (0.5)	334 (18.0)
2083 (9.0)	1176 (0.226)	1525 (12.4)	617 (0.6)	907 (20.4)

#### 4. Conclusions

Reverse osmosis using commercial SW30-2540 membrane, from DOW FILMTEC™, was proved to be a feasible technology in the recovery of thiocyanates from the coke gas condensates. The transmembrane pressure, temperature and feed concentration were the main operating variables. The permeate flux increased with temperature and transmembrane pressure but decreased with the feed concentration. On the other hand, NH<sub>4</sub>SCN rejection increased with pressure (especially at low feed concentrations), but decreased with concentration and temperature.

The pilot plant runs were conducted to validate the lab-scale experiments with fresh condensate feed, which typically show daily variation in concentration, and was a major concern for plant performance. Confirmation of the absence of short-term fouling observed in lab-scale experiments was also targeted. No fouling was observed throughout all the pilot runs carried out, despite the variable feed concentration and temperature. Therefore, no cleaning cycles were needed. However, for a full-scale plant it is recommended to install—as backup—a clean-in-place unit, for eventual rinsing, cleaning or maintenance of the RO plant. The precaution that was required in the onsite testing was a prefiltration step to remove suspended tar particles.

Experiments performed with samples in the laboratory and with fresh wastewater in the steel factory were in good agreement. The solution-diffusion model and the classic film theory can be combined for representing the process, fitting only three parameters. These models together with mass balances were applied for designing a full RO plant for treating 50 m<sup>3</sup>/day of condensates in a continuous mode (with NH<sub>4</sub>SCN concentrations in the range 1–3 g/L, but that can reach eventually values of 9 g/L). The most appropriate design has two stages with internal recycle, with 50 m<sup>2</sup> of membrane area in the first stage and 41 m<sup>2</sup> in the second stage. In this way, permeates with concentrations of thiocyanate under 0.3 mg/L and retentate streams concentrated up to more than 20 g/L were obtained.

**Author Contributions:** Conceptualization, J.R.Á. and S.L.; methodology, F.E.A., S.Á.-G. and S.L.; validation, F.E.A. and J.R.Á.; formal analysis and investigation, F.E.A., J.R.Á. and S.L.; resources, J.R.Á.; writing—original draft preparation, F.E.A. and S.Á.-G.; writing—review and editing, J.R.Á. and S.L.; supervision, S.L. All authors have read and agreed to the published version of the manuscript.

**Funding:** This research was funded by Consejería de Educación y Ciencia—Principado de Asturias, Spain, grant number FC-08-PEST08-14-4.

**Conflicts of Interest:** The authors declare no conflict of interest.

#### References

- Kim, Y.M.; Park, D.; Jeon, C.O.; Lee, D.S.; Park, J.M. Effect of HRT on the biological pre-denitrification process for the simultaneous removal of toxic pollutants from cokes wastewater. *Biores Technol.* **2008**, *99*, 8824–8832. [[CrossRef](#)] [[PubMed](#)]
- Wei, X.-X.; Zhang, Z.-Y.; Fan, Q.-L.; Yuan, X.-Y.; Guo, D.-S. The effect of treatment stages on the coking wastewater hazardous compounds and their toxicity. *J. Hazard. Mater.* **2012**, *239–240*, 135–141. [[CrossRef](#)] [[PubMed](#)]
- Staib, C.; Lant, P. Thiocyanate degradation during activated sludge treatment of coke-ovens wastewater. *Biochem. Eng. J.* **2007**, *34*, 122–130. [[CrossRef](#)]
- Balawejdar, E.K. A macromolecular *N,N*-dichloro-sulfonamide as oxidant for thiocyanates. *Eur. Polym. J.* **2000**, *36*, 1137–1143. [[CrossRef](#)]
- Sharma, V.K.; Burnett, C.R.; O'Connor, D.B.; Cabelli, D. Iron(VI) and iron(V) oxidation of thiocyanate. *Environ. Sci. Technol.* **2002**, *36*, 4182–4186. [[CrossRef](#)] [[PubMed](#)]
- Jensen, J.N.; Tuan, Y.-J. Chemical Oxidation of Thiocyanate Ion by Ozone. *Ozone Sci. Eng.* **1993**, *15*, 343–360. [[CrossRef](#)]
- Lay-Son, M.; Drakides, C. New approach to optimize operational conditions for the biological treatment of a high-strength thiocyanate and ammonium waste: pH as key factor. *Water Res.* **2008**, *42*, 774–780. [[CrossRef](#)]

8. Jeong, Y.S.; Chung, J.S. Biodegradation of thiocyanate in biofilm reactor using fluidized-carriers. *Proc. Biochem.* **2006**, *41*, 701–707. [[CrossRef](#)]
9. Hung, C.-H.; Pavlostathis, S.G. Aerobic biodegradation of thiocyanate. *Water Res.* **1997**, *31*, 2761–2770. [[CrossRef](#)]
10. Kirk, R.E.; Othmer, D.F. *Encyclopedia of Chemical Technology*, 4th ed.; John Wiley & Sons: New York, NY, USA, 1997; Volume 23, p. 322.
11. Kawasaki, S.; Kohara, N. Process for Recovering Thiocyanate. U.S. Patent Number 5.344.564, 6 September 1994.
12. Minhalma, M.; de Pinho, M.N. Integration of nanofiltration/steam stripping for the treatment of coke plant ammoniacal wastewaters. *J. Membrane Sci.* **2004**, *242*, 87–95. [[CrossRef](#)]
13. Sridhar, S.; Smith, B. New Developments in Nanofiltration Technology: A Case Study on Recovery of Impurity-Free Sodium Thiocyanate for Acrylic Fiber Industry. In *Handbook of Membrane Separations. Chemical, Pharmaceutical, Food, and Biotechnological Applications*; Pabby, A.K., Rizvi, S.H., Sastre, A.M., Eds.; Taylor & Francis Group: Boca Raton, FL, USA, 2008; pp. 1101–1129.
14. Ozyonar, F.; Karagozoglu, B. Treatment of pretreated coke wastewater by electrocoagulation and electrochemical peroxidation processes. *Sep. Purif. Technol.* **2015**, *150*, 268–277. [[CrossRef](#)]
15. Kumar, R.; Pal, P. A novel forward osmosis-nano filtration integrate system for coke-oven wastewater reclamation. *Chem Eng. Res. Des.* **2015**, *100*, 542–553. [[CrossRef](#)]
16. Sridhar, S.; Gorugantu, S.M.; Duraiswamy, S.; Biduru, S.; Machiraju, R. Recovery of Sodium Thiocyanate from Industrial Process Solution using Nanofiltration Technique. U.S. Patent Number 7,314,606, 1 January 2008.
17. Bódalo-Santoyo, A.; Gómez-Carrasco, J.L.; Gómez-Gómez, E. Application of reverse osmosis to reduce pollutants present in industrial wastewater. *Desalination* **2003**, *155*, 101–108. [[CrossRef](#)]
18. Yin, N.; Liu, F.; Zhong, Z.; Xing, W. Integrated Membrane Process for the Treatment of Desulfurization Wastewater. *Ind. Eng. Chem. Res.* **2010**, *49*, 3337–3341. [[CrossRef](#)]
19. Yin, N.; Liu, F.; Zhong, Z.; Xing, W. Separation of ammonium salts from coking wastewater with nanofiltration combined with diafiltration. *Desalination* **2011**, *268*, 233–237. [[CrossRef](#)]
20. Cho, Y.; Cattrall, R.W.; Kolev, S.D. A novel polymer inclusion membrane based method for continuous clean-up of thiocyanate from gold mine tailings water. *J. Hazard. Mater.* **2018**, *341*, 297–303. [[CrossRef](#)]
21. Jin, X.; Li, E.; Lu, S.; Qiu, Z.; Sui, Q. Coking wastewater treatment for industrial reuse purpose: Combining biological processes with ultrafiltration, nanofiltration and reverse osmosis. *J. Environ. Sci.* **2013**, *25*, 1565–1574. [[CrossRef](#)]
22. Bhattacharyya, D.; Williams, M.E.; Ray, R.J.; McGray, S.B. Theory of Reverse Osmosis. In *Membrane Handbook*; Ho, W.S., Sirkar, K.K., Eds.; Van Nostrand Reinhold: New York, NY, USA, 1992; pp. 269–280.
23. Field, R.W. Mass transport and the design of membrane systems. In *Industrial Membrane Separation Technology*; Scott, K., Hughes, R., Eds.; Blackie Academy and Professionals; Imprint of Chapman and Hall: Glasgow, UK, 1996; pp. 67–113.
24. American Public Health Association, American Water Works Association, Water Pollution Control Federation. *Standard Methods for the Examination of Water and Wastewater*, 17th ed.; Spanish Translation; Ediciones Diaz de Santo: Madrid, Spain, 1992; pp. 2-80–2-85, 4-23–4-43, 4-48–4-50, 5-19.
25. Knutsson, M.; Johnson, J.A. Determination of phenolic compounds in water. In *Handbook of Water Analysis*; Nollet, L.M.L., Ed.; Marcel Dekker: New York, NY, USA, 2000; pp. 347–366.
26. ISO 14403 (2002). *Water Quality—Determination of Total Cyanide and Free Cyanide by Continuous Flow Analysis*; ISO: Geneva, Switzerland, 2002.
27. ISO 6778 (1984). *Water Quality—Determination of Ammonium—Potentiometric Method*; ISO: Geneva, Switzerland, 1984.
28. Rohman, N.; Wahab, A.; Daas, N.N.; Mahiuddin, S. Viscosity, electrical conductivity, shears relaxation time and Raman spectra of aqueous and methanolic sodium thiocyanate solutions. *Fluid Phase Equil.* **2001**, *178*, 277–297. [[CrossRef](#)]
29. Sagiv, A.; Avraham, N.; Dosoretz, C.G.; Semiat, R. Osmotic backwash mechanism of reverse osmosis membranes. *J. Membr. Sci.* **2008**, *322*, 225–233. [[CrossRef](#)]
30. Vegas, R.; Moure, A.; Dominguez, H.; Parajo, J.C.; Alvarez, J.R.; Luque, S. Evaluation of ultra- and nanofiltration for refining soluble products from rice husk xylan. *Biores. Technol.* **2008**, *99*, 5341–5351. [[CrossRef](#)]

31. Chen, K.L.; Song, L.; Ong, S.L.; Ng, W.J. The development of membrane fouling in full-scale RO processes. *J. Membr. Sci.* **2004**, *232*, 63–72. [[CrossRef](#)]

**Publisher’s Note:** MDPI stays neutral with regard to jurisdictional claims in published maps and institutional affiliations.



© 2020 by the authors. Licensee MDPI, Basel, Switzerland. This article is an open access article distributed under the terms and conditions of the Creative Commons Attribution (CC BY) license (<http://creativecommons.org/licenses/by/4.0/>).

Article

# Pertraction of Co(II) through Novel Ultrasound Prepared Supported Liquid Membranes Containing D2EHPA. Optimization and Transport Parameters

Gerardo León <sup>1,\*</sup>, Asunción María Hidalgo <sup>2</sup>, Beatriz Miguel <sup>1</sup> and María Amelia Guzmán <sup>1</sup>

<sup>1</sup> Departamento de Ingeniería Química y Ambiental, Universidad Politécnica de Cartagena, Paseo Alfonso XIII, 30203 Cartagena, Spain; beatriz.miguel@upct.es (B.M.); maguzmanmv@gmail.com (M.A.G.)

<sup>2</sup> Departamento de Ingeniería Química, Campus de Espinardo, Universidad de Murcia, 30100 Murcia, Spain; ahidalgo@um.es

\* Correspondence: gerardo.leon@upct.es

Received: 30 November 2020; Accepted: 15 December 2020; Published: 17 December 2020



**Abstract:** Pertraction of Co(II) through novel supported liquid membranes prepared by ultrasound, using bis-2-ethylhexyl phosphoric acid as carrier, sulfuric acid as stripping agent and a counter-transport mechanism, is studied in this paper. Supported liquid membrane characterization through scanning electron microscopy, energy-dispersive X-ray spectroscopy and Fourier transform infrared spectroscopy shows the impregnation of the microporous polymer support by the membrane phase by the action of ultrasound. The effect on the initial flux of Co(II) of different experimental conditions is analyzed to optimize the transport process. At these optimal experimental conditions (feed phase pH 6, 0.5 M sulfuric acid in product phase, carrier concentration 0.65 M in membrane phase and stirring speed of 300 rpm in both phases) supported liquid membrane shows great stability. From the relation between the inverse of Co(II) initial permeability and the inverse of the square of carrier concentration in the membrane phase, in the optimized experimental conditions, the transport resistance due to diffusion through both the aqueous feed boundary layer ( $3.7576 \times 10^4 \text{ s}\cdot\text{m}^{-1}$ ) and the membrane phase ( $1.1434 \times 10^{10} \text{ s}\cdot\text{m}^{-1}$ ), the thickness of the aqueous feed boundary layer ( $4.0206 \times 10^{-6} \text{ m}$ ) and the diffusion coefficient of the Co(II)-carrier in the bulk membrane ( $4.0490 \times 10^{-14} \text{ m}^2\cdot\text{s}^{-1}$ ), have been determined.

**Keywords:** cobalt(II); supported liquid membranes; ultrasound; D2EHPA; counter-transport; transport parameters

## 1. Introduction

Cobalt is associated with many industrial and technological activities such as mining, hydrometallurgy, medicine and the manufacture of batteries, steels, magnetic alloys, catalysts, glass, ceramics, paints, lacquers, etc. [1]. Due to its industrial significance, cobalt production has grown steadily over the last two decades, from 56,635 tons in 2005 [2] to 124,344 tons in 2018 [3], leading to both the decrease of primary cobalt resources and the increase in cobalt waste.

Moreover, the presence of cobalt in the wastewater of the above industries is an important environmental problem because, like other heavy metals, it is not biodegradable and tends to accumulate in living organisms, causing diseases and disorders. The acute effects of cobalt on humans affect cardiovascular, endocrine, hematological, respiratory and nervous systems [4].

All this makes the recovery of cobalt from raw materials and secondary sources very interesting from both environmental and economic reasons.



Different techniques have been described for cobalt removal from aqueous solutions, including flocculation [5], adsorption [6–9], biosorption [10–12], phytoremediation [13], solvent extraction [14,15], ion exchange [16] capacitive deionization [17], electrowinning [18], micellar enhanced ultrafiltration [19], nanofiltration [20], reverse and forward osmosis [21,22], membrane distillation [23], liquid membranes [24–27] and combined methods [28].

Liquid membranes are receiving great attention as a separation process because they combine the extraction and the recovery processes in a single continuous stage [29]. In a liquid membrane, two miscible phases (feed and product phases) are separated by an immiscible phase (membrane phase). Supported liquid membranes (SLM) are obtained when the pores of a thin microporous solid support are filled with the membrane phase [29].

Traditionally, the filling of these pores has been carried out by impregnation of the microporous support by the liquid membrane solution under pressure or under vacuum. In this paper, we use a novel method based on the effects of ultrasound. The application of ultrasound to a liquid medium causes mechanical vibration and acoustic streaming. As the liquid medium usually contains dissolved gaseous nuclei, ultrasound generates acoustic cavitation (expanding and collapsing them), releasing large amounts of energy that generate, among other effects, shock waves and micro jets [30]. Polyvinylidene fluoride (PVDF) has been selected as the microporous support, due to its greater resistance to the ultrasound mechanical effects [31,32].

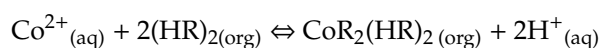
Transport in a liquid membrane system is usually improved by adding to the membrane phase a complexing agent (carrier) to carry the diffusing species across the membrane to the product phase [33]. This process can be accompanied by the transport of other chemical species from the product to the feed phase (coupled counter-transport mechanism), which offers the possibility of transporting a component against its own concentration gradient [34].

In this paper we study the Co(II) pertraction from an acetate buffered aqueous feed phase to an aqueous product phase which contains sulfuric acid as stripping agent (protons as counter ions), through an ultrasound prepared supported liquid membrane containing D2EHPA in kerosene, by using a coupled counter-transport mechanism.

To optimize the pertraction process, the effect on Co(II) initial flux of different experimental conditions (pH of the feed phase, carrier concentration in the membrane phase, stripping agent concentration in the product phase and stirring rate in both feed and product phases) is analyzed. From the relation between the inverse of Co(II) initial permeability and the inverse of the square of carrier concentration in the membrane phase, at the optimal experimental conditions, the transport resistance due to diffusion through both the aqueous feed boundary layer and the membrane phase, the thickness of the aqueous feed boundary layer and the diffusion coefficient of the Co(II)-carrier in the bulk membrane phase are determined.

## 2. Theoretical Background

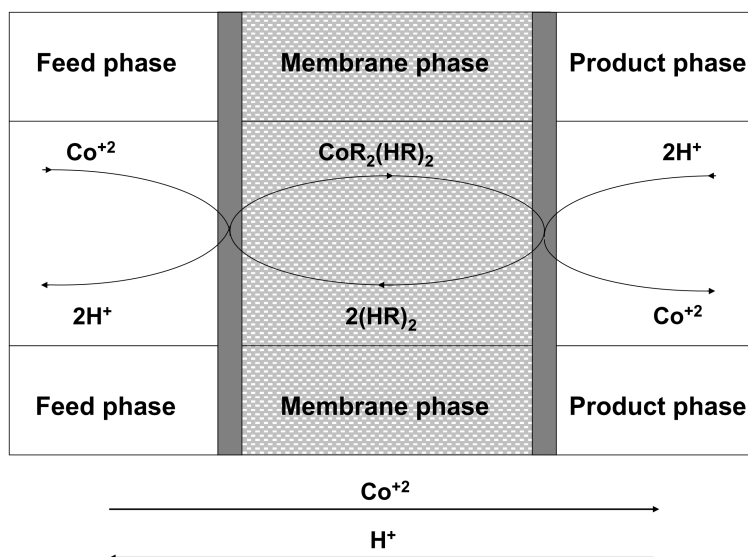
The coupled counter-transport of Co(II) ions through a liquid membrane using D2EHPA as carrier and H<sup>+</sup> as counter ion (sulfuric acid as a stripping agent) is illustrated in Figure 1. Dimerized molecules of carrier (HR)<sub>2</sub> [35] diffuse from the membrane phase to the feed/membrane interface where they undergo reaction with Co(II). Each Co(II) ion is exchanged for two protons, according to the following equation [36]:



The Co(II)-carrier complex, CoR<sub>2</sub>(HR)<sub>2</sub>, diffuses through the membrane phase to the membrane/product interface where due to the high acidic conditions of product phase, the described reaction is reversed and protons are exchanged for Co(II) ions, which are released into the product phase, the carrier being regenerated to begin a new separation cycle. A coupled counter-transport mechanism takes place, so that Co(II) and H<sup>+</sup> travel in opposite directions.

The equilibrium constant of the described reversible reaction ( $K_e$ ) can be expressed by Equation (1).

$$K_e = \frac{[\text{CoR}_2(\text{HR})_2]_{\text{org}} \times [\text{H}^+]_{\text{aq}}^2}{[\text{Co}^{2+}]_{\text{aq}} \times [(\text{HR})_2]_{\text{org}}^2} \quad (1)$$



**Figure 1.** Diagram of the coupled counter-transport of Co(II) ions using D2EHPA as carrier and  $\text{H}^+$  as counter-ion.

It can be considered that chemical reactions that take place at the feed/membrane and membrane/product interfaces occur faster than the diffusion processes [37] and the Co(II) transport rate is determined by the rate of diffusion of Co(II) through the feed diffusion layer and the rate of diffusion of the Co(II)-carrier complex through the membrane. The Co(II) flux across the membrane can be obtained by applying Fick's first diffusion law to the diffusion layer on the feed side ( $J_{fbl}$ ) and to the membrane ( $J_m$ ) through the following equations [38]:

$$J_{fbl} = \frac{[\text{Co}^{2+}]_f - [\text{Co}^{2+}]_{i,f/m}}{\Delta_{fbl}} \quad (2)$$

$$J_m = \frac{[\text{CoR}_2(\text{HR})_2]_{i,f/m} - [\text{CoR}_2(\text{HR})_2]_{i,m/p}}{\Delta_m} \quad (3)$$

where  $\Delta_{fbl}$  is the transport resistance due to diffusion through the aqueous feed boundary layer ( $\delta_{fbl}/D_{aq}$ ) ( $\text{s}\cdot\text{m}^{-1}$ ),  $\Delta_m$  is the transport resistance due to diffusion through the membrane phase ( $\delta_m/D_{ps}$ ) ( $\text{s}\cdot\text{m}^{-1}$ ),  $[\text{Co}^{2+}]_f$  is the cobalt concentration in the feed phase,  $[\text{Co}^{2+}]_{i,f/m}$  is the cobalt concentration in the feed/membrane interface,  $[\text{CoR}_2(\text{HR})_2]_{i,f/m}$  is the complex concentration in the feed/membrane interface,  $[\text{CoR}_2(\text{HR})_2]_{i,m/p}$  is the complex concentration in the membrane/product interface,  $\delta_{fbl}$  is the thickness of the aqueous feed boundary layer (m),  $D_{aq}$  is the average aqueous diffusion coefficient of the Co(II) ( $\text{m}^2\cdot\text{s}^{-1}$ ),  $\delta_m$  is the thickness of the membrane phase (m) and  $D_{ps}$  is the diffusion coefficient of the Co(II)-carrier in the polymeric support.

Due to the different pH values of the feed and the product phases, the distribution coefficient of Co(II) between the membrane phase and the product phase is much lower than that between the feed phase and the membrane phase. Consequently, the concentration of the Co(II)-carrier complex at the

membrane/product interface may be considered negligible compared to that at the feed/membrane interface and Equation (3) can be rewritten as

$$J_m = \frac{[\text{CoR}_2(\text{HR})_2]_{i,f/m}}{\Delta_m} \quad (4)$$

If, as assumed above, chemical reactions are fast compared with the diffusion rate, local equilibrium is reached at the interface, where concentrations are related through Equation (1). Thus, in the steady state,  $J_{fb} = J_m = J$ , and by combining Equations (1), (2) and (4), the following flux expression can be obtained:

$$J = \frac{K_e \cdot [(\text{HR})_2]^2 \cdot [\text{Co}^{2+}]_f}{\Delta_m \cdot [\text{H}^+]^2 + \Delta_{fb} \cdot K_e \cdot [(\text{HR})_2]^2} \quad (5)$$

Thus, the permeability coefficient,  $P = J/[\text{Co(II)}]_f$ , can be written as [38]

$$P = \frac{K_e \cdot [(\text{HR})_2]^2}{\Delta_m \cdot [\text{H}^+]^2 + \Delta_{fb} \cdot K_e \cdot [(\text{HR})_2]^2} \quad (6)$$

From Equation (6), the following expression for  $1/P$  is obtained

$$\frac{1}{P} = \Delta_{fb} + \frac{\Delta_m \cdot [\text{H}^+]^2}{K_e \cdot [(\text{HR})_2]^2} \quad (7)$$

By plotting  $1/P$  as a function of  $1/[(\text{HR})_2]_2$ , at constant pH, a straight line should be obtained with slope  $(\Delta_m \cdot [\text{H}^+]^2)/K_e$  and ordinate  $\Delta_{fb}$ . Knowing  $K_e$  and the pH of the feed solution,  $\Delta_m$  can be obtained from the slope.

Since  $\Delta_{fb} = \delta_{fb}/D_{aq}$ , the value of the thickness of the aqueous feed boundary layer can be calculated if the average aqueous diffusion coefficient is known.

Similarly, since  $\Delta_m = \delta_m/D_{ps}$ , knowing the thickness of the supported liquid membrane,  $D_{ps}$  can be calculated, while the diffusion coefficient of the Co(II)-carrier in the bulk membrane phase ( $D_{bm}$ ) can be obtained by the following equation [39]:

$$D_{bm} = \frac{D_{ps} \cdot \tau^2}{\varepsilon} \quad (8)$$

The porosity of the membrane ( $\varepsilon$ ) is usually given by the membrane supplier and the tortuosity of the membrane ( $\tau$ ) can be calculated according to the relationship [40]:

$$\tau = \frac{1 + V_p}{1 - V_p} \quad (9)$$

where the volume fraction of polymeric support ( $V_p$ ) is  $1 - \varepsilon$  [41].

### 3. Materials and Methods

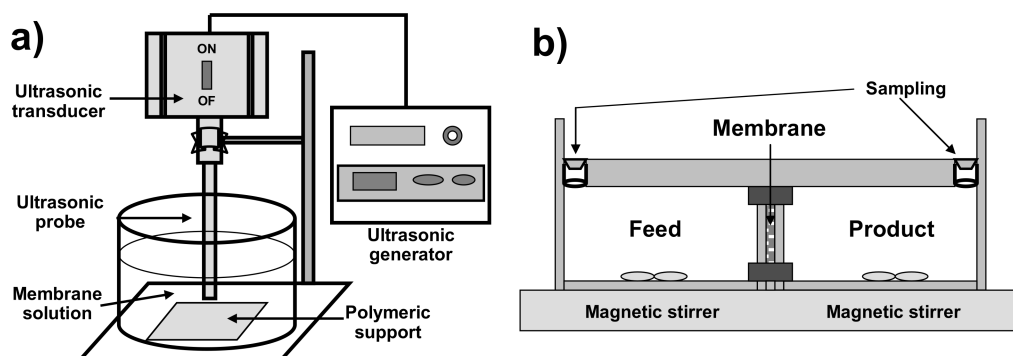
#### 3.1. Materials

Cobalt(II) chloride (98%), sodium acetate (99%), acetic acid (95%) and sulfuric acid (95–98%) were purchased from Panreac. Bis-2-ethylhexyl phosphoric acid (97%) was obtained from Sigma-Aldrich, Madrid, Spain. Kerosene (99%) was supplied by BDH Middle East, Dubai, UAE. A microporous hydrophobic PVDF ultrafiltration membrane (Millipore Durapore GVHP 10, Merck, Madrid, Spain), was utilized as support for the liquid membrane (geometrical area 20 cm<sup>2</sup>, porosity of 75%, pore size of 0.22 μm and thickness of 125 μm).

### 3.2. Methods

#### 3.2.1. Preparation of Supported Liquid Membrane

The liquid membrane phase was constituted by kerosene solutions of D2EHPA at concentrations between 0.2 and 0.8 M. The pores of the microporous support were filled with the membrane solution by applying ultrasound, using Labsonic M (Sartorius SA, Madrid, Spain) ultrasound equipment (titanium probe 10 mm diameter, sound rating density  $130 \text{ W/cm}^2$ ), at 30 KHz,  $150 \mu\text{m}$ , for 30 min (three times for 10 min, with 5 min intervals between them), and the active layer of the polymeric support at a distance of 16 mm from the ultrasound probe [24] (Figure 2a).



**Figure 2.** Schematic representations of: (a) sonication system; (b) experimental transport cell.

#### 3.2.2. Supported Liquid Membrane Characterization

Scanning electron microscopy (SEM), energy-dispersive X-ray spectroscopy (EDX) and infrared spectrometry (IR) were used to study the impregnation of the pristine PVDF porous polymeric support with the liquid membrane phase by the effect of ultrasound (PVDF-USLM).

The outer surface and elemental composition of both PVDF and PVDF-USLM were analyzed by SEM using a HITACHI S-3500N apparatus, containing secondary and backscattered electron detectors (Hitachi High-Technologies Corporation, Tokyo, Japan), equipped with an EDX XFlash 5010 analysis system (Bruker AXS, Karlsruhe, Germany). 15 kV, 10 mm work distance, samples sputtered with a thin layer of platinum during 90 s by a sputter coater Polaron SC 7640 (Quorum Technologies, Newhaven, UK) and  $5000\times$  magnification were used in SEM study, while 15 kV and 15 mm work distance were used in EDX analysis.

The outer surface chemical functional groups of both PVDF and PVDF-USLM were analyzed by using a NICOLET 5700 FTIR equipment (ThermoFischer Scientific, Waltham, MA, USA), in transmittance mode from  $400 \text{ cm}^{-1}$  to  $4000 \text{ cm}^{-1}$ .

#### 3.2.3. Transport Experiments

Transport studies were carried out using a permeation cell consisting of two identical compartments, containing  $250 \text{ cm}^3$  (V) of feed or product phase, separated by the supported liquid membrane with an effective area (A) of  $15 \text{ cm}^2$  [24] (Figure 2b). As feed phase, aqueous solutions of Co(II) between 0.010 M to 0.200 M ( $10 \text{ mol/m}^3$  to  $200 \text{ mol/m}^3$ ) in 0.2 M acetate buffer, with pH ranging from 3 to 7, were used, and aqueous sulfuric acid solutions between 0.005 and 1 M were used as product phase. Both phases were mechanically stirred at speeds ranging from 50 to 400 rpm, at room temperature.

#### 3.2.4. Analytical Methods and Calculations

Samples from the product phase compartment were taken every 30 min and Co(II) concentrations were determined by flame atomic absorption spectrophotometry at 240.7 nm using a Shimadzu AA-2600

apparatus (Duisburg, Germany). The experiments were carried out in duplicate and the results obtained showed less than 3% deviation.

Initial Co(II) fluxes were determined, according to Equation (10) [42], from the slope of the straight line obtained when plotting the Co(II) concentration in the product phase ( $[Co^{2+}]_{pt}$ ) as a function of time during the first four hours of the experiment, because of the linear relationship observed during that time.

$$J = \frac{V}{A} \frac{d[Co^{2+}]_{pt}}{dt} \quad (10)$$

Initial Co(II) permeability values (P) were determined, according to Equation (11) [43], from the straight line obtained when plotting  $\ln[C_0/(C_0 - C_{pt})]$  versus time during the first four hours of the experiment, when a linear relationship was observed

$$\ln \frac{[Co^{2+}]_{f0}}{[Co^{2+}]_{f0} - [Co^{2+}]_{pt}} = \frac{A}{V} P t \quad (11)$$

where  $[Co^{2+}]_{f0}$  is the initial Co(II) concentration in the feed phase.

The instability of the supported liquid membrane was determined from the decrease in Co(II) flux through the membrane in four successive experiments using the same membrane at the optimal experimental conditions.

## 4. Results

### 4.1. Membrane Characterization

Figure 3 shows SEM, EDX and FTIR of both PVDF and PVDF-USLM.

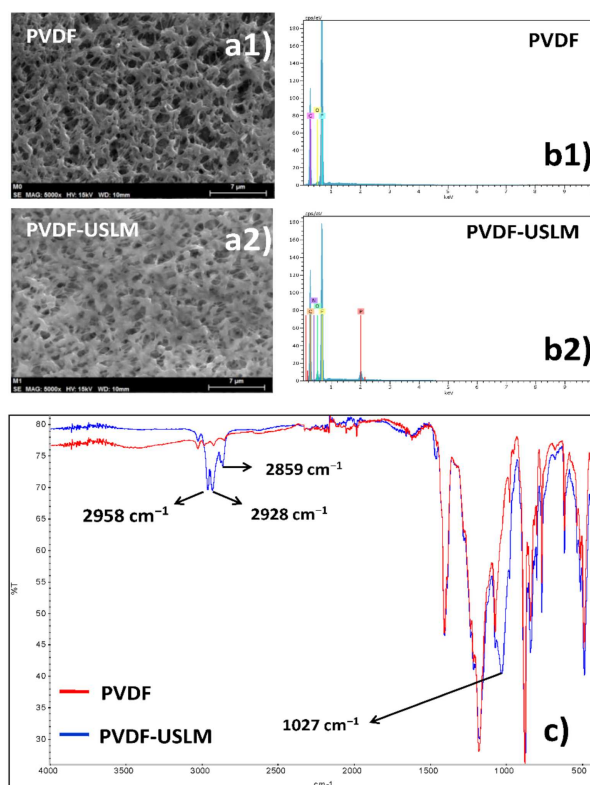


Figure 3. Membrane characterization of PVDF and PVDF-USLM by (a1,a2) SEM; (b1,b2) EDX; (c) FTIR.

SEM shows that the surface microstructure, in terms of the surface morphology and porous structure, was not significantly changed after sonification/impregnation process, though the surface roughness of the impregnated support slightly decreased, which must be a consequence of filling the pores with the liquid membrane phase.

EDX characterization results of the shell surface shows the absence of phosphorus in the original PVDF support but its presence in the PVDF-USLM membrane. This confirms that the polymeric porous support has been adequately impregnated with the liquid membrane phase through the application of ultrasound.

The analysis of the FTIR of PVDF-USLM film shows the presence of several significant bands which are not present in PVDF film. The bands between 2958 and 2859  $\text{cm}^{-1}$  (corresponding to C-H stretching) show the presence of methyl and ethyl groups and the band at 1027  $\text{cm}^{-1}$  (corresponding to P-O-C stretching) shows the presence of P-O-CH<sub>2</sub>- groups. This supports the incorporation of the liquid membrane phase (D2EHPA in kerosene) into the PVDF microporous support during the sonification process with the liquid membrane phase.

#### 4.2. Optimization of Co(II) Transport Process

The influence on the Co(II) pertraction (expressed in terms of flux) of different parameters such as feed phase Co(II) concentration and pH, sulfuric acid concentration in the product phase, carrier concentration in the membrane phase and stirring speed in both feed and product phases, is shown in Figure 4a–f.

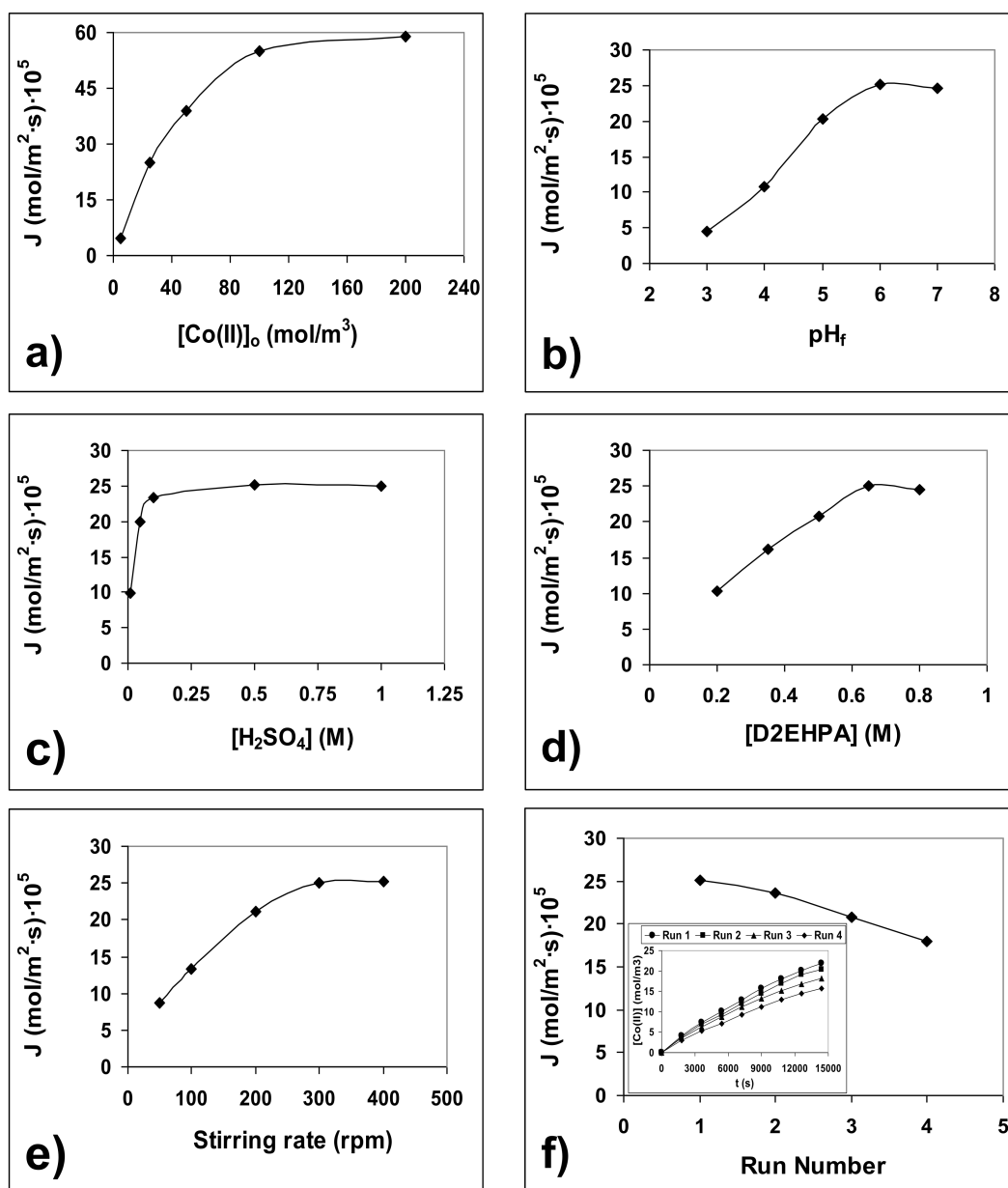
Figure 4a shows the effect of Co(II) concentration in the feed phase on Co(II) flux. The flux increased as the Co(II) concentration in the feed phase increased from 10  $\text{mol/m}^3$  to 100  $\text{mol/m}^3$  due to the presence of a higher number of Co(II) ions in the feed/membrane interface, which facilitated the formation of Co(II)-carrier complex leading to a higher transport. A further increase in Co(II) concentration has no significant effect on flux due to saturation of the feed/membrane interface by the Co(II) ions. A Co(II) concentration of 0.025 M (25  $\text{mol/m}^3$ ) was selected for subsequent experiments as it is the lowest concentration at which significant flux variations were observed with the other parameters studied.

As shown in Figure 4b, the flux increased when feed pH increased between pH 3 and pH 6 and then remained constant. At low feed pH (high  $[\text{H}^+]$ ), the equilibrium of the extraction reaction was highly displaced to the left, and no Co(II)-carrier complex was formed. Moreover, the low proton gradient between product and feed phases generated a low driving force. As the feed pH increased ( $[\text{H}^+]$  decrease), both the equilibrium of the extraction reaction shifted towards the right (more Co(II) carrier complex is formed) and the proton gradient between the product and the feed phases increased. Consequently, Co(II) transport from the feed to the permeate phase increased. Above pH 6, the OH<sup>-</sup> competes with the carrier to form a Co(II) complex and so its transport decreases. Thus, a pH of 6 in the feed phase was maintained throughout the study.

The pertraction of Co(II) from aqueous feed phase across the membrane phase is dependent on the concentration of the stripping agent ( $\text{H}_2\text{SO}_4$ ) present in the product phase (Figure 4c). The results show that the Co(II) flux increased sharply as the sulfuric acid concentrations raised from 0.005 to 0.100 M, and then more slowly up to 0.5 M. At higher sulfuric acid concentrations, the Co(II) flux remained practically constant. These results confirm that the presence of a proton gradient between the product and the feed phases is essential for a high mass transfer. Therefore, a sulfuric acid concentration of 0.5 M in the permeate phase was chosen for further experiments.

The effect of the carrier concentration in the membrane phase on Co(II) flux is shown in Figure 4d. As can be seen, Co(II) flux increased as the carrier concentration increased from 0.2 to 0.65 M, but further increases in carrier concentration had no significant effect on Co(II) flux. According to the equilibrium of the extraction reaction (reaction 1), the higher the carrier concentration in the membrane phase, the more Co(II)-carrier complex is formed. Above 0.65 M, both the saturation of the feed/membrane

interface by the carrier and the higher viscosity of the membrane phase led to the Co(II) flux remaining constant. Therefore, a carrier concentration of 0.65 M was used in subsequent experiments.



**Figure 4.** Influence on Co(II) flux of: (a) initial feed pH; (b) sulfuric acid concentration in product phase; (c) carrier concentration in membrane phase; (d) stirring rate in both aqueous and product phases; (e) initial Co(II) concentration in feed phase; (f) successive runs with the same membrane.

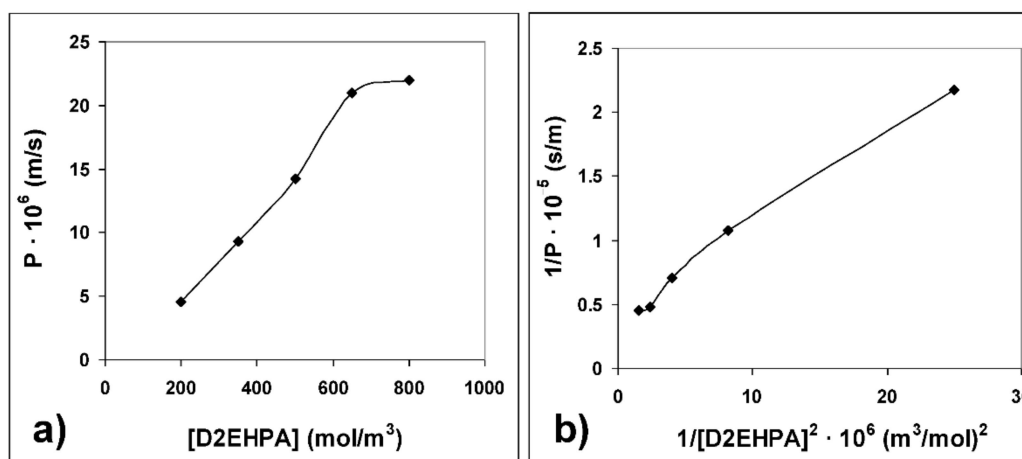
The effect of stirring rate on Co(II) flux is shown in Figure 4e. The flux increased as the stirring rate increased from 50 to 300 rpm, above which no appreciable variation was observed. This indicates that the boundary layers thickness diminished continuously as the stirring rate increased and that minimum values of these boundary layers (minimal diffusion resistance due to the boundary layers) are reached at 300 rpm and above. Therefore, further experiments were carried out at 300 rpm.

The instability of the supported liquid membrane, measured as the decrease in Co(II) flux in four successive runs, is shown in Figure 4f, where the variation of Co(II) concentration with time in those four successive experiments with the same membrane is also shown. The flux in runs 2, 3 and 4, expressed as percentage with respect to the flux in run 1, were 94%, 83% and 71%, respectively.

These flux decreases are lower than those found by other authors using similar supported liquid membranes, but prepared by immersion of the polymeric support in the liquid membrane phase [44].

### 4.3. Determination of Transport Parameters

The effect of the carrier concentration in the membrane phase on Co(II) initial permeability is shown in Figure 5a. As in the case of initial flux, initial permeability increased as the carrier concentration increased from 200 to 650 mol·m<sup>-3</sup>, but further increases in carrier concentration had no significant effect on Co(II) permeability.



**Figure 5.** (a) Effect of the carrier concentration in the membrane phase on Co(II) initial permeability; (b) inverse of Co(II) initial permeability versus the inverse of the square of carrier concentration in the membrane phase.

From data obtained when plotting the inverse of Co(II) initial permeability versus the inverse of the square of carrier concentration in the membrane phase (Figure 5b,  $R^2 = 0.9908$ ), at constant pH (pH = 6), knowing the value of  $K_e$  of D2EHPA ( $K_e = 1.1 \times 10^{-7}$  [45]) and using Equation (7), the transport resistance due to diffusion through the aqueous feed boundary layer ( $\Delta_{fb1}$ ) and due to diffusion through the membrane ( $\Delta_m$ ) were calculated (Table 1). From these values and data for the membrane polymeric support provided by the supplier ( $\delta_m$ ), the  $D_{aq}$  value of  $1.07 \times 10^{-10}$  m<sup>2</sup>·s<sup>-1</sup> [46] and the Equations (8) and (9), the thickness of the aqueous feed boundary layer ( $\delta_{fb1}$ ) and the diffusion coefficient of the Co(II)-carrier complex in the bulk membrane phase ( $D_{bm}$ ) were obtained (Table 1).

**Table 1.** Transport parameters of Co(II) pertraction through ultrasound prepared supported liquid membranes containing D2EHPA as carrier.

$\Delta_{fb1}$ (sm <sup>-1</sup> )	$\Delta_m$ (sm <sup>-1</sup> )	$\delta_{fb1}$ (m)	$D_{bm}$ (m <sup>2</sup> ·s <sup>-1</sup> )
$3.7576 \times 10^4$	$1.1434 \times 10^{10}$	$4.0206 \times 10^{-6}$	$4.0490 \times 10^{-14}$

## 5. Conclusions

This paper has analyzed the optimization and the determination of transport parameters of the Co(II) pertraction through novel ultrasound prepared supported liquid membranes by using a coupled counter-transport mechanism, with D2EHPA as carrier in the membrane phase and sulfuric acid as stripping agent (protons as counter-ions) in the product phase. SEM, EDX and FTIR characterization of the supported liquid membrane show good impregnation of the microporous polymer support by the membrane phase through the action of ultrasound. To optimize the pertraction process, the effect of different experimental conditions on Co(II) initial fluxes was studied. The optimal experimental conditions were: feed phase pH 6, 0.5 M sulfuric acid in product phase, carrier concentration 0.65 M in



membrane phase and stirring speed of 300 rpm in both phases. Supported liquid membrane shows great stability (71%) after four successive runs (four hours each run). From the relation between the inverse of Co(II) initial permeability and the inverse of the square of carrier concentration in the membrane phase, in the optimized conditions, transport resistance due to diffusion through the aqueous feed boundary layer ( $\Delta_{fbl}$ ) and transport resistance due to diffusion through the membrane ( $\Delta_m$ ) were calculated as being  $3.7576 \times 10^4 \text{ sm}^{-1}$  and  $1.1434 \times 10^{10} \text{ sm}^{-1}$ , respectively. The thickness of the aqueous feed boundary layer ( $\delta_{fbl}$ ) was  $4.0206 \times 10^{-6} \text{ m}$  and the membrane diffusion coefficient of the Co(II)-carrier complex through the membrane ( $D_{bm}$ ) was  $4.0490 \times 10^{-14} \text{ m}^2\text{-s}^{-1}$ .

**Author Contributions:** G.L., B.M. and M.A.G. conceived, designed and performed the experiments. G.L., A.M.H., M.A.G. and B.M. analyzed the data and contributed to the interpretation of the results. G.L. and A.M.H. wrote the paper. All authors have read and agreed to the published version of the manuscript.

**Funding:** This research has not received external funding.

**Acknowledgments:** The authors are grateful for the support provided by the Technological Research Support Service of the Technical University of Cartagena (UPCT).

**Conflicts of Interest:** The authors declare no conflict of interest.

## References

1. Cote, G. Hydrometallurgy of strategic materials. *Solvent Extr. Ion. Exch.* **2000**, *18*, 703–727. [[CrossRef](#)]
2. Kapusca, J.P.T. Cobalt production and markets: A brief overview. *Cobalt News* **2007**, *7*, 9–12.
3. Weight, D. *Cobalt Production Statistics*; Cobalt Development Institute: Surrey, UK, 2018; Available online: <https://www.cobaltinstitute.org/statistics.html> (accessed on 28 July 2020).
4. Leyssensa, L.; Vincka, B.; Van Der Straeten, C.; Wuytse, F.; Maesa, L. Cobalt toxicity in humans. A review of the potential sources and systemic health effects. *Toxicology* **2017**, *387*, 43–56. [[CrossRef](#)] [[PubMed](#)]
5. Wang, G.; Zhang, Y.; Jiang, S.; Ma, X.; Wei, B. Removal and recovery of cobalt from Co(II)-Containing water samples by dithiocarboxyl polyethyleneimine. *Sep. Purif. Technol.* **2020**, *251*, 117338. [[CrossRef](#)]
6. Zhang, X.; Wang, X.; Chen, Z. Radioactive Cobalt(II) Removal from aqueous solutions using a reusable nanocomposite: Kinetic, isotherms, and mechanistic study. *Int. J. Environ. Res. Public Health* **2017**, *14*, 1453. [[CrossRef](#)]
7. Islam, M.A.; Morton, D.W.; Johnson, B.B.; Pramanik, B.K.; Mainali, B.; Angove, M.J. Opportunities and constraints of using the innovative adsorbents for the removal of cobalt(II) from wastewater: A review. *Environ. Nanotechnol. Monit. Manag.* **2018**, *10*, 435–456. [[CrossRef](#)]
8. Salmani, M.H.; Ehrampoush, M.H.; Eslami, H.; Eftekhari, B. Synthesis, characterization and application of mesoporous silica in removal of cobalt ions from contaminated water. *Groundw. Sustain. Dev.* **2020**, *11*, 100425. [[CrossRef](#)]
9. Dehghani, M.H.; Yetilmezsoy, K.; Salari, M.; Heidarinejad, Z.; Yousefi, M.; Sillanpää, M. Adsorptive removal of cobalt(II) from aqueous solutions using multiwalled carbon nanotubes and  $\gamma$ -alumina as novel adsorbents: Modelling and optimization based on response surface methodology and artificial neural network. *J. Mol. Liq.* **2020**, *299*, 112154.
10. Vafajoo, L.; Cheraghi, R.; Dabbagh, R.; McKay, G. Removal of cobalt (II) ions from aqueous solutions utilizing the pre-treated 2-Hypnea Valentiae algae: Equilibrium, thermodynamic, and dynamic studies. *Chem. Eng. J.* **2018**, *331*, 39–47. [[CrossRef](#)]
11. Qian Zhang, Q.; Zhuang, S.; Wang, J. Biosorptive removal of cobalt(II) from aqueous solutions using magnetic cyanoethyl chitosan beads. *J. Environ. Chem. Eng.* **2020**, *8*, 104531. [[CrossRef](#)]
12. Iáñez-Rodríguez, I.; Calero, M.; Blázquez, G.; Martín-Lara, M.Á. Greenhouse crop residue and its derived biochar: Potential as adsorbent of cobalt from aqueous solutions. *Water* **2020**, *12*, 1282. [[CrossRef](#)]
13. Mosoarca, G.; Vancea, C.; Popa, S.; Boran, S. Adsorption, bioaccumulation and kinetics parameters of the phytoremediation of cobalt from wastewater using elodea canadensis. *Bull. Environ. Contam. Toxicol.* **2018**, *100*, 733–739. [[CrossRef](#)] [[PubMed](#)]
14. Quintero-Almanza, D.; Gamiño-Arroyo, Z.; Sánchez-Cadena, L.E.; Gómez-Castro, F.I.; Uribe-Ramírez, A.R.; Aguilera-Alvarado, A.F.; Ocampo-Carmona, L.M. Recovery of cobalt from spent lithium-ion mobile phone batteries using liquid–liquid extraction. *Batteries* **2019**, *5*, 44. [[CrossRef](#)]

15. Wiecka, Z.; Rzelewska-Piekut, M.; Cierpiszewski, R.; Staszak, K.; Regel-Rosocka, M. Hydrometallurgical recovery of Cobalt(II) from spent industrial catalysts. *Catalysts* **2020**, *10*, 61. [[CrossRef](#)]
16. Jamiu, Z.A.; Saleh, T.A.; Ali, S.A. Biogenic glutamic acid-based resin: Its synthesis and application in the removal of cobalt(II). *J. Hazard. Mater.* **2017**, *327*, 44–54. [[CrossRef](#)]
17. Liu, X.; Wu, J.; Wang, J. Electro-enhanced removal of cobalt ions from aqueous solution by capacitive deionization. *Sci. Total Environ.* **2019**, *697*, 134–144. [[CrossRef](#)]
18. Lu, J.; Dreisinger, D.; Glück, T. Cobalt electrowinning. A systematic investigation for high quality electrolytic cobalt production. *Hydrometallurgy* **2018**, *178*, 19–29. [[CrossRef](#)]
19. Kumar, V.A.; Marathe, K.V. Selective separation of copper (II) and cobalt (II) from wastewater by using continuous cross-flow micellar-enhanced ultrafiltration and surfactant recovery from metal micellar solutions. *Can. J. Chem. Eng.* **2011**, *89*, 292–298.
20. Gherasim, C.V.; Hancková, K.; Palarčík, J.; Mikulášek, P. Investigation of cobalt (II) retention from aqueous solutions by a polyamide nanofiltration membrane. *J. Membr. Sci.* **2015**, *490*, 46–56. [[CrossRef](#)]
21. Kryvoruchko, A.P.; Yurlova, L.Y. Influence of some organic and inorganic additives on pressure-driven purification of waters containing cobalt. *J. Water Chem. Technol.* **2015**, *37*, 271–276.
22. Liu, X.; Wu, J.; Liu, C.; Wang, J. Removal of cobalt ions from aqueous solution by forward osmosis. *Sep. Purif. Technol.* **2017**, *177*, 8–20. [[CrossRef](#)]
23. Jia, F.; Yin, Y.; Wang, J. Removal of cobalt ions from simulated radioactive wastewater by vacuum membrane distillation. *Prog. Nucl. Energy* **2018**, *103*, 20–27. [[CrossRef](#)]
24. León, G.; Martínez, G.; Guzmán, M.A.; Moreno, J.I.; Miguel, B.; Fernández-López, J.A. Increasing stability and transport efficiency of supported liquid membranes through a novel ultrasound-assisted preparation method: Its application to cobalt(II) removal. *Ultrason. Sonochem.* **2013**, *20*, 650–654. [[CrossRef](#)] [[PubMed](#)]
25. Hachemaoui, A.; Belhamel, K. Simultaneous extraction and separation of cobalt and nickel from chloride solution through emulsion liquid membrane using Cyanex 301 as extractant. *Int. J. Min. Process.* **2017**, *161*, 7–12. [[CrossRef](#)]
26. Vafaei, F.; Torkaman, R.; Moosavian, M.A.; Zaheri, P. Optimization of extraction conditions using central composite design for the removal of Co(II) from chloride solution by supported liquid membrane. *Chem. Eng. Res. Des.* **2018**, *133*, 126–136. [[CrossRef](#)]
27. Parbat, S.A.; Bhanvase, B.A.; Sonawane, S.H. Investigation on liquid emulsion membrane (LEM) prepared with hydrodynamic cavitation process for cobalt (II) extraction from wastewater. *Sep. Purif. Technol.* **2020**, *237*, 116385. [[CrossRef](#)]
28. Sadyrbaeva, T.Z. Recovery of cobalt(II) by the hybrid liquid membrane—Electrodialysis—Electrolysis process. *Electrochim. Acta* **2014**, *133*, 161–168. [[CrossRef](#)]
29. Sastre, A.M.; Kumar, A.; Shukla, J.P.; Singh, R.K. Improved techniques in liquid membrane separations: An overview. *Sep. Purif. Meth.* **1998**, *27*, 213–298. [[CrossRef](#)]
30. Ashokkumar, M. The characterization of acoustic cavitation bubbles—An overview. *Ultrason. Sonochem.* **2011**, *18*, 864–872. [[CrossRef](#)]
31. Masselin, I.; Chasseray, X.; Durand-Bourlier, L.; Lainé, J.M.; Syzaret, P.I.; Lemordant, D. Effect of sonication on polymeric membranes. *J. Membr. Sci.* **2001**, *181*, 213–220. [[CrossRef](#)]
32. Kallioinen, M.; Mänttari, M. Influence of ultrasonic treatment on various membrane materials: A Review. *Sep. Sci. Technol.* **2011**, *46*, 1388–1395. [[CrossRef](#)]
33. León, G. Facilitated transport. In *Encyclopedia of Membranes*, 1st ed.; Drioli, E., Giorno, L., Eds.; Springer: Berlin/Heidelberg, Germany, 2016; pp. 763–764. ISBN 978-3-642-40872-4.
34. De Gyves, J.; Rodríguez, E. Metal ion separations by supported liquid membranes. *Ind. Eng. Chem. Res.* **1999**, *38*, 2182–2202. [[CrossRef](#)]
35. Biswas, R.K.; Habib, M.A.; Islam, M.N. Some Physicochemical Properties of (D2EHPA). 1. Distribution, dimerization, and acid dissociation constants of D2EHPA in a Kerosene/0.10 kmol m<sup>-3</sup> (Na<sup>+</sup>, H<sup>+</sup>)Cl<sup>-</sup> system and the extraction of Mn(II). *Ind. Eng. Chem. Res.* **2000**, *39*, 155–160. [[CrossRef](#)]
36. Juang, R.S.; Su, J.Y. Thermodynamic equilibria of the extraction of cobalt (II) from sulfate solutions with bis(2-ethylhexyl)phosphoric acid. *Ind. Eng. Chem. Res.* **1992**, *31*, 2395–2400. [[CrossRef](#)]
37. Miyake, Y.; Matsuyama, H.; Nishida, M.; Nakai, M.; Nagase, M.; Teramoto, M. Kinetics and mechanism of metal extraction with acidic organophosphorus extractants (I): Extraction rate limited by diffusion process. *Hydrometallurgy* **1990**, *24*, 19–35. [[CrossRef](#)]

38. Sastre, A.M.; Madi, A.; Alguacil, F.J. Facilitated supported liquid-membrane transport of gold(I) using LIX 79 in cumene. *J. Membr. Sci.* **2000**, *166*, 213–219. [[CrossRef](#)]
39. Huang, T.C.; Juang, R.S. Rate and mechanism of divalent metal transport through supported liquid membrane containing di(2-ethylhexyl)phosphoric acid as mobile carrier. *J. Chem. Technol. Biotechnol.* **1988**, *42*, 1–17. [[CrossRef](#)]
40. Alguacil, F.J.; Coedo, A.G.; Dorado, M.T. Transport of chromium(VI) through a Cyanex 923-xylene flat-sheet supported liquid membrane. *Hydrometallurgy* **2000**, *57*, 51–56. [[CrossRef](#)]
41. Stolwijk, T.B.; Sudhoelter, E.J.R.; Reinhoudt, D.N. Crown ether mediated transport: A kinetic study of potassium perchlorate transport through a supported liquid membrane containing dibenzo-18-crown-6. *J. Am. Chem. Soc.* **1987**, *109*, 7042–7047. [[CrossRef](#)]
42. Zaghbani, A.; Tayeb, R.; Dhahbi, M. Studies on the transport of chromium(III) through a supported liquid membrane containing D2EHPA as carrier. *Desal. Water Treat.* **2009**, *12*, 247–255. [[CrossRef](#)]
43. Ochrowicz, K.; Apostoluk, W. Modelling of carrier mediated transport of chromium(III) in the supported liquid membrane system with D2EHPA. *Sep. Purif. Technol.* **2010**, *72*, 112–117. [[CrossRef](#)]
44. Alguacil, F.J.; Alonso, M. Separation of zinc(II) from cobalt(II) solutions using supported liquid membranes with DP-8R (di(2-ethylhexyl) phosphoric acid) as carrier. *Sep. Purif. Technol.* **2005**, *41*, 179–184. [[CrossRef](#)]
45. Van de Voorde, I.; Pinoy, L.; Courtijn, E.; Verpoort, F. Equilibrium Studies of Nickel(II), Copper(II), and Cobalt(II) Extraction with Aloxime 800, D2EHPA, and Cyanex Reagents. *Solvent Extr. Ion. Exch.* **2006**, *24*, 893–914. [[CrossRef](#)]
46. Rubcumintara, T.; Han, K.N. The effect of concentration and temperature on diffusivity of metal compounds. *Metall. Trans. B* **1990**, *21*, 429–438. [[CrossRef](#)]




**Publisher’s Note:** MDPI stays neutral with regard to jurisdictional claims in published maps and institutional affiliations.



© 2020 by the authors. Licensee MDPI, Basel, Switzerland. This article is an open access article distributed under the terms and conditions of the Creative Commons Attribution (CC BY) license (<http://creativecommons.org/licenses/by/4.0/>).

Article

# Development of Chitosan/Starch-Based Forward Osmosis Water Filtration Bags for Emergency Water Supply

Saiful Saiful <sup>1,\*</sup>, Maurisa Ajrina <sup>1</sup>, Yusuf Wibisono <sup>2</sup> and Marlina Marlina <sup>1</sup>

<sup>1</sup> Chemistry Department, Faculty of Mathematics and Natural Science, Syiah Kuala University, Banda Aceh 23111, Indonesia; maurisaajrina62@gmail.com (M.A.); marlina@unsyiah.ac.id (M.M.)

<sup>2</sup> Department of Bioprocess Engineering, Faculty of Agricultural Technology, Brawijaya University, Malang 65141, Indonesia; y\_wibisono@ub.ac.id

\* Correspondence: saiful@unsyiah.ac.id; Tel.: +62-813-6058-1225

Received: 11 November 2020; Accepted: 8 December 2020; Published: 11 December 2020



**Abstract:** A forward osmosis (FO) membrane was developed from a mixture of chitosan and *Dioscorea hispida* starch, cross-linked using glutaraldehyde. The cross-linked chitosan/starch membrane was revealed to have high mechanical properties with an asymmetric structure. The prepared membrane's performance was investigated as an FO filter assembled in a polypropylene water filter bag and aluminum foil plastic. In order to study the FO process, brackish water was used as a feed solution, drawn using three types of solution (fructose, sucrose, and fructose/sucrose mixture, each with 3 M concentration). The maximum water flux (5.75 L/m<sup>2</sup> h) was achieved using 3 M sucrose. The cross-linked membrane restrained the ions in the feed with a rejection factor value close to 100%. The water quality parameters were evaluated for the physical, chemical, and biological criteria, such as pH, salinity, conductivity, total dissolved solids (TDS), heavy metals, and *Escherichia coli* content. The water quality parameters for the FO-processed water met that set by the World Health Organization for drinking water. FO filter bags with cross-linked chitosan/starch membranes can be an option to produce drinking water during an emergency.

**Keywords:** filter water bag; chitosan; *Dioscorea hispida*; starch; forward osmosis membrane; glutaraldehyde; emergency

## 1. Introduction

Water is a natural resource that is essential for human life and supports various daily activities [1]. Water is the primary component of life and contributes to vital functions within the human body [2]. The demand for clean and fresh water, especially for consumption purposes, is expected to increase annually, along with the surge in human population and an increase in global water pollution [2]. For instance, global water consumption in the 1900s was 358 km<sup>3</sup> per year and it increased five-fold to 1500 km<sup>3</sup> per year in the 2000s. Water sources on earth can be obtained from seawater, spring water, groundwater, freshwater lakes, rivers, and the atmosphere. However, most available water sources in nature cannot be accessed and used directly as a source of clean and safe drinking water. Despite the abundance of the earth's water sources, only about 1% of them can be consumed directly, while the other 97% are in the form of seawater, which is unsafe to consume directly [3]. Therefore, water is considered a significant world resource problem, along with food and energy [4].

Moreover, the demand for clean and fresh water during emergencies, increases compared to normal conditions due to the potential interruption to public utilities. Yet, the water qualities should be maintained to meet the established standards [5]. A more practical alternative method and tool is

needed to provide clean drinking water during insurgencies, such as in disaster areas, conflict zones, water crises, and other emergencies. Membrane technology driven by applied pressure and osmotic gradients is suitable for use in emergencies [6]. The membranes commonly used are microfiltration (MF); followed by ultrafiltration (UF), nanofiltration (NF), reverse osmosis (RO), and forward osmosis (FO) [7,8]. Large contaminants in the range of 0.1–5  $\mu\text{m}$ , such as bacteria, viruses, and protozoa in raw water can be removed using MF and UF membranes. Advantages of MF and UF membranes operating at relative pressures. Nanofiltration (NF) and reverse osmosis (RO) membranes were applied to remove smaller size contaminants (ionic components). NF membranes can effectively detect divalent ions, whereas RO membranes can reject monovalent ions. RO membranes are commonly utilized to produce clean and potable water from brackish and seawater. Meanwhile, the FO membrane is a membrane method currently developing with the driving force of the osmotic gradient, without the need to exert external pressure to force fluid flow across the membrane. For practicality in an emergency, forward osmosis (FO) membrane-based filter bag can be proposed as a potential alternative [5,9]. FO membranes are a water separation process that uses the difference in osmotic pressure to produce a water flow through the semipermeable membrane, for separation of water from the dissolved solute [10]. The process of purifying water with FO is carried out by utilizing an osmotic pressure gradient that draws solutes so that water from the feed solution (FS) passes through the semipermeable membrane towards the draw solution (DS) side [11]. Over the past few years, the FO method attracted much attention on both a laboratory and industrial-scale because FO provides many benefits, such as lower energy use, lower tendency for fouling, and better water purification results [12]. Due to its energy efficiency and simple instrumentation, the FO technology provides a great potential for water purification options during emergencies.

FO membranes are manufactured using polymeric materials, both synthetic and natural polymers. Previous studies showed that chitosan as a natural polymer can be used as a membrane for brackish water purification [5,9] and seawater desalination [13,14]. An initial study on the manufacture of drinking water bags using chitosan-based FO membranes was conducted [9]. The results showed that the chitosan-based FO membrane possesses a great potential in brackish water purification because it can produce water that is free of salt, metals, bacteria, and other dissolved materials, therefore, meeting the standards for drinking water. However, it was also reported that pure chitosan membranes are likely to be rigid, fragile, and not acid-resistant. A potential solution is to modify the chitosan membrane to create a better quality membrane and to overcome the limitation of the pure chitosan membrane [12].

The chitosan membrane can be modified through the addition of other polymers through a cross-linking method. Via the cross-linking method, the polymer becomes resistant to acids, thereby increasing its mechanical and chemical stability [15]. Natural polymers from non-food plants are widely used as a source of starch. *Dioscorea hispida* tubers are known as natural starch sources that are cheap and easily found in tropical regions [16]. The advantage of *D. hispida* is its high starch contents, which surpasses 70% yield [17]. *D. hispida* also contains crude protein around 3.6–9.8%. The fat content is relatively low at 1.99–9.36% and the ash content is at 0.29–1.24%. The main mineral is phosphorus, with a value of 11.7–46.9 mg/100g. The cyanide content in tubers is 379–739 ppm. However, this cyanide can be easily removed by washing, using water repeatedly. The *D. hispida*-based starch can be used for a variety of applications, including membrane preparation [18]. The membranes made from a mixture of natural materials can be used as an alternative, environment-friendly material with a great potential production and economic value. Glutaraldehyde is widely used as a cross-linking agent to produce composite films [19] and chitosan membranes [20]. Meanwhile, the properties of pure chitosan membranes that lead to a stiff form can be overcome by adding plasticizers. Glycerol is a commonly used plasticizer to make starch–chitosan mixture films [21] and starch–chitosan edible films [22].

In this study, FO membrane sheets were synthesized from chitosan–*D. hispida*-starch cross-linked by glutaraldehyde. The FO sheet was further applied to manufacture drinking water filtration bags.

Membrane modification was done by referring to previous studies [18]. The modified membrane was applied to the drinking water bags made of polypropylene (PP) plastic and aluminum foil plastic. The FO filter water bag was evaluated in terms of its performance drinkability substance as draw solution, such as fructose, sucrose, and a mixture of both solutions. Brackish water was used as a feed solution, mimicking the water contamination that might be present in an emergency, while the FO process was intended to produce direct drinking water. The water quality parameters were evaluated based on the physical, chemical, and biological criteria by analyzing pH, salinity, conductivity, metal content (As, Cd, Cr, Cu, Fe, Hg, and Zn), and *Escherichia coli* bacteria content.

## 2. Materials and Methods

### 2.1. Materials

The chitosan was purchased from a local chitosan manufacturer that met international medical and food-grade standards, with an acetylation degree of up to 94 mol% (CV. Multiguna, Cirebon, Indonesia). Starch extracted from *D. hispida* tubers was used as a polymer mixture. Glacial acetic acid (Merck, Darmstadt, Germany) was used as a solvent. Sodium bisulfite (Merck, Darmstadt, Germany) was used to prevent browning in starch isolation. Sodium hydroxide was used to neutralize the acetic acid content during membrane cleaning. Fructose and sucrose (Merck, Darmstadt, Germany) were used as draw solutions. Silver nitrate (Merck, Darmstadt, Germany) was used in cyanide qualitative tests. Glycerol (Merck, Darmstadt, Germany) was used as a plasticizer. Glutaraldehyde (Merck, Darmstadt, Germany) was used as a cross-linking agent. Aluminum foil, packaging caps, and PP plastic were obtained from the local plastic store (Banda Aceh, Indonesia). The FO feed solution was brackish water obtained from the Krueng Aceh River and the dam water was obtained from the Limpok area, Aceh Besar District, Indonesia.

### 2.2. *D. hispida*-Based Starch Extraction

To extract the starch, *D. hispida* tubers were firstly peeled and washed thoroughly, using distilled water. Then, the clean the tubers were sliced into a smaller size and added with sodium bisulfite (1.12 g/L), followed by mashing with a crusher to obtain a tuber pulp. It was soaked into distilled water and squeezed using gauze. The filtrate was allowed to settle for 24 h to produce a precipitate. The water in the upper layer was slowly removed. Distilled water was added to dissolve the precipitate, followed by a filtration using a Buchner vacuum. The tubers were washed several times to remove the cyanides. The successful removal was tested using 2 M silver nitrate, where the addition did not change the color of the mixture solution into brown. The precipitate was oven-dried for 24 h at 70 °C. The dried precipitate was sieved with a 100-mesh sieve to obtain starch flour [16].

### 2.3. Membrane Preparation

The membranes were prepared using a chitosan/starch (2:1) mixture. To obtain the mixture, starch paste and chitosan solution were first produced. To produce a starch paste, starch flour was suspended in distilled water and stirred evenly. The mixture was then heated at 75–80 °C for 10–15 min, to reach gelatinization. Meanwhile, the chitosan was dissolved in a 1% (v/v) acetic acid solution and stirred to obtain a chitosan solution. The chitosan solution and starch paste were mixed and stirred at 75–80 °C for ±10 min, and then it was left at room temperature. Afterward,  $5.6 \times 10^{-5}$  mol glutaraldehyde and 0.4% (v/v) glycerol were added. The solution was stirred for ±20 min until homogeneous, cast on a ceramic plate, and oven-dried at ±30 °C. Once dried, the membrane was removed from the mold, washed with 1% (w/v) NaOH, and rinsed with distilled water. Finally, the membranes were air-dried at room temperature [18]. The membrane was then assembled into a filter water bag and tested for its performance in FO.

#### 2.4. Drinking Water Bags Fabrication

The fabrication of drinking water bags was done by using the prepared membranes, PP plastic, and aluminum foil. Two pieces of PP plastic and one sheet of aluminum foil were cut to a designated size ( $12.5 \times 19 \text{ cm}^2$ ). In the middle of one of the PP plastic pieces, a hole with a size of  $6 \times 10.5 \text{ cm}^2$  was made. After that, the FO membrane ( $8 \times 13 \text{ cm}^2$ ) was attached to a PP plastic that was given a hole. The membrane was attached using VHB double-sided foam tape. Three layers consisted of PP plastic (1), PP plastic with attached FO membrane (2), and aluminum foil (3); all layers were assembled from top to bottom, sequentially. The bags were glued by lamination, using a sealing machine. Finally, the lid was installed on the front and backside of the bag.

#### 2.5. Assessment of Drinking Water Bags

Three different DSs (fructose, sucrose, and fructose/sucrose mixture, each with 3 M concentration) were used, respectively, to assess the FO membrane performance in the drinking water bag. Brackish and dam water was used as an FS. Drinking water bags were filled with 100 mL DS through the front opening. Then, the drinking water bag's back opening was filled with 200 mL FS to initiate the FO process (up to 1 h). The water flux ( $\text{L/m}^2 \text{ h}^{-1}$ ) and rejection factor (%) were then calculated using Equations (1) and (2), respectively.

$$\text{Water flux} = \frac{\Delta V}{A \Delta t} \quad (1)$$

$$\text{Rejection factor} = 1 - \frac{C_p}{C_f} \times 100\% \quad (2)$$

where  $\Delta V$ ,  $\Delta t$ , and  $A$  represent the volume of FO-processed water (L), the FO duration (hour), effective membrane surface area ( $\text{m}^2$ ). Meanwhile,  $C_p$  and  $C_f$  are solute concentrations (TDS) in the processed water and FS, respectively.

#### 2.6. Forward Osmosis Water Product Analysis

The water quality produced was determined by pH, salinity, conductivity, metal content, and *E. coli* bacteria content. The pH, salinity, and TDS level was measured using pH meter CT-6022 (Shenzhen Kedida Electronics Co. Ltd., Shenzhen, China), Salinity Meter SA287 (Guangzhou 3win Electronic Technology Co. Ltd., Guangzhou, China), and conductivity meter WTW LF320 (Wissenschaftlich-Technische-Werkstätten GmbH, Weilheim, Germany), respectively. Metal contents (As, Cd, Cr, Cu, Fe, Hg, and Zn) were measured using atomic absorption spectrometer (AAS) Shimadzu 5960A (Kyoto, Japan). Finally, the *E. coli* content was determined using the most probable number (MPN) method [23].

### 3. Results and Discussion

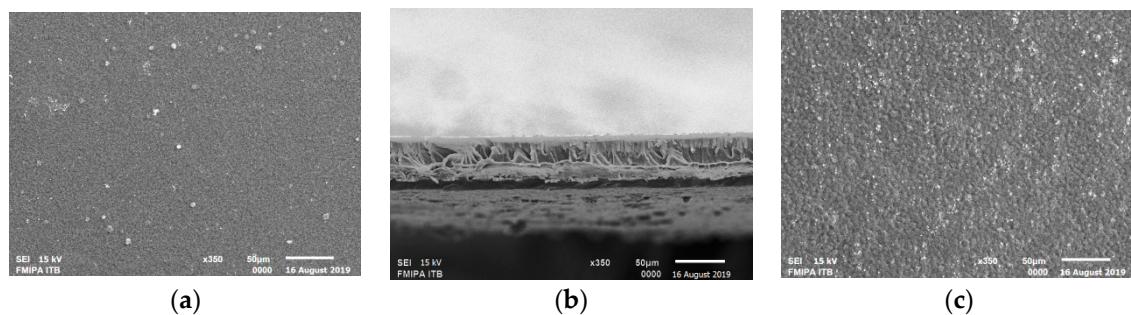
#### 3.1. *D. hispida*-Based Starch Extraction

The isolation of starch was carried out using distilled water as a solvent and the solubility of starch was assisted by the addition of sodium bisulfite into the *D. hispida* slurry. Sodium bisulfite also helps to prevent the browning of starch and activation of bacteria. The process of starch isolation requires repeated washing with water to remove cyanide toxin compounds. Previous studies reported that the cyanide toxin content, in the form of HCN, can reach  $700 \text{ mg/kg}$  [16]. It can be removed by repeated washing. As a result, the starch was free of cyanide toxin, qualitatively marked by the unchanged color after the addition of 1 M silver nitrate addition. Dried *D. hispida*-based starch powder obtained in this study had a yield of 7%.

### 3.2. Forward Osmosis Membrane Preparation

The membrane prepared in this research was based on the optimum condition in our previously published report [18]. During the preparation of starch paste, prior to the making of chitosan/starch mixture, the gelatinization process caused the starch granule crystals to absorb water, swell, then break, and dissolve in water. To cross-link the chitosan and starch, glutaraldehyde was used, where its excessive addition could promote the formation of aggregates, resulting in an inhomogeneous mixture. Hence, the optimum concentration of glutaraldehyde was determined at  $5.6 \times 10^{-5}$  mol. A previous study reported that cross-linking in chitosan causes increased mechanical properties. Meanwhile, the addition of plasticizers in the form of glycerol was intended to overcome the stiffness property of chitosan membranes.

The FO membranes appeared yellowish, thin, and transparent, with strong physical characteristics, a dense porous structure, and a good FO performance [18]. The chitosan/starch FO membrane was revealed to have better characteristics and performance, compared to that made from neat chitosan. The chitosan/starch membrane had a thickness of 0.035 mm, a swelling degree of 28.98%, a porosity of 54.36%, a tensile strength value of 87.63 kgf/mm<sup>2</sup>, and an elongation of 16.08%. The chitosan/starch membrane had an asymmetric structure (as shown in Figure 1), where the top layer was thinner and tighter than the bottom layer. There were no macrovoid found in the membrane structure and the membrane had a stable interconnection, indicating strong mechanical properties [22]. In the FO test, this membrane had a water flux of 4.0 L/m<sup>2</sup> h, where 1 M sucrose was employed as a DS.



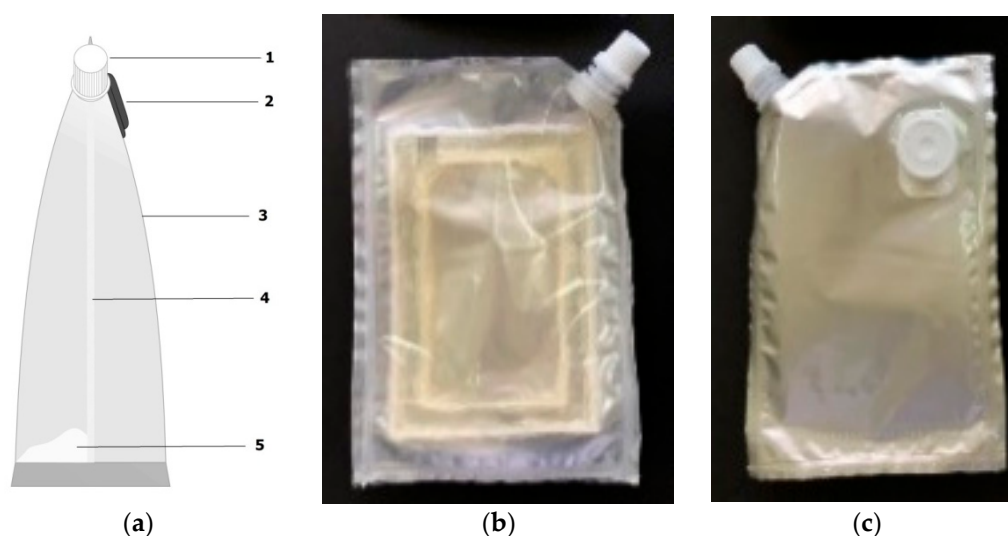
**Figure 1.** SEM Images (350× magnification) of the structure and morphology of the cross-linked chitosan/starch membranes made with a composition of 3% chitosan, 1.5% *D. hispida* starch,  $5.6 \times 10^{-5}$  mol glutaraldehyde, and 0.4% glycerol. (a) Top layer, (b) Cross-section, and (c) Bottom layer.

### 3.3. Drinking Water Bags

The drinking water bags were made by referring to previous studies [9]; illustrated in Figure 2. The bag was made of three main materials, namely PP plastic, aluminum foil, and modified membrane. It is worth noting that the chitosan/starch membrane could not be laminated directly using a simple sealing machine because, based on the thermal analysis, the membrane material did not have a glass transition temperature [18]. After the moisture from the membrane material evaporated, the membrane was immediately observed to decompose at a temperature of 320 °C.

Design of the drinking water bag was similar to commercially available FO filter bags. The three layers were arranged as follows—the PP plastic was assembled as the top layer, the membrane-attached PP plastic as the middle layer, and aluminum foil as the bottom layer. All three were glued altogether through lamination using a sealing machine, where the caps were added to the front and back sides, as shown in Figure 2. The manufactured drinking water bags had a total volume capacity of ±400 mL, with a volume capacity of ±200 mL in each side. The effective surface area of the membrane contact in this bag was 41.25 cm<sup>2</sup>.





**Figure 2.** A drinking water bag made from a combination of aluminum foil and PP plastic with a chitosan/starch membrane filter inside. (a) Water bag design (1 = the lid on the front of the bag, 2 = the lid on the back of the bag, 3 = polypropylene plastic, 4 = chitosan-starch membrane, 5 = draw solution), with the photographs of (b) the front side and (c) backside of the bag.

### 3.4. Forward Osmosis Process

The water bags were used in FO testing with an FS of brackish and dam water. These feed solutions had different chemical characteristics (Table 1). Three types of DSs (fructose, sucrose, and their mixtures) were employed to investigate the chitosan/starch membrane’s performance in the water drinking bag. A total of 200 mL FS was and 100 mL DS was added to the back and front sides of the bag, respectively.

**Table 1.** The quality of the feed water used in the FO process.

Sample	Parameter			
	pH	Salinity (ppt)	Conductivity ( $\mu\text{S}/\text{cm}$ )	TDS (mg/L)
Brackish Water	7.91	9.3	15.83	1297
Dam Water	7.19	0.1	0.39	27

Figure 3 illustrates the water fluxes from the FO process using the three respective DSs. The optimum water flux was evident with a 3 M sucrose DS, which was  $5.75 \text{ L}/\text{m}^2 \text{ h}$ . This value was higher than in the previous study ( $5.25 \text{ L}/\text{m}^2 \text{ h}$ ), which employed an unmodified chitosan membrane and the same DS [9]. The cross-linking using glutaraldehyde was proven to improve membrane performance, where a better flux was observed. Lower water fluxes, 2.5 and  $3.25 \text{ L}/\text{m}^2 \text{ h}$ , were obtained from the fructose and the fructose/sucrose mixture DSs, respectively.

The use of sucrose as a DS was reported in several studies related to the FO process, in which it was found to generate a higher water flux compared to others [9,24–28]. This was ascribed to the higher osmotic pressure produced by the sucrose solution than fructose, glucose, and their mixture. The higher osmotic pressure of the draw solution led to a higher potential of the water flow permeation from the feed, which could be observed, based on the flux differences produced by fructose and sucrose. In this study, the chitosan/starch membrane was also evaluated using dam water; it was carried out with the same effective membrane surface area employing 3 M sucrose. Brackish water and dam water have different characteristics and produce different water flux values, as presented in Figure 4.

Figure 4 shows that the flux value generated from the dam water FS was higher ( $8.5 \text{ L}/\text{m}^2 \text{ h}$ ) than from brackish water ( $5.25 \text{ L}/\text{m}^2 \text{ h}$ ). The results could be associated with the feed water’s different characteristics, including pH, salinity, conductivity, and TDS. The dam water had lower ion contents

than the brackish water; the more significant difference of concentrations between the feed solution and draw solution, and the greater the pressure produced led to a higher water flux [29].

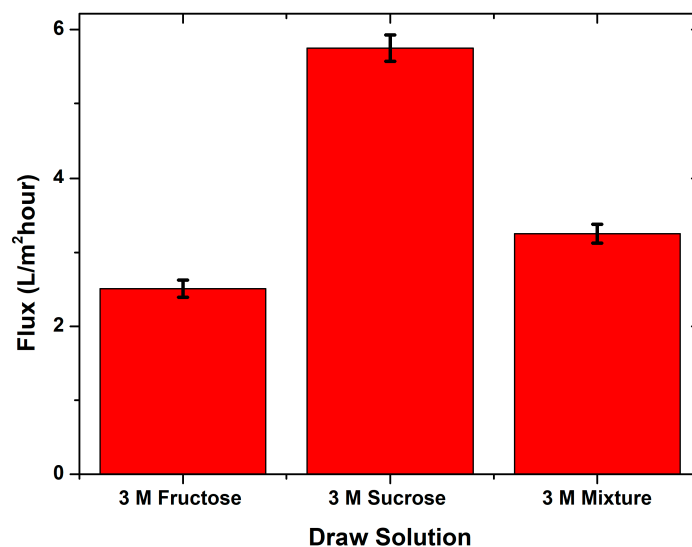


Figure 3. The water flux produced during the FO process brackish water as an FS with different DSs.

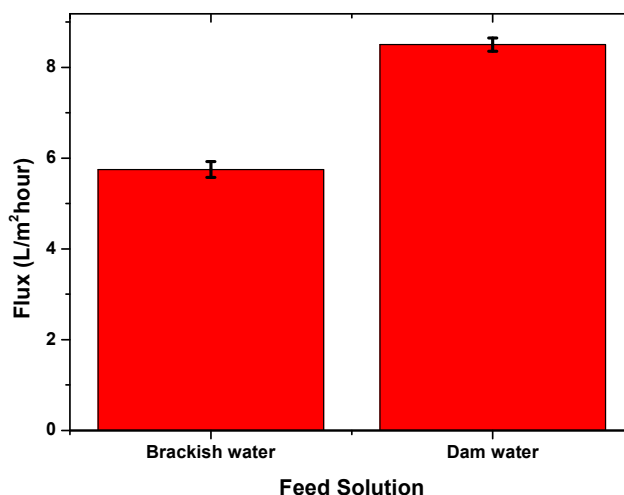
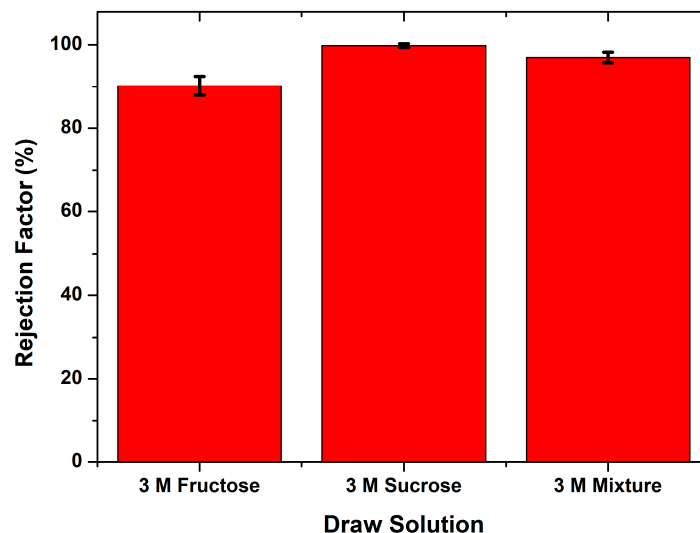


Figure 4. The resulting water flux used 3 M sucrose as a withdrawal solution with different FSs.

In addition to the flux value, the chitosan/starch membrane performance could also be observed from the percent of a rejection factor value. Figure 5 shows the rejection percentage ranging from 90.2–99.8%. Based on the results, the percent rejection in this study showed a high separation of ion particles. The highest rejection percentage (99.8%) was obtained in the FO process from brackish water with a 3 M sucrose draw solution. On the contrary, the lowest percentage of rejection (92.2%) was obtained in the FO process with a 3 M fructose draw solution. The flux value and percent rejection factor obtained from the FO process in this study indicated that the modified chitosan membrane’s performance was better than the unmodified chitosan membrane, as reported in a previous study [9].

Based on the water flux and the rejection factor value, it could be seen that the changes in the membrane water flux affected the rejection factor of the membrane. Changing the draw solution from 3 M Fructose to 3 M sucrose increased the membrane water flux and simultaneously increased the rejection factor. The sucrose 3 M as a draw solution, the amount of water solvent that moved to the draw solution was increased and the feed solution became more concentrated. The salt concentration contributed to the rejection factor’s increase in using the 3 M sucrose draw solution. Increasing

the water flux did not cause the transfer of dissolved ions in the feed solution to the draw solution. The same phenomenon was also observed in using a draw solution for a mixture of fructose and sucrose 3 M, where an increase in the water flux simultaneously resulted in a better rejection factor from the membrane.



**Figure 5.** The rejection factor percentage of ion particles in the FO process from brackish water with different draw solutions.

### 3.5. FO Water Quality

Several water quality parameters was analyzed to assess the water quality of the Lamnyong River, Limpok village, Aceh Besar district. The main parameters related to brackish water quality are salinity, TDS, pH, conductivity, heavy metal content, and *E. coli* bacteria content. The results are shown in Tables 1 and 2. According to the WHO [30] and Indonesian Health Ministry standards [31], several brackish water characteristics do not meet acceptable drinking water quality standards. According to the brackish water properties, the brackish water sample has a salinity value of 9 ppt, which indicates the dissolved salt contents. The presence of dissolved salts was also evidenced by the high TDS value of 1297 mg/L, attributed to the number of ions in the water. The high salinity value and dissolved ion contents in the water were expected to be separated by a forward osmosis membrane. However, low concentration heavy metal contents were observed in brackish water, which was still acceptable for quality drinking water and sanitation standards. All the metals analyzed (As, Cd, Cr, Cu, Fe, Hg, Mn, and Zn) were still relatively low in drinking water content. Moreover, the brackish water samples also tested negative for *E.coli* and *coliform* bacteria.

**Table 2.** The results of the analysis of heavy metal contents in brackish water and FO-processed water.

No	Parameter	Metal Content (mg/L)				Standard (mg/L)
		FO Product Water				
		Brackish Water	Sucrose	Fructose	Mixture	
1	Mercury (Hg)	<0.001	<0.001	<0.001	<0.001	0.006
2	Arsenic (As)	<0.003	<0.003	<0.003	<0.003	0.01
3	Zinc (Zn)	<0.01	<0.01	<0.01	<0.01	3
4	Copper (Cu)	<0.0007	<0.0007	<0.0007	<0.0007	2
5	Chromium (Cr)	<0.002	<0.002	<0.002	<0.002	0.05
6	Iron (Fe)	0.1071	0.0634	0.0214	0.0219	0.2
7	Cadmium (Cd)	<0.002	<0.002	<0.002	<0.002	0.003

For cases where the parameters fell behind the quality standard, the water could be drinkable afterward by using our drinking water bag. The water would then contain sugar from the DS. The use of sucrose and fructose as a draw solution contributed to adding this drinking water bag’s practicality. The quality of the processed water was analyzed against the changes in all parameters of the brackish water. The following was the water quality produced after the FO process, carried out for one hour.

### 3.5.1. Physicochemistry Water Properties

The water produced from the FO process was evaluated for pH, salinity, conductivity, and TDS, as shown in Figure 6. The draw solution’s pH value did not significantly change from before the FO process, ranging from 7.6–7.45 pH (Figure 6a). In line with these findings, the previous research reported that the FO process did not result in significant changes in pH values [5]. Hence, it could be expected that the pH values of the processed water, using the three DSs, were within the allowed range for drinking water quality standards (pH 6.5–8.5), according to the WHO [30] and the Indonesian government [32]. In addition to the pH, the salinity, conductivity, and TDS also showed promising results. The salinity of the FO-processed water (Figure 6b) ranged from 0.1 to 0.8 ppt. The lowest salinity (0.1 ppt) was obtained in the FO-processed water using 3 M sucrose DS. Meanwhile, the highest salinity value (0.8 ppt) was obtained from the water drawn using 3 M fructose. The salinity obtained from this study was lower than those in previous studies. It was reported that the salinity values obtained from FO with neat chitosan membranes were within the range of 0–1.3 ppt [5]. The chitosan/starch membrane could restrain salt particles better, as indicated by the lower salinity in the processed water. Based on these results, water produced by the FO process in this study was classified as freshwater with salinity levels that met the general quality standard (0.5 ppt) used for drinking water [33].

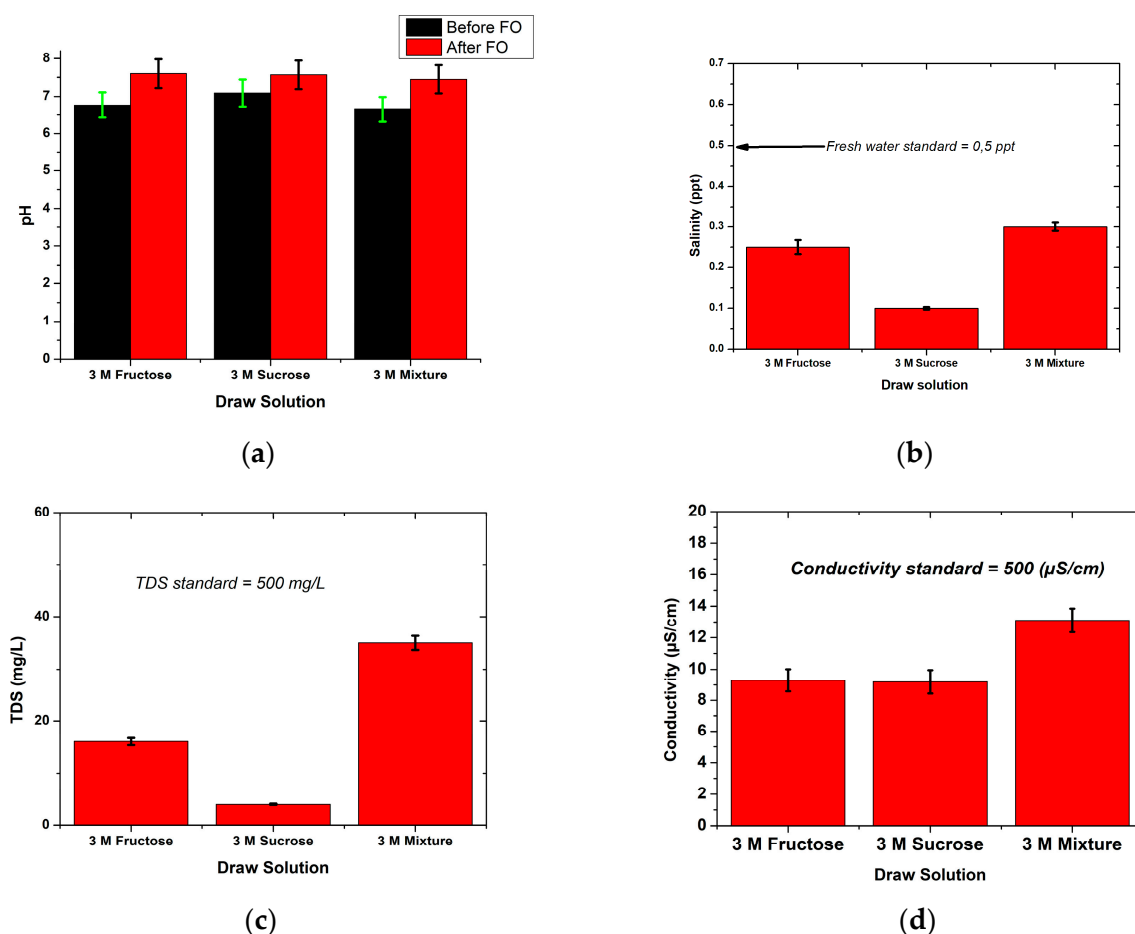


Figure 6. (a) pH, (b) salinity, (c) TDS, and (d) conductivity of the FO-processed water.

The water produced by the FO process in this study was also evaluated for TDS and conductivity to determine its ability to conduct electricity and also the number of dissolved solids present in the water. Figure 6c,d show the value of TDS and water conductivity resulting from the FO process. TDS values obtained were in the range of 2–116 mg/L and the conductivity values were in the range of 0.3–1.43  $\mu\text{S}/\text{cm}$ . These results are known to be better than the TDS and conductivity values reported in previous studies [5]. It was reported that TDS and conductivity values after the FO process using an unmodified chitosan membrane ranged from 2–353 mg/L and 1.92–393  $\mu\text{S}/\text{cm}$ . Based on these results, it was concluded that the modified chitosan membrane can hold particles better than the unmodified chitosan membrane. The maximum TDS value determined as the quality standard for drinking water by the WHO [30] was less than 600 mg/L.

### 3.5.2. Heavy Metal Content

The FO process's water was evaluated for the content of heavy metals As, Cd, Cr, Cu, Fe, Hg, Mn, and Zn, using an AAS. The content of heavy metals in water was essential because it is one of the WHO's mandatory parameters in drinking water quality standards. The results of testing heavy metal content are shown in Table 2.

Table 2 above shows that the feed solution used in this experiment contained heavy metals in low concentrations. Thus, the change of heavy metal contents in the water after the FO process was also minimal. However, if the brackish water feed contained monovalent, divalent, or multivalent ions, based on the literature, it was possible to be retained by the chitosan-based FO [5]. The cross-linked chitosan/starch membrane in this study had a rejection factor above 90%, indicating a high ability to retain dissolved salt in brackish water. Most studies report high rejections of almost every type of heavy metal by FO-like membranes [32,34–36]. You et al. [37] reported that the FO membrane was able to reject heavy metals whose hydrated ion diameters were smaller than the membrane pore size; the charge–interaction should be responsible for heavy metal rejection. The FO water filtration membrane bags have N- and O-containing functional groups that allows heavy metal ions retention via electrostatic repulsion and chelation [38]. However, the FO's heavy metal rejection could also be attributed to the role of the retained multivalent anions from the FS in maintaining the electroneutrality [39]. High diffusion during the FO process, as a consequence of maintaining the DS's electroneutrality, led to a counter ion transfer. Hence, ion exchange between the two solutions did not occur, proven by our FO-processed water's low ion contents.

### 3.5.3. Biological Water Properties

Other than being beneficial to humans, water is also a good medium for bacterial life. Bacteria are divided into two categories, namely pathogenic and non-pathogenic bacteria. Pathogenic bacteria can cause disease and diarrhea. Clean water that is safe to drink must meet the requirements set by the government and WHO. One of these standards relates to the microbiological conditions, where the *E. coli* should not be found in 100 mL of the water. *E. coli* itself is one of the pathogenic bacteria.

Saiful et al. reported that the chitosan-based drinking water bags are able to filter all types of *E. coli* and coliform bacteria [5,9]. *Escherichia coli* is a rod-shaped bacterium. Each of the bacteria was measured approximately to be 0.5  $\mu\text{m}$  in width by 2.0  $\mu\text{m}$  in length. Its dimensions are those of a cylinder 1.0–2.0  $\mu\text{m}$  long, with a radius of about 0.5  $\mu\text{m}$  [40,41]. *E. coli* and coliform bacteria have a larger size and are retained by the chitosan-dense membrane; bacteria from the FS side cannot pass through the membrane to the DS side. Moreover, chitosan is well-known for its antibacterial properties, by changing the permeability of the bacterial cell wall. It allows the bacteria to be killed on the membrane surface, leading to its application in anti-biofouling membranes [42]. However, based on the test results from the Aceh Health Laboratory Aceh Province and FMIPA Chemistry Laboratory, Department of Chemistry, Syiah Kuala University, the brackish water used in the FO process did not contain *E. coli* and coliform bacteria. As a result, the contribution of the FO process carried out by the drinking water bag in eliminating the *E. coli* was insignificant. Nonetheless, the process could be very helpful to

sterilize the water from microbial content during an emergency, where the level of contamination was expected to be high [43].

### 3.6. FO Filter Bag Durability

As a filter bag, this cross-linked chitosan/starch filter bag has some advantages despite the facts that there are always more room for improvement. First, with chitosan and starch raw materials available in nature that can be processed quickly, the price of drinking water bags can be competitive with existing products in the market. Moreover, with regards to membrane lifetime, as a drinking water bag is mostly made for single-use, the chitosan/starch membrane used in this study can be stored for a relatively long time. In a preliminary study, the FO drinking water bag did not change and leaked for about two weeks, which was indicated by no change in the TDS of the feed solution and the withdrawal solution, after reaching an equilibrium osmotic pressure that led to zero net flux.

## 4. Conclusions

This study indicated that the modified chitosan membrane was successfully applied to manufacture drinking water bags for the FO process. The different flux values produced in this study were attributed to the type of draw solution and ion content in the FS. The highest water flux was generated by the FO-drinking water bag using 3 M sucrose DS with values of 5.75 L/m<sup>2</sup> h and 8.5 L/m<sup>2</sup> h for brackish water and dam water FSs, respectively. The percentage of rejection produced in this study also showed a positive performance of the modified chitosan membrane, with a 99.8% value. This research also showed that the modified chitosan membrane was indicated to be successful in retaining salt, metals, bacteria, and other solutes. During the FO process, the filtered water met the WHO's quality standards set for drinking water. Based on these results, it can be concluded that the modified chitosan membrane has the potential to be used as an alternative water purification process in emergency water purification in order to produce drinking water containing sugar as an energy source for the body.

**Author Contributions:** Conceptualization, methodology, formal analysis, supervision, funding acquisition, S.S., M.A., and M.M.; resources, writing—original draft preparation, S.S., and M.A.; writing—review and editing, Y.W., S.S. All authors have read and agreed to the published version of the manuscript.

**Funding:** The APC was funded by the Ministry of Education and Culture Republic of Indonesia. The PDUPT research program supported this work.

**Acknowledgments:** The authors appreciate the Ministry of Education and Culture of the Republic of Indonesia for funding support and the Department of Chemistry at Syiah Kuala University, Indonesia, for the support of laboratory facilities.

**Conflicts of Interest:** The authors declare no conflict of interest.

## References

1. Hossain, M. Water: The most precious resource of our life. *Glob. J. Adv. Res.* **2015**, *2*, 1436–1445.
2. Bidaisee, S. The importance of clean water. *Biomed. J. Sci. Tech. Res.* **2018**, *8*, 17–20. [[CrossRef](#)]
3. Nugroho, W.A.; Nugraha, R.; Wibisono, Y. Autonomous framework on governing water for sustainable food and energy. In Proceedings of the Sharia Economic Conference, Hannover, Germany, 9 February 2013; pp. 37–41.
4. Wibisono, Y.; Nugroho, W.A.; Devianto, L.A.; Sulianto, A.A.; Bilad, M.R. Microalgae in food-energy-water nexus: A review on progress of forward osmosis applications. *Membranes* **2019**, *9*, 166. [[CrossRef](#)] [[PubMed](#)]
5. Saiful, S.; Borneman, Z.; Wessling, M. Double layer mixed matrix membrane adsorbers improving capacity and safety hemodialysis. In Proceedings of the IOP Conference Series: Materials Science and Engineering, Banda Aceh, Indonesia, 12–20 October 2018; Volume 352, p. 012048. [[CrossRef](#)]
6. Shamsuddin, N.; Das, D.B.; Starov, V. Membrane-based point-of-use water treatment (PoUWT) system in emergency situations. *Sep. Purif. Rev.* **2014**, *45*, 50–67. [[CrossRef](#)]
7. Peter-Varbanets, M.; Zurbrugg, C.; Swartz, C.; Pronk, W. Decentralized systems for potable water and the potential of membrane technology. *Water Res.* **2009**, *43*, 245–265. [[CrossRef](#)]

8. Loo, S.L.; Fane, A.G.; Krantz, W.B.; Lim, T.-T. Emergency water supply: A review of potential technologies and selection criteria. *Water Res.* **2012**, *46*, 3125–3151. [[CrossRef](#)]
9. Saiful; Riana, U.; Marlina; Ramli, M.; Mahmud, N. Drinking water bags based on chitosan forward osmosis membranes for emergency drinking water supply. In Proceedings of the IOP Conference Series: Materials Science and Engineering, Banda Aceh, Indonesia, 12–20 October 2018; Volume 273, p. 012047. [[CrossRef](#)]
10. Haupt, A.; Lerch, A. Forward osmosis application in manufacturing industries: A short review. *Membranes* **2018**, *8*, 47. [[CrossRef](#)]
11. Wibisono, Y.; Bilad, M.R. Design of forward osmosis system. In *Current Trends and Future Developments on (Bio-) Membranes*; Basile, A., Cassano, A., Rastogi, N.K., Eds.; Elsevier: Amsterdam, The Netherlands, 2020; pp. 57–83.
12. Zhao, S.; Zou, L.; Tang, C.Y.; Mulcahy, D. Recent developments in forward osmosis: Opportunities and challenges. *J. Membr. Sci.* **2012**, *396*, 1–21. [[CrossRef](#)]
13. Padaki, M.; Isloor, A.M.; Fernandes, J.; Prabhu, K.S. New polypropylene supported chitosan NF-membrane for desalination application. *Desalination* **2011**, *280*, 419–423. [[CrossRef](#)]
14. Shakeri, A.; Salehi, H.; Rastgar, M. Chitosan-based thin active layer membrane for forward osmosis desalination. *Carbohydr. Polym.* **2017**, *174*, 658–668. [[CrossRef](#)]
15. Igberase, E.; Osifo, P. Equilibrium, kinetic, thermodynamic and desorption studies of cadmium and lead by polyaniline grafted cross-linked chitosan beads from aqueous solution. *J. Ind. Eng. Chem.* **2015**, *26*, 340–347. [[CrossRef](#)]
16. Saiful, S.; Helwati, H.; Saleha, S.; Iqbalsyah, T.M. Development of bioplastic from wheat Janeng starch for food packaging. In Proceedings of the IOP Conference Series: Materials Science and Engineering, Banda Aceh, Indonesia, 12–20 October 2018; Volume 523, p. 012015. [[CrossRef](#)]
17. Saleha, S.; Saidi, N.; Rasnovi, S.; Iqbalsyah, T.M. Nutritional composition of *Dioscorea hispida* from different locations around leuser ecosystem area. *J. Nat.* **2018**, *18*, 1–6. [[CrossRef](#)]
18. Saiful, S.; Rahmah, Z.; Ajrina, M.; Marlina, R. Chitosan-starch forward osmosis membrane for desalination of brackish water. *Rasayan J. Chem.* **2020**, *13*, 13. [[CrossRef](#)]
19. Li, H.; Gao, X.; Wang, Y.; Zhang, X.; Tong, Z. Comparison of chitosan/starch composite film properties before and after cross-linking. *Int. J. Biol. Macromol.* **2013**, *52*, 275–279. [[CrossRef](#)] [[PubMed](#)]
20. Silva, R.M.; Silva, G.A.; Coutinho, O.P.; Mano, J.F.; Reis, R.L. Preparation and characterisation in simulated body conditions of glutaraldehyde crosslinked chitosan membranes. *J. Mater. Sci. Mater. Electron.* **2004**, *15*, 1105–1112. [[CrossRef](#)]
21. Li, F.H.; Chen, Y.M.; Li, L.; Bai, X.L.; Li, S. Starch-chitosan blend films prepared by glutaraldehyde cross-linking. *Adv. Mater. Res.* **2012**, *415–417*, 1626–1629. [[CrossRef](#)]
22. Narlis, J.; Rahmi, H.H. Effect of plasticizers on mechanical properties of edible film from janeng starch—Chitosan. *Natural* **2016**, *16*, 4. [[CrossRef](#)]
23. Fahrina, A.; Arahman, N.; Mulyati, S.; Aprilia, S.; Nawi, N.I.M.; Aqsha, A.; Bilad, M.R.; Takagi, R.; Matsuyama, H. Development of polyvinylidene fluoride membrane by incorporating bio-based ginger extract as additive. *Polymers* **2020**, *12*, 2003. [[CrossRef](#)]
24. Su, J.; Chung, T.S.; Helmer, B.J.; De Wit, J.S. Enhanced double-skinned FO membranes with inner dense layer for wastewater treatment and macromolecule recycle using Sucrose as draw solute. *J. Membr. Sci.* **2012**, *396*, 92–100. [[CrossRef](#)]
25. Chekli, L.; Phuntsho, S.; Shon, H.K.; Vigneswaran, S.; Kandasamy, J.; Chanan, A. A review of draw solutes in forward osmosis process and their use in modern applications. *Desalin. Water Treat.* **2012**, *43*, 167–184. [[CrossRef](#)]
26. Ge, Q.; Ling, M.; Chung, T.S. Draw solutions for forward osmosis processes: Developments, challenges, and prospects for the future. *J. Membr. Sci.* **2013**, *442*, 225–237. [[CrossRef](#)]
27. Hamdan, M.; Sharif, A.O.; Derwish, G.; Al-Aibi, S.; Altaee, A. Draw solutions for Forward Osmosis process: Osmotic pressure of binary and ternary aqueous solutions of magnesium chloride, sodium chloride, sucrose and maltose. *J. Food Eng.* **2015**, *155*, 10–15. [[CrossRef](#)]
28. Alaswad, S.O.; Al Aibi, S.; Alpay, E.; Sharif, A.O. Efficiency of organic draw solutions in a forward osmosis process using nano-filtration flat sheet membrane. *J. Biosens. Bioelectron.* **2018**, *9*, 10. [[CrossRef](#)]

29. Chen, G.; Wang, Z.; Nghiem, L.D.; Li, X.M.; Xie, M.; Zhao, B.; Zhang, M.; Song, J.; He, T. Treatment of shale gas drilling flowback fluids (SGDFs) by forward osmosis: Membrane fouling and mitigation. *Desalination* **2015**, *366*, 113–120. [[CrossRef](#)]
30. WHO. *Guidelines for Drinking-Water Quality*; WHO-Press: Geneva, Switzerland, 2017.
31. KepMenkes. *Regulation of the Minister of Health of the Republic of Indonesia Number 492/2010*; Quality of Drinking Water; Ministry of Health of the Republic of Indonesia: Jakarta, Indonesia, 2010.
32. Liu, C.; Lei, X.; Wang, L.; Jia, J.; Liang, X.; Zhao, X.; Zhu, H. Investigation on the removal performances of heavy metal ions with the layer-by-layer assembled forward osmosis membranes. *Chem. Eng. J.* **2017**, *327*, 60–70. [[CrossRef](#)]
33. Maity, J.P.; Ho, P.R.; Huang, Y.H.; Sun, A.C.; Chen, C.Y. The removal of arsenic from arsenic-bearing groundwater in In-situ and Ex-situ environment using novel natural magnetic rock material and synthesized magnetic material as adsorbent: A comparative assessment. *Environ. Pollut.* **2019**, *253*, 768–778. [[CrossRef](#)]
34. Zhao, X.; Liu, C. Efficient removal of heavy metal ions based on the optimized dissolution-diffusion-flow forward osmosis process. *Chem. Eng. J.* **2018**, *334*, 1128–1134. [[CrossRef](#)]
35. Wu, C.-Y.; Mouri, H.; Chen, S.-S.; Zhang, D.; Koga, M.; Kobayashi, J. Removal of trace-amount mercury from wastewater by forward osmosis. *J. Water Process. Eng.* **2016**, *14*, 108–116. [[CrossRef](#)]
36. Mondal, P.; Tran, A.T.K.; Van Der Bruggen, B. Removal of As(V) from simulated groundwater using forward osmosis: Effect of competing and coexisting solutes. *Desalination* **2014**, *348*, 33–38. [[CrossRef](#)]
37. You, S.; Lu, J.; Tang, C.Y.; Wang, X. Rejection of heavy metals in acidic wastewater by a novel thin-film inorganic forward osmosis membrane. *Chem. Eng. J.* **2017**, *320*, 532–538. [[CrossRef](#)]
38. Iqhrammullah, M.; Marlina, M.; Khalil, H.P.S.A.; Lahna, K.; Suyanto, H.; Hedwig, R.; Karnadi, I.; Olaya, N.G.; Abdullah, C.K.; Abdulmadjid, S.N. Characterization and performance evaluation of cellulose acetate–polyurethane film for lead II ion removal. *Polymers* **2020**, *12*, 1317. [[CrossRef](#)] [[PubMed](#)]
39. Irvine, G.J.; Rajesh, S.; Georgiadis, M.; Phillip, W.A. Ion selective permeation through cellulose acetate membranes in forward osmosis. *Environ. Sci. Technol.* **2013**, *47*, 13745–13753. [[CrossRef](#)] [[PubMed](#)]
40. Council, N.R. Size limits of very small microorganisms: Proceedings of a workshop. In Proceedings of the Workshop on Size Limits of Very Small Microorganisms, Washington, DC, USA, 22–23 October 1998.
41. Wibisono, Y.; Sucipto, S.; Perdani, C.G.; Astuti, R.; Dahlan, M. Halal compliance on drinking water industries: A future perspective. In Proceedings of the 3rd International Halal Conference (INHAC 2016), Singapore, 21–23 November 2018; pp. 555–564.
42. Li, J.; Xie, B.; Xia, K.; Zhao, C.; Li, Y.; Li, N.; Han, J. Facile synthesis and characterization of cross-linked chitosan quaternary ammonium salt membrane for antibacterial coating of piezoelectric sensors. *Int. J. Biol. Macromol.* **2018**, *120*, 745–752. [[CrossRef](#)] [[PubMed](#)]
43. Sari, P.N.; Nofriya, N. The relationship of flood disaster with the incidence of diarrhea, water quality and community resilience in water supply: A case study in the city of Bukittinggi. *J. Kesehat. Masy. Andalas* **2018**, *12*, 77–83. [[CrossRef](#)]

**Publisher’s Note:** MDPI stays neutral with regard to jurisdictional claims in published maps and institutional affiliations.






© 2020 by the authors. Licensee MDPI, Basel, Switzerland. This article is an open access article distributed under the terms and conditions of the Creative Commons Attribution (CC BY) license (<http://creativecommons.org/licenses/by/4.0/>).





Article

# Removal of Different Dye Solutions: A Comparison Study Using a Polyamide NF Membrane

Asunción María Hidalgo <sup>1,\*</sup>, Gerardo León <sup>2</sup>, María Gómez <sup>1</sup>, María Dolores Murcia <sup>1</sup>,  
Elisa Gómez <sup>1</sup> and José Antonio Macario <sup>1</sup>

<sup>1</sup> Departamento de Ingeniería Química, Facultad de Química, Campus de Espinardo, Universidad de Murcia, 30100 Murcia, Spain; maria.gomez@um.es (M.G.); md.murcia@um.es (M.D.M.); egomez@um.es (E.G.); joseantonio.macario@um.es (J.A.M.)

<sup>2</sup> Departamento de Ingeniería Química y Ambiental, Universidad Politécnica de Cartagena, 30202 Cartagena, Spain; gerardo.leon@upct.es

\* Correspondence: ahidalgo@um.es; Tel.: +34-868-887-353

Received: 9 November 2020; Accepted: 9 December 2020; Published: 10 December 2020



**Abstract:** The removal of organic dyes in aquatic media is, nowadays, a very pressing environmental problem. These dyes usually come from industries, such as textiles, food, and pharmaceuticals, among others, and their harm is produced by preventing the penetration of solar radiation in the aquatic medium, which leads to a great reduction in the process of photosynthesis, therefore damaging the aquatic ecosystems. The feasibility of implementing a process of nanofiltration in the purification treatment of an aqueous stream with small size dyes has been studied. Six dyes were chosen: Acid Brown-83, Allura Red, Basic Fuchsin, Crystal Violet, Methyl Orange and Sunset Yellow, with similar molecular volume (from 250 to 380 Å). The nanofiltration membrane NF99 was selected. Five of these molecules with different sizes, shapes and charges were employed in order to study the behavior of the membrane for two system characteristic parameters: permeate flux and rejection coefficient. Furthermore, a microscopy study and a behavior analysis of the membrane were carried out after using the largest molecule. Finally, the Spiegler–Kedem–Katchalsky model was applied to simulate the behavior of the membrane on the elimination of this group of dyes.

**Keywords:** characterization; dyes; molecular structure; nanofiltration; physico-chemical properties

## 1. Introduction

Organic dyes (such as Acid Brown-83, Allura Red, Basic Fuchsin, Crystal Violet, Methyl Orange and Sunset Yellow) can be found in effluents of different industries (food, medical, painting) but the most pollutant industry is the textile.

The discharge of these pollutants into the aquatic environment has a strong environmental impact due to the amount of toxic compounds they have and also due to the fact that they cause a decrease in the self-purification capacity of the water they are discharged into. This phenomenon prevents plants from performing photosynthesis and microorganisms from developing their biological activity [1].

Therefore, there are numerous methods of disposal of dye aqueous solutions, which can be grouped into physical, chemical and biological methods, but none of them stand out among the others [2–5]. Following this, new techniques are being investigated, including membrane technologies, because they offer low costs and give good yields [1,6].

As a result, membrane technology is attracting great interest. This technology is based on the separation of compounds by size and charge, as the membrane acts as a filter that retains the molecules which are larger than the pore and allows the water to pass through. In the last decade, more than 65% of research works have been based on the fabrication strategies of nanoporous membranes and their

applications in the field of water purification [7–12]. According to Wang et al. the solute and water permeability play important roles in the membrane performance. The membrane is able to separate pollutants from water mainly through size exclusion and solute diffusion [7].

The application of pressure driven membrane processes for the removal of low molecular weight organic compounds from aqueous solutions has been described in several recent publications—for example, phenol and chlorophenol compounds [13]. A comparative study, using different organic compounds (atrazine, aniline and phenol, and their derivatives 4-chlorophenol, 4-nitrophenol and 4-nitroaniline) in aqueous solution and their elimination through NF-97 polyamide membrane, was carried out. The different physicochemical parameters of the organic compounds, the permeate flux and the rejection coefficient values were found to be correlated. The best correlation for the rejection coefficient was obtained using the molar refractivity and the water solubility of the compound simultaneously. For permeate flux, the best correlation value was obtained using the surface tension and molecular weight [14].

It is clear that removal efficiency depends on the membrane type and solute, and the interaction between them. Temperature, pH, pressure and concentration also influence rejection [15]. Whether nanofiltration should be used in the treatment of wastewater containing dyes depends on the rejection capacity of the membranes and the permeate flux.

In addition, distilled water tests were performed in order to characterize the membrane, and selectivity tests facing salt solutions before and after dyes tests were carried out in order to know the membrane permeability, studying performance and its changes during the process. In that way, membrane fouling can be analyzed, as well as the phenomenon in which membrane pores get wider because substances passing, known as swelling, can be observed [16–18].

The discussion on membrane-based treatment processes is incomplete without an elaborate perception of the mechanism governing the transport of solute across the membrane and compressive modeling of a membrane-based technique [1].

The main goal of this research work is to study the behavior of the NF99 membrane on the elimination of several dyes, which are molecules of different structure, charge and shape, the following ones being chosen: Allura Red, Basic Fuchsin, Crystal Violet, Methyl Orange and Sunset Yellow. These molecules were selected since in the bibliography there are no studies for some of them, such as Basic Fuchsin and Allura Red. Solutions of each dye were used to characterize the system and to obtain the values of the permeate flux and rejection coefficient. Furthermore, a preliminary study on the characterization of the membrane treated with salt solutions was carried out before and after the dye treatment. Such a study was complemented by scanning electric microscopy (SEM) morphologic study of the membrane using the Acid Brown-83 dye. This molecule was selected because it is a real case of a leather tanning industry located in Murcia (Spain). Finally, the Spiegler–Kedem–Katchalsky model was applied to simulate the behavior of the membrane on the elimination of this group of dyes.

## 2. Materials and Methods

### 2.1. Materials

#### 2.1.1. Membrane

A nanofiltration membrane was employed in this research. Its main technical characteristics are shown in Table 1.

**Table 1.** Characteristics of the membrane used in the experimental test module.

<b>Manufacturer</b>	Alfa Laval (Denmark)
<b>Product denomination</b>	NF99
<b>Type</b>	Thin-film composite on polyester
<b>Composition</b>	Polyamide
<b>Membrane surface area (m<sup>2</sup>)</b>	0.003
<b>Maximum pressure (N m<sup>-2</sup>)</b>	55 × 10 <sup>5</sup>
<b>MgSO<sub>4</sub> rejection (%) (2 kg m<sup>-3</sup>, 9·10<sup>5</sup> N m<sup>-2</sup>)</b>	≥98
<b>NaCl rejection (%)</b>	>90
<b>pH range</b>	3–10
<b>Temperature range (°C)</b>	5–50

### 2.1.2. Reagents

The following reagents were used in the assays:

- Acid Brown-83 (AB83), C<sub>18</sub>H<sub>13</sub>N<sub>6</sub>NaO<sub>8</sub>S and its molecular weight is 496.39 g/mol. Supplied by Alfa Industries (Spain).
- Allura Red (AR), C<sub>18</sub>H<sub>14</sub>N<sub>2</sub>Na<sub>2</sub>O<sub>8</sub>S<sub>2</sub>. Its molecular weight is 496.44 g/mol, 80% of purity. Supplied by Sigma-Aldrich INC (Germany).
- Basic Fuchsin (BF), C<sub>20</sub>H<sub>20</sub>ClN<sub>3</sub>. Its molecular weight is 337.86 g/mol. Supplied by Sigma-Aldrich (Germany).
- Crystal Violet (CV), C<sub>20</sub>H<sub>11</sub>N<sub>2</sub>Na<sub>3</sub>O<sub>10</sub>S<sub>3</sub>. Its molecular weight is 407.98 g/mol and ≥90% of purity. Supplied by Sigma-Aldrich INC (Germany).
- Methyl Orange (MO), C<sub>14</sub>H<sub>14</sub>N<sub>3</sub>O<sub>3</sub>NaS. Its molecular weight is 327.33 g/mol. Supplied by Probus (Spain).
- Sunset Yellow (SY), C<sub>16</sub>H<sub>10</sub>N<sub>2</sub>Na<sub>2</sub>O<sub>7</sub>S<sub>2</sub>. Its molecular weight is 452.37 g/mol and 80% of purity. Supplied by Sigma (Germany).
- Sodium Chloride (NaCl). Its molecular weight is 58.4 g/mol. Supplied by Panreac (Spain).
- Hydrous magnesium chloride, MgCl·6H<sub>2</sub>O. Its molecular weight is 203.30 g/mol. Supplied by Panreac (Spain).

In Table 2, Log K<sub>wo</sub>, pK<sub>a</sub> and water solubility data, obtained using PubChem, are shown.

**Table 2.** Chemical properties of some of the dyes employed in the study. Data obtained using PubChem. <https://pubchem.ncbi.nlm.nih.gov/>.

Dyes	Log K <sub>ow</sub>	pK <sub>a</sub>	Water Solubility (g L <sup>-1</sup> )
AB83	-	-	>100
AR	-0.55	-	225
BF	1.632 (*)	-	1–5
CV	0.96	pK <sub>a1</sub> = 5.31	4
	0.51	pK <sub>a2</sub> = 8.64	
MO	-0.66 (*)	-	0.2
			5.0 (*)
SY	-1.18	pK <sub>a1</sub> = 0.82	190
		pK <sub>a2</sub> = 1.46	

(\*) <https://www.carlroth.com/medias/>.

### 2.2. Equipment

The research was carried out in a membrane module from INDEVEN CF (Spain), which has been designed at laboratory scale to obtain further information on the behavior of plane membranes with small surface area. In addition to the membrane module, other equipment was used to obtain valuable parameters for further comparison and discussion among the different dyes.

### 2.2.1. Membrane Module

The membrane module consists of three main stages of installation: feed tank, fluid impulsion pump and membrane settlement. Furthermore, there is a manometer and a rotameter that measure rejection pressure.

The feed tank is cylindric and it maintains the internal fluid at a constant temperature. Its capacity is of 12 L. The fluid passes from the feed tank to the driving pump through a flexible rubber pipe. The pump is a triple plunger pump from Flowmax (Spain). It consists of three AISI 316 Steel valves and of corrosion resistant double collectors. Flow rate is controlled by a manual needle valve.

The membrane inflows are divided into two: permeate flow and concentrate flow. The last one re-enters the feed tank. Moreover, the vent plug discharge and the caudal control are carried out by a flow that leaves the impulsion pump and arrives to the feed tank.

The membrane, whose surface is 30 cm<sup>2</sup>, is placed near the feeding spacer, with the active layer looking towards the mainboard. The following step involves placing the permeate spacer and finally the closing plate. Two o-rings seal the set.

Continuous functioning is guaranteed because the concentrate flow discharges in the feed tank. Operating pressure is regulated by a valve and a manometer, and the flow is measured by a rotameter from TechFluid, which detects flows ranging from 50 to 400 L/h.

### 2.2.2. Spectrophotometer

A spectrophotometer from Shimadzu (UV-160) (Japan) was employed to measure the absorbance of the dye samples. The measurements were carried out at specific wavelengths, which were 443 nm for Acid Brown-83, 485 nm for Sunset Yellow, 596 nm for Crystal Violet, 500 nm for Allura Red, 460 nm for Methyl Orange and 550 nm for Basic Fuchsin.

### 2.2.3. Variable Pressure Scanning Electron Microscope

To develop the membrane fouling study, a scanning electron microscope from Hitachi (S-3500N model) (Japan) was employed; its main characteristics are the following:

- Resolution: 3 nm (high vacuum mode) or 4.5 nm (low vacuum mode);
- Zoom: 15–300,000;
- Accelerating voltage: 0.3–30 kv;
- Variable pressure range: 1–270 Pa;
- Secondary electrons detector;
- Robinson's backscattered electron detector;
- Secondary electrons in variable pressure detector;
- X-ray detector;
- Eucentric plate with computer control and motorized movements in X, Y, Z, R and T;
- Crio-SEM cooling plate ( $-190 \pm 60$  °C);
- Peltier's cooling sample holder ( $-15 \pm 50$  °C).

## 2.3. Experimental Series

In order to obtain further knowledge about the membrane behavior, a series of experiments with different dyes were carried out. In these series of experiments, all the operating conditions remained unchanged excluding that which was subject of study.

### 2.3.1. Distilled Water Assays

The tank was filled with distilled water and afterwards a series of experiments were carried out. The experiments were of 15 min of length, at 5, 10 and 15 bar operating pressures and with a 150 L/h flow. The main goal of these assays was to get to know the permeability of the membrane.

### 2.3.2. Salts Assays

The objective of the experimental assays using salt solutions was to obtain the membrane rejection coefficient and, as a result, its selectivity. In the same way that distilled water assays, the experiments were carried out at 5, 10 and 15 bar operating pressure and with a 150 L/h flow; however, the duration time was of 20 min. Aqueous solutions of 1 g/L were used to carry out the experimental assays. The salts employed in the experiments were magnesium chloride and sodium chloride.

### 2.3.3. Dyes Assays

In order to elucidate the membrane elimination power in detail, a 50 mg/L dye dissolution was employed to fill the feed tank and 30 min assays were carried out, in which the samples were taken every 5 min with different operating pressures. Duplicate assays were carried out.

- Firstly, while the pH was maintained constant at 7 and the flow at 150 L/h, the operating pressure was varied: 10 and 15 bar.
- With the aim of finding out the influence of the pH, the previous experimental series were repeated, changing the pH: first at 8 and afterwards at 3.
- Finally, once all of these assays were carried out, the distilled water assay and the salts assay were repeated to check if the membrane had lost permeability after its use.

## 3. Results and Discussion

### 3.1. Membrane Characterization

The initial membrane characterization was carried out by determining its permeability coefficient, its performance regarding flows and its selectivity against two different salt solutions: sodium chloride and magnesium chloride.

#### Permeability Coefficient Determination

In order to determine the permeability coefficient, the following equation was used:

$$J_v = L_p \cdot (\Delta P - \Delta \Pi) \tag{1}$$

The osmotic pressure gradient can be ignored only if the solvent is employed alone. As a result, the previous equation can be described as:

$$J_v = L_p \cdot \Delta P \tag{2}$$

The permeability coefficient value is obtained by representing the final values of the solvent mass flow against applied pressure.

In Table 3, the permeability coefficient for the solvent ( $L_p$ ) values obtained in this research for different pressure ranges and the permeability coefficient values found in the literature are shown. As can be observed, the values obtained in this research are of the same order as those found in the literature [19–21].

Table 3. Properties of the membrane used in the experimental assays.

Membrane	Water Permeability $L_p$ ( $m\ s^{-1}$ )	Solute Permeability $P_s$ ( $m \cdot s^{-1}$ )	
		NaCl	MgCl <sub>2</sub>
NF99	$1.665 \times 10^{-8}$	$6.705 \times 10^{-6}$	$1.632 \times 10^{-7}$
References[13,19,20]	$1.5 \times 10^{-8}$	-	-

### 3.2. Determination of Selectivity and Performance of the Membrane against Salt Solutions

The characterization of NF membranes is often carried out using divalent salt solutions. In this research, two salt solutions were used: sodium chloride and magnesium chloride.

To determinate the selectivity of the membrane, the rejection coefficient was established:

$$\%R = \frac{(C_0 - C_p)}{C_0} \cdot 100 \quad (3)$$

The experimental values obtained for permeate flux and rejection coefficient were treated by applying the solution-diffusion model [22]. As a result, the permeability coefficient for the solute (Ps) for each salt solution was obtained.

Table 2 shows the Ps values for each salt solution assayed, which are very close to those obtained by previous authors [13].

### 3.3. Influence of the Chemical Structure of Different Dyes

Usually, parameters such as molecular weight, log Kw and pKa, were used to explain the membrane selectivity and the rejection coefficient. However, in recent years, to attempt to explain the behavior of the nanofiltration systems, based on the two characteristic parameters, the permeate flux and the rejection coefficient, the influence of chemical structure parameters could represent an important factor to consider.

Table 4 shows the chemical structure parameters of the dye molecules. The parameters, such as area, radio, length and volume were obtained by the program, MarvinSketch version 15.12.7, using ChemAxon. Furthermore, Figure 1 shows the charge, shape and geometry of different molecules using a tridimensional draw. These parameters were proven to influence permeate flux and rejection coefficient.

**Table 4.** Structure parameters of the dye molecules. Data obtained using ChemAxon. <https://chemaxon.com/products/marvin>.

Dyes	Allura Red	Basic Fuchsin	Crystal Violet	Methyl Orange	Sunset Yellow
Dreiding energy (kcal/mol)	318.39	186.09	294.85	237.39	311.43
MMFF94 energy (kcal/mol)	196.18	69.17	121.74	93.12	184.7
Minimal projection area (Å <sup>2</sup> )	51.15	55.59	71.18	30	46.88
Maximal projection area (Å <sup>2</sup> )	117.52	81.35	105.67	93.1	105.50
Minimal projection radius (Å)	5.33	6.28	7.49	3.96	5.78
Maximal projection radius (Å)	8.57	6.76	8.06	8.58	8.40
Length perpendicular to the max area (Å)	8.44	7.46	8.24	5.88	9.43
Length perpendicular to the min area (Å)	16.78	12.60	14.84	17.33	16.22
Van der Waals volume (Å <sup>3</sup> )	338.50	270.57	378.31	254.85	295.56


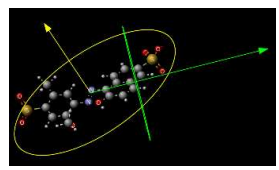
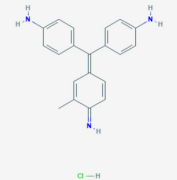
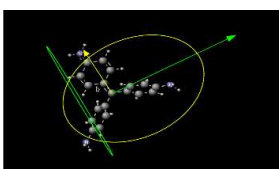
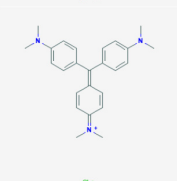
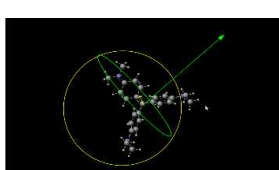
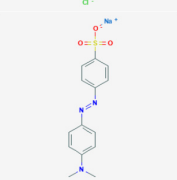
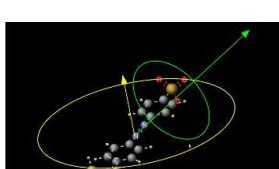
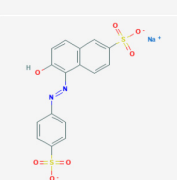
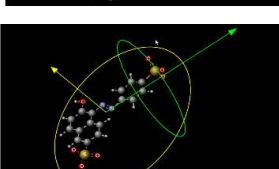
Dyes	Chemical Structure	Shape	Charge	Molecular Structure
Allura Red		Lineal	-2	
Basic Fuchsin		Flat disc	+1	
Crystal Violet		Flat disc	+1	
Methyl Orange		Lineal	-1	
Sunset Yellow		Lineal	-2	

Figure 1. Molecular properties of the dyes.

In the literature, some authors have described that the most influential parameter is molecular volume, but other parameters related to chemical properties can also be used to predict the behavior of these systems. Figure 2 shows the influence of molecular volume in rejection coefficients and permeate flux using a pressure of 10 bar (a), and 15 bar (b) for the different dyes.

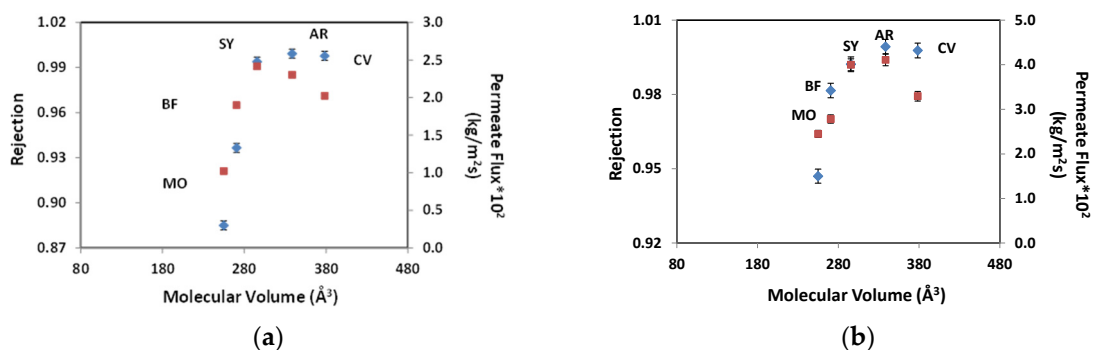


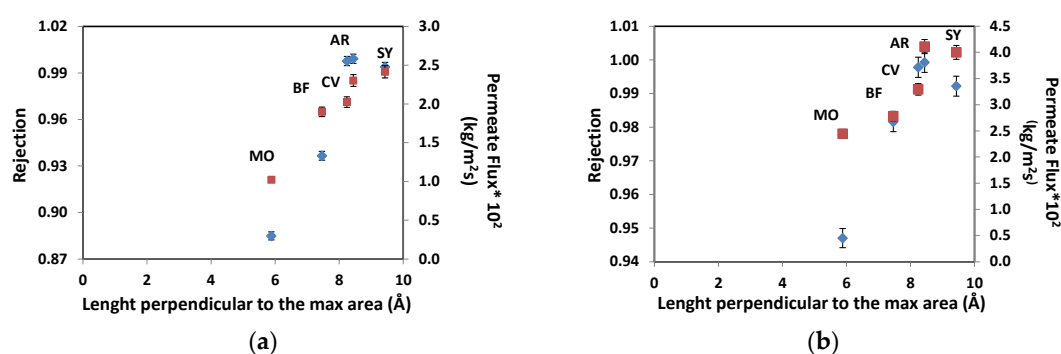
Figure 2. Rejection coefficient (◆) and permeate flux (■) variation with molecular volume for colorants: (MO) Methyl Orange, (BF) Basic Fuchsin, (SY) Sunset Yellow, (AR) Allura Red, (CV) Crystal Violet. Experimental conditions: pH = 7, [Dyes] = 50 mg/L and pressure values (a) 10 bar and (b) 15 bar.



As can be seen in Figure 2a, when the molecular volume is increased, the selectivity of the membrane increases too. When comparing the values obtained for the different pressures applied, it is seen that high-volume molecules present a small decrease in the rejection coefficient when the pressure applied is high (15 bar). Besides that, the permeate flux has no predictive behavior because both the small dye molecules (MO and BF) that have a similar size to the molecular weight cut off MWCO of the membrane and the large dye molecules (CV) have low permeate fluxes.

According to Cheng et al. (2016), membrane water permeability and solute rejection can be attributed to sensitive pore size and membrane charge. This separation discerned three mechanisms, size exclusion (sieving), electrostatic repulsion (Donnan exclusion) and adsorption. The rejection of neutral molecules and large dye molecules (CV) was mostly size exclusion. The rejection of the low-charged solutes was dominated by the electrostatic interactions, including repulsion (cations) and attraction (anions) (BF) [15].

Furthermore, different parameters of the structure of the molecules were correlated with the permeate fluxes and rejection coefficients obtained (Figures S1–S4, Supplementary Material), and it was tested that the parameter that presents a greater incidence is length perpendicular to the maximum area. Figure 3 shows the influence of perpendicular length to the maximum area on permeate flux and rejection coefficient for (a) 10 bar and (b) 15 bar pressures. In this case, the highest value of length perpendicular to the maximum area corresponds to Sunset Yellow dye, and the values obtained for permeate flux and rejection coefficient show a lineal correlation with this parameter, in this particular range studied.



**Figure 3.** Rejection coefficient (◆) and permeate flux (■) variation with length perpendicular to the maximum area for colorants: (MO) Methyl Orange, (BF) Basic Fuchsin, (SY) Sunset Yellow, (AR) Allure Red, (CV) Crystal Violet. Experimental conditions: pH = 7, [Dyes] = 50 mg/L and pressure values (a) 10 bar and (b) 15 bar.

### 3.4. Influence of pH: Comparison of Electrostatic Interaction and Membrane Performance

The permeate fluxes and rejection coefficients obtained from the dye molecule assays were studied with different pH values using the NF99 membrane under identical conditions and the obtained values are shown in Table 5.

**Table 5.** Rejection coefficient and permeate flux variation with pH of feed for the different dyes. P = 15 bar; [Dye] = 50 mg/L.

Dyes	Permeate Flux (kg/m <sup>2</sup> s) × 10 <sup>3</sup>			Rejection Coefficients (%)		
	pH = 3	pH = 7	pH = 8	pH = 3	pH = 7	pH = 8
AB83	35.44	33.50	33.33	99.40	99.48	99.56
AR	39.20	41.11	38.40	99.99	99.93	99.95
BF	-	30.86	-	-	98.78	-
CV	38.66	32.96	16.75	99.91	99.78	99.98
MO	37.87	31.72	19.17	97.27	87.47	99.02
SY	34.67	40.00	38.67	99.78	99.22	99.88

According to different authors [11,15,16], electrostatic interactions between the membrane and charged molecules is an important parameter which determines flux decline. Usually, the pH values of effluents from the dyeing industry are between neutral and basic pH [4]. In this pH range, the polyamide NF99 membrane possesses negative charge, and therefore the negatively charged dye molecules (AB83, AR, MO and SY) are not electrostatically attracted towards the membrane, and hence they do not significantly reduce the permeate flux. However, AB83 and MO dyes molecules showed a decrease in permeate flux, being more significant in the case of MO. This behavior could be explained due to other types of interactions, such as hydrophobic ones (between the aromatic rings of both the dyes and the polyamide membrane selective layer) or hydrogen bonds that can play an important role in membrane blocking, especially under the conditions in which the acidic or basic groups in dyes are partially dissociated.

Positively charged dye molecules (CV) of relatively low molecular weight exhibit a strong fouling effect in the neutral as well as the alkaline pH of the feed solution. This behavior is according to the results obtained by Chindambaram et al. [16].

### 3.5. Fouling Phenomenon after Treatment of Dyes Solutions

A simple means of evaluating the fouling phenomenon effect on the membrane is to repeat the distilled water assays after the dye assays are carried out. In this research, the fouling factor of the membrane, %FF, was calculated in order to quantify the fouling phenomenon by comparing the initial,  $L_{p0}$ , and final,  $L_{pf}$ , values of the permeability coefficient. The equation is the following:

$$\%FF = \frac{(L_{p0} - L_{pf})}{L_{p0}} \cdot 100 \quad (4)$$

Table 6 shows the results of the fouling factor of the membrane after the use of the different dyes studied.

**Table 6.** Values of fouling factor of the membrane for the different dye assays.

Dyes	AB83	AR	BF	CV	MO	SY
FF (%)	10.65	0.6	87.23	24.13	35.29	3.44

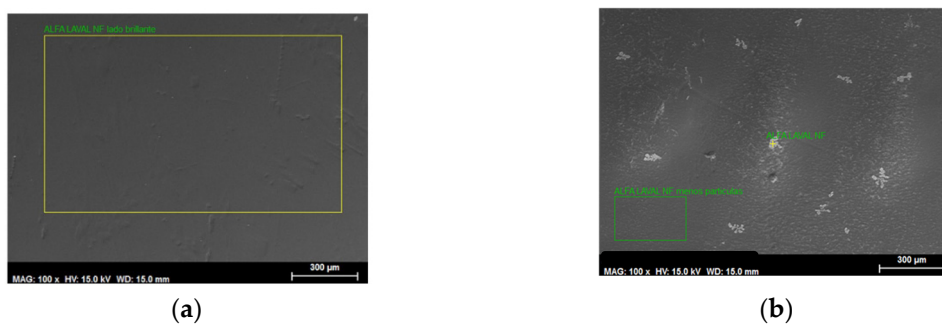
Considering the molecular weight and molecular volume values obtained for each dye, it was found that the smaller dye molecules (MO and BF), whose sizes were close to the molecular weight cut-off (MWCO) of the membrane (200 Da), presented a higher fouling factor. This fact showed that these dyes were absorbed in the membrane and, consequently, the fluxes were reduced. Some authors also described adsorption phenomena for SY [15]. When comparing two dyes of similar molecular size (MO and BF, or CV and AB83), the dye molecules with negative charges and of a linear size gave a lower fouling factor than those of positive charges and with flat disc shape. These results were already described in other studies [23,24].

### 3.6. Morphologic Study of the Membrane

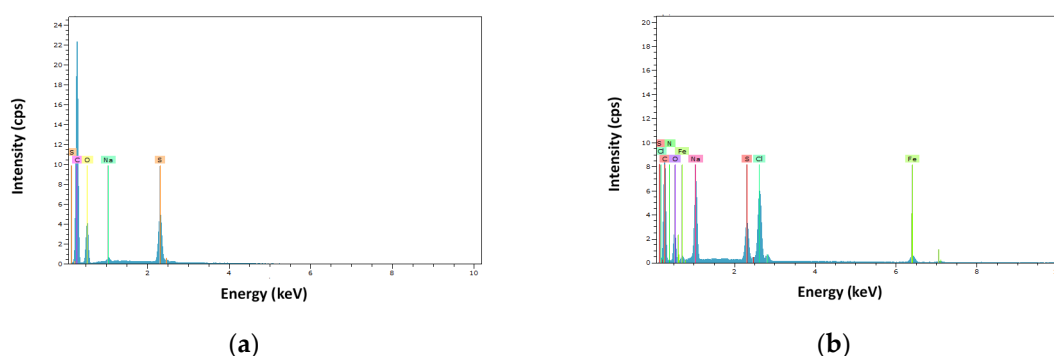
Even though there are many available techniques for observing the membrane surface (including the active layer and the sublayer that sustains it), the most employed technique for nanofiltration membrane characterization is Scanning Electron Microscopy (SEM).

In this research, the samples of native membrane and used membrane (after carrying out the assay of the dye of higher molecular weight, AB83) were analyzed.

Figure 4a,b shows an SEM picture (300×) of the membrane Alfa Laval NF before starting the assays and after them. Figure 5 shows the energy-dispersive X-ray spectrum of the membrane (a) before the initial assay and (b) after the pass of Acid Brown-83 solutions through the membrane.



**Figure 4.** SEM taken picture (300x) of the Alfa Laval NF membrane (a) before starting the assays and (b) after them.



**Figure 5.** EDX analysis of the membrane (a) before the initial assay and (b) after the pass of Acid Brown-83 solutions through the membrane.

When comparing Figures 4 and 5 for the study of the evolution of the Alfa Laval NF membrane after its use, it can be observed that the SEM picture shows that there is a certain degree of fouling. Membrane fouling is mainly observed on the active layer.

Furthermore, according to the energy-dispersive X-ray spectrum, new elements, such as chlorine, iron and nitrogen appear to be on the membrane surface after the assays. The presence of these elements can be explained because of the pass of Sodium Chloride and the dye solution through the membrane, and because of metallic rests from the installation.

### 3.7. Application of the Spiegler–Kedem–Katchalsky Model

In the bibliography, some adequate models to explain the behavior of the separation process for a thin-layer membrane have been described [25–27]—for example, the solution-diffusion model. Therefore, other models are based on the use of coefficients that relate the permeate flux and the fouling factor of the membrane, but in recent years, the most-used models are based on phenomenological transport.

Those models correlate driving force and flow linearly:

$$J_i = L_{i,j} \cdot X_j \tag{5}$$

where  $J_i$  is the flow density of the component,  $X_j$  is the driving force and  $L_{i,j}$  is the proportionality coefficient.

The driving forces that dominate the transference of matter in membrane processes are the gradient of pressure and the gradient of concentration.

The Spiegler–Kedem–Katchalsky model [28,29] expresses the initial equations of the previous model in a differential way; not linearly. As a result, it considers that the densities of flux vary through the thickness of the membrane.

$$J_v = L_p \cdot \left( \frac{dP}{dx} - \sigma \frac{d\Pi}{dx} \right) \tag{6}$$

$$J_s = P_s \cdot \frac{dC_s}{dx} + (1 - \sigma) \cdot C_s \cdot J_v \tag{7}$$

When expressing both equations incrementally:

$$J_v = L_p \cdot (\Delta P - \sigma \cdot \Delta \Pi) \tag{8}$$

$$J_s = P_s \cdot (C_m - C_p) + (1 - \sigma) \cdot J_v \cdot C_s \tag{9}$$

The Spiegler–Kedem–Katchalsky model was initially developed for reverse osmosis processes; however, it has been proven that it is also applicable in some nanofiltration processes [30,31].

This model assumes that transport coefficients are independent of solute concentration. Nevertheless, these coefficients depend on solute concentration for ionic solutions in nanofiltration membranes. As a result, some authors made some changes in the model to consider this fact [32].

There are two parameters to be determined for the Spiegler–Kedem–Katchalsky model:

- Reflection coefficient ( $\sigma$ ). This indicates the capacity of the membrane to be permeated by the solute. A  $\sigma = 0$  value indicates that the membrane is completely permeable for the solute, whereas a  $\sigma = 1$  value indicates that the solute is unable to go through the membrane, as it is completely impermeable (total reflection).
- Solute permeability coefficient ( $P_s$ ). It is defined as the speed at which the solute passes through the membrane. It is unique for each compound and membrane. It is measured in m/s.

The pass of a solute flux through the membrane is caused by two different fluxes: a convective flux, which is caused by the application of a gradient of pressure through the membrane, and a diffusive flux, which is caused by the gradient of concentration in both sides of the membrane. The reflection coefficient is also an indicator of what type of flux prevails: the closer the  $\sigma$  values are to 1, the lower participation has the convective flux [33].

For ideal reverse osmosis membranes,  $\sigma$  values are close to 1 as they present a dense structure and no pores that would enable convective transport.

The observed rejection was calculated using the following expression:

$$\%R_{obs} = \frac{(1 - F)}{1 - \sigma \cdot F} \cdot 100 \tag{10}$$

where  $F$  is a parameter that depends on the reflection coefficient, solvent flux, and solute permeability coefficient [34]:

$$F = e^{(1 - \frac{\sigma}{P_s}) \cdot J_v} \tag{11}$$

The transport phenomenon through the membrane is, in fact, a combination of convection, solution, and diffusion. In this case, the transport process can be described as an irreversible thermodynamic phenomenon. The following relations among the parameters of the process: reflection coefficient and solute permeability ( $\sigma$  and  $P_s$ ), solvent flux ( $J_v$ ) and observed rejection ( $R_{obs}$ ) were proposed by Spiegler, Kedem and Katchalsky:

$$Ln[X] = 1 - \frac{1 - \sigma}{P_s} \cdot J_v \tag{12}$$

$$X = \left( \frac{1}{(1 - \sigma)} - \frac{1}{1 - R_{obs}} \right) \cdot \frac{(1 - \sigma)}{\sigma} \tag{13}$$

The parameters of the model were obtained by employing both Equations (12) and (13) along with (9). When combining Equations (12) and (13), Equation (14) is obtained:

$$\text{Ln} \left[ \left( \frac{1}{(1-\sigma)} - \frac{1}{1-R_{obs}} \right) \cdot \frac{(1-\sigma)}{\sigma} \right] = 1 - \frac{1-\sigma}{P_s} \cdot J_v \tag{14}$$

The average  $R_{obs}$  value was calculated from the experimental data of rejection coefficients; thus it is now a known value. From this value, a parameter  $z$  ( $\frac{1}{1-R_{obs}}$ ) was calculated.

Equations (9) and (14) were employed to determine the rejection coefficient ( $\sigma$ ) and the permeability coefficient ( $P_s$ ). It was determined that solute concentration in the feed was the same as the solute concentration in the membrane ( $C_m \approx C_0$ ), as few polarization processes occur. The analyzed solute feeding and permeate concentrations are converted to mol/m<sup>3</sup> by dividing by the molecular weight of the different dyes.

When replacing  $J_s$ ,  $J_v$ ,  $C_0$  and  $C_p$  in Equation (9), and after isolating  $P_s$ , the following value, dependent on  $\sigma$ , is obtained:

$$P_s = \frac{J_s - J_v \cdot C_s \cdot (1 - \sigma)}{C_0 - C_p} \tag{15}$$

This would lead to a  $P_s = a - b \cdot (1 - \sigma)$  type of equation, so Equation (14) would become the following:

$$\text{Ln} \left[ \left( \frac{1}{(1-\sigma)} - z \right) \cdot \frac{(1-\sigma)}{\sigma} \right] - 1 + \frac{1-\sigma}{a-b \cdot (1-\sigma)} \cdot J_v = 0 \tag{16}$$

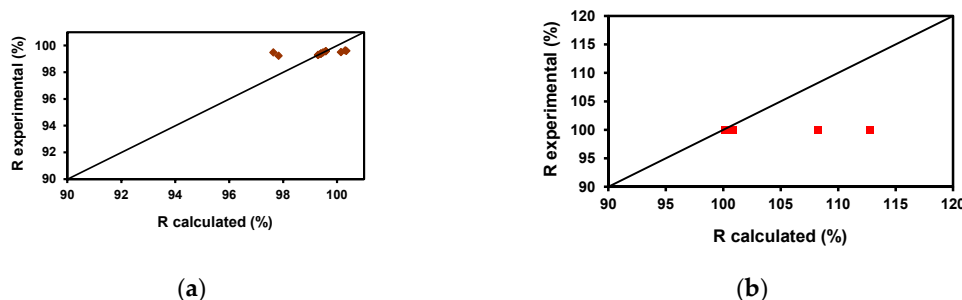
where  $a = \frac{J_s}{C_0 - C_p}$  and  $b = \frac{J_v \cdot C_s}{C_0 - C_p}$ .

In order to solve this equation of one unknown parameter ( $\sigma$ ), it is necessary to use a numeric method, since there is no analytical solution. The program Solver from Excel was employed for that purpose. As a result, the parameters  $\sigma$  and  $P_s$  were obtained for each different case. The results are shown in Table 7.

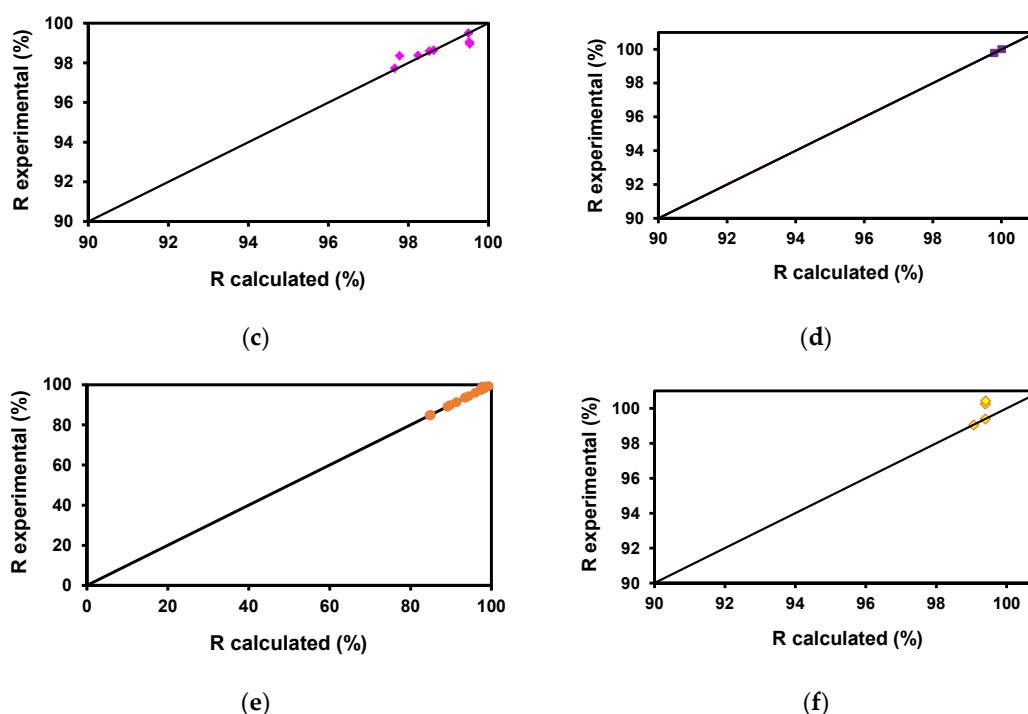
**Table 7.** Solute permeability coefficient and reflection parameter for the different dyes obtained using SKK model.

Dyes	$P_s$ (m s <sup>-1</sup> )	$\sigma$	Standard Deviation
AB83	$1.6418 \times 10^{-7}$	0.9954	0.3605
AR	$2.6624 \times 10^{-8}$	0.9994	3.8356
BF	$2.021 \times 10^{-7}$	0.9887	0.1692
CV	$1.0198 \times 10^{-7}$	0.9974	1.0023
MO	$7.8114 \times 10^{-7}$	0.9563	0.2147
SY	$2.5221 \times 10^{-7}$	0.9942	0.3382

To verify the model, the values of F and Robs were calculated. The following figures (Figure 6a–f) show the good correlation in most cases between the experimental values of the rejection coefficient and those calculated by the model. Table 5 shows the standard deviation values being the highest lower than 4%.



**Figure 6.** Cont.



**Figure 6.** Correlation between the experimental values of the rejection coefficient and those calculated by the model. (a) ◆ AB83, (b) ■ AR, (c) ◆ BF, (d) ■ CV, (e) ● MO, (f) ◆ SY.

### 3.8. Comparative Study of the Results

A comparison of the results obtained on permeate flux and rejection coefficient using NF99 for the different dyes molecules was carried out. Table S1 (Supplementary Material) shows the results obtained by other authors using other membranes (native and modified) for the removal of dyes.

## 4. Conclusions

The performance of a polyamide nanofiltration membrane on the removal of six different dyes, Acid Brown-83, Allura Red, Basic Fuchsin, Crystal Violet, Methyl Orange and Sunset Yellow, has been studied. Firstly, the membrane characterization was carried out, obtaining a water permeability coefficient value of  $1.665 \times 10^{-8} \text{ s m}^{-1}$ . The membrane selectivity was also determined, and the solute permeability coefficients were  $6.705 \times 10^{-6}$  and  $1.632 \times 10^{-7}$  for NaCl and MgCl<sub>2</sub>, respectively. It has been proven that the chemical structure of the dyes has an important influence on the permeate fluxes and rejection coefficients obtained, these being the molecular volume and the length perpendicular to the maximum area the most relevant parameters. The pH influence was also studied, these being the membrane negatively charged at neutral and basic pH and therefore being repelled by the dye molecules of negative charge (AB83, AR, MO and SY). However, AB83 and MO dye molecules showed a decrease in permeate flux, which can be explained due to other types of interactions (hydrophobic interactions and the presence of hydrogen bonds that cause membrane blocking). Membrane fouling was determined by calculating a fouling factor, showing that the smaller dye molecules (Methyl Orange and Basic Fuchsin) presented the highest fouling. Additionally, when comparing dyes of similar molecular sizes, those with negative charges and linear size gave lower values of fouling factor. The morphologic study of the membrane by Scanning Electron Microscopy (SEM) and infrared spectrum confirmed the observed degree of fouling. Finally, the Spiegler–Kedem–Katchalsky model that simulates the membrane behavior was successfully applied, with a high degree of agreement between the experimental and calculated rejection coefficients.

**Supplementary Materials:** The following are available online at <http://www.mdpi.com/2077-0375/10/12/408/s1>, Figure S1: Rejection coefficient (◆) and permeate flux (■) variation with dreiding energy (A&B) and with MMFF94

Energy (C&D) for colorants: (MO) Methyl Orange, (BF) Basic Fuchsin, (SY) Sunset Yellow, (AR) Allure Red, (CV) Crystal Violet. Experimental conditions: pH = 7, [Dyes] = 50 mg/L and pressure 10 bar (A&C) and 15 bar (B&D). Figure S2: Rejection coefficient (◆) and permeate flux (■) variation with minimal projection area (A&B) and with maximal projection area (C&D) for colorants: (MO) Methyl Orange, (BF) Basic Fuchsin, (SY) Sunset Yellow, (AR) Allure Red, (CV) Crystal Violet. Experimental conditions: pH = 7, [Dyes] = 50 mg/L and pressure 10 bar (A&C) and 15 bar (B&D). Figure S3: Rejection coefficient (◆) and permeate flux (■) variation with minimal projection radius (A&B) and with maximal projection radius (C&D) for colorants: (MO) Methyl Orange, (BF) Basic Fuchsin, (SY) Sunset Yellow, (AR) Allure Red, (CV) Crystal Violet. Experimental conditions: pH = 7, [Dyes] = 50 mg/L and pressure 10 bar (A&C) and 15 bar (B&D). Figure S4: Rejection coefficient (◆) and permeate flux (■) variation with length perpendicular to the minimal area (A&B) and with molecular weight (C&D) for colorants: (MO) Methyl Orange, (BF) Basic Fuchsin, (SY) Sunset Yellow, (AR) Allure Red, (CV) Crystal Violet. Experimental conditions: pH = 7, [Dyes] = 50 mg/L and pressure 10 bar (A&C) and 15 bar (B&D), Table S1: Comparison of dye removal between previous studies and this study in terms of water flux and rejection.

**Author Contributions:** Conceptualization, A.M.H. and G.L.; methodology, A.M.H. and G.L.; investigation, J.A.M.; resources, J.A.M.; writing—original draft preparation, A.M.H., M.G. and M.D.M.; writing—review and editing, A.M.H., G.L., J.A.M., M.G., M.D.M. and E.G.; supervision, A.M.H., G.L. and E.G. All authors have read and agreed to the published version of the manuscript.

**Funding:** This research received no external funding.

**Acknowledgments:** The authors would like to thank SAIT, from Polytechnic University of Cartagena for the SEM made to the membrane.

**Conflicts of Interest:** The authors declare no conflict of interest.

## Nomenclature

$C_0$	solute concentration in the feed (kg/m <sup>3</sup> )
$C_m$	solute concentration in the membrane (kg/m <sup>3</sup> )
$C_p$	solute concentration in the permeate (kg/m <sup>3</sup> )
$C_s$	logarithmic average solute concentration between feeding and permeate (kg/m <sup>3</sup> )
$FF$	fouling factor (%)
$J_s$	solute flux density (kg/m <sup>2</sup> s)
$J_v$	solvent flux density (kg/m <sup>2</sup> s)
$L_p$	solvent permeability coefficient (m/s)
$L_{p0}$	initial solvent permeability coefficient (m/s)
$L_{pf}$	final solvent permeability coefficient (m/s)
$P_s$	solute permeability coefficient (m/s)
$r$	rejection (dimensionless)
$R$	rejection coefficient (%)
$R_{obs}$	observed rejection coefficient (%)
$\Delta P$	operating pressure (Pa)
$\Delta \Pi$	osmotic pressure (Pa)
$\sigma$	reflection coefficient

## References

1. Dasgupta, J.; Sikder, J.; Chakraborty, S.; Curcio, S.; Drioli, E. Remediation of textile effluents by membrane based treatment techniques: A state of the art review. *J. Environ. Manag.* **2015**, *147*, 55–72. [[CrossRef](#)]
2. Donkadokula, N.Y.; Kola, A.K.; Naz, I.; Saroj, D. A review on advanced physico-chemical and biological textile dye wastewater treatment techniques. *Rev. Environ. Sci. Biotechnol.* **2020**, *19*, 543–560. [[CrossRef](#)]
3. De Jager, D.; Sheldon, M.S.; Edwards, W. Colour removal from textile wastewater using a pilot-scale dual-stage MBR and subsequent RO system. *Sep. Purif. Technol.* **2014**, *135*, 135–144. [[CrossRef](#)]
4. Verma, A.K.; Dash, R.R.; Bhunia, P. A review on chemical coagulation/flocculation technologies for removal of colour from textile wastewater. *J. Environ. Manag.* **2012**, *93*, 154–168. [[CrossRef](#)] [[PubMed](#)]
5. Liang, C.Z.; Sun, S.P.; Li, F.Y.; Ong, Y.K.; Chung, T.S. Treatment of highly concentrated wastewater containing multiple synthetic dyes by a combined process of coagulation/flocculation and nanofiltration. *J. Membr. Sci.* **2014**, *469*, 306–315. [[CrossRef](#)]

6. Lau, W.J.; Ismail, A.F. Polymeric nanofiltration membranes for textile dye wastewater treatment: Preparation, performance evaluation, transport modelling, and fouling control—a review. *Desalination* **2009**, *245*, 321–348. [[CrossRef](#)]
7. Wang, Z.; Wu, A.; Ciacchi, L.C.; Wei, G. Recent Advances in Nanoporous Membranes for Water Purification. *Nanomaterials* **2018**, *8*, 65. [[CrossRef](#)]
8. Ghadhbhan, M.Y.; Majdi, H.S.; Rashid, K.T.; Alsahy, Q.F.; Lakshmi, D.S.; Salih, I.K.; Figoli, A. Removal of dye from a leather tanning factory by flat-sheet ultrafiltration (UF) membrane. *Membranes* **2020**, *10*, 47. [[CrossRef](#)]
9. Guo, D.; Xiao, Y.; Li, T.; Zhou, Q.; Shen, L.; Li, R.; Xu, Y.; Lin, H. Fabrication of high-performance composite nanofiltration membranes for dye wastewater treatment: Mussel-inspired layer-by-layer self-assembly. *J. Colloid Interface Sci.* **2020**, *560*, 273–283. [[CrossRef](#)]
10. Jun, B.M.; Yoon, Y.; Park, C.M. Post-treatment of nanofiltration polyamide membrane through alkali-catalyzed hydrolysis to treat dyes in model wastewater. *Water* **2019**, *11*, 1645. [[CrossRef](#)]
11. Li, Y.; Wong, E.; Mai, Z.; Der Bruggen, B.V. Fabrication of composite polyamide/Kevlar aramid nanofiber nanofiltration membranes with high permselectivity in water desalination. *J. Membr. Sci.* **2019**, *592*, 117396–117407. [[CrossRef](#)]
12. Benkhaya, S.; M´rabet, S.; Hsissou, R.; El Harfi, A. Synthesis of new low-cost organic ultrafiltration membrane made from Polysulfone/Polyetherimide blends and its application from soluble azoic dyes removal. *J. Mater. Res. Technol.* **2020**, *9*, 4763–4772.
13. Hidalgo, A.M.; Leon, G.; Gómez, M.; Murcia, M.D.; Gómez, E.; Penalva, P. Removal of 4-chloro-2-methyl-phenol from aqueous solutions by nanofiltration and reverse osmosis. *Desalin. Water Treat.* **2015**, *53*, 1499–1505. [[CrossRef](#)]
14. Hidalgo, A.M.; Murcia, M.D.; Gómez, E.; Leon, G.; Cascales, E. Influence of physicochemical parameters of organic solutes on the retention and flux in nanofiltration process. *Chem. Eng. Technol.* **2016**, *39*, 1177–1184. [[CrossRef](#)]
15. Cheng, L.; Zhu, L.P.; Zhang, P.B.; Sun, J.; Zhu, B.K.; Xu, Y.Y. Molecular separation by poly (N-vinyl imidazole) gel-filled membranes. *J. Membr. Sci.* **2016**, *497*, 472–484. [[CrossRef](#)]
16. Chidambaram, T.; Oren, Y.; Noel, M. Fouling of nanofiltration membranes by dyes during brine recovery from textile dye bath wastewater. *Chem. Eng. J.* **2015**, *262*, 156–168. [[CrossRef](#)]
17. Li, C.; Yang, Y.; Liu, Y.; Hou, L. Removal of PhACs and their impacts on membrane fouling in NF/RO membrane filtration of various matrices. *J. Membr. Sci.* **2018**, *548*, 439–448. [[CrossRef](#)]
18. Zhang, N.; Huang, Z.; Yang, N.; Zhang, L.; Jiang, B.; Sun, Y.; Ma, J. Nanofiltration membrane via EGCG-PEI co-deposition followed by crosslinking on microporous PTFE substrates for desalination. *Sep. Purif. Technol.* **2020**, *232*, 115964–115974. [[CrossRef](#)]
19. Restolho, J.A.; Prates, A.; Pinho, M.N.; Afonso, M.D. Sugars and lignosulphonates recovery from eucalyptus spent sulphite liquor by membrane processes. *Biomass Bioenergy* **2009**, *33*, 1558–1566. [[CrossRef](#)]
20. Catarino, M.; Mendes, A. Dealcoholizing wine by membrane separation processes. *Innov. Food Sci. Emerg. Technol.* **2011**, *12*, 330–337. [[CrossRef](#)]
21. Labarca, F.; Bórquez, R. Comparative study of nanofiltration and ion exchange for nitrate reduction in the presence of chloride and iron in groundwater. *Sci. Total Environ.* **2020**, *723*, 137809–137821. [[CrossRef](#)] [[PubMed](#)]
22. Wijmans, J.G.; Baker, R.W. The solution-diffusion model: A review. *J. Membr. Sci.* **1995**, *107*, 1–21. [[CrossRef](#)]
23. Revchuk, A.D.; Suffet, I.N. Ultrafiltration separation of aquatic natural organic matter: Chemical probes for quality assurance. *Water Res.* **2009**, *43*, 3685–3692. [[CrossRef](#)] [[PubMed](#)]
24. Hidalgo, A.M.; Gómez, M.; Murcia, M.D.; Serrano, M.; Rodríguez-Schmidt, R.; Escudero, P.A. Behaviour of polysulfone ultrafiltration membrane for dyes removal. *Water Sci. Technol.* **2018**, *77*, 2093–2100. [[CrossRef](#)]
25. Lee, A.; Elamb, J.W.; Darling, S.B. Membrane materials for water purification: Design, development, and application. *Environ. Sci. Water Res. Technol.* **2016**, *2*, 17–42. [[CrossRef](#)]
26. Abdel-Fatah, M.A. Nanofiltration systems and applications in wastewater treatment: Review article. *Ain Shams Eng. J.* **2018**, *9*, 3077–3092. [[CrossRef](#)]
27. Yang, Z.; Zhou, Y.; Feng, Z.; Rui, X.; Zhang, T.; Zhang, Z. A review on reverse osmosis and nanofiltration membranes for water purification. *Polymers* **2019**, *11*, 1252. [[CrossRef](#)] [[PubMed](#)]
28. Kedem, O.; Katchalsky, A. Thermodynamics of flow processes in biological systems. *Biophys. J.* **1962**, *2*, 53–78.



29. Spiegler, K.S.; Kedem, O. Thermodynamics of hyperfiltration (reverse osmosis): Criteria for efficient membranes. *Desalination* **1966**, *1*, 311–326. [[CrossRef](#)]
30. Ben-David, A.; Bason, S.; Jopp, J.; Oren, Y.; Freger, V. Partitioning of organic solutes between water and polyamide layer of RO and NF membranes: Correlation of rejection. *J. Membr. Sci.* **2006**, *281*, 480–490. [[CrossRef](#)]
31. Hidalgo, A.M.; León, G.; Gómez, M.; Murcia, M.D.; Gómez, E.; Gómez, J.L. Application of the Spiegler-Kedem-Kachalsky model to the removal of 4-chlorophenol by different nanofiltration membranes. *Desalination* **2013**, *315*, 70–75. [[CrossRef](#)]
32. Yaroshchuk, A.E. Rejection of singles salts versus transmembrane volume flow in RO/NF: Thermodynamic properties, model of constant coefficients, and its modification. *J. Membr. Sci.* **2002**, *198*, 285–297. [[CrossRef](#)]
33. Pontie, M.; Buisson, H.; Diawara, C.K.; Essis-Tome, H. Studies of halide ions mass transfer in nanofiltration application to selective defluorination of brackish drinking water. *Desalination* **2003**, *157*, 127–134. [[CrossRef](#)]
34. Nora'aini, A.; Abdul Wahab, M. Regional Symposium on Membrane Science and Technology. In *The Development of Predictive Modeling of Nanofiltration Membrane Properties: A Review*; Kolej Universiti Sains & Teknologi: Johor, Malaysia; Universiti Kebangsaan: Johor, Malaysia, 2004.

**Publisher's Note:** MDPI stays neutral with regard to jurisdictional claims in published maps and institutional affiliations.



© 2020 by the authors. Licensee MDPI, Basel, Switzerland. This article is an open access article distributed under the terms and conditions of the Creative Commons Attribution (CC BY) license (<http://creativecommons.org/licenses/by/4.0/>).

Article

# Dependence of Water-Permeable Chitosan Membranes on Chitosan Molecular Weight and Alkali Treatment

Ryo-ichi Nakayama \*, Koki Katsumata, Yuta Niwa and Norikazu Namiki

Department of Environmental Chemistry & Chemical Engineering, School of Advanced Engineering, Kogakuin University, 2665-1 Nakano-machi, Hachioji, Tokyo 192-0015, Japan; s316020@ns.kogakuin.ac.jp (K.K.); st13562@g.kogakuin.jp (Y.N.); nnamiki@cc.kogakuin.ac.jp (N.N.)

\* Correspondence: bionakayama.ryo@cc.kogakuin.ac.jp; Tel.: +81-42-628-4876; Fax: +81-42-628-4531

Received: 1 September 2020; Accepted: 6 November 2020; Published: 18 November 2020



**Abstract:** Chitosan membranes were prepared by the casting method combined with alkali treatment. The molecular weight of chitosan and the alkali treatment influenced the water content and water permeability of the chitosan membranes. The water content increased as the NaOH concentration was increased from 1 to 5 mol/L. The water permeation flux of chitosan membranes with three different molecular weights increased linearly with the operating pressure and was highest for the membrane formed from chitosan with the lowest molecular weight. Membranes with a lower water content had a higher water flux. The membranes blocked 100% of compounds with molecular weights above methyl orange (MW = 327 Da). At  $60 \leq MW \leq 600$ , the blocking rate strongly depended on the substance. The results confirmed that the membranes are suitable for compound separation, such as in purification and wastewater treatment.

**Keywords:** chitosan; membrane; water content; water permeability; alkali treatment

## 1. Introduction

Chitin and chitosan are biopolymers contained in the exoskeletons of crustaceans that have recently attracted attention as reproducible biogenic components [1,2]. They are significant for effective resource utilization, because they can be obtained from shells that are discarded during the processing of crabs and shrimps for food products [3,4].

Chitin is formed from N-acetyl-D-glucosamine that is linked linearly with  $\beta$ -1,4 units, whereas chitosan is formed from D-glucosamine (i.e., the deacetylation product of chitin). Both structures are similar to cellulose [5,6].

Conventional industrial applications of chitosan include as a flocculent [7], adsorbent [8,9], and fiber [10], because it is commercially and continuously available at low cost. Chitosan is also anticipated to be a biocompatible material in functional gels for drug delivery systems [11–13] and as a membrane material for industrial separation tools [14–16]. Membranes offer several advantages over other separation techniques because of their low energy consumption, bulk production at continuous operation, and production of bio-products that are not thermally denatured. Industrial applications of membrane separation are wide-ranging and include fruit-juice condensation [17], artificial dialysis [18], desalination of seawater [19], and wastewater treatment [20–22].

A membrane is characterized by its mechanical strength (i.e., stress–strain relationship) and mass-transfer characteristics. The mechanical strength determines the handling fatigue life of the membrane in a module. The mass-transfer characteristics determine the molecular diffusion rate through the membrane, which is the main rate-limiting step of the separation process. In general,

chitosan is dissolved in aqueous acetic acid [23]. To form a water-insoluble chitosan membrane, the acetic acid must be neutralized by basic components such as sodium hydroxide (NaOH). During preparation, the type and concentration of the basic aqueous solution is known to influence the coagulation rate and structure of the chitosan gel. Moreover, the deacetylation degree of chitosan affects the distilled water permeation characteristics of the membrane [24]. The film-forming properties of chitosan are affected by the molecular weight of the chitosan and the alkali treatment at the time of membrane formation. The latter is essential to stabilizing the film formation against dissolution in water.

In this study, the water content, mechanical strength, water permeability, and mass-transfer characteristics of chitosan membranes were regulated by controlling the molecular weight of chitosan and the alkali treatment of the casting solution.

## 2. Materials and Methods

### 2.1. Materials

Powders of chitosan with three different molecular weights were purchased from Sigma-Aldrich (St Louis, MO, USA). Table 1 lists the mean molecular weights of the chitosan powders, which were determined from the measured viscosity. The guaranteed viscosity range of chitosan in the database was based on special-grade sodium hydroxide. Acetic acid and other chemicals were purchased from Fujifilm Wako Pure Chemical Industries, Ltd. (Osaka, Japan).

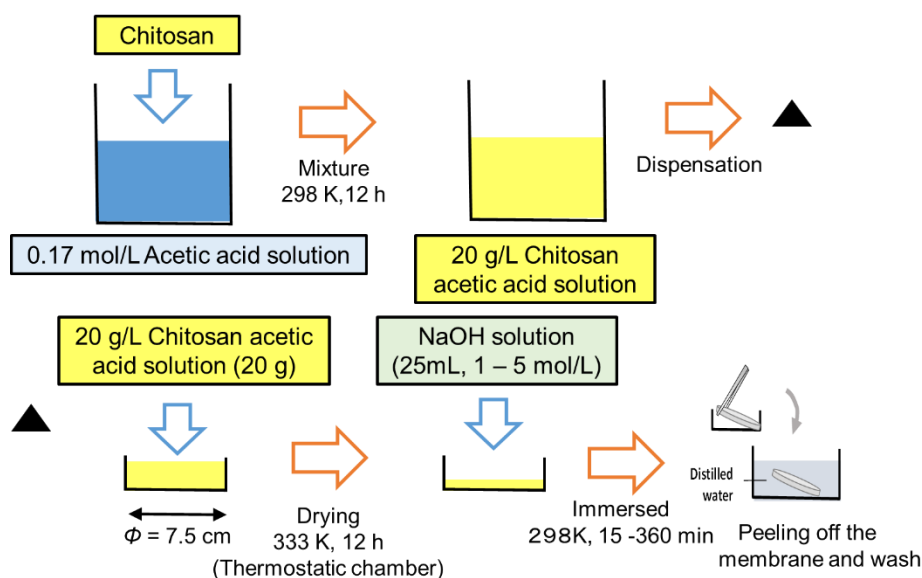
**Table 1.** Measured molecular weights of chitosan powders.

Type of Chitosan	Manufacture	Intrinsic Viscosity	Mean Molecular Weight, MW [Da] *	Guarantee Viscosity [cP] **
Chitosan (Low Viscosity)	Sigma-Aldrich	8.2	$3.81 \times 10^5$	20–200
Chitosan (Medium Viscosity)	Sigma-Aldrich	10.5	$4.45 \times 10^5$	200–800
Chitosan (High Viscosity)	Sigma-Aldrich	14.9	$7.15 \times 10^5$	800–2000

\* Mean molecular weight of chitosan was determined by viscosity measurement. \*\* The range of viscosity was quoted from Sigma-Aldrich.

### 2.2. Preparation of Chitosan Membrane

Figure 1 shows the procedure for preparing the chitosan membranes. Chitosan was dissolved in 1.7 mol/L of acetic acid solution (20 g/L). The chitosan solution (20 g) was dispensed into a petri dish (diameter of 7.5 cm) and then dried for 12 h at 333 K in a thermostatic chamber. Subsequently, the chitosan was gelled by immersion in NaOH at a sufficient concentration (volume of = 25 mL, NaOH concentration = 1–5 mol/L). The chitosan in the petri dish was continuously immersed in the NaOH solution for 15–360 min. The resulting membrane was washed with distilled water. After the alkali treatment, the swollen membrane easily separated from the glass plate; it was thoroughly washed with distilled water to remove any excess NaOH. The neutralized state was checked by immersing pH paper in the wash water.



**Figure 1.** Experimental procedure for preparing the chitosan membranes.

### 2.3. Scanning Electron Microscopy

The membranes were snap-frozen in liquid nitrogen and then dried in a vacuum freeze dryer (RLE-103, Kyowa Vacuum Engineering Co., Ltd., Tokyo, Japan) at 298 K for 24 h. Then, the dried membranes were sputter-coated with a thin Pt membrane, using a sputter-coater (E-1010 Ion Sputter, Hitachi, Ltd., Tokyo, Japan). Finally, cross-sectional images of the membranes were obtained using a scanning electron microscope (SEM) (Miniscope TM-1000, Hitachi, Ltd., Tokyo, Japan).

### 2.4. Water Content

To determine the internal structure of a swollen membrane, the volumetric water content ( $H_V$ ) was determined from the water content of the membrane. For this purpose, each membrane was cut into  $4 \times 4$  cm squares. Because a membrane sequesters water in its void spaces, the volumetric water content reasonably approximates the void fraction of a membrane in the swollen state. Each membrane square was blotted with filter paper to remove the excess surface water and was then dried in a thermo-controlled oven (333 K, 24 h). The water loss was measured gravimetrically with an electronic balance (ER-180A; A&D Co. Ltd., Tokyo). The volumetric water content each membrane square was obtained by calculating its gravimetric change after swelling:

$$H_V = \frac{V_w}{V_m} \quad (1)$$

where  $V_w$  is the volume of water in the membrane, and  $V_m$  is the volume of the membrane.

### 2.5. Mechanical Strength

The mechanical strengths of the membranes were measured with a rheometer (CR-DX500, Sun Scientific Co., Ltd., Tokyo, Japan). The swollen membranes were cut into  $1 \times 4$  cm samples and stretched at a rate of  $1.0 \text{ mm s}^{-1}$ . The maximum stress and maximum strain were measured to characterize the mechanical strength. The maximum stress  $\sigma$  was calculated as follows:

$$\sigma = \frac{B_{max}}{A_c} \quad (2)$$

where  $B_{max}$  is the maximum pre-breaking load, and  $A_c$  is the cross-sectional area of the initial membrane. The maximum strain  $\lambda$  was calculated as follows:

$$\lambda = \frac{L_0 - L_i}{L_i} \times 100 \quad (3)$$

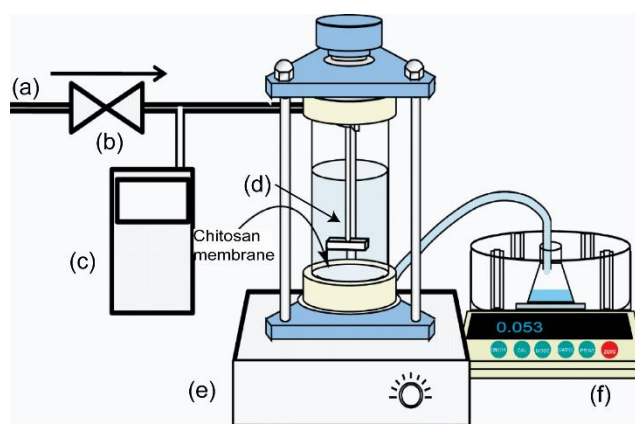
where  $L_i$  and  $L_0$  are the membrane lengths in the initial and breaking states, respectively.

### 2.6. Water Permeability

The water permeability of the membrane was measured with an ultrafiltration apparatus (UHP-62K, Advantec Tokyo Kaisha, Ltd., Tokyo, Japan) [25]. Figure 2 presents a schematic of the module and the setup for testing the water permeation. The initial volume of the aqueous phase was 200 mL, and the effective membrane surface area was  $2.13 \times 10^{-3} \text{ m}^2$ . The operating pressure  $\Delta P$  (50–200 kPa) was adjusted by introducing  $\text{N}_2$  gas at room temperature (298 K). A magnetic stirring bar was installed near the membrane surface and stirred at a constant speed of  $3 \text{ s}^{-1}$  in the aqueous phase. The mass of the permeated water was measured on an electric balance and was converted to the volumetric amount of permeated water according to the permeated water density. The volumetric water flux  $J_v$  was then calculated as follows:

$$J_V = \frac{V_p}{A_m \cdot \ell \cdot t} \quad (4)$$

where  $V_p$  is the volumetric amount of permeated water,  $A_m$  is the membrane surface area,  $\ell$  is the thickness of the swollen membrane, and  $t$  is the operating time. These tests were replicated three times. The results of the water permeability test of the membranes were presented with the associated standard deviation ( $\pm \text{SD}$ ).



**Figure 2.** Schematic of the water permeation apparatus: (a)  $\text{N}_2$  gas inlet, (b) regulator, (c) transducer, (d) magnetic stirring bar, (e) magnetic stirrer, and (f) electronic balance.

### 2.7. Measurement of the Mass Transfer Flux

A chitosan membrane prepared by the method described in Section 2.2 was installed in the ultrafiltration device, and 190 mL of the sample solution was poured in the permeation cell. After the device was filled with the sample solution, it was sealed, and a vial was attached to the permeation outlet. The experiment was started by pressurizing the device to 100 kPa with  $\text{N}_2$  gas. The stirring speed was  $190 \text{ min}^{-1}$ . Each experimental sample solution (urea (MW = 60 Da), D-glucose (MW = 180 Da), methyl orange (MW = 327 Da), and bordeaux S (MW = 604 Da)) was dissolved in water as a solvent. After the substance permeation experiment, the absorbance of the sample solution before and after permeation was measured with an extra-visible visible spectrophotometer (V-630IRM, JASCO). After the absorbance was measured, the concentrations  $C_f$  and  $C_p$  before and after permeation,

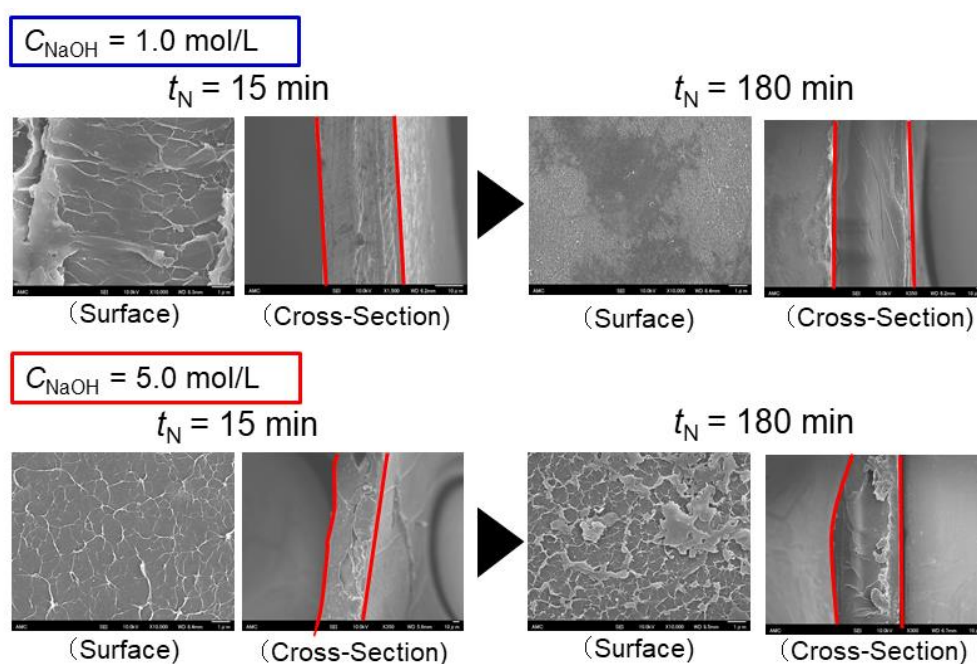
respectively, were determined from the calibration curve of each sample solution. The apparent rejection rate  $R$  was then calculated as follows:

$$R = \frac{(C_f - C_p)}{C_f} \times 100 \quad (5)$$

### 3. Results and Discussion

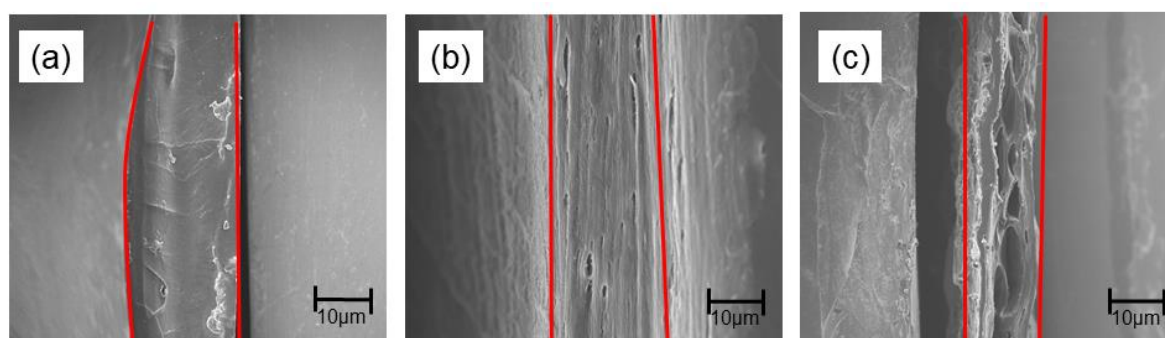
#### 3.1. Scanning Electron Microscopy

Figure 3 shows scanning electron microscopy (SEM) images of the surfaces and cross-sections of the chitosan membranes prepared in solutions with various NaOH concentrations ( $C_{\text{NaOH}} = 1.0$  and 5.0 mol/L) and crosslinking times ( $t_N = 15$  and 180 min). The surfaces of chitosan membranes prepared in 1.0 mol/L NaOH were smooth, and more membrane formed with a longer crosslinking time. Meanwhile, the cross-section showed that the structure became denser with a longer crosslinking time. The chitosan membranes prepared in 5.0 mol/L NaOH developed a rough surface with a longer crosslinking time, and the membrane surface peeled off and deteriorated. Furthermore, the cross-section of the membrane showed voids in the internal structure with a shorter crosslinking time. Previous SEM images demonstrated a measurable change in the biopolymer networks induced by the alkali treatment [26,27].



**Figure 3.** SEM images of the surfaces and cross-sections of chitosan membranes prepared in 1.0 mol/L NaOH ( $t_N = 15$  and 180 min, upper panels) and 5.0 mol/L NaOH ( $t_N = 15$  and 180 min, lower panels).

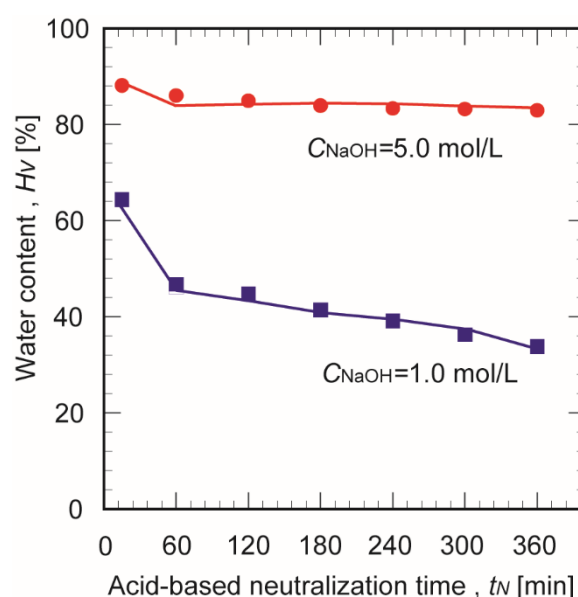
Figure 4 shows SEM images of the membranes prepared from chitosans with different molecular weights (low, medium, and high) in 5 mol/L NaOH. All of the membranes had uniform and dense internal structures in the thickness direction, but the membrane prepared from chitosan with a high molecular weight developed voids through its cross-section.



**Figure 4.** Cross-sectional SEM images of membranes prepared in 5 mol/L NaOH ( $t_N = 180$  min) from chitosan of different molecular weights: (a) low, (b) medium, and (c) high.

### 3.2. Volumetric Water Content

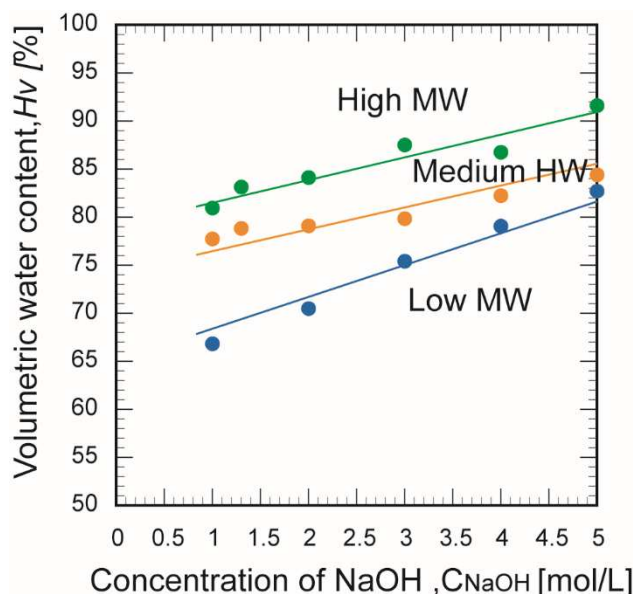
Figure 5 shows the effect of the crosslinking time on the water contents of chitosan membranes prepared in 1.0 and 5.0 mol/L NaOH. For the chitosan membranes prepared in 1.0 mol/L NaOH, the water content decreased with increasing crosslinking time. This is probably because the network structure within the membrane densified as the crosslinking progressed. Conversely, the water content of the chitosan membranes prepared in 5.0 mol/L NaOH showed no significant change regardless of the crosslinking time. This was attributed to the rapid progression of the crosslinking in the concentrated NaOH aqueous solution, so the membrane was fully formed within a short time.



**Figure 5.** Effect of crosslinking time on the water content of chitosan membranes prepared in 1.0 and 5.0 mol/L NaOH.

Figure 6 shows the effects of the chitosan molecular weight and NaOH concentration on the volume porosity. For all chitosan membranes, the volumetric water content increased with the NaOH concentration. This trend can be explained by the hydrogen bonds that crosslink the amino and hydroxyl groups of chitosan [28]. Chitosan polymer networks are principally crosslinked by hydrogen bonds between hydrogel groups and amino groups. Increasing the concentration of the basic aqueous solution is equivalent to increasing its ionic strength; thus, when the NaOH concentration was high, the ionic strength was also high and the hydrogen bonds were weakened. This may have increased the clearance between polymer chains owing to the weakened hydrogen bonds from the higher ionic

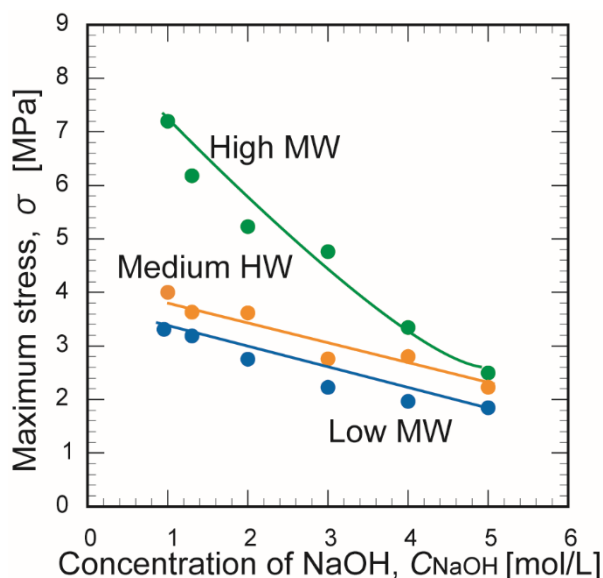
strength of NaOH [29]. This suggests that the concentration of the basic aqueous solution contributes greatly to the surface and cross-sectional structures of chitosan membranes.



**Figure 6.** Effect of the chitosan molecular weight on the porosity and concentration of the aqueous NaOH solution during membrane formation.

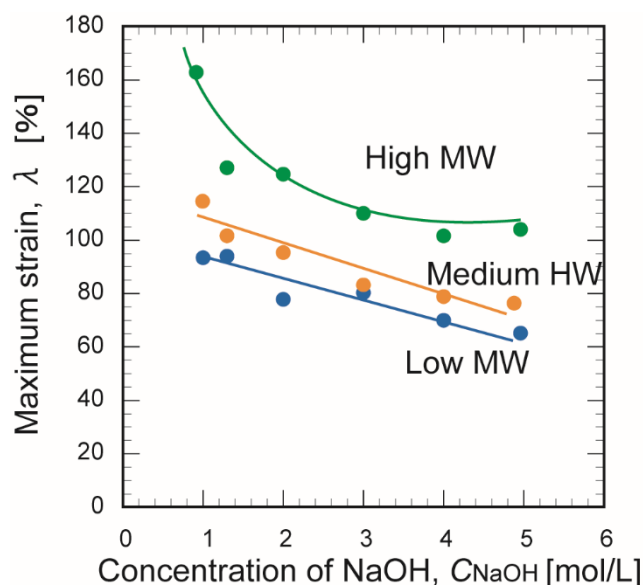
### 3.3. Mechanical Strength

Figures 7 and 8 show the effect of the NaOH concentration on the maximum stress and maximum strain, respectively, at the time of membrane rupture. Increasing the NaOH concentration decreased the maximum breaking stress and the maximum strain. These trends might be explained by the decreased number of hydrogen bonds and weakening bonds between chitosan molecules as the NaOH concentration increased. The membrane prepared from chitosan with a high molecular weight exhibited greater mechanical strength than the other two membranes. This may be explained by the stronger crosslinking of its polymer chains, which contained many crosslinking points [30].



**Figure 7.** Effect of the NaOH concentration on the maximum stress of the three chitosan membranes at the time of rupture.

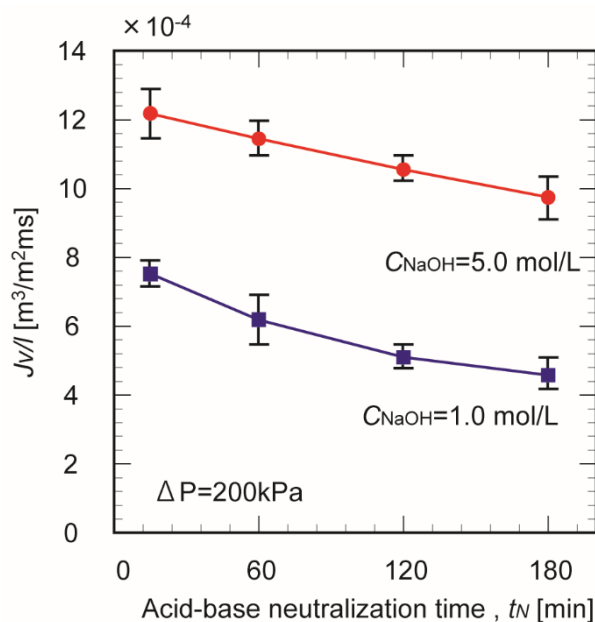




**Figure 8.** Effect of the NaOH concentration on the maximum strain of the three chitosan membranes at the time of rupture.

### 3.4. Water Permeability

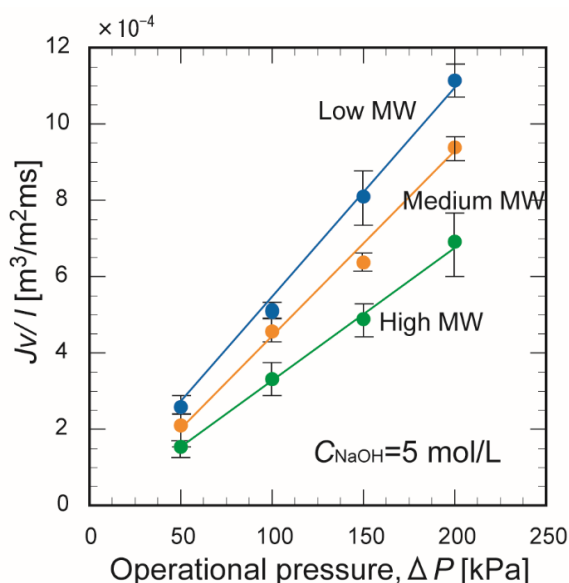
Figure 9 shows the effect of the crosslinking time on the water flux through the chitosan membranes prepared in 1.0 and 5.0 mol/L NaOH. The water permeation flux decreased with increasing crosslinking time, regardless of the NaOH concentration. At longer crosslinking times, the interior of the membrane grew denser and suppressed the water flux. Lengthening the crosslinking time probably increased the tortuosity of the permeation pathway through the membrane.



**Figure 9.** Effect of crosslinking time on the water permeation flux through chitosan membranes prepared in 1.0 and 5.0 mol/L NaOH.

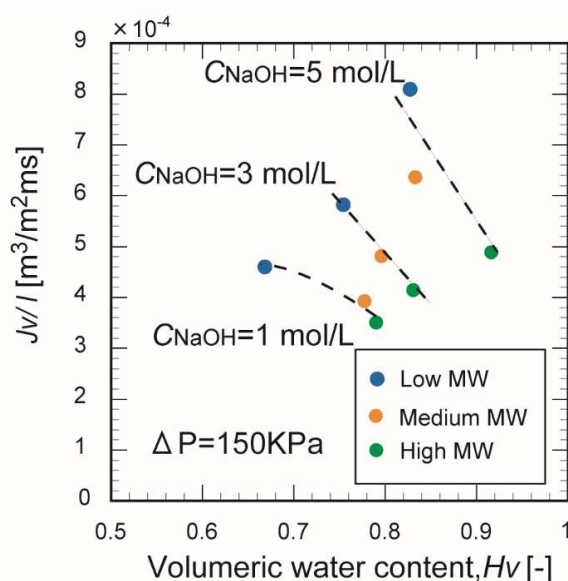
Figure 10 shows the effect of the operating pressure on the water permeation flux through the membranes prepared from chitosan with different molecular weights. The water permeation flux increased linearly with the operating pressure for all membranes and was highest for the membrane

formed from chitosan with a low molecular weight. This appears to be because the molecular chain length of the chitosan influences the water permeation pathway through the membrane.



**Figure 10.** Effect of the operating pressure on the water flux through the chitosan membranes ( $t_N = 180$  min).

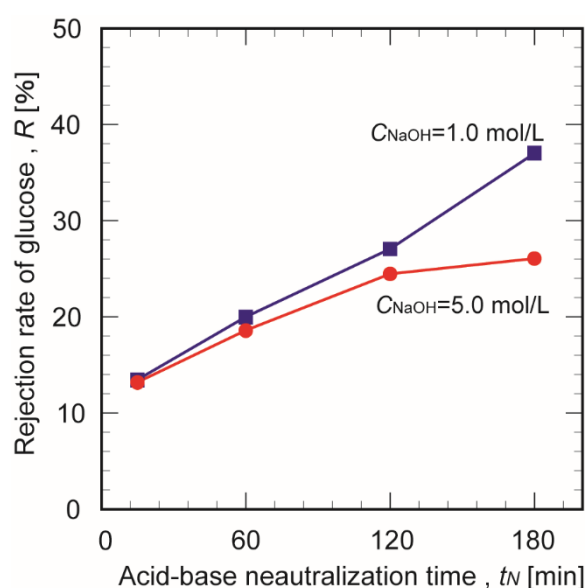
Figure 11 plots the water flux as a function of porosity for the membranes prepared from different-molecular-weight chitosan in different NaOH concentrations. Increasing the molecular weight of chitosan increased the volumetric water content and decreased the water permeation flux of the membrane. In general, the water permeation path increased with porosity. These results suggest that many moisture regions were immobilized by the molecular chains in the cell structure of the chitosan membrane. These regions could not function as permeation pathways for water. However, in the membrane formed from chitosan with a low molecular weight, the volumetric water content decreased and the permeation flux of pure water increased. The superior water permeation performance of this sample can be explained by the molecular chain length of the chitosan.



**Figure 11.** Correlation between the pure water flux and porosity of the chitosan membranes in different NaOH concentrations.

### 3.5. Mass Permeation Performance of the Chitosan Membranes

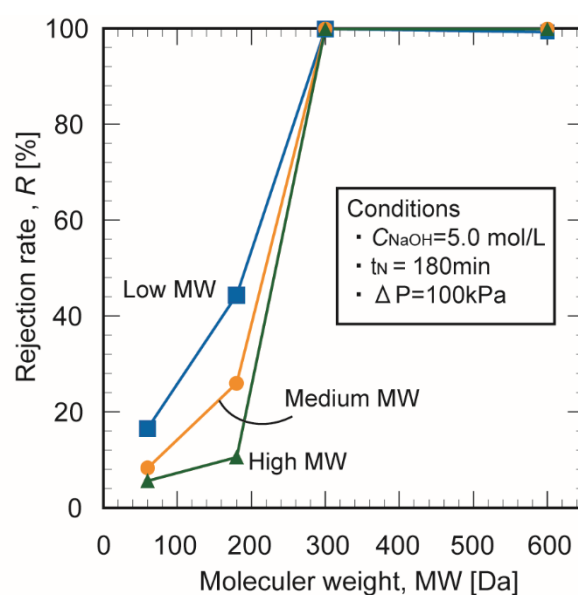
Figure 12 plots the glucose inhibition rate a function of the crosslinking time for chitosan membranes prepared in 1.0 and 5.0 mol/L NaOH. Increasing the crosslinking time increased the glucose inhibition rate of the chitosan membranes in 1.0 mol/L NaOH. This trend can be explained by the reduced number of pores in the membrane as the crosslinking time elapsed; this blocked or narrowed the permeation channels to below the molecular size of glucose (8.7 Å). In contrast, the inhibition rate of membranes prepared in 5.0 mol/L NaOH did not change significantly after 120 min. Since the crosslinking in the membrane was rapidly completed during the formation process with excessive NaOH, the diameters of the mass permeation channels may have been robust against extended crosslinking times.



**Figure 12.** Effect of crosslinking time on the apparent rejection rate of the glucose ratio for chitosan membranes prepared in different NaOH concentrations ( $\Delta P = 100$  kPa).

When molecules with high and low molecular weights are separated with a polymer, the membrane must block the target polymer and pass the smaller molecules. This property can be evaluated with the membrane fractionation performance. The fractional molecular weight of a membrane is defined as the molecular weight at which the apparent rejection is 90% or more. Since the separation by molecular weight is non-uniform, the fractional molecular weight covers a range of molecular weights. Thus, the molecular weight cutoff is an important performance index of biopolymer membranes and is a helpful guide for selecting a suitable membrane for a given purpose.

Figure 13 shows the fractional molecular curve of membranes prepared from chitosan with different molecular weights in 1.0 mol/L NaOH. The rejection rate increased with the molecular weight of the chitosan. The inhibition rate of particles with molecular weights above methyl orange (327 Da) was 100%. At  $60 \leq MW \leq 600$ , the blocking rate changed remarkably with the molecular weight, which indicates that a fractional molecular weight was identified. This range includes the molecular weights of many functional food components such as amino acids, saccharides, and food polyphenols.



**Figure 13.** Fractional molecular curves of the chitosan membranes.

#### 4. Conclusions

Membranes were successfully prepared from chitosan powder of different molecular weights of chitosan and with different alkali treatments. The volumetric water content of the chitosan membranes increased with the NaOH concentration regardless of the molecular weight of the chitosan. The membrane prepared from chitosan with a high molecular weight exhibited greater mechanical strength than the other membranes. The molecular weight and alkali treatment significantly affected the water permeation flux and mass transfer the prepared chitosan membranes. The water permeability was highest in the membrane prepared from chitosan with a low molecular weight. The water permeation flux increased 1.8-fold as the NaOH concentration was raised from 1.0 to 5.0 mol/L. The membranes had an inhibition rate of 100% for tested components with molecular weights above MW = 327 Da. At  $60 \leq MW \leq 600$ , the blocking rates changed remarkably with the molecular weight, which indicates that a fractional molecular weight was identified.

In this study, the volumetric water flux increased with the NaOH concentration and molecular weight of the chitosan. The findings regarding the dominant role of the alkali treatment on both the physical properties and water permeability of chitosan membranes will help facilitate the production of chitosan membranes as a separation technology for water treatment and environment-compatible engineering.

**Author Contributions:** Conceptualization, R.-i.N.; methodology, R.-i.N.; formal analysis, K.K. and Y.N.; investigation, K.K. and Y.N.; writing-original draft preparation, R.-i.N.; writing-review and editing, R.-i.N.; visualization, R.-i.N., K.K. and Y.N.; supervision, N.N. All authors have read and agree to the published version of the manuscript.

**Funding:** This research received no external funding.

**Acknowledgments:** The authors sincerely thank Masanao Imai of Nihon University, who provide the rheometer for measuring mechanical strength of the membrane.

**Conflicts of Interest:** The authors declare no conflict of interest.

#### References

1. Kumar, S.; Ye, F.; Dobretsov, S.; Dutta, J. Chitosan nanocomposite coatings for food, paints, and water treatment applications. *Appl. Sci.* **2019**, *9*, 2409. [[CrossRef](#)]
2. Dodane, Y.; Vilivalam, V.D. Pharmaceutical applications of chitosan. *Pharm. Sci. Technol. Today* **1998**, *1*, 246–253. [[CrossRef](#)]

3. Kumar, M.N.V.R. A review of chitin and chitosan application. *React. Funct. Polym.* **2000**, *46*, 1–27. [[CrossRef](#)]
4. Gierszewska, M.; Czubenko, J.O.; Chrzanowska, E. pH-responsive chitosan/alginate polyelectrolyte complex membranes reinforced by tripolyphosphate. *Euro. Polym. J.* **2018**, *101*, 282–290. [[CrossRef](#)]
5. Du, J.R.; Hsu, L.H.; Xiao, E.S.; Guo, X.; Zhang, Y. Using genipin as a “green” crosslinker to fabricate chitosan membranes for pervaporative dehydration of isopropanol. *Sep. Purif. Technol.* **2020**, *244*, 116843. [[CrossRef](#)]
6. Rinaudo, M. Chitin and chitosan: Properties and applications. *Prog. Polym. Sci.* **2006**, *31*, 603–632. [[CrossRef](#)]
7. Yang, Z.; Shang, Y.; Lu, Y.; Chen, Y.; Huang, X. Flocculation properties of biodegradable amphoteric chitosan-based flocculants. *Biochem. Eng. J.* **2011**, *172*, 287–295.
8. Igberase, E.; Osifo, P. Equilibrium, kinetic, thermodynamic and desorption studies of cadmium and lead by polyaniline grafted cross-linked chitosan beads from aqueous. *J. Ind. Eng. Chem.* **2015**, *26*, 340–347. [[CrossRef](#)]
9. Wu, F.C.; Tseng, R.L.; Juang, R.S. A review and experimental verification of using chitosan and its derivatives as adsorbents for selected heavy metals. *J. Environ. Manag.* **2010**, *91*, 798–806. [[CrossRef](#)]
10. Pillai, C.K.S.; Paul, W.; Sharma, C.P. Chitin and chitosan polymers: Chemistry, solubility and fiber formation. *Prog. Polym. Sci.* **2009**, *34*, 641–678. [[CrossRef](#)]
11. Luo, Y.; Teng, Z.; Wang, X.; Wang, Q. Development of carboxymethyl chitosan hydrogel beads in alcohol-aqueous binary solvent for nutrient delivery applications. *Food Hydrocoll.* **2013**, *31*, 332–339. [[CrossRef](#)]
12. Kofuji, K.; Murata, Y.; Kawashima, S. Sustained insulin release with biodegradation chitosan gel beads prepared by copper ions. *Int. J. Pharm.* **2005**, *303*, 95–103. [[CrossRef](#)] [[PubMed](#)]
13. Akhtar, F.; Rizvi, M.M.; Kar, S.K. Oral delivery of curcumin bound to chitosan nanoparticles cured *Plasmodium yoelii* infected mice. *Biotechnol. Adv.* **2012**, *30*, 310–320. [[CrossRef](#)] [[PubMed](#)]
14. Juang, R.S.; Shiau, R.C. Metal removal from aqueous solutions using chitosan-enhanced membrane filtration. *J. Membr. Sci.* **2000**, *165*, 159–167. [[CrossRef](#)]
15. Wang, H.D.; Chu, L.Y.; Song, H.; Yang, J.P.; Xie, R.; Yang, M. Preparation and enantiomer separation characteristics of chitosan/ $\beta$ -cyclodextrin composite membranes. *J. Membr. Sci.* **2007**, *297*, 262–270. [[CrossRef](#)]
16. El-Azzanmi, L.A.; Grulke, E.A. Carbon dioxide separation from hydrogen and nitrogen by fixed facilitated transport in swollen chitosan membranes. *J. Membr. Sci.* **2008**, *323*, 225–234. [[CrossRef](#)]
17. Aguiar, I.B.; Miranda, N.G.M.; Gomes, F.S.; Santos, M.C.S.; Freitas, D.G.C.; Tonon, R.V.; Cabral, L.M.C. Physicochemical and sensory properties of apple juice concentrated by reverse osmosis and osmotic evaporation. *Innov. Food Sci. Emerg. Technol.* **2012**, *16*, 137–142. [[CrossRef](#)]
18. Stamatialis, D.F.; Papenburg, B.J.; Girones, M.; Saiful, S.; Mettahalli, S.N.M.; Schmitmeier, S.; Wessling, M. Medical applications of membranes: Drug delivery, artificial organs and tissue engineering. *J. Membr. Sci.* **2008**, *308*, 1–34. [[CrossRef](#)]
19. Liu, M.; Yu, S.; Gao, C. Preparation, structure characteristics and separation properties of thin-film composited polyamideurethane seawater reverse osmosis membrane. *J. Membr. Sci.* **2008**, *325*, 947–956. [[CrossRef](#)]
20. Klimczak, K.; Stanislawek, E. Reclamation of water from dairy wastewater using polymeric nanofiltration membranes. *Desalin. Water Treat.* **2018**, *128*, 364–371. [[CrossRef](#)]
21. Guibal, E.; Milot, C.; Eterradosi, O.; Gauffier, C.; Domar, A. Study of molybdate ion sorption on chitosan gel beads by different spectrometric analyses. *Int. J. Biol. Macromol.* **1999**, *24*, 49–59. [[CrossRef](#)]
22. Krajewska, B. Pore structure of gel chitosan membrane III. Pressure-driven mass transport measurements. *Polym. Gles. Netw.* **1996**, *4*, 55–63. [[CrossRef](#)]
23. Aznar, E.; Oroval, M.; Pascual, L.; Murguia, J.R.; Manez, M.R.; Sancenon, F. Gated materials for on-command release of guest molecules. *Chem. Rev.* **2016**, *116*, 561–718. [[CrossRef](#)] [[PubMed](#)]
24. Osifo, P.O.; Neomagus, H.W.J.P.; Merwe, H.V.D.; Branken, D.J. Transport properties of chitosan membranes for zinc (II) removal from aqueous systems. *Sep. Purif. Technol.* **2017**, *179*, 428–437. [[CrossRef](#)]
25. Nakayama, R.; Yano, T.; Imai, M.; Namiki, N. Highly Size-Selective Water-Insoluble Cross-Linked Carboxymethyl Cellulose Membranes. *J. Polym. Environ.* **2019**, *27*, 2439–2444. [[CrossRef](#)]
26. Yang, G.; Zhang, L.; Cao, X.; Liu, Y. Structure and microporous formation of cellulose/silk fibroin blend membranes Part II. Effect of post-treatment by alkali. *J. Membr. Sci.* **2003**, *210*, 379–387. [[CrossRef](#)]
27. Wang, S.; Copeland, L. Effect of alkali treatment on structure and function of pea starch granules. *Food Chem.* **2002**, *135*, 1635–1642. [[CrossRef](#)]

28. Uragami, T.; Matsuda, T.; Okuno, H.; Miyata, T. Structure of chemically modified chitosan membranes and their characteristics of permeation and separation of aqueous ethanol solutions. *J. Membr. Sci.* **1994**, *88*, 243–251. [[CrossRef](#)]
29. Siroky, J.; Blackburn, R.S.; Bechtold, T.; Taylor, J.; White, P. Alkali treatment of cellulose II fibers and effect on dye sorption. *Carbohydr. Polym.* **2011**, *84*, 299–307. [[CrossRef](#)]
30. Zuluaga, R.; Putaux, J.L.; Cruz, J.; Velez, J.; Mondragon, I.; Ganan, P. Cellulose microfibrils from banana rachis: Effect of alkaline treatments on structural and morphological features. *Carbohydr. Polym.* **2009**, *76*, 51–59. [[CrossRef](#)]

**Publisher’s Note:** MDPI stays neutral with regard to jurisdictional claims in published maps and institutional affiliations.



© 2020 by the authors. Licensee MDPI, Basel, Switzerland. This article is an open access article distributed under the terms and conditions of the Creative Commons Attribution (CC BY) license (<http://creativecommons.org/licenses/by/4.0/>).



Article

# Treatment of Olive Mill Wastewater through Integrated Pressure-Driven Membrane Processes

Aldo Bottino, Gustavo Capannelli, Antonio Comite \* , Camilla Costa, Raffaella Firpo, Anna Jezowska and Marcello Pagliero

Department of Chemistry and Industrial Chemistry, University of Genoa, via Dodecaneso 31, 16141 Genova, Italy; bottino@chimica.unige.it (A.B.); gustavo.capannelli@gmail.com (G.C.); camilla.costa@unige.it (C.C.); firpolella00@gmail.com (R.F.); aniajez@yahoo.com (A.J.); marcello.pagliero@unige.it (M.P.)

\* Correspondence: antonio.comite@unige.it; Tel.: +39-0103536197

Received: 14 August 2020; Accepted: 9 November 2020; Published: 11 November 2020



**Abstract:** The disposal of wastewater resulting from olive oil production (olive mill wastewater, OMW) is a major issue for olive oil producers. This wastewater is among the most polluting due to the very high concentration of organic substances and the presence of hardly degradable phenolic compounds. The systems proposed for OMW treatment are essentially based either on conventional chemical-physical, biological and thermal processes, or on membrane processes. With respect to conventional methods, membrane processes allow to separate different species without the use of chemicals or heat. This work deals with the use of the integrated pressure-driven membrane processes for the treatment of OMW. They consist of a first stage (microfiltration, MF) in which a porous multichannel ceramic membrane retains suspended materials and produces a clarified permeate for a second stage (reverse osmosis, RO), in order to separate (and concentrate) dissolved substances from water. Laboratory scale experiments with different small flat sheet RO membranes were first carried out in order to select the most appropriate one for the successive bench scale tests with a spiral wound module having a large membrane surface. The aim of this test was to concentrate the dissolved substances and to produce water with low salinity, chemical oxygen demand (COD), and reduced phytotoxicity due to a low content of phenolic compounds. The trend of the permeate flux and membrane retention as a function of the volume concentration ratio was investigated. The influence of OMW origin and its aging on the membrane performance was also studied.

**Keywords:** olive mill wastewater; membrane separation process; microfiltration; reverse osmosis; water recovery

## 1. Introduction

Olive oil mill wastewater (OMW) is a by-product of the olive oil extraction process produced seasonally in a large quantity. Niaounakis and Halvadakis in their book [1] estimated a generation of OMW in the range of 10–30 million m<sup>3</sup>/year in 2006 and we should expect that since then, its quantity has increased in accordance with the increase in world olive oil consumption, which from 2006 to 2019 has grown from about 2.6 to 2.97 million tons [2,3].

### 1.1. OMW Composition

The OMW consists mainly of olive fruit vegetation water (more than 50% of the fruit) and water added during the extraction process. The composition of OMW is affected by the variety and ripeness of the olives and by the system used for their processing (pressure or centrifugation mills). For example, the centrifugation step in three-phase olive mill processing, the most common olive oil extraction



system, generates an amount of OMW more than two times higher than that of olive oil produced. An average OMW composition can be given as 83.2% of water, 1.8% of inorganic salts and 15% of organic constituents, among which 7.5% of sugars [4]. OMW is characterized by a low pH, a high electrical conductivity and a chemical oxygen demand (COD), which can be as high as 200 g/L. The three-phase process (3P) generates the greatest amount of OMW, about 1–1.2 m<sup>3</sup>/tons of olives, while the two-phase process generates the least amount, about 0.085–0.1 m<sup>3</sup>/tons of olives. The batch-pressing process produces about 0.4–0.6 m<sup>3</sup>/tons of olives of OMW [5]. Nevertheless, all the three types of OMW are highly pollutant. Due to the presence of several organic compounds, among which there is a phenolic fraction, untreated OMW has broad-spectrum toxicity against bacteria, plants and animals [6], which implies treatment and environmental problems. However, phenols presence in OMW makes this problematic by-product (wastewater) a potential source for recovery of precious antioxidants. For the abovementioned reasons, OMW treatment systems are not only supposed to be flexible and efficient in reducing COD and salinity, they also should be a viable alternative for recovery of high added value phenolic compounds.

### 1.2. OMW Membrane-Based Treatment Processes

The systems proposed for OMW treatment are essentially based either on conventional biological, chemical, physicochemical and thermal processes [7–9] or advanced membrane processes [10–16]. The latter, especially pressure-driven processes (microfiltration (MF), ultrafiltration (UF), nanofiltration (NF) and reverse osmosis (RO)), offer several advantages over traditional technologies, mainly in terms of low energy consumption, no additive requirements and no phase change, and thus, the possibility to preserve the original characteristics of treated effluents.

Gebreyohannes et al. [17] in 2016 reviewed both the literature and patents about the application of integrated membrane technologies for OMW treatment and they highlighted the polarization and fouling problems occurring in the pressure-driven membrane processes, which are mainly related to the particular composition of the OMW (e.g., solids, pectins, etc.). Again in 2016, Pulido [18] reviewed in detail the open literature on the application of membrane technologies in OMW treatment as well as on the main obstacles for their cost-effective utilization, namely the related fouling problems. He highlighted the need for a pretreatment before the integrated membrane process to limit the fouling phenomena and to achieve more stable operating permeate fluxes.

Typically, the proposed integrated pressure-driven membrane processes are based on the combination of steps for the removal of suspended solids (e.g., microfiltration or ultrafiltration) and of a second step aimed at the pollutant concentration and clean water recovery (e.g., nanofiltration and/or reverse osmosis). A fractionation of the pollutants contained in the OMW is technically feasible [19,20] but the application of such a process scheme composed by several steps of MF and UF with different molecular weight cut-off (MWCO), NF and RO is very expensive and often quite sophisticated for its implementation into small and medium olive mills.

Membrane processes have been applied to all the three types of OMWs (Table 1). The content of total suspended solids (TSS) and others minor components such as fats and pectins makes imperative a feed pretreatment before the NF or RO processes. Considering that the pH for the types of OMWs is similar, the electrical conductivity (EC) reflects the concentration of organic electrolytes and salts. The two-phase process shows the lowest electrical conductivity or solid residue. On the other hand, the two-phase process generates a solid, known as alperujo, which is a very pollutant waste to handle since it contains most of the organic compounds that in the three-phase process are released in the wastewater [5].

**Table 1.** Analytical characteristics of olive mill wastewater (OMWs) from the batch (BP), two-phase (2P) and three-phase (3P) processes and some integrated membrane processes proposed in literature.

Process	pH	EC (mS/cm)	TSS (g/L)	COD (g/L)	Ph (mg/L)	Ch (g/L)	Proposed Process	References
BP	4.5–5		0.1–2.7	65.7–130	1.2–2.4%	2.2–4.5		[5]
	4.5	9.0	12%	–180.0	-	-		[21]
	4.5	-	8.0	47.8	3740	-	UF-NF	[22]
	4.7	-	7.8	59.1	4560	-		
2P	5.1	1.8	-	13.4	749	-	NF	[23]
	5.25	2.1	-	14.0	776	-		
	5.5	2.2	-	4.2	-	-	NF	[24]
	4.9	1.7	5.6	16.4	181	-	RO	[25]
	4.9	1.3	0.6%	7.8	-	-		[21]
3P	4.7–5.2	-	0.9–27.6	40–103.4	0.37–0.5%	1.5–4.7		[5]
	5.0	-	17.6		212	-	MF-NF-OD	[11]
	-	-	44	107.2	2640	12.3	UF-NF-RO	[26]
	5.4	7.9	6.6%	151.4	-	-		[21]
	5.13	5.08	11.7	16.5	850	13.1	UF-NF-RO	[27]

EC = Electrical conductivity; TSS = Total Suspended Solids; TOC = Total Organic Compounds; COD = Chemical Oxygen Demand; Ph = Polyphenols; Ch = Carbohydrates.

Cassano et al. [9] studied the application of UF polymeric membranes (MWCO between 4 and 10 kDa) and they observed a flux decrement up to 50% over 300 min operating time. The best performing membrane was made of regenerated cellulose. The flux recovery after cleaning with an alkaline detergent at 40 °C was claimed enough to recover the initial water flux. In any case, the raw OMW was subjected to preventive microfiltration step at 0.2 micron. Garcia Castello et al. [11] studied the combination of MF, NF followed by an osmotic distillation. In the MF step a 0.2 µm membrane was used and a strong flux decrease was observed without any tendency of stabilization. The cleaning procedure was carried out by using a concentrated alkaline solution of 20 g/L NaOH at 40 °C for 30 min followed by tap water rinsing. An irreversible fouling was observed with a loss of flux of about 50%. The flux reduction in the NF membrane (Nadir N30F spiral-wound membrane module) was about 35% after about 1 h operation at a volume reduction factor of about 3. The NF membrane after cleaning with 1g/L of NaOH as done for MF completely recovered its initial water flux. From the cited investigations it seems that although UF underwent severe fouling the initial flux could be recovered in most of the cases by a chemical alkaline cleaning procedure.

Bazzarelli et al. [28] proposed an integrated membrane process based on a MF/NF and osmotic distillation and membrane emulsification. For the MF step, a 0.14 µm ceramic membrane was used and the good results in the MF flux stability were ascribed to an acidification step at pH 1.8 and a subsequent filtration on a stainless steel filter [29]. The chemical cleaning protocol was still based on the use of an alkaline detergent at 40 °C for 30 min. Chemical physical pretreatments before the integrated pressure-driven membrane processes were studied in order to improve the performance of the integrated membrane process. Pulido et al. [30] applied a pretreatment based on a Fenton process, then directly followed by NF. Nevertheless, the direct application of tighter membrane processes (NF or RO) after a physical chemical secondary treatment can lead to cake formation on the membrane surface as reported for RO membranes [31].

Recently, the possibility of using a water-ethanol mixture for the extraction of polyphenols and their purification by integrated membrane processes was explored [32]. Although it opens up an interesting perspective, additional investigations should be carried out in order to define the quality of the reverse osmosis permeate and its ethanol content. With the aim of recovering valuable polyphenols, most of the studies investigated the integration of ultrafiltration (UF) and (NF). De Almeida et al. [22] showed that despite the combination of UF and NF, the COD and total phenols removal can be 83.3 and 93.1%, respectively. Despite the interesting results, the quality of the permeate water is still far from being disposed in the sewage under the parameters imposed by the legislation. Therefore,

to meet the current disposal regulations a further treatment or filtration step of the NF permeate is clearly necessary.

Another integration scheme relied on the direct use of RO instead or in addition to the NF. Tundis et al. [33] showed the recovery and classification of polyphenols by using a MF step on a 0.1  $\mu\text{m}$   $\text{TiO}_2$  membrane followed by a NF step and a RO step based on a membrane typically applied to brackish water. Although a flux decay was observed for all the membrane filtrations, as the aim of the work was about the characterization of the polyphenols in the concentrate, the quality of the final NF and RO permeates was not assessed by the authors. Zagklis et al. [34] in a recent paper mentioned the design of a full system based on UF/NF/RO integrated with adsorption steps and solid-liquid extraction with the aim of recovering the polyphenolic fractions from both OMW and other types of phenolic containing wastewater (e.g., grape marc and olive leaves). Coskun et al. [35] in their lab scale study proposed centrifugation as a primary step followed by UF and finally by RO. Their study was exclusively focused on the rejection performance of the different membranes. Petrotos et al. [36] studied some relevant operational parameters on a pilot scale, a process integrating MF followed by a NF (or open RO) and then by RO using tubular membranes.

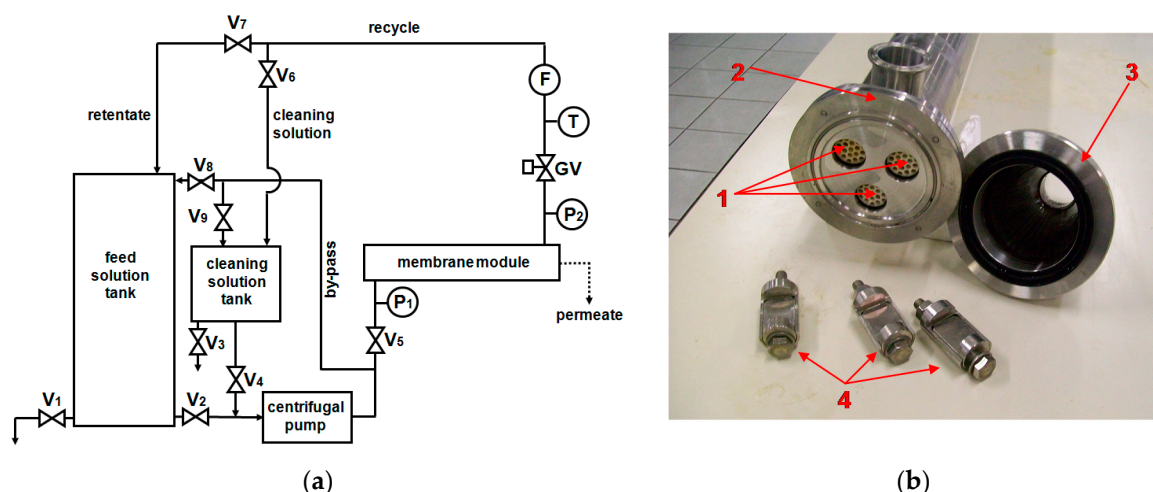
The problem of OMW is clearly urgent from the point view of its environmental impact and the technological solution that requires it to be simple, cost-effective and reliable, especially in countries where the size of working olive mills is still small. Integrated pressure-driven processes, which include RO as a final step, should enable the production of a permeate water of sufficient quality not only for its safe discharge into sewage, but also for any kind of reuse into a farm or olive oil production process.

Membrane processes were shown to be very effective in the treatment of numerous industrial effluents and wastewaters. However, their successful application depends on the proper choice of process configuration and process conditions, and these are the focus of the experimental study presented here. In this work, two consecutive pressure-driven membrane processes, namely microfiltration and reverse osmosis, are proposed for OMW treatment in order to obtain a RO permeate composed of water with a low salinity, COD, and reduced phytotoxicity due to very low content of phenolic compounds, which are retained and concentrated by the RO membrane. To this aim, laboratory scale tests were first carried out with small flat sheet RO membrane samples in order to select the most suitable membrane for the successive pilot scale investigation with a spiral wound element with a large membrane surface area. The high concentrations of suspended materials in OMW imposed the use of microfiltration as a pretreatment system for the RO, in order to avoid plugging of the feed spacer of the spiral wound elements. Ceramic multichannel elements with excellent thermal stability and chemical resistance to withstand severe cleaning cycles were used for microfiltration in order to easily remove particulates that can foul the membrane or plug the channels. This work deals with practical aspects and problems connected to the concentration of large volumes of OMW with MF/RO pilot plants and to OMW storage that were not investigated enough in the literature.

## 2. Materials and Methods

Since characteristics of OMW may differ significantly from mill to mill, OMWs from three different olive mills, two located in Liguria and one in Tuscany, were employed. The names of these mills cannot be revealed for confidentiality reasons and a generic code composed of letters and numbers will be used to identify the three types of OMWs. OMWs were first stored in reservoir tanks to allow sedimentation of a large part of suspended materials and separation of a supernatant fluid, which was filtered through a filter bag with an opening of 200  $\mu\text{m}$  prior to microfiltration.

Microfiltration of prefiltered OMW was performed in a batch operation mode with the plant schematically shown in Figure 1a, using three ceramic membranes (Membralox EP19-40, Pall Corp., Port Washington, NY, USA) arranged in parallel into a stainless steel housing (Figure 1b). The main properties of these membranes are shown in Table 2.



**Figure 1.** (a) Schematic of the plant used for MF tests: V1-9 ball valves; GV gate valve; P1,2 manometers, T thermometer; F flowmeter. (b) Membralox module: 1—ceramic multi-channel membranes, 2—stainless steel membrane housing, 3—module end-cup, 4—clamps.

**Table 2.** Main properties of Pall–Membralox EP19-40 membrane used for MF tests.

Channel Diameter	4 mm
Number of Channels	19
Filtration Surface Area	0.24 m <sup>2</sup>
Length	1020 mm
Material	Ultrapure $\alpha$ -alumina (>99.7%)
Pore size of the inner layer	0.2 $\mu$ m

The MF retentate was completely recycled to the feed tank while the clean permeate was continuously withdrawn to be used for RO test. As can be seen from Figure 1a, OMW is fed by the centrifugal pump to the membrane module with a velocity  $v = 3.9$  m/s (calculated from the ratio between the feed flow rate measured by the flow meter, F, and the membrane channels cross-section) at an average pressure  $P = 2.3$  bar, unless otherwise reported, measured by two manometers, P1 and P2, located before and after the membrane module, respectively. The permeate flow rate is simply evaluated by measuring with a graduated tank the time necessary to produce a given permeate volume. Permeate flux is then calculated from the ratio between the permeate flow rate and the overall filtration surface area. The temperature measured by the thermometer, T, is kept constant at 30 °C by a cooling device immersed into the feed tank. An electric immersion heater in the cleaning tank provides a rapid heating of the cleaning solutions (NaOH and/or NaOCl solutions) used to remove foulants from the membrane.

The scheme of the RO plant is very similar to that of the MF plant shown in Figure 1a. The main differences are related to the feed pump (piston), the pressure control valve (globe valve), and the use of a variable frequency drive ‘inverter’ to control the feed flow rate, Q (speed pump). The experimental conditions adopted for RO experiments were:  $P = 30$  bar (unless otherwise reported),  $Q = 1000$  L/h,  $T = 25$  °C. A small cell was used for preliminary tests with flat sheet membrane samples (surface 0.0066 m<sup>2</sup>) listed in Table 3. A cylindrical vessel was employed to house a spiral wound membrane module (SW30HR Dow-Filmtec, now DuPont, Wilmington, Delaware; 4” diameter, 40” length, membrane surface 7.9 m<sup>2</sup>) during the successive bench scale experiments. Preliminary tests with small flat membranes were carried out keeping the feed concentration constant, and continuously recycling both permeate and concentrate streams to the feed tank. Concentration tests with spiral wound module were performed in a batch operation mode, following the same procedure previously described for microfiltration of OMW. During both RO and MF experiments samples of different streams were collected for analysis.

**Table 3.** NF and RO membrane used during test cell experiments.

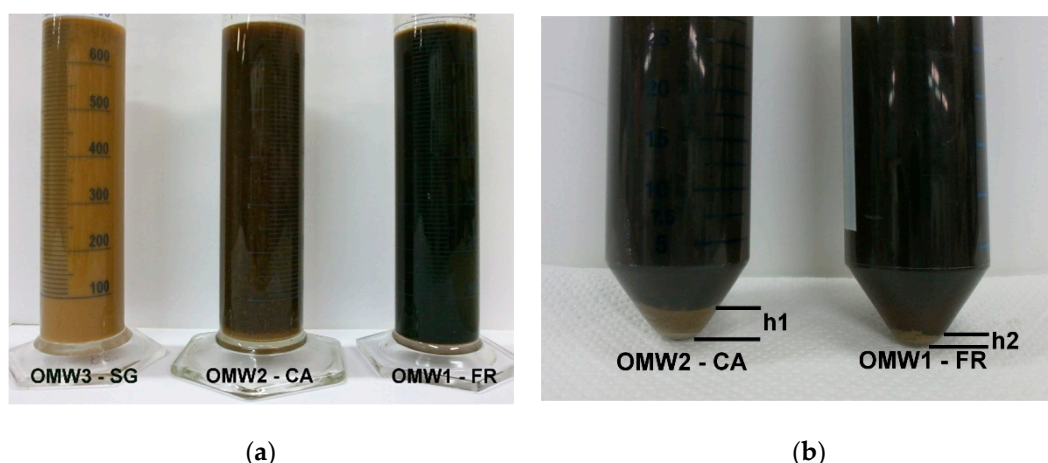
Membrane	Manufacturer	Minimum Rejection	Application
Desal AG	GE Power&Water	99.3% (NaCl)	Brackish water RO
Desal SC	GE Power&Water	98.5% (NaCl)	Brackish water RO
Desal DK	GE Power&Water,	98% (MgSO <sub>4</sub> )	NF
SW30 HR	DOW	99.6% (NaCl)	Seawater RO
SW30 ULE	DOW	99.55% (NaCl)	Seawater RO
BW30	DOW	99.0% (NaCl)	Brackish water RO
NF 90	DOW	97.0% (MgSO <sub>4</sub> ), 85.0% (NaCl)	NF

Electrical conductivity, pH and suspended solids content were measured according to Standard Methods [37]. COD was determined with the spectrophotometric method using Merck Spectroquant® test kits (Merck KGaA, Darmstadt, Germany). The method is analogous to EPA 410.4, US Standard Methods 5220 D, and ISO 15705. Phenols were determined with Folin–Ciocalteu reagent [38].

### 3. Results

#### 3.1. Feed Pretreatment and Microfiltration

OMWs with quite different characteristics were received from three mills. In particular, the OMW3-SG was characterized by a very high load of suspended solids of small size with a negligible settling velocity and poorly retained by the filter bag as can be seen in Figure 2a, where the images of the three types of OMWs after settling and filtration treatment are reported for comparison. The darker color of samples OMW1-FR and OMW2-CA is connected to a high particle removal efficiency. However, even in these two cases (especially for OMW2-CA) the produced filtrates did not satisfy the requirements for the RO feed. This is apparent from the images of Figure 2b, where deposited solids after centrifugation (8000 rpm for 10 min) can be observed on the bottom of the centrifuge tube. Therefore, a post-filtration treatment with ceramic membrane with 0.2 µm pore size was employed for the removal of fine suspended solids and production of a suitable feed for RO [39]. The main physicochemical characteristics of the three types of OMW (after settling and bag filtration) fed to the microfiltration plant are reported in Table 4.

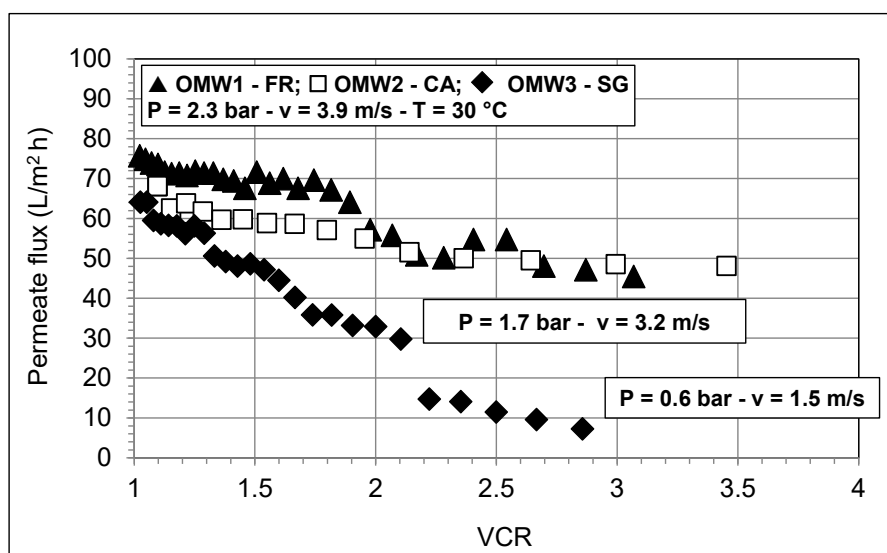


**Figure 2.** (a) Images of OMWs after settling and bag filtration. (b) Images of OMWs after centrifugation (h = TSS volume).

**Table 4.** Physicochemical properties of OMWs fed to the microfiltration plant.

	pH (—)	TSS (mg/L)	COD (mg/L)	Conductivity ( $\mu$ S/cm)	Phenols (mg/L)
OMW1-FR	4.43	870	30,000	5310	2000
OMW2-CA	5.80	1700	66,500	13,940	1500
OMW3-SG	5.17	15,000	159,500	12,780	3300

Figure 3 refers to the microfiltration tests and shows the behavior of permeate flux as a function of volume concentration ratio, VCR (i.e., the ratio between the volume of the initial feed and the volume of the final concentrate) for the three different pretreated (settled and filtered) OMWs. Gentle heating at 30 °C makes the feed (especially the OMW3-SG) more fluid with consequent reduction of the friction loss along the plant and improved performance of the centrifugal pump. The permeate flux at the beginning of the MF tests appears very close for the three OMWs, while increasing the VCR, OMWs behave differently, especially OMW3-SG. As far as OMW1-FR and OMW2-CA are considered, the permeate flux first slightly decreases and then tends to level off. With OMW3-SG, which contains a relevant amount of suspended materials, a strong and almost proportional decline of permeate flux with increasing the VCR is observed.



**Figure 3.** Permeate flux versus volume concentration ratio (VCR) during the MF tests with different OMWs.

After a VCR = 2.1, the high viscosity of the concentrated OMW3-SG (Figure 4a) considerably reduces the performance (head and flow rate) of the centrifugal pump, thus the fluid velocity through the membrane channels is progressively lowered and membrane channels begin to plug. The permeate flux first falls and then continues the decrease slowly. Immediately after VCR = 2.85, a sudden increase of the pressure occurred and the pump reached its shut-off pressure. The test had to be stopped immediately and it was necessary to use a metal probe to unclog membrane channels (Figure 4b).

Moreover, an intense membrane cleaning with NaOH solution (2% w/w) and NaOCl (500 ppm Cl) at 60 °C for at least 60 min was used to remove the deposit remaining on the membrane surface and into the membrane pores. By measuring pure water flux before ( $J_{W,0}$ ) and after ( $J_{W,F}$ ) OMW filtration, a flux recovery ratio  $FRR = (J_{W,F}/J_{W,0}) \cdot 100$  very close to 100% was achieved, thus demonstrating the effectiveness of the cleaning procedure. The other two types of OMWs (1-FR and 2-CA) did not plug membrane channels but severely fouled the membrane. The pure water flux after MF was around 30% of the original membrane flux, but even in this case a  $FRR \approx 100\%$  was obtained after the cleaning with NaOH and NaOCl.



**Figure 4.** (a) OMW3-SG viscous concentrate after VCR = 2.1. (b) Removal of OMW3-SG muddy concentrate from the membrane channel with a metallic probe.

The main physicochemical properties of feed (FD) and permeate (PR) samples collected at increasing VCR during the MF of the three types of OMW are listed in Table 5. Both pH and electrical conductivity of feed and permeate are substantially similar since dissolved ions pass through the pore of the membrane while a given retention is observed for COD due to the removal of suspended organic part, which contributes to this parameter. Phenol retentions seem to be high for the MF membrane, but according to previous literature findings [8], this fact can be ascribed to fouling, which may deeply alter the retention characteristics of membrane by itself.

**Table 5.** Main physicochemical properties of feed (FD) and permeate (PR) samples collected during the MF tests with three different types of OMW.

VCR	pH		Conductivity (µs/cm)			COD (mg/L)			Phenols (mg/L)		
	FD	PR	FD	PR	R (%)	FD	PR	R (%)	FD	PR	R (%)
OMW1-FR											
1.00	4.43	4.39	5310	5050	4.90	30,000	19,780	34.07	2000	1430	28.50
1.29	4.44	4.39	5450	5330	2.20						
1.82	4.44	4.4	5420	5290	2.40	33,425	20,450	38.82	3900	2820	27.69
3.07	4.5	4.41	5450	5260	3.49	38,700	23,100	40.31	4500	3200	28.89
OMW2-CA											
1.00	5.8	5.9	13,940	13,690	1.79	66,500	43,370	34.78	1500	996	33.60
1.22	5.79	5.88	13,600	13,350	1.84	70,889	40,990	42.18			
1.55	5.77	5.91	13,560	13,410	1.11	75,500	42,440	43.79	1590	1050	33.96
2.14	5.79	5.87	13,920	13,650	1.94	85,000	40,740	52.07			
3.45	5.81	5.9	13,990	13,500	3.50	95,000	42,850	54.89	1910	1200	37.17
OMW3-SG											
1.00	5.17	5.23	12,780	12,240	4.23	128,800	49,490	61.58	3300	1950	40.91
1.67	5.37	5.38	12,470	12,060	3.29	164,350	55,350	66.32			
2.86	5.37	5.39	12,470	12,050	3.37	209,000	64,590	69.10	4800	2820	41.25

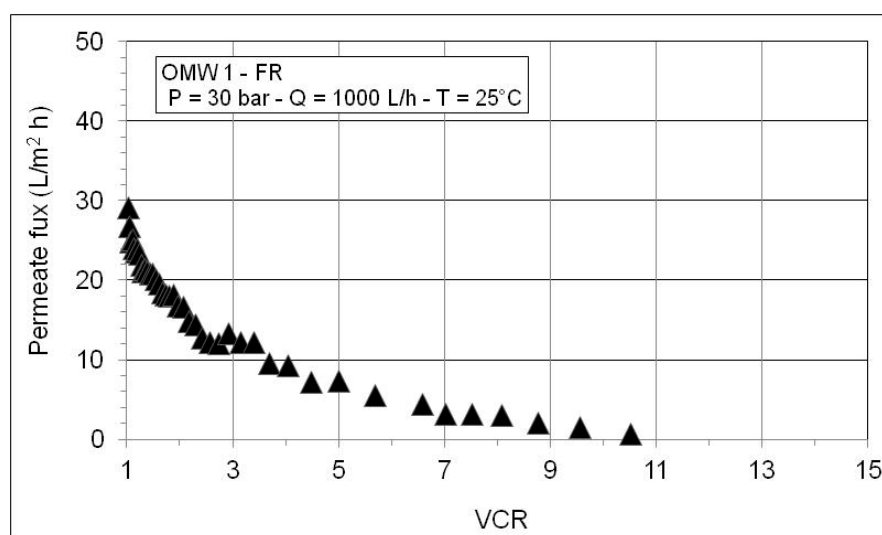
### 3.2. Nanofiltration and Reverse Osmosis

The results of NF/RO screening tests with small flat sheet membranes carried out by using the MF permeate of OMW2-CA as feed are reported in Table 6. Except for Desal DK, all the other membranes present very high solute retention. To obtain useful products from OMW such as purified water (permeate) and a polyphenols rich solution (concentrate), a membrane with the highest possible retention to salts, COD and phenols are required. Table 6 reveals that SW30HR membrane (DOW) completely meets these requirements. Therefore, this membrane in a spiral wound configuration was selected for successive bench-scale tests.

**Table 6.** Results of the RO screening tests with different types of NF and RO membranes (P = 30 bar, T = 25 °C). Feed: MF permeate of OMW2-CA (Conductivity = 13,200 µS/cm; COD = 40,180 mg/L; Phenols = 1070 mg/L).

Membrane	Permeate Flux (L/m <sup>2</sup> h)	Conductivity		COD		Phenols	
		PR (µS/cm)	R (%)	PR (mg/L)	R (%)	PR (mg/L)	R (%)
Desal AG	7.00	138.6	98.95	2608	93.51	6.0	99.44
Desal SC	14.35	170.3	98.71	2326	94.21	9.1	99.15
Desal DK	60.61	1473	88.84	8249	79.47	112.8	89.46
SW30 HR	12.66	109.6	99.17	1736	95.68	2.9	99.73
SW30 ULE	12.04	151.8	98.85	2359	94.13	4.4	99.59
BW30	33.26	159.7	98.79	2387	94.06	9.0	99.16
NF 90	27.27	150.5	98.86	2668	93.36	7.5	99.30

The results of the RO concentration test carried out with the MF permeate of OMW1-FR are shown in Figure 5. By increasing the VCR, the permeate flux decreases first rapidly and then slowly until reaching VCR = 10.5, a value (around 1 L/(m<sup>2</sup>·h)) ca. 30 times lower than that of the initial flux (VCR = 1). The observed flux decline with increasing VCR can be ascribed to the increase of the osmotic pressure of the feed, as well as concentration polarization and fouling phenomena.

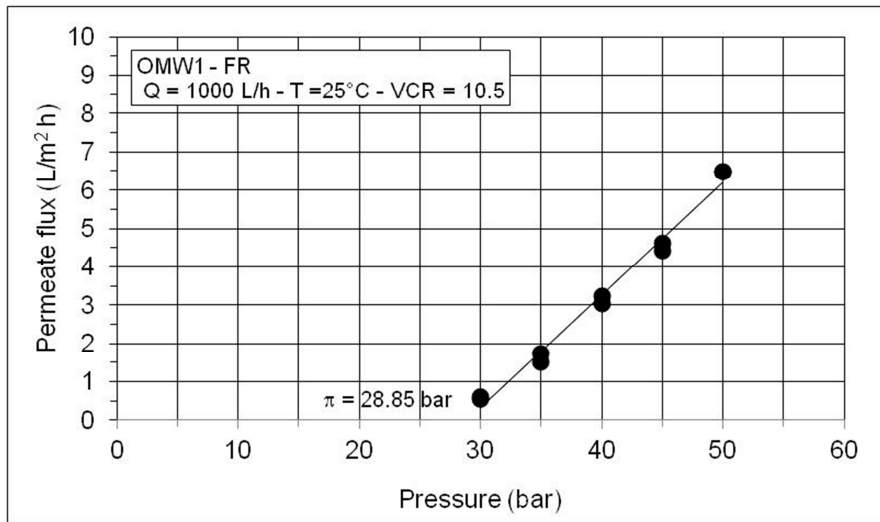


**Figure 5.** Permeate flux as a function of VCR during RO test with the MF permeate of OMW1-FR.

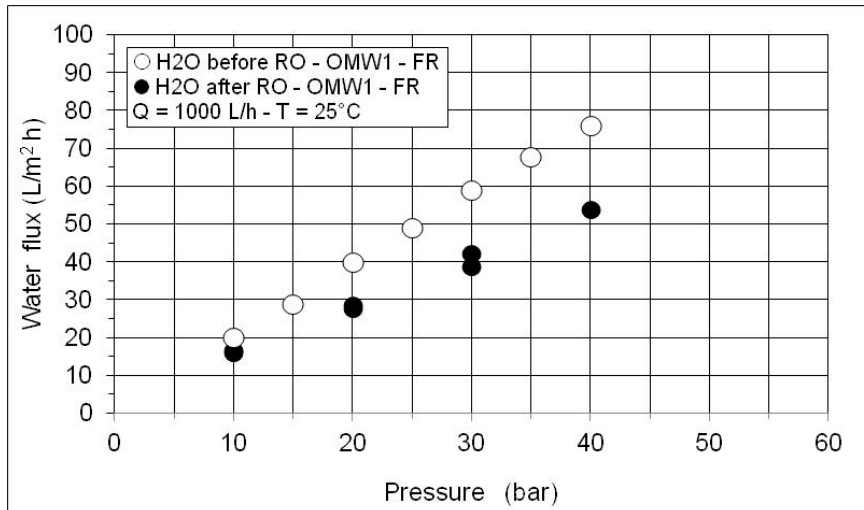
The osmotic pressure of the concentrated solution (VCR = 10.5) can be estimated by measuring the permeate flux at increasing pressures and a constant feed concentration as shown in Figure 6. The differences in pure water flux (Figure 7) measured before and after OMW treatment are connected to the membrane fouling. Only a moderate cleaning with a NaOH solution (pH = 11) at 40°C was sufficient for eliminating fouling and achieving FRR around 100%.

Figures 8 and 9 show the behavior of the permeate flux as a function of VCR during the RO concentration of the permeates produced by microfiltration of OWM2-CA and OWM3-SG. The trends are similar to that shown in Figure 5. The permeate flux improves at higher pressure but continues to fall with the increase in the VCR. A worse membrane performance is observed according to the considerably higher solute content of these OMWs as shown in Table 7. Further inspection of Table 7 reveals high retention values for conductivity and COD and an excellent abatement of phytotoxic phenol fraction. As expected, the retention worsens with VCR and improves with the pressure (since water flux through the membrane increases with the pressure while the solute diffusion is independent of pressure).

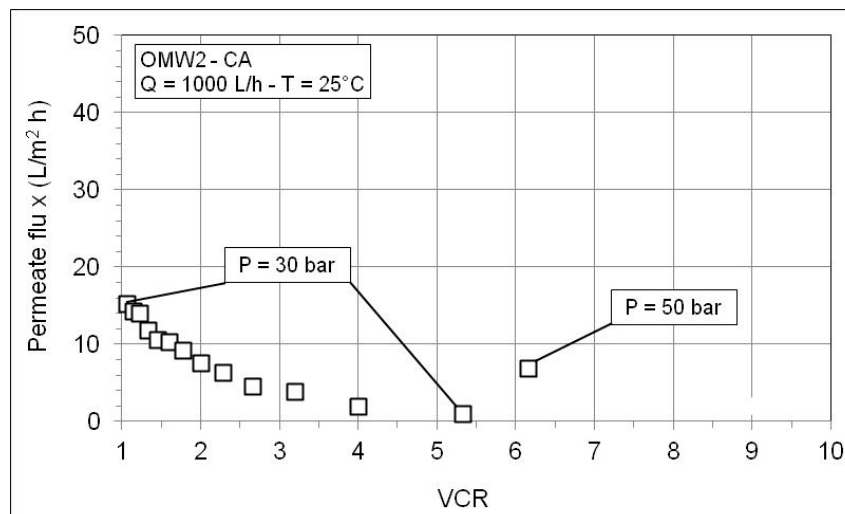




**Figure 6.** Permeate flux as a function of operating pressure at VCR = 10.5 (Feed: MF permeate of OMW1-FR).



**Figure 7.** Pure water flux as a function of operating pressure before and after RO test with MF permeate of OMW1-FR.



**Figure 8.** Permeate flux as a function of VCR during RO test with the MF permeate of OMW2-CA.

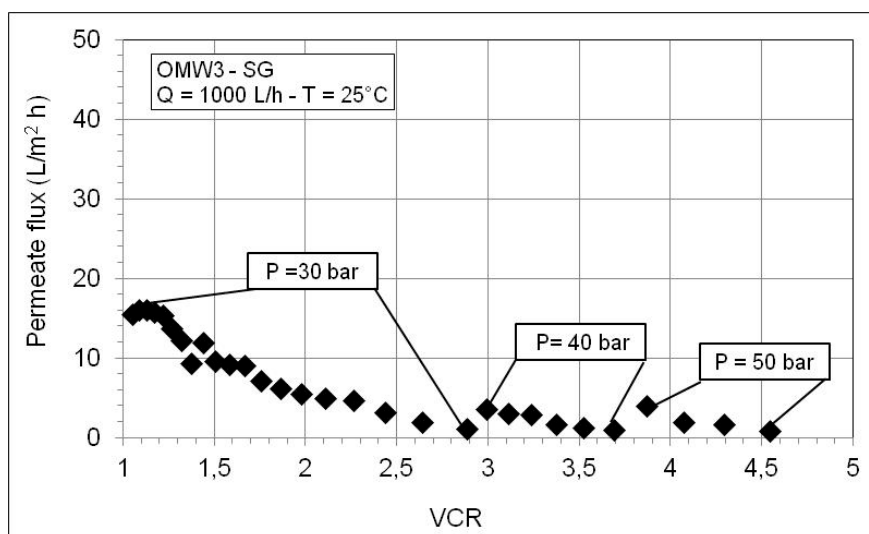


Figure 9. Permeate flux as a function of VCR during RO test with the MF permeate of OMW3-SG.

Table 7. Main physicochemical properties of feed (FD) and permeate (PR) samples collected during RO test with the MF permeates of three different types of OMW.

VCR	P (bar)	pH		Conductivity (µS/cm)			COD (mg/L)			Phenols (mg/L)		
		FD	PR	FD	PR	R (%)	FD	PR	R (%)	FD	PR	R (%)
OMW1-FR												
1.00	30	4.48	3.79	5100	89.7	98.24	19,650	628	96.80	2900	6.0	99.79
1.96	30	4.58	3.61	8880	109.0	98.77	36,170	926	97.44			
6.56	30	4.68	3.83	20,900	253.0	98.79						
10.50	30			26,700	1382	94.82	140,120	2558	98.17	24300	28.0	99.88
OMW2-CA												
1.00	30	5.88	4.81	13,200	116.3	99.12	40,180	2010	95.00	1070	5.0	99.53
1.23	30	5.87	4.84	15,200	133.4	99.12	53,990	2231	95.87			
1.60	30	5.86	4.86	16,370	199.2	98.78	65,860	2495	96.21			
2.29	30	5.9	4.9	18,910	239.7	98.73	86,960	3840	95.58			
4.00	30	5.98	4.92	20,490	318.9	98.44	109,220	8855	91.89			
5.33	30	6.02	4.96	27,400	904.0	96.70	151,700	15,325	89.90	5600	57.3	98.98
6.15	50	6.12	4.89	30,200	702.0	97.68	191,350	4075	97.87	6420	24.2	99.62
OMW3-SG												
1.00	30	5.45	5.27	12,100	115.2	99.05	58,560	2933	94.99	2250	2.2	99.90
1.24	30			17,130	128.4	99.25	78,280	3189	95.93			
1.62	30			20,500	192.7	99.06	104,320	4543	95.65			
2.33	30	5.5	5.21	25,800	738.0	97.14	120,800	10,000	91.72			
2.74	30			29,000	1592	94.51	159,220	13,855	91.30	7500	54.0	99.28
3.62	40			33,800	1734	94.87	215,850	16,620	92.30			
4.57	50	5.59	5.16	36,100	3320	90.80	261,900	8720	96.67	9850	26.0	99.74

The effect of OMW age on the performance of the membrane is shown in the following Figures 10 and 11 and in Table 8. It is worth noticing that olive oil extraction is a seasonal operation whose duration is around 4–5 months during the winter. The amount of OMW is much higher than that of olive oil produced, and consequently very large plants are necessary for the treatment of all the wastewater generated daily, otherwise it must be stored. To obtain preliminary information on the influence of OMW storage/aging on the performance of the integrated membrane process, a given amount of OMW2-CA was allowed to rest for ca. 4 months. After this long settling period, the supernatant liquid was filtered through the usual filter bag and the resulting filtrate was sent to the MF plant. From the results reported in Figure 10, a given increase of the permeate flux of the stored OMW is observed. This increase is connected to a lower content of suspended material (TSS = 420 mg/L) due to the 4 months settling period. Conversely, only a moderate variation of the permeate flux during the RO experiments (Figure 11) occurs since the amount of dissolved solids does not practically change

during the storage, as can be seen from physicochemical characterization results shown in Table 8. From the same table it is apparent that the storage period does not affect membrane retention.

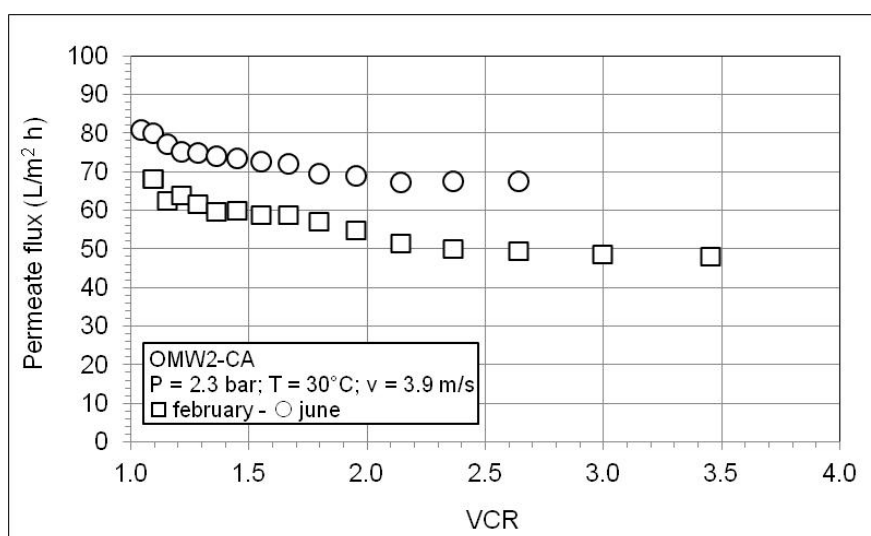


Figure 10. Effect of storage of OMW2-CA on the permeate flux as a function of VCR during MF test.

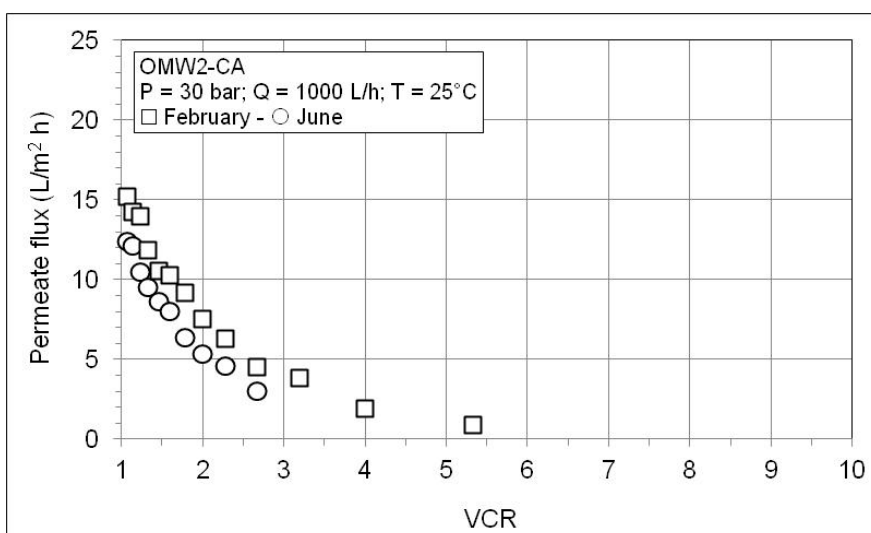


Figure 11. Effect of storage of OMW2-CA on the permeate flux as a function of VCR during RO test with the MF permeate of OMW2-CA.

Table 8. Main physicochemical properties of feed (FD) and permeate (PR) samples collected during the RO test with “aged” OMW2-CA.

VCR	P (bar)	pH		Conductivity (µs/cm)			COD (mg/L)			Phenols (mg/L)		
		FD	PR	FD	PR	R (%)	FD	PR	R (%)	FD	PR	R (%)
1.00	30	5.91	4.82	13,500	117.4	99.13	40,200	2050	94.90	1025	5.2	99.49
1.14	30	5.87	4.84	14,200	135.2	99.05	44,500	2120	95.24			
1.33	30	5.93	4.85	15,300	198.7	98.70	55,450	2290	95.87			
1.60	30	5.94	4.87	16,450	240.1	98.54	67,800	2370	96.50			
2.00	30	5.89	4.83	17,930	303.8	98.31	84,300	3540	95.80	2320	11.0	99.53
2.67	30	5.93	4.90	19,800	318.4	98.39	98,650	5900	94.02			

## 4. Discussion

### 4.1. Pretreatment and Microfiltration

As reported in Tables 1 and 3, OMW contains relevant concentrations of TSS. Therefore, any type of membrane process aimed at polyphenol recovery as well as water reuse needs a pretreatment to remove TSS. The removal of TSS is of crucial importance for the fouling control of the NF or RO process.

Cassano et al. [12] pretreated the raw OMWs by using a commercial tubular MF membrane module (pore size 0.2  $\mu\text{m}$ , polypropylene, 5.5 mm inner diameter). Then, UF polymeric membranes were used to produce a clear permeate to be fed to the nanofiltration unit. Nevertheless, for all the UF membranes, a flux decay was observed. Bazzarelli et al. [29] studied the change of pH to destabilize the solid suspension in OMW and they showed that a pretreatment based on MF or UF can be effective at removing the suspended solids. MF exhibits higher fluxes than UF and ceramic membranes showed the highest fluxes. In another interesting approach of MF by using polymeric hollow fiber membranes, a fouling control was attempted by the deposition on the membrane surface of a photoactive gel [40].

García–Castello et al. [11] reported the performance of a 0.2  $\mu\text{m}$  alumina membrane after several filtration runs. During each run, a consistent flux decay was observed and even after a cleaning procedure with 20 g/L NaOH at 40 °C the water flux of the virgin membrane was not fully recovered.

In our work, we proposed the use of a ceramic MF membrane due to its high chemical and thermal stability during the cleaning procedures to restore its performance. We also observed an evident decay of the flux (Figure 3), but on the other hand, a chemical cleaning with alkaline agents combined with the use of a sufficiently high temperature (about 60 °C for at least 1 h) we restored the initial membrane performance. The effect of the temperature during the chemical cleaning was remarked in a recent work also by Fraga et al. [41], where the use of high permeability silicon carbide MF membranes was investigated.

The MF ceramic membrane module tested with all the three OMWs was able to preserve the subsequent NF or RO spiral wound modules from plugging problems. Since MF can seriously suffer from plugging and fouling phenomena at high TSS, the use of chemically-resistant membranes seems to be essential, especially if the plant is designed to be used only seasonally.

### 4.2. Nanofiltration and Reverse Osmosis

SW30HR membrane showed the best retention of COD and phenols among the tested NF and RO membranes. By increasing the VCR, the retention to phenols was always very high (>99.3%) and the retention to COD had generally been about 95%. The highest VCR obtained was limited by the increase of the osmotic pressure. As shown, at VCR = 10.5 the experimental osmotic pressure was approaching 29 bars. The electrical conductivity of pristine OMW1-FR was 5310  $\mu\text{S}/\text{cm}$ , while for OMW2-CA and OMW3-SG, the electrical conductivities were very close, 13,940  $\mu\text{S}/\text{cm}$ , 12,780  $\mu\text{S}/\text{cm}$ , respectively (Table 4). Since the electrical conductivity is mainly related to the concentration of dissolved salts, with the OMW1-CA it was possible to achieve a higher VCR than for the other two OMWs. The different behavior between OMW2-CA and OMW3-SG during the RO concentration is therefore mainly related to the different level of organic compounds, considering that the ratio of COD between the OMW3-SG and OMW2-CA is about 2. A pressure increase seems to be beneficial to both the flux and the retention.

### 4.3. Remarks

On the basis of our results and of the findings reported in the literature, integrated membrane processes are able to efficiently produce a polyphenols-rich concentrate. The recovery of polyphenols is very interesting, since they are valuable compounds that can be supplied to cosmetic and pharmaceutical industries. Nevertheless, the exploitation of polyphenols-rich streams is still facing some technological challenges related to the polyphenol fractionation. The main driver to develop processes for the treatment of OMW is the environmental pressure in order to limit the pollution related to their production and disposal. A clean water stream can be obtained when an RO process is considered as a

final step. In the proposed integrated membrane process, the high retention of polyphenols can allow the separation of good quality water already after a first RO stage, which can be more easily accepted by a sewage depuration system since the residual COD is no longer related to the presence of polyphenols. The permeate water can be considered also for an internal reuse in the olive mill after and eventual refining treatment (a second RO stage or adsorption) as well as for irrigation purposes. The main process issues are related to controlling the fouling. Ceramic membranes have proved their suitability since they can withstand aggressive chemical cleaning procedures, and although their cost is still high compared to that of polymeric membranes, they can guarantee a longer lifetime. Since in many countries olive mills are still small enterprises, the investment costs for a membrane-based treatment plant can be more easily faced if there is the possibility of storing part of the OMWs generated during the milling season. In this work, we proved that the aging of the OMW does not critically affect the performance of the integrated membrane process.

Pulido and Martinez-Ferez in their review [42] identified the control of fouling as one of the limits of membrane technologies applied to OMW. Another bottleneck for a wide field application of the integrated membrane process remains, related to the options available for either the disposal or chemical/energetic valorization of the concentrate stream. These options should be evaluated on the specific characteristics and constraints of the olive mill willing to apply membrane technology.

## 5. Conclusions

MF/RO integrated membrane processes have been proposed for the treatment of OMW. The MF can be considered a suitable pretreatment for RO process since it provides a clean permeate, which does not cause plugging of the spiral wound element. RO separates dissolved substances from water, thus allowing the concentration of valuable products and produces water with a low salinity, COD, and phytotoxicity. Channel plugging and fouling of MF membrane represent a serious problem during the treatment of OWM, characterized by a high load of fine particles, which cannot be properly removed by simple settling or bag filtration. Therefore, ceramic membranes capable of withstanding hard cleaning agents are necessary. Membrane performance is not deeply affected by OWM aging and consequently, the wastewater may be treated gradually, without the need of large plants operating only a few months a year. This may involve important benefits connected to the reduction of investment costs and of bactericide solutions, which are necessary for a long-term storage of delicate RO membranes. The commercial RO membrane for seawater treatment, SW30 HR (Dow), showed a very high retention to polyphenols and dissolved species, which contribute to electrical conductivity. The increase of both osmotic pressure and organics concentration limited the maximum volume concentration ratio that could be achieved.

**Author Contributions:** Conceptualization, A.B. and G.C.; data curation, C.C. and A.J.; funding acquisition, G.C.; investigation, A.B., R.F., A.J. and M.P.; methodology, A.B. and A.J.; project administration, G.C. and A.C.; resources, A.C. and A.J.; supervision, A.B. and A.C.; visualization, A.J. and M.P.; writing—original draft, A.B. and A.J.; writing—review & editing, A.C. and M.P. All authors have read and agreed to the published version of the manuscript.

**Funding:** This research was conducted in the framework of the ENPI CBC Med Project: MEDOLICO I-B/2.1/090 (Mediterranean Cooperation in the Treatment and Valorisation of Olive Mill Wastewater, OMW).

**Conflicts of Interest:** The authors declare no conflict of interest. The funders had no role in the design of the study; in the collection, analyses, or interpretation of data; in the writing of the manuscript, or in the decision to publish the results.

## References

1. Niaounakis, M.; Halvadakis, C.P. *Olive Processing Waste Management: Literature Review and Patent Survey*, 2nd ed.; Waste Management Series; Elsevier: Amsterdam, The Netherlands, 2006; pp. 1–498.
2. Trends in World Olive Oil Consumption. Available online: <https://www.oliveoilmarket.eu/trends-in-world-olive-oil-consumption> (accessed on 10 August 2020).

3. Consumption of Olive Oil Worldwide from 2012/13 to 2019/20. Available online: <https://www.statista.com/statistics/940491/olive-oil-consumption-worldwide/> (accessed on 10 August 2020).
4. Kiritsakis, A.K. *Olive Oil: From the Tree to the Table*; Food & Nutrition Press Inc.: Trumbull, CT, USA, 1998.
5. Tsagaraki, E.; Lazarides, H.N.; Petrotos, K.B. Olive Mill Wastewater Treatment. In *Utilization of By-Products and Treatment of Waste in the Food Industry*; Oreopoulou, V., Russ, W., Eds.; Springer: Boston, MA, USA, 2007; pp. 133–157.
6. Obied, H.K.; Bedgood, D.R., Jr.; Prenzler, P.D.; Robards, K. Bioscreening of Australian olive mill waste extracts: Biophenol content, antioxidant, antimicrobial and molluscicidal activities. *Food Chem. Toxicol.* **2007**, *45*, 1238–1248. [[CrossRef](#)]
7. Caputo, C.; Scacchia, F.; Pelagagge, P.M. Disposal of by-products in olive oil industry: Waste-to-energy solutions. *Appl. Therm. Eng.* **2003**, *23*, 197–214. [[CrossRef](#)]
8. Paraskeva, P.; Diamadopoulos, E. Technologies for olive mill wastewater (OMW) treatment: A review. *J. Chem. Technol. Biotechnol.* **2006**, *81*, 1475–1485. [[CrossRef](#)]
9. Yonar, T.; Mert, B.K.; Kestioglu, K.; Hung, Y.-T. Treatment of olive oil production wastewaters. In *Handbook of Environment and Waste Management: Air and Water Pollution Control*; Hung, Y.-T., Wang, L.K., Shammas, N.K., Eds.; World Scientific Pub: Singapore, 2012; Chapter 22; pp. 979–1014.
10. Turano, E.; Curcio, S.; De Paola, M.G.; Calabrò, V.; Iorio, G. An integrated centrifugation–ultrafiltration system in the treatment of olive mill wastewater. *J. Membr. Sci.* **2002**, *209*, 519–531. [[CrossRef](#)]
11. Garcia-Castello, E.; Cassano, A.; Criscuoli, A.; Conidi, C.; Drioli, E. Recovery and concentration of polyphenols from olive mill wastewaters by integrated membrane system. *Water Res.* **2010**, *44*, 3883–3892. [[CrossRef](#)] [[PubMed](#)]
12. Cassano, A.; Conidi, C.; Drioli, E. Comparison of the performance of UF membranes in olive mill wastewater treatment. *Water Res.* **2011**, *45*, 3197–3204. [[CrossRef](#)]
13. Ochando-Pulido, J.M.; Rodriguez-Vives, S.; Hodaifa, G.; Martinez-Ferez, A. Impacts of operating conditions on reverse osmosis performance of pretreated olive mill wastewater. *Water Res.* **2012**, *46*, 4621–4632. [[CrossRef](#)]
14. El-Abbassi, A.; Kiai, H.; Raiti, J.; Hafidi, A. Application of ultrafiltration for olive processing wastewaters treatment. *J. Cleaner Prod.* **2014**, *65*, 432–438. [[CrossRef](#)]
15. Zirehpour, A.; Rahimpour, A.; Jahanshahi, M. The filtration performance and efficiency of olive mill wastewater treatment by integrated membrane process. *Desalin. Water Treat.* **2015**, *53*, 1254–1262. [[CrossRef](#)]
16. Hamza, M.; Sayadi, S. Valorisation of olive mill wastewater by enhancement of natural hydroxytyrosol recovery. *Int. J. Food Sci. Tech.* **2015**, *50*, 826–833. [[CrossRef](#)]
17. Gebreyohannes, A.Y.; Mazzei, R.; Giorno, L. Trends and current practices of olive mill wastewater treatment: Application of integrated membrane process and its future perspective. *Sep. Purif. Technol.* **2016**, *162*, 45–60. [[CrossRef](#)]
18. Pulido, J.M.O. A review on the use of membrane technology and fouling control for olive mill wastewater treatment. *Sci. Total Environ.* **2016**, *563–564*, 664–675. [[CrossRef](#)] [[PubMed](#)]
19. Pizzichini, M.; Russo, C. Process for Recovering the Component of Olive Mill Wastewater with Membrane Technologies. WIPO Patent WO2005123603 A1, 29 December 2005.
20. Galanakis, C.M.; Tornberg, E.; Gekas, V. Clarification of high-added value products from olive mill wastewater. *J. Food Eng.* **2010**, *99*, 190–197. [[CrossRef](#)]
21. Ochando-Pulido, M.; Martinez-Ferez, A. Chapter 7: On the Purification of Agro-Industrial Wastewater by Membrane Technologies: The Case of Olive Mill Effluents. In *Desalination*; Taner, Y., Ed.; IntechOpen: London, UK, 2017; pp. 127–142. [[CrossRef](#)]
22. De Almeida, M.S.; Martins, R.C.; Quinta-Ferreira, R.M.; Gando-Ferreira, L.M. Optimization of operating conditions for the valorization of olive mill wastewater using membrane processes. *Environ. Sci. Pollut. Res.* **2018**, *25*, 21968–21981. [[CrossRef](#)] [[PubMed](#)]
23. Ochando-Pulido, M.; Corpas-Martinez, J.R.; Vellido-Perez, J.A.; Martinez-Ferez, A. Optimization of polymeric nanofiltration performance for olive-oil-washing wastewater phenols recovery and reclamation. *Sep. Purif. Technol.* **2020**, *236*, 116261. [[CrossRef](#)]
24. Ochando-Pulido, J.M.; Stoller, M.; Martinez-Fereza, A. Boundary flux modelling for purification optimization of differently-pretreated agro-industrial wastewater with nanofiltration. *Sep. Purif. Technol.* **2018**, *93*, 147–154. [[CrossRef](#)]

25. Ochando-Pulido, J.M.; Stoller, M.; Víctor-Ortega, M.D.; Martínez-Férez, A. Analysis of the Fouling Build-up of a Spiral Wound Reverse Osmosis Membrane in the Treatment of Two-phase Olive Mill Wastewater. *Chem. Eng. Trans.* **2016**, *47*, 403–408.
26. Zagklis, D.P.; Vavouraki, A.I.; Kornaros, M.E.; Paraskeva, C.A. Purification of olive mill wastewater phenols through membrane filtration and resin adsorption/desorption. *J. Hazard. Mater.* **2015**, *285*, 69–76. [[CrossRef](#)]
27. Paraskeva, C.A.; Papadakis, V.G.; Tsarouchi, E.; Kanellopoulou, D.G.; Koutsoukos, P.G. Membrane processing for olive mill wastewater fractionation. *Desalination* **2007**, *213*, 218–229. [[CrossRef](#)]
28. Bazzarelli, F.; Piacentini, E.; Poerio, T.; Mazzei, R.; Cassano, A.; Giorno, L. Advances in membrane operations for water purification and biophenols recovery/valorization from OMWWs. *J. Membr. Sci.* **2016**, *497*, 402–409. [[CrossRef](#)]
29. Bazzarelli, F.; Poerio, T.; Mazzei, R.; D’Agostino, N.; Giorno, L. Study of OMWWs suspended solids destabilization to improve membrane processes performance. *Sep. Purif. Technol.* **2015**, *149*, 183–189. [[CrossRef](#)]
30. Ochando-Pulido, J.M.; Martinez-Ferez, A. Operation setup of a nanofiltration membrane unit for purification of two-phase olives and olive oil washing wastewaters. *Sci. Total Environ.* **2018**, *612*, 758–766. [[CrossRef](#)] [[PubMed](#)]
31. Ochando-Pulido, J.M.; Víctor-Ortega, M.D.; Martínez-Ferez, A. Membrane fouling insight during reverse osmosis purification of pretreated olive mill wastewater. *Sep. Purif. Technol.* **2016**, *168*, 177–187. [[CrossRef](#)]
32. Sygouni, V.; Pantziaros, A.G.; Iakovides, I.C.; Sfetsa, E.; Bogdou, P.I.; Christoforou, E.A.; Paraskeva, C.A. Treatment of two-phase olive mill wastewater and recovery of phenolic compounds using membrane technology. *Membranes* **2019**, *9*, 27. [[CrossRef](#)] [[PubMed](#)]
33. Tundis, R.; Conidi, C.; Loizzo, M.R.; Sicari, V.; Cassano, A. Olive Mill Wastewater Polyphenol-Enriched Fractions by Integrated Membrane Process: A Promising Source of Antioxidant, Hypolipidemic and Hypoglycaemic Compounds. *Antioxidants* **2020**, *9*, 602. [[CrossRef](#)]
34. Zagklis, D.P.; Paraskeva, C.A. Preliminary design of a phenols purification plant. *J. Chem. Technol. Biotechnol.* **2020**, *95*, 373–383. [[CrossRef](#)]
35. Coskun, T.; Debik, E.; Demir, N.M. Treatment of olive mill wastewaters by nanofiltration and reverse osmosis membranes. *Desalination* **2010**, *259*, 65–70. [[CrossRef](#)]
36. Petrotos, K.B.; Kokkora, M.I.; Papaioannou, C.; Gkoutisidis, P.E. Olive mill wastewater concentration by two-stage reverse osmosis in tubular configuration, in a scheme combining open and tight membranes. *Desalin. Water Treat.* **2016**, *57*, 20621–20630. [[CrossRef](#)]
37. American Public Health Association. *Standard Methods for the Examination of Water and Wastewater*, 15th ed.; American Public Health Association, American Water Works Association, Water Environment Federation: Washington, DC, USA, 1981.
38. Singleton, V.L.; Orthofer, R.; Lamuela-Raventos, R.M. Analysis of total phenols and other oxidation substrates and antioxidants by means of Folin-Ciocalteu reagent. *Methods Enzymol.* **1999**, *299*, 152–178.
39. Rodriguez, S.G.S. *Particulate and Organic Matter Fouling of Seawater Reverse Osmosis Systems, Characterization, Modeling and Applications*; CRC Press: Boca Raton, FL, USA, 2011.
40. Han, Y.; Giorno, L.; Gugliuzza, A. Photoactive Gel for Assisted Cleaning during Olive Mill Wastewater Membrane Microfiltration. *Membranes* **2017**, *7*, 66. [[CrossRef](#)]
41. Fraga, M.C.; Sanches, S.; Crespo, J.G.; Pereira, V.J. Assessment of a New Silicon Carbide Tubular Honeycomb Membrane for Treatment of Olive Mill Wastewaters. *Membranes* **2017**, *7*, 12. [[CrossRef](#)]
42. Ochando-Pulido, J.M.; Martinez-Ferez, A. On the Recent Use of Membrane Technology for Olive Mill Wastewater Purification. *Membranes* **2015**, *5*, 513–531. [[CrossRef](#)] [[PubMed](#)]

**Publisher’s Note:** MDPI stays neutral with regard to jurisdictional claims in published maps and institutional affiliations.



© 2020 by the authors. Licensee MDPI, Basel, Switzerland. This article is an open access article distributed under the terms and conditions of the Creative Commons Attribution (CC BY) license (<http://creativecommons.org/licenses/by/4.0/>).

Article

# Diversity of Acyl Homoserine Lactone Molecules in Anaerobic Membrane Bioreactors Treating Sewage at Psychrophilic Temperatures

Shamas Tabraiz<sup>1,\*</sup>, Burhan Shamurad<sup>1</sup> , Evangelos Petropoulos<sup>1</sup>, Alex Charlton<sup>2</sup>,  
Obaidullah Mohiudin<sup>1</sup>, Mohammad Danish Khan<sup>1</sup>, Emeka Ekwenna<sup>3</sup> and Paul Sallis<sup>1</sup>

<sup>1</sup> School of Engineering, Newcastle University, Newcastle Upon Tyne NE1 7RU, UK; b.a.s.shamurad@newcastle.ac.uk (B.S.); vagpetrop@gmail.com (E.P.); O.Mohiuddin2@newcastle.ac.uk (O.M.); danishkhan2547upss@gmail.com (M.D.K.); paul.sallis@newcastle.ac.uk (P.S.)

<sup>2</sup> School of Natural and Environmental Sciences, Newcastle University, Newcastle Upon Tyne NE1 7RU, UK; alex.charlton@ncl.ac.uk

<sup>3</sup> Department of Engineering, Durham University, Durham DH1 3LE, UK; emeka.b.ekwenna@durham.ac.uk

\* Correspondence: S.Tabraiz2@newcastle.ac.uk

Received: 17 September 2020; Accepted: 25 October 2020; Published: 30 October 2020



**Abstract:** This study explores the types of acyl homoserine lactone (AHL) and their concentrations in different compartments of different conventional anaerobic bioreactors: (i) an upflow anaerobic membrane bioreactor (UAnMBR, biofilm/mixed liquor (sludge)); (ii) an anaerobic membrane bioreactor (AnMBR, biofilm/mixed liquor (sludge)); and (iii) an upflow sludge blanket (UASB, sludge only), all operating at 15 °C. Ten types of the AHL, namely C4-HSL, 3-oxo-C4-HSL, C6-HSL, 3-oxo-C6-HSL, C8-HSL, 3-oxo-C8-HSL, C10-HSL, 3-oxo-C10-HSL, C12-HSL, and 3-oxo-C12-HSL, which were investigated in this study, were found in UAnMBR and UASB, whilst only six of them (C4-HSL, 3-oxo-C4-HSL, C8-HSL, C10-HSL, 3-oxo-C10-HSL, and C12-HSL) were found in AnMBR. Concentrations of total AHL were generally higher in the biofilm than the sludge for both membrane bioreactors trialed. C10-HSL was the predominant AHL found in all reactors (biofilm and sludge) followed by C4-HSL and C8-HSL. Overall, the UAnMBR biofilm and sludge had 10-fold higher concentrations of AHL compared to the AnMBR. C10-HSL was only correlated with bacteria ( $p < 0.05$ ), whilst other types of AHL were correlated with both bacteria and archaea. This study improves our understanding of AHL-mediated Quorum Sensing (QS) in the biofilms/sludge of UAnMBR and AnMBR, and provides new information that could contribute to the development of quorum quenching anti-fouling strategies in such systems.

**Keywords:** quorum sensing; acyl homoserine lactone; anaerobic membrane bioreactor

## 1. Introduction

Anaerobic treatment is considered a more suitable option for wastewater treatment (focusing on the organic fraction) due to the low energy requirement, the potential for resource recovery (methane production and/or other intermediates), and the lower sludge production [1] compared to conventional aerobic treatment that has been used historically. Recently, to improve anaerobic treatment, membranes have been introduced internally and/or externally to anaerobic bioreactors [2–5]. However, membrane fouling, particularly through biofilm formation, is a perpetual challenge that hampers the widespread use of anaerobic membrane bioreactors (AnMBR) for wastewater treatment applications. Typically, the energy required for gas sparging to control the membrane fouling in AnMBR could be up to 86% of the total energy requirement [6]. Thus, the AnMBR technology could have a greater appeal if the energy requirement for mixing/gas sparging could be substantially reduced [7].



Hence, there is a need for improvements related to membrane operation and fouling mitigation, especially for substrates that are low in organic matter, and consequently have low potential for energy recovery (i.e., domestic wastewater).

Bacteria initiate biofilm formation through a mechanism of excretion and sensing diffusible molecules (autoinducers), which is known as quorum sensing (QS). Numerous Gram-negative bacteria have been reported previously to express QS activity via acyl homoserine lactones (AHL) [8–11]. The structure of AHL consists of a homoserine lactone (HSL) ring attached to an acyl chain length of between C4 and C18; the acyl chain comes with or without “oxo” or “hydroxyl” groups at the C3 position [12–15].

Biofilm formation in aerobic MBR has been previously linked with AHL [16–18]. The increased AHL concentration has been found to correlate with extracellular polymeric substances (EPS), which subsequently increase fouling [19–21]. Since biofouling is connected with the presence of AHL in aerobic MBR [22–25], AHL have been successfully targeted to control biofilm formation and reduce biofouling in aerobic systems. Among the AHL, most studies on aerobic MBR have targeted the C8-HSL molecule, and consider it a plausible cause of fouling [16,26,27]. However, the presence of AHL in anaerobic engineered systems has been reported rarely and not investigated in detail. The formation of anaerobic granules in an UASB reactor has also been linked to AHL [28]. The majority of studies used synthetic wastewater anaerobic granules to study AHL, whilst to date only one study reported the AHL status in actual industrial wastewater using anaerobic granular sludge [29]. Different types of AHL molecules have been investigated in different processes of anaerobic digestion [30]. A recent study also investigated the exogenous addition of AHL in anaerobic granules and reported this enhanced the performance of granules in terms of removal efficiencies for organic carbon [31].

Although several studies report the presence of AHL in UASB reactors, more information is required with regard to the types and quantities of AHL in anaerobic membrane bioreactors treating real wastewater. Therefore, this study investigated the status of AHL in the sludge and biofilm of conventional AnMBR and upflow anaerobic membrane bioreactor (UAnMBR), as well as in the sludge of a UASB reactor, all treating real sewage. Specifically, the work focuses on the relationship between the microbial community profile and the AHL detected in these membrane/sludge-based anaerobic systems, especially when they operate under extreme conditions (i.e., low temperatures). Low-temperature anaerobic treatment (with and without a membrane) has been investigated previously, but no information was provided about the AHL status [32,33]. Only a few studies have reported the AHL status in anaerobic systems (specifically UASB) operated at mesophilic conditions (30–37 °C) [28–30]. However, the current study explores the AHL status in conventional AnMBR and UAnMBR as well as in the sludge of a UASB reactor treating sewage at a psychrophilic temperature (15 °C).

## 2. Materials and Methods

### 2.1. Experimental Setup

All the bioreactors had been previously operated continuously for 1 year prior to sampling. Experimentation took place in the Environmental Engineering Laboratory, School of Engineering, Newcastle University, UK. The AnMBR, UAnMBR, and UASB were run continuously for 200 days during the current experiment. The bioreactors had originally been inoculated with cold adapted biomass acclimated to “cold” naturally due to its origin (Lake Geneva, Switzerland and Savalbard, Norway) and further acclimated to UV-sterilized wastewater as a substrate through numerous feed batches over a 12-month period [34]. The influent was primary settled sewage collected from the Northumbrian Water Tudhoe Mill wastewater treatment plant, Durham, UK, which was collected monthly and stored at 4 °C. For this trial, unsterilized substrate was fed to the reactors. No pH adjustment was made to the substrate, as it ranged between 6.7 and 7.2. The operational parameters of the bioreactors and wastewater characteristics are given in Table 1. The membrane flux of AnMBR and

UAnMBR was estimated by measuring the volume of the effluent on a daily basis (collected in 24 h). The membranes were backwashed daily for 30 min with permeate effluent.

**Table 1.** Operational parameters of upflow anaerobic membrane bioreactor (UAnMBR), membrane bioreactor AnMBR, and upflow anaerobic sludge blanket (UASB) reactor.

Reactor Type	AnMBR	UAnMBR	UASB
Membrane type	Hollow fiber, PVDF (0.1 $\mu\text{m}$ )	Hollow fiber, PVDF (0.1 $\mu\text{m}$ )	-
Plant scale (volume)	Lab scale (1 L)	Lab scale (1 L)	Lab scale (1 L)
Wastewater feed	Domestic sewage	Domestic sewage	Domestic sewage
Influent COD ( $\text{mg L}^{-1}$ )	$269.5 \pm 22.7$	$269.5 \pm 22.7$	$269.5 \pm 22.7$
Organic loading rate ( $\text{kgCOD}\cdot\text{m}^{-3}\text{d}^{-1}$ )	$0.108 \pm 0.011$	$1.2 \pm 0.17$	$1.2 \pm 0.17$
pH	6.7–7.2	6.7–7.2	6.7–7.2
Temperature ( $^{\circ}\text{C}$ )	15	15	15
HRT (Hours)	60	7	7
SRT (days)	60	60	60
Flux ( $\text{L m}^{-2}\text{hr}^{-1}$ )	0.75	2.18	-

## 2.2. AHL Molecules Investigated in the Study

The types of acyl homoserine lactones (AHL) used in the current study were selected after an extensive literature review. Only AHL which had been reported in activated sludge, or in the strain cultures isolated from it, were selected [35,36]; N-butanoyl-L-homoserine lactone (C4-HSL), N-3-oxo-butanoyl-L-homoserine lactone (3-oxo-C4-HSL), N-hexanoyl-L-homoserine lactone (C6-HSL), N-3-oxo-hexanoyl-L-homoserine lactone (3-oxo-C6-HSL), N-octonoyl-L-homoserine lactone (C8-HSL), N-3-oxo-octonoyl-L-homoserine lactone (3-oxo-C8-HSL), N-decanoyl-L-homoserine lactone (C10-HSL), N-3-oxo-decanoyl-L-homoserine lactone (3-oxo-C10-HSL), N-dodecanoyl-L-homoserine lactone (C12-HSL), and N-3-oxo-dodecanoyl-L-homoserine lactone (3-oxo-C12-HSL). These AHL were purchased from Chemodex, St. Gallen, Switzerland.

## 2.3. Sludge and Biofilm Collection and AHL Extraction

Sludge and biofilm were collected from AnMBR and UAnMBR, while only sludge was collected from UASB. Two samples of biofilm and sludge were collected on the 170th and 180th day of experimentation. The sample collection time was selected when steady-state conditions were evident from the operational parameters after a prolonged period ( $\approx 2$  months).

AHL from the biofilm and sludge were extracted using a modified Lade et al. (2014) method [35]. Briefly, the used membrane from the AnMBR and UAnMBR was disconnected and placed in a tube containing 50 mL phosphate buffer solution (PBS) solution. The tube was closed tightly and shaken for 2 min by hand. The suspension of the biofilm (BF) and mixed liquor sludge (S), 50 mL each, were centrifuged at  $10,000\times g$  for 10 min. The supernatant was filtered through a 0.2  $\mu\text{m}$  cellulose acetate filter. The filtrate was mixed with an equal volume of ethyl acetate and shaken at 180 rpm for 2 h. The top organic layer was collected and dried via nitrogen gas (99.9%) purging. The dried residue was dissolved in 0.5 mL solution of acetonitrile and formic acid (0.1%) [23].

## 2.4. AHL Identification and Quantification

Standard stock solutions of each AHL at  $1\text{ mg mL}^{-1}$  were prepared in acetonitrile. AHL standards of different concentrations—0.015  $\mu\text{M}$ , 0.03125  $\mu\text{M}$ , 0.0625  $\mu\text{M}$ , 0.125  $\mu\text{M}$ , 0.25  $\mu\text{M}$ , 0.5  $\mu\text{M}$  and 1.0  $\mu\text{M}$ —were made by diluting the stock solution in acetonitrile/0.1% formic acid solution in appropriate proportions to prepare the standard curve. An ultra-performance liquid chromatograph coupled with triple quadrupole mass spectrometer (UPLC-MS/MS) (Waters, Xevo TQ-XS, Milford, MA, USA) was used to identify and quantify the AHL. The column used for the analysis was an Acquity BEH C18 ( $2.1 \times 100\text{ mm}$ ; 1.7  $\mu\text{m}$  Particle Size) (Waters, UK). The temperature of the column was kept at  $20\text{ }^{\circ}\text{C}$ . Two mobile phases were used: (a) water + formic acid (0.1%) and (b) acetonitrile + formic acid (0.1%).

The solvent gradients (time: % B) used were (0.0: 30), (5.0: 30), (12.0: 90), (12.5: 90), (15: 30), (17: 95), (18: 30), and (20: 30).

Standards and AHL extracts from the biofilm and mixed liquor sludge were injected at the rate of 0.25 mL min<sup>-1</sup>. The MS settings were as follows: ionization mode, positive; ionization source, electrospray ionization; capillary voltage, 3.0 kV; cone voltage, 30 V; source offset, 50 V; desolvation gas glow, 650 L h<sup>-1</sup>; desolvation temperature, 350 °C; cone gas flow, 150 L h<sup>-1</sup>; collision gas flow, 0.2 mL min<sup>-1</sup>; nebulizer gas pressure, 7.0 bar and collision energy, 2 eV. Column effluent was detected using the multiple reaction monitoring approach. The specific liquid chromatography time, appearance of precursor's ions (m/z) and two transition ions, and the relative intensity of the two transition ions was used as a reference (m/z; 102, m/z; 74). A standard curve was prepared from the transition ions with the highest intensity.

### 2.5. Influent/Effluent Quality Analysis

The chemical oxygen demand (COD) in the influent and effluent were measured using standard methods, APHA (2006). The COD removal efficiency was estimated using the formula below. The mixed liquor suspended solids (MLSS) content of the biomass in the bioreactors was quantified gravimetrically [37].

$$\text{Removal efficiency} = \frac{\text{COD}_{in} - \text{COD}_{out}}{\text{COD}_{in}} \times 100 \quad (1)$$

### 2.6. EPS Extraction, Proteins, and Polysaccharides Measurement

The scraped biofilm was suspended in phosphate buffer solution (PBS) to make a 10 mL sample volume. The biofilm and PBS suspension were shaken well by hand to disperse the biofilm thoroughly. Sludge and biofilm suspension (10 mL) were centrifuged for 5 min at 6000 × g (4 °C). The supernatant was collected, and a 0.2 µm cellulose acetate filter (Millipore, Merck UK) was used to filter the suspended particles. The content of the proteins (PN) and polysaccharides (PS) in the solution represented the soluble EPS/soluble microbial product (SMP). The sludge and biofilm sample pellets were resuspended in 10 mL PBS and sonicated for 2 min using ultrasonic cleaner (9USC-TH, VWR, Bristol, UK). The suspension was placed in a shaker (KS400i, IKA, Oxford, UK) at 150 rpm for 10 min and centrifuged at 8000 × g for 10 min. The harvested supernatant was filtered, and the PN and PS present in the filtrate were denoted loosely bound EPS (LB-EPS). The pellets in tubes were re-suspended in 10 mL PBS and re-sonicated for 3 min. Subsequently, the sludge was exposed to sonication for 3 min. In each tube (10 mL), 2 g of hydrated CER (cation exchange resin) (Dowex® Marathon® C sodium form, Sigma-Aldrich, Kent, UK) was added in the suspension. Then, the solution was centrifuged at 12,000 × g (30 min) and the content of PS and PN in the supernatant was defined as tightly bound EPS (TB-EPS) [38–40].

### 2.7. Molecular Microbial Analysis

**DNA Extraction:** Due to the nature of the inoculum (soils and sediments), a phenol extraction method was used with minor modification for the DNA extraction [41]. Briefly, the biomass obtained from the biofilm and mixed liquor sludge was centrifuged at 4000 × g for 30 min, and the supernatant was removed. The CTAB buffer (0.5 mL), phenol:chloroform:isoamyl alcohol (25:24:1) (Sigma Aldrich) solution, was added, and the pellets were resuspended. The mixture was transferred to the lysing matrix-E tubes (Sigma, UK). Afterwards, the tubes were placed in a ribolyzer (30 sec, 4.0 m sec<sup>-1</sup>) followed by centrifugation for 5 min at 16,000 × g and 5 °C. The supernatant was transferred to the phase lock gel®, green tubes (VWR, UK). Then, 0.5 mL of phenol/isoamyl alcohol (24:1) was added to the phase lock gel tubes, mixed well, and centrifuged at 16,000 × g and 5 °C for 5 min. To remove the phenol completely and produce a high-quality supernatant, the phase lock gel (green tube) step was repeated twice. Supernatant was transferred to a 2 mL Eppendorf tube, precipitated by adding two volume of 30% PEG (6000) (Sigma Aldrich, UK) solution, and mixed well. The sample was placed at 5

°C overnight. The mixture was centrifuged for 20 min at 16,000× *g* and 5 °C. The supernatant was discarded, and 1 mL of ethanol (70%, ice-cold, filtered) was added. The solution was centrifuged at 16,000× *g* and 5 °C for 20 min. The supernatant was discarded and tubes were spun down for 1–2 s. The remaining ethanol was removed, and tubes were dried at 55 °C for 1–2 min. The DNA eluted with ultrapure DPEC water (ThermoFisher, Dartford, UK). The quantity and quality of the extracted DNA was checked by Nano-drop (ThermoFisher, UK). The DNA was saved at –80 °C for further use.

**Sequencing:** Polymerase chain reaction (PCR) of the extracted DNA was carried out using the pair of universal reverse; primer 806R (GGACTACHVGGGTWTCTAAT) and the forward primer 515F (GTGCCAGCMGCCGCGGTAA), targeting the V4 region of 16S rRNA gene [42,43]. The GoTaq® Hot Start master mix (Thermo Fisher Scientific, UK) was used for the PCR with the following conditions: initial denaturation (94 °C, 3 min), denaturation 35 cycles (94 °C, 45 s), annealing (50 °C, 30 s), extension (70 °C, 90 s). The quality control was carried out by agarose gel, library preparation including adaptors tagging, and an equal concentration of all samples were mixed and cleaned up. After amplification, sequencing was carried out at the prepared samples using the Illumina MiSeq platform (NU-OMICS, Northumbria University, Newcastle Upon Tyne, UK) to identify the 16S rDNA amplicon.

The raw data obtained from the illumina MisSeq were de-multiplexed and filtered using dada2 for quality control [44] within the QIIME2 analysis pipeline, <https://qiime.org> [45]. To get the close-reference amplicon sequence variant (ASV), VSEARCH was used by plug in the cluster-features-closed-reference in QIIME2 [46]. Adding to it, the SILVA119 database was used to produce the table with frequencies of the taxonomically assigned representative sequences.

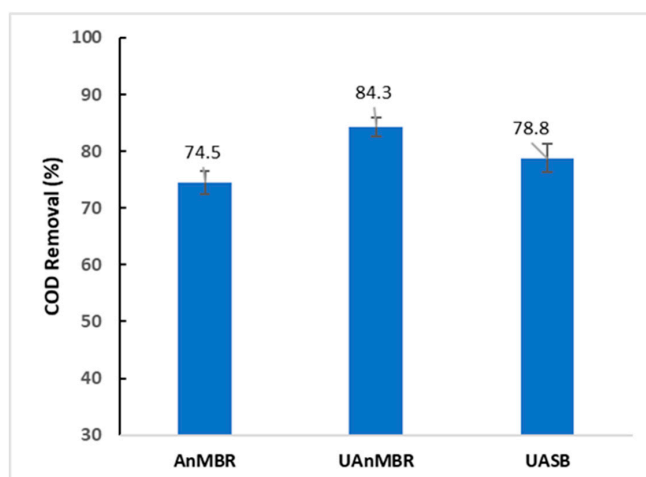
## 2.8. Data Visualization

Non-metric multidimensional scaling (NMDS) plots of the microbial communities in biofilm and sludge samples from all bioreactors was performed using Phyloseq Package [47]. The relative abundance bar chart, the canonical correspondence analysis (CCA) between AHL and the microbial community, and a heat map of correlation between proteins/polysaccharides and AHL concentration were prepared using Microbiome Package [48] in R (R Studio v3.6.3) following the procedures described by Shamurad et al. [49,50]. For co-occurrence analysis, a correlation matrix was developed by calculating all possible pairwise Spearman correlations among the AHL and microbial community (genus level) of UASB, UAnMBR, and AnMBR ( $n = 5$ ). A correlation between AHL and microbial community was considered if the Spearman's correlation coefficient was  $\geq 0.8$  and the  $p$  value was  $\leq 0.05$ . To reduce the chances of obtaining false-positive results, the  $p$  values were adjusted with a multiple testing correction using the Benjamini–Hochberg method [51]. The pairwise correlations of the AHL and the bacterial/archaea genus formed their co-occurrence networks. Network analyses were performed in R environment and the microbial communities were further visualized and explored to identify their topological properties (i.e., clustering coefficient, shortest average path length and modularity) in Gephi [52].

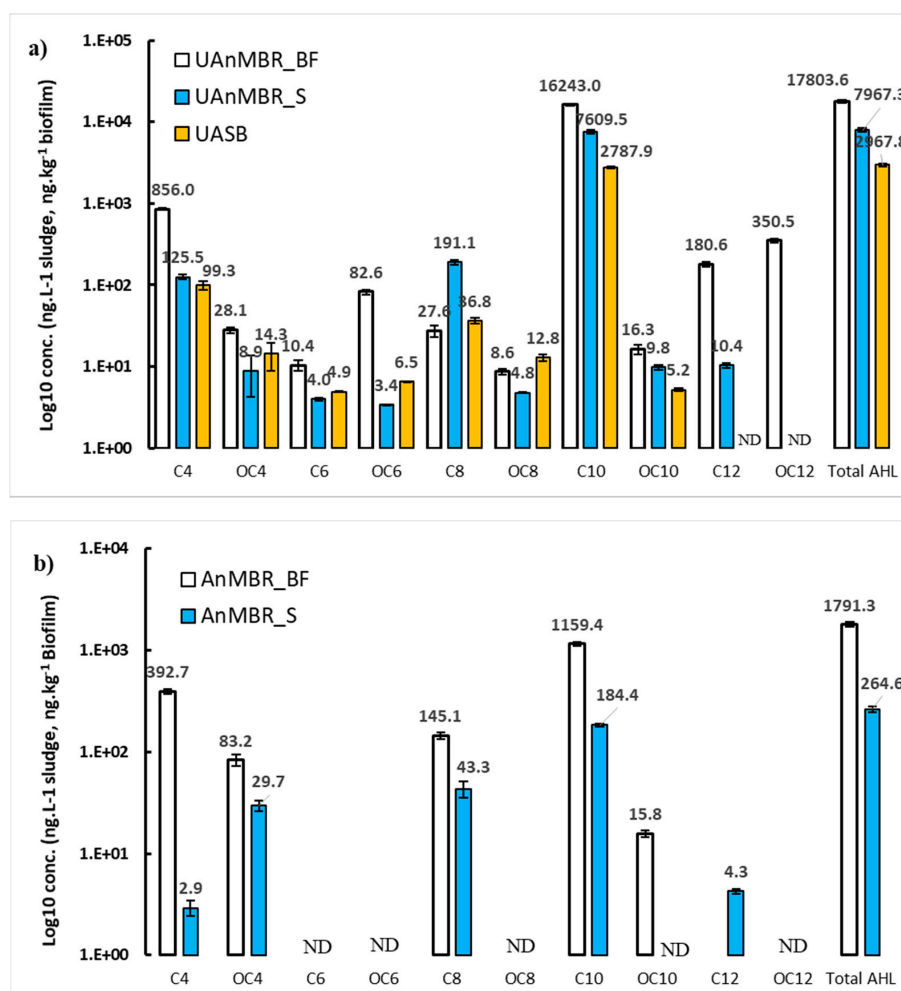
## 3. Results

### 3.1. AHL Types and Concentrations

Ten types of AHL were evaluated in the biofilm and sludge of the two conventional anaerobic membrane bio-reactor types: (i) UAnMBR, (ii) AnMBR, and in the (iii) sludge of a UASB reactor. The samples for AHL analysis were taken when the bioreactor reached a pseudo-steady state condition. This condition was determined from the COD removal efficiencies of the bioreactors, which were consistent through the final two months of operation (Figure 1). The concentration and types of these AHL varied with reactor type (Figure 2a,b). Biofilms in both membrane systems had a higher concentration of AHL than the sludge. The C10-HSL was the most abundant AHL at all treatments (present in both sludge and biofilm for all setups), followed by C4-HSL and C8-HSL.



**Figure 1.** Chemical oxygen demand (COD) percentage removal efficiencies monitored in the last two months of operation to access the steady-state conditions of all the bioreactors. Sample were taken after every 5 days ( $n = 12$ ). The error bar represents standard deviation.



**Figure 2.** Acyl homoserine lactone (AHL) concentrations in the biofilm (ng kg<sup>-1</sup>) and sludge (mg L<sup>-1</sup>) of (a) UAnMBR and UASB (sludge only), (b) AnMBR (error bars show standard deviation of replicates;  $n = 2$ ); the  $y$ -axis is a log scale. AHL abbreviations are; C4: C4-HSL; C6: C6-HSL; C8: C8-HSL; C10: C10-HSL; C12: C12-HSL; OC4: 3-oxo-C4-HSL; OC6: 3-oxo-C6-HSL; OC8: 3-oxo-C8-HSL; OC10: 3-oxo-C10-HSL; OC12: 3-oxo-C12-HSL. The abbreviation of ND; not detected.

Overall, 10 different AHL were found in the UAnMBR biofilm, showing greater diversity than AnMBR biofilm where only six AHL were detected. The AHL:C6-HSL, 3-O-oxo-C6-HSL, 3-oxo-C8-HSL, and 3-oxo-C12-HSL were not detected in the AnMBR biofilm. In addition to the lower AHL diversity, the concentrations of the total AHL in the AnMBR biofilm were also lower (10-fold) compared to the UAnMBR biofilm. Briefly, the concentrations of C4-HSL and C10-HSL in UAnMBR were 2.2- and 14-fold higher than the those in AnMBR, respectively, while the concentration of 3-oxo-C10-HSL was found to be similar in both biofilms. In contrast, the concentrations of 3-oxo-C4-HSL and C8-HSL were 3- and 5-fold higher in AnMBR biofilm than in the UAnMBR biofilm. The sludge of the UAnMBR had a higher concentration of all AHL than UASB sludge except for 3-oxo-C4-HSL, C6-HSL, 3-oxo-C6-HSL, and 3-oxo-C8-HSL.

The total AHL concentrations in the UAnMBR sludge were 30- and 2.7-fold higher than those found in the AnMBR and UASB sludge, respectively. Similarly, the concentration of C10-HSL in the sludge of UAnMBR was 41- and 2.7-fold higher than that in the AnMBR and UASB sludge, respectively. The C4-HSL concentration in the AnMBR sludge was 30- to 40-fold lower than that in the UASB and UAnMBR sludge, while C8-HSL in the UAnMBR sludge was 4- to 5-fold higher than that in the UASB and UAnMBR sludge.

### 3.2. Protein and Polysaccharide Correlations with AHL

The concentration of polysaccharides was found to be higher than that of proteins in both the biofilms and the sludge samples for all three reactors. The biofilms of the AnMBR and UAnMBR had higher concentrations of polysaccharides and proteins as compared to the sludge for all reactors. Interestingly, despite the relatively low organic loading rates, the concentrations of both polysaccharides and proteins were higher in the AnMBR biofilm than those found in the UAnMBR biofilm. On the contrary, the polysaccharide concentration in the AnMBR sludge was lower than that in the UAnMBR sludge, whilst the polysaccharide concentration was the highest in the UASB sludge (Figure 3a–d). Three AHL (C4-HSL, 3-oxo-C4-HSL, and 3-oxo-C10-HSL) were correlated significantly ( $p < 0.05$ ) with the concentration of polysaccharides and proteins (Figure 3e).

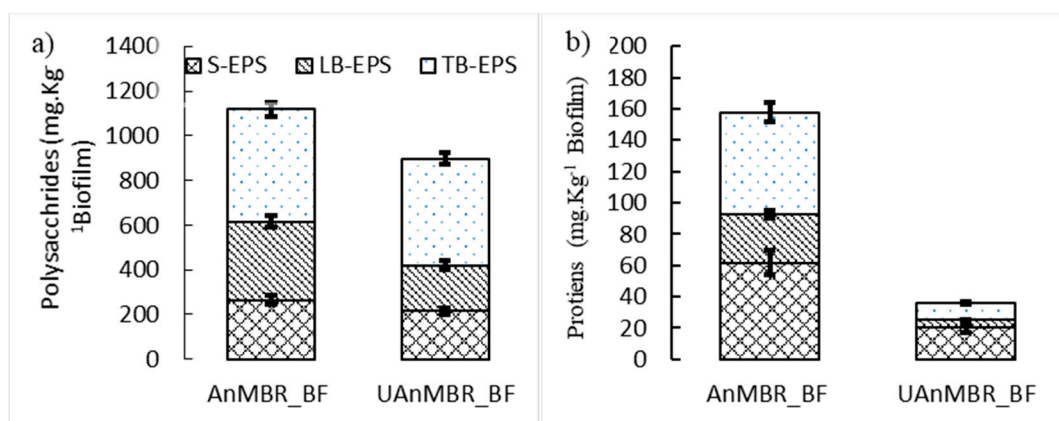
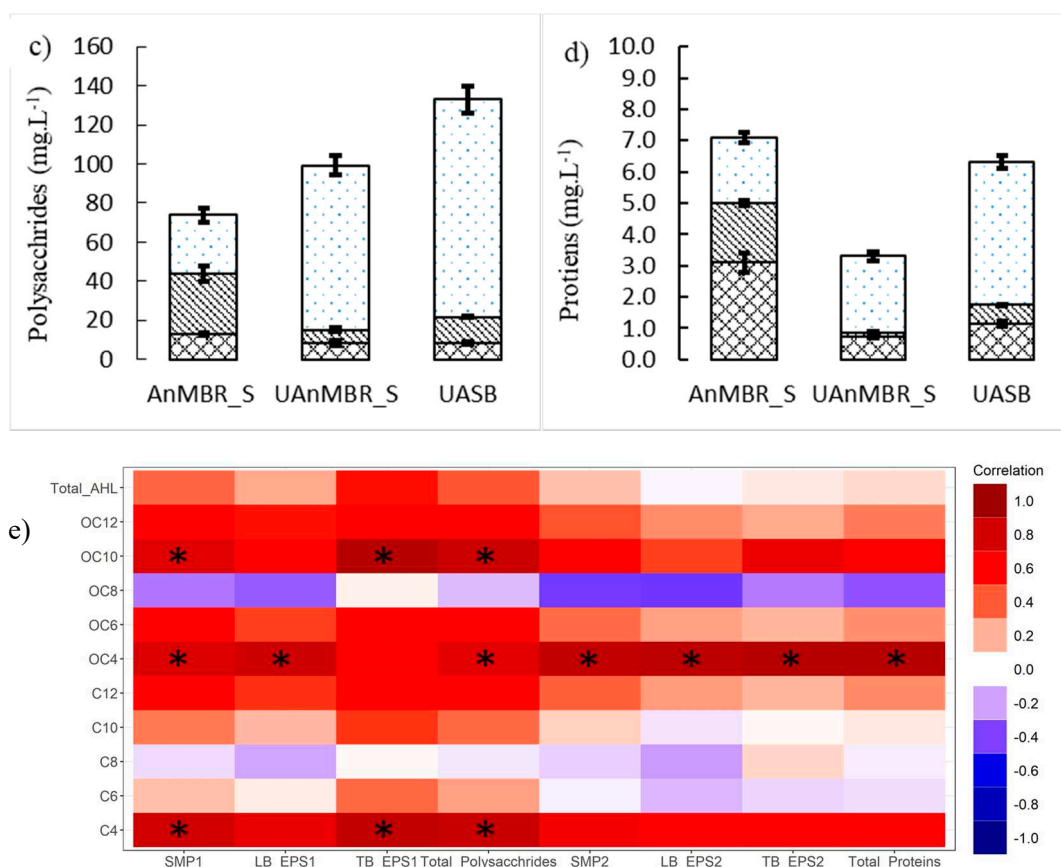


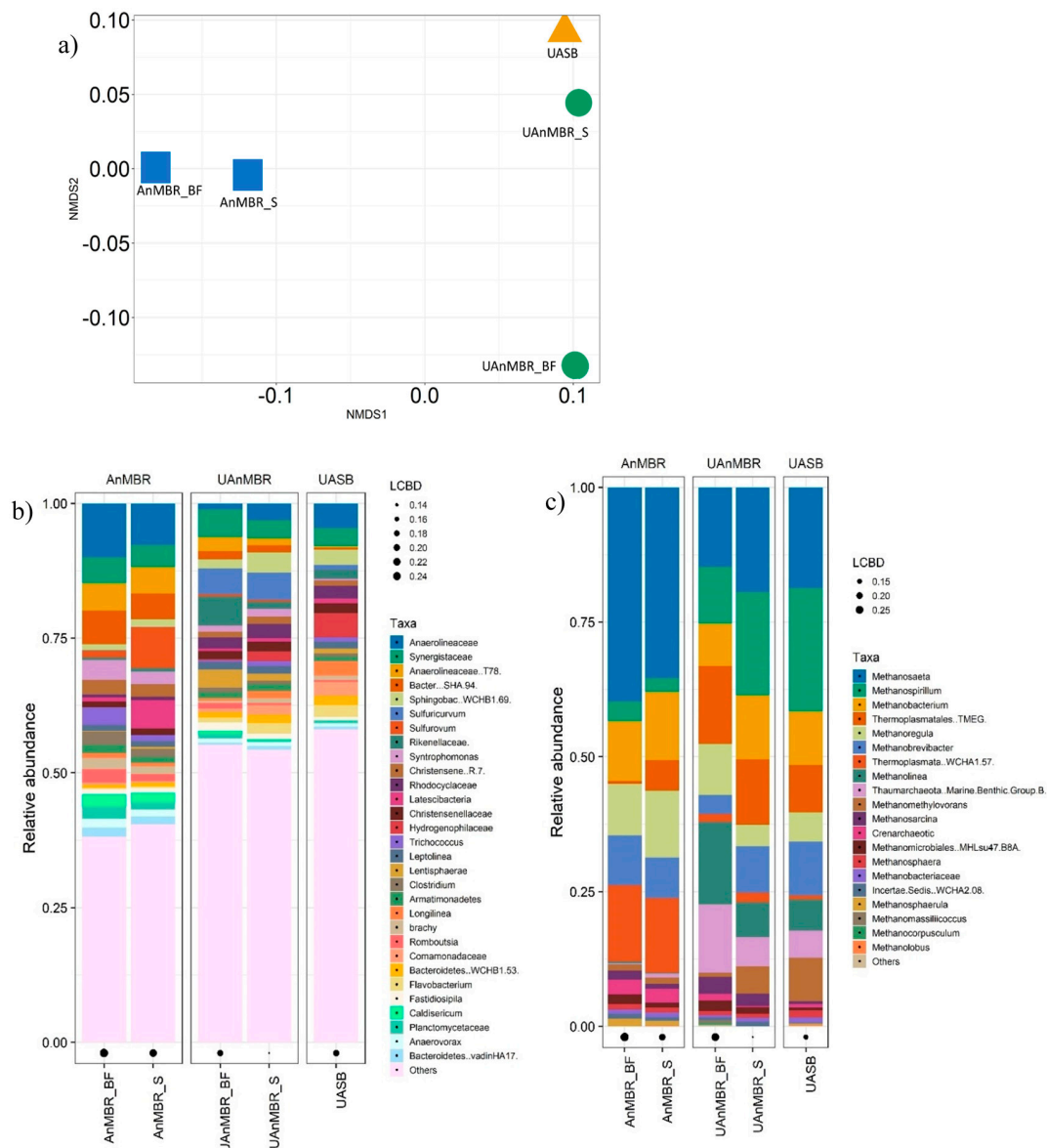
Figure 3. Cont.



**Figure 3.** (a) Polysaccharides in soluble extracellular polymeric substance (S\_EPS), loosely bound extracellular polymeric substance (LB\_EPS), and tightly bound extracellular polymeric substance (TB\_EPS) in AnMBR\_BF and UAnMBR\_BF; (b) proteins in S\_EPS, LB\_EPS, and TB\_EPS in AnMBR\_BF and UAnMBR\_BF; (c) polysaccharides in S-EPS, LB-EPS, and TB-EPS in AnMBR\_S, UAnMBR\_S, and UASB; (d) proteins in S\_EPS, LB\_EPS, and TB\_EPS in AnMBR\_S, UAnMBR\_S, and UASB. The concentrations of the proteins and polysaccharides in the biofilms are reported in mg kg<sup>-1</sup>, while in the sludge, they are reported in mg L<sup>-1</sup> (error bars represent standard deviation of replicates; *n* = 2). (e) Pearson correlation between proteins, polysaccharides, and AHL present in the biofilm and sludge of the AnMBR, UAnMBR, and UASB. S\_EPS1: polysaccharides in soluble extracellular polymeric substances; LB.EPS1: polysaccharides in loosely bound extracellular polymeric substances; TB.EPS1: polysaccharides in tightly bound extracellular polymeric substances; S.EPS2: proteins in soluble extracellular polymeric substances; LB.EPS2: proteins in loosely bound extracellular polymeric substances; TB.EPS2: proteins in tightly bound extracellular polymeric substances. The asterisk (\*) indicates *p* < 0.05. AHL abbreviations are; C4: C4-HSL; C6: C6-HSL; C8: C8-HSL; C10: C10-HSL; C12: C12-HSL; OC4: 3-oxo-C4-HSL; OC6: 3-oxo-C6-HSL; OC8: 3-oxo-C8-HSL; OC10: 3-oxo-C10-HSL; OC12: 3-oxo-C12-HSL.

### 3.3. Microbial Community in AnMBR, UAnMBR, and UASB

The microbial communities in the sludge and biofilm of the AnMBR and UAnMBR were found to be different, but as expected, the UASB sludge community was similar to the sludge of the UAnMBR (Figure 4a). Both archaeal and bacterial communities were different in the AnMBR and UAnMBR (Figure 4 b,c).



**Figure 4.** (a) Non-metric multidimensional scaling (NMDS) plot of reactor communities, (b) relative abundance of the 30 most abundant bacteria; (c) relative abundance of the 20 most abundant archaea. AnMBR\_BF is the biofilm from AnMBR, AnMBR\_S is the sludge from AnMBR, UAnMBR\_BF is the biofilm from UAnMBR, and UASB represents sludge from the UASB.

The genus *Methanosaeta* was the main archaea (14.7–39.7% relative to total archaea) present in all three bioreactors followed by *Methanospirillum* (2.6–22.9%) and *Methanobacterium* (7.9–12.7%). In general, the genera *Methanosaeta*, *Methanoregula*, and *Thermoplasmatales* (WCHA1.57) had higher relative abundance in the AnMBR (both biofilm and sludge) than UAnMBR (biofilm and sludge) and UASB (sludge), while *Methanospirillum*, *Thermoplasmatales* (TMEG), and *Methanomethylovorans* tended to be richer in the UAnMBR and UASB compared to the AnMBR. The archaea *Thaumarchaeota* (*Marine benthic group B*) and *Methanolinea* were only present in the UASB and the UAnMBR (present in negligible abundance in AnMBR), with the UAnMBR biofilm showing the highest abundance. The relative abundance of *Methanosarcina*, *Crenarchaeotic*, *Methanomicrobiales* (MHLsu47, B8A), and *Methanosphaera* were generally higher in the biofilms than in the sludge of both membrane bioreactors (AnMBR and UAnMBR).



In the case of bacteria (at the genus level), *Anaerolineaceae* (unclassified) (1.1–10% relative to total bacteria) and *Synergistaceae* (unclassified) (3.3–5.1%) were the most abundant taxa in all three bioreactors. The genus *Anaerolineaceae* T78, *Anaerolineaceae* (unclassified), *Bacteroidetes* (*vadinHA17*, SHA94), and *Sulfurovum* showed higher abundance in the AnMBR than UAnMBR and UASB. Generally, *Synergistaceae* (unclassified), *Anaerolineaceae* (T78), *Bacteroidetes* (*vadinHA17*, SHA 94), and *Clostridium* had higher relative abundance in the biofilms than the sludge. The genus *Sulfuricurvum*, *Longilinea*, *Lentisphaerae*, *Sphingobacteriaceae* (WCHB1-69), and *Leptolinea*, an amplicon sequence variant (ASV) from the family *Rikenellaceae* (unclassified) and *Hydrogenophilaceae* (unclassified) were the most abundant taxa in the UAnMBR and the UASB, but not in the AnMBR.

The relative abundance of *Anaerolineaceae* (unclassified) in the AnMBR biofilm and sludge was 10.0% and 7.7%, while in the UAnMBR biofilm and sludge, the proportion was 1.1% and 3.1%, respectively; for the UASB, this reached up to 4.6%. The relative abundance of the genus *Anaerolineaceae* (T78) was found in the AnMBR biofilm and sludge at 5.0% and 4.9%, while in the UAnMBR biofilm and sludge, its relative abundance was 2.6% and 1.3%, respectively, and this genus reached 2.7% in the UASB. The relative abundance of *Synergistaceae* (unclassified) in the AnMBR biofilm and sludge, UAnMBR sludge and biofilm, and UASB sludge was 4.8%, 4.1%, 5.1%, 3.3%, and 3.4%, respectively.

#### 4. Discussion

The current study has investigated and compared AHL-mediated QS activity in the biofilm and the sludge of three different anaerobic bioreactors (AnMBR, UAnMBR, and UASB). To date, only a limited number of studies have briefly mentioned the status of AHL in relation to QS in anaerobic bioreactors [53,54], and so far, no study has focused specifically on the existence of AHL in the biofilms of such systems operating at low temperatures. This renders this study critical, as it could pave the way towards a better understanding of excessive biofilm formation on the surface of a membranes in MBR systems; this process leads inevitably to membrane fouling, which is the main cause of the increased operational and maintenance cost of membrane bioreactors [55]. Therefore, providing an insight into the status of AHL-mediated QS activity in these systems could eventually enable operators to devise new strategies for a fouling mitigation process that would reduce operating costs. This is critical for anaerobic bioreactors treating domestic wastewater, because the energy yields (as biogas) from such substrates are not sufficient to support their sustainable operation [6].

The importance of AHL C4-HSL, C6-HSL, 3-oxo-C6-HSL, C8-HSL, 3-oxo-C8-HSL, C10-HSL, 3-oxo-C10-HSL, C12-HSL, 3-oxo-C12-HSL, C14-HSL, and 3-oxo-C14-HSL has been reported recently in relation to different bacteria-mediated processes in mesophilic (37 °C) batch-fed anaerobic digesters, (organic loading rate of 1.5–2 kg COD m<sup>-3</sup> day<sup>-1</sup>) fed with synthetic wastewater [30]. In that study, the total AHL concentrations were generally higher than those observed in the current study. However, the concentrations of all AHL present in a conventional UASB (37 °C, 2 kg COD m<sup>-3</sup> day<sup>-1</sup>) were considerably lower (at 0–6 ng L<sup>-1</sup>) than those observed in the UASB, AnMBR, and UAnMBR of the current study (Figure 2), with C4-HSL being the highest (6 ng L<sup>-1</sup>) [30]. Additionally, C8-HSL, 3-oxo-C8-HSL, C10-HSL, and C12-HSL were not detectable in the conventional mesophilic UASB, but they were present in the UASB of the current study. A plausible reason could be the higher temperature (37 °C) of their experiment and use of synthetic wastewater (absence of non-acclimated cells). It may be significant that some AHL, namely C6-HSL, 3-oxo-C6-HSL, and 3-oxo-C8-HSL were not detected in the sludge or biofilm of the AnMBR, but they were found in the UASB and UAnMBR (both sludge and biofilm). Therefore, since these bioreactors both contained a more structured biomass in the form of granular sludge (or at least denser flocs), it is possible that the microbial communities in these UASB setups could have excreted these specific AHL as part of the granulation formation process that occurs naturally in upflow systems, which agrees with observations reported previously [53].

Recently, Ma et al. [28] has reported the presence of only two kinds of AHL, C8-HSL (up to 250.0 ng L<sup>-1</sup>) and C10 HSL (up to 500.0 ng L<sup>-1</sup>), in mature anaerobic granules from a mesophilic digester fed with synthetic wastewater (OLR 4.0 kg COD m<sup>-3</sup> day<sup>-1</sup>). The concentration of C10-HSL

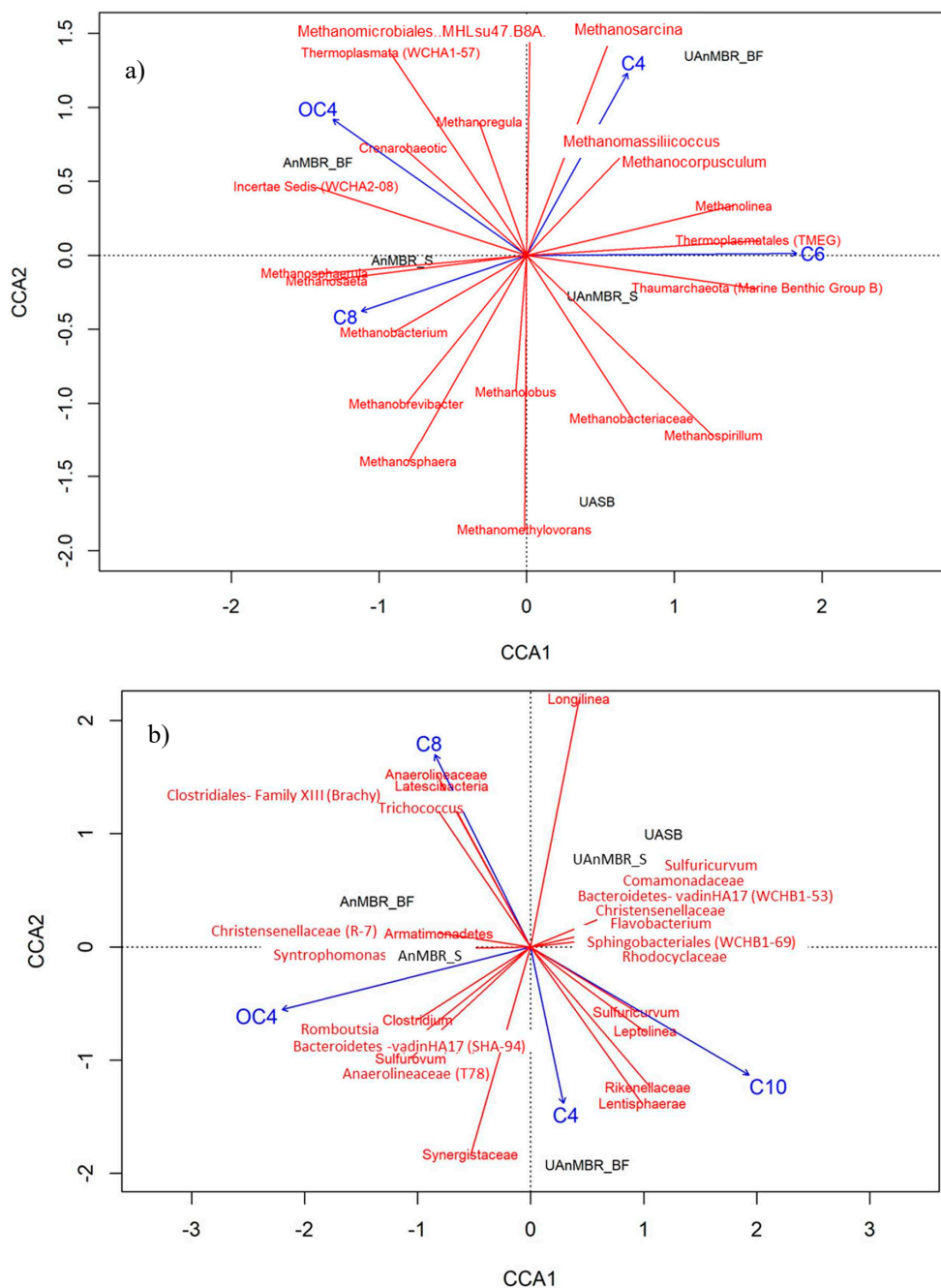
reported in their study [28] was 10-fold lower than the C10-HSL concentration found in our UASB and UAnMBR (both in sludge and biofilms) and comparable to the C10-HSL concentration in the AnMBR biofilm and sludge (1159.0 ng kg<sup>-1</sup> and 184.4 ng L<sup>-1</sup>). Similarly, Ma et al. [29] also observed four AHL with maximum concentrations of C6-HSL (25 ng L<sup>-1</sup>), C8-HSL (420 ng L<sup>-1</sup>), C10-HSL (240 ng L<sup>-1</sup>), and C12-HSL (180 ng L<sup>-1</sup>) in a UASB treating industrial wastewater. The C6-HSL, C8-HSL, and C12-HSL concentrations were similar, whereas the C10-HSL concentration was 10-fold lower than that of the UASB sludge, UAnMBR biofilm, and UAnMBR sludge of the current study. Their maximum organic loading rate was 24.0 kg COD m<sup>-3</sup> day<sup>-1</sup> [29] (typical for an industrial wastewater), was 20-fold higher than the OLR of the current study which treated sewage (a low strength wastewater). This indicates that at higher OLR, the concentration of C10-HSL reduces; this suggests that C10-HSL is the main QS molecule used by the microbial community during low nutrient (low OLR) conditions and starvation stress. The use of AHL by microbial populations in upflow anaerobic bioreactors (UASB) has been reported previously to induce a k-strategy during starvation for reproduction and regulating cooperation [30]. The higher concentration (2-fold) of C10-HSL in UAnMBR biofilms as compared to UAnMBR sludge strengthens this argument. The biofilm would have had a higher microbial density than the sludge and hence greater competition for substrate between cells (or less substrate per unit of cells); consequently, higher concentrations of C10-HSL and other AHL were to be expected. Under substrate competition conditions, bacteria are known to produce more glucose-dominated EPS [56], which was the case observed in the current study based on the higher concentrations of polysaccharides in the biofilm (Figure 3). Furthermore, the canonical analysis linking community abundance with AHL concentrations showed that only bacteria were correlated with C10-HSL (Figures 5b and 6).

Furthermore, C10-HSL concentrations in the AnMBR were lower than in the UAnMBR, despite the lower OLR of the former (0.10 kg COD m<sup>-3</sup> day<sup>-1</sup>) compared to the latter (1.2 kg COD m<sup>-3</sup> day<sup>-1</sup>). Regardless, the polysaccharides concentration was higher in the AnMBR biofilm, which was plausibly attributed to the higher concentration of 3-oxo-C4-HSL. The significant correlation ( $p < 0.05$ ) of 3-oxo-C4-HSL with polysaccharides and proteins in EPS (Figure 3e) strengthens this argument. Furthermore, the C8-HSL concentration in the AnMBR biofilm was higher than UAnMBR biofilm (Figure 2a), which could be the reason for the higher level of polysaccharides. Similarly, higher fouling rates were observed in the AnMBR compared to UAnMBR. High OLR has been reported previously as a cause for higher fouling rates [57,58]. However, low COD removal efficiencies means that some of the organic matter remains untreated; this could potentially block the membrane pores and increase fouling rates [59] (i.e., particulate matter). This plausibility explains the reason behind the higher fouling rates in the AnMBR compared to UAnMBR (Figure 7). The food to microorganism ratio (F:M) has been reported as an important parameter controlling fouling. A lower F:M leads to starvation and bacteria excrete glucose-dominant SMP under such conditions [56], and this could lead to higher fouling rates. The same trend was observed in the AnMBR biofilm and sludge (higher concentrations of polysaccharide in SMP and LB-EPS) compared to the UAnMBR. The higher HRT in the AnMBR decreases the OLR and subsequently lowers F:M compared to the UAnMBR. In addition, the potential of granulation has been reported previously for alleviating fouling compared to suspended flocculant sludge [60]; this could have been another plausible reason related to the low fouling rates in UAnMBR. We propose that the higher AHL concentration in UAnMBR could have been most likely factor associated with the granulation that usually occurs in such upflow systems.

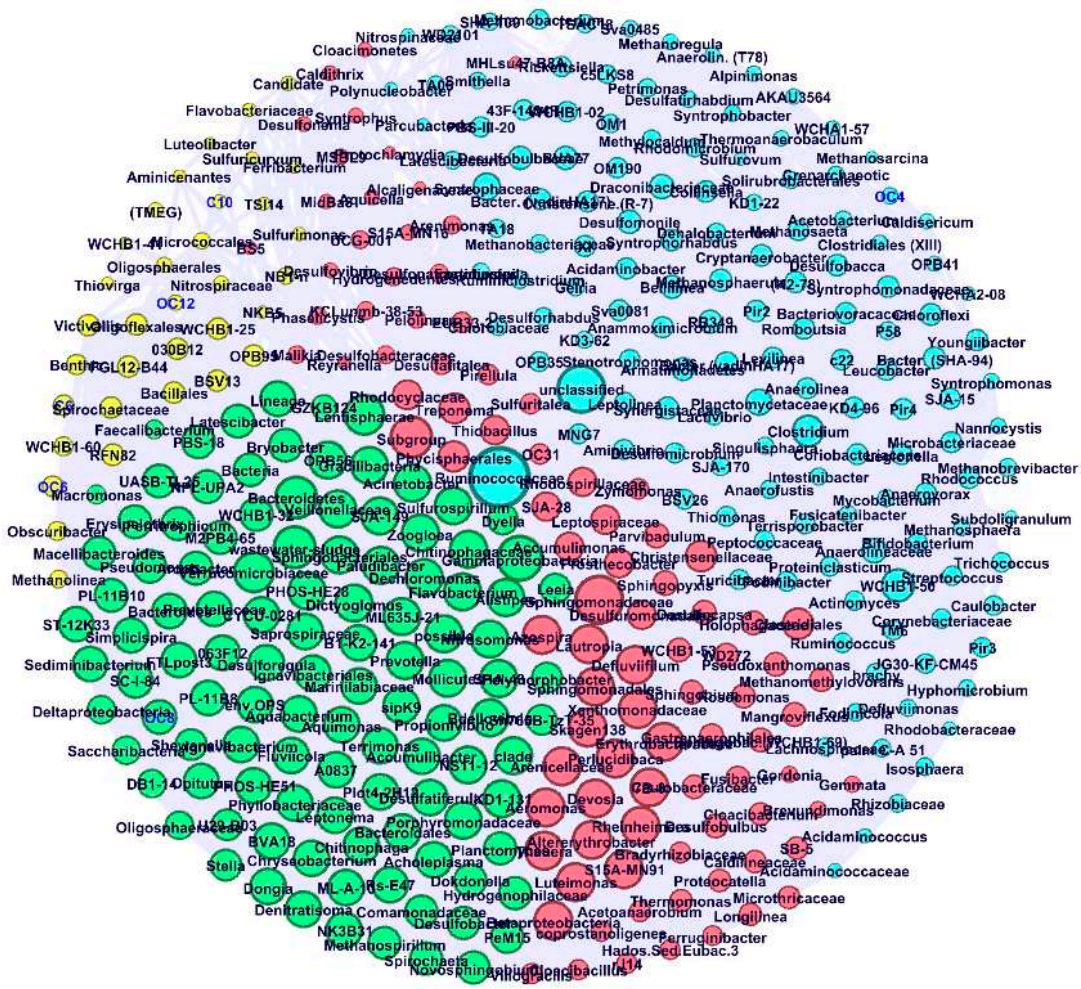
The non-metric multidimensional scaling showed that the microbial communities varied in the different reactors. Canonical correlation analysis (CCA) was carried out to find the correlation between the core communities (both archaea and bacteria) of the bioreactors (sludge and biofilm) and the AHL.

In the case of the archaea, C4-HSL correlated with *Methanosarcina*, *Methanomassiliicoccus*, and *Methanocorpusculum*; 3-oxo-C4-HSL correlated with *Crenarchaeotic* and *Incertae Sedis (WCHA2-08)*; C6-HSL correlated with *Thermoplasmatales (TMEG)*, *Thaumarchaeota (Marine Benthic Group.B)*, and *Methanolinea*; and C8-HSL correlated with *Methanobacterium*, *Methanosaeta*, and *Methanosphaera*.

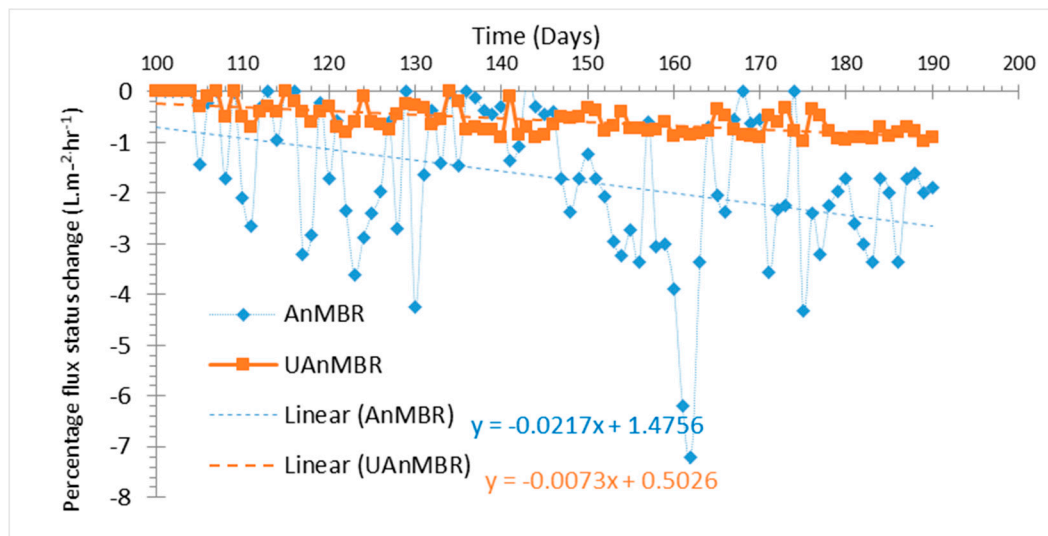
Previous studies [61,62] have reported *Methanosaeta harundinacea*, *Methanobacterium thermautotrophicus*, *Methanobacterium formicicum*, and *Methanosarcina mazei* as key archaeal genera and species linked to the production of AHL in anaerobic reactors; this observation shows some similarity with the current study (Figure 5a). However, further detailed genomic studies are required to investigate the genes involved in the production of AHL molecules in the archaea and whether there is any link between them and methane production, or any other step in the archaeal metabolism.



**Figure 5.** Canonical correspondence analysis (CCA) of acyl homoserine lactones (AHL) concentrations with (a) all archaea and (b) the 30 most abundant bacteria. AnMBR\_BF is the biofilm from AnMBR, AnMBR\_S is the sludge from AnMBR, UAnMBR\_BF is the biofilm from UAnMBR, and UASB represents sludge from the UASB. AHL abbreviations are as follows; C4: C4-HSL; C6: C6-HSL; C8: C8-HSL; C10: C10-HSL; C12: C12-HSL; OC4: 3-oxo-C4-HSL; OC6: 3-oxo-C6-HSL; OC8: 3-oxo-C8-HSL; OC10: 3-oxo-C10-HSL; OC12: 3-oxo-C12-HSL.



**Figure 6.** Co-occurrence network of biofilm and sludge of all reactors at genus level and AHL concentrations. The modularity of the nodes is differentiated by colors at genus level and AHL concentration. Only strong (Pearson’s R > 0.8) and significant ( $p < 0.05$ ) correlation connections were included, and nodes were labeled for genus (black) and AHL concentration (blue).



**Figure 7.** Percentage flux reduction in AnMBR and UAnMBR from the 100th (new membrane installed) to the 190th day.

In the case of bacteria, C10-HSL correlated with *Sulfuricurvum*, *Leptolinea*, *Lentisphaerae*, and *Rikenellaceae*; C8-HSL correlated with *Anaerolineaceae* (family), *Latescibacteria*, *Trichococcus*, and *Clostridiales*-family XIII (*Brachy*); 3-oxo-C4-HSL correlated with *Syntrophomonas*, *Clostridium*, *Romboutsia*, *Bacteroidetes vadinHA17 (SHA-94)*, and *Christensenellaceae* (R-7).

In addition, a co-occurrence network revealed that long and medium-chain AHL (C6-HSL, 3-oxo-C6-HSL, C12-HSL, and 3-oxo-C12-HSL) correlated with the community that clustered in one of the modules (Yellow) (Figure 6). This indicates that the group of a particular community is closely associated with QS through these molecules.

A recent study reported *Romboutsia* was responsible for QS through the AI-2 molecule [63], but not through AHL. Similarly, a *Clostridium* species has been reported to mediate QS through peptides as their autoinducer QS molecules to make spores and excrete exotoxins [64,65]. Additionally, a few studies also reported correlations between AHL and taxa in the granular sludge of a UASB. Specifically, Ma reported that *Christensenellaceae* and *Longilinea* were correlated with C10-HSL and C8-HSL [28]. *Latescibacteria*, *Bacteroidetes vadinHA17*, *Syntrophomonas*, *Clostridium*, *Christensenellaceae* (R-7), and *Anaerolineaceae* (family) were reported as having a strong correlation with the AHL concentration in industrial anaerobic granules [29,53], which corroborates the observations in the current study. However, bacteria that correlate with AHL may not necessarily be producing these molecules themselves, but responding to them or adopting phenotypic behavior after sensing AHL in their environment [31,66]. So, single-strain studies in an anaerobic environment are required to further understand whether the QS is mediated or is a phenotypic behavior adopted in response to the presence of autoinducers. Bacteria from different environments have previously been separated and examined for QS activity i.e., flocculant sludge in sequencing batch bioreactors [53], sludge of aerobic MBR [23], activated sludge [67], bovine rumen [68], plants [69], but there is no published study that reports the isolation of these bacteria, especially from anaerobic systems, and tests them for QS activity mediated through AHL.

Furthermore, in the current study, the AHL status and the corresponding microbial community was investigated; however, the operational parameters were not exactly similar. Hence, it is not yet certain which variable affected AHL differentiation the most: the organic loading per gram of VS, the HRT, the membrane flux (LMH) and/or others. Further studies using similar operational parameters would be critical to understand the routes to AHL diversity.

Therefore, further research is required to establish the roles of different types of QS autoinducers in the biofilms and sludge of AnMBR/UAnMBR to allow the development of strategies to control fouling without affecting treatment and methane production efficiency, especially at relatively cold but sustainable (for domestic wastewater) temperatures.

## 5. Conclusions

The concentration of the total AHL was higher in the biofilm of the membranes of the anaerobic bioreactors compared to the sludge (in both AnMBR types). AHL concentration was found to be higher in the UAnMBR than in the AnMBR. However, the EPS concentration and fouling rates were lower in the UAnMBR than in AnMBR. This suggests that the different operational conditions of different reactor types do affect the microbial communities, and subsequently the AHL response, which is expressed in divergent AHL concentrations. This study reports that the C10-HSL, C4-HSL, 3-oxo-C4-HSL, and C8-HSL are the main AHL present in anaerobic reactors (with or without membranes), these molecules require special attention in future work to further understand their role in biofilm formation/fouling and granulation.

**Author Contributions:** Conceptualization, S.T.; methodology, S.T. and E.P.; software, B.S. and S.T.; validation, S.T.; formal analysis, A.C., O.M., and M.D.K.; resources, S.T.; data curation, S.T.; writing—original draft preparation, S.T.; writing—review and editing, P.S., E.E.; visualization, S.T., B.S.; supervision, P.S.; funding acquisition, S.T. All authors have read and agreed to the published version of the manuscript.

**Funding:** This research was funded by Commonwealth Commission UK (PKCA-91-2016), and The APC was funded by Newcastle University UK.

**Conflicts of Interest:** The authors declare no conflict of interest.

## References

1. Van Lier, J.B.; Mahmoud, N.; Zeeman, G. *Anaerobic Wastewater Treatment*; IWA Publishing: London, UK, 2008; pp. 415–456.
2. He, Y.; Xu, P.; Li, C.; Zhang, B. High-concentration food wastewater treatment by an anaerobic membrane bioreactor. *Water Res.* **2005**, *39*, 4110–4118. [[CrossRef](#)] [[PubMed](#)]
3. Berkessa, Y.W.; Yan, B.; Li, T.; Tan, M.; She, Z.; Jegatheesan, V.; Jiang, H.; Zhang, Y. Novel anaerobic membrane bioreactor (AnMBR) design for wastewater treatment at long HRT and high solid concentration. *Bioresour. Technol.* **2018**, *250*, 281–289. [[CrossRef](#)]
4. Vincent, N.M.; Tong, J.; Yu, D.; Zhang, J.; Wei, Y. Membrane fouling characteristics of a side-stream tubular anaerobic membrane bioreactor (AnMBR) treating domestic wastewater. *Processes* **2018**, *6*, 50. [[CrossRef](#)]
5. Lew, B.; Tarre, S.; Beliavski, M.; Dosoretz, C.G.; Green, M. Anaerobic membrane bioreactor (AnMBR) for domestic wastewater treatment. *Desalination* **2009**, *243*, 251–257. [[CrossRef](#)]
6. Smith, A.L.; Stadler, L.B.; Cao, L.; Love, N.G.; Raskin, L.; Skerlos, S.J. Navigating wastewater energy recovery strategies: A life cycle comparison of anaerobic membrane bioreactor and conventional treatment systems with anaerobic digestion. *Environ. Sci. Technol.* **2014**, *48*, 5972–5981. [[CrossRef](#)]
7. Shoener, B.D.; Bradley, I.M.; Cusick, R.D.; Guest, J.S. Energy positive domestic wastewater treatment: The roles of anaerobic and phototrophic technologies. *Environ. Sci. Process. Impacts* **2014**, *16*, 1204–1222. [[CrossRef](#)] [[PubMed](#)]
8. Patel, N.M.; Moore, J.D.; Blackwell, H.E.; Amador-Nogues, D. Identification of unanticipated and novel N-acyl L-homoserine lactones (AHLs) using a sensitive non-targeted LC-MS/MS method. *PLoS ONE* **2016**, *11*, e0163469. [[CrossRef](#)]
9. Girard, L.; Blanchet, E.; Intertaglia, L.; Baudart-Lenfant, J.; Stien, D.; Suzuki, M.T.; LeBaron, P.; Lami, R. Characterization of N-Acyl Homoserine Lactones in *Vibrio tasmaniensis* LGP32 by a biosensor-based UHPLC-HRMS/MS method. *Sensors* **2017**, *17*, 906. [[CrossRef](#)] [[PubMed](#)]
10. Mukherji, R.; Prabhune, A. Enzyme purification and kinetic characterization of AHL lactonase from *Bacillus* sp. RM1 a novel and potent quorum quencher isolated from Fenugreek root nodule rhizosphere. *Int. J. Curr. Microbiol. Appl. Sci.* **2015**, *4*, 909–924.
11. Doberva, M.; Stien, D.; Sorres, J.; Hue, N.; Sanchez-Ferandin, S.; Eparvier, V.; Ferandin, Y.; LeBaron, P.; Lami, R. Large Diversity and Original Structures of Acyl-Homoserine Lactones in Strain MOLA 401, a Marine Rhodobacteraceae Bacterium. *Front. Microbiol.* **2017**, *8*, 1152. [[CrossRef](#)]
12. Krick, A.; Kehraus, S.; Eberl, L.; Riedel, K.; Anke, H.; Kaesler, I.; Graeber, I.; Szewzyk, U.; König, G. A marine Mesorhizobium sp. produces structurally novel long-chain N-acyl-L-homoserine lactones. *Appl. Environ. Microbiol.* **2007**, *73*, 3587–3594. [[CrossRef](#)] [[PubMed](#)]
13. Milton, D.L.; Hardman, A.; Camara, M.; Chhabra, S.R.; Bycroft, B.W.; Stewart, G.S.; Williams, P. Quorum sensing in *Vibrio anguillarum*: Characterization of the vanI/vanR locus and identification of the autoinducer N-(3-oxodecanoyl)-L-homoserine lactone. *J. Bacteriol.* **1997**, *179*, 3004–3012. [[CrossRef](#)]
14. Milton, D.L.; Chalker, V.J.; Kirke, D.; Hardman, A.; Cámara, M.; Williams, P. The LuxM Homologue VanM from *Vibrio anguillarum* Directs the Synthesis of N-(3-Hydroxyhexanoyl) homoserine Lactone and N-Hexanoylhomoserine Lactone. *J. Bacteriol.* **2001**, *183*, 3537–3547. [[CrossRef](#)]
15. Schaefer, A.L.; Hanzelka, B.L.; Parsek, M.R.; Greenberg, E.P. Detection, purification, and structural elucidation of the acylhomoserine lactone inducer of *Vibrio fischeri* luminescence and other related molecules. *Methods Enzymol.* **1999**, *305*, 288–301.
16. Lee, S.H.; Lee, S.; Lee, K.; Nahm, C.H.; Kwon, H.; Oh, H.-S.; Won, Y.-J.; Choo, K.-H.; Lee, C.-H.; Park, P.-K. More efficient media design for enhanced biofouling control in a membrane bioreactor: Quorum quenching bacteria entrapping hollow cylinder. *Environ. Sci. Technol.* **2016**, *50*, 8596–8604. [[CrossRef](#)]
17. Naik, M.M.; Bhangui, P.; Bhat, C. The first report on *Listeria monocytogenes* producing siderophores and responds positively to N-acyl homoserine lactone (AHL) molecules by enhanced biofilm formation. *Arch. Microbiol.* **2017**, *199*, 1409–1415. [[CrossRef](#)]

18. Naik, M.M.; Naik, S.P.; Dubey, S.K.; Bhat, C.; Charya, L.S. Enhanced exopolysaccharide production and biofilm forming ability in methicillin resistant *Staphylococcus sciuri* isolated from dairy in response to acyl homoserine lactone (AHL). *J. Food Sci. Technol.* **2018**, *55*, 2087–2094. [[CrossRef](#)]
19. Kim, S.-R.; Oh, H.-S.; Jo, S.-J.; Yeon, K.-M.; Lee, C.-H.; Lim, D.-J.; Lee, C.-H.; Lee, J.-K. Biofouling control with bead-entrapped quorum quenching bacteria in membrane bioreactors: Physical and biological effects. *Environ. Sci. Technol.* **2013**, *47*, 836–842. [[CrossRef](#)]
20. Yeon, K.-M.; Cheong, W.-S.; Oh, H.-S.; Lee, W.-N.; Hwang, B.-K.; Lee, C.-H.; Beyenal, H.; Lewandowski, Z. Quorum sensing: A new biofouling control paradigm in a membrane bioreactor for advanced wastewater treatment. *Environ. Sci. Technol.* **2008**, *43*, 380–385. [[CrossRef](#)]
21. Shrout, J.D.; Nerenberg, R. Monitoring bacterial twitter: Does quorum sensing determine the behavior of water and wastewater treatment biofilms? *Environ. Sci. Technol.* **2012**, *46*, 1995–2005. [[CrossRef](#)]
22. Siddiqui, M.F.; Sakinah, M.; Singh, L.; Ab Wahid, Z. Targeting N-acyl-homoserine-lactones to mitigate membrane biofouling based on quorum sensing using a biofouling reducer. *J. Biotechnol.* **2012**, *161*, 190–197. [[CrossRef](#)]
23. Lade, H.; Paul, D.; Kweon, J.H. Isolation and molecular characterization of biofouling bacteria and profiling of quorum sensing signal molecules from membrane bioreactor activated sludge. *Int. J. Mol. Sciences* **2014**, *15*, 2255–2273. [[CrossRef](#)]
24. Xiao, Y.; Waheed, H.; Xiao, K.; Hashmi, I.; Zhou, Y. In tandem effects of activated carbon and quorum quenching on fouling control and simultaneous removal of pharmaceutical compounds in membrane bioreactors. *Chem. Eng. J.* **2018**, *341*, 610–617. [[CrossRef](#)]
25. Waheed, H.; Xiao, Y.; Hashmi, I.; Stuckey, D.; Zhou, Y. Insights into quorum quenching mechanisms to control membrane biofouling under changing organic loading rates. *Chemosphere* **2017**, *182*, 40–47. [[CrossRef](#)]
26. Oh, H.-S.; Yeon, K.-M.; Yang, C.-S.; Kim, S.-R.; Lee, C.-H.; Park, S.Y.; Han, J.Y.; Lee, J.-K. Control of membrane biofouling in MBR for wastewater treatment by quorum quenching bacteria encapsulated in microporous membrane. *Environ. Sci. Technol.* **2012**, *46*, 4877–4884. [[CrossRef](#)]
27. Yu, H.; Lee, K.; Zhang, X.; Choo, K.-H. Core-shell structured quorum quenching beads for more sustainable anti-biofouling in membrane bioreactors. *Water Res.* **2019**, *150*, 321–329. [[CrossRef](#)]
28. Ma, H.; Ma, S.; Hu, H.; Ding, L.; Ren, H. The biological role of N-acyl-homoserine lactone-based quorum sensing (QS) in EPS production and microbial community assembly during anaerobic granulation process. *Sci. Rep.* **2018**, *8*, 15793. [[CrossRef](#)]
29. Ma, H.; Wang, X.; Zhang, Y.; Hu, H.; Ren, H.; Geng, J.; Ding, L.-L. The diversity, distribution and function of N-acyl-homoserine lactone (AHL) in industrial anaerobic granular sludge. *Bioresour. Technol.* **2018**, *247*, 116–124. [[CrossRef](#)]
30. Zhang, Y.; Li, J.; Liu, F.; Yan, H.; Li, J.; Zhang, X.; Jha, A.K. Specific quorum sensing signal molecules inducing the social behaviors of microbial populations in anaerobic digestion. *Bioresour. Technol.* **2019**, *273*, 185–195. [[CrossRef](#)]
31. Lv, L.; Li, W.; Zheng, Z.; Li, N.; Zhang, N. Exogenous acyl-homoserine lactones adjust community structures of bacteria and methanogens to ameliorate the performance of anaerobic granular sludge. *J. Hazard. Mater.* **2018**, *354*, 72–80. [[CrossRef](#)]
32. Petropoulos, E.; Shamurad, B.; Acharya, K.; Tabraiz, S. Domestic wastewater hydrolysis and lipolysis during start-up in anaerobic digesters and microbial fuel cells at moderate temperatures. *Int. J. Environ. Sci. Technol.* **2020**, *17*, 27–38. [[CrossRef](#)]
33. Petropoulos, E.; Yu, Y.; Tabraiz, S.; Yakubu, A.; Curtis, T.P.; Dolfing, J. High rate domestic wastewater treatment at 15 °C using anaerobic reactors inoculated with cold-adapted sediments/soils–shaping robust methanogenic communities. *Environ. Sci. Water Res. Technol.* **2019**, *5*, 70–82. [[CrossRef](#)]
34. Petropoulos, E.; Dolfing, J.; Davenport, R.J.; Bowen, E.J.; Curtis, T.P. Developing cold-adapted biomass for the anaerobic treatment of domestic wastewater at low temperatures (4, 8 and 15 C) with inocula from cold environments. *Water Res.* **2017**, *112*, 100–109. [[CrossRef](#)] [[PubMed](#)]
35. Lade, H.; Paul, D.; Kweon, J.H. N-Acyl homoserine lactone-mediated quorum sensing with special reference to use of quorum quenching bacteria in membrane biofouling control. *BioMed Res. Int.* **2014**, *2014*, 1–25. [[CrossRef](#)] [[PubMed](#)]

36. Morohoshi, T.; Okutsu, N.; Xie, X.; Ikeda, T. Identification of Quorum-Sensing Signal Molecules and a Biosynthetic Gene in *Alicyclophilus* sp. isolated from activated sludge. *Sensors* **2016**, *16*, 1218. [CrossRef] [PubMed]
37. Apha, W. *Standart Methods for Examination of Water and Wastewater*, 19th ed.; American Public Health Association: Washington, DC, USA, 2006.
38. Zhang, H.; Xia, J.; Yang, Y.; Wang, Z.; Yang, F. Mechanism of calcium mitigating membrane fouling in submerged membrane bioreactors. *J. Environ. Sci.* **2009**, *21*, 1066–1073. [CrossRef]
39. Jiang, W.; Xia, S.; Liang, J.; Zhang, Z.; Hermanowicz, S.W. Effect of quorum quenching on the reactor performance, biofouling and biomass characteristics in membrane bioreactors. *Water Res.* **2013**, *47*, 187–196. [CrossRef] [PubMed]
40. Maqbool, T.; Khan, S.J.; Waheed, H.; Lee, C.-H.; Hashmi, I.; Iqbal, H. Membrane biofouling retardation and improved sludge characteristics using quorum quenching bacteria in submerged membrane bioreactor. *J. Membr. Sci.* **2015**, *483*, 75–83. [CrossRef]
41. Griffiths, R.I.; Whiteley, A.S.; O'Donnell, A.G.; Bailey, M.J. Rapid method for coextraction of DNA and RNA from natural environments for analysis of ribosomal DNA-and rRNA-based microbial community composition. *Appl. Environ. Microbiol.* **2000**, *66*, 5488–5491. [CrossRef]
42. Kozich, J.J.; Westcott, S.L.; Baxter, N.T.; Highlander, S.K.; Schloss, P.D. Development of a dual-index sequencing strategy and curation pipeline for analyzing amplicon sequence data on the MiSeq Illumina sequencing platform. *Appl. Environ. Microbiol.* **2013**, *79*, 5112–5120. [CrossRef]
43. Caporaso, J.G.; Lauber, C.L.; Walters, W.A.; Berg-Lyons, D.; Lozupone, C.A.; Turnbaugh, P.J.; Fierer, N.; Knight, R. Global patterns of 16S rRNA diversity at a depth of millions of sequences per sample. *Proc. Natl. Acad. Sci. USA* **2011**, *108* (Suppl. S1), 4516–4522. [CrossRef] [PubMed]
44. Callahan, B.J.; McMurdie, P.J.; Rosen, M.J.; Han, A.W.; Johnson, A.J.; Holmes, S.P. DADA2: High-resolution sample inference from Illumina amplicon data. *Nat. Methods* **2016**, *13*, 581. [CrossRef] [PubMed]
45. Caporaso, J.G.; Kuczynski, J.; Stombaugh, J.; Bittinger, K.; Bushman, F.D.; Costello, E.K.; Fierer, N.; Pena, A.G.; Goodrich, J.K.; Gordon, J.I.; et al. QIIME allows analysis of high-throughput community sequencing data. *Nat. Methods* **2010**, *7*, 335. [CrossRef]
46. Rognes, T.; Flouri, T.; Nichols, B.; Quince, C.; Mahé, F. VSEARCH: A versatile open source tool for metagenomics. *PeerJ* **2016**, *4*, e2584. [CrossRef]
47. McMurdie, P.J.; Holmes, S. phyloseq: An R package for reproducible interactive analysis and graphics of microbiome census data. *PLoS ONE* **2013**, *8*, e61217. [CrossRef]
48. Leo Lahti, S.S. Tools for Microbiome Analysis in R. 2017. Available online: <http://microbiome.github.com/microbiome> (accessed on 17 September 2020).
49. Shamurad, B.; Gray, N.; Petropoulos, E.; Tabraiz, S.; Acharya, K.; Quintela-Baluja, M.; Sallis, P. Data of metal and microbial analyses from anaerobic co-digestion of organic and mineral wastes. *Data Brief* **2019**, *24*, 103934. [CrossRef]
50. Shamurad, B.; Gray, N.; Petropoulos, E.; Tabraiz, S.; Acharya, K.; Quintela-Baluja, M.; Sallis, P. Co-digestion of organic and mineral wastes for enhanced biogas production: Reactor performance and evolution of microbial community and function. *Waste Manag.* **2019**, *87*, 313–325. [CrossRef] [PubMed]
51. Benjamini, Y.; Hochberg, Y. Controlling the false discovery rate: A practical and powerful approach to multiple testing. *J. R. Stat. Soc. Ser. B (Methodological)* **1995**, *57*, 289–300. [CrossRef]
52. Bastian, M.; Heymann, S.; Jacomy, M. Gephi: An open source software for exploring and manipulating networks. In *Third International AAAI Conference on Weblogs and Social Media*; Aalborg Universitet: Aalborg, Denmark, 2009.
53. Tan, C.H.; Koh, K.S.; Xie, C.; Tay, M.; Zhou, Y.; Williams, R.; Ng, W.J.; Rice, S.A.; Kjelleberg, S. The role of quorum sensing signalling in EPS production and the assembly of a sludge community into aerobic granules. *ISME J.* **2014**, *8*, 1186–1197. [CrossRef] [PubMed]
54. Zhang, Z.; Cao, R.; Jin, L.; Zhu, W.; Ji, Y.; Xu, X.; Zhu, L. The regulation of N-acyl-homoserine lactones (AHLs)-based quorum sensing on EPS secretion via ATP synthetic for the stability of aerobic granular sludge. *Sci. Total Environ.* **2019**, *673*, 83–91. [CrossRef]
55. Judd, S. *The MBR Book: Principles and Applications of Membrane Bioreactors for Water and Wastewater Treatment*; Elsevier: Amsterdam, The Netherlands, 2010.



56. Myszka, K.; Czaczyk, K. Characterization of adhesive exopolysaccharide (EPS) produced by *Pseudomonas aeruginosa* under starvation conditions. *Curr. Microbiol.* **2009**, *58*, 541–546. [[CrossRef](#)]
57. Johir, M.; Vigneswaran, S.; Sathasivan, A.; Kandasamy, J.; Chang, C. Effect of organic loading rate on organic matter and foulant characteristics in membrane bio-reactor. *Bioresour. Technol.* **2012**, *113*, 154–160. [[CrossRef](#)] [[PubMed](#)]
58. Sharghi, E.A.; Shourgashti, A.; Bonakdarpour, B. Considering a membrane bioreactor for the treatment of vegetable oil refinery wastewaters at industrially relevant organic loading rates. *Bioprocess Biosyst. Eng.* **2020**, *43*, 981–995. [[CrossRef](#)] [[PubMed](#)]
59. Brink, P.V.D.; Satpradit, O.-A.; Van Bentem, A.; Zwijnenburg, A.; Temmink, H.; Van Loosdrecht, M.C. Effect of temperature shocks on membrane fouling in membrane bioreactors. *Water Res.* **2011**, *45*, 4491–4500. [[CrossRef](#)] [[PubMed](#)]
60. Jun, Z.; Yang, F.L.; Meng, F.G.; Peng, A.N.; Di, W.A.N.G. Comparison of membrane fouling during short-term filtration of aerobic granular sludge and activated sludge. *J. Environ. Sci.* **2007**, *19*, 1281–1286.
61. Guo, X.; Zhang, G.; Liu, X.; Ma, K.; Dong, X. Detection of the quorum sensing signals in methanogenic archaea. *Acta Microbiol. Sin.* **2011**, *51*, 1200–1204.
62. Zhang, G.; Zhang, F.; Ding, G.; Li, J.; Guo, X.; Zhu, J.; Zhou, L.; Cai, S.; Liu, X.; Luo, Y.; et al. Acyl homoserine lactone-based quorum sensing in a methanogenic archaeon. *ISME J.* **2012**, *6*, 1336. [[CrossRef](#)]
63. Gerritsen, J.; Hornung, B.; Ritari, J.; Paulin, L.; Rijkers, G.T.; Schaap, P.J.; De Vos, W.M.; Smidt, H. A comparative and functional genomics analysis of the genus *Romboutsia* provides insight into adaptation to an intestinal lifestyle. *BioRxiv* **2019**, 845511. [[CrossRef](#)]
64. Steiner, E.; Scott, J.; Minton, N.P.; Winzer, K. An agr quorum sensing system that regulates granulose formation and sporulation in *Clostridium acetobutylicum*. *Appl. Environ. Microbiol.* **2012**, *78*, 1113–1122. [[CrossRef](#)]
65. Christiaen, S.E.; Brackman, G.; Nelis, H.J.; Coenye, T. Isolation and identification of quorum quenching bacteria from environmental samples. *J. Microbiol. Methods* **2011**, *87*, 213–219. [[CrossRef](#)]
66. Hu, H.; He, J.; Liu, J.; Yu, H.; Tang, J.; Zhang, J. Role of N-acyl-homoserine lactone (AHL) based quorum sensing on biofilm formation on packing media in wastewater treatment process. *RSC Adv.* **2016**, *6*, 11128–11139. [[CrossRef](#)]
67. Valle, A.; Bailey, M.J.; Whiteley, A.S.; Manefield, M. N-acyl-L-homoserine lactones (AHLs) affect microbial community composition and function in activated sludge. *Environ. Microbiol.* **2004**, *6*, 424–433. [[CrossRef](#)]
68. Hughes, D.T.; Terekhova, D.A.; Liou, L.; Hovde, C.J.; Sahl, J.W.; Patankar, A.V.; Gonzalez, J.E.; Edrington, T.S.; Rasko, D.A.; Esperandio, V. Chemical sensing in mammalian host–bacterial commensal associations. *Proc. Natl. Acad. Sci. USA* **2010**, *107*, 9831–9836. [[CrossRef](#)] [[PubMed](#)]
69. Smadja, B.; Latour, X.; Faure, D.; Chevalier, S.; Dessaux, Y.; Orange, N. Involvement of N-acylhomoserine lactones throughout plant infection by *Erwinia carotovora* subsp. *atroseptica* (*Pectobacterium atrosepticum*). *Mol. Plant-Microbe Interact.* **2004**, *17*, 1269–1278. [[CrossRef](#)] [[PubMed](#)]



**Publisher’s Note:** MDPI stays neutral with regard to jurisdictional claims in published maps and institutional affiliations.



© 2020 by the authors. Licensee MDPI, Basel, Switzerland. This article is an open access article distributed under the terms and conditions of the Creative Commons Attribution (CC BY) license (<http://creativecommons.org/licenses/by/4.0/>).

Article

# Scaling Risk Assessment in Nanofiltration of Mine Waters

Krzysztof Mitko <sup>1,\*</sup>, Ewa Laskowska <sup>2</sup>, Marian Turek <sup>1</sup>, Piotr Dydo <sup>1</sup>  
and Krzysztof Piotrowski <sup>3</sup>

<sup>1</sup> Department of Inorganic, Analytical Chemistry and Electrochemistry, Faculty of Chemistry, Silesian University of Technology, ul. B. Krzywoustego 6, 44-100 Gliwice, Poland; marian.turek@polsl.pl (M.T.); piotr.dydo@polsl.pl (P.D.)

<sup>2</sup> PolymemTech Sp. z o.o., Al. Niepodległości 118/90, 05-577 Warsaw, Poland; laskowska.ewi@gmail.com

<sup>3</sup> Department of Chemical Engineering and Process Design, Faculty of Chemistry, Silesian University of Technology, ul. M. Strzody 7, 44-100 Gliwice, Poland; krzysztof.piotrowski@polsl.pl

\* Correspondence: krzysztof.mitko@polsl.pl; Tel.: +48-322-372-805

Received: 15 August 2020; Accepted: 14 October 2020; Published: 15 October 2020



**Abstract:** Nanofiltration can be applied for the treatment of mine waters. One of the main problems is the risk of crystallization of sparingly soluble salts on the membrane surface (scaling). In this work, a series of batch-mode nanofiltration experiments of the mine waters was performed in a dead-end Sterlitech<sup>®</sup> HP 4750X Stirred Cell. Based on the laboratory results, the concentration profiles of individual ions along the membrane length in a single-pass industrial-scale nanofiltration (NF) unit was calculated, assuming the tanks-in-series flow model inside the membrane module. These calculations also propose a method for estimating the maximum achievable recovery before the occurrence of the calcium sulfate dihydrate scaling in a single-pass NF 40' length spiral wound module, simultaneously allowing metastable supersaturation of calcium sulfate dihydrate. The performance of three membrane types (NF270, NFX, NFDL) has been evaluated for the nanofiltration of mine water.

**Keywords:** membrane module modeling; calcium sulfate precipitation risk; ionic rejection coefficients

## 1. Introduction

Nanofiltration (NF) and reverse osmosis (RO) are widely used for water and wastewater treatment. Nanofiltration, due to its high rejection of all ions except the monovalent ones, is widely used to eliminate the groundwater hardness [1] or to recover important substances, such as proteins and sugars. NF may also be considered as an alternative to RO for desalination of brackish waters, where  $\text{SO}_4^{2-}$  is the prevailing anion [2]. Nanofiltration is also used as a pretreatment [3] before other methods, such as reverse osmosis, as well as for the treatment of various mine waters, including acidic mine waters [4,5], discharge from oil sand mining [6], saline waters from the mining industry [7].

With the increase in the permeate recovery, concentration polarization rises, increasing the probability of membrane fouling (especially in the form of scaling) because of increasing concentration of sparingly soluble substances in the close vicinity of the membrane surface (e.g.,  $\text{CaSO}_4 \cdot 2\text{H}_2\text{O}$ ,  $\text{CaSO}_4 \cdot 1/2 \text{H}_2\text{O}$ ,  $\text{CaSO}_4$ ,  $\text{BaSO}_4$ ,  $\text{SrSO}_4$ ,  $\text{CaCO}_3$ ,  $\text{SiO}_2$ , etc.) [8–11]. Thus, scaling leads to significant degradation of membrane performance, shortening of membrane lifetime, decrease in permeate quality, increase in the energy consumption as higher pressure difference is necessary, increased cleaning frequency, higher consumption of antiscalants, and in the worst cases, irreversible membrane degradation. Antiscalant treatment and/or pH adjustment are usually used as the feed water pretreatment methods to decrease the mineral scale formation [12,13]. Various cleaning procedures and surface modifications are also applied in membrane scaling control [14]. An accurate prediction

and monitoring of scaling probability and its progress are important. In practice, all these methods are usually applied together to decrease or eliminate the membrane scaling consequences [14]. From the economic and environmental points of view, the earliest possible detection of the scaling onset is crucial. To estimate the calcium sulfate dihydrate solubility in various electrolyte solutions, a reference state for different supersaturated systems, different methods based on specific correlations for the activity coefficients that include the Debye–Hückel, Guggenheim–Davies expressions, Bromley, Meissner or Pitzer models are proposed [15].

One possible approach to prevent scaling formation is to design the membrane process taking into account the hydrodynamic apparatus conditions and scaling kinetics. This approach has been used in the electrodialysis of waters having high scaling potential [16,17].

In the presented work, a methodology of estimating the maximum allowable permeate recovery in the nanofiltration module is presented, with the aim of meeting the needs of increasing the permeate recovery and the process safety, in particular for the application of nanofiltration membranes for the treatment of mine waters. Based on the own laboratory test results and model calculations, the ion concentration profiles along a single-pass industrial-scale NF 40" length spiral wound membrane element were estimated, assuming the tanks-in-series reactor model describing the module performance. These calculations allowed estimating the maximum allowable recovery still preventing the calcium sulfate dihydrate coupled nucleation and scaling occurrence on the membrane surface established in this single-pass NF module construction. The software provided by the manufacturers typically predicts final parameters of the retentate/permeate; however, modeling the nanofiltration in the manner presented in the manuscript can give additional information, such as concentration profile along the membrane, the place inside the module where the scaling risk increase.

## 2. Materials and Methods

### 2.1. Chemistry of Raw Water

Investigation of scaling risk assessment in nanofiltration membranes (Table 1) was carried out using two different mine waters of different composition, denoted as "A" and "B". Mine water "A" (representing the brackish water) has total dissolved salts (TDS) content of 1.8 g/L and has higher sulfate ions concentration than the chloride ones. Real samples collected at the premises of mines were used. The mine water "B" (representing the brine) has TDS of 55 g/L and significantly higher chloride ions concentration compared to sulfates one. The original pH of mine water "A" was adjusted to 5.7 before the experiment to prevent the CaCO<sub>3</sub> scaling. The carbonate ions are relatively easy to remove in the plant pretreatment (i.e., by decarbonization using acid dosing or weak ion exchangers). As such, the focus was put on a more difficult scale-forming compound, calcium sulfate. Ionic composition of each mine water sample was determined using ion chromatography (ICS-5000 Thermo Dionex, Waltham, MA, USA). Concentrations of the main ions are presented in Table 1.

Table 1. Properties of the nanofiltration (NF) membranes were applied.

Mine Water	Langelier Saturation Index (LSI)	Gypsum Saturation	Concentration, g/L				
			Cl <sup>-</sup>	SO <sub>4</sub> <sup>2-</sup>	Na <sup>+</sup>	Mg <sup>2+</sup>	Ca <sup>2+</sup>
A	-2.4	34%	0.384	1.02	0.107	0.142	0.312
B	-2.0	11%	33.2	0.937	19.5	0.990	0.771

### 2.2. NF Membranes

Three commercially available nanofiltration membranes—NF270 (Filmtec), NFX (Synder), and NFDL-5 (Suez) were tested in this study. The properties of these NF membranes are summarized in Table 2. All of the used membranes are thin-film composite polyamide and are negatively charged at the experimental conditions.

**Table 2.** Properties of the NF membranes were applied.

	NFX <sup>1</sup>	NFDL <sup>1</sup>	NF270 <sup>1</sup>
Supplier	Synder Filtration	Suez	Dow FilmTec
Maximum Operating Temperature, °C	50	50	45
pH range	3–10.5	3–9	2–11
Minimum MgSO <sub>4</sub> rejection, %	99	96	99.2
Membrane material	Polyamide thin-film composite	Polyamide thin-film composite	Polyamide thin-film composite
Isoelectric point	3.2	4	3.0
Molecular weight cut-off, Da	150–300	150–300	200–400
Average pore width, nm	n/a	9.6 [18]	7.9 [18]
Contact angle, °	n/a	37.9 [18]	15.9 [18]

<sup>1</sup> Test conditions according to membrane supplier information: 2000 ppm MgSO<sub>4</sub> inlet solution at 110 psi (760 kPa) operating pressure, isothermal process conditions at 77 °F (25 °C), tests at 15% permeate recovery after 24 h of filtration.

### 2.3. Experimental Procedure

Because the mine water samples contained a large amount of total suspended solids, preliminary purification was necessary. Microfiltration (microfilter with pore size 0.45 µm) was used as a pretreatment for “A” and “B” mine waters. Nanofiltration experiments were carried out in a laboratory-scale dead-end Sterlitech® HP 4750 Stirred Cell stainless steel membrane module equipped with a cooling jacket to keep the stable module temperature set at 21 °C. The commercial flat sheet nanofiltration membranes were cut into circular-shaped pieces, with an effective membrane area of 14.6 cm<sup>2</sup>, and then used in all NF procedures (for every single experiment, some new, “fresh” piece of the membrane was applied). Compressed argon was used as a pressure difference source, and the applied pressure was 40 bar.

Each experiment consisted of the following steps:

1. Place the freshly cut membrane in the membrane module.
2. Pour 300 mL of deionized water (Millipore Elix 10 system, conductivity 0.066 µS) into the feed/retentate chamber of the membrane module.
3. Start the filtration; note the time required to collect every 30 mL of permeate. If the pure water flux at constant pressure doesn't change between each 30 mL of permeate collected, the membrane is assumed as conditioned. If not, go back to step 2.
4. Pour out the retentate, fill the feed/retentate chamber with the tested solution.
5. Start the filtration and collect 30 mL of permeate. Pour out the retentate and permeate out; fill the feed/retentate chamber with 300 mL of tested solution.
6. Start the filtration and collect 90 mL of permeate. Stop the filtration, recycle the collected permeate back to the feed/retentate chamber, and collect the feed sample for analysis.
7. Start the filtration. Collect each 30 mL of permeate into a separate sample container.

Ionic composition of all solutions (permeate, feed, retentate after finished experiments) was determined using ion chromatography (ICS-5000 Thermo Dionex, Waltham, MA, USA). Experimental rejection of *i*-th ion was calculated using the Equation (1):

$$R_i = (1 - C_{p,i}/C_{f,i}) \cdot 100\%, \quad (1)$$

where  $C_{p,i}$  and  $C_{f,i}$  are the concentrations of the *i*-th ion in permeate and feed, respectively.

### 2.4. Modeling

The idea is to use the rejection coefficients observed in the dead-end filtration in the modeling of the cross-flow filtration. The necessary condition is to create hydrodynamic conditions which assure

the concentration polarization is negligible and does not affect the conditions during the batch studies. For instance, in other studies that use the dead-end filtration, it was observed that the stirred cell, the concentration polarization became negligible at  $\text{rpm} > 100$  and  $\text{Re} > 12,000$  [19]. To assure minimized concentration polarization, we have used a very high-speed mixer (1200 rpms)—which, together with the dimensions of the system, resulted in turbulent flow and good mixing near the membrane surface ( $57,522 < \text{Re} < 60,802$ ,  $836 < \text{Sc} < 883$ ,  $1533 < \text{Sh} < 1569$ —the calculations are presented in Appendix C). It should be stressed, however, that the mixing speed at which the concentration polarization becomes minimized strongly depends on the design and size of the tank and the mixer. The effect of stirrer design on the mixing is particularly important at very turbulent flows; for instance, above  $\text{Re} > 10,000$  increasing the Reynolds number have no effect on Power number, but the impeller geometry can still significantly affect the quality of mixing.

The purpose of the proposed method is to estimate the borderline conditions for the high-recovery nanofiltration of the waters having high scaling risk. Although the batch-mode nanofiltration works in a discontinuous unsteady state and doesn't fully translate into a steady-state single pass nanofiltration, the presented approach could be used to set the boundaries for a pilot-scale verification of the high recovery nanofiltration, such as which membrane to use, what recovery limit should not be crossed, how to position scaling detectors (e.g., ultrasonic ones) along the module for the detection of scaling onset, etc.

To simulate the performance of a spiral-wound NF module, it was assumed that a single feed/retentate channel has a cuboid shape, i.e., any folding of a feed/retentate channel is neglected. The flow channel can then be conventionally regarded as a set of elementary units for each of the shapes depicted in Figure 1—a cuboid of a height  $h$ , length  $\Delta l$ , and of width  $s$ . The liquid flows between the NF membranes, with the permeate flowing vertically to the direction of the feed flow.

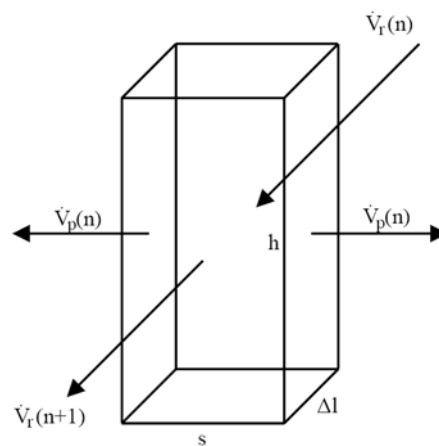


Figure 1. Scheme of an elementary NF module unit.

Mass balance of the elementary unit is given as (total—Equation (2), for individual  $i$ -th ion—Equation (3)):

$$\rho_r(n) \cdot V_r(n) = 2 \rho_p(n) \cdot V_p(n) + \rho_r(n+1) \cdot V_r(n+1), \tag{2}$$

$$C_{r,i}(n) \cdot V_r(n) = 2 C_{p,i}(n) \cdot V_p(n) + C_{r,i}(n+1) \cdot V_r(n+1), \tag{3}$$

where  $\rho$  and  $C$  represent the solution density ( $r$ —retentate,  $p$ —permeate), and  $i$ -th ion molar concentration, respectively. Volumetric flow rate of permeate  $V_p$  can be expressed in terms of the permeate flux  $J_v$  providing Equation (4):

$$V_p(n) = J_v(n) \cdot h \cdot \Delta l \tag{4}$$

Assuming constant density ( $\rho_r = \rho_p = \rho$ ), symmetric permeate outflow in respect to both parallel NF membrane planes and taking into account the assumed dimensions of the elementary unit (Figure 1), the Equations (2)–(4) can be rearranged to Equations (5) and (6):

$$u_r(n) = 2 J_v(n) \cdot \Delta l / s + u_r(n + 1) \tag{5}$$

$$C_{r,i}(n) \cdot u_r(n) = 2 C_{p,i}(n) \cdot J_v(n) \cdot \Delta l / s + C_{r,i}(n + 1) \cdot u_{r,i}(n + 1) \tag{6}$$

where  $u$  is the retentate linear flow rate, defined as Equation (7):

$$u_r(n) = V_r(n) / (hs), \tag{7}$$

Permeate recovery,  $Y$ , and rejection coefficient of  $i$ -th ion,  $R_i$ , are defined as (where 0—inlet,  $n$ — $n$ -th elementary unit)—Equation (8):

$$Y(n) = [u_r(0) - u_r(n)] / u_r(0) = u_p(n) / u_r(0), \tag{8}$$

$$R_i(n) = [C_{r,i}(n) - C_{p,i}(n)] / C_{r,i}(n) = f(Y, C_{r,i}), \tag{9}$$

The rejection coefficients of the ions depend on the permeate recovery, membrane type, and in this case study, feed water composition (mine water “A” and “B”). Substitution of Equation (9) into Equation (6) results in a set of equations making the calculation of linear flow rate and the individual ions concentration profiles along the membrane length knowing appropriate starting values at the module inlet ( $n = 0$ ) possible—Equations (10) and (11):

$$V_r(n + 1) = V_r(n) - 2 J_v(n) \cdot \Delta l \cdot h, \tag{10}$$

$$C_{r,i}(n + 1) = \{V_r(n) \cdot C_{r,i}(n) - 2 \cdot J_v(n) \cdot \Delta l \cdot h \cdot C_{r,i}(n) \cdot [1 - R_i(n)]\} / [V_r(n + 1)], \tag{11}$$

Each  $n$ -th elementary unit was treated as a separate entity, with all the inflow originating from the elementary unit ( $n - 1$ ) and the outflow going directly to the elementary unit ( $n + 1$ )—it was assumed that no back-mixing or longitudinal dispersion exists to simulate the plug flow conditions.

To assess the membrane scaling risk, the saturation level of a given sparingly soluble salt has to be considered at the membrane surface facing the retentate channel instead of the saturation level at the retentate bulk. The following concentration polarization profile was assumed—Equation (12):

$$C_{r,i}^m = C_{r,i} \cdot \exp[J(n)/k], \tag{12}$$

where  $k$  denotes the mass transfer coefficient at the wall (the membrane), calculated using Equation (13) [20]:

$$Sh(n) = k(n) \cdot d_h / D_i = 1.85 [Re(n) \cdot Sc(n) \cdot d_h / s]^{1/3}, \tag{13}$$

where  $Sh$ ,  $Re$ ,  $Sc$  denote the Sherwood, Reynolds, and Schmidt dimensionless numbers,  $d_h$  is the hydraulic diameter of the channel,  $s$  is the channel’s length, and  $D_i$  is the diffusion coefficient of the  $i$ -th ion—calculated according to procedure described in Reference [21]. Knowing the predicted ions related directly to at the membrane surface, gypsum saturation level  $\sigma$  may be calculated with Equation (14) [22]:

$$\sigma = a_{Ca^{2+}} \cdot a_{SO_4^{2-}} \cdot (a_{H_2O})^2 / K_{sp}, \tag{14}$$

where  $a_i$  is the activity of  $i$ -th ion, based on the Bromley equation for a high ionic strength solution [23]; and  $K_{sp}$  is the solubility product of the calcium sulfate dihydrate, calculated with Equation (15) for a given process temperature  $T$  [K] [24]:

$$\ln(K_{sp}) = 390.9619 - 152.624 \log(T) - 12545.62/T + 0.0818493 T, \tag{15}$$

Nucleation induction time  $t_{\text{ind}}$  of calcium sulfate dihydrate was calculated with the semi-empirical Equation (16) [22,24]:

$$t_{\text{ind}} = K \cdot \sigma^{-r}, \quad (16)$$

where the constants  $K = 1.3 \times 10^5$  s, and  $r = 5.6$  [22].

Geometric parameters of the experimental test module under study were as follows: total module length,  $L$ : 0.916 m; length of elementary unit assumed for the calculations,  $\Delta l$ : 0.001 m; intermembrane distance,  $s$ :  $7.87 \times 10^{-4}$  m (31 mil spacer).

Scaling indices were estimated using the Phreeqc aqueous phase thermodynamic modeling package from the U.S. Geological Survey [25]. The Phreeqc software uses the extended Debye–Huckel and the Davies equation to model the activity coefficients in the liquid phase. Scaling potential of both mine waters, A and B, was confirmed using the ROSA package from DOW Filmtec [26]. The ROSA software simulates the membrane treatment operations based on empirically determined separation factors for different ions and under the given operating conditions.

### 3. Results and Discussion

#### 3.1. Nanofiltration

Laboratory tests were carried out in a Sterlitech® HP 4750 Stirred Cell membrane module. The individual effect of permeate recovery  $Y$  on  $\text{SO}_4^{2-}$ ,  $\text{Cl}^-$ ,  $\text{Ca}^{2+}$ ,  $\text{Mg}^{2+}$ , and  $\text{Na}^+$  rejection coefficients  $R_i$  for both analyzed waters “A” and “B”, as well as for three types of NF membranes (NFX, NF270, and NFDL), are presented in Appendix A. Based on the laboratory results, the rejection coefficients were calculated with Equation (1), and a set of empirical equations correlating the resulting rejection coefficients  $R_i$  of common ions with permeate recovery  $Y$  [%], and ion concentration in the elementary cell ( $n - 1$ ),  $C_i$  [ $\text{mg}/\text{dm}^3$ ], were established—see Appendix B.

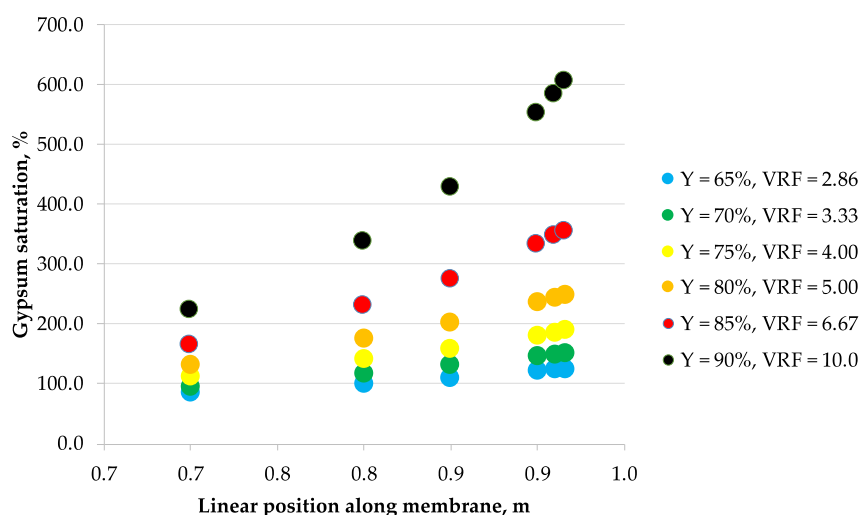
The rejection coefficients for brackish water “A” are considerably higher (for all ions considered) than for brine “B”. This may be caused by the different composition of each feed water. The water “A” contains less chloride, sodium, calcium, and magnesium ions, which causes a smaller diffusion driving force across the membrane, resulting in lower flux of these ions across the membrane; simultaneously, the water flux across the membrane is higher in the case of less saline water “A”, causing overall lower rejection coefficients of calcium and magnesium. This effect does not happen in the case of the sulfate, as both waters contain similar amounts of this ion. The rejection of sulfate was significantly higher than the rejection of calcium and magnesium, which was caused by the negative surface charge of the membrane at the experimental conditions ( $\text{pH} \geq 5.7$ ).

The highest chloride rejection was observed when the NFDL membrane was used. Moreover, in most cases, NDFL membrane type demonstrates the highest rejection of both univalent cations and bivalent cations, while the NFX membrane generally shows the lowest rejection among all three types studied. The results are in line with the ionic rejection coefficients previously reported in the literature; for instance, Hilal et al. [27] reported achieving low rejection coefficients of monovalent ions and high rejection coefficients of multivalent ions when applying nanofiltration with polyamide membranes, including the NF270, to process concentrated solutions. Kelewou et al. [28] achieved similar results using polyamide-based membranes, including the NF270 membrane used in the presented experiments. They have concluded that the chloride ion is mostly transported through the nanofiltration membrane by diffusion, while the sulfate ion was mostly removed by the convection.

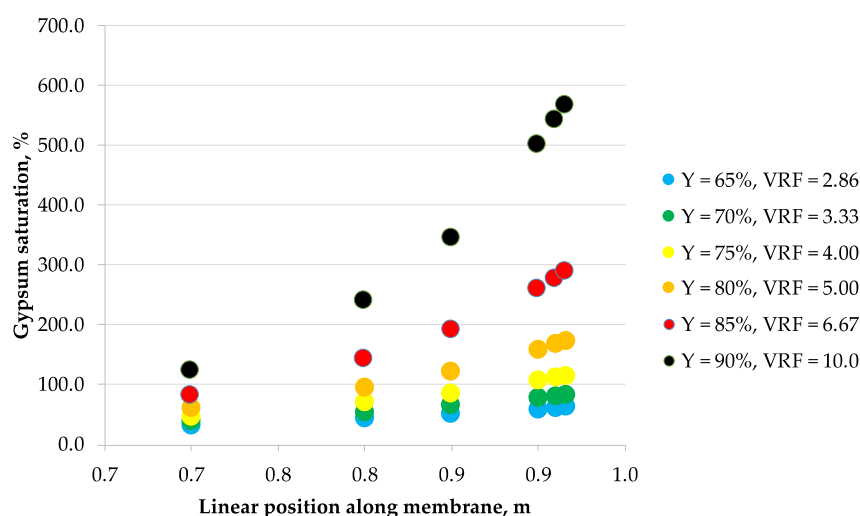
#### 3.2. Scaling

The correlations obtained from laboratory data were then used to calculate the concentration profiles of the considered 5 ionic species along the membrane module length arranged in a single-pass industrial-scale NF unit, assuming the tanks-in-series reactor model of a flow inside the membrane module. These calculations allowed to estimate the maximum allowable recovery that would effectively prevent the membrane surface scaling phenomena in a single-pass NF module. Figures 2–7 show

the calcium sulfate dihydrate saturation profiles along the simulated NF membrane length for the assumed: 65%, 70%, 75%, 80%, 85%, and 90% of the permeate recovery, Y. Saturation of calcium sulfate dihydrate increases along the membrane module length with the permeate recovery, Y in all considered cases. However, the nonlinearity effect is different depending on the Y parameter assumed, processed solution and membrane type. Mine water “A” is supersaturated as early as at 65% of the permeate recovery, while mine water “B” becomes supersaturated later—starting from 75% recovery. Only for NFDL membrane type and “B” mine water, supersaturation of calcium sulfate dihydrate rises sharply exceeding over 600% as early as at 90% recovery. In other cases, at 80% (and lower) recovery, it is typically below 300%. In the practical applications, it is usually assumed that while the solution becomes supersaturated at calcium sulfate saturation of 100%, but it is safe to operate nanofiltration modules up to saturation of ca. 160–200% at best, due to the wide metastable zone of calcium sulfate. There are known examples of operating nanofiltration modules at 300%–400% of calcium sulfate saturation [29], but 600% is way beyond any safety limits of water treatment operations, as it indicates immediate and severe scaling on the membrane surface. However, to assess the scaling severity, one should also take into account the nucleation kinetics and residence time of the supersaturated solution.

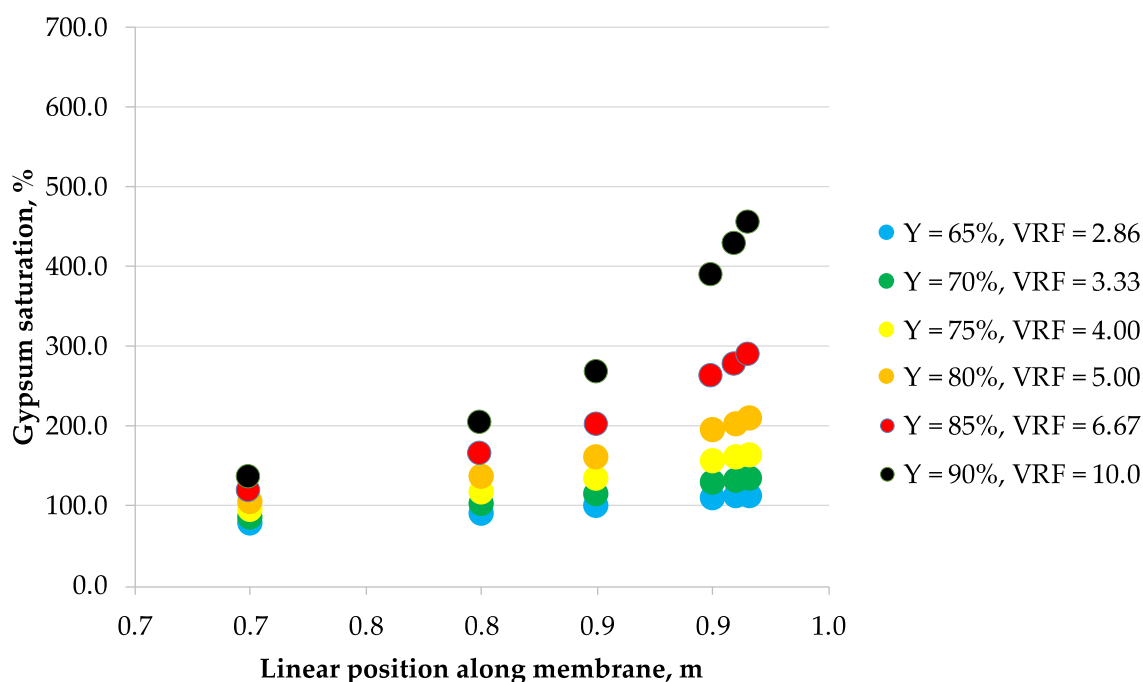


**Figure 2.** Saturation vs. position along the membrane for mine water A (0.384 g/L as  $\text{Cl}^-$ , 1.02 g/L as  $\text{SO}_4^{2-}$ , 0.107 g/L as  $\text{Na}^+$ , 0.142 g/L as  $\text{Mg}^{2+}$ , 0.312 g/L as  $\text{Ca}^{2+}$ ) and NF270 nanofiltration membrane.

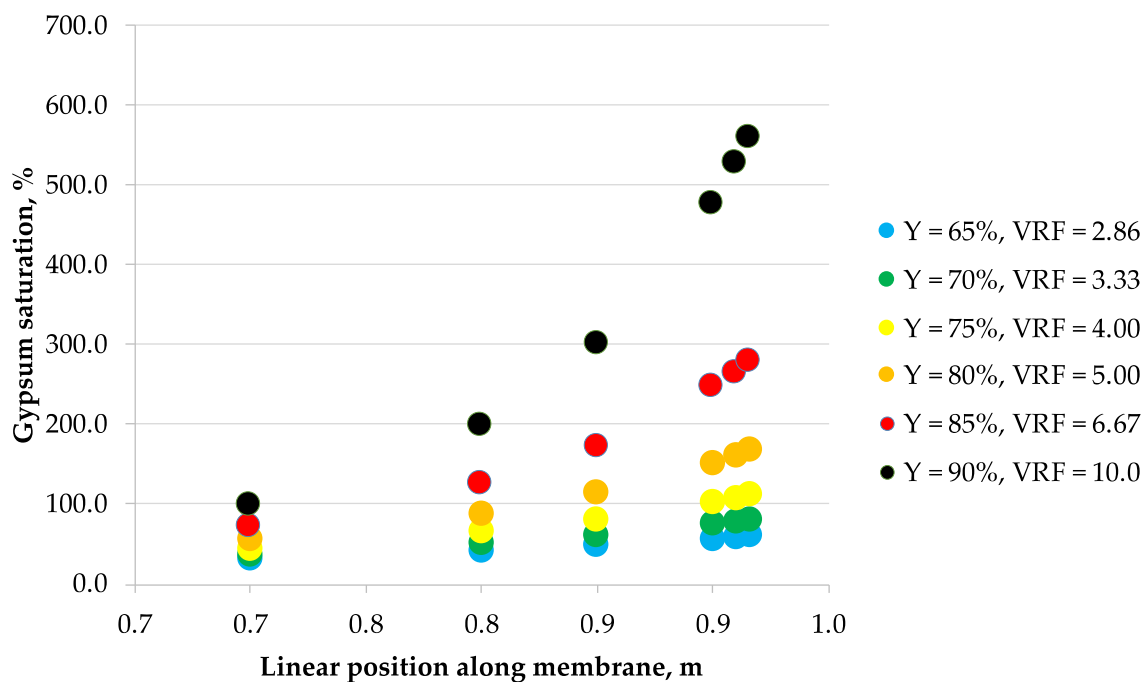


**Figure 3.** Saturation vs. position along the membrane for mine water B (33.2 g/L as  $\text{Cl}^-$ , 0.937 g/L as  $\text{SO}_4^{2-}$ , 19.5 g/L as  $\text{Na}^+$ , 0.990 g/L as  $\text{Mg}^{2+}$ , 0.771 g/L as  $\text{Ca}^{2+}$ ) and NF270 nanofiltration membrane.

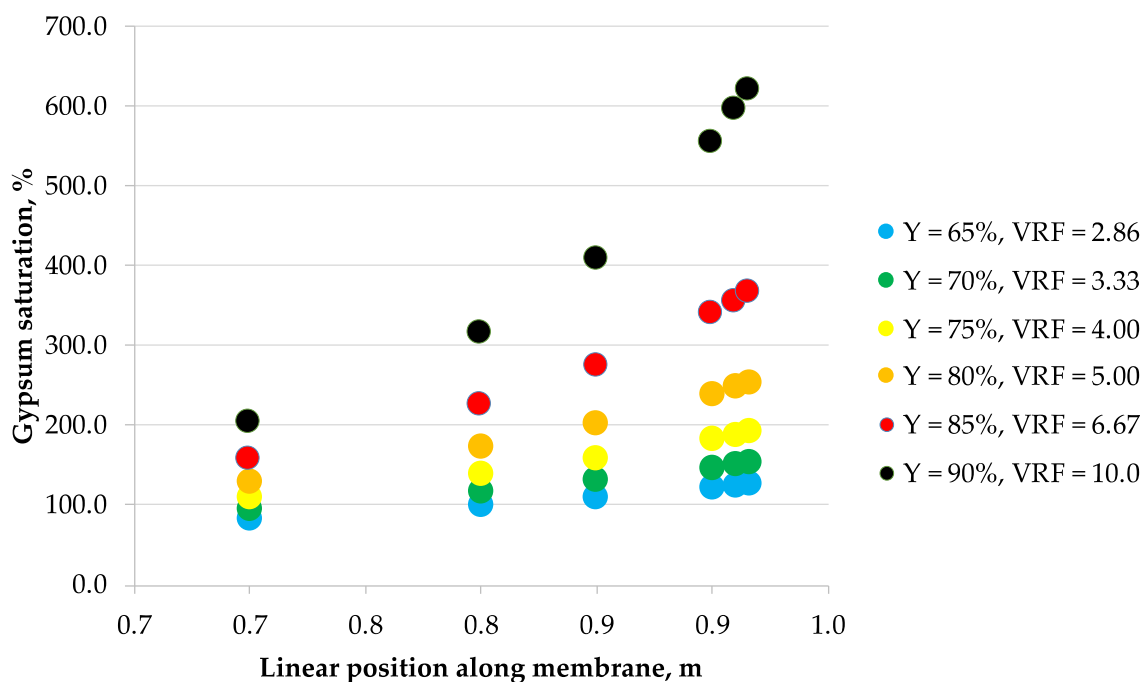




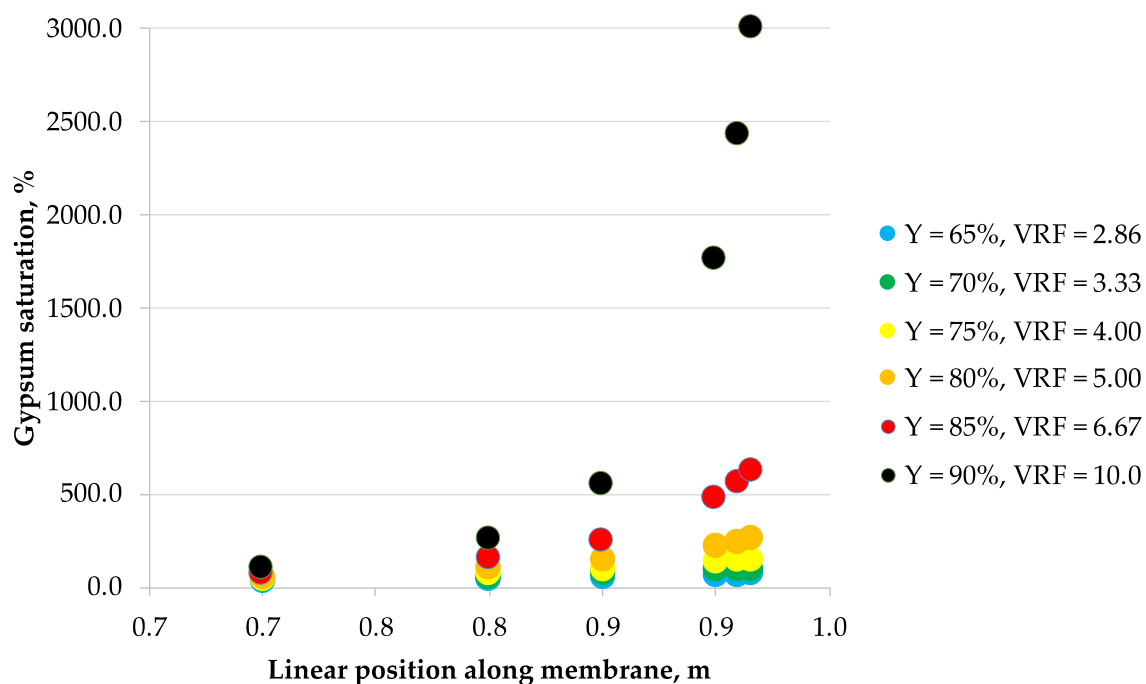
**Figure 4.** Saturation vs. position along the membrane for mine water A (0.384 g/L as  $\text{Cl}^-$ , 1.02 g/L as  $\text{SO}_4^{2-}$ , 0.107 g/L as  $\text{Na}^+$ , 0.142 g/L as  $\text{Mg}^{2+}$ , 0.312 g/L as  $\text{Ca}^{2+}$ ) and NFX nanofiltration membrane.



**Figure 5.** Saturation vs. position along the membrane for mine water B (33.2 g/L as  $\text{Cl}^-$ , 0.937 g/L as  $\text{SO}_4^{2-}$ , 19.5 g/L as  $\text{Na}^+$ , 0.990 g/L as  $\text{Mg}^{2+}$ , 0.771 g/L as  $\text{Ca}^{2+}$ ) and NFX nanofiltration membrane.



**Figure 6.** Saturation vs. position along the membrane for mine water A (0.384 g/L as  $\text{Cl}^-$ , 1.02 g/L as  $\text{SO}_4^{2-}$ , 0.107 g/L as  $\text{Na}^+$ , 0.142 g/L as  $\text{Mg}^{2+}$ , 0.312 g/L as  $\text{Ca}^{2+}$ ) and NFDL nanofiltration membrane.



**Figure 7.** Saturation vs. position along the membrane for mine water B (33.2 g/L as  $\text{Cl}^-$ , 0.937 g/L as  $\text{SO}_4^{2-}$ , 19.5 g/L as  $\text{Na}^+$ , 0.990 g/L as  $\text{Mg}^{2+}$ , 0.771 g/L as  $\text{Ca}^{2+}$ ) and NFDL nanofiltration membrane.

Tables 3 and 4. Show the induction time values for calcium sulfate dihydrate in the retentate corresponding to the nanofiltration conditions under study and theoretical time needed for the solution to flow last 30 cm of the module at: 65%, 70%, 75%, 80%, 85%, or 90% recovery, appropriately. One should keep in mind, however, that these results are valid for nanofiltration working at 40 bar of hydraulic pressure. As the pressure can influence the rejection coefficients, the batch mode experiments should be repeated if this method is to be applied for different hydraulic pressure.

**Table 3.** Induction time of calcium sulfate dihydrate during the NF process at the retentate outlet (0.916 m of module length)—effect of permeate recovery  $Y$ , mine water (“A”: 0.384 g/L as  $Cl^-$ , 1.02 g/L as  $SO_4^{2-}$ , 0.107 g/L as  $Na^+$ , 0.142 g/L as  $Mg^{2+}$ , 0.312 g/L as  $Ca^{2+}$ ; “B”: 33.2 g/L as  $Cl^-$ , 0.937 g/L as  $SO_4^{2-}$ , 19.5 g/L as  $Na^+$ , 0.990 g/L as  $Mg^{2+}$ , 0.771 g/L as  $Ca^{2+}$ ) and nanofiltration membrane type.

Y, %	$t_{ind}, s$					
	NF270 “A”	NFX “A”	NFDL “A”	NF270 “B”	NFX “B”	NFDL “B”
65	28,560	48,900	27,180	1,156,440	1,403,220	657,900
70	11,100	20,760	10,440	283,320	348,900	126,780
75	3648	7560	3384	53,340	65,880	15,540
80	930	2202	846	7080	8520	894
85	153.6	447	136.8	560.4	648	12.24
90	10.8	46.62	9.18	19.2	20.7	$4.60 \times 10^{-3}$

**Table 4.** The maximum allowable recovery for each membrane type and feed water (“A”: 0.384 g/L as  $Cl^-$ , 1.02 g/L as  $SO_4^{2-}$ , 0.107 g/L as  $Na^+$ , 0.142 g/L as  $Mg^{2+}$ , 0.312 g/L as  $Ca^{2+}$ ; “B”: 33.2 g/L as  $Cl^-$ , 0.937 g/L as  $SO_4^{2-}$ , 19.5 g/L as  $Na^+$ , 0.990 g/L as  $Mg^{2+}$ , 0.771 g/L as  $Ca^{2+}$ ).

	Membrane Type					
	NF270 “A”	NFX “A”	NFDL “A”	NF270 “B”	NFX “B”	NFDL “B”
Maximum allowable recovery [%]	90.1	91.6	89.8	89.3	89.5	84.6

To assess the scaling risk on the membrane surface following methodology is proposed, based on the earlier research [16,17]:

1. Calculate the permeate recovery  $Y$  of the module by assuming the feed linear flow velocity (refer to Section 2.3 Modeling).
2. Assume a point along the module membrane length.
3. Calculate the bulk retentate ionic concentrations and retentate concentrations at the membrane surface for a chosen point using the previously discussed model.
4. Calculate the theoretical time needed for the solution to flow from the chosen point to the retentate outlet. The gradual change in the volumetric flow along the membrane module length, due to the flow across the membrane is taken into account when calculating the time needed to leave the module has been taken into account by calculating the mean residence time in each of the elementary units separately and adding them.
5. If the theoretical time needed for the solution is not at least six times higher than the induction time, the scaling risk is unacceptably high.

Using the above assumptions, a maximum allowable recovery was calculated for each feed water and membrane type, defined as the maximum permeate recovery for which there is no unacceptable high risk of scaling at any point along the membrane module length—the results are presented in Table 4.

The results suggest that performing the nanofiltration at high permeate recovery (even above 90%) should be possible without the scaling on the membrane surface. One should remember, however, that in reality the supersaturated solution doesn’t leave the module precisely at the last point along the membrane and can stay for some time in the piping. In practical operation, a lower permeate recovery value (~ 85%) would be more recommended, as well as placing the precipitator for supersaturated retentate immediately after the pressurized device, to avoid unnecessary holdup in the piping.

The scaling risk is the highest when applying the NFDL membrane and the lowest when applying the NFX membrane. This can be explained as a result of different chemistry of the obtained retentate: The NFDL membrane has shown the highest rejection coefficients of bivalent ions during the bench-scale

tests, which means the retentate obtained using this membrane is the most supersaturated with calcium sulfate. On the other hand, NFDL is more hydrophobic than NF270, so it may show less tendency for scale layer growth in the same saturation conditions.

#### 4. Conclusions

Based on the permeate flux and sodium, magnesium, calcium, chloride, and sulfate ions concentration measurements in the dead-end experiments, the scaling risk of calcium sulfate dihydrate in the NF 40" length spiral wound membrane module was estimated. The dead-end experiments showed that the nanofiltration process may be safely operated even at 80% recovery of permeate. A method of predicting the operational limits of nanofiltration modules working in high scaling risk situations, e.g., when the feed water is rich in calcium and sulfate, was proposed. Comparing the theoretical time needed for solution to flow through the module and calculated nucleation induction time of calcium sulfate dihydrate for a given final retentate concentration, it is possible to predict maximal safe recovery level  $Y$  for each specific process conditions; the established model, however, is valid only at given hydraulic pressure (40 bar) and would need an additional set of experiments to include pressure as a variable. Experimental tests clearly demonstrated that scaling-free operation of the 40" length spiral wound NF module is possible at 75% to permeate recovery in the case of highly concentrated mine water and with 80% permeate recovery considering brackish water. A possibility of working at 75% to permeate recovery level should improve the performance of the integrated salt production systems using NF as pretreatment step, since they are limited in terms of overall recovery by the pretreatment (NF) recovery. The establishment of the reliable and mathematical model to simulate the nanofiltration in large-scale systems creates an opportunity for the investigation of NF applicability in several technologically important processes.

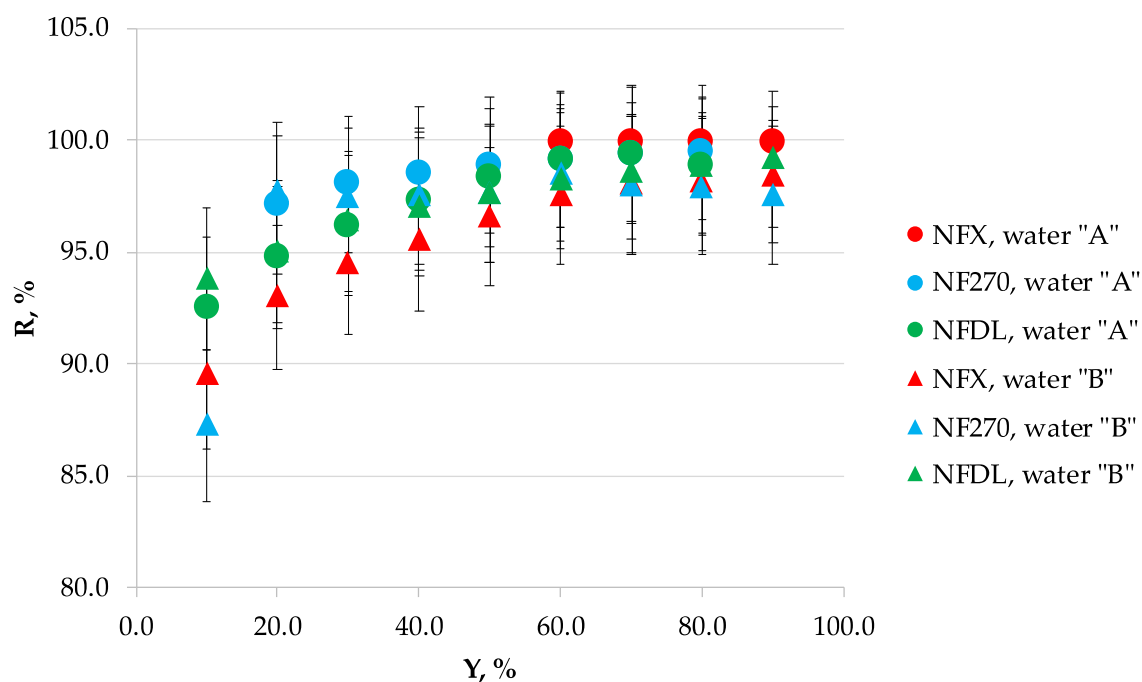
**Author Contributions:** Conceptualization, K.M.; methodology, K.M., E.L.; formal analysis, K.M.; investigation, E.L., P.D.; resources, P.D.; data curation, K.M.; writing—original draft preparation, E.L., K.M.; writing—review and editing, K.M., K.P.; visualization, K.M.; supervision, M.T.; project administration, M.T.; funding acquisition, M.T. All authors have read and agreed to the published version of the manuscript.

**Funding:** This research was funded by POLISH NATIONAL CENTRE FOR RESEARCH AND DEVELOPMENT, contract number TANGO2/340568/NCBR/2017. The APC was funded by POLISH NATIONAL CENTRE FOR RESEARCH AND DEVELOPMENT.

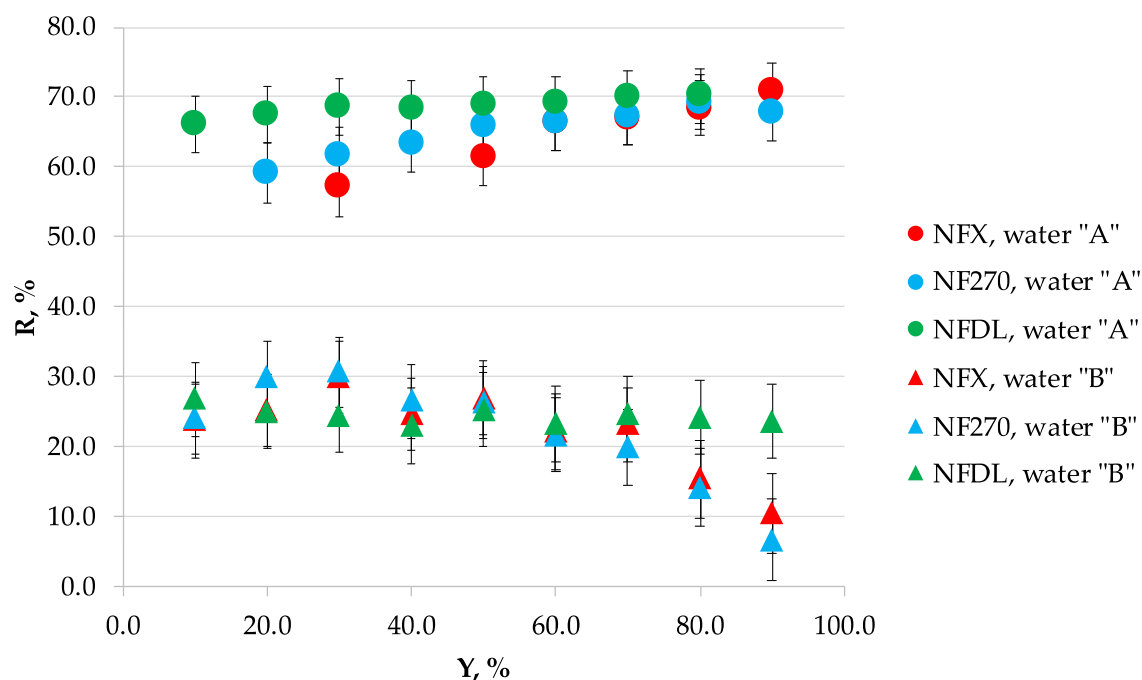
**Conflicts of Interest:** The authors declare no conflict of interest.

#### Appendix A

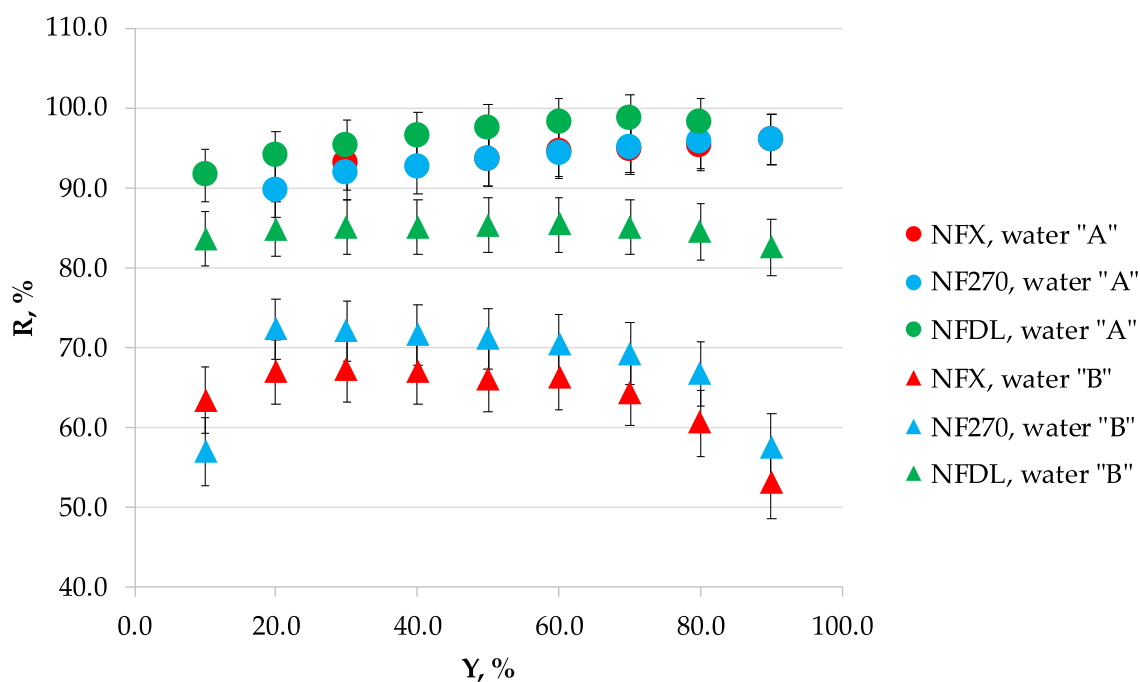
Individual effect of permeate recovery  $Y$  on  $\text{SO}_4^{2-}$ ,  $\text{Cl}^-$ ,  $\text{Ca}^{2+}$ ,  $\text{Mg}^{2+}$ , and  $\text{Na}^+$  rejection coefficients  $R_i$  for both analyzed waters "A" and "B", as well as for three types of NF membranes (NFX, NF270, and NFDL), is demonstrated in Figures A1–A5.



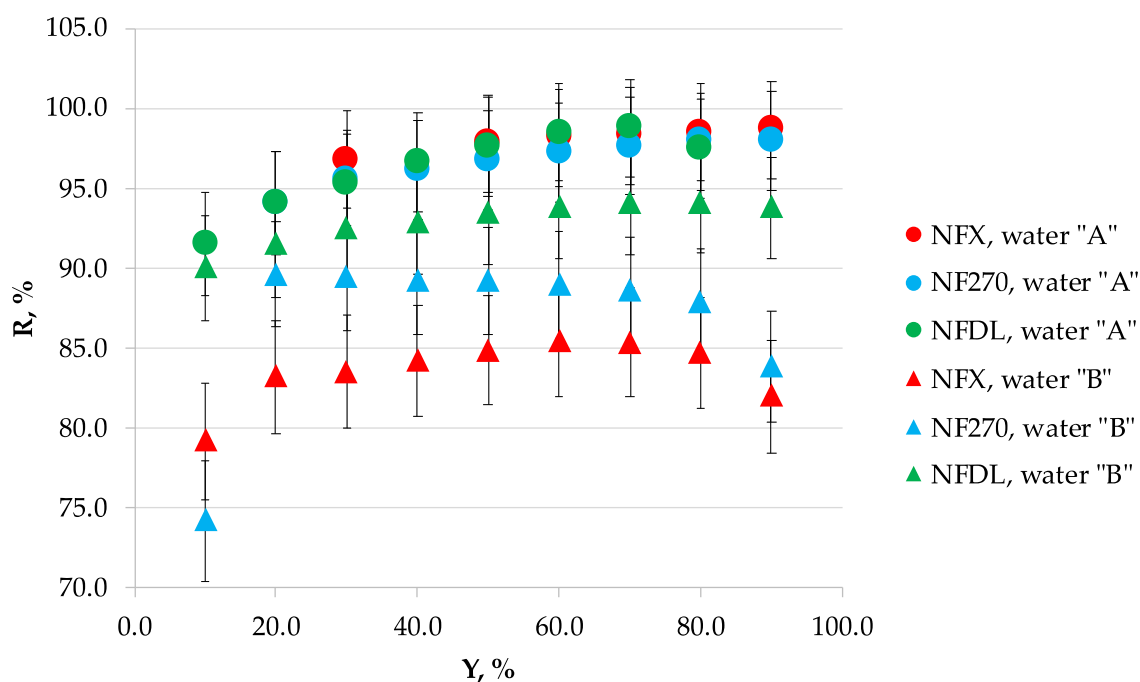
**Figure A1.** Rejection coefficient, R, of  $\text{SO}_4^{2-}$  as a function of permeate recovery, Y, for NFX, NF270 and NFDL nanofiltration membranes and mine waters "A" (0.384 g/L as  $\text{Cl}^-$ , 1.02 g/L as  $\text{SO}_4^{2-}$ , 0.107 g/L as  $\text{Na}^+$ , 0.142 g/L as  $\text{Mg}^{2+}$ , 0.312 g/L as  $\text{Ca}^{2+}$ ) and "B" (33.2 g/L as  $\text{Cl}^-$ , 0.937 g/L as  $\text{SO}_4^{2-}$ , 19.5 g/L as  $\text{Na}^+$ , 0.990 g/L as  $\text{Mg}^{2+}$ , 0.771 g/L as  $\text{Ca}^{2+}$ ).



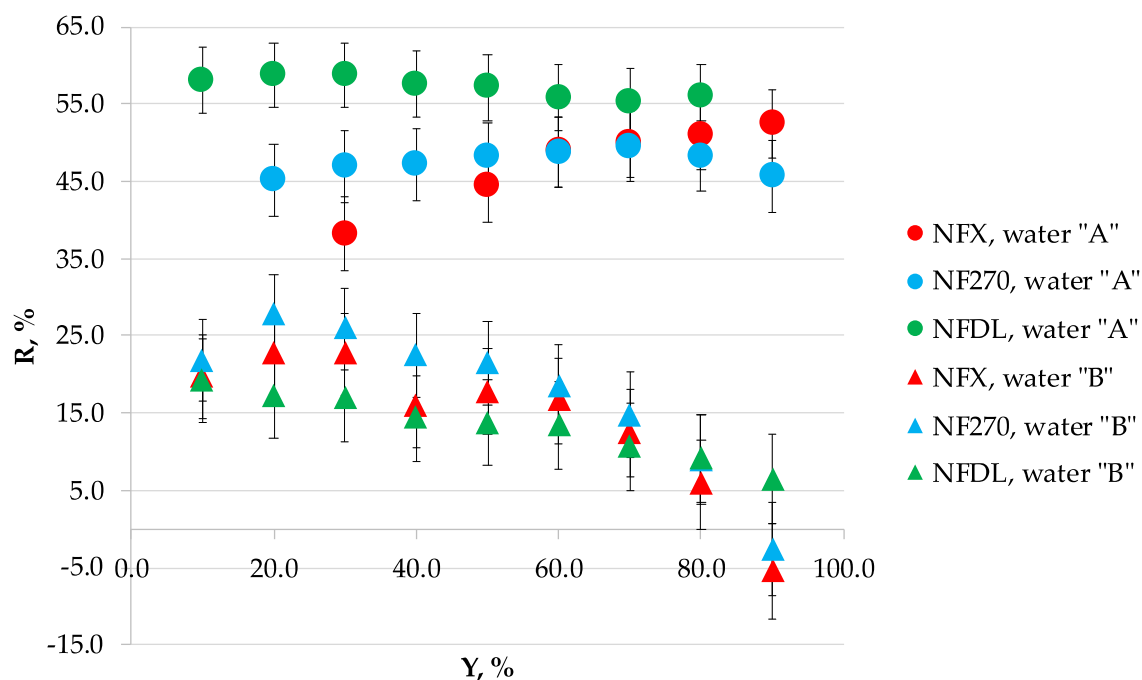
**Figure A2.** Rejection coefficient, R, of  $\text{Cl}^-$  as a function of permeate recovery, Y, for NFX, NF270 and NFDL nanofiltration membranes and mine waters "A" (0.384 g/L as  $\text{Cl}^-$ , 1.02 g/L as  $\text{SO}_4^{2-}$ , 0.107 g/L as  $\text{Na}^+$ , 0.142 g/L as  $\text{Mg}^{2+}$ , 0.312 g/L as  $\text{Ca}^{2+}$ ) and "B" (33.2 g/L as  $\text{Cl}^-$ , 0.937 g/L as  $\text{SO}_4^{2-}$ , 19.5 g/L as  $\text{Na}^+$ , 0.990 g/L as  $\text{Mg}^{2+}$ , 0.771 g/L as  $\text{Ca}^{2+}$ ).



**Figure A3.** Rejection coefficient,  $R$ , of  $\text{Ca}^{2+}$  as a function of permeate recovery,  $Y$ , for NFX, NF270 and NFDL nanofiltration membranes and mine waters "A" (0.384 g/L as  $\text{Cl}^-$ , 1.02 g/L as  $\text{SO}_4^{2-}$ , 0.107 g/L as  $\text{Na}^+$ , 0.142 g/L as  $\text{Mg}^{2+}$ , 0.312 g/L as  $\text{Ca}^{2+}$ ) and "B" (33.2 g/L as  $\text{Cl}^-$ , 0.937 g/L as  $\text{SO}_4^{2-}$ , 19.5 g/L as  $\text{Na}^+$ , 0.990 g/L as  $\text{Mg}^{2+}$ , 0.771 g/L as  $\text{Ca}^{2+}$ ).



**Figure A4.** Rejection coefficient,  $R$ , of  $\text{Mg}^{2+}$  as a function of permeate recovery,  $Y$ , for NFX, NF270 and NFDL nanofiltration membranes and mine waters "A" (0.384 g/L as  $\text{Cl}^-$ , 1.02 g/L as  $\text{SO}_4^{2-}$ , 0.107 g/L as  $\text{Na}^+$ , 0.142 g/L as  $\text{Mg}^{2+}$ , 0.312 g/L as  $\text{Ca}^{2+}$ ) and "B" (33.2 g/L as  $\text{Cl}^-$ , 0.937 g/L as  $\text{SO}_4^{2-}$ , 19.5 g/L as  $\text{Na}^+$ , 0.990 g/L as  $\text{Mg}^{2+}$ , 0.771 g/L as  $\text{Ca}^{2+}$ ).



**Figure A5.** Rejection coefficient,  $R$ , of  $\text{Na}^+$  as a function of permeate recovery,  $Y$ , for NFX, NF270 and NFDL nanofiltration membranes and mine waters “A” (0.384 g/L as  $\text{Cl}^-$ , 1.02 g/L as  $\text{SO}_4^{2-}$ , 0.107 g/L as  $\text{Na}^+$ , 0.142 g/L as  $\text{Mg}^{2+}$ , 0.312 g/L as  $\text{Ca}^{2+}$ ) and “B” (33.2 g/L as  $\text{Cl}^-$ , 0.937 g/L as  $\text{SO}_4^{2-}$ , 19.5 g/L as  $\text{Na}^+$ , 0.990 g/L as  $\text{Mg}^{2+}$ , 0.771 g/L as  $\text{Ca}^{2+}$ ).

The permeate flows observed in the study are presented in Table A1.

**Table A1.** Permeate flow observed during the batch-mode studies with three different membranes (NF270, NFX, NFDL) and mine waters “A” (0.384 g/L as  $\text{Cl}^-$ , 1.02 g/L as  $\text{SO}_4^{2-}$ , 0.107 g/L as  $\text{Na}^+$ , 0.142 g/L as  $\text{Mg}^{2+}$ , 0.312 g/L as  $\text{Ca}^{2+}$ ) and “B” (33.2 g/L as  $\text{Cl}^-$ , 0.937 g/L as  $\text{SO}_4^{2-}$ , 19.5 g/L as  $\text{Na}^+$ , 0.990 g/L as  $\text{Mg}^{2+}$ , 0.771 g/L as  $\text{Ca}^{2+}$ ).

Recovery, %	Volume Reduction Fraction	Permeate Flux, $\text{dm}^3/\text{m}^2\cdot\text{h}$					
		“A”			“B”		
		NF270	NFX	NFDL	NF270	NFX	NFDL
10%	1.11	273	62	206	76	64	67
20%	1.25	264	59	223	71	61	68
30%	1.43	255	56	211	71	58	61
40%	1.67	247	56	204	62	56	56
50%	2.00	223	56	187	55	50	53
60%	2.50	211	28	169	49	45	51
70%	3.33	185	-	154	39	41	50
80%	5.00	145	-	120	25	35	46
90%	10.0	65	-	-	76	29	42

## Appendix B

Empirical correlations used to calculate ionic rejection coefficients were as follows:

For mine water “A” and membrane type NF270:

$$R_{\text{Cl}^-} = -2.0012662 \times 10^{-3} \cdot Y^2 + 0.3514697 \cdot Y + 52.82125, \quad (\text{A1})$$

$$R_{\text{SO}_4^{2-}} = -6.171004 \times 10^{-4} \cdot Y^2 + 9.84534268 \times 10^{-2} \cdot Y + 95.482911691, \quad (\text{A2})$$

$$R_{\text{Mg}^{2+}} = -7.993941 \times 10^{-4} \cdot Y^2 + 0.1408108 \cdot Y + 91.724665, \quad (\text{A3})$$

$$R_{Ca^{2+}} = -8.968448 \times 10^{-4} \cdot Y^2 + 0.185505 \cdot Y + 86.43278, \quad (A4)$$

For mine water “A” and membrane type NFX:

$$R_{Cl^-} = 0.231046 \cdot Y + 50.55687, \quad (A5)$$

$$R_{SO_4^{2-}} = -1.6965 \times 10^{-5} \cdot Y^2 + 4.209337 \times 10^{-3} \cdot Y + 99.6657, \quad (A6)$$

$$R_{Mg^{2+}} = -4.511 \times 10^{-4} \cdot Y^2 + 8.3874 \times 10^{-2} \cdot Y + 94.69, \quad (A7)$$

$$R_{Ca^{2+}} = 5.1136 \times 10^{-2} \cdot Y + 91.23656, \quad (A8)$$

For mine water “A” and membrane type NFDL:

$$R_{Cl^-} = -4.539 \times 10^{-4} \cdot Y^2 + 9.2025 \times 10^{-2} \cdot Y + 65.579, \quad (A9)$$

$$R_{SO_4^{2-}} = -1.8305 \times 10^{-3} \cdot Y^2 + 0.256961 \cdot Y + 90.1299, \quad (A10)$$

$$R_{Mg^{2+}} = -2.1816374 \times 10^{-3} \cdot Y^2 + 0.28643 \cdot Y + 88.884, \quad (A11)$$

$$R_{Ca^{2+}} = -1.73443 \times 10^{-3} \cdot Y^2 + 0.2494767 \cdot Y + 89.27368, \quad (A12)$$

For mine water “B” and membrane type NF270:

$$R_{Cl^-} = -5.502 \times 10^{-8} \cdot (C_{Cl^-})^2 + 2.691 \times 10^{-3} \cdot C_{Cl^-} + 1.201, \quad (A13)$$

$$R_{SO_4^{2-}} = 97.767, \quad (A14)$$

$$R_{Mg^{2+}} = -7.356 \times 10^{-7} \cdot (C_{Mg^{2+}})^2 + 1.5346 \times 10^{-3} \cdot C_{Mg^{2+}} + 88.57, \quad (A15)$$

$$R_{Ca^{2+}} = -6.312 \times 10^{-6} \cdot (C_{Ca^{2+}})^2 + 8.53 \times 10^{-3} \cdot C_{Ca^{2+}} + 69.0976, \quad (A16)$$

For mine water “B” and membrane type NFX:

$$R_{Cl^-} = -4.45122 \times 10^{-8} \cdot (C_{Cl^-})^2 + 2.0857 \times 10^{-3} \cdot C_{Cl^-} + 7.624313, \quad (A17)$$

$$R_{SO_4^{2-}} = -10717627 / (C_{SO_4^{2-}})^2 + 5059.293 / C_{SO_4^{2-}} + 97.77344, \quad (A18)$$

$$R_{Mg^{2+}} = -1.683707 \times 10^{-6} \cdot (C_{Mg^{2+}})^2 + 6.8848 \times 10^{-3} \cdot C_{Mg^{2+}} + 78.35183, \quad (A19)$$

$$R_{Ca^{2+}} = -9.012477 \times 10^{-6} \cdot (C_{Ca^{2+}})^2 + 1.071 \times 10^{-2} \cdot C_{Ca^{2+}} + 63.9628, \quad (A20)$$

For mine water “B” and membrane type NFDL:

$$R_{Cl^-} = -1.337313 \times 10^{-4} \cdot C_{Cl^-} + 29.21885, \quad (A21)$$

$$R_{SO_4^{2-}} = -4960805.8 / (C_{SO_4^{2-}})^2 + 984.06223 / C_{SO_4^{2-}} + 99.23215, \quad (A22)$$

$$R_{Mg^{2+}} = -8647516 / (C_{Mg^{2+}})^2 + 6582.018 / C_{Mg^{2+}} + 92.737, \quad (A23)$$

$$R_{Ca^{2+}} = -1.852922 \times 10^{-6} \cdot (C_{Ca^{2+}})^2 + 4.792406 \times 10^{-3} \cdot C_{Ca^{2+}} + 82.14258, \quad (A24)$$

The recovery, Y, can be calculated using the Volume Reduction Factor (VRF) as:

$$Y = 100\% \cdot (1 - 1/VRF) \quad (A25)$$



## Appendix C

The Reynolds number in the dead-end filtration module was calculated using the equation:

$$Re = \omega \cdot \rho \cdot r^2 / \mu \quad (A26)$$

where  $\omega$  is the mixer 63,200 rotational speed (1200 rpm = 126 rad/s),  $r$  is the radius of the effective area of the membrane (0.022 m),  $\rho$  is the density (ranging from 1003 kg/m<sup>3</sup> for the least concentrated water sample—water “A”—to 1047 kg/m<sup>3</sup> for the most concentrated water sample—retentate during nanofiltration of water “B” at 90% permeate recovery),  $\mu$  is the viscosity (ranging from 1.006 × 10<sup>−3</sup> Pas to 1.11 × 10<sup>−3</sup> Pas). The Reynolds number during the experiments ranged from 836 to 883.

The Schmidt number in the dead-end filtration module was calculated using the equation:

$$Sc = \mu / (\rho \cdot D) \quad (A27)$$

where  $D$  is the diffusion coefficient of sodium chloride (1.2 × 10<sup>−9</sup> m<sup>2</sup>/s). The Schmidt number during the experiments ranged from 57,522 to 60,802.

The Sherwood number in the dead-end filtration module was calculated using the equation:

$$Sh = 0.044 \cdot Re^{0.75} \cdot Sc^{0.33} \quad (A28)$$

The Sherwood number in the experiments ranged from 1533 to 1569.

## References

1. Mohammad, A.W.; Teow, Y.H.; Ang, W.L.; Chung, Y.T.; Oatley-Radcliffe, D.L.; Hilal, N. Nanofiltration membranes review: Recent advances and future prospects. *Desalination* **2015**, *356*, 226–254. [[CrossRef](#)]
2. Mohsen, M.S.; Jaber, J.O.; Afonso, M.D. Desalination of brackish water by nanofiltration and reverse osmosis. *Desalination* **2003**, *157*, 167. [[CrossRef](#)]
3. Al-Amoudi, A.S.; Farooque, A.M. Performance, restoration and autopsy of NF membranes used in seawater pretreatment. *Desalination* **2005**, *178*, 261–271. [[CrossRef](#)]
4. Lopez, J.; Reig, M.; Vecino, X.; Gibert, O.; Cortina, J.L. From nanofiltration membrane permeances to design projections for the remediation and valorisation of acid mine waters. *Sci. Total Environ.* **2020**, *738*, 139780. [[CrossRef](#)]
5. Lopez, J.; Reig, M.; Gibert, O.; Cortina, J.L. Recovery of sulphuric acid and added value metals (Zn, Cu, and rare earths) from acidic mine waters using nanofiltration membranes. *Sep. Purif. Technol.* **2019**, *212*, 180–190. [[CrossRef](#)]
6. Voigt, I.; Richter, H.; Weyd, M.; Milew, K.; Haseneder, R.; Günther, C.; Prehn, V. Treatment of oily and salty mining water by ceramic nanofiltration membranes. *Chem. Ing. Tech.* **2019**, *91*, 1454–1459. [[CrossRef](#)]
7. Laskowska, E.; Turek, M.; Mitko, K.; Dydo, P. Concentration of mine saline water in high-efficiency hybrid RO-NF system. *Desalin. Water Treat.* **2018**, *128*, 414–420. [[CrossRef](#)]
8. Shirazi, S.; Lin, C.J.; Chen, D. Inorganic fouling of pressure-driven membrane processes—A critical review. *Desalination* **2010**, *250*, 236–248. [[CrossRef](#)]
9. Sweity, A.; Ronen, Z.; Herzberg, M. Induced organic fouling with antiscalants in seawater desalination. *Desalination* **2014**, *352*, 158–165. [[CrossRef](#)]
10. Hao, W.; Yang, M.; Zhao, K.; Tang, J. Dielectric measurements of fouling of nanofiltration membranes by sparingly soluble salts. *J. Membr. Sci.* **2016**, *497*, 339–347. [[CrossRef](#)]
11. Meng, X.; Yang, R.; Zhang, X. Enhanced gypsum scaling by organic fouling layer on nanofiltration membrane: Characteristics and mechanisms. *Water Res.* **2016**, *91*, 203–213.
12. Chesters, S.P. Innovations in the inhibition and cleaning of reverse osmosis membrane scaling and fouling. *Desalination* **2009**, *238*, 22–29. [[CrossRef](#)]
13. Shih, W.Y.; Gao, J.; Rahardianto, A.; Glater, J.; Cohen, Y.; Gabelich, C.J. Ranking of antiscalant performance for gypsum scale suppression in the presence of residual aluminum. *Desalination* **2006**, *196*, 280–292. [[CrossRef](#)]

14. Al-Amoudi, A.; Lovitt, R.W. Fouling strategies and the cleaning system of NF membranes and factors affecting cleaning efficiency. *J. Membr. Sci.* **2007**, *303*, 4–28. [[CrossRef](#)]
15. Tomaszewska, B.; Kmieciak, E.; Wątor, K.; Tyszer, M. Use of numerical modelling in the prediction of membrane scaling. Reaction between antiscalants and feedwater. *Desalination* **2018**, *427*, 27–34. [[CrossRef](#)]
16. Turek, M.; Waś, J.; Mitko, K. Scaling prediction in electro-dialytic desalination. *Desalin. Water Treat.* **2012**, *44*, 255–260. [[CrossRef](#)]
17. Mitko, K.; Turek, M. Concentration distribution along the electro-dialyzer. *Desalination* **2014**, *341*, 96–100. [[CrossRef](#)]
18. Vieira, G.S.; Moreira, F.K.V.; Matsumoto, R.L.S.; Michelon, M.; Filho, F.M.; Hubinger, M.D. Influence of nanofiltration membrane features on enrichment of jussara ethanolic extract (*Euterpe edulis*) in anthocyanins. *J. Food Eng.* **2018**, *226*, 31–41. [[CrossRef](#)]
19. Imbrogno, A.; Schäfer, A.I. Comparative study of nanofiltration membrane characterization devices of different dimension and configuration (cross flow and dead end). *J. Membr. Sci.* **2019**, *585*, 67–80. [[CrossRef](#)]
20. Noble, R.; Stern, S. *Membrane Separations Technology: Principles and Applications*, 3rd ed.; Elsevier Science: Amsterdam, The Netherlands, 1995; pp. 51–52.
21. Li, Y.-H. Diffusion of ions in sea water and deep-sea sediments. *Geochim. Cosmochim.* **1974**, *38*, 703–714.
22. Packter, A. The precipitation of sparingly soluble alkaline-earth metal and lead salts: Nucleation and growth orders during the induction period. *J. Chem. Soc. A* **1968**, *0*, 859–862. [[CrossRef](#)]
23. Lancia, A.; Musmarra, D.; Prisciandaro, M. Measuring induction period for calcium sulfate dihydrate precipitation. *AIChE J.* **1999**, *45*, 390–397. [[CrossRef](#)]
24. Prisciandaro, M.; Lancia, A.; Musmarra, D. Calcium sulfate dihydrate nucleation in the presence of calcium and sodium chloride salts. *Ind. Eng. Chem. Res.* **2001**, *40*, 2335–2339. [[CrossRef](#)]
25. Parkhurst, D.L.; Appelo, C.A.J. Chapter A43: Description of input and examples for PHREEQC version 3—A computer program for speciation, batch-reaction, one-dimensional transport, and inverse geochemical calculations. In *U.S. Geological Survey Techniques and Methods*; Book 6; US Geological Survey: Reston, VA, USA, 2013; p. 497.
26. ROSA. Available online: <http://web.archive.org/web/20100723021839/http://www.dow.com/liquidseps/design/rosa.htm> (accessed on 13 August 2020).
27. Hilal, N.; Al-Zoubi, H.; Mohammad, A.W.; Darwish, N.A. Nanofiltration of highly concentrated salt solutions up to seawater salinity. *Desalination* **2005**, *184*, 315–326. [[CrossRef](#)]
28. Kelewou, H.; Lhassani, A.; Merkouzi, M.; Drogui, P.; Sellamuthu, B. Salt retention by nanofiltration membranes: Physicochemical and hydrodynamic approaches and modelling. *Desalination* **2011**, *277*, 106–112. [[CrossRef](#)]
29. Turek, M.; Mitko, K.; Laskowska, E.; Chorażewska, M.; Piotrowski, K.; Jakóbiak-Kolon, A.; Dydo, P. Energy Consumption and Gypsum Scaling Assessment in a Hybrid Nanofiltration- Reverse Osmosis-Electrodialysis system. *Chem. Eng. Technol.* **2018**, *41*, 392–400. [[CrossRef](#)]

**Publisher’s Note:** MDPI stays neutral with regard to jurisdictional claims in published maps and institutional affiliations.




© 2020 by the authors. Licensee MDPI, Basel, Switzerland. This article is an open access article distributed under the terms and conditions of the Creative Commons Attribution (CC BY) license (<http://creativecommons.org/licenses/by/4.0/>).



Article

# Hydration and Diffusion of $H^+$ , $Li^+$ , $Na^+$ , $Cs^+$ Ions in Cation-Exchange Membranes Based on Polyethylene- and Sulfonated-Grafted Polystyrene Studied by NMR Technique and Ionic Conductivity Measurements

Vitaliy I. Volkov <sup>1,2,\*</sup>, Alexander V. Chernyak <sup>1,2</sup>, Daniil V. Golubenko <sup>3</sup>, Vladimir A. Tverskoy <sup>4</sup>, Georgiy A. Lochin <sup>1,5</sup>, Ervena S. Odzhigaeva <sup>1,5</sup> and Andrey B. Yaroslavtsev <sup>3</sup> 

<sup>1</sup> Institute of Problems of Chemical Physics RAS, 142432 Chernogolovka, Russia; chernyak@icp.ac.ru (A.V.C.); lochin.g@yandex.ru (G.A.L.); odzhigaeva.ervena@yandex.ru (E.S.O.)

<sup>2</sup> Scientific Center in Chernogolovka RAS, 142432 Chernogolovka, Russia

<sup>3</sup> Kumakov Institute of General and Inorganic Chemistry RAS, 119991 Moscow, Russia; xpman2009@yandex.ru (D.V.G.); yaroslav@igic.ras.ru (A.B.Y.)

<sup>4</sup> Lomonosov Institute of Fine Chemical Technologies, MIREA–Russian Technological University, 119571 Moscow, Russia; tverskoy@mitht.ru

<sup>5</sup> Faculty of Chemistry, Lomonosov Moscow State University, 119991 Moscow, Russia

\* Correspondence: vitwolf@mail.ru or vitwolf@icp.ac.ru

Received: 12 August 2020; Accepted: 28 September 2020; Published: 1 October 2020



**Abstract:** The main particularities of sulfonate groups hydration, water molecule and alkaline metal cation translation mobility as well as ionic conductivity were revealed by NMR and impedance spectroscopy techniques. Cation-exchange membranes MSC based on cross-linked sulfonated polystyrene (PS) grafted on polyethylene with ion-exchange capacity of 2.5 mg-eq/g were investigated. Alkaline metal cation hydration numbers ( $h$ ) calculated from temperature dependences of  $^1H$  chemical shift of water molecule for membranes equilibrated with water vapor at  $RH = 95\%$  are 5, 6, and 4 for  $Li^+$ ,  $Na^+$ , and  $Cs^+$  ions, respectively. These values are close to  $h$  for equimolar aqueous salt solutions. Water molecules and counter ions  $Li^+$ ,  $Na^+$ , and  $Cs^+$  diffusion coefficients were measured by pulsed field gradient NMR on the  $^1H$ ,  $^7Li$ ,  $^{23}Na$ , and  $^{133}Cs$  nuclei. For membranes as well as for aqueous chloride solutions, cation diffusion coefficients increased in the following sequence:  $Li^+ < Na^+ < Cs^+$ . Cation and water molecule diffusion activation energies in temperature range from 20 °C to 80 °C were close to each other (about 20 kJ/mol). The cation conductivity of MSC membranes is in the same sequence,  $Li^+ < Na^+ < Cs^+ \ll H^+$ . The conductivity values calculated from the NMR diffusion coefficients with the use of the Nernst–Einstein equation are essentially higher than experimentally determined coefficients. The reason for this discrepancy is the heterogeneity of membrane pore and channel system. Ionic conductivity is limited by cation transfer in narrow channels, whereas the diffusion coefficient characterizes ion mobility in wide pores first of all.

**Keywords:** sulfonic cation-exchange membrane; hydration number; pulsed field gradient NMR; diffusion coefficient; ionic conductivity

## 1. Introduction

Ion-exchange membranes are widely applied for separation processes, particularly targeted ion extraction from aqueous solutions. Electrochemical technology development and new material generation require the investigation of the ionic transfer mechanism [1–3]. Ion-exchange membrane conductivity is determined by water uptake, charge group nature and polymeric matrix structure [4,5].

The hydration degree of membranes is mainly determined by water coordination to cations. Nuclear magnetic resonance (NMR) techniques provide unique information on the composition of the hydrate complexes and membrane ionic channel framework. The first results of cation hydration in sulfonic cation resins based on sulfonated polystyrene Dowex 50 W and in aqueous acid and salt solutions, as model systems, were published at the end of the 1960s and the beginning of the 1970s just after commercialization of NMR spectrometers [6–10]. It was shown that water molecules in the first hydration sphere of cation are polarized, destroying the hydrogen bond network. Therefore, the water  $^1\text{H}$  NMR line is shifted in a high magnetic field. In the case of the hydrogen ion form, the  $\text{H}^+$  counter ion forms additional hydrogen bonds caused by the low field  $^1\text{H}$  NMR line shift. Hydration cations  $\text{H}(\text{H}_2\text{O})_h^+$  ( $h$  is hydration number) are generated. It was shown that at low humidity in sulfonic cation-exchange resin CU-2 [11], Nafion [12–14] and MF-4SC [15,16] membranes acidic protons form hydroxonium ions  $\text{H}_5\text{O}_2^+$ . The hydration of other cations—for instance, alkaline metal cations—has not been sufficiently studied [15], in spite of it being very important for revelation of membrane ion selectivity mechanism.

For membrane transfer processes investigation, the cation diffusion is especially interesting, as it is directly connected with ionic conductivity. The mobility of water molecules is also very important, since they are directly involved in cations transport [15,17–20]. This leads to a significant dependence of the membrane ionic conductivity on humidity. The diffusion coefficients of water in the ion-exchange membranes decrease by several orders of magnitude with the decreasing of a water uptake  $\lambda$  ( $\lambda$  is amount of water molecules per sulfonate group) if  $\lambda \leq h$  [12,15–18]. Proton conductivity in the Nafion membrane is changed in similar manner [12,21–23]. Pulsed field gradient NMR (PFG NMR) gives a unique opportunity to measure self-diffusion coefficients directly. Till now PFG NMR experiments in membranes were carried out on  $^1\text{H}$  nuclei of water molecules and hydrated  $\text{H}^+$  cations and only their average self-diffusion coefficient was estimated [12,15–18]. In order to determine cation and water molecule self-diffusion coefficients separately, the NMR measurement on cation nuclei like  $^7\text{Li}$ ,  $^{23}\text{Na}$ ,  $^{133}\text{Cs}$  is necessary. It is not simple because of low NMR sensitivity of these nuclei. Therefore, the self-diffusion of  $\text{Li}^+$ ,  $\text{Na}^+$ , and  $\text{Cs}^+$  in ion exchangers is low investigated by PFG NMR technique. Grafted ion-exchange membranes on the basis of manufacturing polymer films are very promising. Cation-exchange membranes based on polyethylene (PE) grafted with sulfonated polystyrene (SPS), which we will call “MSC membranes” in accordance with the originally proposed name [24], have shown excellent transport performance and a high potential for power generation systems such as fuel cells and reverse electro dialysis plants. [24] Hydrophilic segments SPS are formed in hydrophobic PE matrix. Recent years of research have shown that the transport properties of this kind of membranes are not worse than a Nafion membrane [24–26]. The possibility of  $\text{Li}^+$ ,  $\text{Na}^+$ , and  $\text{Cs}^+$  cation diffusion coefficients measurements in grafted ion-exchange membranes by pulsed field gradient NMR on the  $^7\text{Li}$ ,  $^{23}\text{Na}$ , and  $^{133}\text{Cs}$  nuclei was shown for the first time in our previous investigation [27]. Therefore, there is an opportunity to compare the ionic diffusion and conductivity measurements correctly.

The main objective of this work is to characterize hydration, diffusion and conductivity of alkaline metal  $\text{Li}^+$ ,  $\text{Na}^+$ , and  $\text{Cs}^+$  cations in polyethylene membranes with grafted sulfonated polystyrene. To explain the regularities of the transfer processes, a comparative study of the cation hydration and mobility in aqueous solutions of lithium, sodium, and cesium chlorides, as in model systems, has been carried out. The interconnection between cation hydration and diffusion are discussed.

## 2. Materials and Methods

### 2.1. MSC Membrane Synthesis, Ion-Exchange Capacity and Humidity Measurements, and Sample Preparations

Sulfonated cation-exchange membranes were obtained by post-radiation grafting polymerization of styrene on a pre-oxidized low-density PE film with a thickness of 20  $\mu\text{m}$  followed by sulfonation of grafted PS with 96% sulfuric acid at temperature 98  $^\circ\text{C}$ , as described in references [24,27]. To generate

peroxides in a PE film, the latter was irradiated in air at a  $^{60}\text{Co}$   $\gamma$ -radiation source with an irradiation dose power of 5.2 Gy/s to absorbed irradiation doses of 0.05 and 0.1 MGy. Post-radiation chemical-grafting polymerization was carried out in a styrene/methanol mixture (1/1 by volume) containing iron(II) sulfate as a peroxide reducing agent. The degree of PS grafting ( $\Delta p$ ) was calculated from the weight gain of the film.

$$\Delta p = \left[ \frac{(m_1 - m_0)}{m_0} \right] \cdot 100\% \quad (1)$$

where  $m_1$  is the mass of polystyrene grafted sample and  $m_0$  is the mass of the sample (PE film) before grafting.

The measurement of the ion-exchange capacity (IEC, mEq/g) was carried out according to the State Standard GOST 20255.1-89 and GOST 20255.2-89. A sample of the dry cation exchange membrane in proton form was weighed and placed in a dry conical flask with an NaOH solution. The flask was sealed with a stopper and stirred for several hours. The NaOH solution was then poured into a dry beaker, and the sample was titrated with a standard HCl solution. The calculation of IEC was carried out according to the standard procedure. A membrane with IEC of 2.5 mg-eq/g was studied in this work.

To determine the water uptake, the membranes were balanced with saturated salt solutions, after which the membrane was weighed. The membrane was then dried at 80 °C to constant weight in a vacuum created by a foreline pump. The water uptake of the ion exchange membrane was calculated by mass loss, which was characterized by the amount water molecules per sulfonate group ( $\lambda$ )

$$\lambda = \frac{m_{\text{H}_2\text{O}}}{m_{\text{dry}} \cdot M(\text{H}_2\text{O}) \cdot \text{IEC}} \quad (2)$$

where  $m_{\text{H}_2\text{O}}$  and  $m_{\text{dry}}$  are the mass of water in the membrane and mass of the dry membrane and  $M(\text{H}_2\text{O}) = 18 \text{ g/mol}$  is the molar mass of water [12,14,27]. The  $\lambda$  values at different relative humidity RH for  $\text{Li}^+$ ,  $\text{Na}^+$ ,  $\text{Cs}^+$  ionic forms MSC membrane are given in Table 1.

**Table 1.** Water uptake  $\lambda$  at different relative humidity RH for  $\text{Li}^+$ ,  $\text{Na}^+$ , and  $\text{Cs}^+$  ionic forms of MSC membrane.

RH, %	$\lambda$ , $[\text{H}_2\text{O}]/[\text{SO}_3\text{Li}], \text{Li}^+$ Ionic Form	$\lambda$ , $[\text{H}_2\text{O}]/[\text{SO}_3\text{Na}], \text{Na}^+$ Ionic Form	$\lambda$ , $[\text{H}_2\text{O}]/[\text{SO}_3\text{Cs}], \text{Cs}^+$ Ionic Form
12	0.6	0.8	0.0
33	1.4	1.1	1.4
58	3.3	3.1	3.4
75	5.7	3.9	3.7
84	8.1	6.2	6.6
98	23.5	20.9	16.1

To prepare the sample for NMR measurements, the membrane was cut into small strips, weighed, and placed in desiccators containing saturated solutions of salts of  $\text{MgCl}_2$  (RH = 32%),  $\text{NaBr}$  (RH = 58%),  $\text{NaCl}$  (RH = 78%), and  $\text{Na}_2\text{CO}_3$  (RH = 95%). Membrane samples were kept in desiccators until a constant weight. The samples were placed in a standard 5 mm sample tubes, which was hermetically sealed. The measurements were carried out in the 20 °C to 80 °C temperature range.

To standardize membranes in the  $\text{H}^+$  form, the initial samples were kept for 24 h in a 1 M HCl solution and then washed with distilled water. To transfer the membrane to the  $\text{Li}^+$  form, the sample was kept in a 1 M solution of lithium hydroxide (with a tenfold excess) for 24 h, after which it was thoroughly washed with distilled water. The completeness of the conversion to the  $\text{Li}^+$  form was determined by  $^1\text{H}$  NMR spectra.

To transfer the membrane to the Na<sup>+</sup> form, the sample in the Li<sup>+</sup> form was kept in a 1-M solution of sodium chloride (with a tenfold excess) for 24 h, after which it was thoroughly washed with distilled water. The completeness of the conversion to the Na<sup>+</sup> form was determined by <sup>7</sup>Li NMR spectra.

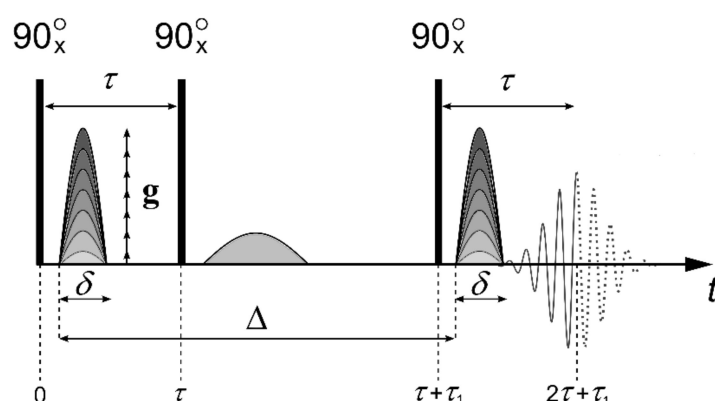
To transfer the membrane to the Cs<sup>+</sup> form, the sample in the Na<sup>+</sup> form was kept for 24 h in a 1-M solution of cesium sulfate or cesium chloride (with a tenfold excess) and thoroughly washed with distilled water. The completeness of the conversion to the Cs<sup>+</sup> form was determined by <sup>23</sup>Na NMR spectra.

## 2.2. Experimental Technique

### 2.2.1. NMR Spectroscopy, Diffusion Coefficient Measurement

High-resolution <sup>1</sup>H, <sup>7</sup>Li, <sup>23</sup>Na, and <sup>133</sup>Cs NMR spectra were recorded with the use of Bruker Avance III-500 and Avance III-400 WB Fourier transform NMR spectrometers (Bruker, Ettlingen, Germany).

Diffusion coefficient (DC) measurement of water molecules and Li<sup>+</sup>, Na<sup>+</sup>, and Cs<sup>+</sup> cations were carried out using a NMR Fourier transform Bruker Avance III-400 WB spectrometer equipped with a pulsed magnetic field gradient probe. The maximum value of the pulsed gradient amplitude was 30 T/m. Diffusion coefficients were measured at frequencies of 400.22, 155.51, 105.84, and 52.48 MHz for <sup>1</sup>H, <sup>7</sup>Li, <sup>23</sup>Na, and <sup>133</sup>Cs nuclei, respectively. The stimulated echo pulse sequence was used to measure diffusion coefficients (Figure 1).



**Figure 1.** Stimulated echo pulse sequence with the magnetic field gradient pulses.

Here,  $\tau$  is the time interval between the first and second radio frequency (RF) pulses,  $\tau_1$  is the time interval between the second and the third pulses,  $\Delta$  is the interval between the gradient pulses,  $\delta$  is duration of the equivalent rectangular magnetic field gradient pulses, and  $g$  is the amplitude of the magnetic field gradient pulse [28].

For the molecules undergoing unhindered isotropic Brownian motion, the evolution of the spin echo signal is described by the following equation:

$$A(2\tau, \tau_1, g) = A(2\tau, \tau_1, 0) \exp(-\gamma^2 g^2 \delta^2 t_d D) \quad (3)$$

where  $\gamma$  is gyromagnetic ratio,  $t_d = \Delta - \delta/3$  is the diffusion time;  $D$  is the diffusion coefficient; and  $\tau$ ,  $\tau_1$ , and  $g$  are parameters explained in Figure 1.

Accordingly,  $A(2\tau, \tau_1, 0)$  is expressed by the following equation:

$$A(2\tau, \tau_1, 0) = \frac{A(0)}{2 \exp(-\frac{2\tau}{T_2} - \frac{\tau_1}{T_1})}$$

where  $A(0)$  is the signal intensity after the first RF pulse (Figure 1).  $T_1$  and  $T_2$  are the spin-lattice and spin-spin relaxation times, respectively. While measuring the echo signal evolution,  $\tau$  and  $\tau_1$  are fixed, and only the dependence  $A$  of as a function of  $g$  is analyzed, which is called the diffusion decay.

In the case of non-exponential decays, the experimental curves

$$A(g) = \frac{A(2\tau, \tau_1, g)}{A(2\tau, \tau_1, 0)}$$

are usually deconvoluted in several exponential components, which are described by Equation (3). For the multiphase system consisting of  $m$  phases in the case of slow (compare to  $t_d$ ) molecular exchange between the phases,

$$A(g) = \sum_{i=1}^m p'_i \exp(-\gamma^2 g^2 \delta^2 t_d D_i) \quad (4)$$

where  $D_i$  is the diffusion coefficient of  $i$ -th component and

$$p'_i = p_i \exp\left(-\frac{2\tau}{T_{2i}} - \frac{\tau_1}{T_{1i}}\right) / \sum_{i=1}^m p_i \exp\left(-\frac{2\tau}{T_{2i}} - \frac{\tau_1}{T_{1i}}\right)$$

$$\sum_{i=1}^m p_i = 1$$

Here,  $p_i$  is the relative amount of the nuclei belong to the molecules characterized by the diffusion coefficient  $D_i$ . The value  $p_i$  is called the population of  $i$ -th phase. For the long  $T_1$  and  $T_2$  values, it is usually assumed that  $p_i \approx p'_i$ . The details of the experimental curve decomposition in several exponential diffusion decays were described previously [27,28].

In the literature, the term “self-diffusion coefficient” is often used for the diffusion coefficient measured by the pulsed field gradient method. We are applying the term “diffusion” because this term is usual among the membrane scientists.

### 2.2.2. Ionic Conductivity Measurement

Ion conductivity was measured using an Elins Z1500J (Chernogolovka, Russia) impedance meter (frequency range 1 kHz–1.5 MHz) on symmetric carbon/membrane/carbon cells with an active surface area  $S$  of 0.5 cm<sup>2</sup>. The conductivity value  $\sigma$  (S·cm<sup>-1</sup>) was calculated from the resistance  $R$  found from the impedance hodographs from the cutoff on the axis of active resistances and the geometric dimensions of the membrane according to the Equation (5) The Binder MKF 115 constant climate chamber was used to set the required humidity and temperature during measurement.

$$\sigma = \frac{l}{S \cdot R} \quad (5)$$

where  $l$  is the membrane thickness in cm,  $S$  is membrane area in cm<sup>2</sup>.

A typical impedance hodograph is shown in Figure S1. We considered the electrical equivalent circuit describing this system in Golubenko, D., Karavanova, Y., Yaroslavtsev’s article [29]. With an increase in the current frequency, the polarizing contribution of diffusion layers decreases, accompanied by a decrease in the real and imaginary parts of the complex resistance. At high frequencies, the imaginary part of the impedance decreases to zero, while the real part of the impedance is equivalent to the membrane’s ohmic resistance. We found the ohmic resistance directly by extrapolating the hodographs to the active resistance axis in this work.



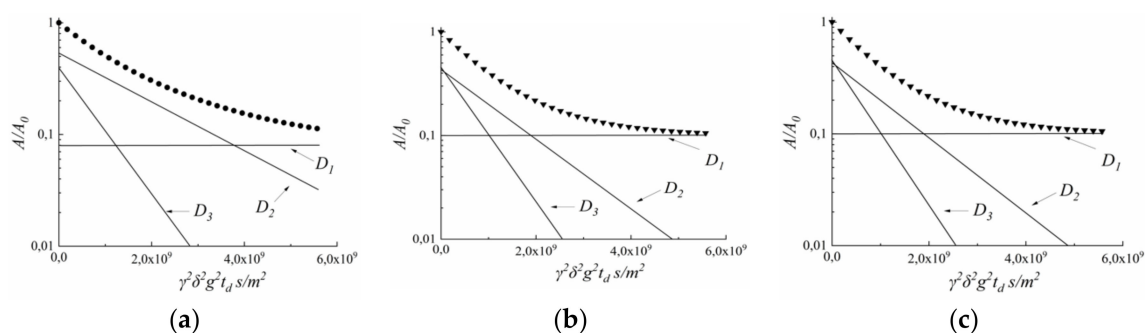
### 3. Results and Discussion

#### 3.1. $^1\text{H}$ , $^7\text{Li}$ , $^{23}\text{Na}$ , $^{133}\text{Cs}$ NMR Spectroscopy. Hydration Numbers

$^1\text{H}$ ,  $^7\text{Li}$ ,  $^{23}\text{Na}$ , and  $^{133}\text{Cs}$  NMR spectra of MSC membranes are represented by narrow lines that belong to water molecules, protons, and  $\text{Li}^+$ ,  $\text{Na}^+$ , and  $\text{Cs}^+$  cations in appropriate ionic forms of the membrane (Figures S2 and S3). A low line width (no more than 1 kHz) indicates high mobility of water and ions in the membranes.  $^1\text{H}$  NMR spectrum of MSC membrane in hydrogen form is represented by two singlet lines (Figure S2).

The line with the highest intensity belongs to the protons of water molecules and hydrated  $\text{H}^+$  cations (in the acidic ionic form of the membrane). The low intensity signal at 2–3 ppm very likely belongs to mobile fragments of polyethylene matrix [27].

Water molecules in MSC membranes are not uniformly distributed. Spin echo attenuation (diffusion decay) of  $^1\text{H}$  nuclei is a non-linear shape it is a sum of three exponential components approximating by Equation (4). The  $^1\text{H}$  diffusion decays in  $\text{Li}^+$ ,  $\text{Na}^+$ , and  $\text{Cs}^+$  ionic forms of MSC membrane at RH = 95% are shown in Figure 2.



**Figure 2.** Spin echo attenuation (diffusion decay) of water molecule  $^1\text{H}$  nuclei in  $\text{Li}^+$  ionic form (a),  $\text{Na}^+$  ionic form (b) and  $\text{Cs}^+$  ionic form (c) of MSC membrane; RH = 95%, T = 293K. Dots are experimental curves; straight lines are decomposition on  $D_1$ ,  $D_2$ ,  $D_3$  components from Equation (4). Components of diffusion coefficients  $D_1$ ,  $D_2$ , and  $D_3$  and relative parts  $p_1$ ,  $p_2$ , and  $p_3$  are the next. For  $\text{Li}^+$  ionic form, MSC  $D_1 = (2.4 \pm 0.5) \cdot 10^{-13} \text{ m}^2/\text{s}$ ,  $D_2 = (5.0 \pm 0.5) \cdot 10^{-10} \text{ m}^2/\text{s}$ ,  $D_3 = (1.3 \pm 0.5) \cdot 10^{-9} \text{ m}^2/\text{s}$  and  $(0.08 \pm 0.01)$ ,  $(0.53 \pm 0.05)$ ,  $(0.39 \pm 0.05)$ , correspondingly. For  $\text{Na}^+$  ionic form, MSC  $(4.5 \pm 0.5) \cdot 10^{-13} \text{ m}^2/\text{s}$ ,  $(7.8 \pm 1) \cdot 10^{-10} \text{ m}^2/\text{s}$ ,  $(1.5 \pm 0.5) \cdot 10^{-9} \text{ m}^2/\text{s}$  and  $(0.1 \pm 0.015)$ ,  $(0.44 \pm 0.05)$ ,  $(0.46 \pm 0.05)$ , correspondingly. For  $\text{Cs}^+$  ionic form MSC  $D_1 = (3.4 \pm 0.3) \cdot 10^{-13} \text{ m}^2/\text{s}$ ,  $D_2 = (1.1 \pm 0.2) \cdot 10^{-9} \text{ m}^2/\text{s}$ ,  $D_3 = (1.7 \pm 0.2) \cdot 10^{-9} \text{ m}^2/\text{s}$ , and  $(0.13 \pm 0.1)$ ,  $(0.49 \pm 0.05)$ ,  $(0.38 \pm 0.04)$ , correspondingly.

Component with the least diffusion coefficient  $D_1$   $(2.4\text{--}4.5) \times 10^{-13} \text{ m}^2/\text{s}$  belongs to signal at 2–3 ppm (Figure S2). It may be proposed that this signal is due to the low molecular weight of polyethylene fragments arising during  $\gamma$ -irradiation.

Diffusion coefficients  $D_2$  and  $D_3$  ( $10^{-10}$ – $10^{-9} \text{ m}^2/\text{s}$ ) are typical of water molecules (or hydrated cation  $\text{H}^+$  in acid ionic form of MSC membrane). The existence of water molecules with different translation mobility denotes on membrane heterogeneity.

The diffusion coefficient  $D_3$  practically does not depend on the type of cation and is  $(1.3\text{--}1.7) \times 10^{-9} \text{ m}^2/\text{s}$ , which is close to the diffusion coefficient of bulk water ( $2.4 \times 10^{-9} \text{ m}^2/\text{s}$ ). These water molecules are rather far from cations are probably belong to the so-called “uncharged solution” in the wide membrane pores. We suppose that translation mobility of water molecules coordinated by cation is partially characterized by diffusion coefficient  $D_2$ . Thermogravimetry techniques enable us to calculate the integral water uptake  $\lambda$  only. The number of water molecules connected with cation  $\lambda_s$  may be calculated as the product of its relative part, and  $\lambda$ :  $\lambda_s = p_2 \lambda / (p_2 + p_3)$ . Namely,  $\lambda_s$  values are using for cation hydration number  $h$  calculation.

Let us mention some features of low field  $^1\text{H}$  signal in  $\text{H}^+$  form of MSC membrane. The NMR line width increases, and the line center position is shifted to the low field with humidity and temperature decrease. This chemical shift is larger compare to bulk water, which indicates proton hydration with the formation of  $\text{H}(\text{H}_2\text{O})^+_h$  [27].

In contrast to the hydrogen form, in salt forms of MSC membranes, the  $^1\text{H}$  NMR line is shifted to strong fields. This is due to the fact that water molecules located in the first coordination sphere of cations do not act as acceptors of hydrogen bonds and turn out to be less polarized compared to bulk water molecules forming a hydrogen bond network. Consequently, the hydrogen bond network is partially destroyed [15].

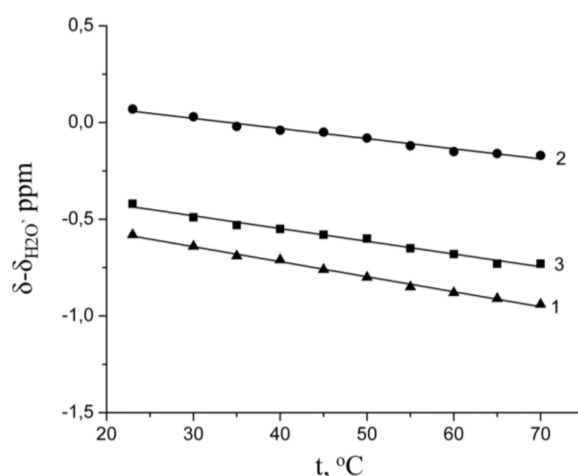
The fast exchange takes place between water molecules in the first hydrated spheres of cation and other water molecules. Therefore, the observed  $^1\text{H}$  signal is singlet of which chemical shift  $\delta$  may be approximate as [7,10]

$$\delta = \frac{\delta_h \cdot h}{\lambda_s} + \frac{\delta_{\text{H}_2\text{O}} \cdot (\lambda_s - h)}{\lambda_s} \tag{6}$$

where  $h$  is the hydration number,  $\lambda_s$  is the water molecule amount per cation (sulfonated group), which we have calculated above from Figure 2. Keeping in mind that  $\delta_h$  is temperature-independent because of water molecules in the first cation hydrated sphere polarization, we have the next equation for chemical shift temperature dependence:

$$\frac{d\delta}{dt} = \frac{(\lambda_s - h)}{\lambda_s} \frac{d\delta_{\text{H}_2\text{O}}}{dt} \tag{7}$$

which is presented by a straight line (Figure 3)



**Figure 3.** Chemical shift of water molecule  $^1\text{H}$  nuclear temperature dependences in  $\text{Li}^+$ (1),  $\text{Na}^+$ (2)  $\text{Cs}^+$ (3) ionic forms at RH = 95%.

From the  $^1\text{H}$  chemical shift, the temperature dependences the hydration numbers  $h$  of  $\text{Li}^+$ ,  $\text{Na}^+$ , and  $\text{Cs}^+$  cations in MSC membrane were calculated for the first time using Equation (8) [7,10].

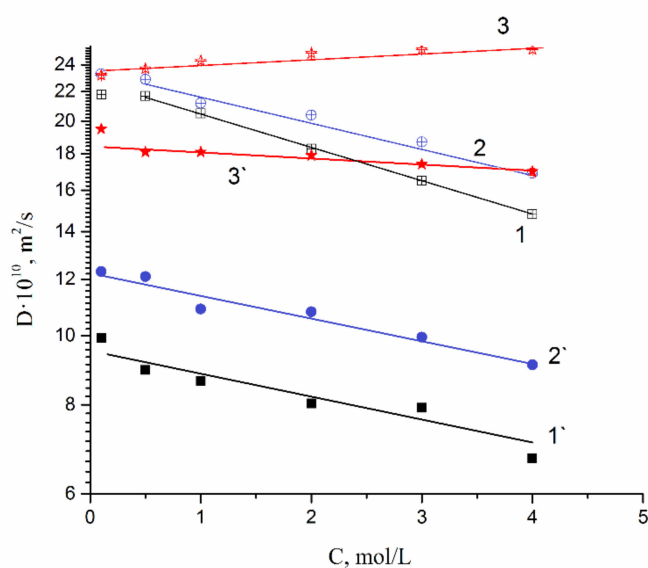
$$h = \lambda_s \left[ 1 - \frac{\frac{d\delta}{dt}}{\frac{d\delta_{\text{H}_2\text{O}}}{dt}} \right] \tag{8}$$

where  $d\delta/dt$  is a chemical shift temperature dependence of membrane water,  $b$  is the slope of  $d\delta/dt$  temperature dependence, which are 0.0068, 0.0052, 0.0066 for  $\text{Li}^+$ ,  $\text{Na}^+$ , and  $\text{Cs}^+$  ionic forms, correspondingly;  $d\delta_{\text{H}_2\text{O}}/dt$  is the a chemical shift temperature dependence of bulk water,  $b$  is 0.01 [8].

Hydration numbers  $h$  of  $\text{Li}^+$ ,  $\text{Na}^+$ , and  $\text{Cs}^+$  are shown in Table 2. The hydration numbers for same cations in equimolar aqueous salt chloride solutions and membrane water uptakes are also shown for comparison. The  $h$  values of  $\text{Li}^+$ ,  $\text{Na}^+$ , and  $\text{Cs}^+$  in MSC membranes at high humidity is practically equal to salt solution ones. The crystallography radii and Stokes–Einstein hydrodynamic ion radii are also presented in Table 2. We have calculated hydrodynamic ion radii from the Stokes–Einstein equation on the basis of ionic diffusion coefficient in chloride aqueous solution. Ion diffusion coefficient concentration dependences (Figure 4) were approximated to an infinite dilute concentration.

**Table 2.** Crystallography radii, Stokes–Einstein hydrodynamic ion radii, and hydration numbers ( $h$ ) of  $\text{Li}^+$ ,  $\text{Na}^+$ , and  $\text{Cs}^+$  cations in appropriate MSC membrane ionic forms at RH = 95% and in equimolar aqueous salt chloride solutions.

Cation	$\text{Li}^+$	$\text{Na}^+$	$\text{Cs}^+$
Crystallography ionic radius, Å [30]	0.69	1.02	1.67
Stokes-Einstein hydrodynamic ionic radius, Å [31]	2.38	1.84	1.19
Stokes-Einstein hydrodynamic radius, estimated from ionic diffusion coefficient in chloride aqueous solution at infinite dilute concentration	2.7	2.2	1.5
Total water uptake of membrane ( $\lambda$ )	24	21	16
Water amount per membrane sulfonate group ( $\lambda_s$ )	13.8	10.3	8.1
Hydration number of cations ( $h$ ) in membrane	$4.1 \pm 1$	$5.0 \pm 1$	$3.1 \pm 1$
Hydration number of cations ( $h$ ) in aqueous solution [7,8]	4	4.6	3.9

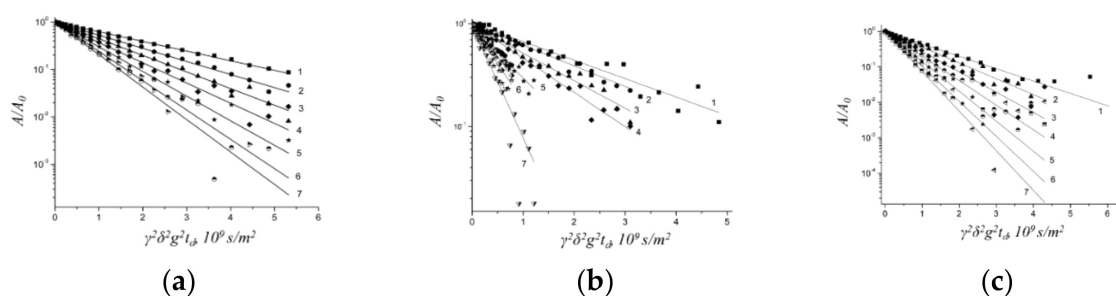


**Figure 4.** Water molecule and cation diffusion coefficient concentration dependences in lithium, sodium, cesium chloride aqueous solutions. 1– $\text{H}_2\text{O}$  in  $\text{LiCl}$ , 2– $\text{H}_2\text{O}$  in  $\text{NaCl}$ , 3– $\text{H}_2\text{O}$  in  $\text{CsCl}$ . 1’– $\text{Li}^+$  in  $\text{LiCl}$ , 2’– $\text{Na}^+$  in  $\text{NaCl}$ , 3’– $\text{Cs}^+$  in  $\text{CsCl}$ .

### 3.2. Diffusion of $\text{Li}^+$ , $\text{Na}^+$ , and $\text{Cs}^+$ Cations and Ionic Conductivity

#### 3.2.1. Diffusion of $\text{Li}^+$ , $\text{Na}^+$ , and $\text{Cs}^+$ Cations in MSC Membrane

Spin echo attenuation (diffusion decay) of  $^7\text{Li}^+$ ,  $^{23}\text{Na}^+$ , and  $^{133}\text{Cs}^+$  is exponential in salt ionic form of MSC membrane. Diffusion decay is well approximated by Equation (3) (Figure 5).

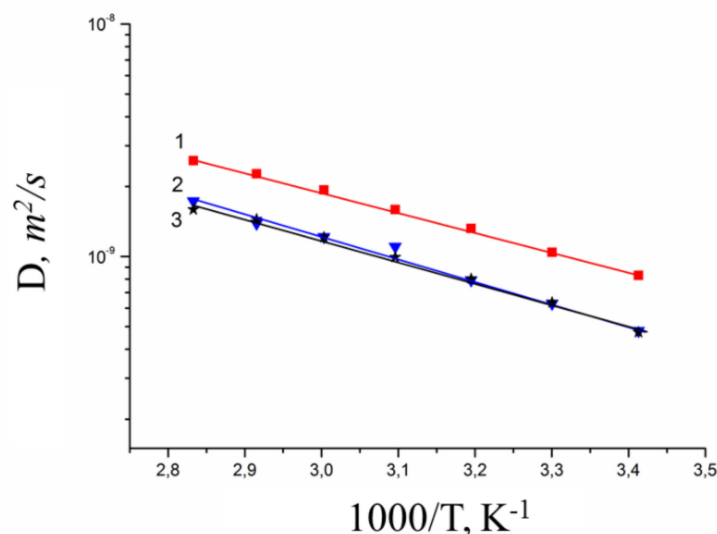


**Figure 5.** Diffusion decays of  ${}^7\text{Li}$  (a),  ${}^{23}\text{Na}$  (b),  ${}^{133}\text{Cs}$  (c) nuclei NMR signals in appropriate ionic form of MSC membrane at RH = 95% and different temperatures 1–20 °C, 2–30 °C, 3–40 °C, 4–50 °C, 5–60 °C, 6–70 °C, 7–80 °C.

Diffusion coefficient temperature dependences are shown in Figure 6. These dependences are linearized in the coordinates of the Arrhenius equation,

$$D = D_0 \cdot e^{-\frac{E_a}{RT}} \tag{9}$$

where  $D_0$  is temperature independent,  $R$  is gas constant,  $T$  is absolute temperature,  $E_a$  is a diffusion activation energy.



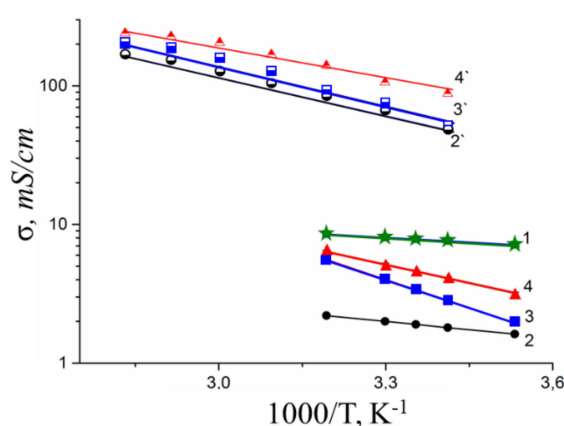
**Figure 6.** Temperature dependences of Cs<sup>+</sup>, Na<sup>+</sup>, and Li<sup>+</sup> diffusion coefficients in appropriate ionic form of MSC membrane at RH = 95%: 1–Cs<sup>+</sup> ionic form,  $E_a = 18.1$  kJ/mol; 2–Na<sup>+</sup> ionic form,  $E_a = 16.5$  kJ/mol; 3–Li<sup>+</sup> ionic form,  $E_a = 17.6$  kJ/mol.

Cation diffusion coefficients increase in a sequence  $\text{Li}^+ \approx \text{Na}^+ < \text{Cs}^+$ . This row is the same for cation diffusion coefficients of chloride aqueous solutions (Figure 4). Cation diffusion activation energies are about 16–18 kJ/mol.

### 3.2.2. Ionic Conductivity of MSC Membrane

Temperature dependences of ionic conductivity of different ionic forms of MSC membranes are shown in Figure 7.

The conductivity values at different humidity and activation energies calculated from Arrhenius equation are listed in Table 3.



**Figure 7.** Temperature dependences of experimental  $\sigma_{\text{exp}}$  (1–4) and calculated  $\sigma_{\text{calc}}$  (2’–4’) ionic conductivities in  $\text{H}^+$  (1),  $\text{Li}^+$  (2) and (2’),  $\text{Na}^+$  (3) and (3’), and  $\text{Cs}^+$  (4) and (4’) ionic forms of MSC membrane at RH = 95%.

**Table 3.** Experimental values of ionic conductivity at 25 °C and conductivity activation energies of  $\text{H}^+$ ,  $\text{Li}^+$ ,  $\text{Na}^+$ , and  $\text{Cs}^+$  cations in MSC membrane with different humidity. IEC = 2.5 mg-eq/g.

Ionic Form	RH, %		95		75		58		32	
	Ea, $\text{kJ}\cdot\text{mol}^{-1}$	$\sigma_{\text{exp}}$ $\text{mS}\cdot\text{cm}^{-1}$	Ea, $\text{kJ}\cdot\text{mol}^{-1}$	$\sigma_{\text{exp}}$ $\text{mS}\cdot\text{cm}^{-1}$	Ea, $\text{kJ}\cdot\text{mol}^{-1}$	$\sigma_{\text{exp}}$ $\text{mS}\cdot\text{cm}^{-1}$	Ea, $\text{kJ}\cdot\text{mol}^{-1}$	$\sigma_{\text{exp}}$ $\text{mS}\cdot\text{cm}^{-1}$	Ea, $\text{kJ}\cdot\text{mol}^{-1}$	$\sigma_{\text{exp}}$ $\text{mS}\cdot\text{cm}^{-1}$
H	4.3	7.8	11	6	12	3	23	0.6		
Li	7.5	1.9	30	0.5	39	0.2	52	0.008		
Na	26	3.4	31	0.7	40	0.2	68	0.01		
Cs	17	4.6	32	0.8	37	0.3	60	0.02		

Ionic conductivity of investigated membranes increases in the sequence  $\text{Li}^+ < \text{Na}^+ < \text{Cs}^+ \ll \text{H}^+$ . It should be noted that the diffusion coefficients of lithium, sodium, and cesium cations in MSC and in aqueous solutions change in the same sequence. Ionic conductivities ( $\sigma_{\text{calc}}$ ) of MSC membranes were calculated using Nernst–Einstein Equation (10).

$$\sigma_{\text{calc}} = \frac{N \cdot D \cdot e^2}{k \cdot T} \tag{10}$$

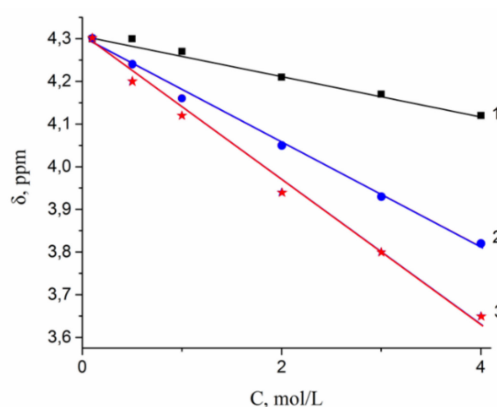
where  $N$  is a number of charge carrier in  $\text{cm}^3$ ;  $D$  is diffusion coefficient,  $\text{m}^2/\text{s}$ ;  $e$  is electron charge,  $1.9 \times 10^{-19}$  C;  $k$ -Boltzmann constant,  $1.38 \times 10^{-23}$  J/K;  $T$  is absolute temperature, K.

As shown in Figure 7, the calculated and experimental conductivity curve are similar. Conductivity activation energies of alkaline metal cations are close to each other. However, the calculated conductivity values are one or two orders of magnitude more in comparison with experimental ones. This difference seems natural. Ionic transport in membranes is realized through the system of channels and pores, which size is depended on polymeric matrix nature and hydration degree. So, for example, in accordance with the well-known Gierke model, at high humidity, the size of pores in perfluorinated membranes of the Nafion type is 4–5 nm. At the same time, the diameter of the channels connecting them is much smaller and is about 2 nm [32,33]. It is well known that ionic conductivity is limited by the transport of ions in the narrow channels. They are usually called the “bottle neck” [34] Ionic transfer in narrow channels namely limits a membrane ionic conductivity [35]. It may be supposed that the diffusion coefficient measured by NMR in the first turn is due to high mobility ions localized in wide pores [27]. Indeed, simple estimation shows that the volume of water in the pores of the Nafion membranes is about an order of magnitude higher than in the channels connecting them. The concentration of cations in membrane’s pore solution increases with decreasing of surrounding relative humidity. The fixed

$-\text{SO}_3^-$  groups are much less hydrated compared to cations. From this point of view, it will be sensible to investigate the chemical shifts and diffusion coefficients of water and cation in aqueous chloride solutions depending on concentration as in a simple model system.

### 3.2.3. $\text{Li}^+$ , $\text{Na}^+$ , and $\text{Cs}^+$ Hydration and Diffusion in Chloride Aqueous Solutions

A dependence of  $^1\text{H}$  water molecule chemical shift on solution concentration is shown in Figure 8. Proton signal shifts to the high field with chloride concentration increasing. This fact is explained by destroying of hydrogen bonds between water molecules [7,8,15,36]. This phenomenon is stronger for the  $\text{CsCl}$  solution, since  $\text{Cs}^+$  possesses low polarizing properties (due to the large ion size), which causes the hydrogen bond system to be destroyed.



**Figure 8.**  $^1\text{H}$  chemical shift dependences on concentration of  $\text{LiCl}$  (1),  $\text{NaCl}$  (2), and  $\text{CsCl}$  (3) aqueous solutions.

As a result, water molecule translational mobility should increase with increasing concentration, which is observed experimentally (curve 3 in Figure 8).

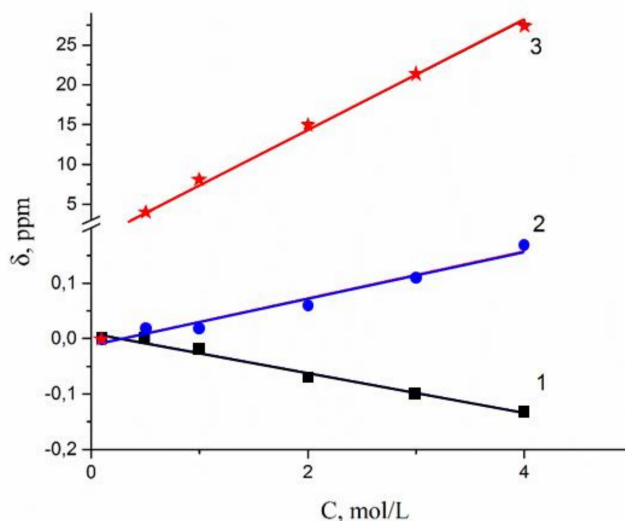
The water molecules and cation diffusion coefficient increase with alkaline metal atomic mass increase. The mobility of cations increases in the sequence  $\text{Li}^+$ ,  $\text{Na}^+$ , and  $\text{Cs}^+$  due to an increase in the water mobility and due to a decrease in the effective radius of the hydrated cation. Both of these phenomena are associated with decreasing the hydration energy in the same order. It is important to note that, in contrast to the data obtained for membranes, the diffusion coefficients of dilute solutions found using NMR practically coincide with the diffusion coefficients described in the literature on the base of ion conductivity data [37]. This emphasizes that the discrepancy between the data for membranes is determined by the difference in the nature of the ion mobility founded by NMR and conductometry. NMR data characterize the ion mobility in the pores of the membrane, but ionic conductivity is limited by the transfer in narrower channels.

It should be mentioned that  $\text{Li}^+$ ,  $\text{Na}^+$  and water diffusion coefficients are reduced greater compared to  $\text{Cs}^+$  ion for which water diffusion coefficient even increases with an increase in electrolyte concentration (curves 1', 2'; 1, 2 (Figure 4) and curves 3', 3 (Figure 4)). The water hydrogen bond network is destroying to a greater extent with increasing in  $\text{Cs}^+$  concentration. As contrasted to  $\text{Cs}^+$ , hydration energy of  $\text{Li}^+$  and  $\text{Na}^+$  ions is more. Therefore, the mobility of water molecules connected with these cations drops and water diffusion coefficient is reduced with the rise in salt concentration.

Now, the reason for the decrease in the diffusion coefficients of cations with an increase in the concentration of solutions should be considered. To understand this, it is worth noting that water molecules are bound by both cations and anions, forming a more or less ordered environment of water molecules around them. To implement the cation transfer, it must destroy its coordination environment and form a new one. Obviously, the formation of a new environment is difficult when the ordered environment of another ion is located nearby. The higher the concentration of the solution, the higher the fraction of relatively tightly bound water molecules surrounded by cations, the more difficult the

process of ion transfer is. In aqueous solutions, this is expressed in a clearly pronounced tendency toward a decrease in the activity coefficient of ions with an increase in their concentration.

In Figure 9,  ${}^7\text{Li}$ ,  ${}^{23}\text{Na}$ , and  ${}^{133}\text{Cs}$  nuclei chemical shift concentration dependences are shown. This dependence is stronger for  ${}^{133}\text{Cs}$ . Chemical shift increases (compare to  ${}^7\text{Li}$ ,  ${}^{23}\text{Na}$ ), while CsCl concentration is varied from 1 mol/L to 4 mol/L (curve 3, Figure 9).



**Figure 9.**  ${}^7\text{Li}$  (1),  ${}^{23}\text{Na}$  (2), and  ${}^{133}\text{Cs}$  (3) nuclear NMR chemical shift concentration dependences in lithium, sodium, cesium chloride aqueous solutions.

The chemical shift of these nuclei is determined by nuclear quadrupole moment interaction with electric field gradient, created by nearest hydrated water molecules. Lithium and sodium cations form of rather stable and symmetric complexes. Therefore, an electric field symmetry and a nuclear chemical shift are changed slightly with concentration variation (curves 1,2 Figure 9). Cesium cation surrounding is not stable because of a weak bond  $\text{Cs}^+$  with water molecules. With an increase of CsCl solution concentration, the symmetry of the surrounding  $\text{Cs}^+$  decreases; this is a reason for the increase of the  ${}^{133}\text{Cs}$  chemical shift (curve 3, Figure 9).

#### 4. Conclusions

The comparison of hydration, diffusion, and ionic conductivity in MSC membranes and chloride aqueous solutions shows that in high humidity membrane (RH = 95%) hydration numbers of  $\text{Li}^+$ ,  $\text{Na}^+$ , and  $\text{Cs}^+$  is closed to those in dilute aqueous solutions. Cation diffusion coefficients and ionic conductivity increase in a sequence of  $\text{Li}^+ < \text{Na}^+ < \text{Cs}^+$ . The conductivity values calculated from the NMR diffusion coefficients using the Nernst–Einstein equation are essentially higher than experimentally determined ones. These results are discussed on the basis of  ${}^1\text{H}$ ,  ${}^7\text{Li}$ ,  ${}^{23}\text{Na}$ , and  ${}^{133}\text{Cs}$  chemical shift and water molecule and  $\text{Li}^+$ ,  $\text{Na}^+$ , and  $\text{Cs}^+$  cation diffusion coefficient experimental dependences in chloride aqueous solutions. In contrast to the data obtained for membranes, the diffusion coefficients of dilute solutions measured by NMR practically coincide with the diffusion coefficients described in the literature, calculated from ion conductivity data. This emphasizes that the discrepancy between the experimental and calculated conductivities for membranes is determined by the difference in the nature of the ionic mobilities determined by NMR and conductometry. NMR characterizes the ion mobility in the wide pores of the membrane, but ionic conductivity is limited by the ion transfer in narrow channels.

**Supplementary Materials:** The following are available online at <http://www.mdpi.com/2077-0375/10/10/272/s1>, Figure S1: (A) EEC for a conductor with predominantly ionic conduction Figure S1 A - EEC for a conductor with predominantly ionic conduction; (B) Typical Nyquist plot of MSC-membrane. Here is Cs-form at 75%

RH; Figure S2:  $^1\text{H}$  NMR spectrum in  $\text{H}^+$  ionic form of MSC membrane at RH = 95% and T = 293K; Figure S3: NMR spectra of  $^7\text{Li}$  (a),  $^{23}\text{Na}$  (b) and  $^{133}\text{Cs}$  (c) nuclei in appropriate ionic form of MSC membrane at RH = 95%.

**Author Contributions:** Study of ionic conductivity, A.B.Y., D.V.G. Membrane synthesis, V.A.T. Carried out NMR studies, V.I.V., A.V.C., G.A.L., E.S.O. All authors have read and agreed to the published version of the manuscript.

**Funding:** This work was supported by the Russian Foundation for Basic Research (project no. 18-08-00423 A). NMR measurements were performed using equipment of the Multi-User Analytical Center of the Institute of Problems of Chemical Physics RAS and Science Center in Chernogolovka RAS with the support of State Assignment of the Institute of Problems of Chemical Physics RAS (state registration nos. AAAA-A19-119071190044-3 and AAAA-A19-119071190017-7).

**Acknowledgments:** The studies of ionic conductivity were performed using equipment at the Center for Collective Use of the Kurnakov Institute (Moscow, Russia), functioning with the support of the State Assignment of the Kurnakov Institute in the field of fundamental scientific research.

**Conflicts of Interest:** The authors declare no conflict of interest.

## References

1. Wenten, I.G.; Khoiruddin, K.; Aryanti, P.T.P.; Hakim, A.N. Scale-up Strategies for Membrane-Based Desalination Processes: A Review. *J. Membr. Sci. Res.* **2016**, *2*, 42–58.
2. Campione, A.; Gurreri, L.; Ciofalo, M.; Micale, G.; Tamburini, A.; Cipollina, A. Electrodialysis for water desalination: A critical assessment of recent developments on process fundamentals, models and applications. *Desalination* **2018**, *434*, 121–160. [[CrossRef](#)]
3. Luo, T.; Abdu, S.; Wessling, M. Selectivity of ion exchange membranes: A review. *J. Membr. Sci.* **2018**, *555*, 429–454. [[CrossRef](#)]
4. Luo, X.Y.; Holdcroft, S. Water transport through short side chain perfluorosulfonic acid ionomer membranes. *J. Membr. Sci.* **2016**, *520*, 155–165. [[CrossRef](#)]
5. Prikhno, I.A.; Safronova, E.Y.; Stenina, I.A.; Yurova, P.A.; Yaroslavtsev, A.B. Dependence of the Transport Properties of Perfluorinated Sulfonated Cation-Exchange Membranes on Ion-Exchange Capacity. *Membr. Membr. Technol.* **2020**, *2*, 265–271. [[CrossRef](#)]
6. Knapp, P.S.; Waite, R.O.; Malinowski, E.R. NMR Studies of Aqueous Electrolyte Solutions. Hydration of Sodium Perchlorate, Hydrochloric Acid, and Perchloric Acid from Temperature Effects on Proton Shifts. *J. Chem. Phys.* **1968**, *49*, 5459–5463. [[CrossRef](#)]
7. Creekmore, R.W.; Reilley, C.N. Nuclear Magnetic Resonance Determination of Hydration Numbers of Electrolytes in Concentrated Aqueous Solutions. *J. Phys. Chem.* **1969**, *73*, 1563–1568. [[CrossRef](#)]
8. Malinowski, E.R.; Knapp, P.S.; Feuer, B. NMR Studies of Aqueous Electrolyte Solutions. I. Hydration Number of NaCl Determined from Temperature Effects on Proton Shift. *J. Chem. Phys.* **1966**, *45*, 4274–4279. [[CrossRef](#)]
9. Creekmore, R.W.; Reilley, C.N. Nuclear Magnetic Resonance Study of Ion-Exchange Resins. *Anal. Chem.* **1970**, *42*, 570–575. [[CrossRef](#)]
10. Gough, T.E.; Sharma, H.D.; Subramanian, N. Proton magnetic resonance studies of ionic solvation in ion-exchange resins. Part, I. Sulfonated cation-exchange resins. *Can. J. Chem.* **1970**, *48*, 917–923. [[CrossRef](#)]
11. Khutsishvili, V.G.; Bogachev, Y.S.; Volkov, V.I.; Serebryanskaya, A.I.; Shapet'ko, N.N.; Timashev, S.F.; Orman, M.L. Water state investigation in sulfocationite CU-2 phase by proton magnetic resonance technique. *Russian. J. Phys. Chem.* **1983**, *57*, 2524–2527.
12. Chernyak, A.V.; Vasiliev, S.G.; Avilova, I.A.; Volkov, V.I. Hydration and Water Molecules Mobility in Acid Form of Nafion Membrane Studied by  $^1\text{H}$  NMR Techniques. *Appl. Magn. Reson.* **2019**, *50*, 677–693. [[CrossRef](#)]
13. Iwamoto, R.; Oguro, K.; Sato, M.; Iseki, Y. Water in perfluorinated, sulfonic acid Nafion membranes. *J. Phys. Chem. B* **2002**, *106*, 6973–6979. [[CrossRef](#)]
14. Maldonado, L.; Perrin, J.-C.; Dillet, J.; Lottin, O. Characterization of polymer electrolyte Nafion membranes: Influence of temperature, heat treatment and drying protocol on sorption and transport properties. *J. Membr. Sci.* **2012**, *389*, 43–56. [[CrossRef](#)]
15. Volkov, V.I.; Marinin, A.A. NMR methods for studying ion and molecular transport in polymer electrolytes. *Russ. Chem. Rev.* **2013**, *82*, 248–272. [[CrossRef](#)]
16. Volkov, V.I.; Vasilyak, S.L.; Park, I.W.; Kim, H.J.; Ju, H.; Volkov, E.V.; Choh, S.H. Water behavior in perfluorinated ion-exchange membranes. *Appl. Magn. Reson.* **2003**, *25*, 43–53. [[CrossRef](#)]



17. Guillermo, A.; Gebel, G.; Mendil-Jakani, H.; Pinton, E. NMR and Pulsed Field Gradient NMR Approach of Water Sorption Properties in Nafion at Low Temperature. *J. Phys. Chem. B* **2009**, *113*, 6710–6717. [[CrossRef](#)]
18. Ma, Z.; Jiang, R.; Myers, M.E., Jr.; Thompson, E.L.; Gittleman, C.S. NMR studies of proton transport in fuel cell membranes at sub-freezing conditions. *J. Mater. Chem.* **2011**, *21*, 9302–9311. [[CrossRef](#)]
19. Mendil-Jakani, H.; Pouget, S.; Gebel, G.; Pintauro, P.N. Insight into the multiscale structure of pre-stretched recast Nafion (R) membranes: Focus on the crystallinity features. *Polymer* **2015**, *63*, 99–107. [[CrossRef](#)]
20. Stenina, I.A.; Yaroslavtsev, A.B. Low- and intermediate-temperature proton-conducting electrolytes. *Inorg. Mater.* **2017**, *53*, 253–262. [[CrossRef](#)]
21. Nicotera, I.; Coppola, L.; Rossi, C.O.; Youssry, M.; Ranieri, G.A. NMR Investigation of the Dynamics of Confined Water in Nafion-Based Electrolyte Membranes at Subfreezing Temperatures. *J. Phys. Chem. B* **2009**, *113*, 13935–13941. [[CrossRef](#)] [[PubMed](#)]
22. Moster, A.L.; Mitchell, B.S. Hydration and Proton Conduction in Nafion/Ceramic Nanocomposite Membranes Produced by Solid-State Processing of Powders from Mechanical Attrition. *J. Appl. Polym. Sci.* **2009**. [[CrossRef](#)]
23. Thompson, E.L.; Capehart, T.W.; Fuller, T.J.; Jorne, J. Investigation of low-temperature proton transport in Nafion using direct current conductivity and differential scanning calorimetry. *J. Electrochem. Soc.* **2006**, *153*, A2351–A2362. [[CrossRef](#)]
24. Safronova, E.Y.; Golubenko, D.V.; Shevlyakova, N.V.; D’Yakova, M.G.; Tverskoi, V.A.; Dammak, L.; Grande, D.; Yaroslavtsev, A.B. New cation-exchange membranes based on cross-linked sulfonated polystyrene and polyethylene for power generation systems. *J. Membr. Sci.* **2016**, *515*, 196–203. [[CrossRef](#)]
25. Jannasch, P.; Weiber, E.A. Configuring Anion Exchange Membranes for High Conductivity and Alkaline Stability by Using Cationic Polymers with Tailored Side Chains. *Macromol. Chem. And Phys.* **2016**, *217*, 1108–1118.
26. Oh, K.; Ketpang, K.; Kim, H.; Shanmugam, S. Synthesis of sulfonated poly(arylene ether ketone) block copolymers for proton exchange membrane fuel cells. *J. Membr. Sci.* **2016**, *507*, 135–142. [[CrossRef](#)]
27. Volkov, V.I.; Chernyak, A.V.; Golubenko, D.V.; Shevlyakova, N.V.; Tverskoy, V.A.; Yaroslavtsev, A.B. Mobility of Cations and Water Molecules in Sulfocation-Exchange Membranes Based on Polyethylene and Sulfonated Grafted Polystyrene. *Membr. Membr. Tech.* **2020**, *2*, 54–62. [[CrossRef](#)]
28. Avilova, I.A.; Smolina, A.V.; Kotelnikov, A.I.; Kotelnikova, R.A.; Loskutov, V.V.; Volkov, V.I. Self-diffusion of Water and Blood Lipids in Mouse Erythrocytes. *Appl. Magn. Reson.* **2016**, *47*, 335–347. [[CrossRef](#)]
29. Golubenko, D.; Karavanova, Y.; Yaroslavtsev, A. Effects of the surface layer structure of the heterogeneous ion-exchange membranes on their impedance. *J. Electroanal. Chem.* **2016**, *777*, 1–7. [[CrossRef](#)]
30. Shannon, R.D.; Prewitt, C.T. Effective ionic radii in oxides and fluorides, *Acta Crystallogr. Sect. B Struct. Crystallogr. Cryst. Chem.* **1969**, *25*, 925–946. [[CrossRef](#)]
31. Nightingale, E.R. Phenomenological theory of ion solvation. Effective radii of hydrated ions. *J. Phys. Chem.* **1959**, *63*, 1381–1387. [[CrossRef](#)]
32. Gierke, T.D.; Munn, G.E.; Wilson, F.C. Ion transfer in and through charged membranes. Structure, properties, theory. *Sci. Polym. Phys.* **1981**, *19*, 1687–1704. [[CrossRef](#)]
33. Nikonenko, V.V.; Yaroslavtsev, A.B.; Pourcelly, G.; Ciferri, A. *Ionic Interactions in Natural and Synthetic Macromolecules*; Ciferri, A., Perico, A., Eds.; John Wiley & Sons, Inc.: Hoboken, NJ, USA, 2012; pp. 267–335.
34. Yaroslavtsev, A.B. Solid electrolytes: Main prospects of research and development. *Russ. Chem. Rev.* **2016**, *85*, 1255–1276. [[CrossRef](#)]
35. Yaroslavtsev, A.B.; Stenina, I.A.; Golubenko, D.V. Membrane materials for energy production and storage. *Pure Appl. Chem.* **2020**. [[CrossRef](#)]
36. Voropaeva, E.Y.; Sanginov, E.A.; Volkov, V.I.; Pavlov, A.A.; Shalimov, A.S.; Stenina, I.A.; Yaroslavtsev, A.B. Transport Properties of MF-4SK Membranes Modified with Inorganic Dopants. *Russ. J. Inorg. Chem.* **2008**, *53*, 1536–1541. [[CrossRef](#)]
37. Lide, D.R. *CRC Handbook of Chemistry and Physics*; CRC Press: Boca Raton, FL, USA, 2004; p. 2660.



Article

# Impact of MWCO and Dopamine/Polyethyleneimine Concentrations on Surface Properties and Filtration Performance of Modified Membranes

Mariane Carolina Proner<sup>1</sup>, Ingrid Ramalho Marques<sup>1</sup>, Alan Ambrosi<sup>1</sup> , Katia Rezzadori<sup>1,†</sup>,  
Cristiane da Costa<sup>2</sup>, Guilherme Zin<sup>1</sup>, Marcus Vinícius Tres<sup>3,\*</sup>  and Marco Di Luccio<sup>1,\*</sup> 

<sup>1</sup> Laboratory of Membrane Processes, LABSEM, Department of Chemical and Food Engineering, Federal University of Santa Catarina, Florianópolis 88040-970, Brazil; mariproner@gmail.com (M.C.P.); ingrid\_ra\_malho@hotmail.com (I.R.M.); alan.ambrosi@ufsc.br (A.A.); katia.rezzadori@ufsc.br (K.R.); guilhermezin@gmail.com (G.Z.)

<sup>2</sup> Laboratory of Control and Polymerization Processes, LCP, Department of Chemical and Food Engineering, Federal University of Santa Catarina, Florianópolis 88040-970, Brazil; cristiane.costa@ufsc.br

<sup>3</sup> Laboratory of Agroindustrial Processes Engineering, LAPE, Federal University of Santa Maria, Cachoeira do Sul 96508-010, Brazil

\* Correspondence: marcus.tres@ufsm.br (M.V.T.); di.luccio@ufsc.br (M.D.L.);  
Tel.: +55-51-3724-8417 (M.V.T.); +55-48-3721-2529 (M.D.L.)

† Current address: Department of Food Science and Technology, Federal University of Santa Catarina, Rod. Admar Gonzaga, 1346, Itacorubi, Florianópolis 88034-001, Brazil.

Received: 17 August 2020; Accepted: 15 September 2020; Published: 18 September 2020



**Abstract:** The mussel-inspired method has been investigated to modify commercial ultrafiltration membranes to induce antifouling characteristics. Such features are essential to improve the feasibility of using membrane processes in protein recovery from waste streams, wastewater treatment, and reuse. However, some issues still need to be clarified, such as the influence of membrane pore size and the polymer concentration used in modifying the solution. The aim of the present work is to study a one-step deposition of dopamine (DA) and polyethyleneimine (PEI) on ultrafiltration membrane surfaces. The effects of different membrane molecular weight cut-offs (MWCO, 20, 30, and 50 kDa) and DA/PEI concentrations on membrane performance were assessed by surface characterization (FTIR, AFM, zeta potential, contact angle, protein adsorption) and permeation of protein solution. Results indicate that larger MWCO membranes (50 kDa) are most benefited by modification using DA and PEI. Moreover, PEI is primarily responsible for improving membrane performance in protein solution filtration. The membrane modified with 0.5:4.0 mg mL<sup>-1</sup> (DA: PEI) presented a better performance in protein solution filtration, with only 15% of permeate flux drop after 2 h of filtration. The modified membrane can thus be potentially applied to the recovery of proteins from waste streams.

**Keywords:** membrane surface modification; antifouling; hydrophilicity; mussel-inspired; protein

## 1. Introduction

Membrane separation processes (MSP) are widely applied in several industry sectors, whether directly on the production line, in the treatment of residual streams, or water recovery/treatment, for their low energy consumption, simplicity of operation, and high separation efficiency [1–3]. In the food industry, large volumes of protein-rich waste streams are produced, especially in animal protein and dairy processing plants, and need treatment. In this context, ultrafiltration (UF) is highlighted and commonly used as a suitable alternative to conventional methods for recovery and concentration of proteins from waste streams, and as a way to minimize water loss and up-cycle byproducts like

cheese whey and other animal proteins [2,4–9]. However, the formation of a polarized layer, and fouling, is still a challenging issue in the treatment of wastewaters containing proteins, due to the high interaction that they have with the membrane surface. The fouling caused, promotes decline of the permeate flux and consequent reduction in the performance of the membranes, which have to be constantly cleaned, increasing process costs [10–12]. In this sense, efforts are focused on methods to minimize fouling effects [13–17], and membrane surface modification (MSM) is currently considered the most favorable strategy [13,18–24].

Among the MSM techniques, the mussel-inspired method (MI) has gained interest [25–35]. Based on the adhesive capacity of mussels, Lee, Dellatore, Miller, and Messersmith (2007) [36] proposed the immersion of material in a solution of dopamine (DA), with slightly alkaline pH and in the presence of oxygen (conditions for DA polymerization), to form a thin adhesive polymeric layer on the surface, known as polydopamine (PDA). The PDA exhibits chemical stability, from the interactions of the catechol group, and hydrophilic characteristics, due to the presence of the amino group [27,37–46]. As a result of the hydrophilic character and affinity with several polymers, DA is a strategy highly used in MSM to create anti-fouling characteristics; reducing the interaction of the membrane surface with various solutes, including proteins, which are usually hydrophobic, improving filtration performance, and reducing cleaning cycles [30,37,38,43,47–51]. As an improvement of the method, Yang et al. (2014) [52] proposed a single-step deposition of DA with a hydrophilic polymer, polyethyleneimine (PEI). According to the authors, the concomitant deposition of DA and PEI generated a cross-linked polymer chain, increasing the chemical stability and dispersing polymeric agglomerates of the PDA. Furthermore, it provided a surface with a higher hydrophilic character [52].

Later studies related to the surface modification of membranes with the deposition of DA and PEI by the mussel-inspired method also identified that modified membranes presented an antifouling property, an increase in the degree of hydrophilicity, and high water permeance. Yang et al. (2016) [26] investigated the effects of varying the amount PEI used in the modification solution, and PEI molecular weight, on the properties of the polypropylene microfiltration (MF) membrane. Xue et al. (2017) [53] used the co-deposition of DA and PEI to modify polytetrafluoroethylene MF membranes, while Lv et al. (2015) [27] carried out the deposition of DA/PEI to produce nanofiltration (NF) membranes, using a polyacrylonitrile UF membrane as support. However, most studies focus on MF membranes [25,26,38,47,54], and there are only a few reports about the modification of UF membranes by co-deposition of DA with PEI [27,55,56]. Knowledge on the effect of chemical modification on membrane performance, and about different pore size or molecular weight cut-off (MWCO) of UF membranes is also important and needed. Moreover, the effect of different concentrations of DA and PEI on UF performance, and which polymer exerts the most influence on the protein solution filtration efficiency are still unclear.

In this context, we present an extensive investigation about the impact of membrane pore size, and concentration of DA: PEI solutions, on the surface properties and on the filtration performance of modified UF membranes. The work was carried out in two parts: (i) different MWCO UF membranes (20, 30, and 50 kDa) were modified by the co-deposition of DA and PEI, using a solution containing 2 mg mL<sup>-1</sup> of both species; (ii) a 50 kDa UF membrane was modified through the co-deposition of DA and PEI using solutions with different concentrations. The membrane performance was evaluated in terms of physicochemical characterizations, hydraulic performance, and bovine serum albumin (BSA) filtration.

## 2. Material and Methods

### 2.1. Material

Three commercial UF polymeric membranes were acquired from Microdyn-Nadir (Wiesbaden, Hesse, Germany). UP020, UH030, and UH050 are hydrophilic polyethersulfone (PES) membranes

that support temperature up to 95 °C and a pH range from 0 to 14. MWCO are equal to 20, 30, and 50 kDa, respectively.

The solution of DA and PEI was prepared with dopamine hydrochloride, polyethyleneimine (Mw = 800 Da), and tris (hydroxymethyl) aminomethane (Tris) (Sigma-Aldrich, Saint Louis, MO, USA). The model protein used in the filtration and protein adsorption tests was bovine serum albumin (BSA; code A2153; purity >96% and molecular mass of 66 kDa), purchased from Sigma-Aldrich (Brazil). The cleaning procedures were performed with ultrapure water and 0.02% sodium hydroxide (pH 10) (P.A., Lafan, Várzea Paulista, SP, Brazil).

## 2.2. Methods

### 2.2.1. Membrane Modification

The membranes were cut into disks (9.2 cm diameter), conditioned, and fixed in Petri dishes. The conditioning consisted of immersing the samples in ethanol (99%, Synth, Diadema, SP, Brazil) for 2 h, followed by rinsing and immersion in water (ultra-purified by reverse osmosis) for 12 h to remove preservatives and ensure the complete membrane wetting.

This study was carried out in two separate parts: the first part refers to the modification of UF membranes with different MWCO (20, 30, and 50 kDa), and with a fixed concentration of the DA/PEI solution (2 mg mL<sup>-1</sup> each). In the second part, the modification of the UH050 membrane with different concentrations of DA and PEI (Table 1) was assessed. The modification solution was prepared by dissolving the DA and PEI in a Tris buffer solution (pH 8.5, 50 mM). The modification process was performed by immersing the membrane in the DA/PEI solution and shaking for 12 h in an orbital shaker (TECNAL TE-420, Piracicaba, SP, Brazil) at 50 rpm and 25 ± 1 °C. After reaching the reaction time, the membrane was rinsed with water to eliminate excess of the solution, and stored in water. The modification was carried out in duplicate, with two different membrane sheets; the reaction time (12 h) was determined in preliminary tests, and the concentration of DA and PEI (2 mg mL<sup>-1</sup>) was chosen based on previous works [50,54].

**Table 1.** Dopamine (DA) and polyethyleneimine (PEI) concentrations used for UH050 membrane modification.

DA (mg mL <sup>-1</sup> )	PEI (mg mL <sup>-1</sup> )
2.0	0.5, 2.0
0.5	1.0, 2.0, 4.0, 8.0

### 2.2.2. Membrane Characterization

The chemical structure of the control and modified membranes was analyzed through Fourier transform infrared spectrometry, with an attenuated total reflection accessory (FTIR, model Tensor 27, Bruker Scientific LLC, Billerica, MA, USA). The polymer mass adhered to the membrane was analyzed by weighing the membrane samples (diameter 9.2 cm) before and after the modification. Before each weighing, the membranes were dried for 2 h at 40 ± 1 °C and placed in a desiccator for 1 h. The deposited polymer mass was estimated by calculating the mass difference of the samples. Membrane roughness was evaluated by surface topography with atomic force microscope (AFM) analysis (Easyscan2 Flex AFM, Nanosurf, Liestal, Switzerland), using WS × M 5.0 software (Nanosurf, Liestal, Switzerland). An electrokinetic analyzer (SurPASS, Anton-Paar GmbH, Graz, Austria) was used to determine the zeta potential of the membranes before and after modification. The analysis was carried out using a solution of KCl (1 mM), varying the pH range from 3 to 10.5 by the addition of sodium hydroxide, at room temperature (25 °C). The zeta potential of the BSA solution (2.5 g L<sup>-1</sup>; pH 6.5) was measured in a dynamic light scattering device, with a capillary cell and two electrodes (Zeta sizer Nano ZS3600, Malvern Instruments, Malvern, England, UK).

Membrane wettability was evaluated by two methods. First, control and modified membranes were cut into samples of 1 cm x 2 cm and dried for 2 h at  $40 \pm 2$  °C. In the first method (treatment 1), the samples were only immersed in water for 12 h, while in the second treatment (treatment 2), the samples were previously immersed in ethanol for 2 h, then followed by water immersion for 12 h. Immersion in ethanol in the second method was carried out to secure the total wetting of the membrane pores. This test was carried out in duplicates, and the mass water gain is given in g water/g dry membrane based on the difference in wet and dry membrane masses. The sessile drop method (Ramé–Hart, 250-F1) was used for obtaining a pure water contact angle, which was measured in five different positions on the membrane surface. The assay was performed in triplicate.

In protein adsorption assays, control and modified membranes were cut into samples of 1 cm x 2 cm and conditioned as described in the wettability tests. Then, the membranes were placed in a desiccator for 1 h, weighed, and conditioned again before being immersed in a tube with 7 mL of  $0.5 \text{ g L}^{-1}$  BSA solution at pH 6.5. The tube with the membrane and the BSA solution was shaken for 6 h in an orbital shaker (TECNAL TE-420, Piracicaba, SP, Brazil) at 130 rpm and  $25 \pm 1$  °C. Then, protein solution aliquots were collected to determine the protein concentration by Bradford's method. The mass of protein adsorbed to the membrane in  $\mu\text{g protein/mg dry membrane}$  was calculated with Equation (1).

$$q = \frac{(C_i - C)V}{M_d} \quad (1)$$

where  $M_d$  (g) is the mass of the dry membrane and  $V$  (L) is the volume of the solution in the tube.  $C_i$  ( $\text{g L}^{-1}$ ) and  $C$  ( $\text{g L}^{-1}$ ) are BSA initial, and over time, concentrations, respectively.

### 2.2.3. Filtration Performance

The water permeance and the permeate flux of the BSA solution were evaluated using a conventional stirred cell (dead-end), with a volume of 500 mL and an effective membrane area of  $9.6 \text{ cm}^2$ . The driving force was the pressure exerted by the injection of nitrogen into the cell headspace, regulated by a digital manometer (0–5 bar). The tests were performed at  $23 \pm 2$  °C and under agitation with a magnetic stirrer (1000 rpm). Before the filtration tests, the control membrane (unmodified) was conditioned in ethanol for 2 h and immersed in ultrapure water for 12 h. The modified membranes were used directly from the storage vessel (ultrapure water).

The water permeance was obtained according to a procedure adapted from Zin et al. (2019) [57]. The filtration system was filled with water and pressurized at 5 bar, keeping the permeate collecting valve open until constant flux (membrane compaction), then the permeate flux was collected, varying the pressure from 4 to 1 bar. For the protein solution filtration and fouling tests, 100 mL of BSA solution ( $2.5 \text{ g L}^{-1}$ , pH 6.5) was used. The tests were performed under agitation (magnetic stirrer, 1000 rpm) and the constant pressure of 4 bar for 2 h. Permeate flux was obtained every 15 min. At the end of the process, samples of permeate and concentrate were collected to analyze the total protein content by the Bradford method [58], and to calculate the membrane retention. After the protein solution filtration, physical and chemical cleaning procedures were carried out in sequential steps. The physical cleaning (PC) was performed with 100 mL of ultrapure water under agitation for 10 min. Chemical cleaning (CC) was carried out with 100 mL of 0.02% sodium hydroxide solution (pH 10) for 30 min, with a solution refresh after 15 min. At the end of the CC, the membrane was washed with 100 mL of water for 5 min. All cleaning procedures were performed with the membrane coupled to the system under agitation (magnetic stirrer, 1000 rpm). After each cleaning procedure, a water permeation test was performed.

Experiments to evaluate the membrane regeneration, with the control and modified membrane, were performed with three consecutive cycles of protein filtration (2 h each), interleaved by physical cleanings. At the end of the third filtration, a complete cleaning procedure (PC + CC) was carried out, and water permeance determined after each cleaning procedure.

### 2.3. Statistical Analysis

The results were presented as an arithmetic mean  $\pm$  the standard deviation of two replicates, and the Tukey test (significance of 5%) was used to identify significant differences.

## 3. Results and Discussion

### 3.1. Influence of Membrane Molecular Weight Cut-off

The effect of different MWCOs on the membrane modification by the mussel-inspired method was assessed through testing 20 (UP020), 30 (UH030), and 50 kDa (UH050) PES UF membranes, modified with DA and PEI concentration of 2 mg mL<sup>-1</sup> and 12 h of reaction time.

#### 3.1.1. Physicochemical Characteristics of Control and Modified Membranes

The chemical structure of the control and modified membranes was analyzed by FTIR-ATR to check the effective reaction of DA and PEI, which is reported to occur through a Michael addition or Schiff base reaction between the catechol and amine groups [52]. The spectra of the modified membranes (Figure 1a) shows a band between 1600 and 1630 cm<sup>-1</sup>, attributed to vibrations of the C = N bond [52,59]. This band suggests the primary amine (PEI) and the carbonyl group (catechol) formed a Schiff base, confirming the incorporation of PDA/PEI on the surface of the PES membrane [55,57,60]. Moreover, the larger the MWCO, the higher the amount of DA/PEI mass deposited on the membrane, as shown in Figure 1b. The UP020, UH030, and UH050 modified membranes presented a gain of polymer mass equal to 0.16, 0.23, and 0.35 mg cm<sup>-2</sup>, respectively, which is an indication that as the membrane pore size increases, the polymeric solution penetrates more easily into the membrane pores, which can lead, not only to the membrane surface modification, but also to changes of the inner surface of the pores. Nevertheless, the average roughness (Figure S1 of Supplementary Material) was not modified. The roughness of the UP020, UH030, and UH050 control membranes was 6.79, 4.86, 17.75 nm, while the modified ones were 6.69, 6.63, 17.87 nm, respectively.

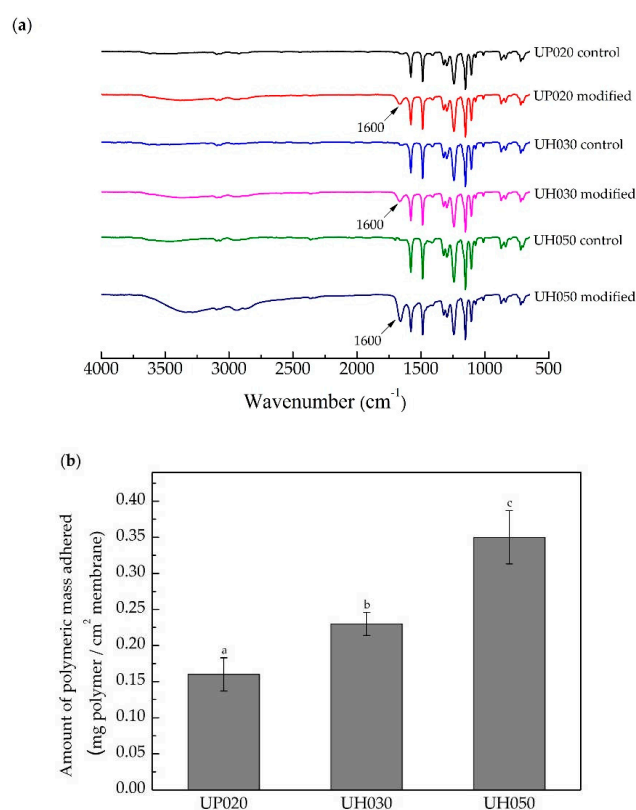
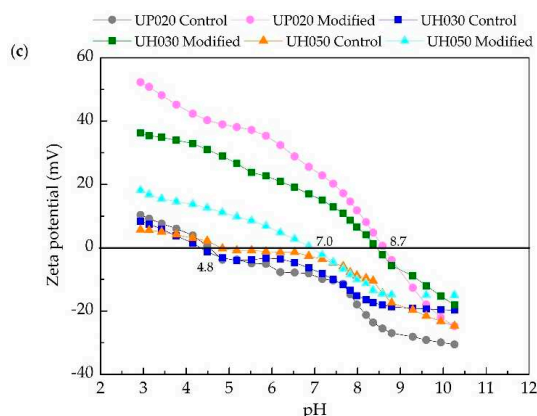


Figure 1. Cont.



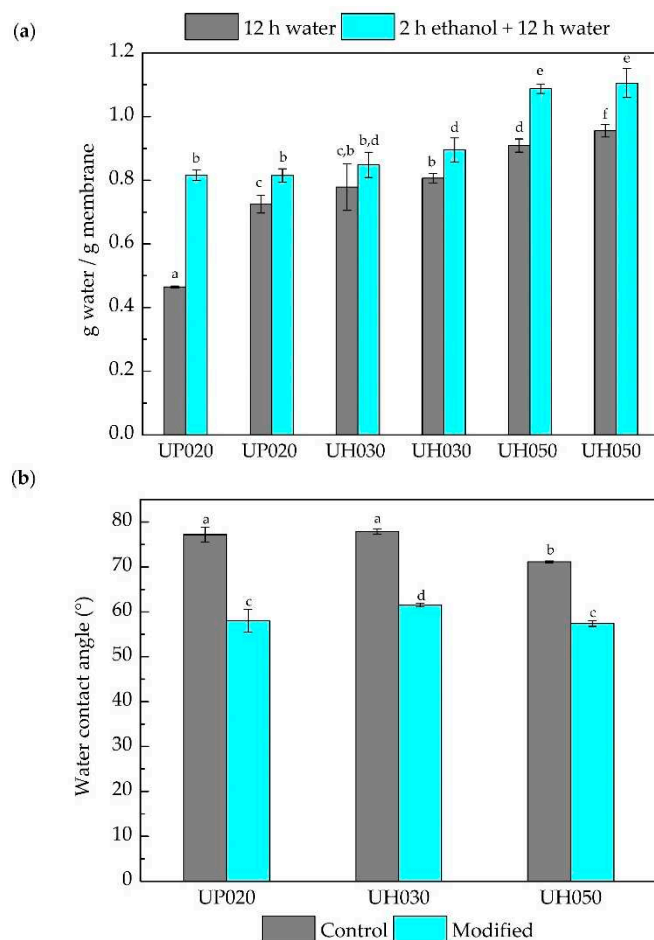
**Figure 1.** (a) ATR-FTIR spectra of the control and modified membranes. (b) Polymeric mass deposited on modified membranes with DA and PEI concentrations of  $2 \text{ mg mL}^{-1}$  and a deposition time of 12 h. Bars with different letters show the statistical difference ( $p < 0.05$ ). (c) Zeta potential of control and modified membrane with DA and PEI concentrations of  $2 \text{ mg mL}^{-1}$  and deposition time of 12 h.

Thus, for better comprehension of the effects of the modification on membrane properties and their relationship to MWCO, zeta potential analysis was performed. With this analysis, it is possible to gather information on the surface charges and to identify possible changes after the modification reaction. Figure 1c shows the zeta potential of the control and modified membrane surfaces within the pH range 3–10.5.

The control membranes, independently of the MWCO, have a similar distribution of charges (Figure 1c). Their isoelectric point (IP) is around pH 4.8, which shows that the membrane surface is mostly negatively charged in the evaluated pH range. The simultaneous deposition of DA/PEI on the membrane surface considerably changed the surface zeta potential, and the IP of the UP020 and UH030 membranes moved to approximately pH 8.7. In contrast, the IP of the UH050 membrane moved to pH 7.0. A more positive membrane zeta potential was expected after the modification, due to the upturn of the number of amino groups on its surface. These results confirm that the membrane modifications were successfully carried out.

The MWCO also caused variation in zeta potential after the modification process. Figure 1c shows that the modified membrane with the larger average pore size, i.e., UH050, exhibited fewer positive charges on its surface when compared with the other two modified membranes (UH030 and UH020). Such behavior implies that the smaller pore size hinders the penetration of the DA/PEI solution into the membrane pores, and the modification process tends to occur only on its surface. Thus, due to the higher number of amino groups present on its surface, the membranes with smaller pore sizes are more positively charged. This behavior corroborates the discussion related to the polymer mass adhered to the membrane, since the zeta potential is a surface analysis. In other words, the results infer that the deposition of DA/PEI on the membrane with the higher MWCO occurs both on the surface and onto the pore walls.

The hydration properties (wettability and hydrophilicity) of the control and modified membranes are shown in Figure 2. The amount of water absorbed after the two treatments (treatment 1—12 h water and treatment 2—2 h ethanol + 12 h water) was similar for UH030 and UH050 control, and modified membranes, except for the UP020 membrane (Figure 2a). The larger the pore size, the more water is absorbed, which is reasonable since there is more pore volume available to be filled in with water.



**Figure 2.** (a) Wettability of control and modified membranes measured after two different treatments. In the first bar, membranes were immersed in water for 12 h (treatment 1). In the second adjacent bar, the membranes were immersed in ethanol for 2 h and then immersed in water for 12 h (treatment 2). (b) Water contact angles for control and modified membranes. Bars with different letters show a statistical difference ( $p < 0.05$ ).

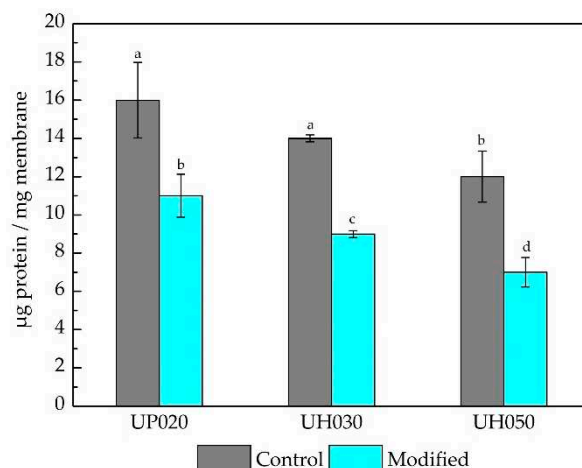
The different behavior presented by the UP020 control compared to the controls UH030 and UH050 after treatment 1 (only water) can be explained by the difference in the membrane pore sizes. Since all the control membranes had a hydrophilic character, the UH030 and UH050 showed lower resistance to water absorption owing to their larger pore size. For the UP020 control, this absorption was more difficult because of the smaller pore size and the consequent higher Laplace pressure for water intrusion. However, after the treatment with ethanol, which has a lower surface tension than water (22.1 and 72.3 mN/m at 20 °C, respectively), the water can fill the membrane pores more easily. It is worth noting that wettability assay shows the amount of water that the membrane is able to retain both in the pores and absorbed in the polymer matrix. Since the UF membrane is porous, we can consider that the amount of water inside the pores is much larger than that absorbed by the polymer. Thus, the membrane can absorb a limited amount of water, which is slightly increased by the ethanol conditioning. Moreover, membranes composed of the same polymeric material, but with a larger pore size, retain more water than membranes with a smaller pore size due to capillarity.

As expected, all the membranes presented a hydrophilic character (contact angle  $< 90^\circ$ ) (Figure 2b); the lower contact angle of the UH050 control membrane ( $\sim 70^\circ$ ) may be related to its larger pore size than the other two membranes tested ( $\sim 75^\circ$ ). Additionally, the membranes presented a decrease ( $\sim 20\%$ ) in contact angle after the chemical modification, regardless of pore size. Wang et al. (2020) [3] modified



PES ultrafiltration membranes with dopamine and surfactant, and obtained similar contact angle results for control and modified membranes.

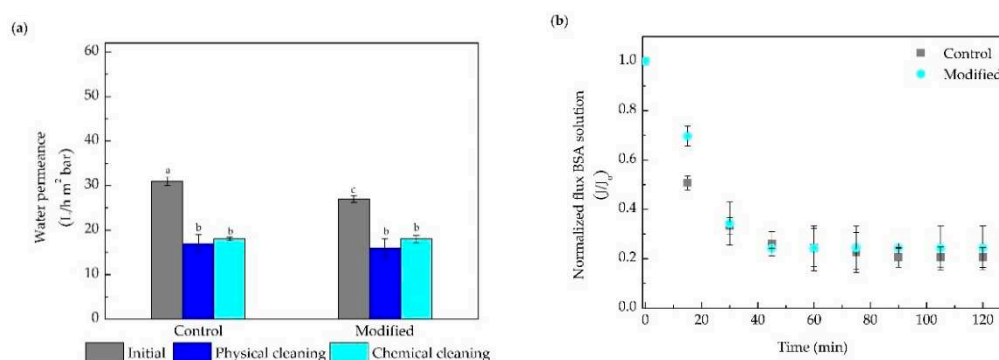
The increase of the hydrophilic character was responsible for the decrease of BSA protein adsorbed on the membrane surface, as we can observe in Figure 3. All modified membranes adsorbed a lower amount of protein (31%, 36%, and 42% for the UP020, UH030, and UH050 modified membranes, respectively) compared to their controls. Likewise, the higher the MWCO, the lower the mass of protein adsorbed. This behavior matches the results presented in Figure 1b,c, which evidence that with increasing the membrane pore size, the DA/PEI solution modifies the membrane surface and the walls of the membrane pores, therefore decreasing the interaction PES/protein.



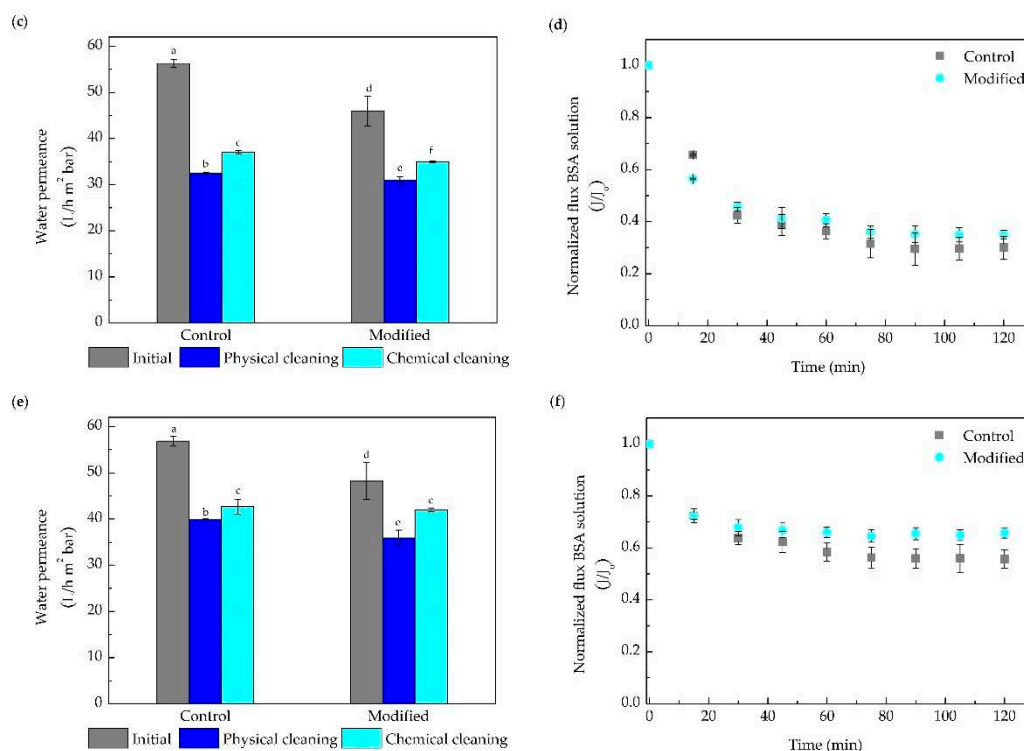
**Figure 3.** Bovine serum albumin (BSA) adsorption on the surface of control and modified membranes at a concentration of  $0.5 \text{ g L}^{-1}$  for 6 h. Bars with different letters show a statistical difference ( $p < 0.05$ ).

### 3.1.2. Membrane Filtration Performance of Control and Modified Membranes

The filtration performance of the modified membranes, evaluated in terms of water permeance (before protein filtration and after cleaning steps) and normalized BSA solution permeate flux is presented in Figure 4. All the membranes presented a slight reduction (10% for UH030 and UH050, and 15% for UP020) in the initial water permeance after modification (Figure 4a). The difference in the water permeance drop may be due to the larger MWCO of the UH030 and UH050 membranes, which facilitates the entrance of the DA/PEI solution into the membrane pores, and leading to a slight reduction of the membrane pore size when compared with the UH020 modified membranes. Similar behavior was observed elsewhere [27,31]. Membrane retentions were all above 98% since the membrane MWCOs were smaller than the molecular size of the BSA, which is around 65 kDa.



**Figure 4.** Cont.



**Figure 4.** Water permeance before the protein filtration (initial) and after the physical and chemical cleaning for the membranes (a) UP020, (c) UH030, and (e) UH050. Normalized permeate flux of the BSA solution (b) UP020, (d) UH030, and (f) UH050. Bars with different letters show a statistical difference ( $p < 0.05$ ).

Despite the lower BSA adsorption presented by the modified membranes in comparison to the control (Figure 3), the normalized permeate flux of BSA solution over 2 h filtration (Figure 4b,d,f) was similar for the UP020 and UH030 membranes. On the other hand, the UH050 modified membrane showed a 20% drop in permeate flux when compared to the control membrane after 2 h of filtration. However, it is important to consider that the concentration of the solution used in the filtration tests was five times higher ( $2.5 \text{ g L}^{-1}$ ) than that used in the protein adsorption test ( $0.5 \text{ g L}^{-1}$ ). With a high protein concentration in the feed solution, differences are less prone to be detected by the filtration tests. The increase in MWCO induced an improvement in filtration, both in control and in the modified membrane, due to the reduction of the membrane resistance to water flux. As previously discussed, the DA/PEI solution can penetrate the pores more easily in larger pore size membranes, forming not only a thin layer on the surface but also coating the pore walls. Thus, when the aqueous protein solution comes into contact with the membrane, the water quickly bonds with the membrane surface creating a higher resistance to fouling, which is reflected in the increase in the permeate flux of the membranes with larger pore size. This behavior is supported by the results of polymeric mass adhered, zeta potential, and adsorption tests (Figures 1 and 3).

Figure 4a,c,e also show that the UP020, UH030, and UH050 control membranes recovered around 60, 66, and 73% of the initial water permeance after chemical cleaning, while the modified membranes recovered 67, 75, and 85%, respectively. Concerning MWCO, when increasing the pore size of the membrane, the recovery of water permeance increased significantly; a remarkable result pointing to a possible application in industry. The results of BSA normalized permeate flux (Figure 4b,d,f) and recovery of the water permeance after the cleaning procedures (Figure 4a,c,e) indicate that the membrane modification in larger MWCO membranes improves the protein filtration performance.

In general, the results observed indicate that the modification of the membrane surface by the co-deposition of DA/PEI is affected by MWCO. With the increase in the MWCO, the improvement in the filtration performance of the modified membrane became more evident, when compared to its

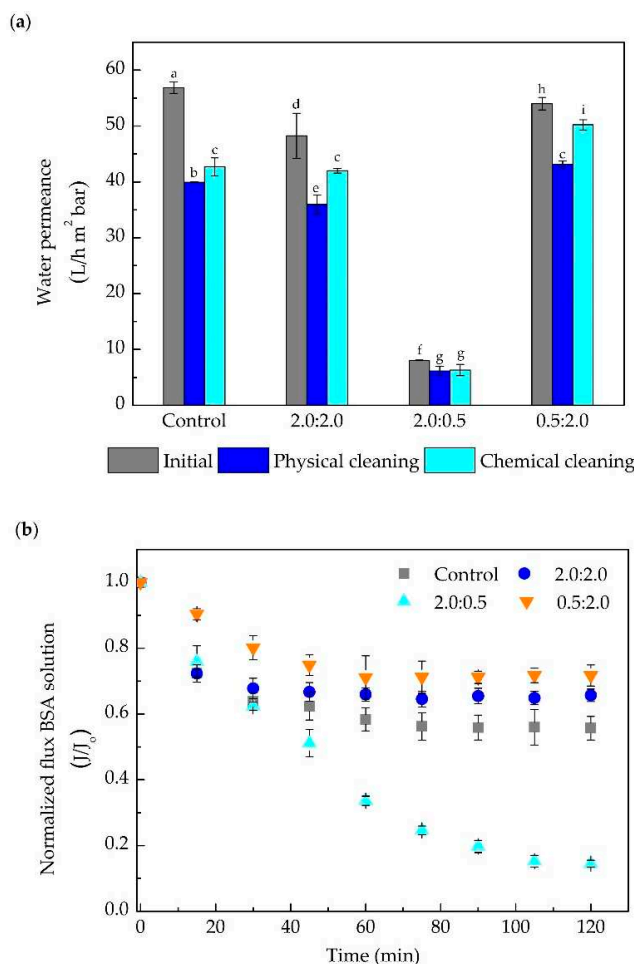
control, and with a lower decline in permeate flux compared to the initial flux, and an increase in the recovery of the water flux after cleaning procedures. Thus, the UH050 membrane was chosen to proceed to Part 2 and evaluate the different DA/PEI concentrations.

### 3.2. Influence of DA and PEI Concentration

Although the results presented in Section 3.1 indicated an improvement in the performance of protein solution filtration through UF membranes modified with DA and PEI, with more intensity of the membrane with higher MWCO, tests varying the concentration of these polymers were performed to investigate the direct influence of the polymers on the filtration performance. Initially, we sought to identify which polymer, DA or PEI, would be responsible for the greatest effect on the membrane performance when filtering protein solutions. Then, the concentration was varied.

#### 3.2.1. Effects of Different DA and PEI Concentrations

Different polymeric blends of DA and PEI (2.0:0.5 and 0.5:2.0 mg mL<sup>-1</sup>) were used to modify the membranes for 12 h, making it possible to compare with the results from Section 3.1.2 (UH050 membrane, 2.0: 2.0 mg mL<sup>-1</sup> of DA/PEI). The performance of control and modified membranes in the permeation of the BSA protein solution are presented in Figure 5.



**Figure 5.** Performance of control and modified UH050 membrane with different concentrations of DA:PEI (2.0:2.0; 2.0:0.5, and 0.5:2.0 mg mL<sup>-1</sup>) in the filtration of BSA solution (2.5 g L<sup>-1</sup>). (a) Water permeance before the protein filtration (initial) and after the physical and chemical cleaning. (b) Normalized permeate flux of the BSA solution. Bars with different letters show a statistical difference ( $p < 0.05$ ).

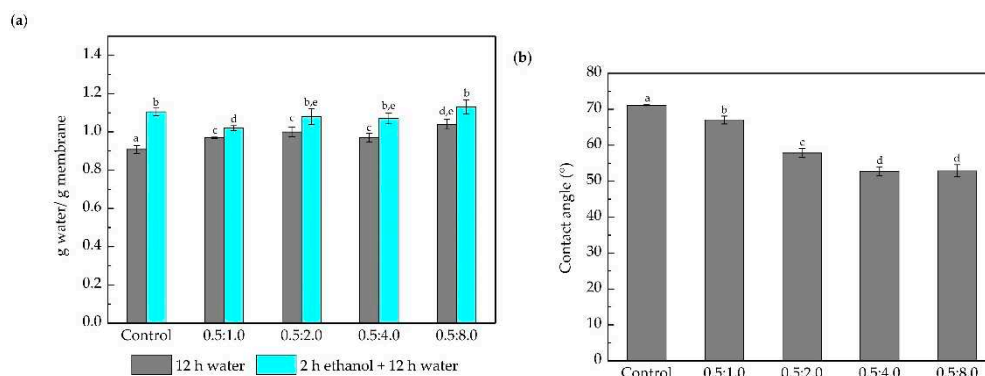
Figure 5a shows that the different polymeric blends of DA:PEI used in the modifying solution considerably interfere with the water permeance. While the modified membranes with DA:PEI concentration 2.0:2.0 and 0.5:2.0 mg mL<sup>-1</sup> presented initial water permeance (before the protein filtration) close to that of the control membrane, the modified membrane with the concentration 2.0:0.5 mg mL<sup>-1</sup> showed a 80% drop in the permeance. This behavior can be explained by the higher hydrophilic character of the PEI in comparison to the DA. Another fact that should be highlighted is the increase in the polymeric growth rate of the PDA film on the membrane surface when using modification solutions with a higher concentration (m/m) of DA (a good binding agent). This explanation agrees with some studies claiming that the small pore size of UF membranes can be blocked by the thicker polymeric films formed after modification with polymeric blends with higher concentrations of DA [40,50]. Moreover, Yang et al. (2014) [52] suggested that the incorporation of PEI through crosslinking with the catechol and amino groups eliminates the PDA aggregates, helping to increase the hydrophilicity of the membrane, without significantly affecting the permeate flux that could be compromised by pore blockage. Such behavior can be seen in the water permeance results obtained in this part of the study. All membranes presented retention values above 98% (data not shown), an expected result since the membrane had a molecular weight cut-off lower than the molecular size of the BSA.

Figure 5b presents the normalized flux of BSA solution for the control and modified membranes at 2 h of permeation. The normalized flux was around 20% and 35% higher than the control for the membranes modified with 2.0:2.0 and 0.5:2.0 mg mL<sup>-1</sup> of DA/PEI, respectively. In turn, a normalized flux decrease of around 70% at the end of the filtration was observed for the membrane modified with 2.0:0.5 mg mL<sup>-1</sup> of DA/PEI, when compared to the control. Such behavior is in agreement with the discussion concerning the water permeance, increasing the amount of PEI (a super hydrophilic polymer) reduces polymeric aggregates and enhances the interaction of the surface with water, increasing the water permeance and BSA solution permeation.

The recovery of the water permeance after the cleaning procedure is shown in Figure 5a. Results indicate that at least 70% of the water permeance can be recovered by using only physical cleaning (pure water under stirring), as in the case of the control membrane. A gain of up to 15% can be noticed for the modified membranes, with the best result obtained by the 0.5:2.0 DA:PEI sample (80% recovery). Similar behavior is observed for the permeance recovery regarding chemical cleaning, in which the membrane modified with the highest proportion of PEI, i.e., 0.5:2.0 mg mL<sup>-1</sup>, was the one that presented the highest permeance recovery (93%). In turn, the control membrane showed the lowest recovery percentage after chemical cleaning (73%). These results suggest that the use of a higher amount of PEI in the modification solution decreases the solute/membrane interaction, favoring the cleaning procedure (results of the zeta-potential analysis presented in the next section prove this hypothesis). Moreover, PEI, a highly hydrophilic polymer, is mainly responsible for increasing the permeate flux and decreasing the fouling effect; the lower the DA:PEI ratio, the more promising results were obtained. To understand the extent to which reducing this ratio impacted the process, we investigated the membrane modification by increasing the PEI concentration and keeping DA concentration constant.

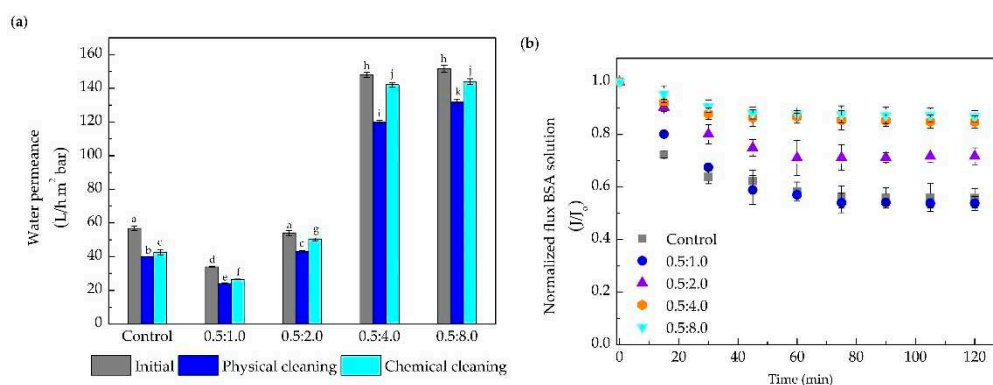
### 3.2.2. Influence of PEI Concentration

Membrane surface modification was performed with a reaction time of 12 h and different polymeric blends of DA:PEI. The DA concentration was fixed at 0.5 mg mL<sup>-1</sup> and the concentrations of PEI evaluated were 1.0, 2.0, 4.0, and 8.0 mg mL<sup>-1</sup>. The hydrophilicity of the membranes was evaluated by contact angle and water mass gain (Figure 6).



**Figure 6.** (a) Mass water uptake of control and membranes modified with different concentrations of DA and PEI after the immersion for 12 h in water (treatment 1), and the immersion for 2 h in ethanol and then 12 h in water (treatment 2). (b) Water contact angle of the control and membranes modified with different concentrations of DA and PEI. Bars with different letters show a statistical difference ( $p < 0.05$ ).

The increase in the capacity of the modified membranes to interact with water, when compared to the control membrane is observed in water uptake results (Figure 6a). After treatment 1 (water), the water uptake slightly increased (~10%) with the PEI concentration increase. After treatment 2 (ethanol + water), it can be observed that the modified membranes present a similar water uptake to the control membrane. It is important to point out the limit of water that can be absorbed by the membrane, as explained previously (Figure 2). The increase in PEI concentration from 0.5 to 4.0 g L<sup>-1</sup> caused the contact angle (Figure 6b) to decrease by about 20%. Zin et al. (2019) [57] modified a poly (vinylidene difluoride) microfiltration membrane with DA/PEI to treat oily wastewater, and observed similar behavior. According to Yang et al. (2016) [26], the increase in the degree of hydrophilicity is a result of a large number of amino groups present in the PEI molecule, and consequently in the PDA/PEI coatings. The augmentation of membrane hydrophilicity may induce a higher resistance to the adhesion of hydrophobic components on its surface, and further investigation, by evaluating the hydraulic performance of the membranes in the UF of BSA solution supported this hypothesis. The results are shown in Figure 7.



**Figure 7.** Performance of the control and modified membranes with different concentrations of DA and PEI (0.5:1.0, 0.5:2.0, 0.5:4.0, and, 0.5:8.0 mg mL<sup>-1</sup>) in the permeation of BSA solution (2.5 g L<sup>-1</sup>). (a) Water permeance before the protein filtration (initial) and after the physical and chemical cleaning. (b) Normalized permeate flux of the BSA solution. Bars with different letters show a statistical difference ( $p < 0.05$ ).

Figure 7a illustrates that the water permeance before the protein filtration (initial) varied by increasing the PEI concentration from 1.0 to 8.0 mg mL<sup>-1</sup>. Membranes modified with high PEI concentration presented higher permeance. Water permeance augmented by about 170%, compared to

the control membrane, when using 4.0 and 8.0 mg mL<sup>-1</sup>. This behavior corroborates the discussion in Section 3.2.2, in which the PEI, due to its super hydrophilic characteristic, and capacity to reduce polymeric aggregates, is mainly responsible for the increase of the water permeate flux. In addition, the increase in hydrophilic groups on the membrane surface due to the DA/PEI coating facilitates the water flux through the pores, reflected in the higher permeance observed [61]. All the membranes evaluated presented the same protein retention, around 98%.

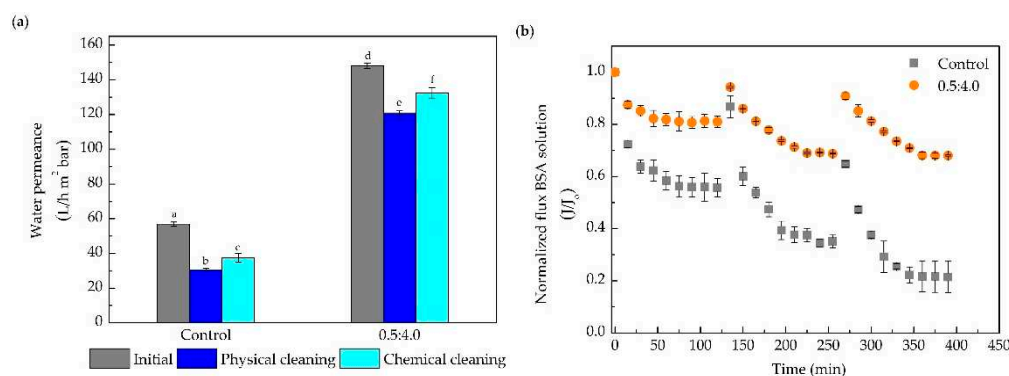
All the membranes presented a similar behavior regarding the normalized flux of BSA solution over time, as illustrated in Figure 7b. Control and modified membranes with 0.5:1.0 mg mL<sup>-1</sup> of DA/PEI presented almost equal values of normalized flux, with a 45% drop at 2 h of filtration. In turn, the membranes modified with higher concentrations of DA/PEI showed a lower decline in permeate flux. For the 0.5:4.0 and 0.5:8.0 mg mL<sup>-1</sup> modified membranes, a decline of only 15% was noticed, proving that the increase in the PEI concentration, in relation to DA in the modification process, is beneficial to the performance of the membrane. In addition, this result corroborates the indication that an increase in the concentration of PEI generates an increase in the affinity with water, which reduces possible interactions of solute/membrane, and is reflected in a smaller drop in flux over the filtration period. Zin et al. (2019) [57] suggested that the formed DA/PEI film provides a hydration layer, making it difficult for hydrophobic solutes to adhere into the modified membrane surface. This is also supported by the protein adsorption test (Figure S2 of Supplementary Material), in which modified membranes adsorbed 60% less BSA. This reduction in the amount of adsorbed protein corroborates that a possible increase in the number of hydrophilic groups favors the interaction of water with membrane surface, and increases resistance to adsorption of hydrophobic compounds (BSA). Other authors have also observed that membranes modified by PDA or co-deposition with other polymers adsorbed smaller amounts of protein than unmodified membranes [25,62].

The results presented in Figure 7a also show a better performance in terms of water permeance recovery was achieved with the membranes modified with higher concentrations of PEI. After the physical cleaning, the permeance recovery of the membranes modified with 0.5:2.0; 0.5:4.0, and 0.5:8.0 mg mL<sup>-1</sup> was around 80%. On the other hand, for the control and modified membranes with a lower concentration of PEI, this recovery was around 70%. When analyzing the recoveries after the chemical cleaning step, the modified membranes with concentrations of 0.5:2.0, 0.5:4.0, and 0.5:8.0 mg mL<sup>-1</sup> achieved recoveries of 93, 96, and 95%, respectively, which are excellent results for the membrane cleaning process.

Differences were also found for the membrane zeta potential over the pH range evaluated (Figure S3 of Supplementary Material). The control membrane was predominantly negatively charged, presenting a point of zero charges (PZC) at pH 4.5. In turn, for 0.5:4.0 and 0.5:8.0 mg mL<sup>-1</sup> DA/PEI membranes, the PZC was increased to pH 5.3 and 5.7, respectively. The differences among the membranes can be attributed to the increase in the number of amino groups, as discussed in item 3.1.1. Additionally, the zeta potential results help to evaluate the attraction or repulsion between the protein molecules and the membrane surfaces at pH 6.5 (filtration pH). At pH 6.5, the BSA solution showed zeta potential values equaling -8.9. Control, 0.5:4.0 and 0.5:8.0, membranes showed zeta potential values equaling -8.6, -14.4, and -17.7, respectively. Thus, as the BSA solution and membranes showed negative zeta potential values, the protein tends to be repelled when in contact with the membrane surface, thus avoiding adsorption and fouling. The modified membranes were also more negatively charged when compared to the control membranes, increasing the repulsion between the protein and the membrane surface. These results, associated with the hydrophilicity (Figure 6), corroborate the hypotheses discussed for the filtrations of the BSA solution (Figure 7) in which, PEI, a highly hydrophilic polymer, is mainly responsible for the improvement in performance of PES UF membranes modified by the present method.

### 3.2.3. Membrane Regeneration

Membrane regeneration assays consisted of three consecutive cycles of protein filtration (2 h each) interleaved by physical cleanings that were also performed (Figure 8). Since no differences between the membranes modified with 4.0 and 8.0 mg mL<sup>-1</sup> of PEI were observed, this assay was carried out with the control and the membrane modified with 0.5:4.0 mg mL<sup>-1</sup> of DA, and PEI.



**Figure 8.** Membrane regeneration experiments of the control and modified membranes with 0.5:4.0 mg mL<sup>-1</sup> of DA and PEI in the filtration of BSA solution (2.5 g L<sup>-1</sup>). (a) Water permeance before the protein filtration (initial) and after the physical and chemical cleaning (after three cycles of BSA filtration). (b) Normalized permeate flux of the BSA solution. Bars with different letters show a statistical difference ( $p < 0.05$ ).

The modified membrane, which exhibited an increase in the water permeance and protein retention similar to the control (above 98%), was able to conduct the protein filtration with a decline in permeate flux (protein permeate flux) three times smaller on average. The modified membrane showed better resistance to fouling, with a reduction of only 30% of the permeate flux at the end of the third cycle, in relation to the initial flux of the first cycle (Figure 8b). On the other hand, the control membrane presented a permeate flux decline close to 80% at the end of three filtration cycles. Substantial recovery of water permeance after the cleaning procedures (Figure 8a) was obtained with a modified membrane, when compared with the control membranes (around 50% higher for the physical cleaning and 40% for the chemical cleaning).

As a final consideration, the results presented here corroborate the assumption that modification by coating with DA/PEI can increase the affinity with water, and probably reduces the protein adsorption on the membrane surface, improving the resistance to fouling. Moreover, the choice of PEI concentration used to modify the UF membranes, through co-deposition with DA, plays an essential role in the improvement of the protein solution filtration performance.

## 4. Conclusions

This study explored the impact of membrane pore size and concentration of dopamine and polyethyleneimine (DA:PEI) solutions used to modify membrane surface and improve filtration performance, when treating wastewaters containing protein. PES ultrafiltration membranes modified by the co-deposition of DA/PEI increased the resistance to fouling in protein solution (BSA) filtration. The performance of the modification process was affected by the MWCO of the membrane and also by the DA/PEI concentration used in the modification solution. The modified membrane with larger MWCO (50 kDa) presented the lowest protein adsorption, when compared with control membranes and with UH020 and UH030 modified membranes. In addition, experimental results showed high DA concentration decreases the water permeance and the permeate flux of the protein solution. On the other hand, an increase in the PEI concentration resulted in more hydrophilic membranes and is mainly responsible for the better performance in the protein filtration process. Thus, membranes modified

with 0.5:4.0 and 0.5:8.0 mg mL<sup>-1</sup> of DA and PEI showed better results in BSA solution filtration and antifouling properties.

**Supplementary Materials:** The following are available online at <http://www.mdpi.com/2077-0375/10/9/239/s1>. Figure S1: AFM images of the control and modified membranes, Figure S2: Static adsorption test of BSA on the surface of the control and modified membranes. The test was performed for 6 h with a BSA solution concentration of 0.5 g L<sup>-1</sup>. Bars with different letters show statistical difference ( $p < 0.05$ ), Figure S3: Zeta potential of the control and modified membranes. The DA and PEI concentrations used to modify the membranes were 0.5:4.0 and 0.5:8.0 mg mL<sup>-1</sup>.

**Author Contributions:** Conceptualization: M.C.P., G.Z. and M.D.L.; methodology: M.C.P. and I.R.M.; formal analysis: M.C.P. and I.R.M.; investigation: M.C.P. and I.R.M.; writing—Original draft preparation, M.C.P.; writing – review and editing, A.A., K.R., C.d.C., G.Z., M.V.T. and M.D.L.; supervision, A.A., C.d.C., G.Z. and M.D.L.; funding acquisition: G.Z. and M.D.L.; project administration: A.A., M.D.L. All authors have read and agreed to the published version of the manuscript.

**Funding:** This research was funded by CNPq (420275/2018-5, 307576/2018-3, 307512/2015-0), CAPES (PROEX) and FAPESC (Fundação de Amparo à Pesquisa e Inovação do Estado de Santa Catarina - CP 05/2015).

**Acknowledgments:** Authors acknowledge Multi-user Analytical Lab of the Department of Chemical and Food Engineering for the contact angle analysis, membrane zeta potential, and FTIR. Authors thank LOOSA (Laboratory of Organic Optoelectronics and Anisotropic Systems) for AFM analysis; LCP (Laboratory of Process Control and Polymer) for solution zeta potential analysis. All the laboratories cited here are located at the Federal University of Santa Catarina, Florianópolis, SC, Brazil.

**Conflicts of Interest:** The authors declare no conflict of interest.

## References

1. Barclay, T.G.; Hegab, H.M.; Michelmores, A.; Weeks, M.; Ginic-markovic, M. Multidentate polyzwitterion attachment to polydopamine modified ultrafiltration membranes for dairy processing: Characterization, performance and durability. *J. Ind. Eng. Chem.* **2018**, *61*, 356–367. [[CrossRef](#)]
2. Kumar, P.; Sharma, N.; Ranjan, R.; Kumar, S.; Bhat, Z.F.; Jeong, D.K. Perspective of membrane technology in dairy industry: A review, Asian-Australasian. *J. Anim. Sci.* **2013**, *26*, 1347–1358. [[CrossRef](#)]
3. Wang, J.; Tian, J.; Gao, S.; Shi, W.; Cui, F. Dopamine triggered one step polymerization and codeposition of reactive surfactant on PES membrane surface for antifouling modification. *Sep. Purif. Technol.* **2020**, *249*, 117148. [[CrossRef](#)]
4. Gao, N.; Fan, W.; Xu, Z. Ceramic membrane with protein-resistant surface via dopamine/diglycolamine co-deposition. *Sep. Purif. Technol.* **2020**, *234*, 116135. [[CrossRef](#)]
5. Bennani, C.F.; Ousji, B.; Ennigrou, D.J. Reclamation of dairy wastewater using ultrafiltration process. *Desalin. Water Treat.* **2015**, *55*, 297–303. [[CrossRef](#)]
6. Tonon, R.V.; Bianca, A.; Couto, C.C.; Mellinger-silva, C.; Iraidy, A.; Brígida, S.; Cabral, L.M.C. Coupling of ultrafiltration and enzymatic hydrolysis aiming at valorizing shrimp wastewater. *Food Chem.* **2016**, *198*, 20–27. [[CrossRef](#)]
7. Haberkamp, J.; Ernst, M.; Makdissy, G.; Huck, P.M. Protein fouling of ultrafiltration membranes—Investigation of several factors relevant for tertiary wastewater treatment. *J. Environ. Eng. Sci.* **2009**, *660*, 651–660. [[CrossRef](#)]
8. Lech, M.; Niesobska, A.; Trusek-holownia, A. Dairy wastewater utilization: Separation of whey proteins in membrane and chromatographic processes. *Desalin. Water Treat.* **2016**, *3994*. [[CrossRef](#)]
9. Sioutopoulos, D.; Karabelas, A. Membrane Fouling Due to Protein—Polysaccharide Mixtures in Dead-End Ultrafiltration; the Effect of Permeation Flux on Fouling Resistance. *Membranes* **2019**, *9*, 21. [[CrossRef](#)]
10. Zhou, R.; Ren, P.; Yang, H.; Xu, Z. Fabrication of antifouling membrane surface by poly (sulfobetaine methacrylate)/polydopamine co-deposition. *J. Memb. Sci.* **2014**, *466*, 18–25. [[CrossRef](#)]
11. Tripathi, B.P.; Das, P.; Simon, F.; Stamm, M. Ultralow fouling membranes by surface modification with functional polydopamine. *Eur. Polym. J.* **2018**, *99*, 80–89. [[CrossRef](#)]
12. Yu, C.; Gao, B.; Wang, W.; Xu, X.; Yue, Q. Chemosphere Alleviating membrane fouling of modified polysulfone membrane via coagulation pretreatment/ultrafiltration hybrid process. *Chemosphere.* **2019**, *235*, 58–69. [[CrossRef](#)] [[PubMed](#)]



13. Nthunya, L.N.; Gutierrez, L.; Lapeire, L.; Verbeken, K.; Zaouri, N.; Nxumalo, E.N.; Mamba, B.B.; Verliefe, A.R.; Mhlanga, S.D. Fouling-resistant PVDF nano fiber membranes for the desalination of brackish water in membrane distillation. *Sep. Purif. Technol.* **2019**, *228*, 115793. [[CrossRef](#)]
14. Salama, A.; Zoubek, M.; Henni, A.; El, M. A new modeling approach for flux declining behavior during the filtration of oily-water systems due to coalescence and clustering of oil droplets: Experimental and multicontinuum investigation. *Sep. Purif. Technol.* **2019**, *227*, 115688. [[CrossRef](#)]
15. Cheng, L.; Shaikh, A.R.; Fang, L.; Jeon, S.; Liu, C.; Zhang, L.; Wu, H.; Wang, D.; Matsuyama, H. Fouling-Resistant and Self-Cleaning Aliphatic Polyketone Membrane for Sustainable Oil – Water Emulsion Separation. *ACS Appl. Mater. Interfaces.* **2018**, *10*, 44880–44889. [[CrossRef](#)]
16. Li, Y.; Shi, S.; Cao, H.; Zhao, Z.; Su, C.; Wen, H. Improvement of the antifouling performance and stability of an anion exchange membrane by surface modification with graphene oxide (GO) and polydopamine (PDA). *J. Memb. Sci.* **2018**, *566*, 44–53. [[CrossRef](#)]
17. Guo, Y.; Sun, P.; Wei, J. New insight into the fouling behavior of hydrophobic and hydrophilic polypropylene membranes in integrated membrane bioreactors. *J. Environ. Technol.* **2018**, 3330. [[CrossRef](#)]
18. Huner, I.D.; Gulec, H.A. Fouling behavior of poly (ether) sulfone ultrafiltration membrane during concentration of whey proteins: Effect of hydrophilic modification using atmospheric pressure argon jet plasma. *Colloids Surfaces B Biointerfaces.* **2017**, *160*, 510–519. [[CrossRef](#)]
19. Shen, L.; Wang, H.; Zhang, Y.; Li, R.; Fabien, B.; Yu, G.; Lin, H.; Liao, B. New strategy of grafting hydroxyethyl acrylate (HEA) via  $\gamma$  ray radiation to modify polyvinylidene fluoride (PVDF) membrane: Thermodynamic mechanisms of the improved antifouling performance. *Sep. Purif. Technol.* **2018**, *207*, 83–91. [[CrossRef](#)]
20. Rajakumaran, R.; Boddu, V.; Kumar, M.; Shalaby, M.S.; Abdallah, H. Effect of ZnO morphology on GO-ZnO modified polyamide reverse osmosis membranes for desalination. *Desalination.* **2019**, *467*, 245–256. [[CrossRef](#)]
21. Davenport, D.M.; Lee, J.; Elimelech, M. Efficacy of antifouling modification of ultra filtration membranes by grafting zwitterionic polymer brushes. *Sep. Purif. Technol.* **2017**, *189*, 389–398. [[CrossRef](#)]
22. Chen, X.; He, X.; Suo, X.; Huang, J.; Gong, Y.; Liu, Y.; Li, H. Effect of surface topological structure and chemical modification of flame sprayed aluminum coatings on the colonization of *Cylindrotheca closterium* on their surfaces. *Appl. Surf. Sci.* **2016**, *388*, 385–391. [[CrossRef](#)]
23. Nguyen, A.; Azari, S.; Zou, L. Coating zwitterionic amino acid l-DOPA to increase fouling resistance of forward osmosis membrane. *Desalination* **2013**, *312*, 82–87. [[CrossRef](#)]
24. Chang, X.; Wang, Z.; Quan, S.; Xu, Y.; Jiang, Z.; Shao, L. Exploring the synergetic effects of graphene oxide (GO) and polyvinylpyrrolidone (PVP) on poly (vinylidene fluoride)(PVDF) ultrafiltration membrane performance. *Appl. Surf. Sci.* **2014**, *316*, 537–548. [[CrossRef](#)]
25. Jiang, J.; Zhu, L.; Zhu, L.; Zhang, H.; Zhu, B.; Xu, Y. Antifouling and antimicrobial polymer membranes based on bioinspired polydopamine and strong hydrogen-bonded poly(n-vinyl pyrrolidone). *ACS Appl. Mater. Interfaces.* **2013**, *5*, 12895–12904. [[CrossRef](#)] [[PubMed](#)]
26. Yang, H.C.; Wu, M.B.; Li, Y.J.; Chen, Y.F.; Wan, L.S.; Xu, Z.K. Effects of polyethyleneimine molecular weight and proportion on the membrane hydrophilization by codepositing with dopamine. *J. Appl. Polym. Sci.* **2016**, *133*, 1–10. [[CrossRef](#)]
27. Lv, Y.; Yang, H.; Liang, H.; Wan, L.; Xu, Z. Nanofiltration membranes via co-deposition of polydopamine/polyethylenimine followed by cross-linking. *J. Memb. Sci.* **2015**, *476*, 50–58. [[CrossRef](#)]
28. Wang, Z.-X.; Lau, C.-H.; Zhang, N.-Q.; Bai, Y.-P.; Shao, L. Mussel-inspired tailoring of membrane wettability for harsh water treatment. *J. Mater. Chem. A.* **2015**, *3*, 2650–2657. [[CrossRef](#)]
29. Li, J.; Yuan, S.; Wang, J.; Zhu, J.; Shen, J. Mussel-inspired modification of ion exchange membrane for monovalent separation. *J. Memb. Sci.* **2018**, *553*, 139–150. [[CrossRef](#)]
30. Shi, H.; He, Y.; Pan, Y.; Di, H.; Zeng, G.; Zhang, L.; Zhang, C. A modified mussel-inspired method to fabricate TiO<sub>2</sub> decorated superhydrophilic PVDF membrane for oil/water separation. *J. Memb. Sci.* **2016**, *506*, 60–70. [[CrossRef](#)]
31. Kasemset, S.; Wang, L.; He, Z.; Miller, D.J.; Kirschner, A.; Freeman, B.D.; Sharma, M.M. Influence of polydopamine deposition conditions on hydraulic permeability, sieving coefficients, pore size and pore size distribution for a polysulfone ultrafiltration membrane. *J. Memb. Sci.* **2017**, *522*, 100–115. [[CrossRef](#)]
32. Li, R.; Liu, J.; Shi, A.; Luo, X.; Lin, J.; Zheng, R.; Fan, H.; Selasie, S.V.; Lin, H. A facile method to modify polypropylene membrane by polydopamine coating via inkjet printing technique for superior performance. *J. Colloid Interface Sci.* **2019**, *552*, 719–727. [[CrossRef](#)] [[PubMed](#)]

33. Li, R.; Wu, Y.; Shen, L.; Chen, J.; Lin, H. A novel strategy to develop antifouling and antibacterial conductive Cu/polydopamine/polyvinylidene fluoride membranes for water treatment. *J. Colloid Interface Sci.* **2018**, *531*, 493–501. [[CrossRef](#)] [[PubMed](#)]
34. Chen, X.; Zhai, Y.; Han, X.; Liu, H.; Hu, Y. Surface chemistry-dominated underwater superoleophobic mesh with mussel-inspired zwitterionic coatings for oil/water separation and self-cleaning. *Appl. Surf. Sci.* **2019**, *483*, 399–408. [[CrossRef](#)]
35. Xia, Y.; Dai, X.; Gai, J. Preparation of high-performance reverse osmosis membrane by zwitterionic polymer coating in a facile one-step way. *J. Appl. Polym. Sci.* **2019**, *48355*, 1–11. [[CrossRef](#)]
36. Lee, H.; Dellatore, S.M.; Miller, W.M.; Messersmith, P.B. Mussel-Inspired Surface Chemistry for Multifunctional Coatings. *Science* **2007**, *318*, 426–430. [[CrossRef](#)]
37. Cheng, C.; Li, S.; Zhao, W.; Wei, Q.; Nie, S.; Sun, S.; Zhao, C. The hydrodynamic permeability and surface property of polyethersulfone ultrafiltration membranes with mussel-inspired polydopamine coatings. *J. Memb. Sci.* **2012**, *417–418*, 228–236. [[CrossRef](#)]
38. Xiang, Y.; Liu, F.; Xue, L. Under seawater superoleophobic PVDF membrane inspired by polydopamine for efficient oil/seawater separation. *J. Memb. Sci.* **2015**, *476*, 321–329. [[CrossRef](#)]
39. Wang, R.; Song, X.; Xiang, T.; Liu, Q.; Su, B.; Zhao, W.; Zhao, C. Mussel-inspired chitosan-polyurethane coatings for improving the antifouling and antibacterial properties of polyethersulfone membranes. *Carbohydr. Polym.* **2017**, *168*, 310–319. [[CrossRef](#)]
40. Kasemset, S.; Lee, A.; Miller, D.J.; Freeman, B.D.; Sharma, M.M. Effect of polydopamine deposition conditions on fouling resistance, physical properties, and permeation properties of reverse osmosis membranes in oil/water separation. *J. Memb. Sci.* **2013**, *426*, 208–216. [[CrossRef](#)]
41. Wu, J.; Zhang, L.; Wang, Y.; Long, Y.; Gao, H.; Zhang, X.; Zhao, N.; Cai, Y.; Xu, J. Mussel-inspired chemistry for robust and surface-modifiable multilayer films. *Langmuir.* **2011**, *27*, 13684–13691. [[CrossRef](#)] [[PubMed](#)]
42. Xi, Z.Y.; Xu, Y.Y.; Zhu, L.P.; Wang, Y.; Zhu, B.K. A facile method of surface modification for hydrophobic polymer membranes based on the adhesive behavior of poly(DOPA) and poly(dopamine). *J. Memb. Sci.* **2009**, *327*, 244–253. [[CrossRef](#)]
43. Xue, Q.; Cao, H.; Meng, F.; Quan, M.; Gong, Y.K. Cell membrane mimetic coating immobilized by mussel-inspired adhesion on commercial ultrafiltration membrane to enhance antifouling performance. *J. Memb. Sci.* **2017**, *528*, 1–11. [[CrossRef](#)]
44. Yang, H.-C.; Luo, J.; Lv, Y.; Shen, P.; Xu, Z.-K. Surface Engineering of Polymer Membranes. *J. Memb. Sci.* **2015**, *483*, 42–59. [[CrossRef](#)]
45. Zhang, Y.; Wang, Z.; Lin, W.; Sun, H.; Wu, L.; Chen, S. A facile method for polyamide membrane modification by poly(sulfobetaine methacrylate) to improve fouling resistance. *J. Memb. Sci.* **2013**, *446*, 164–170. [[CrossRef](#)]
46. Yang, J.; Xu, H.; Zhang, L.; Zhong, Y.; Sui, X.; Mao, Z. Lasting superhydrophobicity and antibacterial activity of Cu nanoparticles immobilized on the surface of dopamine modified cotton fabrics. *Surf. Coatings Technol.* **2017**, *309*, 149–154. [[CrossRef](#)]
47. He, Y.; Xu, L.; Feng, X.; Zhao, Y.; Chen, L. Dopamine-induced nonionic polymer coatings for significantly enhancing separation and antifouling properties of polymer membranes: Codeposition versus sequential deposition. *J. Memb. Sci.* **2017**, *539*, 421–431. [[CrossRef](#)]
48. Jiang, J.H.; Zhu, L.P.; Li, X.L.; Xu, Y.Y.; Zhu, B.K. Surface modification of PE porous membranes based on the strong adhesion of polydopamine and covalent immobilization of heparin. *J. Memb. Sci.* **2010**, *364*, 194–202. [[CrossRef](#)]
49. Li, M.; Xu, J.; Chang, C.; Feng, C.; Zhang, L. Bioinspired fabrication of composite nano filtration membrane based on the formation of DA/PEI layer followed by cross-linking. *J. Memb. Sci.* **2014**, *459*, 62–71. [[CrossRef](#)]
50. McCloskey, B.D.; Park, H.B.; Ju, H.; Rowe, B.W.; Miller, D.J.; Chun, B.J.; Kin, K.; Freeman, B.D. Influence of polydopamine deposition conditions on pure water flux and foulant adhesion resistance of reverse osmosis, ultrafiltration, and microfiltration membranes. *Polymer.* **2010**, *51*, 3472–3485. [[CrossRef](#)]
51. Oymaci, P.; Nijmeijer, K.; Borneman, Z. Development of Polydopamine Forward Osmosis Membranes with Low Reverse Salt Flux. *Membranes* **2020**, *10*, 94. [[CrossRef](#)] [[PubMed](#)]
52. Yang, H.-C.; Liao, K.-J.; Huang, H.; Wu, Q.-Y.; Wan, L.-S.; Xu, Z.-K. Mussel-inspired modification of a polymer membrane for ultra-high water permeability and oil-in-water emulsion separation. *J. Mater. Chem. A.* **2014**, *2*, 10225–10230. [[CrossRef](#)]

53. Xue, S.; Li, C.; Li, J.; Zhu, H.; Guo, Y. A catechol-based biomimetic strategy combined with surface mineralization to enhance hydrophilicity and anti-fouling property of PTFE flat membrane. *J. Membr.* **2017**, *524*, 409–418. [[CrossRef](#)]
54. Shi, H.; Xue, L.; Gao, A.; Fu, Y.; Zhou, Q.; Zhu, L. Fouling-resistant and adhesion-resistant surface modification of dual layer PVDF hollow fiber membrane by dopamine and quaternary polyethyleneimine. *J. Memb. Sci.* **2016**, *498*, 39–47. [[CrossRef](#)]
55. Xu, Y.C.; Wang, Z.X.; Cheng, X.Q.; Xiao, Y.C.; Shao, L. Positively charged nanofiltration membranes via economically mussel-substance-simulated co-deposition for textile wastewater treatment. *Chem. Eng. J.* **2016**, *303*, 555–564. [[CrossRef](#)]
56. Yang, Q.; Luo, J.; Guo, S.; Hang, X.; Chen, X.; Wan, Y. Threshold flux in concentration mode: Fouling control during clarification of molasses by ultrafiltration. *J. Memb. Sci.* **2019**, *586*, 130–139. [[CrossRef](#)]
57. Zin, G.; Wu, J.; Rezzadori, K.; Petrus, J.C.C.; Di Luccio, M.; Li, Q. Modification of hydrophobic commercial PVDF microfiltration membranes into superhydrophilic membranes by the mussel-inspired method with dopamine and polyethyleneimine. *Sep. Purif. Technol.* **2019**, *212*, 641–649. [[CrossRef](#)]
58. Bradford, M.M. A Rapid and Sensitive Method for the Quantitation Microgram Quantities of Protein Utilizing the Principle of Protein-Dye Binding. *Anal. Biochem.* **1976**, *254*, 248–254. [[CrossRef](#)]
59. Li, F.; Meng, J.; Ye, J.; Yang, B.; Tian, Q.; Deng, C. Surface modification of PES ultrafiltration membrane by polydopamine coating and poly(ethyleneglycol) grafting: Morphology stability, and anti-fouling. *Desalination* **2014**, *344*, 422–430. [[CrossRef](#)]
60. Guan, N.; Chew, P.; Zhao, S.; Malde, C.; Wang, R. Superoleophobic surface modification for robust membrane distillation performance. *J. Memb. Sci.* **2017**, *541*, 162–173. [[CrossRef](#)]
61. Xu, F.; Wei, M.; Zhang, X.; Song, Y.; Zhou, W.; Wang, Y. How Pore Hydrophilicity Influences Water Permeability? *Research* **2019**, *2019*, 1–10. [[CrossRef](#)]
62. Azari, S.; Zou, L. Using zwitterionic amino acid L-DOPA to modify the surface of thin film composite polyamide reverse osmosis membranes to increase their fouling resistance. *J. Memb. Sci.* **2012**, *401–402*, 68–75. [[CrossRef](#)]



© 2020 by the authors. Licensee MDPI, Basel, Switzerland. This article is an open access article distributed under the terms and conditions of the Creative Commons Attribution (CC BY) license (<http://creativecommons.org/licenses/by/4.0/>).

Article

# Effect of pH on Total Volume Membrane Charge Density in the Nanofiltration of Aqueous Solutions of Nitrate Salts of Heavy Metals

Agata Marecka-Migacz <sup>1</sup>, Piotr Tomasz Mitkowski <sup>1,\*</sup> , Arkadiusz Nędzarek <sup>2</sup> ,  
Jacek Różański <sup>1</sup> and Waldemar Szaferski <sup>1</sup>

<sup>1</sup> Division of Chemical Engineering and Equipment, Institute of Chemical Technology and Engineering, Poznan University of Technology, 60-965 Poznań, Poland; agata.j.marecka@doctorate.put.poznan.pl (A.M.-M.); jacek.rozanski@put.poznan.pl (J.R.); waldemar.szaferski@put.poznan.pl (W.S.)

<sup>2</sup> Department of Aquatic Bioengineering and Aquaculture, West Pomeranian University of Technology in Szczecin, 71-550 Szczecin, Poland; Arkadiusz.Nedzarek@zut.edu.pl

\* Correspondence: piotr.mitkowski@put.poznan.pl; Tel.: +48-61-665-3334

Received: 30 July 2020; Accepted: 11 September 2020; Published: 14 September 2020



**Abstract:** The separation efficiencies of aqueous solutions containing nitric salts of Zn, Cu, Fe or Pb at various pH in process of nanofiltration have been investigated experimentally. These results were used to obtain the total volume membrane charge densities, through mathematical modelling based on the Donnan–Steric partitioning Model. The experimentally obtained retention values of individual heavy metal ions varied between 36% (Zn<sup>2+</sup> at pH = 2), 57% (Pb<sup>2+</sup> at pH = 2), 80% (Fe<sup>3+</sup> at pH = 9), and up to 97% (Cu<sup>2+</sup> at pH = 9). The mathematical modelling allowed for fitting the total volume membrane charge density ( $X_d$ ), which yielded values ranging from  $-451.90$  to  $+900.16$  mol/m<sup>3</sup> for different non-symmetric ions. This study presents the application of nanofiltration (NF) modelling, including a consideration of each ion present in the NF system—even those originating from solutions used to adjust the pH values of the feed.

**Keywords:** nanofiltration; DSPM model; heavy metals; total volume membrane charge density; ceramic membrane

## 1. Introduction

Nowadays, dynamically thriving chemical plants produce high volumes of wastewaters, and, therefore, in many cases, they are a source of polluted water containing heavy metals. In many references, Cu, Pb and Zn have been mentioned as the most dangerous heavy metals, which are produced by chemical-intensive industries at a large scale [1–3]. Based on the information placed on the website of the United States Environmental Protection Agency and according to The National Primary Drinking Water Regulations (NPDWR) [4], the concentration of heavy metals such as Cu, Fe, Zn or Pb in drinking water cannot exceed 1.3 mg/L, 0.3 mg/L, 5 mg/L and 0.015 mg/L, respectively. The origins of pollution with heavy metals are various; however, the sources can be related to the corrosion of household plumbing systems, the erosion of natural deposits across liquid industrial wastes in ore enrichment plants, inorganic paint factories, production involving galvanization, etc.

Current knowledge indicates that it is better to prevent than combat the effects; therefore, recent research has been directed towards methods of preventing the migration of heavy metals from industrial wastewaters to the environment at the source, rather than through their treatment later on. The removal of heavy metals from inorganic effluents can be achieved by conventional treatment processes, such as chemical precipitation, flotation, ion exchange and electrochemical deposition. These processes

have significant disadvantages, which include: incomplete removal, high-energy requirements, and the production of toxic sludge [2]. Newer processes, such as adsorption on novel adsorbents (natural materials) [5], photocatalytic processes [6], electro dialysis [7] or membrane processes [8–13], appear to be more effective than traditional treatment methods [14]. When high contaminant removal is a goal, nanofiltration is generally found to be cost-effective [14,15]. However, wide industrial applications are limited by the relatively high operational costs [14]. In the last 20 years, membrane processes have gained significant attention in the field of separation processes [16–18]. The continuous development of new polymeric and inorganic membranes with high efficiency and selectivity as well as the improved knowledge regarding separation mechanisms allowed for the replacement of conventional techniques using membrane processes [19]. Nanofiltration (NF) is a process with low power demand in comparison to reverse osmosis or distillation, which works in the pressure range of 0.4–3 MPa, and also it does not introduce any additional ingredients that may pose problems with their removal, or affect the purity of the product [17,19–21].

One of the most important features of nanofiltration membranes is their ability to separate ions from water. The NF process can recover metallic ions, or at least retain them, and it can be used to concentrate solutions containing multivalent salts or to fractionate salts based on the different charge densities and hydrated sizes of the ions [22,23]. Examples of applications of ions and hardness recovery with use of NF processes are presented in many reports [16,24–26]. With the growing interest in NF as a separation technique for a wide range of applications, even under harsh conditions, ZrO<sub>2</sub> or TiO<sub>2</sub> membranes are increasingly preferred due to their high chemical, thermal and mechanical resistance [27,28] and easy interaction between metallic species and ceramic materials [25]. Therefore, the use of ceramic membranes in aggressive systems, including extreme pH values, is recommended [29–31].

In general, transport during NF depends on diffusion, convection and electrostatic interactions [32]. For a charged compound, both steric hindrance and electrostatic interactions are responsible for rejection [33,34]. Another important parameter in the transport and interpretation of retention is the membrane charge present along the surface of a membrane and also through the pores [35]. A strong charge present at the membrane surface has a crucial effect on the ion retention of the membrane [36]; unfortunately, the experimental determination of the membrane charge, which could explain ion transport through a NF membrane, is challenging. Therefore, a modelling-based approach has been published [23]. However, there is no experimental technique which would enable the quantification of the membrane charge value in direct way, especially during separation. Nowadays, the only possible way is to use streaming potential techniques [37–39]. As a result, zeta-potential values are obtained, while such measurement methods require a sample in a flat, powder or even fibre form, which requires the destruction of a membrane. Therefore, the authors of this study postulate using mathematical modelling to determine the total volume membrane charge density and correlate the pH of separated solutions, which would help in the assessment of membrane performance.

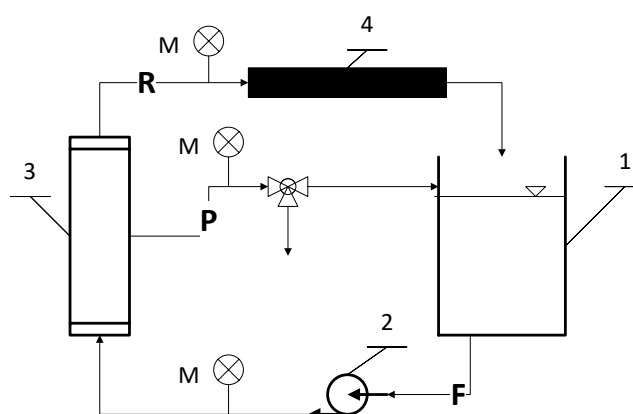
In the mathematical modelling of NF, three groups of models describing transport across a membrane can be distinguished. The first group of models is derived from irreversible thermodynamics and considers the membrane as a black box. The other two groups of models additionally take into account the properties of the membrane and are divided into: solution-diffusion and pore-flow models [19]. Over the last few decades many transport models have been proposed such as the Steric-Hindrance-Pore model, Electric-Steric-Hindrance-Pore model, Teorell–Mayer–Sievers model, Frictional model, or Space-Charge model [19,40,41]. More recently, Nair et al. [42] determined membrane transport parameters and effective pore size with the Spiegler–Kedem model and the Steric-Hindrance-Pore model. In 2019 Nair et al. [43] explained the effect of pH on flux variation with the use of the Spiegler–Kedem and Steric-Hindrance-Pore models. Bowen et al. [44–47] proposed the Donnan–Steric partitioning model (DSPM), which has also been used by others [48–54] with fairly good results. Xu et al. [55] investigated temperature influences on the retention of fourteen kinds of pharmaceuticals and personal care products by NF membranes and predicted their performances at given feed temperatures with the use of refined DSPM and a Dielectric-Exclusion model incorporated

with temperature functions. Kingsbury and co-authors [56] used the solution-diffusion model as a common framework to compare the permeability, partition and diffusion coefficients, water permeance, and salt rejection of twenty commercial ion exchange membranes. Despite the modelling approaches presented above, the novel computational methodology was developed by Rall et al. [57], who integrated accurate physical models of ion transport—valid on the nano-scale—into the large-scale superstructure optimization of the membrane. Nevertheless, none of these models are fully predictive, due to the difficulties associated with the identification of certain model parameters [58].

In order to predict the separation performance, it is important to evaluate the membrane charge density in well-defined solutions. To the best of our knowledge, there is no paper presenting the volume charge membrane densities obtained with the DSPM model correlated with values of pH. Therefore, the authors aim to consider each ion and water in modelling, to therefore provide values of the total volume membrane charge densities—along with their correlation to the pH of separated solutions—through mathematical modelling. As a case study, the nanofiltration of aqueous solutions of nitric salts of  $\text{Cu}^{2+}$ ,  $\text{Zn}^{2+}$ ,  $\text{Fe}^{3+}$  and  $\text{Pb}^{2+}$ , at various pH values, was studied experimentally and with the described DSPM model.

## 2. Materials and Methods

All experiments were conducted using the experimental set-up schematically presented in Figure 1, equipped with 19-channel ceramic  $\text{Al}_2\text{O}_3/\text{TiO}_2$  nanofiltration membranes (Inopor, Germany) with the following characteristics: cut-off at 450 Da, porosity of 0.3, membrane active layer thickness  $0.5 \mu\text{m}$  [59], pore radius 0.9 nm, length of 1178 mm, external diameter of 25 mm, channel diameter of 3.5 mm, and a filtration area of  $0.25 \text{ m}^2$ . The Point of Zero Charge (PZC) of the membrane used in the NF process was equal to  $6.0 \pm 0.9$  (reported by the manufacturer). Transmembrane pressure (TMP) was set to 0.4 MPa and the cross-flow velocity was equal to 4 m/s. The process temperature was fixed and amounted to  $293 \pm 1.0 \text{ K}$ . The system operated in continuous mode. Thus, both permeate and retentate were driven to the feed reservoir to keep the concentration of the experiments constant and simulate a continuous filtration process. The steady state was usually obtained after 90 min of operation in continuous mode. More details regarding the experimental set-up can be found in [60]. After each filtration, the membrane was chemically cleaned according to the manufacturer's recommendations, described by Nędzarek et al. [30] and Bonisławska et al. [61]: washing with 2% NaOH solution ( $T = 360 \text{ K}$ ,  $t = 40 \text{ min}$ ), rinsing with ultra-pure water, washing with 0.5%  $\text{HNO}_3$  solution ( $T = 320 \text{ K}$ ,  $t = 30 \text{ min}$ ), and, finally, rinsing three times with ultra-pure water. Chemical washing resulted in a performance characteristic for a clean membrane.



**Figure 1.** Schema of the laboratory plant: 1—feed/retentate tank; 2—pump; 3—membrane module; 4—radiator; F—feed; R—retentate; P—permeate; M—manometer.

Working solutions subjected to nanofiltration contained single aqueous solutions of  $\text{Zn}(\text{NO}_3)_2$ ,  $\text{Cu}(\text{NO}_3)_2$ ,  $\text{Pb}(\text{NO}_3)_2$  and  $\text{Fe}(\text{NO}_3)_3$ . The initial concentration of each heavy metal ion in the solution

before filtration was equal to 500 µg/dm<sup>3</sup>, and no precipitation was observed in all investigated systems. The retention levels of the metals were measured for the following pH values: 2.0, 4.6, 6.0, 6.9, and 9.0. The pH values were controlled using 0.1 M NaOH and 0.1 M HCl. In the feeds and permeates obtained at the respective pH values, heavy metals were traced by a cathodic stripping voltammetry method (CSV). The heavy metal retention (*R*) was calculated according to Equation (1):

$$R = \left(1 - \frac{C_{p,i}}{C_{f,i}}\right) \cdot 100\%, \tag{1}$$

where *C<sub>f,i</sub>* is the concentration of individual ion in the feed and *C<sub>p,i</sub>* in the permeate solution.

#### Determination of Effective Membrane Charge Density in Nanofiltration

In order to describe the ion transport through the NF ceramic membrane, the DSPM model was utilized. In comparison with other reports [44–52,62], the modelling in this contribution considered each ion present in the system—even ions originating from solutions used to set the desired values of pH. Such a detailed approach is innovative in terms of modelling NF processes. To date, researchers who exploited the DSPM model did not take ions originating from solutions used for regulating pH, such as NaOH or HCl, into account, or at least did not show it explicitly. The solutes in aqueous solutions dissociate, then deliver specific ionic forms to the separated system. The authors are convinced that the presence of additional ions (such as Na<sup>+</sup>, OH<sup>−</sup> or H<sup>+</sup>, Cl<sup>−</sup>) may influence the total volume membrane charge density. In the model, it was also assumed that the concentrations of the components in the feed are constant (i.e., steady state model), that the transmembrane pressure for the entire duration of the process is constant, that the straight cylindrical pores of length are equal to the effective membrane layer thickness, and that the concentration polarization effect and fouling phenomena are negligible. The Reynolds number at the feed side was equal to 13,309 (*Re* = *w*·*d*·*ρ*/*η*). The solvent viscosity values were assumed to be equal to water at a process temperature equal to 20 °C, which is (*η<sub>s</sub>*) 0.00105 Pa·s. Therefore, the schematic representation of the concentration profiles is shown in Figure 2, which can be described in detail using the following set of model Equations (2)–(17).

$$V_s = \frac{r_p^2(\Delta P - \Delta\pi)}{8\eta_s\Delta x} \tag{2}$$

$$\Delta\pi = \pi_{feed} - \pi_{permeate} \tag{3}$$

$$\pi_{feed} = \frac{RT}{\tilde{V}_w} \sum_{i=1}^{NoComp} x_{f,i} \tag{4}$$

$$\pi_{permeate} = \frac{RT}{\tilde{V}_w} \sum_{i=1}^{NoComp} x_{p,i} \tag{5}$$

$$\lambda_i = \frac{r_{s,i}}{r_p} \tag{6}$$

$$\phi_i = (1 - \lambda_i)^2 \tag{7}$$

$$K_{d,i} = 1 - 2.3\lambda_i + 1.154\lambda_i^2 + 0.224\lambda_i^3 \tag{8}$$

$$K_{c,i} = (2 - \phi_i)(1 + 0.054\lambda_i - 0.988\lambda_i^2 + 0.441\lambda_i^3) \tag{9}$$

$$\frac{dc_i}{dx} = \frac{V_s}{K_{d,i}D_i} (K_{c,i}c_i - C_{p,i}) - \frac{F}{RT} z_i c_i \frac{d\psi}{dx} \tag{10}$$

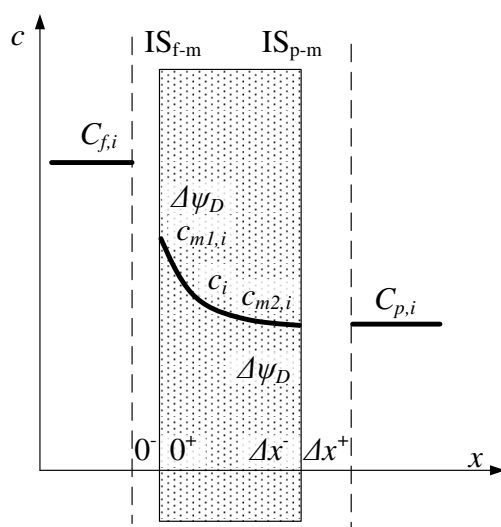
$$\frac{d\psi}{dx} = \frac{\sum_{i=1}^{NoComp} \left( \frac{z_i V_s}{D_i} (K_{c,i} c_i - C_{p,i}) \right)}{\frac{F}{RT} \sum_{i=1}^{NoComp} (z_i^2 c_i)} \quad (11)$$

$$\sum_{i=1}^{NoComp} c_{m1,i} z_i = -X_d \quad (12)$$

$$\sum_{i=1}^{NoComp} C_{p,i} z_i = 0 \quad (13)$$

$$c_{m,i} = C_{f,i} \phi_i \exp\left(-\frac{z_i F}{RT} \psi_D\right) \quad (14)$$

$$R_i = 1 - \frac{C_{p,i}}{C_{f,i}} \quad (15)$$



**Figure 2.** Concentration profiles of ions in the membrane active layer and external solutions, considering the Donnan potentials, where  $C_{f,i}$  and  $C_{p,i}$  are the concentrations of individual ion in the feed and permeate solution, respectively;  $\Delta x$  is the membrane active layer thickness;  $c_{m1,i}$  and  $c_{m2,i}$  are the concentrations of the individual ion at both the feed and permeate boundaries, respectively;  $c_i$  is the concentration of individual ion along the pores.  $IS_{f-m}$  and  $IS_{p-m}$  represent the interfacial surfaces of feed–membrane and permeate–membrane, respectively.

Boundary conditions:

$$c_i(0^+) = c_{m1,i} \quad (16)$$

$$c_i(\Delta x^-) = C_{p,i} \quad (17)$$

All model variables and model equations were reported and described in Tables 1 and 2, respectively. The degree of freedom (DOF) of the presented model is equal to  $8 + 8 \cdot NC$ , where NC stands for number of compounds present in the mixture. The values of diffusion coefficients and sizes of ions were reported in Table 3, while the permeate fluxes obtained for each variant were around  $8.06 \times 10^{-5}$  m/s.



**Table 1.** Variables in Donnan–Steric partitioning model (DSPM) (NC—number of components).

Differential Variables		Number
Concentration of ion in the membrane [mol/m <sup>3</sup> ]	$c_i$	NC
Algebraic and Implicit Variables		Number
Potential gradient inside membrane pore [V]	$\psi$	1
Ratio of solute to pore radius [-]	$\lambda_i$	NC
Steric term [-]	$\varphi_i$	NC
Hindrance factor for diffusion [-]	$K_{d,i}$	NC
Hindrance factor for convection [-]	$K_{c,i}$	NC
Ion concentration in the permeate [mol/m <sup>3</sup> ]	$C_{p,i}$	NC
Retention coefficient [-]	$R_i$	NC
Solvent velocity [m <sup>3</sup> /m <sup>2</sup> /s]	$V_s$	1
Donnan potential [V]	$\psi_D$	1
Osmotic pressure difference [Pa]	$\Delta\pi$	1
Osmotic pressure on the feed side [Pa]	$\pi_{feed}$	1
Osmotic pressure on the permeate side [Pa]	$\pi_{permeate}$	1
Parameters and Known Variable		Number
Effective membrane charge density [mol/m <sup>3</sup> ]	$X_d$	1
Molar fraction on the feed side [mol/mol]	$x_{f,i}$	NC
Molar fraction on the permeate side [mol/mol]	$x_{p,i}$	NC
Pore radii [m]	$r_p$	1
Ion radii [m]	$r_{s,i}$	NC
Transmembrane pressure [Pa]	$\Delta P$	1
Ideal gas constant [J/(mol·K)]	$R$	1
Faraday constant [C/mol]	$F$	1
Temperature [K]	$T$	1
Solvent viscosity [Pa·s]	$\eta_s$	1
Thickness of membrane active layer [m]	$\Delta x$	1
Molar volume of water [m <sup>3</sup> /mol]	$\tilde{V}_w$	1
Diffusion coefficient of ion [m <sup>2</sup> /s]	$D_i$	NC
Charge of individual ion [e]	$z_i$	NC
Ion concentration in the feed [mol/m <sup>3</sup> ]	$C_{f,i}$	NC
Ion concentration in the membrane in the surface directly contacting with the feed [mol/m <sup>3</sup> ]	$c_{m1,i}$	NC
Ion concentration in the membrane in the surface directly contacting with the permeate [mol/m <sup>3</sup> ]	$c_{m2,i}$	NC
<b>Total number of variables: 15 + 15·NC</b>		

**Table 2.** List of equations in the DSPM model (NC—number of components).

Equation Description	Equations	Number of Equations
Solvent velocity based on Hagen–Poiseuille-type relationship	(2)	1
Osmotic pressure difference across the membrane	(3)	1
Osmotic pressure at the feed side	(4)	1
Osmotic pressure at the permeate side	(5)	1
Ratio of the solute radii to the pore radii	(6)	NC
Steric partitioning coefficient	(7)	NC
Hindrance factor for diffusion	(8)	NC
Hindrance factor for convection	(9)	NC
Concentration gradient inside the membrane pore	(10)	NC

Table 2. Cont.

Equation Description	Equations	Number of Equations
Potential gradient inside the membrane pore	(11)	1
Electroneutrality conditions in the membrane	(12)	1
Electroneutrality conditions in the permeate	(13)	1
Donnan–Steric partitioning	(14)	NC
Retention coefficient	(15)	NC
<b>Total Number of Equations: 7 + 7·NC</b>		

Table 3. Values of diffusion coefficients and size of ions.

Ion	Diffusion Coefficient, $D_i$ [m <sup>2</sup> /s]	Size of Ion/Molecule, $r_{s,i}$ [m]
Cu <sup>2+</sup>	$1.24 \times 10^{-9}$ [63]	$7.7 \times 10^{-11}$ [64]
Fe <sup>3+</sup>	$7.19 \times 10^{-9}$ [65]	$6.0 \times 10^{-11}$ [64]
Zn <sup>2+</sup>	$5.18 \times 10^{-8}$ [65]	$7.4 \times 10^{-11}$ [64]
Pb <sup>2+</sup>	$8.45 \times 10^{-9}$ [65]	$11.9 \times 10^{-11}$ [64]
NO <sub>3</sub> <sup>-</sup>	$1.25 \times 10^{-9}$ [66]	$1.79 \times 10^{-10}$ [67]
H <sup>+</sup>	$4.50 \times 10^{-9}$ [68]	$0.9 \times 10^{-9}$ [64]
Na <sup>+</sup>	$1.33 \times 10^{-9}$ [69]	$0.1 \times 10^{-9}$ [64]
OH <sup>-</sup>	$5.27 \times 10^{-9}$ [69]	$1.33 \times 10^{-10}$ [67]

Using the mathematical model presented above, it was possible to obtain the total volume membrane charge density ( $X_d$ ). The parameter estimations of total volumetric membrane charge density were performed for the sets of variants listed in Table 4. The parameter estimation computations were conducted using the gPROMS software. Parameter estimation in gPROMS is based on the maximum likelihood formulation, which provides a simultaneous estimation of parameters in the physical model of the process [70]. Assuming independent, normally distributed measurement errors—with zero means and standard deviations—the maximum likelihood goal can be achieved through the objective function presented in Equation (18) [70]. In the cases discussed in this study, the parameter estimation problems gave the following values of parameters following Equation (18):  $NE = 3$ ,  $NV = 1$ ,  $NM = 1$ ,  $N = 3$ .

$$\Phi = \frac{N}{2} \ln(2\pi) + \frac{1}{2} \min X_d \left\{ \sum_{i=1}^{NE} \sum_{j=1}^{NV_i} \sum_{k=1}^{NM_{ij}} \left[ \ln(\sigma_{ijk}^2) + \frac{(c_{ijk,mes} - c_{ijk})^2}{\sigma_{ijk}^2} \right] \right\} \quad (18)$$

where:  $\Phi$ —set of model parameters to be estimated,  $N$ —total number of measurements taken during all the experiments,  $NE$ —number of experiments performed,  $NV_i$ —number of variables measured in the  $i$ -th experiment,  $NM_{ij}$ —number of measurements of the  $j$ -th variable in the  $i$ -th experiment,  $\sigma_{ijk}^2$ —variance of the  $k$ -th measurement of variable  $j$  in experiment  $i$ ,  $c_{ijk}$ — $k$ -th measured value of variable  $j$  in experiment  $i$ ,  $c_{ijk,mes}$ — $k$ -th predicted value of variable  $j$  in experiment  $i$ .

Table 4. Variants of parameters estimation.

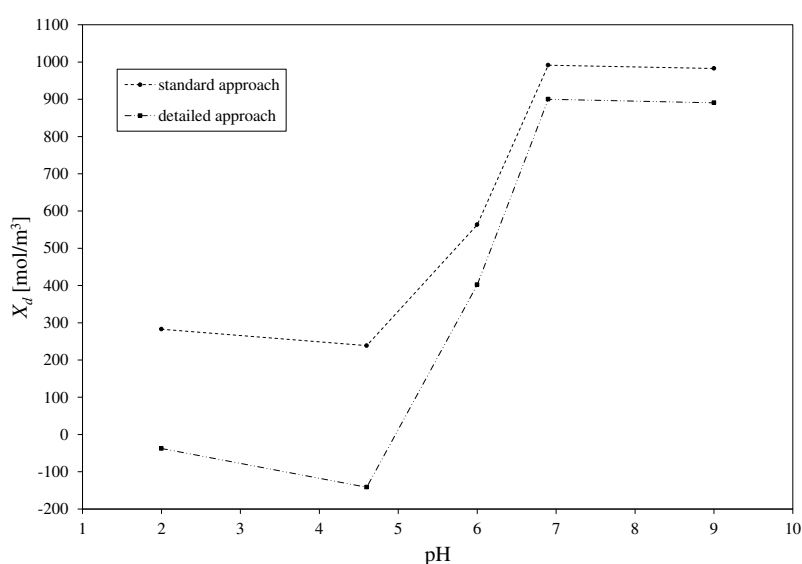
Variant	Heavy Metal Ion *	Heavy Metal Ion Concentration [mol/m <sup>3</sup> ]	pH				
			1-Set	2-Set	3-Set	4-Set	5-Set
1.	Cu <sup>2+</sup>	$7.87 \times 10^{-3}$	2.0	4.6	6.0	6.9	9.0
2.	Fe <sup>3+</sup>	$8.95 \times 10^{-3}$	2.0	4.6	6.0	6.9	9.0
3.	Zn <sup>2+</sup>	$7.69 \times 10^{-3}$	2.0	4.6	6.0	6.9	9.0
4.	Pb <sup>2+</sup>	$2.41 \times 10^{-3}$	2.0	4.6	6.0	6.9	9.0

\* All ions were introduced as nitric salts of specific heavy metal.

### 3. Results and Discussion

#### 3.1. Comparison of Standard and Detailed DSPM Nanofiltration Modelling

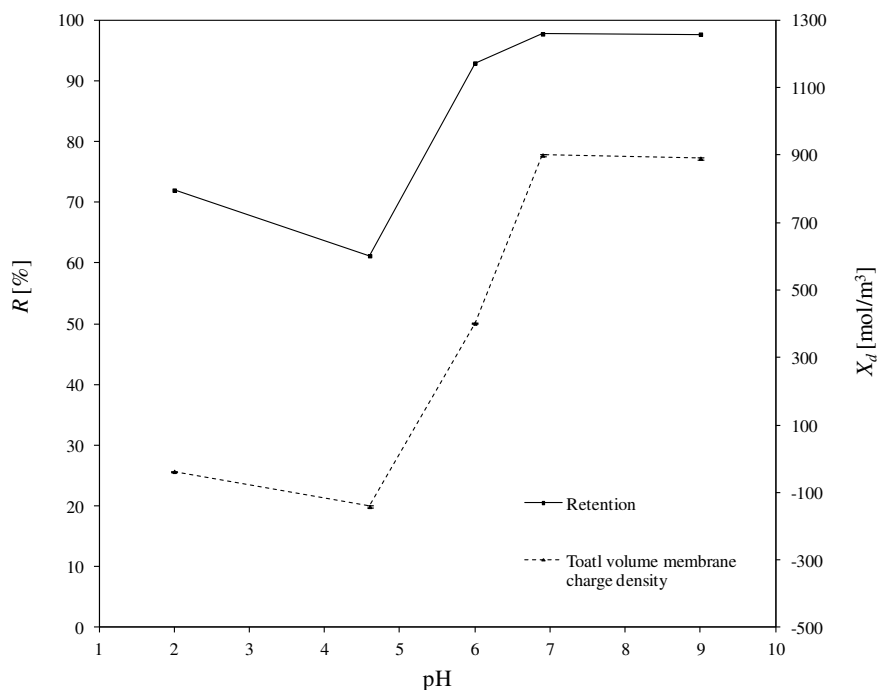
The parameter estimations were performed with the use of the above presented mathematical model. The correctness of the presented modelling approach can be acknowledged through a comparison of the estimated  $X_d$  values for the standard approach—when only ions coming from the salt are considered—with  $X_d$  values estimated with use of the detailed modelling, which takes into account each existing ion in the feed solution. Such a comparison was presented for aqueous solutions of  $\text{Cu}(\text{NO}_3)_2$ . The obtained results are presented in Figure 3. In the standard approach,  $X_d$  ranged between +282.79 and +982.87 [ $\text{mol}/\text{m}^3$ ], with a pH increase from 2 to 9, while in the detailed approach, it changed from  $-37.57$  to  $+890.62$  [ $\text{mol}/\text{m}^3$ ]. It is important to notice that the detailed DSPM model revealed a shift of total volume membrane charge to negative values between pH values equal to 4.8 and 6, which can be related to the presence of a specific isoelectric point of the separated mixture. It can be concluded that the presence of ions originating from the solution regulating the pH influenced the membrane  $X_d$  values, which is clearly visible in the detailed model. This is related to the fact that all ions and molecules present in the system may interact with each other and, therefore, influence the charge present on and in the membrane. Therefore, all results presented hereafter were obtained with use of the detailed described DSPM model.



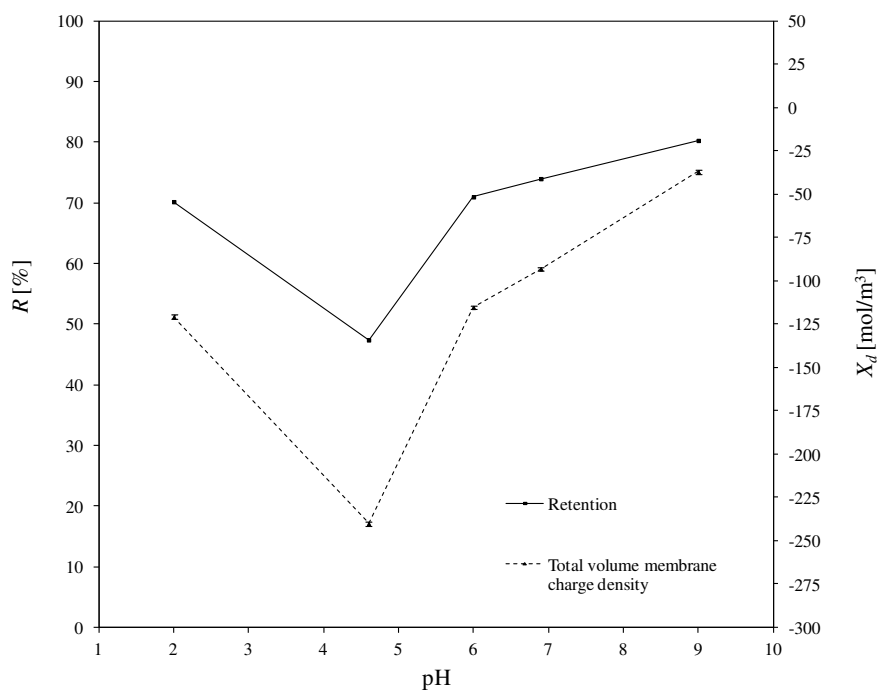
**Figure 3.** Comparison of estimated total volume membrane charge densities  $X_d$  for standard and proposed modelling approach with detailed described DSPM model, for aqueous solution of  $\text{Cu}(\text{NO}_3)_2$ .

#### 3.2. Estimated Values of Total Volume Membrane Charge Density

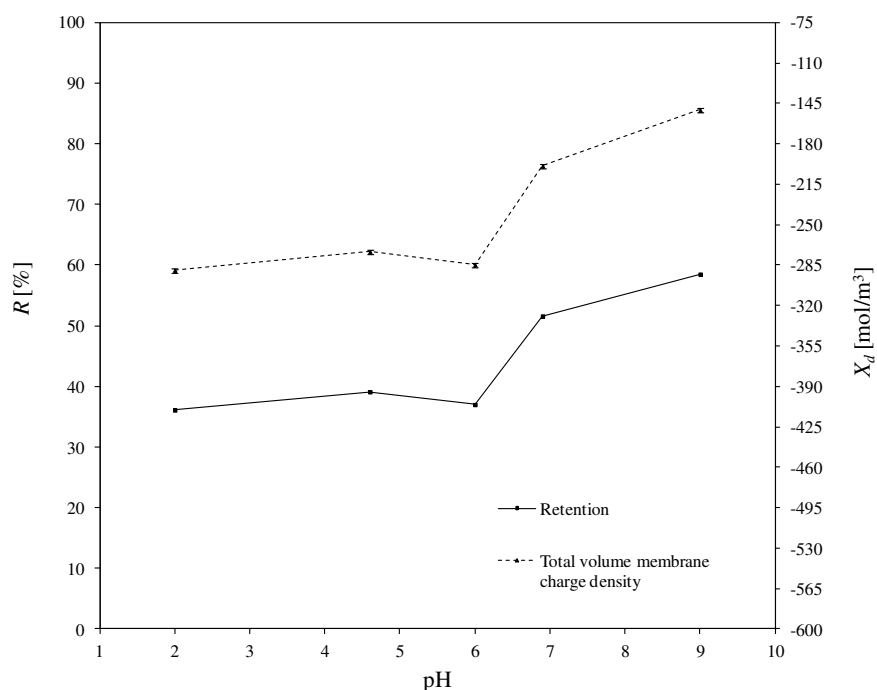
The total volume charge densities of the ceramic  $\text{TiO}_2$  membrane as a function of pH for all the experimentally investigated solutions of asymmetric salts (namely:  $\text{Cu}(\text{NO}_3)_2$ ,  $\text{Pb}(\text{NO}_3)_2$ ,  $\text{Fe}(\text{NO}_3)_3$ ,  $\text{Zn}(\text{NO}_3)_2$ ), and the influence of pH on the retention of heavy metals, are presented in Figures 4–7. For all ions, the trends of the retention curves were the same as the charge density curves in terms of their qualitative manner. All  $R = f(\text{pH})$  and  $X_d = f(\text{pH})$  curves possess the S-shape, with the inflexion in the range of pH between 4.9 and 6.0. In the case of asymmetric salt, Labbez et al. [62] have already shown that the dependency of the retention as a function of pH is described by the S-shaped curve. The values of retention rates obtained experimentally and by means of the detailed DSPM model were identical, and therefore, in this work, there is no difference in plotting experimental or calculated retentions.



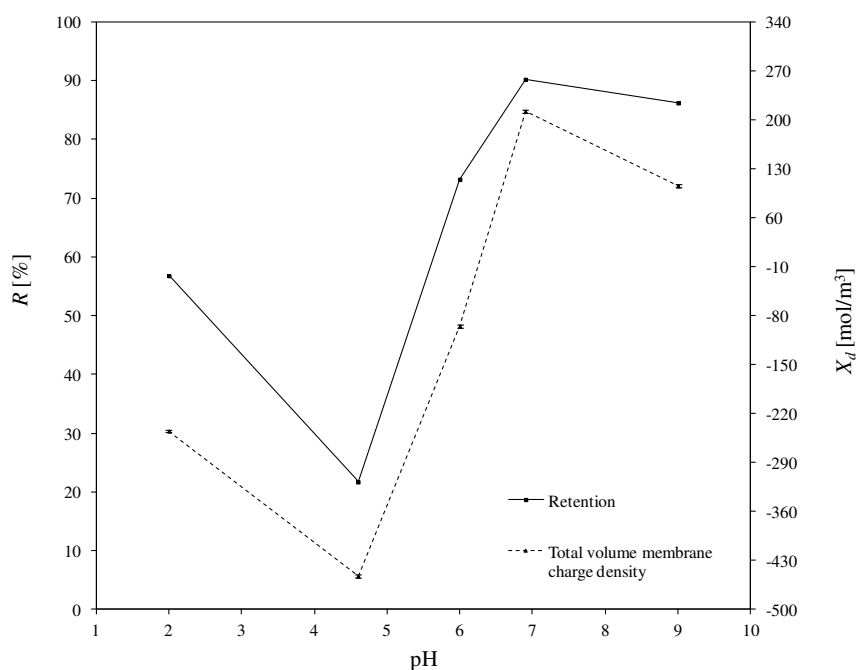
**Figure 4.** The influence of pH on the total volume charge density in aqueous solution of  $\text{Cu}(\text{NO}_3)_2$  and the influence of pH on the  $\text{Cu}^{2+}$  retention. Retention values obtained experiments.



**Figure 5.** The influence of pH on the total volume charge density in aqueous solution of  $\text{Fe}(\text{NO}_3)_3$  and the influence of pH on the  $(\text{Fe}^{3+})$  retention. Retention values obtained experiments.



**Figure 6.** The influence of pH on the total volume charge density in aqueous solution of  $Zn(NO_3)_2$  and the influence of pH on the  $(Zn^{2+})$  retention. Retention values obtained experiments.



**Figure 7.** The influence of pH on the total volume charge density in aqueous solution of  $Pb(NO_3)_2$  and the influence of pH on the  $(Pb^{2+})$  retention. Retention values obtained experiments.

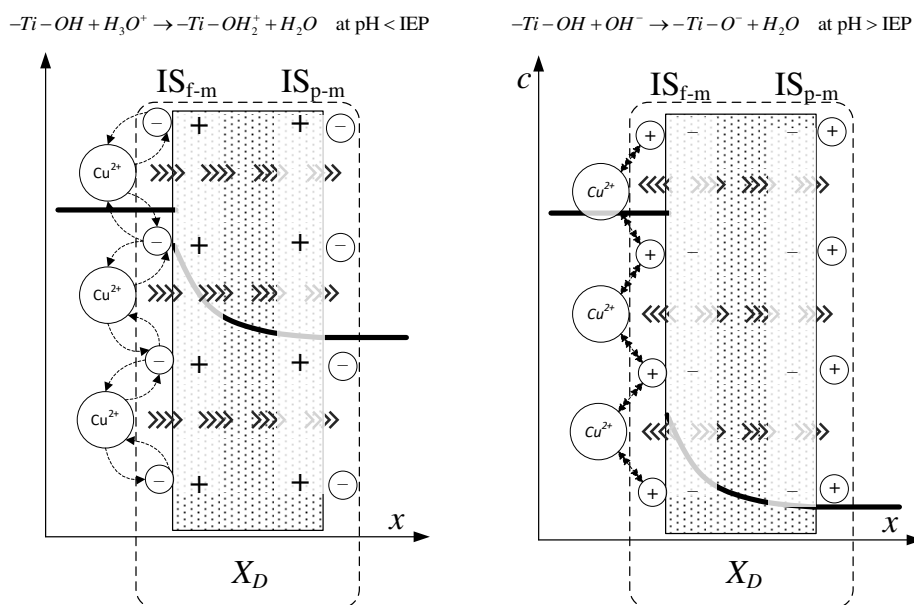
In general, the possible mechanisms for the separation of electrolytes are sieving, electrostatic interactions between the membrane and the ions or between the ions mutually, differences in diffusivity and solubility, or a combination of all those listed [19,71]. A high retention for multivalent ions is frequently combined with a moderate retention for monovalent ions. In our study, the pore size of the membrane was large enough to demonstrate that salt retention is only affected by size effects to very little extent. Taking into account the difference between the membrane cut-off (which is equal to 450 Da) and the studied ion radii—which, e.g., for the  $Pb^{2+}$  ion (the largest of the investigated ions) is

equal to  $11.9 \cdot 10^{-11}$  m—the steric effect may not justify the obtained ions retentions. For all experiments, the highest retention was achieved for  $\text{Cu}^{2+}$ . At a pH equal to 9, retention reached values above 97%. For the  $\text{Fe}^{3+}$  and  $\text{Zn}^{2+}$  ions, the highest degrees of retention rates was also achieved for a pH = 9, but the values were much lower and equal to 80.3% and 58.8%, respectively. Whereas for the  $\text{Pb}^{2+}$  ion, the highest retention was achieved for pH = 6.9 which was 90.2%. Such values of retention could be related to the differences in diffusivities and electrostatic interactions between ions and membrane. The maximum retention for  $\text{Cu}^{2+}$  may have resulted from the lowest values of diffusion coefficient of all ions and the minimum retention of  $\text{Zn}^{2+}$  from the highest diffusion coefficient of all ions (compare with Table 3).

For the estimated values of the total volume charge density for each set of ions present in the aqueous solutions, the membrane becomes different in terms of individual charge, or—in other words—the apparent charge densities on and in the membrane are significantly different. That dependence is associated with the nature of the electrolyte in the system and with the specific adsorption on the membrane surface and pore walls. For solutions containing  $\text{Cu}^{2+}$  ions (1st variant in Table 4), the  $X_d$  varied with pH changes in the range from 37.6 to 890.6 mol/m<sup>3</sup>; for the 2nd variant (Table 4), for solutions containing  $\text{Fe}^{3+}$  ions from −120.9 to −37.0 mol/m<sup>3</sup>; for the 3rd variant (Table 4), containing  $\text{Zn}^{2+}$  ions from −289.4 to −150.9 mol/m<sup>3</sup> and for last variant, which contained  $\text{Pb}^{2+}$  ions, from −245.0 to 105.6 mol/m<sup>3</sup>. At first glance, the variation of the  $X_d$  sign is surprising, especially due to the fact that all of the investigated heavy metals were in ion forms. It should also be noted that  $\text{NO}_3^-$  ions were present in all the listed variants. They were present because the investigated cations were introduced into the solution in the form of nitric (V) salt. Moreover,  $\text{Na}^+$ ,  $\text{OH}^-$  and  $\text{Cl}^-$ ,  $\text{H}^+$  ions were present in the aqueous solution, which originate from sodium base and hydrochloric acid, respectively—used for the regulation of pH.

The obtained inflections of the membrane charge density curves for all ions were confirmed; in each system, the minimal value of total volume membrane charge density was in the range of pH 4.5–6.0, which corresponds to the IEP of the studied membrane. For the  $\text{Cu}^{2+}$ ,  $\text{Fe}^{3+}$ , and  $\text{Pb}^{2+}$  ions, the minimal values of  $X_d$  were for pH = 4.6 and for  $\text{Zn}^{2+}$  for pH = 6. The type of membrane material used for the active layer influences the membrane structure, and thereby affects the membrane separation ability, but also has an influence on membrane surface charge, which depends on the material isoelectric point value. The membrane possessed a positive charge during the filtration of separated solutions with pH lower than the IEP value, whereas during the filtration of solutions with a pH higher than IEP, the membrane possessed a negative charge. Therefore, the obtained trend of total volume membrane charge densities is correct. For example, when  $\text{Cu}^{2+}$  ions are present in the system at a pH below IEP, the  $\text{Cu}^{2+}$  ions are repelled and the anions present in the feed solution are bound to the membrane, so that the overall stable charge on the membrane during that separation is negative and the retention level is lower due to the formed negative layer which attracts  $\text{Cu}^{2+}$  cations. In cases when the pH of the feed is higher than that of the IEP, the  $\text{Cu}^{2+}$  ions are attracted, and thus retention increases and the change in overall membrane charge  $X_d$  might reflect the partial surface adsorption of cations. Such behaviour of the membrane at different pH values is explained by the amphoteric behaviour of the  $\text{TiO}_2$  active membrane layer reported by Van Gestel et al. [27], which is schematically visualised in Figure 8. Unfortunately, the relation between IEP and the inflection point for the obtained curves for all investigated cases—when di(tri)-monovalent salts were studied—does not work properly for mono-monovalent salts. Van Gestel et al. [27] studied zeta potential measurements as a function of pH for mono-monovalent and mono-divalent salts ( $\text{Na}_2\text{SO}_4$ ,  $\text{CaCl}_2$ ). They concluded that mono-monovalent salts can be considered as indifferent electrolytes for the NF membrane, and that the inherent charge is due to the protonation and dissociation of surface hydroxyl groups (IEP = 6). Whereas for mono-divalent salts, that trend was totally different. The sign of the zeta potential is altered with the type of salts and salt concentrations. Those phenomena were explained by the selective adsorption of cations or anions. Depending on the forms of  $-\text{Ti}-\text{OH}$  surface groups, ions are able to form complexes. Increasing values of membrane charge densities may be caused by the selective

adsorption and additional ions adsorption; the first stage is complexation and the next is the adsorption of additional ions. Moreover, some ions may be adsorbed by the pore wall and influence the membrane charge, as suggested by Takagi et al. [72].



**Figure 8.** Schematic representation of amphoteric behavior of  $\text{TiO}_2/\text{Al}_2\text{O}_3$  active layer of membrane during separation of aqueous solution of  $\text{Cu}(\text{NO}_3)_2$ .

It is postulated that the total volume membrane charge density is determined by the sum of the fixed membrane charge density and the number of adsorbed ions. The possible mechanism for the formation of the membrane charge assumes that the ions are partitioned from the bulk solution into the membrane pore under the influence of the Donnan potential. Among the partitioned ions in the membrane pores, either cations or anions are adsorbed selectively by the pore wall. Next, the adsorbed ions are bound on the pore wall and give the electric charge to the membrane. In our opinion, the electric charge given to the membrane, which includes all these phenomena, can be seen as the total volume membrane charge density, as presented in Figure 8. In view of this, the values of total volume membrane charge density  $X_d$  will always be different depending on the type of solute (electrolyte) which is subjected to the NF process, and hence, on the ion types and the pH values as well. Such dependence was obtained for the investigated solutions. For each studied solution, the  $X_d$  values in pH range varied from 2.0 to 9.0 are different. Therefore, it can be assumed that the mechanism of selective ion adsorption acts according to the membrane sign, which is positive at a low pH and negative at a high pH; cations or anions are adsorbed on the membrane (see Figure 8), changing the values and, in two cases, the charge of  $X_d$ , which is also visible in Figures 4–7. Figure 8 shows the possible explanations of the transport of copper ions below and above IEP; however, it also should be considered as a general explanation of ion transport, whether transports of di- or tri-valent ions are studied.

Normally, the membrane became more negative at a higher pH of the feed. It needs to be highlighted that such a trend exists for monovalent salts—for example, NaCl. In this work, asymmetrical salts were considered and the observed trends were similar to those presented by Mazzoni et al. [73]. Additionally, the  $X_d$  values stated in this work are values of membrane charge density after nanofiltration process stabilization, i.e., in steady state operation. The membrane active layer functional groups ( $\text{TiO}_2$ ) take forms which depend on the pH of the feed solution contacting the membrane surface, therefore obtaining the adequate surface charge. With the advent of such charge, adsorption and charge exclusion occur, leading to stable separation and reaching the estimated  $X_d$  values.

In an acidic environment, metals occur in the form of free ions, and the absence of soluble charged metal hydroxides render the formation of an additional active separation layer on the membrane surface impossible. At low pH values, retentions are always lower than when pH increases. As the pH of the environment increases, so too does the amount of soluble metal hydroxides. Due to electrostatic effect of the separated mixture, i.e., metal hydroxides–membrane interaction, an active filtration layer can form on the membrane surface, and the retention rate increases, for  $\text{Cu}^{2+}$  from 72% (pH = 2) to 97.7% (pH = 9), for  $\text{Fe}^{3+}$  from 70.2% (pH = 2) to 80.3% (pH = 9), for  $\text{Pb}^{2+}$  from 56.8% (pH = 2) to 86.20% (pH = 9), and for  $\text{Zn}^{2+}$  from 36.1% (pH = 2) to 58.5% (pH = 9). The formation of that layer results in an increase in the density of positive charge in the membrane, which causes the cation retention to increase for all of the investigated experimental variants, as is also presented in [60]; the values of total volume membrane charge density for each variant increase, which is also presented in Figures 4–7.

Divalent ions have an important effect on the surface charge—divalent cation adsorption on the membrane surface reduces its negative charge. On the other hand, when both divalent cations and anions are present in the solution, the effect of the divalent anion is opposite to the effect of the divalent cation [35]. Therefore, the obtained total volume membrane charge densities can be related to the apparent interactions between ions present in the mixtures. These phenomena can explain the observed different values of  $X_d$  for different ions, because, as mentioned above, for each variant, all ions present in each system were taken into account. For example, for the  $\text{Cu}^{2+}$  variant in the system, ions such as  $\text{NO}_3^-$ ,  $\text{OH}^-$ ,  $\text{Na}^+$ ,  $\text{H}^+$  were also considered. Therefore, besides  $\text{Cu}^{2+}$  and membrane interactions, all various phenomena associated with those ion–ions interactions (selective absorption, Donnan partitioning) occur, which significantly influence the total volume membrane charge density values which are inherently included. Additionally, changes in the additional ions ratio in the systems influence the pH values of the feeds.

Generally, when the membrane makes contact with the aqueous electrolyte solution, it takes the electric charge according to a few possible mechanisms: functional group dissociation, the adsorption of ions from solution, and the adsorption of polyelectrolytes, ionic surfactant or charged nanoparticles. Such charge has an influence on ions distribution in the solution, in view of the electroneutrality requirements of the separated system [74]. This charging mechanism can occur on the exterior membrane surface and in the interior pore surface, due to the distribution of ions in the solution to maintain the electroneutrality of the system [75]. The membrane has the internal and surface charge density. Surface charge may be assigned to constant membrane charge (intrinsic), which is generated when the membrane is soaked in the electrolyte. This is caused in view of the acid/base dissociation or ionization of other functional groups, or ions adsorption on the membrane surface from the solution. Therefore, in this study, the overall membrane charge was considered, which presents the total volume membrane charge density created during the NF separation.

In order to enable a comparison of the obtained data with the literature data, the effective membrane charge density was rearranged to the surface charge density according to Equation (19), with the assumption that membrane surface charge is uniformly distributed on the entire intergranular volume between cylindrical pores [39]:

$$\sigma = \frac{X_d r_p F}{2} \quad (19)$$

where  $\sigma$  is the surface charge density [ $\text{C}/\text{m}^2$ ],  $r_p$  is the pore radius [m], and  $F$  is the Faraday constant [ $\text{C}/\text{mol}$ ]. The values of the total volume membrane charge densities after conversion to surface charge densities  $\sigma$  [ $\text{C}/\text{m}^2$ ] are presented in Table 5. These values are in good qualitative agreement with the values presented in [76].



**Table 5.** Values of effective charge density after conversion to surface charge density  $\sigma$ .

pH	Cu <sup>2+</sup>	Fe <sup>3+</sup>	Zn <sup>2+</sup>	Pb <sup>2+</sup>
2.0	−0.00082	−0.00262	−0.00628	−0.00532
4.6	−0.00307	−0.00521	−0.00594	−0.00981
6.0	0.00873	−0.00250	−0.00618	−0.00207
6.9	0.01954	−0.00202	−0.00432	0.00461
9.0	0.01933	−0.00080	−0.00328	0.00229

### 3.3. Determination of Corellation of the Total Volume Membrane Charge Density

In order to determine the correlation which would provide at least limited re-use of the obtained estimation results of the presented modelling, the correlations of the estimated total volume membrane charge densities were obtained. In the trial-and-error search of the feasible form of a correlation relating  $X_d$  and pH, including the Newton’s and Lagrange’s interpolating polynomial methods, Equation (20) was finally proposed:

$$\hat{X}_{d,i}(pH) = \frac{a(pH)^2 + b(pH) + c}{d(pH)^2 + e(pH) + f} \tag{20}$$

where  $a, b, c, d, e, f$  are the coefficients, the values of which are presented in Table 6 as first set of parameters.

**Table 6.** Values of parameters in Equation (20).

Set of Parameters	Parameters	Fe <sup>3+</sup>	Cu <sup>2+</sup>	Zn <sup>2+</sup>	Pb <sup>2+</sup>
First set of parameters	a	4.44	342.07	−76.42	−247.56
	b	−199.89	−2251.68	1557.69	3754.86
	c	−40.6	2369.91	−6684.97	−14,589.5
	d	1	1	1	1
	e	−6.55	−12.30	−11.72	−14.27
	f	12.59	40.73	35.28	53.18
	$S_e$	8.03	0.549	14.276	0.408
Second set of parameters	a	-	277.57	−92.68	−223.51
	b	-	−1795.30	2263.50	3104.14
	c	-	1630.37	−10,754.65	−11,272.98
	d	-	1.00	1.00	1.00
	e	-	−12.77	−12.77	−12.77
	f	-	43.06	43.06	43.06
	$S_e$	-	3.19	106.74	24.85

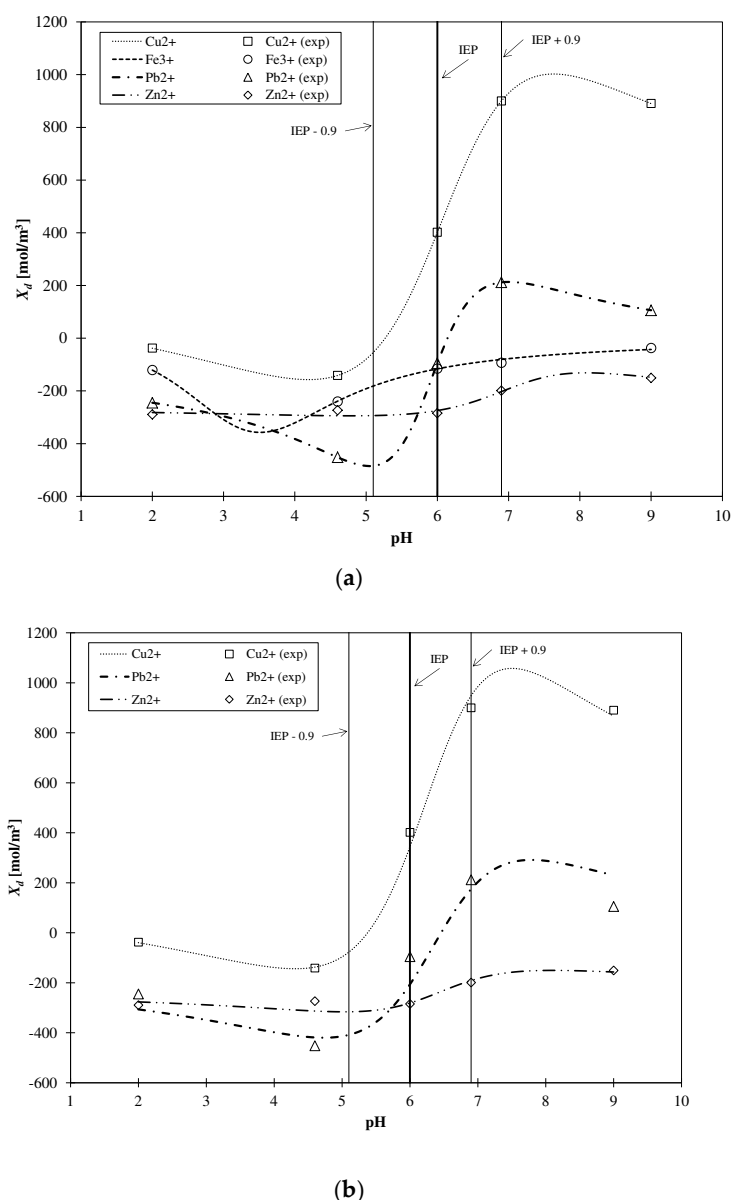
The parameters of correlation were regressed with use of the least squares method, and the so-defined objective function reached values between 0.50 for Pb<sup>2+</sup> and 611.44 for Zn<sup>2+</sup>. The presented form of Equation (20) gives the first view of how function  $X_d = f(pH)$  might be shaped, and through which values it can progress.

In this study, the measure of model compatibility with empirical data was based on the variance of random component method. The starting point was model residuals. The assessment of the random component variance, the so-called remainder variance, is expressed by Equation (21):

$$S_e^2 = \frac{\sum_{i=1}^n (X_{d,i}(pH) - \hat{X}_{d,i}(pH))^2}{n - m - 1} \tag{21}$$

where  $X_{d,i}(pH)$  is the total volume membrane charge density determined experimentally [mol/m<sup>3</sup>],  $\hat{X}_{d,i}(pH)$  is the total volume membrane charge density calculated with regression model [mol/m<sup>3</sup>],  $n$  is the number of observations, and  $m$  is the number of estimated model parameters.

The root of the remainder variance is the standard deviation of the residues  $S_e$  (also known as the estimation standard error). This value indicates the average difference between the observed values of the explanatory variable and theoretical values. As seen in Figure 9a, the obtained correlations converge well with the computationally obtained results of  $X_d$ . In Figure 9, the horizontal thin lines mark the range of IEP, whereas the horizontal bold line marks the value of the IEP of the TiO<sub>2</sub> membrane. As mentioned earlier, the obtained inflection of the membrane charge density curves for all ions is confirmed, and in each system the minimal value of total volume membrane charge density was in the range of pH 4.5–6.0. The shapes of the obtained correlation functions are in good agreement, and the inflection points of each ion are generally close to the limits of IEP, except for solutions containing Fe<sup>3+</sup>.



**Figure 9.** Performance of correlation Equation(20), with parameters listed in Table 6, with respect to estimated  $X_d$  values. (a) first set of parameters from Table 6; (b) second set of parameters from Table 6.

After the analysis of the first set of parameters reported in Table 6, it was proposed to unify the parameters present in the denominator of Equation (19) for divalent cations and perform the parameter optimization. The results of those optimizations are reported as the second set

of parameters in Table 6. Although the second set of parameters exhibit higher values of  $S_e$  in comparison to the first set, they are still in good quantitative agreement (see Figure 9b).

#### 4. Conclusions

The main aim of the computer-aided estimations and simulations performed was to estimate the total volume membrane charge density using the Donnan–Steric partitioning model, derived from the extended Nernst–Planck equation with the Donnan partitioning assumption, which finally resulted in a relation between the total membrane charge density and the pH of separated solutions. The obtained total volume membrane charge densities reflect the experimental values of ion retention very well. The values of such charge densities of the membrane are very important for the explanation of the possible mechanisms of ions transport across the membrane, which regulate the value of the solute retention and influence the electrostatic repulsion between the ions and the membrane.

The value of total volume membrane charge density is influenced by several factors. One of the key factors is the type of the solution, which is directly related to the valance of present ions. However, the determination of the  $X_d$  value requires an experimental investigation for each NF system.

The obtained results of total volumetric membrane charge densities confirm the amphoteric behavior of ceramic  $\text{Al}_2\text{O}_3/\text{TiO}_2$  NF membranes. The  $X_d$  values change with the increase in the pH of feeds. Initially, at low pH values, when the membrane is positively charged, all types of ions obtained negative values for the total volume membrane charge densities. This is associated with the adsorption of  $\text{NO}_3^-$  ions due to electrostatic attraction. Next, when the pH values began to increase, the  $X_d$  also changed. For all types of ions, the  $X_d$  increased, but in a different manner. For solutions containing  $\text{Cu}^{2+}$  and  $\text{Pb}^{2+}$  ions, their  $X_d$  values increase from negative to positive values, and for  $\text{Fe}^{3+}$  and  $\text{Zn}^{2+}$ , increases were also observed, but the values nevertheless remained negative. For  $\text{Cu}^{2+}$  from pH 2 to pH 9, the total volume membrane charge density changed dramatically, by approx. 738%, and for  $\text{Pb}^{2+}$ , the change was the smallest, at approx. 292%. The fact that the values for each ion variants increase is undoubtedly associated with ions–membrane interactions, precisely the with electrostatic attraction of cations. Our studies provide an interesting unexplained observation, that for  $\text{Fe}^{3+}$  and  $\text{Zn}^{2+}$ , the values of the total membrane charge densities are negative in the whole range of pH. Additionally, lower retention rates were achieved for those two ions in comparison to solutions that contained  $\text{Cu}^{2+}$  or  $\text{Pb}^{2+}$ . This effect may be caused by ions complexation and a strong interaction between ions and ions present in the feeds. It is also worth noting that, if the total membrane charge density is strongly positive, the retention rate is significantly better than when the membrane charge is negative. Equation (20) in the presented form may allow for the easier prediction of the retention rate of the studied solutions. Such a correlation allows its use in process simulations, i.e., by knowing values of pH of aqueous solution of specific ion, the values of  $X_d$  in the considered system can be computed, therefore leading to the calculation of metal ion retention.

The total volume membrane charge density is very difficult to determine without performing any experiments. Based on the obtained results, it can be seen that even for groups of cations with the same valance, the  $X_d$  has significantly different values. It is also difficult to assess which mechanisms play a key role in shaping the membrane charge, whether Donnan partitioning, selective adsorption, electrostatic interaction, diffusion difference, or other, as-yet-unexplored phenomena. Therefore, mathematical modelling with closely associated experimental studies must be further carried out.

The additional and highly important output from this study is that the presented method based on the model and parameter estimation allows for a first view of the separation mechanism without time consuming studies of intrinsic charge. Therefore, knowledge regarding the total volume membrane charge density helps in the systematic investigation of the influence of membrane charge on the behaviour of salts, even if it is computation-based and obtained through the parameter estimation of rejection experiments. The value of total volume membrane charge density in the presence of a few ions cannot be interpreted in the same way when a single pair of ions are present in the system. In other words, interactions between all ions in the investigated systems should be taken into account.

However, the authors consider that, in the future, it should be possible to define the relation between specific ions and total volume membrane charge density through some mixing rules, which would allow for the real predictive modelling of NF separations based on a few retention experiments.

**Author Contributions:** The following contributions are recognized: conceptualization, A.M.-M., P.T.M. and A.N.; methodology, A.N., P.T.M. and J.R.; modelling, A.M.-M. and P.T.M.; simulation, A.M.-M.; validation, A.M.-M. and P.T.M.; experimental investigation, A.M.-M. and A.N.; resources, P.T.M., J.R. and A.N.; writing—original draft preparation, A.M.-M. and P.T.M.; writing—review and editing, A.M.-M., P.T.M., A.N., J.R. and W.S.; visualization, A.M.-M. and W.S.; supervision, P.T.M. and J.R. All authors have read and agreed to the published version of the manuscript.

**Funding:** This research was supported by the Ministry of Science and Higher Education in Poland subsidy for Poznan University of Technology, Faculty of Chemical Technology.

**Conflicts of Interest:** The authors declare no conflict of interest.

## References

1. Wuana, R.A.; Okieimen, F.E. Heavy metals in contaminated soils: A review of sources, chemistry, risks and best available strategies for remediation. *ISRN Ecol.* **2011**, *2011*, 402647. [CrossRef]
2. Barakat, M.A. New trends in removing heavy metals from industrial wastewater. *Arab. J. Chem.* **2011**, *4*, 361–377. [CrossRef]
3. Arbabi, M.; Hemati, S.; Amiri, M. Removal of lead ions from industrial wastewater: A review of removal methods. *Int. J. Epidemiol. Res.* **2015**, *2*, 105–109.
4. National Primary Drinking Water Regulations. Available online: [https://www.epa.gov/sites/production/files/2016-06/documents/npwdr\\_complete\\_table.pdf](https://www.epa.gov/sites/production/files/2016-06/documents/npwdr_complete_table.pdf) (accessed on 18 October 2017).
5. Hegazi, H.A. Removal of heavy metals from wastewater using agricultural and industrial wastes as adsorbents. *HBRC J.* **2013**, *9*, 276–282. [CrossRef]
6. Skubal, L.R.; Meshkov, N.K.; Rajh, T.; Thurnauer, M. Cadmium removal from water using thiolactic acid-modified titanium dioxide nanoparticles. *J. Photochem. Photobiol. A Chem.* **2002**, *148*, 393–397. [CrossRef]
7. Prochaska, K.; Woźniak-Budych, M.J. Recovery of fumaric acid from fermentation broth using bipolar electro dialysis. *J. Membr. Sci.* **2014**, *469*, 428–435. [CrossRef]
8. Qdais, H.A.; Moussa, H. Removal of heavy metals from wastewater by membrane processes: A comparative study. *Desalination* **2004**, *164*, 105–110. [CrossRef]
9. Staszak, K.; Woźniak, M.; Sottek, M.; Karaś, Z.; Prochaska, K. Removal of fumaric acid from simulated and real fermentation broth. *J. Chem. Technol. Biotechnol.* **2015**, *90*, 432–440. [CrossRef]
10. Staszak, K.; Woźniak, J.M.; Staniewski, J.; Prochaska, K. Application of nanofiltration in the process of the separation of model fermentation broths components. *Polish J. Chem. Technol.* **2013**, *15*, 3–6. [CrossRef]
11. Chaudhari, L.B.; Murthy, Z.V.P. Treatment of landfill leachates by nanofiltration. *J. Environ. Manag.* **2010**, *91*, 1209–1217. [CrossRef]
12. Religa, P.; Kowalik-Klimczak, A.; Gierycz, P. Study on the behavior of nanofiltration membranes using for chromium(III) recovery from salt mixture solution. *Desalination* **2013**, *315*, 115–123. [CrossRef]
13. Religa, P.; Kowalik, A.; Gierycz, P. Application of nanofiltration for chromium concentration in the tannery wastewater. *J. Hazard. Mater.* **2011**, *186*, 288–292. [CrossRef] [PubMed]
14. Shah, A.I.; Din Dar, M.U.; Bhat, R.A.; Singh, J.P.; Singh, K.; Bhat, S.A. Prospectives and challenges of wastewater treatment technologies to combat contaminants of emerging concerns. *Ecol. Eng.* **2020**, *152*, 105882. [CrossRef]
15. Shen, J.; Huang, J.; Ruan, H.; Wang, J.; Van der Bruggen, B. Techno-economic analysis of resource recovery of glyphosate liquor by membrane technology. *Desalination* **2014**, *342*, 118–125. [CrossRef]
16. Mohammad, A.W.; Teow, Y.H.; Ang, W.L.; Chung, Y.T.; Oatley-Radcliffe, D.L.; Hilal, N. Nanofiltration membranes review: Recent advances and future prospects. *Desalination* **2014**, *356*, 226–254. [CrossRef]
17. Hilal, N.; Al-Zoubi, H.; Darwish, N.A.; Mohamma, A.W.; Abu Arabi, M. A comprehensive review of nanofiltration membranes: Treatment, pretreatment, modelling, and atomic force microscopy. *Desalination* **2004**, *170*, 281–308. [CrossRef]

18. Schmidt, P.; Lutze, P. Characterisation of organic solvent nanofiltration membranes in multi-component mixtures: Phenomena-based modelling and membrane modelling maps. *J. Membr. Sci.* **2013**, *445*, 183–199. [[CrossRef](#)]
19. Marchetti, P.; Jimenez Solomon, M.F.; Szekely, G.; Livingston, A.G. Molecular separation with organic solvent nanofiltration: A critical review. *Chem. Rev.* **2014**, *114*, 10735–10806. [[CrossRef](#)]
20. Broniarz-Press, L.; Mitkowski, P.T.; Szaferski, W.; Marecka, A. Modelowanie procesu odzysku fumaranu diamonu metodą nanofiltracji. *Inżynieria Apar. Chem.* **2014**, *53*, 223–224.
21. Mulder, M. *Basic Principles of Membrane Technology*, 2nd ed.; Kluwer Academic Publishers: Dordrecht, The Netherlands, 1996.
22. Tanninen, J.; Mänttari, M.; Nyström, M. Nanofiltration of concentrated acidic copper sulphate solutions. *Desalination* **2006**, *189*, 92–96. [[CrossRef](#)]
23. Marecka-Migacz, A.; Mitkowski, P.T.; Antczak, J.; Róžański, J.; Prochaska, K. Assessment of the Total Volume Membrane Charge Density through Mathematical Modeling for Separation of Succinic Acid Aqueous Solutions on Ceramic Nanofiltration Membrane. *Processes* **2019**, *7*, 559. [[CrossRef](#)]
24. Izadpanah, A.A.; Javidnia, A. The ability of a nanofiltration membrane to remove hardness and ions from diluted seawater. *Water* **2012**, *4*, 283–294. [[CrossRef](#)]
25. Bernata, X.; Fortuny, A.; Stüber, F.; Bengoa, C.; Fabregat, A.; Font, J. Recovery of iron (III) from aqueous streams by ultrafiltration. *Desalination* **2008**, *221*, 413–418. [[CrossRef](#)]
26. Ramadan, Y.; Pátzay, G.; Szabó, G.T. Transport of NaCl, MgSO<sub>4</sub>, MgCl<sub>2</sub> and Na<sub>2</sub>SO<sub>4</sub> across DL type nanofiltration membrane. *Period. Polytech. Chem. Eng.* **2010**, *54*, 81–86. [[CrossRef](#)]
27. Van Gestel, T.; Vandecasteele, C.; Buekenhoudt, A.; Dotremont, C.; Luyten, J.; Leysen, R.; Van der Bruggen, B.; Maes, G. Salt retention in nanofiltration with multilayer ceramic TiO<sub>2</sub> membranes. *J. Membr. Sci.* **2002**, *209*, 379–389. [[CrossRef](#)]
28. Drost, A.; Nędzarek, A.; Tórz, A. Reduction of proteins and products of their hydrolysis in process of cleaning post-production herring (*Clupea harengus*) marinating brines by using membranes. *Membr. Water Treat.* **2016**, *7*, 451–462. [[CrossRef](#)]
29. Drost, A.; Nędzarek, A.; Bogusławska-Was, E.; Tórz, A.; Bonisławska, M. UF application for innovative reuse of fish brine: Product quality, CCP management and the HACCP system. *J. Food Process Eng.* **2014**, *37*, 396–401. [[CrossRef](#)]
30. Nędzarek, A.; Drost, A.; Harasimiuk, F.; Tórz, A.; Bonisławska, M. Application of ceramic membranes for microalgal biomass accumulation and recovery of the permeate to be reused in algae cultivation. *J. Photochem. Photobiol. B Biol.* **2015**, *153*, 367–372. [[CrossRef](#)]
31. Kujawski, W.; Kujawa, J.; Wierzbowska, E.; Cerneaux, S.; Bryjak, M.; Kujawski, J. Influence of hydrophobization conditions and ceramic membranes pore size on their properties in vacuum membrane distillation of water-organic solvent mixtures. *J. Membr. Sci.* **2016**, *499*, 442–451. [[CrossRef](#)]
32. Braeken, L.; Bettens, B.; Boussu, K.; Van der Meeren, P.; Cocquyt, J.; Vermant, J.; Van der Bruggen, B. Transport mechanisms of dissolved organic compounds in aqueous solution during nanofiltration. *J. Membr. Sci.* **2006**, *279*, 311–319. [[CrossRef](#)]
33. Jun, B.M.; Cho, J.; Jang, A.; Chon, K.; Westerhoff, P.; Yoon, Y.; Rho, H. Charge characteristics (surface charge vs. zeta potential) of membrane surfaces to assess the salt rejection behavior of nanofiltration membranes. *Sep. Purif. Technol.* **2020**, *247*. [[CrossRef](#)]
34. Oatley, D.L.; Llenas, L.; Pérez, R.; Williams, P.M.; Martínez-Lladó, X.; Rovira, M. Review of the dielectric properties of nanofiltration membranes and verification of the single oriented layer approximation. *Adv. Colloid Interface Sci.* **2012**, *173*, 1–11. [[CrossRef](#)] [[PubMed](#)]
35. Teixeira, M.; Rosa, M.; Nystrom, M. The role of membrane charge on nanofiltration performance. *J. Membr. Sci.* **2005**, *265*, 160–166. [[CrossRef](#)]
36. Puhlfürß, P.; Voigt, A.; Weber, R.; Morbé, M. Microporous TiO<sub>2</sub> membranes with a cut off <500 Da. *J. Membr. Sci.* **2000**, *174*, 123–133.
37. Su, B.; Duan, X.; Dou, M.; Gao, X.; Gao, C. Charge characteristics of nanofiltration membrane by streaming potential method. *Adv. Mater. Res.* **2011**, *396–398*, 547–551. [[CrossRef](#)]
38. Peeters, J.M.M.; Mulder, M.H.V.; Strathmann, H. Streaming potential measurements as a characterization method for nanofiltration membranes. *Colloids Surf. A Physicochem. Eng. Asp.* **1999**, *150*, 247–259. [[CrossRef](#)]

39. Pérez-González, A.; Ibáñez, R.; Gómez, P.; Urriaga, A.M.; Ortiz, I.; Irabien, J.A. Nanofiltration separation of polyvalent and monovalent anions in desalination brines. *J. Membr. Sci.* **2015**, *473*, 16–27.
40. Darvishmanesh, S.; Buekenhoudt, A.; Degève, J.; Van der Bruggen, B. General model for prediction of solvent permeation through organic and inorganic solvent resistant nanofiltration membranes. *J. Membr. Sci.* **2009**, *334*, 43–49. [[CrossRef](#)]
41. Tanimura, S.; Nakao, S.-I.; Kimura, S. Transport equation for a membrane based on a frictional model. *J. Membr. Sci.* **1993**, *84*, 79–91. [[CrossRef](#)]
42. Nair, R.R.; Protasova, E.; Strand, S.; Bilstad, T. Implementation of spiegler–Kedem and steric hindrance pore models for analyzing nanofiltration membrane performance for smart water production. *Membranes* **2018**, *8*, 78. [[CrossRef](#)]
43. Nair, R.R.; Protasova, E.; Strand, S.; Bilstad, T. Effect of pH on produced water treatment using nanofiltration membranes: Artificial neural network for performance assessment and steric hindrance pore model for flux variation evaluation. *Desalin. Water Treat.* **2019**, *146*, 120–130. [[CrossRef](#)]
44. Bowen, W.R.; Mukhtar, H. Characterisation and prediction of separation performance of nanofiltration membranes. *J. Membr. Sci.* **1996**, *112*, 263–274. [[CrossRef](#)]
45. Bowen, W.R.; Mohammad, A.W. Diafiltration by nanofiltration: Prediction and optimization. *AIChE J.* **1998**, *44*, 1799–1812. [[CrossRef](#)]
46. Bowen, W.R.; Mohammad, A.W. A theoretical basis for specifying nanofiltration membranes—Dye/salt/water streams. *Desalination* **1998**, *117*, 257–264. [[CrossRef](#)]
47. Bowen, W.R.; Welfoot, J.S. Predictive modelling of nanofiltration: Membrane specification and process optimisation. *Desalination* **2002**, *147*, 197–203. [[CrossRef](#)]
48. Déon, S.; Dutournié, P.; Bourseau, P. Modeling nanofiltration with Nernst-Planck approach and polarization layer. *AIChE J.* **2007**, *53*, 1952–1969. [[CrossRef](#)]
49. Santafé-Moros, A.; Gozálviz-Zafrilla, J.M.; Lora-García, J. Applicability of the DSPM with dielectric exclusion to a high rejection nanofiltration membrane in the separation of nitrate solutions. *Desalination* **2008**, *221*, 268–276. [[CrossRef](#)]
50. Fadaei, F.; Shirazian, S.; Ashrafzadeh, S.N. Mass transfer modeling of ion transport through nanoporous media. *Desalination* **2011**, *281*, 325–333. [[CrossRef](#)]
51. Szymczyk, A.; Lanteri, Y.; Fievet, P. Modelling the transport of asymmetric electrolytes through nanofiltration membranes. *Desalination* **2009**, *245*, 396–407. [[CrossRef](#)]
52. Szymczyk, A.; Sbaï, M.; Fievet, P.; Vidonne, A. Transport properties and electrokinetic characterization of an amphoteric nanofilter. *Langmuir* **2006**, *22*, 3910–3919. [[CrossRef](#)]
53. Kowalik-Klimczak, A.; Zalewski, M.; GIERYCZ, P. Prediction of the Chromium (Iii) Separation From Acidic Salt Solutions on Nanofiltration Membranes Using Donnan and Steric Partitioning Pore (Dsp) Model. *Archit. Civ. Eng. Environ.* **2016**, *9*, 135–140. [[CrossRef](#)]
54. Kowalik-Klimczak, A.; Zalewski, M.; Gierycz, P. Removal of Cr(III) ions from salt solution by nanofiltration: Experimental and modelling analysis. *Polish J. Chem. Technol.* **2016**, *18*, 10–16. [[CrossRef](#)]
55. Xu, R.; Zhou, M.; Wang, H.; Wang, X.; Wen, X. Influences of temperature on the retention of PPCPs by nanofiltration membranes: Experiments and modeling assessment. *J. Membr. Sci.* **2020**, *599*, 117817. [[CrossRef](#)]
56. Kingsbury, R.S.; Wang, J.; Coronell, O. Comparison of water and salt transport properties of ion exchange, reverse osmosis, and nanofiltration membranes for desalination and energy applications. *J. Membr. Sci.* **2020**, *604*, 117998. [[CrossRef](#)]
57. Rall, D.; Schweidtmann, A.M.; Kruse, M.; Evdochenko, E.; Mitsos, A.; Wessling, M. Multi-scale membrane process optimization with high-fidelity ion transport models through machine learning. *J. Membr. Sci.* **2020**, *608*, 118208. [[CrossRef](#)]
58. Farsi, A.; Boffa, V.; Christensen, M.L. Electroviscous effects in ceramic nanofiltration membranes. *ChemPhysChem* **2015**, *16*, 3397–3407. [[CrossRef](#)]
59. Van Gestel, T.; Vandecasteele, C.; Buekenhoudt, A.; Dotremont, C.; Luyten, J.; Leysen, R.; Van Der Bruggen, B.; Maes, G. Alumina and titania multilayer membranes for nanofiltration: Preparation, characterization and chemical stability. *J. Membr. Sci.* **2002**, *207*, 73–89. [[CrossRef](#)]
60. Nędzarek, A.; Drost, A.; Harasimiuk, F.B.; Tórz, A. The influence of pH and BSA on the retention of selected heavy metals in the nanofiltration process using ceramic membrane. *Desalination* **2015**, *369*, 62–67. [[CrossRef](#)]


61. Bonisławska, M.; Nędzarek, A.; Rybczyk, A. Assessment of the use of precipitating agents and ceramic membranes for treatment of effluents with high concentrations of nitrogen and phosphorus from recirculating aquaculture systems. *Aquac. Res.* **2019**, *50*, 1248–1256. [CrossRef]
62. Labbez, C.; Fievet, P.; Szymczyk, A.; Vidonne, A.; Foissy, A.; Pagetti, J. Analysis of the salt retention of a titania membrane using the “DSPM” model: Effect of pH, salt concentration and nature. *J. Membr. Sci.* **2002**, *208*, 315–329. [CrossRef]
63. Ribeiro, A.C.F.; Esteso, M.A.; Lobo, V.M.M.; Valente, A.J.M.; Simões, S.M.N.; Sobral, A.J.F.N.; Burrows, H.D. Diffusion coefficients of copper chloride in aqueous solutions at 298.15 K and 310.15 K. *J. Chem. Eng. Data* **2005**, *50*, 1986–1990. [CrossRef]
64. Atomic and Ionic Radii. Available online: <http://www.wiredchemist.com/chemistry/data/atomic-and-ionic-radii> (accessed on 7 July 2018).
65. Kariuki, S.; Dewald, H.D. Evaluation of diffusion coefficients of metallic ions in aqueous solutions. *Electroanalysis* **2005**, *8*, 307–313. [CrossRef]
66. Perry, R.; Green, D.; Maloney, J. *Perry's Chemical Engineers' Handbook*; McGraw-Hill: New York, NY, USA, 1997; ISBN 0-07-115448-5.
67. Jenkins, H.D.B.; Thakur, K.P. Reappraisal of thermochemical radii for complex ions. *J. Chem. Educ.* **1979**, *56*, 576. [CrossRef]
68. Krishna, R.; Wesselingh, J.A. The Maxwell-Stefan approach to mass transfer. *Chem. Eng. Sci.* **1997**, *52*, 861–911. [CrossRef]
69. Samson, E.; Marchand, J.; Snuder, K.A. Calculation of ionic diffusion coefficients on the basis of migration test results. *Mater. Struct.* **2003**, *36*, 156–165. [CrossRef]
70. Process Systems Enterprise Limited. *gPROMS Model Builder Documentation 2014*; Release 4.0.0; Process Systems Enterprise Limited: London, UK, April 2014.
71. Peeters, J.M.M.; Boom, J.P.; Mulder, M.H.V.; Strathmann, H. Retention measurements of nanofiltration membranes with electrolyte solutions. *J. Membr. Sci.* **1998**, *145*, 199–209. [CrossRef]
72. Takagi, R.; Larbot, A.; Cot, L.; Nakagaki, M. Effect of Al<sub>2</sub>O<sub>3</sub> support on electrical properties of TiO<sub>2</sub>/Al<sub>2</sub>O<sub>3</sub> membrane formed by sol–gel method. *J. Membr. Sci.* **2000**, *177*, 33–40. [CrossRef]
73. Mazzoni, C.; Bruni, L.; Bandini, S. Nanofiltration: Role of the electrolyte and pH on Desal DK performances. *Ind. Eng. Chem. Res.* **2007**, *46*, 2254–2262. [CrossRef]
74. Elimelech, M.; Chen, W.H.; Waypa, J.J. Measuring the zeta (electrokinetic) potential of reverse osmosis membranes by a streaming potential analyzer. *Desalination* **1994**, *95*, 269–286. [CrossRef]
75. Schaep, J.; Vandecasteele, C. Evaluating the charge of nanofiltration membranes. *J. Membr. Sci.* **2001**, *188*, 129–136. [CrossRef]
76. Mullet, M.; Fievet, P.; Reggiani, J.; Pagetti, J. Surface electrochemical properties of mixed oxide ceramic membranes: Zeta-potential and surface charge density. *J. Membr. Sci.* **1997**, *123*, 255–265. [CrossRef]



© 2020 by the authors. Licensee MDPI, Basel, Switzerland. This article is an open access article distributed under the terms and conditions of the Creative Commons Attribution (CC BY) license (<http://creativecommons.org/licenses/by/4.0/>).

Article

# Long-Term Investigation into the Membrane Fouling Behavior in Anaerobic Membrane Bioreactors for Municipal Wastewater Treatment Operated at Two Different Temperatures

Yi Ding <sup>1</sup>, Zhansheng Guo <sup>1</sup>, Zhenlin Liang <sup>1</sup>, Xuguang Hou <sup>1</sup>, Zhipeng Li <sup>2,\*</sup> , Dashuai Mu <sup>1</sup>, Changzi Ge <sup>1</sup>, Chunpeng Zhang <sup>3</sup> and Chao Jin <sup>4,\*</sup>

<sup>1</sup> Marine College, Shandong University, Weihai 264209, China; dingyi@sdu.edu.cn (Y.D.); guozhansheng@sdu.edu.cn (Z.G.); liangzhenlin@sdu.edu.cn (Z.L.); richardhoukk@163.com (X.H.); dashuai.mu@sdu.edu.cn (D.M.); changzige@sdu.edu.cn (C.G.)

<sup>2</sup> State Key Laboratory of Urban Water Resources and Water Environment, School of Marine Science and Technology, Harbin Institute of Technology at Weihai, Weihai 264200, China

<sup>3</sup> Key Laboratory of Groundwater Resources and Environment (Ministry of Education), Jilin University, Changchun 130021, China; zhang\_cp@jlu.edu.cn

<sup>4</sup> School of Environmental Science and Engineering, Sun Yat-Sen University, Guangzhou 510275, China

\* Correspondence: lizhipengcn@hit.edu.cn (Z.L.); jinchao3@mail.sysu.edu.cn (C.J.)

Received: 21 July 2020; Accepted: 11 September 2020; Published: 13 September 2020



**Abstract:** In this study, the characteristics of activated sludge flocs were investigated and their effects on the evolution of membrane fouling were considered in the anaerobic membrane bioreactors (AnMBR), which were operated at 25 and 35 °C for municipal wastewater treatment. It was found that the membrane fouling rate of the AnMBR at 25 °C was more severe than that at 35 °C. The membrane fouling trends were not consistent with the change in the concentration of soluble microbial product (SMP). The larger amount of SMP in the AnMBR at 35 °C did not induce more severe membrane fouling than that in the AnMBR at 25 °C. However, the polysaccharide and protein concentration of extracellular polymeric substance (EPS) was higher in the AnMBR at 25 °C in comparison with that in the AnMBR at 35 °C, and the protein/polysaccharide ratio of the EPS in the AnMBR at 25 °C was higher in contrast to that in the AnMBR at 35 °C. Meanwhile, the fouling tendencies measured for the AnMBRs could be related to the characteristics of loosely bound EPS and tightly bound EPS. The analysis of the activated sludge flocs characteristics indicated that a smaller sludge particle size and more fine flocs were observed at the AnMBR with 25 °C. Therefore, the membrane fouling potential in the AnMBR could be explained by the characteristics of activated sludge flocs.

**Keywords:** anaerobic membrane bioreactor; temperature; membrane fouling behavior; sludge flocs characteristics; soluble microbial product; extracellular polymeric substance

## 1. Introduction

Membrane separation technology coupled with an anaerobic bioreactor can be used for municipal sewage treatment [1]. The anaerobic membrane bioreactor (AnMBR) has attracted a lot of attention due to the advantages of less sludge production, higher loading rate, better quality effluent, and lower energy consumption [2]. The anaerobic process can be operated under different temperature [3]. As a result of the slow anaerobic microorganism growth, a long sludge retention time (SRT) is needed to achieve better pollutant removal efficiency, especially for municipal wastewater treatment [4]. Although the SRT should be longer than that commonly used at mesophilic temperatures, AnMBR operation near room temperature is technically feasible for municipal wastewater treatment [5].



However, due to the limitation of anaerobic microbial metabolism at 25 °C, the increased colloid and dissolved solids content during the anaerobic process may enhance the membrane fouling propensity. Membrane fouling still is one of the key problems of membrane bioreactor research. Extracellular polymeric substances (EPS) and soluble microbial products (SMP) are the major causes of membrane fouling. SMPs are the soluble cellular components secreted by microorganisms, and the EPSs have been differentiated into the inner layer and the outer layer [6]. The inner layer is mainly composed of tightly bound EPSs (TB-EPS), and the outer layer is mainly referred to as loosely bound EPSs (LB-EPS) [7]. The content of the LB-EPS and TB-EPS has some effect on the microbial aggregates [8]. Moreover, some authors indicated that the protein and carbohydrate were considered to be the main reason for flux reduction [9,10], and other researchers observed that pore blockage and cake layer formation were significantly enhanced by EPS during MBR operation [11,12]. It has been reported that the proteinous and carbohydrate EPSs and SMPs were strongly correlated with the type of wastewater [13,14].

Therefore, the purpose of this research was to discuss the membrane fouling mechanisms in an anaerobic membrane bioreactor for municipal wastewater treatment under two different temperature conditions. We sought to (1) assess the membrane fouling behavior; (2) investigate the EPS and SMP characteristics, and (3) analyze the size distribution and morphology of the sludge flocs. This study would further improve the understanding of membrane fouling behaviors in AnMBR for wastewater treatment.

## 2. Materials and Methods

### 2.1. AnMBRs Operating at Two Different Temperatures

The anaerobic process can be conducted at psychrophilic, mesophilic, and thermophilic temperature ranges [15]. Under the mesophilic condition, the reactor was usually operated at 35 °C [16]. During the conventional experiment, the MBR was often operated under the room temperature condition, at a temperature of  $25 \pm 0.5$  °C [17]. Therefore, two identical AnMBRs operated at 25 and 35 °C were used in this study to discuss the membrane fouling mechanisms in an anaerobic membrane bioreactor for municipal wastewater treatment under different temperature conditions. The experimental set-up of the AnMBRs at 25 and 35 °C is shown in a previous study [18]. The cylindrical anaerobic MBR was made of a polymethyl methacrylate, and the volume was 8.0 L. The AnMBR was equipped with a rounding polyvinylidene fluoride (PVDF) membrane module with a membrane pore size of 0.22  $\mu\text{m}$  and membrane surface area of 0.2  $\text{m}^2$ . A water level controller was utilized to maintain the wastewater volume. The transmembrane pressure (TMP) was recorded by a vacuum meter (YB150, Yangquan, China). The TMP data presented were based on the measurements conducted after the AnMBRs reached steady state. The steady state herein refers to the experimental period approximately after 200 days. Once the TMP reached 30 kPa in the AnMBRs, the membrane modules were taken out and cleaned. The modules were reloaded into the bioreactors to run the next hydraulic retention time (HRT) after cleaning. Furthermore, the effluent pump was operated intermittently in scheduled mode. The bioreactor temperature was maintained at scheduled temperatures.

### 2.2. Operating Parameters of the AnMBRs

Simulated municipal sewage was used as feed water for the AnMBRs at 25 and 35 °C, according to previous study [18]. Activated sludge from sewage treatment plant (Harbin, China) was used as inoculum for the AnMBRs at 25 and 35 °C. The sludge retention time (SRT) and the HRT were maintained at 370 days and 24 h, respectively. The sludge concentration (MLSS) was 5861 mg/L and 6024 mg/L for the AnMBR at 25 and 35 °C, respectively, and the MLSS concentrations of the AnMBRs had little change during the whole long-term operation process.

### 2.3. SMP and EPS Preparation from Anaerobic Membrane Bioreactor

The SMP and EPS was prepared based on the following procedure. First, the sludge mixture was centrifuged for 5 min with 5000 rpm. Second, the collected supernatant was filtered by microporous membrane. The collected filtrate was considered to be SMP. The LB-EPS and TB-EPS were extracted according to previous research and measured for the amount of proteins and carbohydrates [19]. EPS content was characterized by the sum of protein and polysaccharide per gram of dry sludge. All the above analyses were performed in triplicate, and their average values were listed.

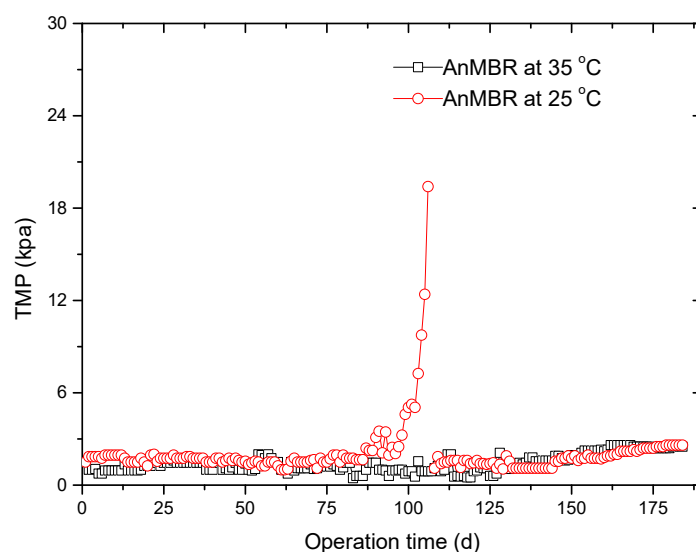
### 2.4. Analytical Methods

Proteins and carbohydrates were analyzed by the Lowry method [20] and the phenol–sulfuric method [21], respectively. Excitation–emission matrix (EEM) spectra (FP 6500, JASCO, Tokyo, Japan) were obtained according to a previous study [22]. The morphological characteristics of the activated sludge were investigated by the floc size distribution and sludge flocs morphology. Particle size distribution (PSD) was analyzed through a Mastersizer 2000 coupled to Hydro 2000SM (A) with a detection range of 0.02–2000  $\mu\text{m}$  (Mastersizer 2000, Malverin, England). The sludge floc morphology was investigated by microscopy (BX51, Olympus, Tokyo, Japan) and the images were obtained. The EEM spectra and PSD were conducted in triplicate, and only the representative results are reported in the paper. In total, 12 different sludge floc morphology images of each sample were obtained, and the representative images are shown in the research.

## 3. Results and Discussion

### 3.1. Membrane Fouling Behavior

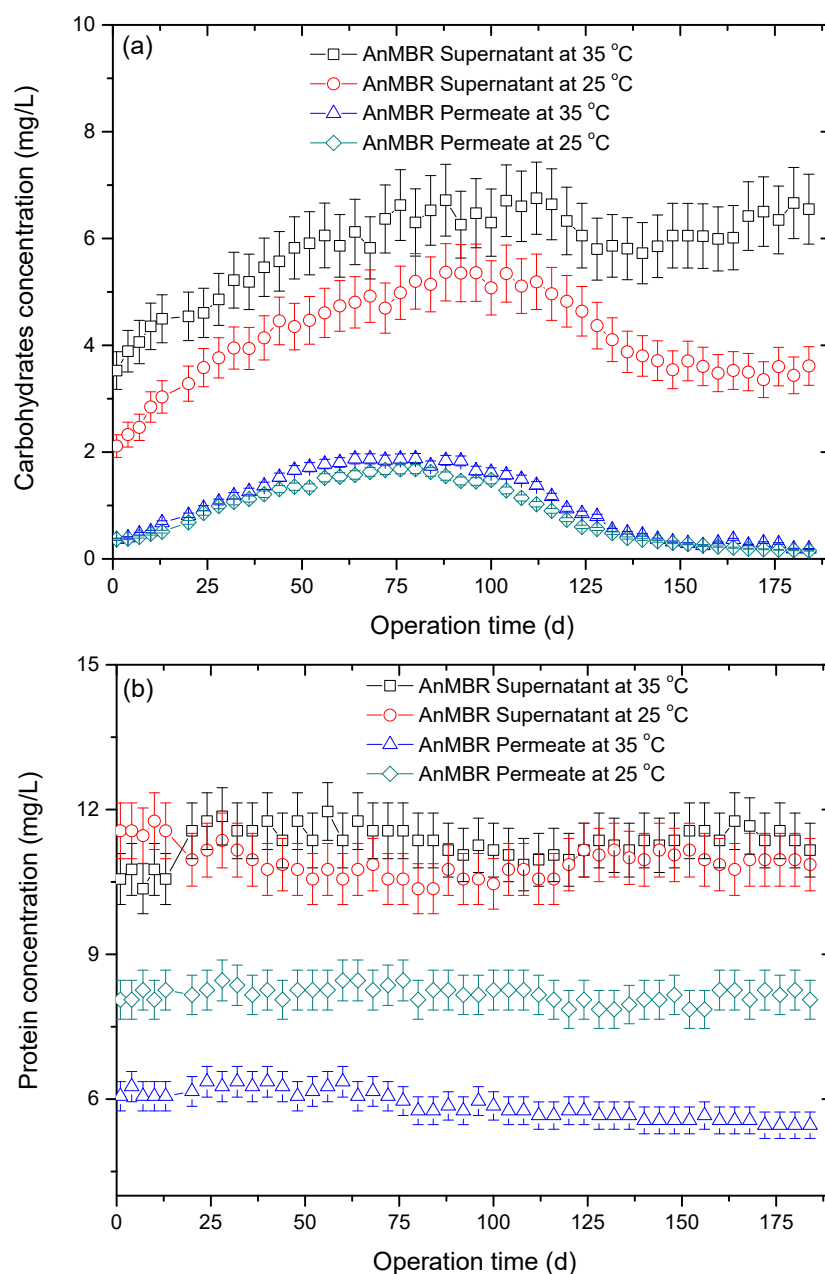
The changes in TMP throughout the experimental period are illustrated in Figure 1. The TMP generally increased with time and reached low values (1.45 kpa for the AnMBR at 35 °C, 3.1 kpa for the AnMBR at 25 °C) at the initial 90 d in the two AnMBRs. However, the TMP jumped to 19.4 kpa at 106 d in the AnMBR at 25 °C, while the TMP in the AnMBR at 35 °C remained stable and never underwent transition during the 180-day operation. Obviously, the membrane fouling rate of the AnMBR at 25 °C increased more slowly than that of the AnMBR at 35 °C. The mixed liquor in the AnMBR at 25 °C exhibited consistently higher membrane fouling propensity than the mixed liquor in the AnMBR at 35 °C. It is believed that membrane fouling is mainly induced by SMP and EPS [23,24]. We aimed to clarify the reason for different membrane fouling rates between the AnMBR at 25 °C and the AnMBR at 35 °C; the characteristics of the SMP and EPS are studied in the following sections.



**Figure 1.** The variations in transmembrane pressure (TMP) throughout the experimental period.

### 3.2. Changes in Concentrations of SMP

The variations in carbohydrate and protein contents for SMP are illustrated in Figure 2 during the operation time. This shows that the content of SMP of the two AnMBRs at 35 and 25 °C had the same tendency. Figure 2a illustrates the variations in the carbohydrate concentration in SMP throughout the experimental period. It was found that the carbohydrate concentrations were increased in the beginning 120 days in the supernatant and permeate of the anaerobic membranes, and then the carbohydrate concentrations were kept relatively stable in the following period.



**Figure 2.** The changes in carbohydrate (a) and protein (b) contents in soluble microbial products (SMP) during the operation time.

Figure 2b shows the protein concentration in SMP of the two AnMBRs at 35 and 25 °C. The protein content seemed to be less affected by the long-term operation. Though the protein content in SMP of the AnMBR at 35 °C was slightly higher than that in SMP of the AnMBR at 25 °C, the protein content in the permeate of the AnMBR at 35 °C was dramatically lower than that in the permeate of the AnMBR

at 25 °C. Although the carbohydrate and protein contents of the AnMBR at 35 °C in the supernatant were slightly higher than those of the AnMBR at 25 °C, this difference was small and was assumed not to cause a significant change in sludge filterability. Therefore, the membrane fouling trends were not consistent with the change in the concentrations of SMP, and the content of SMP was obviously not indicative of the fouling tendencies of the two AnMBRs.

### 3.3. Changes in Concentrations of EPS

EPS was commonly considered to be the main reason for membrane fouling in MBR [25]. The content changes in carbohydrate and protein of LB-EPS and TB-EPS are shown in Figure 3a,b in the two AnMBRs at 35 and 25 °C against the operation time. It can be seen from Figure 3a that the carbohydrate in TB-EPS was more than that in LB-EPS in both the two AnMBRs at 35 and 25 °C. Meanwhile, the carbohydrate in LB-EPS and TB-EPS of the AnMBR at 35 °C was less than that in LB-EPS and TB-EPS of the AnMBR at 25 °C.

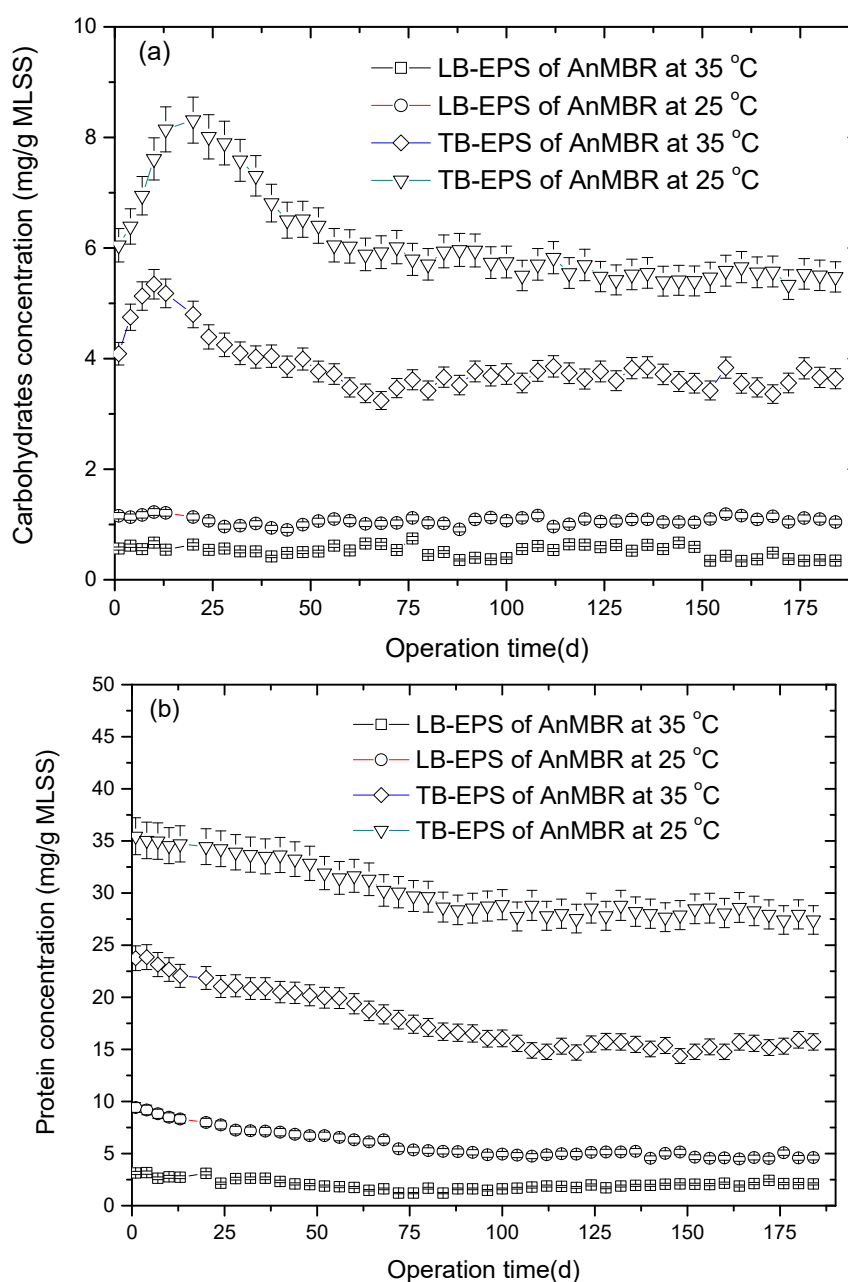
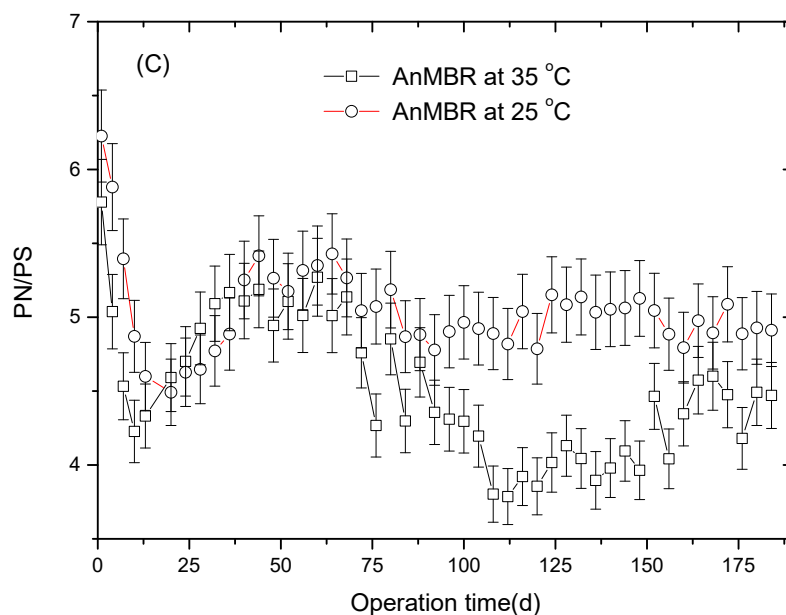


Figure 3. Cont.



**Figure 3.** The variations in carbohydrate (a) and protein (b) contents and the proteins (PN)/polysaccharides (PS) ratio for extracellular polymeric substances (EPS) (c) in the two anaerobic membrane bioreactors (AnMBRs) at 35 and 25 °C against the operation time.

The protein content of LB-EPS and TB-EPS in the two AnMBRs at 35 and 25 °C is listed in Figure 3b. It was found that the protein concentrations declined slowly for the LB-EPS and TB-EPS in the two AnMBRs at 35 and 25 °C, but the values for the LB-EPS and TB-EPS in the AnMBR at 25 °C were significantly higher than those in the AnMBR at 35 °C. It was seen that protein was the main component of the EPS. It has been reported that LB-EPS plays a more important role in membrane fouling compared to TB-EPS [26]. In this research, the content of LB-EPS and TB-EPS in the sludge flocs showed a relationship with the fouling tendency. The polysaccharide and protein concentration of LB-EPS and TB-EPS were higher at the AnMBR with 25 °C compared those at AnMBR with 35 °C, which may result in the faster fouling propensity in AnMBR at 25 °C.

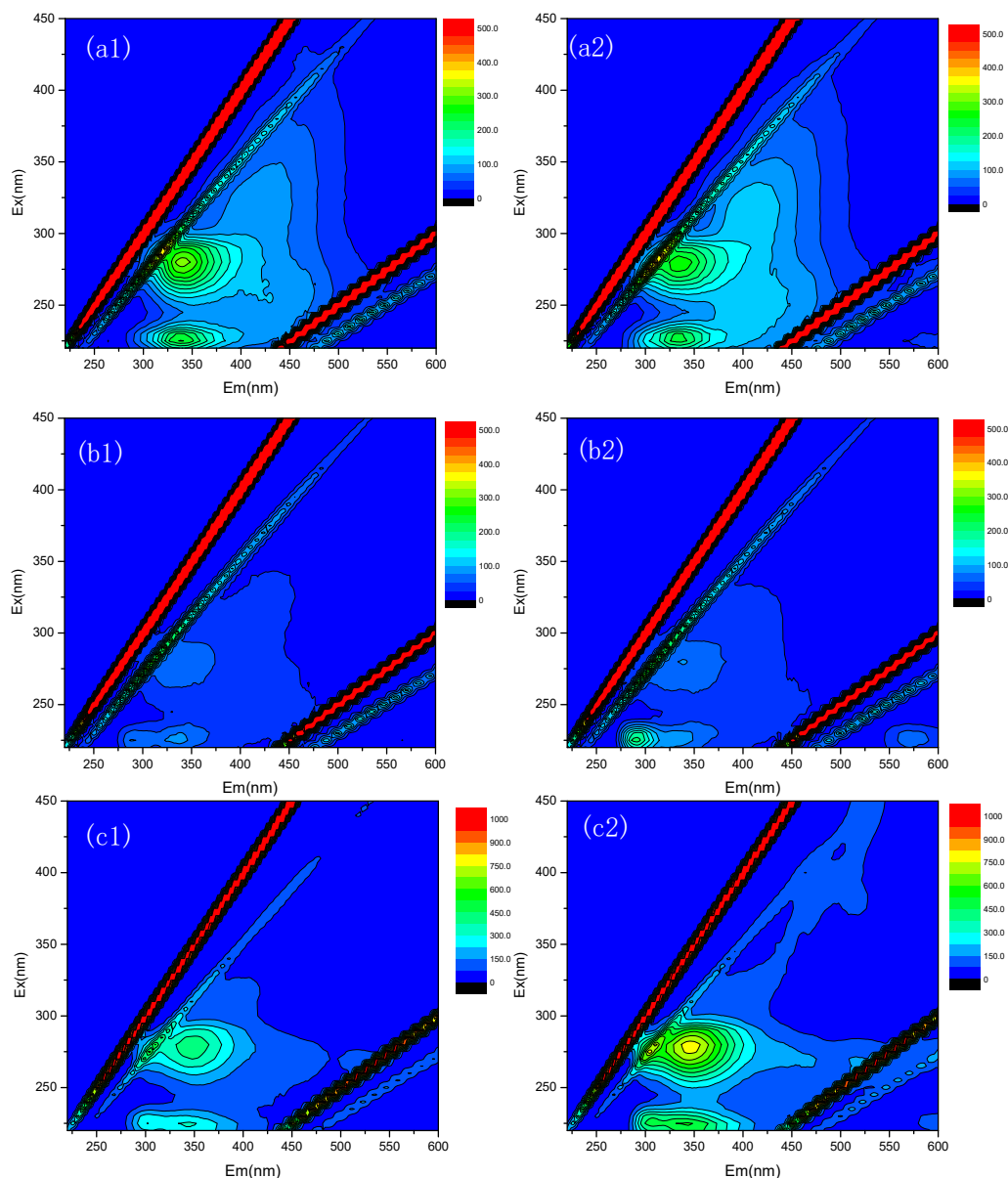
The variation in the proteins (PN)/polysaccharides (PS) ratio for EPS with operation time is presented in Figure 3c. Obviously, the PN/PS ratio for EPS of AnMBR at 35 °C was lower than that for EPS of AnMBR at 25 °C. In the course of the experiment, the average PN/PS ratio for EPS in the AnMBR at 35 °C was 4.88, which was 10% lower than that in the AnMBR at 25 °C (5.40). It has been found that the PN/PS ratio of EPS could indicate the membrane fouling trend of sludge flocs [27]. Therefore, with respect to the AnMBR at 35 °C, the lower PN/PS ratio for the EPS could lead to less membrane fouling than that in the AnMBR at 25 °C. Additionally, it had been reported that the PN/PS ratio reduction of EPS could cause a decrease in floc hydrophobicity [27]. It was for this reason that the sludge deposition on the membranes was reduced and the fouling layer caused by the sludge flocs would be mitigated in the AnMBR at 35 °C.

In the present study, mixed liquor samples with higher polysaccharide and protein content and protein/polysaccharide ratio in EPS were observed to have greater potential to foul membranes during the AnMBR operation at 25 °C. It was suggested that the EPS in the mixed liquor, particularly the carbohydrates and protein substances, were the major substances that accumulated on the membranes and consequently caused membrane fouling.

### 3.4. Characteristics of SMP and EPS

EEM analysis was used to study the characteristics of SMP and EPS in the two AnMBRs at 35 and 25 °C, which provides spectral information about the aromatic protein-like and tryptophan protein-like compounds [28]. It can be seen from Figure 4 that the EEM spectra all showed two peaks for the SMP

and EPS in the mixed liquor suspension of the two AnMBRs at 35 and 25 °C. At the excitation/emission wavelengths (Ex/Em) of 230–240 nm/335–350 nm (Peak A), the peak was considered to reflect aromatic protein-like substances, and at the Ex/Em of 280 nm/330–340 nm (Peak B), the peak was associated with the tryptophan protein-like substances [29].



**Figure 4.** Excitation–emission matrix (EEM) spectra of SMP (a), loosely bound EPS (LB-EPS) (b) and tightly bound EPS (TB-EPS) (c) in the AnMBR at 35 °C (1) and the AnMBR at 25 °C (2).

It was found that the peak relative dominance for protein-like substances in the SMP extracted from AnMBR at 35 °C was stronger than that extracted from AnMBR at 25 °C; however, the peak intensity of protein-like substances for the LB-EPS and TB-EPS extracted from AnMBR at 25 °C were stronger than those extracted from AnMBR at 35 °C. The trends in the EEM spectra intensity for LB-EPS and TB-EPS coincided with the fouling tendencies monitored for the two AnMBRs at 35 and 25 °C. It was demonstrated that the protein-like substances in the LB-EPS and TB-EPS had an important effect on the membrane fouling development in the AnMBR at 35 °C and the AnMBR at 25 °C. Taking into consideration the results of EEM fluorescence spectra analyses, indicating that the EPS in the AnMBR

at 25 °C showed more proteinaceous characteristics, it can be inferred that the protein-like substances are abundant in EPS of the AnMBR at 25 °C, which would cause severe membrane fouling.

### 3.5. Morphology Characteristics of the Sludge Flocs and Their Effects on Membrane Fouling

The PSD of activated sludge in the two AnMBRs at 35 and 25 °C is listed in Figure 5. There are obvious differences between the two AnMBRs at 35 and 25 °C, indicating that operation temperature had significant impact on PSD in the two AnMBRs at 35 and 25 °C. At the steady state of the AnMBR at 35 °C, the particle size of 90% sludge flocs was less than 383.579 μm, and the particle size of 90% sludge flocs was less than 180.043 μm in the AnMBR at 25 °C. A previous study reported that sludge particles with smaller particle sizes could be easily deposited on the membrane surface to form a cake layer [30]. The reason was that the back transport velocity of the particles reduced with the decrease of their size [31]. Thus, one of the reasons for the more severe membrane fouling trend in the AnMBR at 25 °C could be attributed to the smaller particle size of flocs, inducing serious cake formation.

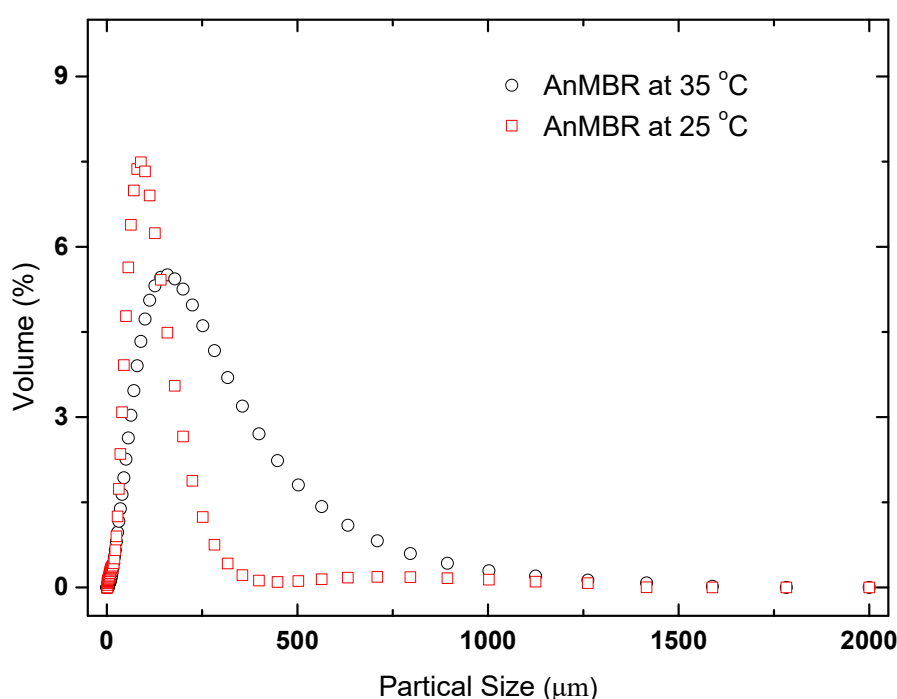
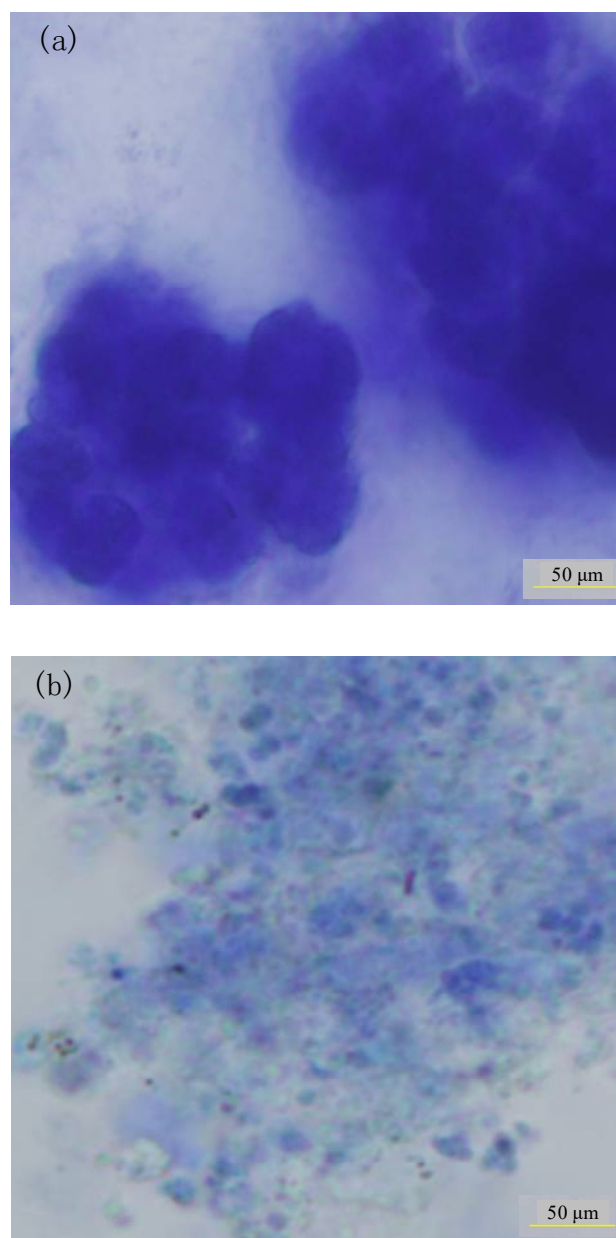


Figure 5. The particle size distribution (PSD) of sludge flocs in the two AnMBRs at 35 and 25 °C.

The sludge floc structure in the two AnMBRs at 35 and 25 °C is shown in Figure 6. It was illustrated that the sludge floc size was lower in the AnMBR with 25 °C condition than that in the AnMBR with 35 °C condition. Compared to that in the AnMBR under 35 °C conditions, the decrease in floc size in the AnMBR under 25 °C conditions could be owing to the effect of the lower temperature on the growth rate of anaerobic microorganisms, which caused the lower sludge aggregation.

As seen from the microscopic analysis, the amount of fine flocs in the AnMBR at 25 °C was more than that in the AnMBR at 35 °C. Consequently, the greater quantity of small sludge flocs in the AnMBR at 25 °C might have contributed to the more severe membrane fouling compared to the AnMBR at 35 °C. Thus, the membrane fouling propensity for the AnMBR at 25 °C was higher than that for the AnMBR at 35 °C. It has been indicated that more LB-EPS in EPS could reduce bioflocculation and affect the floc structure [8]. Therefore, the LB-EPS concentration was higher in the AnMBR at 25 °C compared to that in the AnMBR at 35 °C, which may result in the higher fouling propensity.



**Figure 6.** The sludge floc size and structure in the AnMBRs under 35 (a) and 25 °C (b) conditions.

#### 4. Conclusions

In this study, sludge floc characteristics were analyzed and their effect on membrane fouling was researched for anaerobic membrane bioreactors (AnMBR). The temperature differences between the two AnMBRs resulted in a number of different physical and biochemical properties of mixed liquor that seemed to be related to the differences in the fouling behaviors of the two types of sludge. It was found that the mixed liquor in the AnMBR at 25 °C exhibited consistently higher membrane fouling propensity than the mixed liquor in the AnMBR at 35 °C. The content of EPS in the sludge flocs showed a relationship with fouling tendency. Mixed liquor samples with higher polysaccharide and protein content and protein/polysaccharide ratio in EPS were observed to have greater potential to foul membranes during the AnMBR operation at 25 °C. Meanwhile, the EEM spectra peak intensities of protein-like substance for the LB-EPS and TB-EPS extracted from the AnMBR at 35 °C were stronger than those extracted from the AnMBR at 25 °C. The content of EPS (especially polysaccharide and protein substances) in the activated sludge mixed liquor was concluded to be a key index to assess the



fouling propensity. Furthermore, the sludge particle size was smaller and a larger amount of fine flocs was found in the AnMBR at 25 °C. Thus, one of the reasons for the raised membrane fouling potential in the AnMBR at 25 °C could be attributed to the EPS and sludge floc characteristics.

**Author Contributions:** Data curation, Z.G.; formal analysis, C.J. and C.Z.; investigation, Y.D. and Z.L. (Zhenlin Liang); writing—original draft, Z.L. (Zhipeng Li); writing—review and editing, X.H., C.G. and D.M. All authors have read and agreed to the published version of the manuscript.

**Funding:** This study was supported by the National Natural Science Foundation of China (No. 51408158) and the Natural Science Foundation of Shandong Province of China (No. ZR2019QEE012).

**Conflicts of Interest:** The authors declare that they have no conflict of interest.

## References

1. Lin, H.J.; Peng, W.; Zhang, M.J.; Chen, J.R.; Hong, H.C.; Zhang, Y. A review on anaerobic membrane bioreactors: Applications, membrane fouling and future perspectives. *Desalination* **2013**, *314*, 169–188. [[CrossRef](#)]
2. Aquino, S.F.; Hu, A.Y.; Akram, A.; Stuckey, D.C. Characterization of dissolved compounds in submerged anaerobic membrane bioreactors (SAMBRs). *J. Chem. Technol. Biotechnol.* **2006**, *81*, 1894–1904. [[CrossRef](#)]
3. Gao, W.J.; Leung, K.T.; Qin, W.S.; Liao, B.Q. Effects of temperature and temperature shock on the performance and microbial community structure of a submerged anaerobic membrane bioreactor. *Bioresour. Technol.* **2011**, *102*, 8733–8740. [[CrossRef](#)] [[PubMed](#)]
4. Pretel, R.; Robles, A.; Ruano, M.V.; Seco, A.; Ferrer, J. The operating cost of an anaerobic membrane bioreactor (AnMBR) treating sulphate-rich urban wastewater. *Sep. Purif. Technol.* **2014**, *126*, 30–38. [[CrossRef](#)]
5. Herrera-Robledo, M.; Cid-Leon, D.M.; Morgan-Sagastume, J.M.; Noyola, A. Biofouling in an anaerobic membrane bioreactor treating municipal sewage. *Sep. Purif. Technol.* **2011**, *81*, 49–55. [[CrossRef](#)]
6. Ramesh, A.; Lee, D.J.; Lai, J.Y. Membrane biofouling by extracellular polymeric substances or soluble microbial products from membrane bioreactor sludge. *Appl. Microbiol. Biotechnol.* **2007**, *74*, 699–707. [[CrossRef](#)] [[PubMed](#)]
7. Sheng, G.P.; Yu, H.Q.; Li, X.Y. Extracellular polymeric substances (EPS) of microbial aggregates in biological wastewater treatment systems: A review. *Biotechnol. Adv.* **2010**, *28*, 882–894. [[CrossRef](#)] [[PubMed](#)]
8. Li, X.Y.; Yang, S.F. Influence of loosely bound extracellular polymeric substances (EPS) on the flocculation, sedimentation and dewaterability of activated sludge. *Water Res.* **2007**, *41*, 1022–1030. [[CrossRef](#)]
9. Park, N.; Kwon, B.; Kim, I.S.; Cho, J.W. Biofouling potential of various NF membranes with respect to bacteria and their soluble microbial products (SMP): Characterizations, flux decline, and transport parameters. *J. Membr. Sci.* **2005**, *258*, 43–54. [[CrossRef](#)]
10. Rosenberger, S.; Laabs, C.; Lesjean, B.; Gnirss, R.; Amy, G.; Jekel, M.; Schrotter, J.C. Impact of colloidal and soluble organic material on membrane performance in membrane bioreactors for municipal wastewater treatment. *Water Res.* **2006**, *40*, 710–720. [[CrossRef](#)]
11. Cho, B.D.; Fane, A.G. Fouling transients in nominally sub-critical flux operation of a membrane bioreactor. *J. Membr. Sci.* **2002**, *209*, 391–403. [[CrossRef](#)]
12. Germain, E.; Stephenson, T.; Pearce, P. Biomass characteristics and membrane aeration: Toward a better understanding of membrane fouling in submerged membrane bioreactors (MBRs). *Biotechnol. Bioeng.* **2005**, *90*, 316–322. [[CrossRef](#)]
13. Remmas, N.; Melidis, P.; Zerva, I.; Kristoffersen, J.B.; Nikolaki, S.; Tsiamis, G.; Ntougias, S. Dominance of candidate Saccharibacteria in a membrane bioreactor treating medium age landfill leachate: Effects of organic load on microbial communities, hydrolytic potential and extracellular polymeric substances. *Bioresour. Technol.* **2017**, *238*, 48–56. [[CrossRef](#)] [[PubMed](#)]
14. Remmas, N.; Melidis, P.; Paschos, G.; Statiris, E.; Ntougias, S. Protozoan indicators and extracellular polymeric substances alterations in an intermittently aerated membrane bioreactor treating mature landfill leachate. *Environ. Technol.* **2016**, *38*, 1–33. [[CrossRef](#)]
15. El-Mashad, H.M.; Zeeman, G.; Loon, W.K.P.V.; Bot, G.P.A.; Lettinga, G. Effect of temperature and temperature fluctuation on thermophilic anaerobic digestion of cattle manure. *Bioresour. Technol.* **2004**, *95*, 191–201. [[CrossRef](#)] [[PubMed](#)]

16. Jia, R.X.; Sun, D.Z.; Dang, Y.; Meier, D.; Holmes, D.E.; Smith, J.A. Carbon cloth enhances treatment of high-strength brewery wastewater in anaerobic dynamic membrane bioreactors. *Bioresour. Technol.* **2020**, *298*, 122547. [[CrossRef](#)]
17. Hwang, B.K.; Kim, J.H.; Ahn, C.H.; Lee, C.H.; Song, J.Y.; Ra, Y.H. Effect of disintegrated sludge recycling on membrane permeability in a membrane bioreactor combined with a turbulent jet flow ozone contactor. *Water Res.* **2010**, *44*, 1833–1840. [[CrossRef](#)] [[PubMed](#)]
18. Ding, Y.; Liang, Z.L.; Guo, Z.S.; Li, Z.P.; Hou, X.G.; Jin, C. The Performance and Microbial Community Identification in Mesophilic and Atmospheric Anaerobic Membrane Bioreactor for Municipal Wastewater Treatment Associated with Different Hydraulic Retention Times. *Water-Sui* **2019**, *11*, 160. [[CrossRef](#)]
19. Li, Z.P.; Tian, Y.; Ding, Y.; Wang, H.Y.; Chen, L. Contribution of extracellular polymeric substances (EPS) and their subfractions to the sludge aggregation in membrane bioreactor coupled with worm reactor. *Bioresour. Technol.* **2013**, *144*, 328–336. [[CrossRef](#)]
20. Lowry, O.H.; Rosebrough, N.J.; Farr, A.L.; Randall, R.J. Protein measurement with the Folin phenol reagent. *J. Biol. Chem.* **1951**, *193*, 265–275.
21. Dubois, M.; Gilles, K.A.; Hamilton, J.K.; Rebers, P.; Smith, F. Colorimetric method for determination of sugars and related substances. *Anal. Chem.* **1956**, *28*, 350–356. [[CrossRef](#)]
22. Tian, Y.; Li, Z.P.; Lu, Y.B. Changes in characteristics of soluble microbial products and extracellular polymeric substances in membrane bioreactor coupled with worm reactor: Relation to membrane fouling. *Bioresour. Technol.* **2012**, *122*, 62–69. [[CrossRef](#)] [[PubMed](#)]
23. Wang, Z.W.; Wu, Z.C. A Review of Membrane Fouling in MBRs: Characteristics and Role of Sludge Cake Formed on Membrane Surfaces. *Separ. Sci. Technol.* **2009**, *44*, 3571–3596. [[CrossRef](#)]
24. van den Brink, P.; Zwijnenburg, A.; Smith, G.; Temmink, H.; van Loosdrecht, M. Effect of free calcium concentration and ionic strength on alginate fouling in cross-flow membrane filtration. *J. Membr. Sci.* **2009**, *345*, 207–216. [[CrossRef](#)]
25. Zhang, H.M.; Xia, J.; Yang, Y.; Wang, Z.X.; Yang, F.L. Mechanism of calcium mitigating membrane fouling in submerged membrane bioreactors. *J. Environ. Sci.* **2009**, *21*, 1066–1073. [[CrossRef](#)]
26. Wang, Z.W.; Wu, Z.C.; Tang, S.J. Extracellular polymeric substances (EPS) properties and their effects on membrane fouling in a submerged membrane bioreactor. *Water Res.* **2009**, *43*, 2504–2512. [[CrossRef](#)]
27. Masse, A.; Sperandio, M.; Cabassud, C. Comparison of sludge characteristics and performance of a submerged membrane bioreactor and an activated sludge process at high solids retention time. *Water Res.* **2006**, *40*, 2405–2415. [[CrossRef](#)]
28. Zhang, X.Y.; Wang, Z.W.; Wu, Z.C.; Wei, T.Y.; Lu, F.H.; Tong, J.; Mai, S.H. Membrane fouling in an anaerobic dynamic membrane bioreactor (AnDMBR) for municipal wastewater treatment: Characteristics of membrane foulants and bulk sludge. *Process Biochem.* **2011**, *46*, 1538–1544. [[CrossRef](#)]
29. Chen, W.; Westerhoff, P.; Leenheer, J.A.; Booksh, K. Fluorescence excitation-emission matrix regional integration to quantify spectra for dissolved organic matter. *Environ. Sci. Technol.* **2003**, *37*, 5701–5710. [[CrossRef](#)]
30. Lin, H.J.; Xie, K.; Mahendran, B.; Bagley, D.M.; Leung, K.T.; Liss, S.N.; Liao, B.Q. Sludge properties and their effects on membrane fouling in submerged anaerobic membrane bioreactors (SANMBRs). *Water Res.* **2009**, *43*, 3827–3837. [[CrossRef](#)]
31. Bae, T.H.; Tak, T.M. Interpretation of fouling characteristics of ultrafiltration membranes during the filtration of membrane bioreactor mixed liquor. *J. Membr. Sci.* **2005**, *264*, 151–160. [[CrossRef](#)]



© 2020 by the authors. Licensee MDPI, Basel, Switzerland. This article is an open access article distributed under the terms and conditions of the Creative Commons Attribution (CC BY) license (<http://creativecommons.org/licenses/by/4.0/>).



Article

# Comparison between a Conventional Anti-Biofouling Compound and a Novel Modified Low-Fouling Polyethersulfone Ultrafiltration Membrane: Bacterial Anti-Attachment, Water Quality and Productivity

Norhan Nady <sup>1,\*</sup> , Noha Salem <sup>2</sup>, Ranya Amer <sup>3</sup>, Ahmed El-Shazly <sup>4</sup>, Sherif H. Kandil <sup>5</sup> and Mohamed Salah El-Din Hassouna <sup>2</sup>

<sup>1</sup> Polymeric Materials Research Department, City of Scientific Research and Technological Applications (SRTA-City), Borg El-Arab City, Alexandria 21934, Egypt

<sup>2</sup> Department of Environmental Studies, Institute of Graduate Studies and Research, Alexandria University, Alexandria 21321, Egypt; nohasalem560@yahoo.com (N.S.); s.hassouna@gmail.com (M.S.E.-D.H.)

<sup>3</sup> Environment and Natural Material Research Institute (ENMRI), City of Scientific Research and Technological Applications (SRTA-City), New Borg El-Arab, Alexandria 21934, Egypt; ranyaamer@yahoo.com

<sup>4</sup> Chemicals and Petrochemical Engineering Department, Egypt-Japan University of Science and Technology (E-JUST), Alexandria 21934, Egypt; ahmed.El-shazly@yahoo.com

<sup>5</sup> Department of Materials Science, Institute of Graduate Studies and Research, Alexandria University, Alexandria 21321, Egypt; s.kandil@usa.net

\* Correspondence: norhan.nady77@yahoo.com; Tel.: +20-109-091-8521

Received: 12 August 2020; Accepted: 4 September 2020; Published: 10 September 2020



**Abstract:** In this work, the efficiency of a conventional chlorination pretreatment is compared with a novel modified low-fouling polyethersulfone (PES) ultrafiltration (UF) membrane, in terms of bacteria attachment and membrane biofouling reduction. This study highlights the use of membrane modification as an effective strategy to reduce bacterial attachment, which is the initial step of biofilm formation, rather than using antimicrobial agents that can enhance bacterial regrowth. The obtained results revealed that the filtration of pretreated, inoculated seawater using the modified PES UF membrane without the pre-chlorination step maintained the highest initial flux ( $3.27 \pm 0.13 \text{ m}^3 \cdot \text{m}^{-2} \cdot \text{h}^{-1}$ ) in the membrane, as well as having one and a half times higher water productivity than the unmodified membrane. The highest removal of bacterial cells was achieved by the modified membrane without chlorination, in which about  $12.07 \times 10^4$  and  $8.9 \times 10^4$  colony-forming unit (CFU)  $\text{m}^{-2}$  bacterial cells were retained on the unmodified and modified membrane surfaces, respectively, while  $29.4 \times 10^6$  and  $0.42 \times 10^6$  CFU  $\text{mL}^{-1}$  reached the filtrate for the unmodified and modified membranes, respectively. The use of chlorine disinfectant resulted in significant bacterial regrowth.

**Keywords:** biofouling; ultrafiltration; polyethersulfone; chlorine; membrane modification; low-fouling surface

## 1. Introduction

Proper pretreatment of the feed seawater for reverse osmosis (RO) helps to reduce microorganisms, thus protecting the RO membranes from fouling [1–3]. The ultrafiltration (UF) process is used as a pretreatment step; it serves as a barrier to remove components with a pore size larger than 100 nm, such as fine colloidal particles, bacteria, viruses, and larger molecules such as proteins [4–6]. The UF process has proved to be an effective alternative to conventional technologies in terms of both cost effectiveness and energy efficiency [2,7,8]. Moreover, according to environmental concerns, it is a good

choice as it provides the production of higher quality brine with low levels of toxic chemicals and contaminants compared to conventional pretreatment technologies [3,9].

Generally, membrane systems are prone to several types of fouling depending on the type of foulant itself, e.g., inorganic or scaling fouling, particulate and colloidal fouling, organic fouling and biological fouling [10–13]. However, biological fouling is the most difficult to control in seawater desalination [13]. Biofilm formation consists of three major phases; induction, logarithmical growth, and plateau phases. The induction phase is the phase in which biofouling starts, with bacterial attachment to the membrane surface by weak physicochemical interactions [11,14,15]. The second phase is the logarithmical growth phase of the attached microorganisms. This phase is associated with extracellular polymeric substance (EPS) secretion and biofilm development [11,14]. The third phase is the plateau, where biofilm growth is limited by fluid shear forces. This phase is the detachment process, as bacteria tend to leave the biofilm for another part of the membrane surface due to an increase in population density and a lack of nutrients [11,12]. This stage of biofouling is more difficult control compared to earlier stages and is mainly affected by nutrients, bacterial growth rate, the mechanical stability of the biofilm, and the effective shear forces [13–15]. Generally, the rapid flux decline occurs at the early stage of biofilm formation due to the initial attachment and growth of microorganisms, followed by a gradual decay by the establishment of an equilibrium condition between the growth of biofilm, EPS production, and the detachment of cells [11–15].

There are three major strategies commonly used to control the biofouling phenomenon in membrane-based processes: chemical and physical pretreatment of the feed water to reduce nutrient availability [4,16–18], biocide usage for metabolic inactivation [17,19–21], and membrane modification to make the membrane less prone to biofouling [22–25]. The conventional method of dealing with the incidence of biofouling is to treat feed water with a biocide or disinfectant [18]. Chlorine remains the most commonly used disinfectant because of its availability, reasonable cost, and effectiveness [26–28]. Furthermore, the efficiency of chlorine can be improved with the use of coagulants to remove the suspended materials [29]. However, there are limitations to chlorine usage including the need for controlling pH, turbidity, and contact time [18,26]; also, hypochlorous acid, which is formed at lower pH values, is highly reactive and corrosive [30].

Most of the used membranes are very susceptible to chlorine degradation. Therefore, chlorination has to be followed by dechlorination in the pretreatment strategy when membranes are used for water treatment. It was reviewed that the oxidative nature of hypochlorite may have detrimental effects on polyethersulfone (PES) membranes such as high protein retention [27,30,31], polymer chain breakage, and consequent expansion of the membrane pore size [27,32–34], changes in membrane surface charge (hydrophilicity/hydrophobicity) [31,33,34], and the deterioration of the membrane's mechanical strength [27,33].

Many bacteria can develop resistance against chlorine [28,35,36]. In addition, the removal of 99.9% of bacteria may not be sufficient to prevent their regrowth, as the surviving cells can multiply at the expense of biodegradable substances [37]. Moreover, the inactive biomass left in feed water after chlorination serves as a rich nutrient, resulting in a rapid bacterial growth rate [20,38]. Chlorine can also promote microbial regrowth by breaking down humic acids and producing assimilable organic carbon (AOC), which may act as a supportive nutrient for chlorine-resistant bacteria [18].

On the other hand, chlorine has environmental implications as it reacts with the organic matter of the feed water and produces various disinfection byproducts (DBPs) [39,40]. The types and concentrations of these DBPs depend on several factors such as the type and amount of disinfectant used, contact time, organic and inorganic contents, temperature, turbidity, and pH [13]. DBPs pose potential risks to human health and aquatic ecosystems when they are discharged in brine. Mediterranean seawater is particularly problematic as it usually contains high concentrations of bromide, which raise the risk of the formation of brominated DBPs that are more carcinogenic or mutagenic than their chlorinated analogs [41].

Another strategy used for fouling mitigation is the surface modification of ready-made membranes to acquire an effective anti-biofouling property [42,43]. PES is widely used for the preparation of UF membranes due to its excellent chemical resistance [44], good thermal stability, and mechanical properties [45]. PES membranes also show high flux and have a reasonable cost compared to other membrane materials. However, they are relatively hydrophobic, and their surfaces adsorb the components of the used fluid, which make them more susceptible to fouling [46]. Surface modifications of PES membranes are one of the current trends to control membrane fouling; they increase membrane surface hydrophilicity and consequently reduce the adsorption or adhesion of the different substances in feed water [47]. Surface modifications of PES membranes can be carried out in many ways, such as coating, blending, compositing, or grafting [24]. Several techniques can be used to initiate the grafting process, including chemical, photochemical, and high-energy radiation initiators [23,24,42,48], as well as enzymatic techniques [24].

Laccases are a group of oxidative enzymes whose exploitation as biocatalysts in the modification (grafting) of poly(ethersulfone) (PES) membranes represent a successful example of an environmentally friendly modification of PES membranes [49]. Phenols and aromatic or aliphatic amines are suitable substrates for laccase enzymes. Laccase-catalyzed reactions are preceded by the monoelectronic oxidation of the substrate molecules to the corresponding reactive radicals that can then produce dimers, oligomers, and/or polymers [50,51].

Recently, a PES membrane was modified by the surface grafting of a brush-like hydrophilic polymer layer. This was achieved by enzyme-catalyzed grafting of an amine-bearing modifier, 3-aminophenol (3-AP), to obtain more hydrophilic PES membranes due to the presence of amine groups on the membrane surface. This method is known for its mildness and eco-friendliness as it can be carried out at room temperature, and uses only air as a source of oxygen and aqueous reaction medium, while no harsh chemicals are needed [47].

This study highlights an effective strategy to reduce biofouling in seawater desalination. It compares the effectiveness of membrane modification to reduce bacterial attachment, which is the initial step of biofilm formation, and the traditional strategy of using antimicrobial agents to kill bacteria cells in the seawater feed stream. The main aim of this study is to compare the efficiency of a conventional chlorination pretreatment step for feed water (seawater) with that of a modified PES UF membrane with brush-like oligomers of poly (3-AP) on its surface in terms of the UF membrane biofouling reduction, as well as comparing the environmental impacts of both strategies in terms of membrane performance and filtrate water quality. To the best of our knowledge, this is the first application study that compares the effect of membrane surface modification on the biofouling phenomenon compared to the traditional strategy of using antimicrobial agents that to mitigate biofouling in the membrane-based desalination process.

## 2. Materials and Methods

### 2.1. Materials

3-aminophenol (3-AP,  $C_6H_7NO$ ), dichloromethane (DCM,  $CH_2Cl_2$ ), sodium acetate (anhydrous,  $C_2H_3NaO_2$ ), acetic acid ( $C_2H_4O_2$ ), catechol ( $C_6H_6O_2$ ), and sodium thiosulfate pentahydrate ( $Na_2S_2O_3 \cdot 5H_2O$ ) were obtained from Sigma-Aldrich (Germany). All of them were at least 98% purity. A flat sheet of polyethersulfone (PES; 0.03  $\mu m$  pore size) was purchased from Sterlitech (USA). Laccase from *Trametes versicolor* ( $>0.5 U \cdot mg^{-1}$ ) was obtained from Fluka (Germany). Sodium hypochlorite solution (NaOCl, available chlorine 4%–5%) was purchased from Alpha Chemika (India). Sodium bisulfite (a mixture of  $NaHSO_3$  and  $Na_2S_2O_3$  powder) was obtained from Acros Organics (Belgium). Ethanol (analytical reagent grade) and *N,N*-diethyl-*p*-phenylenediamine 4 (DPD4) Palintest were purchased from Fisher (United Kingdom). Ferric chloride ( $FeCl_3$ , anhydrous) was obtained from Oxford Laboratory (India). Luria–Bertani (LB) agar (Lennox) was obtained from Conda (Spain). Yeast extract was obtained from Bio Basic (Canada Inc., Canada). Peptone water

medium (peptone 5.0, tryptone 5.0, sodium chloride 5.0) was purchased from Lab a Neogen Company (United Kingdom). Sodium phosphate monobasic, disodium hydrogen phosphate-2-hydrate, and potassium iodide (KI) were obtained from Riedel-de Haën (Germany). Soluble starch was purchased from Daejung (Korea).

## 2.2. Methods

### 2.2.1. Laccase Activity

Laccase activity was determined using catechol as a substrate, as previously described [46]. Briefly, the assay mixture contained 0.33 mL of 10 mM catechol, and 2.67 mL of 0.1 M sodium acetate buffer (pH 5), with 0.025 U·mL<sup>-1</sup> laccase. Catechol oxidation was monitored by following the increase in absorbance at 400 nm ( $\epsilon = 26,000 \text{ M}^{-1}\cdot\text{cm}^{-1}$ ) with a reaction time of 20 min. One unit of laccase activity is defined as the amount of enzyme required to oxidize 1  $\mu\text{mol}$  of catechol per minute at 25 °C.

### 2.2.2. Modification of PES Membrane Surfaces

Flat rectangular sheets of commercial PES membrane (200 × 200 mm, 0.03  $\mu\text{m}$  pore size, (Sterlitech, USA) were cut into circles of 4.5 cm diameter to fit in a 50-mL Amicon filtration cell. The membrane modification was carried out as previously described [47,52]. The membrane circles were immersed in 40 mL of 0.1 M sodium acetate buffer (pH 5) containing equal volumes of 15 mM 3-AP and laccase enzyme (0.5 U·mL<sup>-1</sup>). Air was bubbled through the solution for the purpose of good mixing and as a source of oxygen for the enzyme catalytic cycle (i.e., enzyme reactivation). The reaction was carried out for 30 min at room temperature (23 ± 2 °C). After completing the modification, the membrane circles were washed first by spraying with deionized water, followed by dipping in freshly boiled deionized water (95 ± 2 °C), and they were subsequently dried for 24 h in a desiccator.

### 2.2.3. Seawater Sampling

This study was conducted using Mediterranean seawater from the El Max region of west Alexandria, Egypt, in February 2018. Total dissolved salts (TDS), turbidity, and calcium content were measured immediately after sampling using standard methods [53]. The purpose of using seawater was to maintain the natural composition of the feed water used in the experiments. The feed seawater was stored at a controlled room temperature (20 ± 2 °C). Figure 1 shows a schematic diagram of the experimental steps, as described in the following sections.

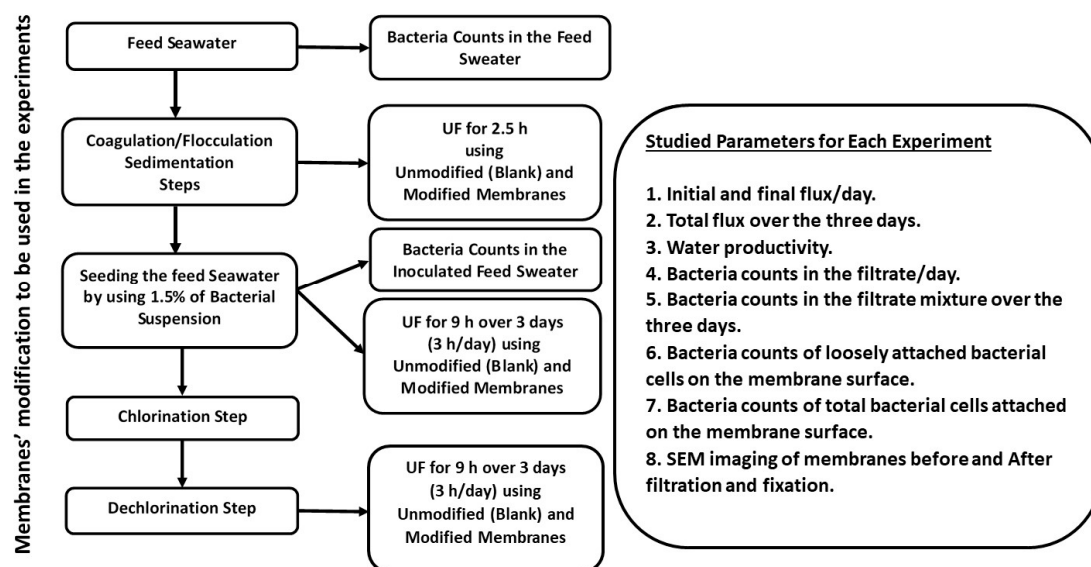


Figure 1. A schematic diagram of the experimental steps.

## 2.2.4. Preparation of the Feed Seawater

### Pretreatment of the Feed Seawater by Coagulation

The collected seawater was pretreated to reduce the suspended matter in order to prevent membrane blockage by other types of fouling rather than biofouling, which was being investigated. Coagulation was carried out using ferric chloride ( $\text{FeCl}_3$ ) by the conventional standard jar test. A stock solution of  $\text{FeCl}_3$  ( $1000 \text{ mg}\cdot\text{L}^{-1}$ ) was prepared, 200 mL samples of seawater were placed in 250 mL beakers, and different concentrations of ferric chloride (2, 4, 6, 8, 10, 15, and  $20 \text{ mg L}^{-1}$ ) were added into the beakers. Samples were stirred for 1 min at 100 rpm followed by 20 min of slow mixing at 30 rpm [54]. Residual turbidity was determined as an indicator of performance, and the optimum dose of the coagulant was identified. The optimum dose of the  $\text{FeCl}_3$  was added to seawater and then kept for a week for sedimentation, and subsequently, the supernatant of clear water was taken.

### Seeding of Seawater with Bacterial Load

The pretreated seawater was inoculated with various bacterial strains that are actually present in seawater in order to investigate the biofouling phenomenon within a relatively short time. Inoculum was prepared by adding 1 mL of seawater into 30 mL sterile Luria–Bertani (LB) broth (consisting of 0.5% tryptone, 0.5% peptone, 0.5% yeast extract, and 0.5% NaCl). The tubes were incubated in a shaker incubator at  $30^\circ\text{C}$  and 150 rpm for five days. Then, the pretreated seawater was inoculated with 1.5% of this bacterial suspension ( $\text{OD}_{680} = 1.8$ ) immediately before the UF experiment.

### Disinfection of the Feed Seawater

The disinfection of the seawater was carried out using chlorine in the form of sodium hypochlorite ( $\text{NaOCl}$ ) solution with 4%–5% available chlorine. Practically, only 3% of the available chlorine was determined by standardization using 0.01 N sodium thiosulfate ( $\text{Na}_2\text{S}_2\text{O}_3$ ) solutions. The standard method of iodometric titration [55] was used: 200 mL of chlorine solution was placed in a conical flask and 5 mL of glacial acetic acid was added to reduce the pH to between 3.0 and 4.0, followed by adding 1 g of potassium iodide, and the solution was mixed well. The potassium iodide solution was titrated against 0.01 N sodium thiosulfate solution until the yellow color of the liberated iodine almost faded away. Then, 1 mL of 1% starch solution indicator was added, producing a blue color, followed by titration again against 0.01 N sodium thiosulfate solution till the blue color disappeared; the total volume of titrant was measured, and total chlorine was determined in  $\text{mg}\cdot\text{L}^{-1}$  from Equation (1):

$$\text{Residual chlorine} = A \times N \times 35.45 \times 1000/\text{mL sample taken} \quad (1)$$

where A is the mL of titrant for the sample and N is the normality of sodium thiosulfate.

In this work, a stock solution of sodium hypochlorite ( $1000 \text{ mg L}^{-1}$ ) was freshly prepared. A chlorine dose of  $6 \text{ mg L}^{-1}$ , which was prepared from this stock solution, was added to the inoculated pretreated feed water (pH 6) and was kept for 90 min contact time in the dark at room temperature ( $23 \pm 3^\circ\text{C}$ ). Then, the free residual chlorine was measured using the standard DPD colorimetric method.

### Dechlorination Process

Sodium bisulfite was added as a dechlorinating agent for the removal of any residual chlorine before UF to protect the membrane from deterioration by chlorine; a stock solution of sodium bisulfite ( $100 \text{ mg L}^{-1}$ ) was prepared using sterile distilled water. Excess sodium bisulfite was used to confirm the complete removal of chlorine (each  $5 \text{ mg L}^{-1}$  of sodium bisulfite was added to remove  $1 \text{ mg L}^{-1}$  of residual chlorine), kept for 30 min contact time at a room temperature of  $23 \pm 2^\circ\text{C}$ . Then, residual free chlorine was measured using the DPD colorimetric method; a chlorine standard curve was established by the preparation of different known concentrations of chlorine (0.05, 0.2, 0.5, 0.8, 1, 2, and  $3 \text{ mg L}^{-1}$ ) in 10 mL sterilized distilled water. The concentration of residual chlorine was measured by adding



DPD tablets into 10 mL of solution and shaking for 2 min. The intensity of the produced red color was measured using a Vis-spectrophotometer at 515 nm wavelength, and the concentration of residual chlorine was determined in  $\text{mg L}^{-1}$  using the prepared chlorine standard curve.

### 2.2.5. Ultrafiltration (UF)

A dead-end stirred filtration cell (Millipore, Amicon Model 8050,  $13.4 \text{ cm}^2$  active filtration area) was used at a constant pressure of 1 bar and 200 rpm stirring at  $23 \pm 2 \text{ }^\circ\text{C}$ . Unmodified and modified PES membranes were used in the filtration of different conditions of feed seawater. Two different feed seawater types, in terms of pretreatment steps, were used: one pretreated by coagulation only, without the chlorination step, and the other pretreated by coagulation followed by chlorination and dechlorination steps. Then, the pretreated feed seawater samples were seeded with a bacterial suspension and filtered for 9 h over three days (3 h/day) of filtration time. UF was also carried out for the pretreated feed seawater without bacterial loading for 2.5 h of filtration time in order to investigate the membrane permeability in the absence of bacterial cells.

First, the filtration cell was immersed in 70% ethanol overnight, and then it was washed three times with sterilized deionized water to remove any traces of ethanol. The membranes were also washed three times with sterilized deionized water before the experiment, and then UF was carried out. At the end of each day, the membrane was placed in 50 mL of initial pretreated seawater without bacterial suspension to avoid any damage caused by drying. The experiment for each tested condition was performed three times; a new membrane was used in each experimental assay. The microbiological results were normalized and their average was taken.

### Water Flux

The pure water flux was determined at the start and end of each day using Equation (2):

$$J_w = \frac{Q}{\Delta t \cdot A} \quad (2)$$

where  $J_w$  = water flux ( $\text{m}^3 \cdot \text{m}^{-2} \cdot \text{s}^{-1}$ ),  $Q$  is the volume of permeate collected ( $\text{m}^3$ ),  $\Delta t$  is the sampling time (s), and  $A$  is the membrane area ( $\text{m}^2$ ) [47].

### Water Productivity

The volume of the output of filtrate from the membrane was determined in  $\text{m}^3 \cdot \text{h}^{-1}$  at the end of each day for three days.

### 2.2.6. Bacterial Count

Bacterial growth was counted in the initial feed seawater and the filtrate produced each day as well as the filtrate mixture produced. Standard plate counts were used by plating 100  $\mu\text{L}$  of suitable serially diluted bacterial suspension in phosphate buffer solution (PBS) pH 7, ranging from  $10^{-1}$  to  $10^{-5}$ , on LB agar in three replicates, followed by incubation at  $30 \text{ }^\circ\text{C}$  overnight. The number of separate colonies was recorded as a colony-forming unit (CFU)  $\text{mL}^{-1}$  [56].

Moreover, at the end of the experiment, the membrane was cut into two identical halves; one half was placed in 30 mL PBS and the bacteria attached on the membrane surface were determined twice; the first bacterial count was determined immediately for the loosely attached bacteria by gently handshaking for a minute, and then the count was determined again for the total bacterial cells attached on the membrane surface using mechanical shaking after incubation overnight in a shaker incubator at 150 rpm,  $30 \text{ }^\circ\text{C}$ . The bacterial counts were determined as the  $\text{CFU m}^{-2}$  of the membrane surface.

### 2.2.7. Scanning Electron Microscope Imaging

Both unmodified and modified membrane surfaces, after UF of both pretreated, inoculated feed seawater without the chlorination step and pretreated, inoculated feed seawater with chlorination and dechlorination steps, were imaged using a JeolJsm 6360 LA scanning electron microscope (SEM, JEOL Ltd., Tokyo, Japan). After the experiment, the membranes were cut using a very sharp blade and were preserved in a fixer composed of 0.3% glutaraldehyde, 5% formaldehyde in phosphate buffer (pH 7.2), and serially dehydrated in modified ethyl alcohol [57]. Moreover, the formed layers on both unmodified and modified PES membranes, after UF of pretreated feed seawater with neither the chlorination step nor bacterial loading and after UF of pretreated feed seawater with the chlorination step and without bacterial loading, were imaged. All surfaces were coated with Au before imaging. A voltage of 20 KV and a resolution of  $1280 \times 960$  pixels were used.

### 2.2.8. Atomic Absorption Spectroscopy Analysis

Atomic absorption spectroscopy (Shimadzu AA-7000, Tokyo, Japan) was used for the analysis of the layers formed on both the unmodified and the modified PES UF membrane surfaces after filtration of the two types of feed seawater, without bacterial loading (feed seawater pretreated without the chlorination step and feed seawater pretreated with chlorination and dechlorination steps), at a constant pressure of 1 bar and 200 rpm, at  $23 \pm 2$  °C, for 2.5 h of filtration time.

## 3. Results and Discussion

### 3.1. Chemical Analysis of the Used Seawater

A chemical analysis of the seawater showed a high calcium content ( $483.36 \pm 8.92$  mg L<sup>-1</sup>) due to the winter season, as previously reported [58]. The turbidity was determined as 3.17 Nephelometric Turbidity Units (NTU). The total dissolved salts (TDS) concentration was 27.2 ppt (ng/L), which is less than the average for Mediterranean seawater [59] because of the proximity of the El-Mahmoudiyah canal outfall to the sampling point.

### 3.2. Membrane Characterization

The membrane characterization was previously performed and published [47], and the obtained results are briefly presented as follows: Thermogravimetric Analyses (TGA) show that the rate of decomposition of the backbone of the modified membranes is somewhat slower than that of the blank membrane. As shown at 800 °C, only 38 wt% of the modified membrane remained, whereas only 15 wt% remained of the blank membrane. Moreover, Differential Scanning Calorimetry (DSC) analysis revealed that the glass transition temperature of the blank PES membrane was 226 °C, and it decreased very slightly upon modification to 224 °C. X-ray diffraction (XRD) analysis shows the effect of the amorphous structure of poly(3-AP) on the intensity of the characteristic peak of the blank membrane; it is proposed that the addition of poly(3-AP) may contribute to the increase in the flux of the modified membranes. The tensile strength test of the membranes showed a very slight decrease in the tensile strength of the blank membranes. However, the modified membranes at a high grafting yield showed slightly stronger mechanical properties than the blank membrane. The Raman spectra of the modified membrane confirm the presence of amine groups on the membrane surface. Scanning Probe Microscope (SPM) images show the formation of a brush-like modifying layer of poly(3-AP). Furthermore, the Nuclear Magnetic Resonance (NMR) integration results of the analyzed peaks do not favor a particular structure. The proposed structure of the formed poly(3-AP) layer is shown in Supplementary Figure S1. The water flux of the most modified membranes increased up to 35% relative to the blank (unmodified) membrane, and an up to 90% reduction in protein adsorption was obtained. In general, this modification does not harmfully affect the bulk properties of the original blank membrane.

### 3.3. Pretreatment of the Feed Seawater (Coagulation–Flocculation)

Coagulation and flocculation are important pretreatment processes for the removal of colloidal particles responsible for the turbidity of seawater [13]. The destabilization of colloidal particles is usually carried out by adding coagulants followed by the clotting of the resulting unstable colloidal particles, which are then removed from water by sedimentation [60]. In this work, coagulation was carried out by the standard jar test using ferric chloride ( $\text{FeCl}_3$ ) due to its proven performance as a coagulant in water treatment plants [61]. The addition of  $\text{FeCl}_3$  resulted in the rapid removal of turbidity as a result of the neutralization of the negatively charged particles with different cationic species produced from the hydrolysis of ferric chloride in water, leading to the destabilization of such particles and subsequently flocculation (Supplementary Figure S2). Maximum turbidity removal was about 82.6% at 8 mg/L of  $\text{FeCl}_3$  (Supplementary Figure S3). However, when high concentrations of  $\text{FeCl}_3$  were used, lower turbidity removal was obtained due to competition between the re-conformation rate of negatively charged particle networks and the collision rate of destabilized colloids [61,62].

### 3.4. Ultrafiltration Process

#### 3.4.1. Water Flux

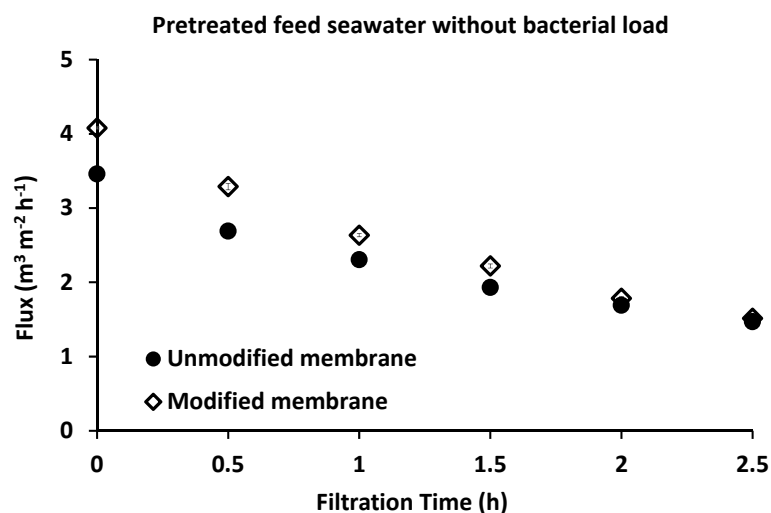
##### Pretreated Feed Seawater without Bacterial Loading

A UF experiment was carried out using pretreated seawater with neither bacterial loading nor the pre-chlorination step in order to investigate the effect of other seawater contents, which can affect membrane performance. As shown in Figure 2, the water flux reduced over time for both unmodified and modified membranes to less than half its initial value (unmodified, 57.5% reduction; modified, 62.9% reduction). Observation of the membrane before and after filtration showed the formation of a colored layer that precipitated on the membrane surface (Figure 3) (unmodified PES, c; modified PES, d). SEM images of this formed layer showed salt precipitation. The presence of calcium was proposed due to its high content in the raw feed seawater ( $483.36 \pm 8.92 \text{ mg L}^{-1}$ ) and was confirmed by atomic absorption analysis. However, there may be other salts/dissolved materials that were precipitated on the membrane surface. It should be noted that, in desalination plants, the inlet feed is usually diluted to reduce the water salinity to around 15,000–20,000 ppm to minimize salt precipitation on the membrane surface. Calcium ions have a negative impact on the membrane flux by altering the surface chemistry through interaction with foulant molecules, such as natural organic materials (NOM) [11,63,64]. Calcium can also link two negatively charged functional groups together to form intermolecular complexes; when the linkage happens between two humic acid molecules, a gel layer of macromolecules can be formed through this intermolecular bridging, and it becomes more compact and cohesive by the cross-linking effect of calcium [64]. As shown in Figure 4, scanning electron microscope images showed that most of the formed layers appeared as separate crystals on the modified membranes, whereas they appeared as a packed gel layer on the unmodified PES membrane. The pre-chlorination step of the feed seawater did not make a significant change to the general performance of both unmodified and modified membranes (i.e., only a fluctuation up to 6%).

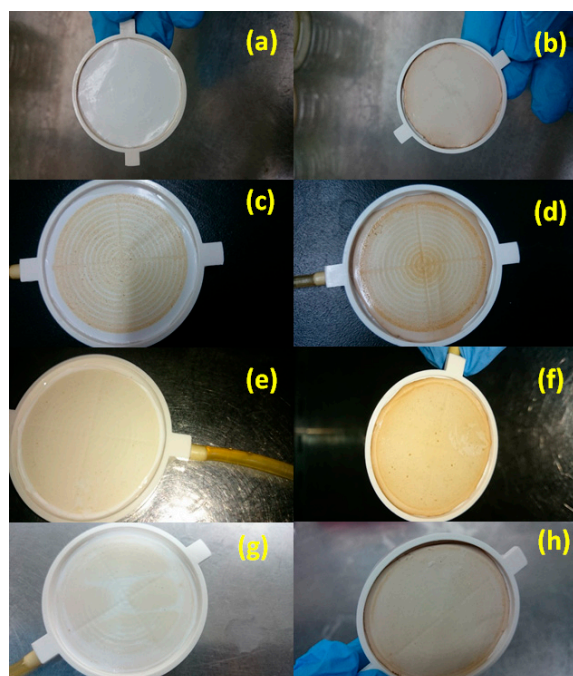
##### Pretreated Feed Seawater with Bacterial Loading

The bacterial count of the seawater sample was determined as  $1600 \text{ CFU mL}^{-1}$ . In order to investigate the biofouling phenomenon within a relatively short time, the pretreated seawater was inoculated with a bacterial load of various bacteria strains that are naturally present in seawater. The seawater was seeded by a 1.5% bacterial suspension of  $\text{OD}_{680} = 1.8$  and was filtered using a dead-end stirred filtration cell at a constant pressure of 1 bar at  $23 \pm 2 \text{ }^\circ\text{C}$  and 200 rpm stirring for 9 h (3 h  $\times$  3 days) filtration time. PES membranes of  $0.03 \text{ }\mu\text{m}$  pore size were used in the filtration of pretreated (i.e., by the coagulation step as described in the previous section) inoculated feed seawater, with or without the pre-chlorination step. The biofouling phenomenon and biofilm formation on

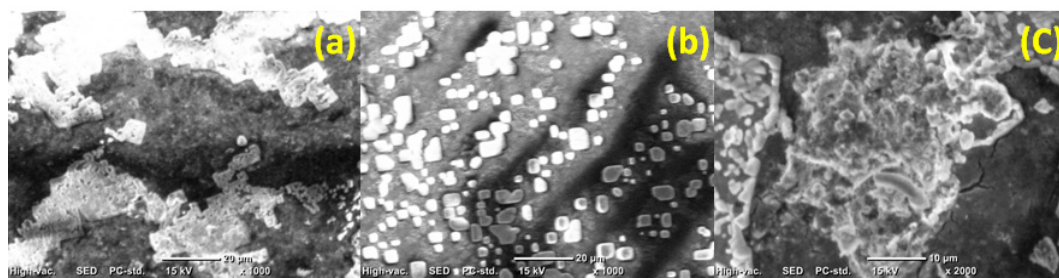
the PES membrane surface with the consequential effect on membrane performance was studied. Membrane performance was evaluated by determining: (1) the initial and final flux of the membrane, (2) water productivity (volume of filtrate), (3) bacterial count of the filtrate on each day, (4) bacterial count of the filtrate mixture produced over three days, (5) bacterial count on the membrane surface and (6) SEM imaging of the membrane surface.



**Figure 2.** The flux of pretreated seawater with neither bacterial load nor the chlorination step. Three samples were tested for both the unmodified and modified membranes. Reference conditions: pressure of 1 bar,  $23 \pm 2$  °C at 200 rpm stirring for 2.5 h filtration time. Unmodified membrane (black filled circle) and modified membrane (black unfilled diamond).



**Figure 3.** Photos of unmodified membrane before (a) and after (c) filtration of pretreated seawater without bacterial loading, and modified membrane before (b) and after (d) filtration of pretreated seawater without bacterial loading. Photo of unmodified membrane after filtration of pretreated, inoculated seawater without chlorination (e) or with the chlorination (g) pretreatment step, and photo of modified membrane after filtration of pretreated, inoculated seawater without chlorination (f) or with the chlorination (h) pretreatment step. Reference conditions: 1 bar,  $23 \pm 2$  °C and 200 rpm stirring for 2.5 h filtration time.



**Figure 4.** SEM images of unmodified ((a),  $\times 1000$ ) and modified ((b),  $\times 1000$ ) polyethersulfone (PES) membranes after filtration of pretreated seawater with neither bacterial loading nor the chlorination step, and modified ((c),  $\times 2000$ ) PES membranes after filtration of pretreated seawater without bacterial loading but after the chlorination step. Reference conditions: 1 bar,  $23 \pm 2$  °C and 200 rpm stirring for 2.5 h filtration time.

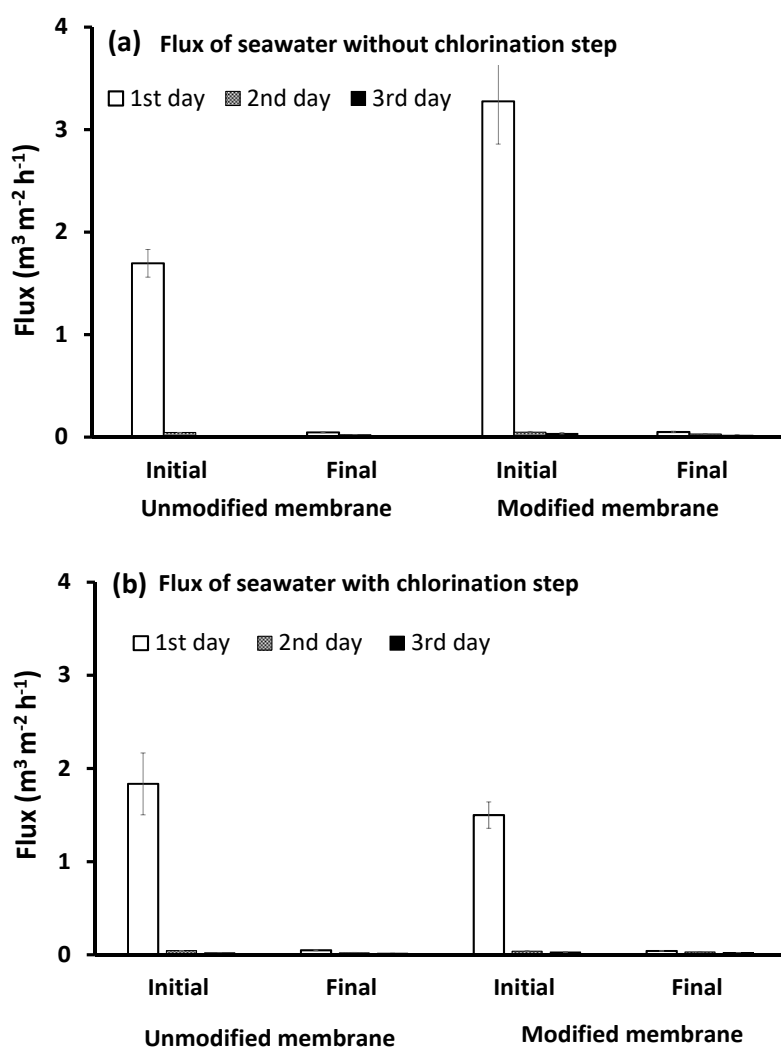
As shown in Figure 5, on the first day of filtration of the pretreated, inoculated feed seawater, without the chlorination step, the initial flux of the unmodified membrane was significantly reduced, and only about 43% of its value was maintained relative to seawater without bacterial loading. Meanwhile, the modified membrane was able to maintain about 76.3% of its initial flux relative to seawater without bacterial loading. The modified membrane had a higher initial flux compared to the unmodified one, which can be attributed to the presence of free polar groups of brush-like oligomers formed on the membrane surface, as previously presented and shown in Supplementary Figure S1 [47], which increased both its hydrophilicity (the static water contact angle of the unmodified and modified PES are  $75.9 \pm 2^\circ$  and  $41.2 \pm 1.7^\circ$ , respectively) and the repellence of bacteria. Both effects can facilitate water permeation. The flux declined rapidly to reach about 1% of its initial flux for both unmodified and modified membranes by the end of the first day (3 h filtration). This rapid flux decline can be correlated with two main effects.

The first effect is concentration polarization, which resulted from the accumulation of larger solutes (such as calcium crystals, as illustrated in the previous section) that were rejected and retained at the membrane surface. As they could not diffuse back to the bulk solution, they caused a concentration gradient above the membrane surface and created an osmotic back pressure that reduced the effective transmembrane pressure of the system [11,64].

The second factor responsible for the rapid flux decline was the early attachment and proliferation of bacterial cells maintained on the membrane surface [11,17,65,66]. Bacterial cells colonized the membrane through the reversible and irreversible attachment of bacteria's surface via electrostatic and hydrophobic interactions [17] as the first step of biofilm formation. Moreover, depositions of bacterial cells on the membrane surface formed hydraulic resistance, which resulted in additional concentration polarization as bacterial cells affected the porosity and pore size distribution on the membrane surface, resulting in the precipitation of salts within membrane pores [20,65].

On the other hand, when the pretreated, inoculated seawater was exposed to chlorination and dechlorination pretreatment steps, it was observed that the chlorination did not cause evident changes in the initial flux of the unmodified membrane, as it decreased to about 53% of its value relative to the feed seawater without bacterial loading. Meanwhile, the chlorination step resulted in a reduction in the modified membrane flux to about 36.7% of its value relative to the case of using feed seawater without bacterial loading, and an even greater reduction compared to the pretreated, inoculated seawater without chlorination (45.8%). There is no obvious explanation for the effect of chlorination on the modified layer; however, SEM images of the salt layer formed on the membrane surface, when UF was carried out using pretreated seawater without bacterial loading, showed a difference in the shape of the formed layer in the presence or absence of chlorine. When the feed water was pretreated without the chlorination step, a continuous gel layer was formed on the unmodified membrane surface (Figure 4a), while clearly separated crystals were formed on the modified membrane surface (Figure 4b). However, when chlorine was used, the salt layer formed on the modified membrane (Figure 4c) was similar to that

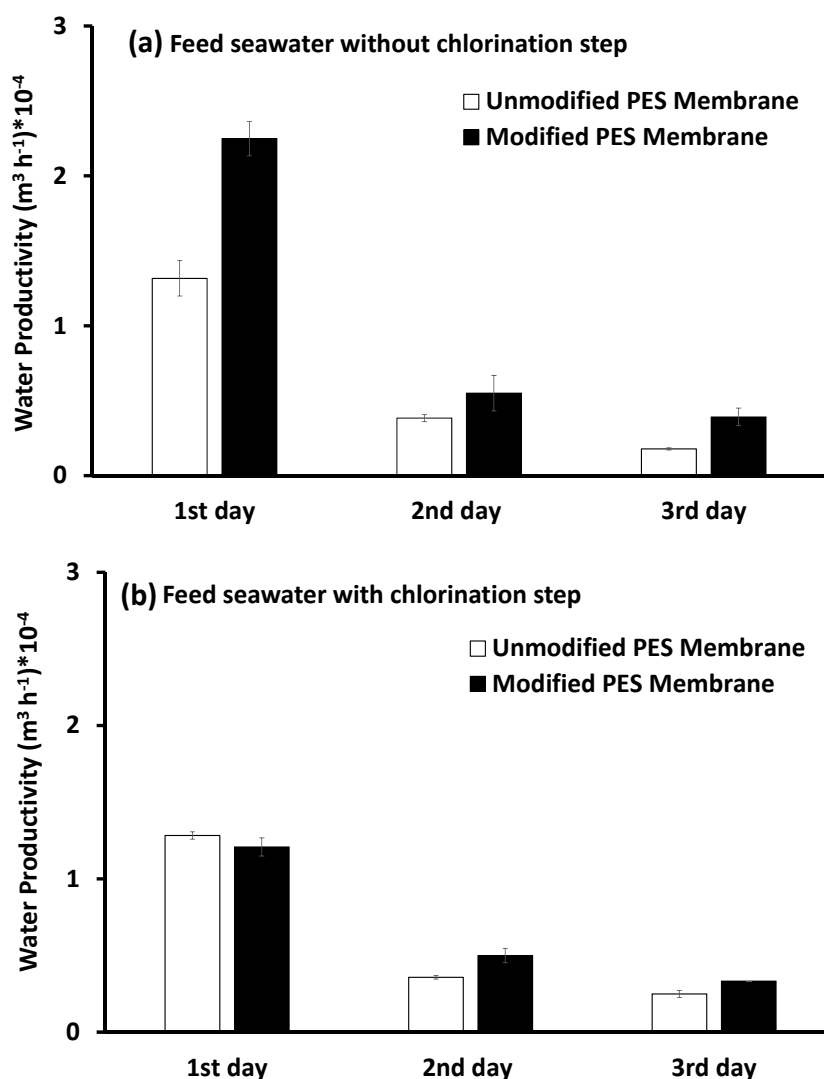
formed on the unmodified membrane. The significant flux reduction in the modified membrane after the filtration of pretreated, inoculated seawater with chlorination and de-chlorination pretreatment steps may be explained by the presence of dead biomass in the feed water which represented a high content of NOM, which could interact with calcium ions and form a thick, packed gel layer that affects membrane permeability. Furthermore, this condensed gel layer could be easily consumed by bacterial cells resulting in a higher bacterial growth rate. However, the effect of the chlorination–dechlorination pretreatment steps on the modified membrane structure and the mechanisms by which these two different layers were formed in the presence or the absence of chlorine require further investigation. The very low flux observed on the second and third days of filtration was a common trend for both the unmodified and modified PES membranes in the two cases of pretreated, inoculated chlorinated or non-chlorinated seawater. However, the rate of flux decline was more gradual, which can be related to the equilibrium condition between biofilm growth, EPS production, and biofilm loss (cell detachment) caused by hydrodynamic shear at the solution–biofilm interface [17,66].



**Figure 5.** Initial and final flux of both the unmodified and modified PES membranes in two cases: bacterial loaded feed seawater without chlorination (a) or with the chlorination (b) pretreatment step. Reference conditions: pressure of 1 bar at  $23 \pm 2 \text{ }^\circ\text{C}$  and 200 rpm stirring for 9 h (3 h  $\times$  3 days) filtration time.

### 3.4.2. Water Productivity

The filtrate volume per unit of time is expressed as water productivity ( $\text{m}^3 \cdot \text{h}^{-1}$ ), as shown in Figure 6. The highest productivity was recorded on the first day for the different testing conditions. Meanwhile, the productivity was greatly decreased on the second and third days of filtration (about 73 and 84%, respectively) as a consequence of flux decline. The largest volume of the filtrate was produced when the modified membrane was used to filter pretreated, inoculated seawater, without the chlorination step (water productivity was almost one and a half times the water productivity of the unmodified membrane). When chlorine was used, the productivity of the modified PES membrane was reduced due to flux decline, as mentioned in the previous section.



**Figure 6.** Water productivity ( $\text{m}^3 \text{h}^{-1}$ ) of both the unmodified and modified PES membranes in two cases: bacterial loaded feed seawater without chlorination (a) or with the chlorination (b) pretreatment step. Reference conditions: pressure of 1 bar at  $23 \pm 2 \text{ }^\circ\text{C}$  and 200 rpm stirring for 9 h ( $3 \text{ h} \times 3 \text{ days}$ ) filtration time.

### 3.4.3. Bacterial Counts

#### Bacterial Counts in the Pretreated Inoculated Feed Seawater over Three Days

Chlorine is usually added to control bacterial growth in most water treatment/desalination plants; the effect of the chlorination step on the feed water was investigated by counting the bacterial cells in

pretreated, inoculated feed seawater over three days. The feed seawater used for the experiments was freshly prepared on the first day and then kept at 4 °C overnight to be used on the second and third days. With the chlorination pretreatment step for feed water, the rate of bacterial growth increased rapidly over the three days relative to the bacterial growth of feed water that was not chlorinated, as shown in Figure 7. This high growth rate may be attributed to the presence of a rich nutrient supply of inactive biomass (dead bacteria) in the feed water [20,38]. This means that chlorine is not the optimum choice to control bacterial growth, even if it is efficient to remove most of the bacteria, as the surviving bacteria can undergo a rapid regrowth.

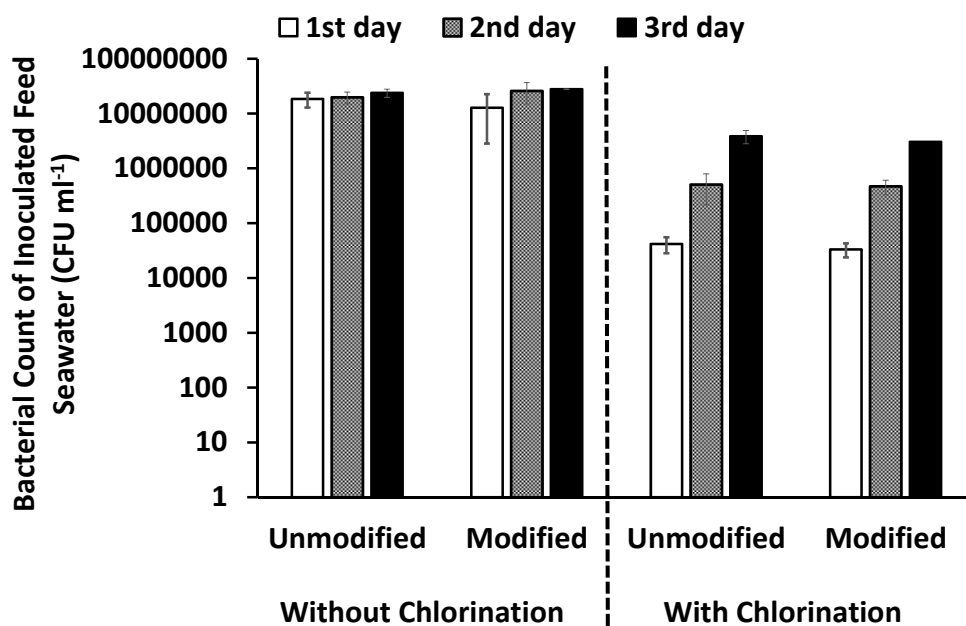
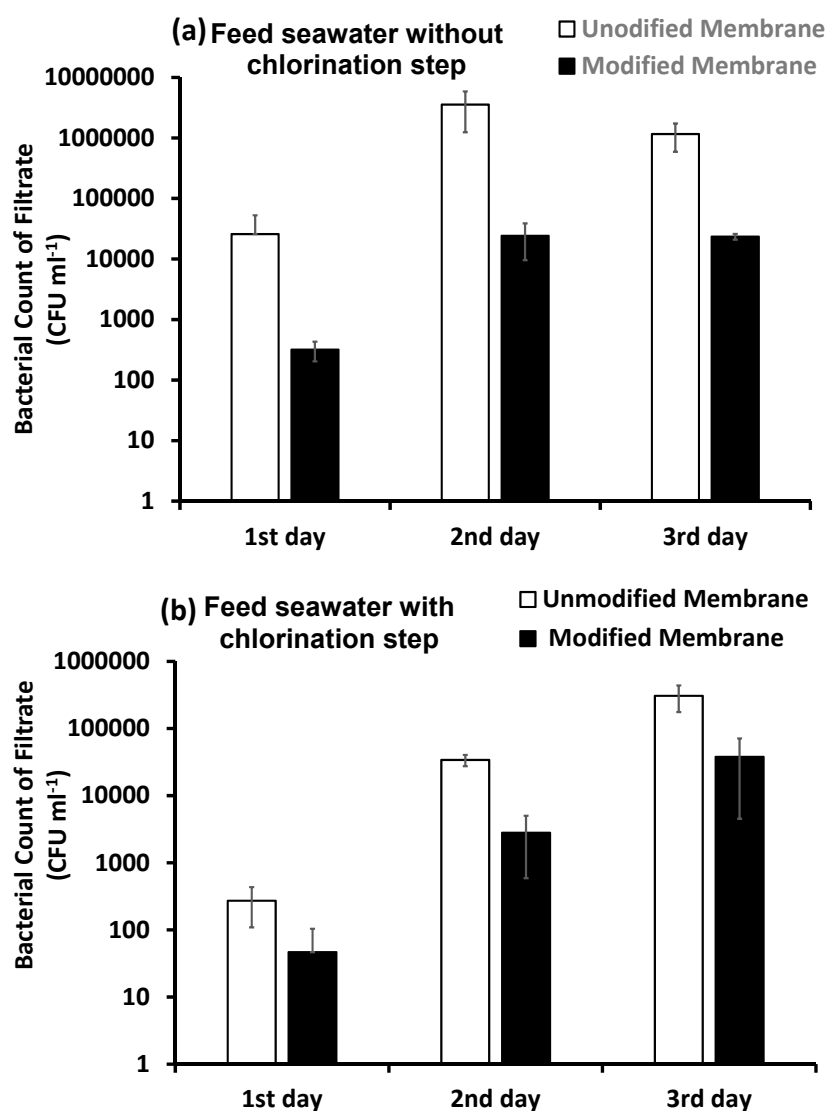


Figure 7. Bacterial count in pretreated, inoculated chlorinated and non-chlorinated feed seawater.

#### Bacterial Counts in the Filtrate Water over Three Days

Since UF is commonly used to remove fine colloidal particles, bacteria, viruses and large molecules such as proteins [5], both unmodified and modified membranes showed a high bacterial removal efficiency under the different testing conditions. On the first day of filtration of the pretreated, inoculated feed seawater (Figure 8), about 99.8% of total bacterial cells were removed by the unmodified membrane (retained on the membrane), while about 0.2% were permeated with the filtrate ( $2.575 \times 10^4$  CFU mL<sup>-1</sup>). The highest removal of bacterial cells was achieved by the modified membrane, in which about 99.99% of total feed bacterial cells were retained on the membrane surface, while only 0.01% of feed bacteria ( $0.318 \times 10^4$  CFU mL<sup>-1</sup>) reached the filtrate. This high bacterial rejection confirms the antifouling ability of such a modification, as illustrated in a previous work [47]. The antifouling mechanism of the modified membrane is based on steric hindrance and the osmotic effect of the hydrated brush-like polymer layer, which keeps bacterial cells as well as macromolecules (nutrients for bacteria) at a distance from the membrane surface [50]. On the second day of filtration, the bacterial cells on the membrane surface began to metabolize and secrete extracellular polymeric substances as the first step of biofilm formation [11,14,15,17]. For this, the filtrate on the second day recorded the highest bacterial count for both the unmodified membrane ( $355 \times 10^4$  CFU mL<sup>-1</sup>) and modified membrane ( $2.41 \times 10^4$  CFU mL<sup>-1</sup>); however, the counted bacterial cells in the filtrate of the modified membrane were much lower than those in the filtrate of the unmodified membrane.





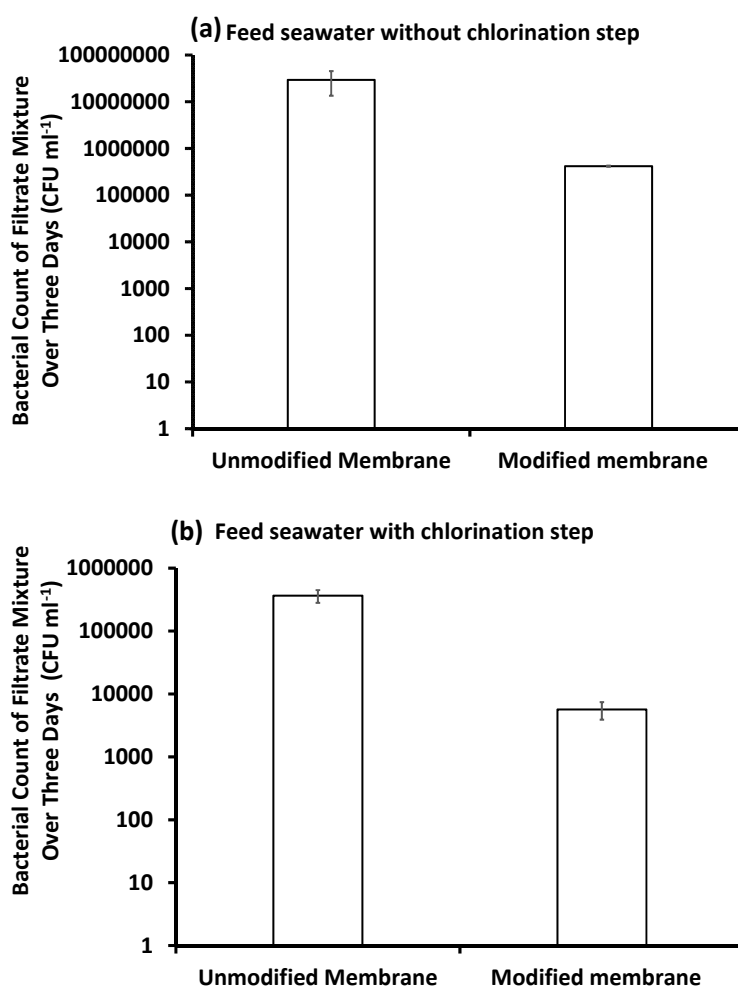
**Figure 8.** Bacterial count of the ultrafiltration (UF) filtrate for pretreated, inoculated feed seawater without chlorination (a) or with the chlorination (b) pretreatment step. Reference conditions: 1 bar,  $23 \pm 2$  °C and 200 rpm stirring for 9 h (3 h  $\times$  3 days) filtration time.

This phenomenon can be attributed to the logarithmical growth phase. Meanwhile, bacterial growth may be promoted by the presence of calcium salts. Calcium not only causes flux decline, as discussed before, but also plays a vital role in bacterial biofilm formation. The calcium ion was reported as a universal messenger, transmitting signals from the cell surface to the interior of the cell [67,68]. Calcium signaling is regulated by calmodulin, which is a calcium-modulating protein that controls cell proliferation, programmed cell death, and autophagy [69]. Moreover, calcium was assigned in specific and non-specific interactions between cells and the localized surface, in which calcium-binding proteins are often involved in bacterial adhesion to a surface. This binding is important for cell–cell aggregation. In addition, calcium is also recorded as an ionic cross-bridging molecule for negatively charged bacterial polysaccharides [68].

On the third day of filtration, the bacterial count recorded in the filtrate of the unmodified membrane was lower than that on the second day. This may be explained as the bacterial growth reaching the plateau phase, in which the biofilm growth phase was limited by the “detachment process” of the fluid shear forces. This phase may be attributed to the increase in population density and the lack of nutrients in the biofilm, and because the bacterial attachment to the membrane is limited [11,14,15].

Another reason for the inability of bacteria to reach the filtrate of the unmodified membrane is the complete blockage of most membrane pores. Regarding this, the bacterial cells were forced to settle on the membrane surface. Meanwhile, in the case of the modified membrane, the bacterial counts of the filtrate on the second and third days were approximately the same. This can be explained by the incomplete blockage of membrane pores. The modified membrane had available spaces for bacterial attachment. This observation was confirmed by SEM images, as will be discussed in the following section.

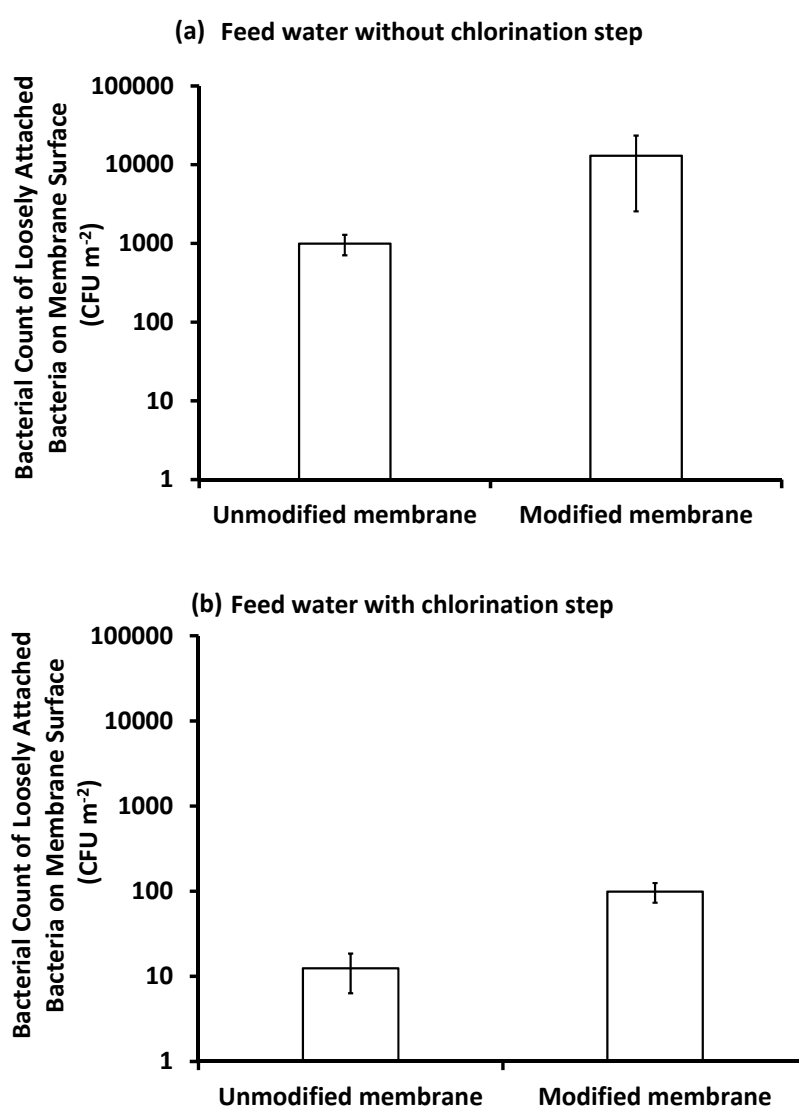
When chlorine was applied in the pretreatment, it removed about 99.6% of the total bacterial cells in the feed water (Figure 9). On the first day of filtration, the unmodified membrane removed about 99.3% of the bacterial cells that remained in the feed water after the chlorination step, and only 0.7% of bacterial cells reached the filtrate. Bacterial counts in the filtrate increased by the second and third days of filtration to reach about  $306.5 \times 10^3 \text{ CFU mL}^{-1}$  by the end of the third day. This was attributed to the growth of bacterial cells on the membrane surface due to dead biomass and calcium ions, as mentioned before. Although the modified membrane showed a significant flux decline in the presence of chlorine, as illustrated in the previous section, it was efficient in removing most of the total bacteria remaining in the feed seawater after the chlorination step over the three days of filtration. In addition, the modified membrane showed the lowest bacterial counts recorded for filtrate mixtures of both chlorinated and non-chlorinated feed seawater.



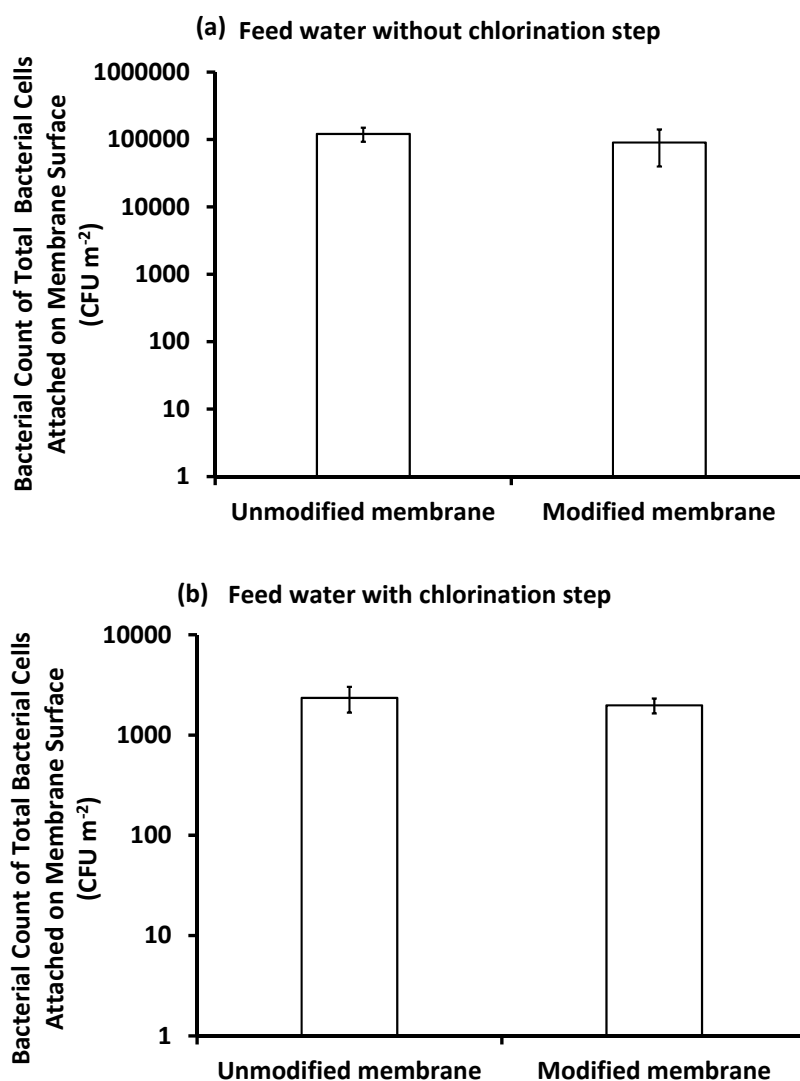
**Figure 9.** Bacterial count of the filtrate mixture produced after three days of filtration using pretreated, inoculated feed seawater without chlorination (a) or with the chlorination (b) pretreatment step. Reference conditions: 1 bar,  $23 \pm 2 \text{ }^\circ\text{C}$ , and 200 rpm stirring for 9 h ( $3 \text{ h} \times 3 \text{ days}$ ) filtration time.

### Bacterial Count on the Membrane Surface

As shown in Figures 10 and 11, the bacteria that were removed from the modified membrane surface after the filtration of inoculated feed seawater, pretreated with or without chlorine, after gentle handshaking for 1 min, were more than those removed from the unmodified membrane. Meanwhile, the total bacterial cells removed from the unmodified membrane surface after mechanical shaking for 24 h were more than those removed from the modified membrane surface. This can be explained as a looser attachment of cells to the modified membrane compared to the unmodified membrane. This, in fact, confirms the antifouling effect of the modified membrane as it can keep bacteria at a distance from the membrane surface [47]. Meanwhile, the bacteria on the unmodified membrane were more closely attached as it is more hydrophobic and hence more favorable for bacterial attachment [17]. This was shown by the thick layer of biofilm and EPS secretion, as evidenced by SEM images. Based on this result, we can say that, after routine washing, the modified membrane can retain its normal flux and performance.

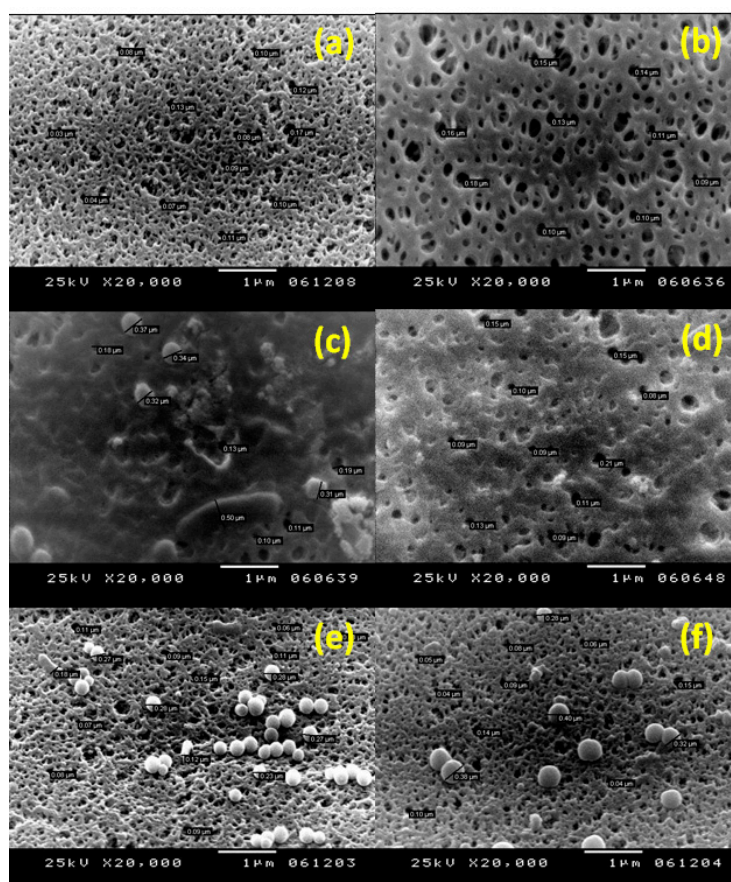


**Figure 10.** Bacterial count of loosely attached bacteria on the surface of unmodified and modified PES membranes after three days of filtration under different conditions of feed water: feed water pretreated without the chlorination step (a), and feed water pretreated with the chlorination step (b) using hand shaking for 1 min. Reference conditions: 1 bar, 23 ± 3 °C at 200 rpm stirring for 9 h (3 h × 3 days) filtration time.



**Figure 11.** Bacterial count of total bacteria attached on the surface of the unmodified and modified PES membranes after three days of filtration under different conditions of feed water: feed water pretreated without the chlorination step (a), and feed water pretreated with the chlorination step (b) using mechanical shaking for 24 h. Reference conditions: 1 bar,  $23 \pm 2$  °C at 200 rpm stirring for 9 h ( $3 \text{ h} \times 3 \text{ days}$ ) filtration time.

Figure 12a,b show SEM images for unmodified PES membrane and modified PES membrane before filtration, respectively. For the feed water pretreated without chlorination, SEM images shown in Figure 12c,d show the formation of a thick layer of biofilm with EPS secretion and the complete blockage of most of the unmodified membrane pores. Meanwhile, the layer of biofilm formed on the modified membrane surface was not as thick as on the unmodified membrane and, clearly, the pores were not completely blocked. On the other hand, in the case of the chlorine disinfection step, the SEM image in Figure 12e shows the presence of bacteria on the unmodified membrane surface in aggregations at the start of biofilm formation, while, on the modified membrane surface, bacteria did not form aggregations. An SEM image (shown in Figure 12f) of the modified membrane surface under both conditions (i.e., chlorinated or non-chlorinated feed seawater) showed that bacteria were more loosely attached, as discussed before.



**Figure 12.** SEM images for unmodified PES membrane (a) and modified PES membrane (b) before filtration, respectively. SEM images of unmodified PES membrane (c) and modified PES membrane (d) after filtration of pretreated, inoculated feed seawater without the chlorination step, respectively. SEM images of unmodified PES membrane (e) and modified PES membrane (f) after filtration of pretreated, inoculated feed seawater pretreated with the chlorination step, respectively. Reference conditions: 1 bar,  $23 \pm 2^\circ\text{C}$  at 200 rpm stirring for 9 h ( $3 \text{ h} \times 3 \text{ days}$ ) filtration time. SEM images were taken at 20,000 $\times$  magnification, and the scale bar is 1  $\mu\text{m}$ .

#### 4. Conclusions

The filtration of pretreated, inoculated seawater using a modified PES UF membrane without the pre-chlorination step maintained the initial flux of the membrane as well as the largest permeated volume (productivity). The modified membrane was able to reject bacteria from the membrane surface in both the presence or absence of chlorine disinfectant. The addition of chlorine generally resulted in a cleaner membrane; however, its usage in conjunction with the modified membrane resulted in a significant reduction in the membrane flux. Furthermore, bacterial counts of chlorinated feedwater over three days of filtration reflected enhanced bacterial regrowth. SEM images showed a looser attachment of bacteria on the modified membrane surface.

In general, the modified PES membrane with a brush-like oligomer of the 3-AP modifier shows a higher membrane performance in terms of improving the quality and productivity of the filtrate as well as reducing the bacterial attachment onto the membrane's surface. Both the steric hindrance and the osmotic effect of the hydrated brush-like polymer layer keep bacteria at a distance from the membrane surface, which facilitates their removal by routine membrane-washing procedures. On the other hand, the use of chlorine disinfectant in the pretreatment of feed water prior to UF had no evident effect; it resulted in a further reduction in both the quality and water productivity of the membrane compared to the modified one. Moreover, significant bacterial regrowth was enhanced by chlorine usage.

Depending on the obtained results from this study, many points still require further investigation to understand the effect of the membrane structure on the biofouling phenomenon. More studies are needed to investigate the effect of chlorination–dechlorination steps on the structure of the modifying layer. Moreover, the interaction between the modifying layer and the bacterial cells and its effect on biofilm formation require further in-depth studies.

**Supplementary Materials:** The following are available online at <http://www.mdpi.com/2077-0375/10/9/227/s1>, Figure S1: Schematic representation of four possible chemical structure(s) of the PES surface after modification with 3-aminophenol (3-AP), containing O-linked and N-linked structures [47]. Figure S2: Photos of seawater (a) before coagulant addition, (b) after sedimentation, and (c) after pretreatment. Figure S3: Residual turbidity as a function of coagulant ( $\text{FeCl}_3$ ) concentration ( $\text{mg}\cdot\text{L}^{-1}$  seawater).

**Author Contributions:** Conceptualization, M.S.E.-D.H., N.N., and R.A.; methodology, M.S.E.-D.H., N.N., R.A., and N.S.; formal analysis, N.N., R.A., N.S., and M.S.E.-D.H.; investigation, M.S.E.-D.H., S.H.K., R.A., N.N., and N.S.; resources, M.S.E.-D.H., R.A., A.E.-S., and N.N.; data curation, N.N., R.A., M.S.E.-D.H., and N.S.; writing—N.N., N.S., and M.S.E.-D.H.; original draft preparation, N.N. and N.S.; writing—review and editing, N.N., M.S.E.-D.H., and S.H.K.; supervision, N.N., R.A., and M.S.E.-D.H. All authors have read and agreed to the published version of the manuscript.

**Funding:** This research received no external funding.

**Conflicts of Interest:** The authors declare no conflict of interest.

## References

1. Malaeb, L.; Ayoub, G.M. Reverse osmosis technology for water treatment: State of the art review. *Desalination* **2011**, *267*, 1–8. [[CrossRef](#)]
2. Khanzada, N.; Khan, S.J.; Davies, P. Performance evaluation of reverse osmosis (RO) pre-treatment technologies for in-land brackish water treatment. *Desalination* **2017**, *406*, 44–50. [[CrossRef](#)]
3. Darre, N.C.; Toor, G.S. Desalination of water: A review. *Curr. Pollut. Rep.* **2018**, *4*, 104–111. [[CrossRef](#)]
4. Hilal, N.; Ogunbiyi, O.O.; Miles, N.J.; Nigmatullin, R. Methods employed for control of fouling in MF and UF membranes: A comprehensive review. *Sep. Sci. Technol.* **2005**, *40*, 1957–2005. [[CrossRef](#)]
5. Fritzmann, C.; Löwenberg, J.; Wintgens, T.; Melin, T. State of the art of reverse osmosis desalination. *Desalination* **2007**, *216*, 1–76. [[CrossRef](#)]
6. Al Aani, S.; Mustafa, T.N.; Hilal, N. Ultrafiltration membranes for wastewater and water process engineering: A comprehensive statistical review over the past decade. *J. Water Process Eng.* **2020**, *35*, 1–14. [[CrossRef](#)]
7. Wolf, P.H.; Siverns, S.; Monti, S. UF membranes for RO desalination pretreatment. *Desalination* **2005**, *182*, 293–300. [[CrossRef](#)]
8. Jamaly, S.; Darwish, N.; Ahmed, I.; Hasan, S.A. short review on reverse osmosis pretreatment technologies. *Desalination* **2014**, *354*, 30–38. [[CrossRef](#)]
9. Elimelech, M.; Phillip, W.A. The future of seawater desalination. *Energy Environ. Sci.* **2011**, *333*, 712–717. [[CrossRef](#)]
10. Bixler, G.D.; Bhushan, B. Biofouling: Lessons from nature. *Philos. Trans. R. Soc. A.* **2012**, *370*, 2381–2417. [[CrossRef](#)]
11. Jiang, S.; Li, Y.; Ladewig, B.P. A review of reverse osmosis membrane fouling and control strategies. *Sci. Total Environ.* **2017**, *595*, 567–583. [[CrossRef](#)] [[PubMed](#)]
12. Sim, L.N.; Chong, T.H.; Taheri, A.H.; Sim, S.; Lai, L.; Krantz, W.B.; Fane, A.G. A review of fouling indices and monitoring techniques for reverse osmosis. *Desalination* **2018**, *434*, 169–188. [[CrossRef](#)]
13. Badruzzaman, M.; Voutchkov, N.; Weinrich, L.; Jacangelo, J.G. Selection of pretreatment technologies for seawater reverse osmosis plants: A review. *Desalination* **2019**, *449*, 78–91. [[CrossRef](#)]
14. Flemming, H.C. Reverse osmosis membrane biofouling. *Exp. Therm. Fluid Sci.* **1997**, *14*, 382–391. [[CrossRef](#)]
15. Al-Ahmad, M.; Aleem, F.A.; Mutiri, A.; Ubaisy, A. Biofouling in RO membrane systems part 1: Fundamentals and control. *Desalination* **2000**, *132*, 173–179. [[CrossRef](#)]
16. Prihasto, N.; Liu, Q.F.; Kim, S.H. Pre-treatment strategies for seawater desalination by reverse osmosis system. *Desalination* **2009**, *249*, 308–316. [[CrossRef](#)]
17. Matin, A.; Khan, Z.; Zaidi, S.; Boyce, M. Biofouling in reverse osmosis membranes for seawater desalination: Phenomena and prevention. *Desalination* **2011**, *281*, 1–16. [[CrossRef](#)]

18. Nguyen, T.; Roddick, F.A.; Fan, L. Biofouling of water treatment membranes: A review of the underlying causes, monitoring techniques and control measures. *Membranes* **2012**, *2*, 804–840. [[CrossRef](#)]
19. Melo, L.; Bott, T. Biofouling in water systems. *Exp. Therm. Fluid Sci.* **1997**, *14*, 375–381. [[CrossRef](#)]
20. Baker, J.; Dudley, L. Biofouling in membrane systems: A review. *Desalination* **1998**, *118*, 81–89. [[CrossRef](#)]
21. Bott, T. Potential physical methods for the control of biofouling in water systems. *Chem. Eng. Res. Des.* **2001**, *79*, 484–490. [[CrossRef](#)]
22. Liu, C.X.; Zhang, D.R.; He, Y.; Zhao, X.S.; Bai, R. Modification of membrane surface for anti-biofouling performance: Effect of anti-adhesion and anti-bacteria approaches. *J. Membr. Sci.* **2010**, *346*, 121–130. [[CrossRef](#)]
23. Rana, D.; Matsuura, T. Surface modifications for antifouling membranes. *Chem. Rev.* **2010**, *110*, 2448–2471. [[CrossRef](#)] [[PubMed](#)]
24. Nady, N.; Franssen, M.C.R.; Zuilhof, H.; Eldin, M.S.M.; Boom, R.; Schroën, K. Modification methods for poly(arylsulfone) membranes: A mini review focusing on surface modification. *Desalination* **2011**, *275*, 1–9. [[CrossRef](#)]
25. Chang, Y.R.; Lee, Y.J.; Lee, D.J. Membrane fouling during water or wastewater treatments: Current research updated. *J. Taiwan Inst. Chem. E.* **2019**, *94*, 88–96. [[CrossRef](#)]
26. Galal-Gorchev, H. Chlorine in water disinfection. *Pure Appl. Chem.* **1996**, *68*, 1731–1735. [[CrossRef](#)]
27. Arkhangelsky, E.; Kuzmenko, D.; Gitis, N.V.; Vinogradov, M.; Kuiry, S.; Gitis, V. Hypochlorite cleaning causes degradation of polymer membranes. *Tribol. Lett.* **2007**, *28*, 109–116. [[CrossRef](#)]
28. Bhojani, G.; Binod Kumar, S.; Kumar Saha, N.; Halder, S. Membrane biofouling by chlorine resistant *Bacillus* spp.: Effect of feedwater chlorination on bacteria and membrane biofouling. *Biofouling* **2018**, *34*, 426–439. [[CrossRef](#)]
29. Yu, W.; Xu, L.; Graham, N.; Qu, J. Pre-treatment for ultrafiltration: Effect of pre-chlorination on membrane fouling. *Sci. Rep.* **2014**, *4*, 5–13. [[CrossRef](#)]
30. Yadav, K.; Morison, K.R. Effects of hypochlorite exposure on flux through polyethersulphone ultrafiltration membranes. *Food Bioprod. Process* **2010**, *88*, 419–424. [[CrossRef](#)]
31. Kuzmenko, D.; Arkhangelsky, E.; Belfer, S.; Freger, V.; Gitis, V. Chemical cleaning of UF membranes fouled by BSA. *Desalination* **2005**, *179*, 323–333. [[CrossRef](#)]
32. Wolff, S.H.; Zydney, A.L. Effect of bleach on the transport characteristics of polysulfone hemodialyzers. *J. Membr. Sci.* **2004**, *243*, 389–399. [[CrossRef](#)]
33. Arkhangelsky, E.; Kuzmenko, D.; Gitis, V. Impact of chemical cleaning on properties and functioning of polyethersulfone membranes. *J. Membr. Sci.* **2007**, *305*, 176–184. [[CrossRef](#)]
34. Levitsky, I.; Duek, A.; Arkhangelsky, E.; Pinchev, D.; Kadoshian, T.; Shetrit, H.; Naim, R.; Gitis, V. Understanding the oxidative cleaning of UF membranes. *J. Membr. Sci.* **2011**, *377*, 206–213. [[CrossRef](#)]
35. Belila, A.; El-Chakhtoura, J.; Otaibi, N.; Muyzer, G.; Gonzalez-Gil, G.; Saikaly, P.E.; Van Loosdrecht, M.C.M.; Vrouwenvelder, J.S. Bacterial community structure and variation in a full-scale seawater desalination plant for drinking water production. *Water Res.* **2016**, *94*, 62–72. [[CrossRef](#)]
36. Kecec, O.; Gokalsin, B.; Karalti, I.; Kayhan, F.E.; Sesal, N.C. Effects of chlorine stress on *Pseudomonas aeruginosa* biofilm and analysis of related gene expressions. *Curr. Microbiol.* **2016**, *73*, 228–235. [[CrossRef](#)]
37. Flemming, H.C. Biofouling in water systems-cases, causes and countermeasures. *Appl. Microbiol. Biotechnol.* **2002**, *59*, 629–640. [[CrossRef](#)]
38. Lee, J.; Kim, I.S. Microbial community in seawater reverse osmosis and rapid diagnosis of membrane biofouling. *Desalination* **2011**, *273*, 118–126. [[CrossRef](#)]
39. Shon, H.K.; Vigneswaran, S.; Kim, I.S.; Cho, J.; Ngo, H.H. The effect of pretreatment to ultrafiltration of biologically treated sewage effluent: A detailed effluent organic matter (EfOM) characterization. *Water Res.* **2004**, *38*, 1933–1939. [[CrossRef](#)]
40. Agus, E.; Sedlak, D.L. Formation and fate of chlorination by-products in reverse osmosis desalination systems. *Water Res.* **2010**, *44*, 1616–1626. [[CrossRef](#)]
41. Agus, E.; Voutchkov, N.; Sedlak, D.L. Disinfection by-products and their potential impact on the quality of water produced by desalination systems: A literature review. *Desalination* **2009**, *237*, 214–237. [[CrossRef](#)]
42. Fane, A.G.; Wang, R.; Hu, M.X. Synthetic membranes for water purification: Status and future. *Angew. Chem.* **2015**, *54*, 368–386. [[CrossRef](#)]

43. Li, D.; Wang, H. Recent developments in reverse osmosis desalination membranes. *J. Mater. Chem.* **2010**, *20*, 4551–4566. [[CrossRef](#)]
44. Tawalbeh, M.; Al-Mojjily, A.; Al-Othman, A.; Hilal, N. Membrane separation as a pre-treatment process for oily saline water. *Desalination* **2018**, *447*, 182–202. [[CrossRef](#)]
45. Bruggen, B.V.D. Chemical modification of polyethersulfone nanofiltration membranes: A review. *J. Appl. Polym.* **2009**, *114*, 630–642. [[CrossRef](#)]
46. Nady, N.; Schroën, K.; Franssen, M.C.; Fokkink, R.; Eldin, M.S.M.; Zuilhof, H.; Boom, R.M. Enzyme-catalyzed modification of PES surfaces: Reduction in adsorption of BSA, dextrin and tannin. *J. Colloid Interface Sci.* **2012**, *378*, 191–200. [[CrossRef](#)] [[PubMed](#)]
47. Nady, N.; Salem, N.; El-Shazly, A.; Soliman, H.; Kandil, S.H. Fouling-resistant brush-like oligomers of poly(3-aminophenol). *Desalin. Water Treat.* **2017**, *73*, 237–248. [[CrossRef](#)]
48. Ulbricht, M. Advanced functional polymer membranes. *Polymer* **2006**, *47*, 2217–2262. [[CrossRef](#)]
49. Nady, N.; Franssen, M.C.R.; Zuilhof, H.; Boom, R.M.; Schroën, K. Enzymatic modification of polyethersulfone membranes. *Water* **2012**, *4*, 932–943. [[CrossRef](#)]
50. van der Veen, V.; Nady, N.; Franssen, M.C.R.; Zuilhof, H.; Boom, R.M.; Abee, T. *Listeria monocytogenes* repellence by enzymatically modified PES surfaces. *J. Appl. Polym. Sci.* **2015**, *132*, 41576. [[CrossRef](#)]
51. Riva, S. Laccases: Blue enzymes for green chemistry. *Trends Biotechnol.* **2006**, *24*, 219–226. [[CrossRef](#)]
52. Nady, N.; El-Shazly, A. Laccase-catalysed modification of PES membranes using amine-bearing modifiers. *Desalination Water Treat.* **2015**, *55*, 2996–3002. [[CrossRef](#)]
53. Rice, E.W.; Baird, R.B.; Eaton, A.D.; Clesceri, L.S. *Standard Methods for the Examination of Water and Wastewater*, 22nd ed.; American Public Health Association: Washington DC, USA, 2012; pp. 183–190.
54. Shon, H.; Kim, S.; Vigneswaran, S.; Aim, R.B.; Lee, S.; Cho, J. Physicochemical pretreatment of seawater: Fouling reduction and membrane characterization. *Desalination* **2009**, *238*, 10–21. [[CrossRef](#)]
55. Wef, A.A. *Standard Methods for the Examination of water and Wastewater*, 21st ed.; American Public Health Association, American Water Works Association, Water Environmental Federation: Washington, DC, USA, 2005; p. 1360.
56. Jett, B.D.; Hatter, K.L.; Huycke, M.M.; Gilmore, M.S. Simplified agar plate method for quantifying viable bacteria. *Biotechniques* **1997**, *23*, 648–650. [[CrossRef](#)] [[PubMed](#)]
57. Bloem, J.; Bär-Gilissen, M.J.B.; Cappenberg, T.E. Fixation, counting, and manipulation of heterotrophic nanoflagellates. *Appl. Environ. Microbiol.* **1986**, *52*, 1266–1272. [[CrossRef](#)] [[PubMed](#)]
58. Nessim, R.B.; Tadros, H.R.; Taleb, A.E.A.; Moawad, M.N. Chemistry of the Egyptian Mediterranean coastal waters. *Egypt. J. Aquat. Res.* **2015**, *41*, 1–10. [[CrossRef](#)]
59. Borghini, M.; Bryden, H.; Schroeder, K.; Sparnocchia, S.; Vetrano, A. The Mediterranean is becoming saltier. *Ocean Sci.* **2014**, *10*, 693–700. [[CrossRef](#)]
60. Almasi, A.; Dargahi, A.; Motlagh, Z.J.; Mahmoodi, M.; Mohammadi, M.; Rezaei, S.; Janjani, H.; Amirian, T. Evaluation of common coagulants and polymeric coagulant aid in the removal of suspended particles and colloidal turbidity of raw water of Gavoshan dam. *J. Chem. Pharm.* **2016**, *9*, 3178–3181.
61. Matilainen, A.; Vepsäläinen, M.; Sillanpää, M. Natural organic matter removal by coagulation during drinking water treatment: A review. *Adv. Colloid Interface Sci.* **2010**, *159*, 189–197. [[CrossRef](#)]
62. Baghvand, A.; Zand, A.D.; Mehrdadi, N.; Karbassi, A. Optimizing coagulation process for low to high turbidity waters using aluminum and iron salts. *Am. J. Environ. Sci.* **2010**, *6*, 442–448. [[CrossRef](#)]
63. Goosen, M.; Sablani, S.; Al-Hinai, H.; Al-Obeidani, S.; Al-Belushi, R.; Jackson, A. Fouling of reverse osmosis and ultrafiltration membranes: A critical review. *Sep. Sci. Technol.* **2005**, *39*, 2261–2297. [[CrossRef](#)]
64. Shi, X.; Tal, G.; Hankins, N.P.; Gitis, V. Fouling and cleaning of ultrafiltration membranes: A review. *J. Water Process Eng.* **2014**, *1*, 121–138. [[CrossRef](#)]
65. Mansouri, J.; Harrisson, S.; Chen, V. Strategies for controlling biofouling in membrane filtration systems: Challenges and opportunities. *J. Mater. Chem.* **2010**, *20*, 4567–4586. [[CrossRef](#)]
66. Goh, P.S.; Lau, W.J.; Othman, M.H.D.; Ismail, A.F. Membrane fouling in desalination and its mitigation strategies. *Desalination* **2018**, *425*, 130–155. [[CrossRef](#)]
67. Dominguez, D.C. Calcium signalling in bacteria. *Mol. Microbiol.* **2004**, *54*, 291–297. [[CrossRef](#)] [[PubMed](#)]



68. Patrauchan, M.A.; Sarkisova, S.; Sauer, K.; Franklin, M.J. Calcium influences cellular and extracellular product formation during biofilm-associated growth of a marine *Pseudoalteromonas*. *Microbiology* **2005**, *151*, 2885–2897. [[CrossRef](#)]
69. Berchtold, M.W.; Villalobo, A. The many faces of calmodulin in cell proliferation, programmed cell death, autophagy, and cancer. *Biochim. Biophys. Acta* **2014**, *1843*, 398–435. [[CrossRef](#)]



© 2020 by the authors. Licensee MDPI, Basel, Switzerland. This article is an open access article distributed under the terms and conditions of the Creative Commons Attribution (CC BY) license (<http://creativecommons.org/licenses/by/4.0/>).

Article

# Technical and Economic Evaluation of WWTP Renovation Based on Applying Ultrafiltration Membrane

He Bai <sup>1</sup>, Yakai Lin <sup>1,2,\*</sup>, Hongbin Qu <sup>1</sup>, Jinglong Zhang <sup>1</sup>, Xiaohong Zheng <sup>1</sup> and Yuanhui Tang <sup>3,\*</sup>

<sup>1</sup> Beijing Scinor Membrane Technology Co. Ltd., Beijing 100083, China; bai.he@scinormem.com (H.B.); qu.hongbin@scinormem.com (H.Q.); zhang.jinglong@scinormem.com (J.Z.); zheng.xiaohong@scinormem.com (X.Z.)

<sup>2</sup> Beijing Key Laboratory of Membrane Materials and Engineering, Department of Chemical Engineering, Tsinghua University, Beijing 100084, China

<sup>3</sup> College of Chemistry and Environmental Engineering, China University of Mining and Technology, Beijing 100083, China

\* Correspondence: yk\_lin@tsinghua.edu.cn (Y.L.); tyh@cumtb.edu.cn (Y.T.)

Received: 6 July 2020; Accepted: 4 August 2020; Published: 7 August 2020



**Abstract:** Nowadays, the standards of discharging are gradually becoming stricter, since much attention has been paid to the protection of natural water resources around the world. Therefore, it is urgent to upgrade the existing wastewater treatment plant (WWTP), to improve the effluent quality, and reduce the discharged pollutants to the natural environment. In this paper, taking the “Liaocheng UESH (UE Envirotech) WWTP in Shandong province of China” as an example, the existing problems and the detailed measures for a renovation were systemically discussed by technical and economic evaluation, before and after the renovation. During the renovation, the ultrafiltration membrane was added as the final stage of the designed process route, while upgrading the operation conditions of biochemical process at the same time. After the renovation, the removal rates of chemical oxygen demand (COD<sub>cr</sub>), biochemical oxygen demand (BOD<sub>5</sub>), total phosphorus (TP) and other major pollutants were improved greatly, and the results fully achieved the standards of surface water class IV. The ultrafiltration system performs a stable permeability around 1.5 LMH/kPa. Besides, the economic performance of the renovation was evaluated via the net present value (NPV) method. The result reveals that the NPV of the renovation of the WWTP within the 20 year life cycle is CNY 72.51 million and the overall investment cost can be recovered within the fourth year after the reoperation of the plant. This research does not only indicate that it is feasible to take an ultrafiltration membrane as the main technology, both from technical and economic perspectives, while upgrading the biochemical process section in the meantime, but also provides a new strategy for the renovation of existing WWTPs to achieve more stringent emission standards.

**Keywords:** WWTP; renovation and upgrading; ultrafiltration membrane; net present value

## 1. Introduction

Pollution to natural water resource is a worldwide emergent and critical problem. It is definite that the severe deterioration of water bodies has both short- and long-term negative effects to human and environmental health [1]. In particular, chemicals and microbial contaminants in treated wastewater would cause public health concerns [2]. In recent years, wastewater discharging has gained increasing attention in many countries, due to reasons of ensuring water security and developing effective strategies for the sustainable utilization of water resources. Some developed countries have formulated different policies or standards on the discharge of wastewater treatment plant (WWTP) [3]. The point

source emission standard of the United States, which has experienced a shift in policy direction from “technologically based” to “water bodies-based” in recent years, requires the limit of water discharged to sensitive water body of total nitrogen (TN) < 3 mg/L, total phosphorus (TP) < 0.1 mg/L [3,4]. The Japanese government also proposed a special emission standard limits for Osaka Bay of BOD<sub>5</sub> < 8 mg/L, TN < 8 mg/L and TP < 0.8 mg/L.

Developing countries are facing a more serious deterioration situation of natural water bodies with the development of their economy and the improvement of industrialization. Many countries have taken steps to limit the emission of pollutants [5]. Taking China as an example, only chemical oxygen demand (COD<sub>cr</sub>), biochemical oxygen demand (BOD<sub>5</sub>), suspended solids (SS) and other major pollutants were taken into consideration for the emission standards in the early years. Later, the nutrient salts, nitrogen and phosphorus were added in the emission standard list that needed to be controlled as conventional indicators. Currently, the Chinese government has further restricted nutrient emissions and many local governments have issued even stricter local emission standards according to the natural environment in different regions [6]. Hence, it is needed to develop simple, reasonable and acceptable treatment strategies for the renovation of existing wastewater plants in response to increasingly stringent emission standards. It will reduce the discharge of pollutants into natural water bodies; and eliminate negative impacts on the environment and human health, which would be in accordance with the national and international water quality regulations and guidelines.

Since normally urban wastewaters are only treated by conventional activated sludge systems without further treatment [7], the effluents quality can no longer meet the requirements of current emission standards, especially the indicators of SS and nutritive salts due to a lack of technical process as well as equipment [6,7]. Because of its potential economic and environmental benefits, the renovation of existing WWTP to fix water deterioration is regarded as one of the best options for protecting natural water bodies and developing sustainable water management strategies. However, the renovation is a difficult decision for many plant managers, because the renovation of a WWTP is directly related to the total construction costs, operating costs, treatment effect, the floor area, the convenience of management and other key issues. The selection of the technology and the full use of existing facilities are important for the renovation. If only simply modifying the existing system but not adding new technology, no remarkable success would be achieved in significantly decreasing the concentrations of major pollutants, to the levels stated in the restricted criteria corresponding to the water discharged to the natural environment. However, there are numerous problems, such as the footprint, time limit and the difficulty in estimating the expected benefit. Moreover, it is the fate that the WWTP effluents flow to densely populated urban cities paradoxically in order to protect the local natural environment. Therefore, there is a growing need for the development of treatment renovation methodologies by considering the cost-effective and technical benefits.

Today, the implementation of ultrafiltration membrane in wastewater reclamation and reuse has become more attractive, since ultrafiltration membrane separation ensures a higher removal rate of particles, bacteria and large molecular weight organic matters as well as reducing chemical usage and better on-stream time [8,9]. However, there are few applications incorporating the biochemical system for the pretreatment that could keep the inlet water quality of ultrafiltration membrane stable. In addition, there is also a lack of systematic experience in the selection of ultrafiltration membrane products. Therefore, although ultrafiltration membrane is receiving more and more attention in recent years, however, some people worry that the investment is too large to be recovered, or about the rapid contamination of the membrane, and others do not know how to systematically evaluate the renovation methodologies. The study of Al Aani et al. shows that fouling (27%), modelling (17%) and wastewater reuse (12%) were the dominant research topics for the ultrafiltration membrane, however, there is very little research on ultrafiltration membrane for the renovation of existing WWTP [10]. Therefore, it results in a lack of evidence for the WWTP manager to follow about the ultrafiltration membrane and the upgrading of pretreatment, either in a technical or an economic aspect. [11]. Moreover, the incomplete or insufficient economic analyses of options by ultrafiltration membrane processes for

wastewater discharge do not allow to balance or accurately evaluate the disparity among the benefits brought by the increase in water price after the renovation and overall investment cost of the whole plant renovation [12].

Considering the current situation summarized above, taking the Liaocheng UESH WWTP in Shandong province of China as an example, this work introduces a renovation process route with ultrafiltration as the main technology and analyzes the existing problems and the specific measures for the renovation. Then, based on continuously monitoring the operation data of ultrafiltration performances, the actual renovation effects and economic feasibilities of membrane treatments were studied using the net present value method. By way of technical and economic perspective, the viability of the renovation methodologies that take ultrafiltration as the main technology and combines with the upgrading of conventional activated sludge systems in the production of discharged water from urban WWTP effluents was elaborately evaluated, in order to provide a new direction for the renovation of existing WWTP to accommodate more stringent emission standards.

## 2. Background

The UESH WWTP is located in the Liaocheng Economic Development Zone (Liaocheng, China) and it was put into operation in May 2009 with a designed capacity of 30,000 m<sup>3</sup>/d. The plant mainly treats the domestic sewage in the economic development zone and a part of industrial sewage from enterprises. The conventional method of A/A/O (Anaerobic-Anoxic-Oxic) technology with steps in anaerobic, anoxic and aerobic was adopted as the main part of the treatment process, supplemented by biological phosphorus removal methods to achieve the purpose of nitrogen and phosphorus removal. The effluent quality met the primary-level A-class standard of “Pollutant Discharge Standards of Urban Sewage Treatment Plants” (GB 18918-2002) that is shown in Table 1, and then the treated wastewater could be discharged into the Haihe River (Liaocheng, China), the local natural water body.

**Table 1.** Pollutant discharge standards of urban sewage treatment plants.

Nr.	Items	Primary-Level	
		A-Class	B-Class
1	Chemical oxygen demand (COD <sub>Cr</sub> )	50 mg/L	60 mg/L
2	Biochemical oxygen demand (BOD <sub>5</sub> )	10 mg/L	20 mg/L
3	Suspended solids (SS)	10 mg/L	20 mg/L
4	Animal and plant oil	1 mg/L	3 mg/L
5	Petroleum	1 mg/L	3 mg/L
6	Anionic surfactant	0.5 mg/L	1 mg/L
7	Total nitrogen (in N)	15 mg/L	20 mg/L
8	Ammonia nitrogen (in N)	5 (8) mg/L	8 (15) mg/L
9	Total phosphorus (in P)	0.5 mg/L	1 mg/L
10	Chroma (dilution)	30 mg/L	30 mg/L
11	pH	6–9	6–9
12	Number of fecal coliforms (1/L)	103	104

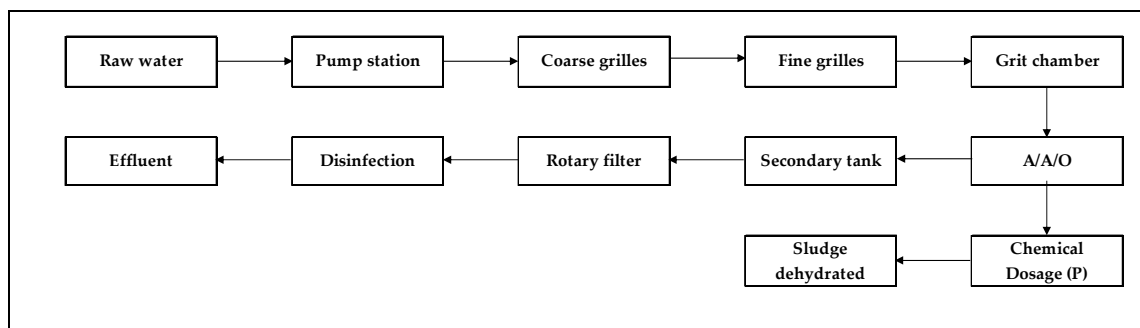
However, with an increase in effort from the Chinese government for the protection of natural water bodies, various policies have been formulated and promulgated, and the discharge standards implemented by the sewage plant could no longer meet the needs of protecting the local natural water environment. Both the “Action Plan for Water Pollution Prevention and Control” that was formulated and promulgated by the State Council in 2015 and the “Work Plan of Liaocheng City Water Pollution Prevention and Control in 2017” that was formulated and issued by the Liaocheng People’s Government clearly require that the water quality of the Haihe River, to which the effluent is discharged from the plant, should reach the Class IV of “Quality Standard of Surface Water” [13], which is shown in Table 2. Therefore, it was urgent for the plant to carry out some renovation in order to reduce the pollution load and protect the local natural environment.

**Table 2.** Water quality standards of surface water.

Nr.	Items	Class I	Class II	Class III	Class IV	Class V
1	Temperature °C	Weekly mean maximum temperature rise ≤ 1 Weekly mean maximum temperature drop ≤ 2				
2	pH	6–9				
3	Dissolved oxygen (DO) ≥ mg/L	7.5	6	5	3	2
4	Chemical oxygen demand (COD <sub>Cr</sub> ) mg/L	15	15	20	30	40
5	Biochemical oxygen demand (BOD <sub>5</sub> ) mg/L	3	3	4	6	10
6	Total nitrogen (in N) (TN) mg/L	0.2	0.5	1.0	1.5	2.0
7	Ammonia nitrogen (in N) (NH <sub>3</sub> -N) mg/L	0.15	0.5	1.0	1.5	2.0
8	Total phosphorus (in P) (TP) mg/L	0.02	0.1	0.2	0.3	0.4

2.1. Plant Current Condition

The plant is running at a full capacity of 30,000 m<sup>3</sup>/d, and the flow diagram of the treatment process is shown in Figure 1. The sewage was pre-treated by a grilles and grit chamber, and then treated by A/A/O conventionally activated sludge method. The effluent from the secondary sedimentation tank was treated by a rotary filter, and then discharged into the receiving water body after disinfection. The concentrated and dehydrated sludge would be transported to a company specializing in sludge disposal for further treatment. The main pollutant indicators of the influent and effluent from the Liaocheng UESH WWTP before the renovation are shown in Table 3.



**Figure 1.** Treatment process of the plant before renovation.

As listed in Table 3, the variation range of organic matter content was large, the BOD<sub>5</sub> of the influent was around 40–80 mg/L, while the COD<sub>Cr</sub> fluctuated between 130 mg/L and 250 mg/L, and the suspended solid was about 100 mg/L. The concentration of nutrient salts was relatively stable, ammonia nitrogen was at about 15 mg/L, and the total phosphorus fluctuated around 3 mg/L. Besides, according to the description of a field operator, the sludge concentration in the aerobic tank was relatively high, with an MLSS (Mixed Liquor Suspended Solid) value at 8000–11,000 mg/L and MLVSS (Mixed Liquor Volatile Suspended Solid) at 3400–4400 mg/L, and the MLVSS was only about 40% and the sludge load was only 0.02 kg BOD<sub>5</sub>/(MLVSS.d), which signified the poor sludge sedimentation ability of the previous treatment process. Therefore, the biochemical properties of the water also needed to be improved.

In addition, due to the long-term full capacity or even overload operation of the plant, there also existed a serious loss of facilities, equipment aging and other problems, such as the bad performance of the aeration distribution system that was caused by the corrosion of the pipelines, which resulted in the uneven mixing of sludge and water in the aerobic tank and an unsatisfactory flow state. The failure

of the propeller affected the uneven mixing of sludge and water even further. Besides, the rotary filter was easily fouled and the inefficient backwash made the SS of the effluent unstable.

As shown in Table 3, although the effluent quality could meet the primary-level A-class standard of “Pollutant Discharge Standards of Urban Sewage Treatment Plants”, however, except for the ammonia nitrogen, the concentration of other main pollutant indicators, especially the total phosphorus and suspended solid, were still much higher than the requirement of the Class IV standard listed in Table 2. In order to improve the effluent quality of the plant, it was necessary to carry out the plant renovation as soon as possible, to reduce the concentration of the main indicators and gradually restore the regional water ecological function.

**Table 3.** Main pollutant indicators of the influent and effluent from the wastewater treatment plant (WWTP) before renovation \*.

Months		1	2	3	4	5	6	7	Average
COD <sub>Cr</sub> (mg/L)	Influent	202	180	237	166	142	142	138	78%
	Effluent	41	47	38	30	28	35	40	
	Removal rate	80%	74%	84%	82%	80%	75%	71%	
BOD <sub>5</sub> (mg/L)	Influent	67.2	61.6	78.4	52.5	56.8	45.2	59.4	91%
	Effluent	5.9	6.4	5.6	5.1	5	4.8	6.2	
	Removal rate	91%	90%	93%	90%	91%	89%	90%	
NH <sub>3</sub> -N (mg/L)	Influent	15.97	14.87	16.47	15.42	17.01	16.14	14.1	98%
	Effluent	0.25	1.21	0.22	0.15	0.26	0.17	0.14	
	Removal rate	98%	92%	99%	99%	98%	99%	99%	
TP (mg/L)	Influent	3.24	3.3	2.71	2.46	2.45	2.43	2.85	85%
	Effluent	0.64	0.74	0.13	0.19	0.35	0.34	0.58	
	Removal rate	80%	78%	95%	92%	86%	86%	80%	
SS (mg/L)	Influent	102	105	146	113	93	117	97	90%
	Effluent	10	10	11	9	9	13	12	
	Removal rate	90%	90%	92%	92%	90%	89%	88%	

The data came from the semi-annual water report of the plant in 2017.

### 2.2. Selection of Renovation Methodologies

The new standard requires the concentration of total nitrogen (TN), total phosphorus (TP) and suspended solid (SS) of the effluent to be much lower. The removal of dissolved substances still needs to be treated by biochemical process, while the removal of suspended solid needed to be further treated. The effluent SS was about 10 mg/L, and it was difficult to achieve the corresponding standards of 6 mg/L only by the rotary filter due to its easily fouling rate and inefficient backwash. Considering the possible high SS that was caused by chemical dosage in the biochemical process after the renovation, a new treatment process needed to be added in order to keep the effluent quality stable. The newly added treatment process should reach the characteristics of small footprint and compact structure because of the limitation of land area, with only 720 m<sup>2</sup> available, which became one of the major difficulties for the renovation. In addition, features such as the high degree of automation and stable effluent water quality also needed to be taken into consideration. The optional processes included the ultrafiltration membrane, sand filtration combined with ozone and other processes, while the ultrafiltration has obvious advantages due to the operational safety and land saving.

The membrane filtration system is a pressure-driven separation process, in which particles and impurities between 0.02 and 0.1 μm in diameter can be intercepted through the micro pores distributed on the membrane surface, which can effectively remove water floc, bacteria and macromolecular organic matter [14]. The ultrafiltration membrane among the relatively mature technologies from recent years, especially after entering the 21st century, which has rapidly developed into a utility engineering technology, which is widely used in various fields of water treatment and become more

competitive compared with traditional technologies, because of the scale production of membrane materials, the integration of membrane modules, the popularization of membrane manufacture and the affordable prices [15]. Not only all bacteria and suspended solids are trapped by the efficient intercept of the ultrafiltration membrane, but also the  $COD_{cr}$ , the total phosphorus and total nitrogen carried by a suspended substance, which realized the further protection of effluent quality after biochemical treatment. Additionally, some refractory macromolecular organic matter can be retained and returned to the biochemical tank by backwashing, in order to prolong its residence time and maximize its degradation.

After a certain period of operation of the ultrafiltration membrane, the retained pollutants will be accumulated on the membrane surface and formed into a filter cake layer that would reduce the membrane flux [14–16]. Therefore, it is necessary to maintain good inlet water quality to protect the stable operation of the ultrafiltration membrane, prolong the cleaning cycle and increase its service life. As a result, the pretreatment facilities also needed to be upgraded.

Through the analysis of the main pollutant of inlet water and production requirements, the effluent  $COD_{cr}$  was about 37 mg/L, so it is necessary to maintain a good biochemical performance, to prevent the membrane from fouling, and at the same time, the ultrafiltration membrane could help to further reduce the concentration of  $COD_{cr}$ . Besides, the high concentration of ammonia nitrogen ( $NH_3-N$ ) and the total nitrogen (TN), as well as the low carbon source in the raw water, were not conducive to denitrification and could affect the performance of phosphorus removal at the same time. Moreover, there was a risk of effluent short circuit on the existing complete mixing of activated sludge that would easily result in sludge swelling, which can also influence the performance of denitrification and phosphorus removal. How to improve the efficiency of denitrification and phosphorus removal in the A/A/O process was one of the technical difficulties for the upgrading of biochemical treatment.

The influent  $BOD_5/NH_3-N$  was about 3.5 while the  $NH_3-N/COD_{cr}$  was about 0.09, showing a lack of carbon source in the biochemical treatment process, which previously resulted in the relatively unstable level of effluent TN content [17]. In addition, as the ratio of  $BOD_5$  to TP was about 20, which meant that the biological phosphorus removal process can be adopted [18], but in order to improve the removal rate of total phosphorus, so as to meet the stricter phosphorus removal target, not only was there a need to optimize the biochemical treatment process, but also to carry out an auxiliary chemical phosphorus removal system.

The renovation was required to tap the potential of the existing facilities, and new technology needed to be added at the same time to make the effluent water quality fully up to the standard. Furthermore, reducing the investment and operation cost as much as possible, as well as achieving the convenient operation and management of the WWTP should also be taken into consideration. Therefore, the final renovation methodology of the plant was determined to be the upgrading of the existing biochemical treatment process, the addition of a chemical phosphorus removal system and an ultrafiltration membrane treatment process. The treatment process after renovation is shown in Figure 2.

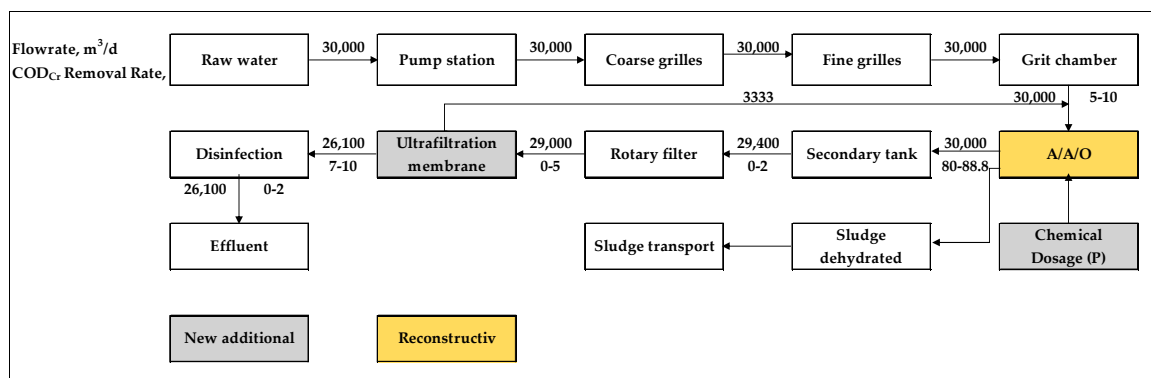


Figure 2. Treatment process of the plant before renovation.

### 2.3. Implementation of Renovation

#### 2.3.1. Upgrading of A/A/O Treatment Process

Considering the existing problems of uneven mixing, short flow and serious sludge accumulation at the bottom of the biochemical tank, which resulted in the unstable performance of the effluent quality, following specific renovation measures should be carried out while keeping the original structure. Giving the returned sludge inlet the same position as the feed water inlet in the anaerobic tank, and optimizing the arrangement of mixer at the same time, allows the water and sludge to fully mix with the kinetic energy during the water feed, meanwhile, it also enables to make full use of the anaerobic tank volume during the mixture. The anoxic tank has the same problems as the anaerobic tank. Similarly, by adjusting the position of the returned sludge inlet port and optimizing the arrangement of mixer, the mixed logistics state of the sludge and water in the anoxic tank can be improved, so as to improve the treatment efficiency of the anoxic zone.

In order to solve the problem of insufficient carbon source in the influent, a carbon source feeding device is set near the anoxic tank to periodically and quantitatively transport a proper amount of high concentration and high biodegradability sewage and sodium acetate, after accounting as a supplementary carbon source.

There used to be a short flow problem for the design of internal reflux, which was that the water could flow from the inlet port of the aerobic tank directly into the anaerobic tank. Therefore, a separation wall was added to block the short flow. In addition, the aeration in the reflux water from the aerobic tank to the anaerobic tank is greatly reduced, to avoid affecting the performance of the anaerobic zone.

#### 2.3.2. Upgrading of Phosphorus Removal System

The original biochemical phosphorus removal process is still used. To increase the phosphorus removal rate, chemical agents are added to make phosphorus form into insoluble substances, so as to be discharged together with the residual sludge [19]. Hence, a new chemical phosphorus removal and dosing device was redesigned in the renovation. The new liquid phosphorus removal agent, whose main component is ferric sulfate, can be used continuously and automatically.

#### 2.3.3. Addition of Ultrafiltration Membrane

The ultrafiltration system includes the ultrafiltration membrane and membrane frame, inlet water pump, backwash system, chemical cleaning system, pipe valve, compressed air system, instrument and automatic control system, among which the core part is the ultrafiltration membrane. The SMT600 series of the pressurized ultrafiltration membrane were selected for the plant renovation. PVDF hollow fiber ultrafiltration membrane is generally produced by thermally induced phase separation (TIPS) process or non-solvent induced phase separation process (NIPS). Compared with NIPS membranes, TIPS membranes, which are prepared driven by a temperature change, have many advantages such as an easily controllable structure, stable membrane quality, narrow micro pore distribution and symmetric structure [20,21]. Moreover, the characteristics of PVDF raw materials can be maintained during manufacturing, which makes the membranes possess higher mechanical strength and chemical resistance. Therefore, the ultrafiltration membranes fabricated by the TIPS method can tolerate a high concentration of soaking and cleaning. Moreover, the advantages of the TIPS membrane can minimize the number of membrane modules due to higher flux and good recoverability, so as to save the floor space and prolong the service life [21]. Table 4 describes the technical parameters of the ultrafiltration membranes used in this renovation.



**Table 4.** Main pollutant indicators of the influent and the effluent from WWTP before renovation.

Items	Parameters
Model	SMT600-P80
Material	PVDF
Pore size (µm)	0.1
Membrane area (m <sup>2</sup> )	80
Nominal size (mm)	Φ225 * 2360
Resistance to NaClO (ppm)	5000

### 3. Evaluation Method

#### 3.1. Technical Analysis

The purpose of the renovation of the Liaocheng UESH WWTP was to improve the removal rate of the main treatment indicators in the water to achieve a level Class IV of “Water Quality Standard of Surface Water”, so as to protect the receiving natural water body. Both the old standard and the new standard did not make clear provisions on calcium, magnesium and carbonate content for the wastewater that discharged into natural water bodies, as new standards mainly made more stringent requirements on COD, nitrogen, phosphorus and other nutritive salts. Moreover, since there is no reverse osmosis after the UF (Ultrafiltration) process, thus the scaling problem does not need to be taken into consideration, hence, the concentration of these ions is not measured by the plant. As the traditional municipal sewage, the content of these ions is not high, which is acceptable for the operation of the UF membrane. Therefore, this paper focuses on the concentration of the main pollutant in the effluent and the change of the removal rate of before and after the renovation as a part of the technical evaluation.

On the other hand, ultrafiltration membrane permeability will be used to investigate the effect of biochemical process upgrading and the stability of the whole process after renovation. One of the characteristics of ultrafiltration membrane fouling is the increase in transmembrane pressure difference (TMP) and the drop of permeability [22]. This paper focuses on the changes of the membrane permeability, which is usually expressed as the flowrate per hour per square meter of membrane area under unit pressure. The influence of pretreatment on the membrane fouling rate as well as the cleaning effect and recovery performance can be evaluated by the continuous monitoring of membrane permeability.

#### 3.2. Economical Analysis

The net present value method of the dynamic evaluation index in engineering economics is used for economic evaluation in this paper. The economic evaluation index is divided into static and dynamic, where static evaluation means that the time value of the fund will be not taken into account and the compound interest will be not calculated when calculating the benefits and costs of the scheme, while they will be taken into account by the dynamic evaluation, of which the calculation process is based on the equivalent basic conversion formula, which includes the net present value [23].

The total cost of the system in its whole life cycle is the sum of the construction, operation, maintenance and energy costs. However, since the changes in the time value of money, the project costs occurring at different points in the asset life cycle cannot be compared or simply added together. They must be discounted to their present value. Appropriate formula for the net present value is as follows [24]:

$$NPV = \sum \frac{(C_I - C_O)}{(1 + i)^t} \tag{1}$$

where, NPV = net present value;  $C_I$  = cash inflows;  $C_O$  = cash outflows;  $i$  = discount rate in decimals;  $t$  = time period.

The result of the NPV method is more realistic because it takes the time value of money into account and it also considers the risk inherent in making projections about the future. Hence this method is useful in the rational arrangement and financial management of the future costs and activities of the WWTP.

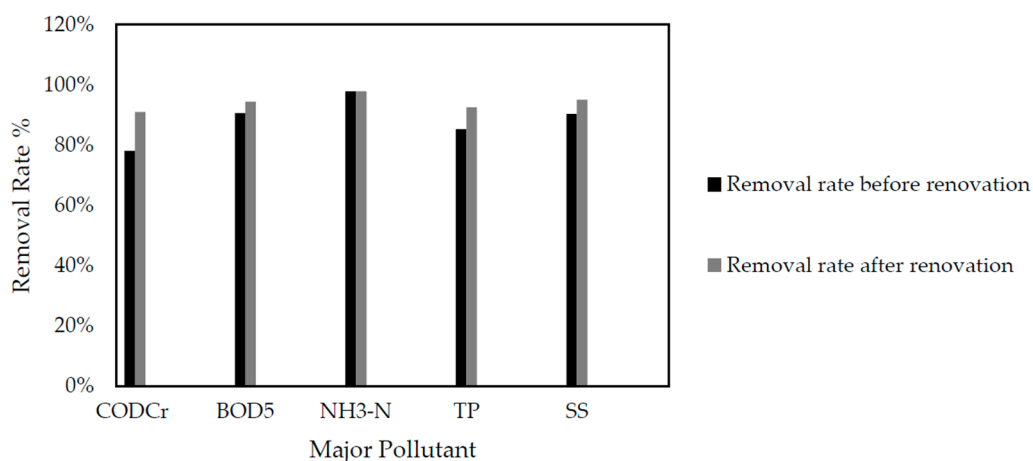
#### 4. Results and Discussion

##### 4.1. Technical Results

Table 5 shows the concentration of a major pollutant in the influent and effluent as well as the removal rate after the plant renovation. Figure 3 shows the improvement of removal rate of major pollutants before and after the plant renovation. The data were collected from the semi-annual water quality analysis report of the plant in 2019.

**Table 5.** Main pollutant indicators of the influent and effluent from the WWTP after renovation.

Months		10	11	12	Average	Standard
COD <sub>Cr</sub> (mg/L)	Influent	171	202	164		
	Effluent	18	17	15	91%	30 mg/L
	Removal rate	89%	92%	91%		
NH <sub>3</sub> -N (mg/L)	Influent	20.3	28.19	27		
	Effluent	0.05	0.05	0.07	99.8%	1.5 mg/L
	Removal rate	99.7%	99.8%	99.7%		
TP (mg/L)	Influent	2.31	3.24	2.42		
	Effluent	0.17	0.16	0.16	93%	0.3 mg/L
	Removal rate	93%	95%	93%		
SS (mg/L)	Influent	72	95	83		
	Effluent	1.65	1.43	1.84	98%	5 mg/L
	Removal rate	98%	98%	98%		



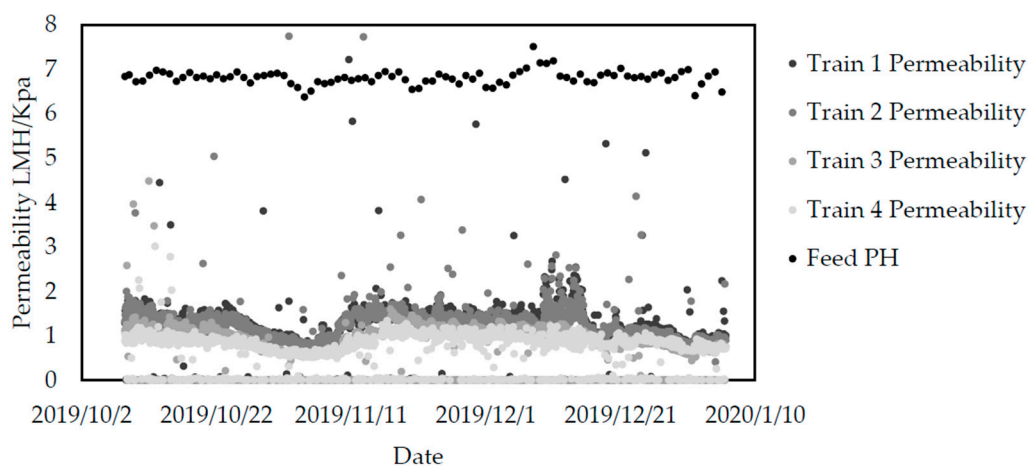
**Figure 3.** Removal rate of the major pollutants before and after the plant renovation, as well as the comparison of effluent water quality with the new discharge standards.

It can be seen from Figure 3, that the removal rates of COD<sub>Cr</sub>, BOD<sub>5</sub>, TN, TP and SS were significantly improved after the renovation, while maintaining the removal rate of ammonia nitrogen in the original level. The concentrations of major pollutants in the effluent are much lower, which totally meet the requirement of the new discharge standard. Among them, the water and sludge can be more fully mixed due to the adjustment of the water inlet port and the sludge inlet port as well as the improvement of the thruster, and the hydraulics flow pattern of the reflux between each biochemical tank is also improved, so as to avoid the formation of dead sludge accumulated in the

tank [25]. The removal rate of BOD<sub>5</sub> is increased to 94% after the renovation, which is better than 91% of that in the original process. In addition, with the interception of a certain amount of macromolecular organic matter by the ultrafiltration membrane, the COD<sub>Cr</sub> removal rate was greatly increased from 78% to 91%.

Chemical agents also have a positive effect on the removal of total phosphorus. Usually the biological phosphorus removal method cannot achieve the ideal effect because it is very sensitive to temperature, water salinity and other aspects. After the additional chemical phosphorus removal method, the phosphorus is changed into insoluble phosphate precipitation form by adding iron salt phosphorus removal agent. On the one hand, iron combines with phosphoric acid, and on the other hand, its hydrolysates can form Fe(OH)<sub>3</sub> and other complexes, which make the original colloids in the water destabilized by adsorption bridging and net capture and sweep, so as to be flocculated and precipitated, which is much easier after it is combined into macromolecules [26]. Compared with the biological phosphorus removal method only, the total phosphorus removal rate was increased from 85% to 93% by adding the chemical phosphorus removal system.

The ultrafiltration membranes, which are the key technology of the renovation, have a significant interception rate for suspended solid, and then the concentration of SS in the effluent is almost impossible to be detected, which is far lower than the required 6 mg/L. Meanwhile, the upgrading of the biochemical treatment also benefits the operation performance of the ultrafiltration membrane. Figure 4 describes the permeability trend of the ultrafiltration membrane within three months after the renovation.



**Figure 4.** Permeability trend of the ultrafiltration membrane within three months after the renovation.

The newly added ultrafiltration membrane was divided into four sets, each set with 80 membrane modules, each of which could operate independently. As shown in Figure 4, the ultrafiltration membrane permeability of the four sets remains basically stable in the operation for three consecutive months. In late October to early November of 2019, there was an impact dosage of the chemical phosphorus removal agent, which resulted in the rapid fouling of the membrane and decline of the permeability [27]. However, it was returned to the initial level after one time of chemical cleaning, which certified a good recoverable performance of the membranes. The permeability of the membrane system was basically maintained at about 1.5 LMH/kPa, which was in the higher level compared with the other ultrafiltration membrane on the market [28].

#### 4.2. Economical Results

The NPV method was used to evaluate the economy performance of the renovation. The cash inflow is the sewage treatment fee charged by the plant after the renovation, while the cash outflow includes the initial investment cost, operation and maintenance cost [29]. The cost of operation and maintenance mainly include the cost of phosphorus removal agent, the cost of carbon source

supplement and the ultrafiltration membrane cleaning agent, power consumption and labor cost of the new equipment, while the data are collected from the plant. The depreciation cost of the ultrafiltration membrane was calculated based on the warranty period given by the membrane manufacturer. The details are as follows:

The total investment cost of this renovation was CNY 25.626 million.

The power consumption mainly included the consumption of ultrafiltration feed pump, backwash pump, metering pump and other power equipment, as well as the power consumption of the newly added lighting and control device. It was calculated that the additional power consumption of the project was 2.199 million KWH per year.

The chemical consumption mainly comes from the chemical phosphor removal, the supplemented carbon source and the cleaning of the ultrafiltration membrane. The main agents that were newly added were sodium acetate, ferric sulfate new agents, sodium hypochlorite, hydrochloric acid and sodium hydroxide. According to the design value, the main chemical consumption was shown in Table 6. According to the three-month operation, the actual consumption was lower than the design value. However, considering uncertain factors such as water quality fluctuation in the future, the design value will be used for the calculation of economic evaluation.

**Table 6.** Additional chemical consumption after renovation.

Nr.	Chemical Agents	Dosage Quantity (kg/d)
1	Sodium hypochlorite	76
2	Sodium hydroxide	14.6
3	Hydrochloric acid	12.78
4	Phosphorus removal agent	6075.4
5	Sodium acetate	8000

The depreciation cost of the ultrafiltration membrane was calculated according to the six year warranty period given by the manufacturer, and the local electricity price, labor cost and pharmaceutical price were calculated according to the local average price of the last two years. The annual maintenance cost was calculated at 2% of the investment cost.

The unit sewage treatment fee charged by the water plant was CNY 2.76/ton after the renovation, and the water treatment fee per ton was CNY 1.58 higher than the original CNY 1.18 before the renovation. Thus, the CNY 1.58/ton will be used as the calculation basis for cash the inflow during the economic evaluation.

In addition, the base year for the NPV calculation WAs 2019, which WAs the commissioning stage after the renovation. The NPV analysis requires a discount rate calculated using interest rates and inflation rates [30]. Interest rates and inflation are based on the historical data of the past 25 years. The average interest rate is calculated as 14% and the average inflation rate is 8% after the average value is collected, hence, the calculated discount rate is 5.55%. All capital inflows and outflows were converted into the present value of the base year in 2019, and then added by the NPV method to obtain the cost of different calculation life cycle. All the calculations were completed using MS Office Excel, and the results are shown in Figure 5.

Due to the improvement of water quality after the renovation, the cost of sewage treatment fee was greatly increased. As shown in Figure 5, the net present value within the 20 year life cycle is CNY 72.51 million, and the overall cost can be recovered in the fourth year after the renovation, which brings considerable economic benefits to the plant.

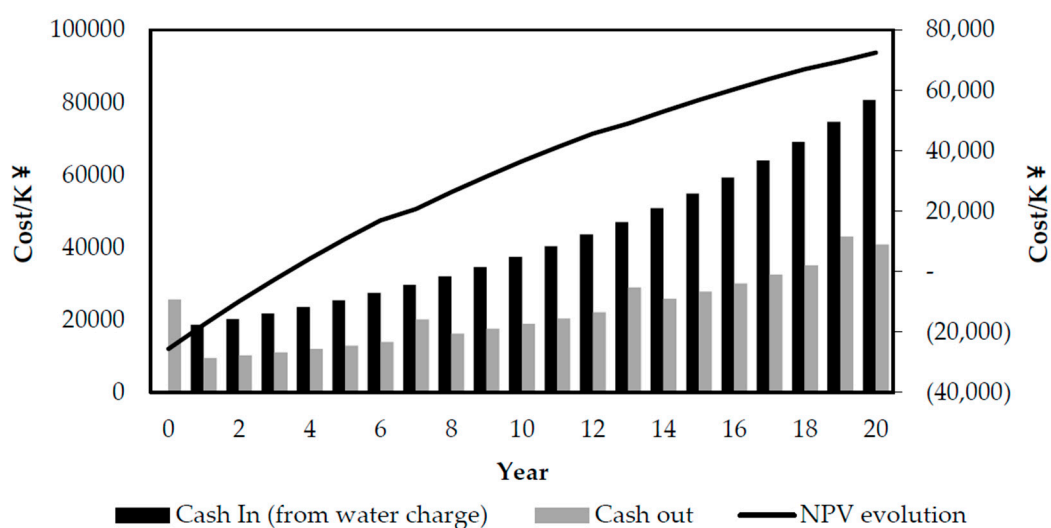


Figure 5. Net present value (NPV) calculation result.

In addition, it can be seen that one of the variables of this renovation methodology was the selection of ultrafiltration membrane. There are different kinds of ultrafiltration membranes with different materials, different performance, operation stabilities and life cycles on the market, which directly affect the economic benefits of water plants by the chemical consumption, membrane depreciation cost and other factors [31]. This paper takes the service life of the ultrafiltration membrane as an example to study the influence of different membrane replacement cycles on the NPV result, as shown in Figure 6.

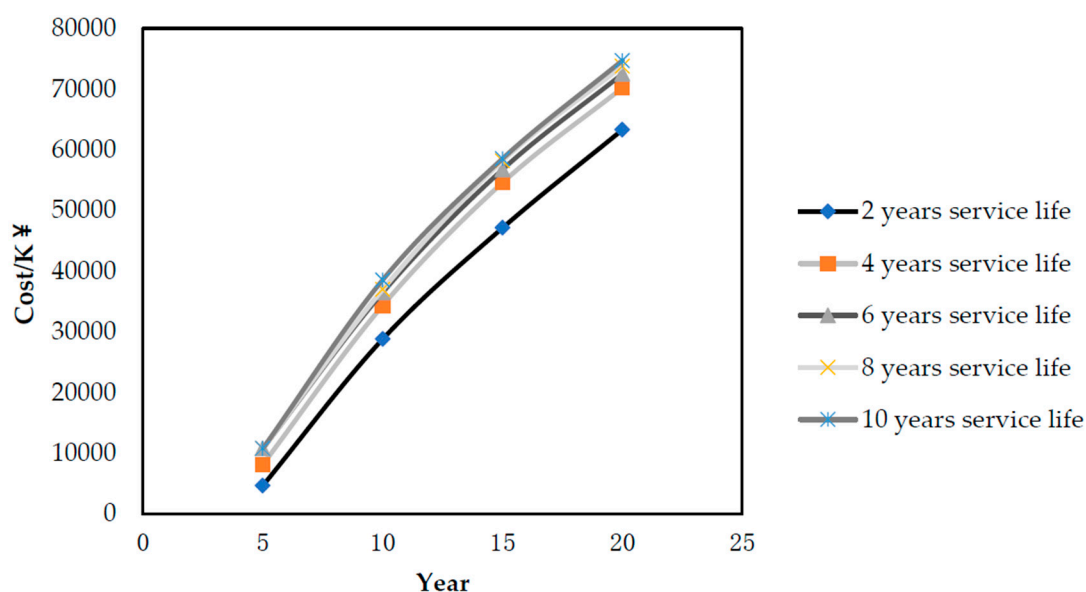


Figure 6. NPV calculation results under the different membrane life cycles.

Figure 6 shows the NPV result of the water plant from 5 to 20 years with the different ultrafiltration membrane service life cycles. It can be seen that different ultrafiltration membranes replacement cycles have a direct impact on the NPV value of the whole life cycle of the plant. When the service life of the membrane is less than 3 years, the influence is much more significant. Ultrafiltration membrane species also affect chemical consumption, power consumption and other factors, and then the selection of ultrafiltration membrane is important in the renovation based on the process route introduced in this paper. The TIPS ultrafiltration membrane was used in the Liaocheng USEH WWTP, which could benefit the water plant continuously due to its good chemical resistance and recoverability.

### 4.3. Challenges and Future Research Orientations

It is obvious that the ultrafiltration membrane will play an increasingly important role in wastewater treatment plant renovation [10]. However, while the ultrafiltration membrane technology is constantly innovating, the research on the mechanism of membrane fouling by specific pollutants is insufficient, moreover, the market supervision is also deficient, which is manifested in the following aspects. Firstly, there is a lack of an integrated outline and systematic standard for ultrafiltration membrane evaluation in the technical and economic dimensions; in addition, there is also no widely accepted operation standards, which result in a lack of evidence for the WWTP to follow during management [10,32,33]. Therefore, it can be predicted that the future research orientation will be more inclined to build the evaluation system of ultrafiltration membrane, and to determine the weight of each indicator, in order to propose a comprehensive and systematic outline of technical and economic dimensions. Additionally, membrane fouling, shrinkage, cycles of operation, and regeneration prospects also need be further studied in the future. In a wastewater treatment process, the physically irreversible fouling of ultrafiltration membranes is severe and inevitable, the permeability loss restricts the application of ultrafiltration for wastewater treatment, and it will also reduce the service life of the membrane and increase the cost of membrane replacement [32–34]. The key issue to solve the fouling problem is to understand the fouling mechanism and cleaning efficiency of a specific pollutant, and find an effective way to regenerate the membrane [35–37]. In addition, how to select and upgrade pretreatments, which can represent important savings in the operational costs related to the membrane’s cleaning procedures and maintenance, will also be one of the future research orientations [38].

However, due to the limitation of the site spaces and time, no other membrane products were performed in this project. Therefore, by reading a large number of studies, the author compared the application of different ultrafiltration membranes in other projects, especially in a municipal wastewater field, and summarized the relevant factors affecting the performance of the ultrafiltration membrane [39]. Meanwhile, we proposed an integrated outline for the evaluation of ultrafiltration membrane-based renovation methodologies of the technical and economic dimensions, which are presented based on the actual Chinese market situation, as shown in Tables 7 and 8 [40,41], which can be regarded as a reference for the establishment of ultrafiltration membrane evaluation systems in the future.

**Table 7.** Technique indexes of the ultrafiltration membrane system-based WWTP renovation methodology evaluation.

Evaluation Item		Weight
Renovation methodologies	Effluent quality	++++
	Automaticity	++
	Security	++
	Installation convenience	++
	Floor space	+
	Construction difficulty	++
	Stability	++
Ultrafiltration membrane	Chemical tolerance	+++
	Material safety	++
	Warranty period	+++
	Cleaning period	+
	Fouling resistant	++
	Integrity	+++
Environmental adaptability		+

**Table 8.** Economic indexes of the ultrafiltration membrane system-based WWTP renovation methodology evaluation.

Evaluation Item		Weight
Total investment costs	Including equipment, materials, construction, installation	+++
Operating costs	Including power consumption costs, chemical consumption, costs, labor costs and management fees	+++
Sewage treatment fee		+++

## 5. Conclusions

In this work, taking the Liaocheng UESH WWTP as an example, this research proves that from the technical perspective, it is a feasible scheme to take the ultrafiltration membrane as the main technology and upgrade the biochemical process section in the meantime. Due to the high efficiency of the ultrafiltration membrane interception characteristics, the main pollutant in the effluent after the renovation could totally meet the Class IV requirement of “Water Quality Standard of Surface Water”. At the same time, the upgrading of the biochemical treatment can also reduce the fouling rate of the ultrafiltration membrane and keep a stable operation status, and thus bring a beneficial impact on the local natural environment. Economic performances evaluated by the NPV method have clearly demonstrated that based on the operational perspective, the ultrafiltration membrane represents a highly competitive technological solution. Thus, we anticipate that the ultrafiltration membrane would play an important role in the renovation of WWTPs. Meanwhile, systematic evaluation systems and research on the fouling mechanism of the ultrafiltration membrane will be the emphases of future research and development.

**Author Contributions:** Conceptualization: Y.L.; data curation: H.B. and H.Q.; investigation: X.Z.; project administration: J.Z.; writing—original draft: H.B.; writing—review and editing: Y.L. and Y.T. All authors have read and agreed to the published version of the manuscript.

**Funding:** This work was financially supported by the Open Project of the State Key Laboratory of Chemical Engineering (no. SKL-ChE-19A02).

**Conflicts of Interest:** The authors declare no conflict of interest.

## References

- Chen, B.; Wang, M.; Duan, M. In search of key: Protecting human health and the ecosystem from water pollution in China. *J. Clean. Prod.* **2019**, *228*, 101–111. [[CrossRef](#)]
- Wang, Q.; Yang, Z. Industrial water pollution, water environment treatment, and health risks in China. *Environ. Pollut.* **2016**, *218*, 358–365. [[CrossRef](#)] [[PubMed](#)]
- Chakraborti, L.; McConnell, K.E. Does ambient water quality affect the stringency of regulations? Plant-level evidence of the clean water act. *Land Econ.* **2012**, *88*, 518–535. [[CrossRef](#)]
- Effluent Limitations Guidelines and Standards for the Construction and Development Point Source Category [DB/OL]*; United States Environmental Protection Agency: Washington, DC, USA, 2013.
- Wang, X.-H.; Wang, X.; Huppel, G.; Heijungs, R.; Ren, N.-Q. Environmental implications of increasingly stringent sewage discharge standards in municipal wastewater treatment plants: Case study of a cool area of China. *J. Clean. Prod.* **2015**, *94*, 278–283. [[CrossRef](#)]
- Zhang, Q.H.; Yang, W.N.; Ngo, H.H.; Guo, W.S. Current status of urban wastewater treatment plants in China. *Environ. Int.* **2016**, *92–93*, 11–22. [[CrossRef](#)]
- Collivignarelli, M.C.; Abbà, A.; Bertanza, G.; Frattarola, A. The upgrading of conventional activated sludge processes with thermophilic aerobic membrane reactor: Alternative solutions for sludge reduction. *J. Environ. Manag.* **2020**, *264*, 110490. [[CrossRef](#)]

8. Tang, Y.H.; Lin, Y.K.; Zhou, B.; Wang, X.L. PVDF membranes prepared via thermally induced (liquidliquid) phase separation and their application in municipal sewage and industry wastewater for water recycling. *Desalin. Water Treat.* **2016**, *57*, 22258–22276. [[CrossRef](#)]
9. Acero, J.L.; Benitez, F.J.; Leal, A.I.; Real, F.J.; Teva, F. Membrane filtration technologies applied to municipal secondary effluents for potential reuse. *J. Hazard. Mater.* **2010**, *177*, 390–398. [[CrossRef](#)]
10. Al Aani, S.; Mustafa, T.N.; Hilal, N. Ultrafiltration membranes for wastewater and water process engineering: A comprehensive statistical review over the past decade. *J. Water Process Eng.* **2020**, *35*, 101241. [[CrossRef](#)]
11. Diaz, S.D.; Peña, L.V.; Cabrera, E.G. Effect of previous coagulation in direct ultrafiltration of primary settled municipal wastewater. *Desalination* **2012**, *204*, 41–48. [[CrossRef](#)]
12. Kajenthira, A.; Siddiqi, A.; Anadon, L.D. A new case for promoting wastewater reuse in Saudi Arabia: Bringing energy into the water equation. *J. Environ. Manag.* **2012**, *102*, 184–192. [[CrossRef](#)] [[PubMed](#)]
13. Xu, Y.; Tang, Q.; Li, D.; Zhou, X.; Sun, G.; Wang, J.; Wang, J. Demonstration project of upgrading reconstruction using ultra-filtration membrane process in Zhaoqing New & High-Tech Zone Waterworks. *Water Technol.* **2012**, *6*, 44–47.
14. Huang, Y.; Feng, X. Polymer-enhanced ultrafiltration: Fundamentals, applications and recent developments. *J. Membr. Sci.* **2019**, *586*, 53–83. [[CrossRef](#)]
15. Kirschner, A.Y.; Cheng, Y.-H.; Paul, D.R.; Field, R.W.; Freeman, B.D. Fouling mechanisms in constant flux crossflow ultrafiltration. *J. Membr. Sci.* **2019**, *574*, 65–75. [[CrossRef](#)]
16. Fuchs, W.; Theiss, M.; Braun, R. Influence of standard wastewater parameters and pre-flocculation on the fouling capacity during dead end membrane filtration of wastewater treatment effluents. *Sep. Purif. Technol.* **2006**, *52*, 46–52. [[CrossRef](#)]
17. Xiong, R.; Yu, X.; Yu, L.; Peng, Z. Biological denitrification using polycaprolactone-peanut shell as slow-release carbon source treating drainage of municipal WWTP. *Chemosphere* **2019**, *235*, 434–439. [[CrossRef](#)]
18. Ren, J.; Li, N.; Wei, H.; Li, A.; Yang, H. Efficient removal of phosphorus from turbid water using chemical sedimentation by FeCl<sub>3</sub> in conjunction with a starch-based flocculant. *Water Res.* **2020**, *170*, 115361. [[CrossRef](#)]
19. Mbamba, C.K.; Lindblom, E.; Flores-Alsina, X.; Tait, S. Plant-wide model-based analysis of iron dosage strategies for chemical phosphorus removal in wastewater treatment systems. *Water Res.* **2019**, *155*, 12–25.
20. Tang, Y.; Lin, Y.; Lin, H.; Li, C.; Zhou, B.; Wang, X. Effects of Room Temperature Stretching and Annealing on the Crystallization Behavior and Performance of Polyvinylidene Fluoride Hollow Fiber Membranes. *Membranes* **2020**, *10*, 38. [[CrossRef](#)]
21. Li, D.; Krantz, W.B.; Greenberg, A.R.; Sani, R.L. Membrane formation via thermally induced phase separation (TIPS): Model development and validation. *J. Membr. Sci.* **2006**, *279*, 50–60. [[CrossRef](#)]
22. Aziz, M.; Ojumu, T. Exclusion of Estrogenic and Androgenic Steroid Hormones from Municipal Membrane Bioreactor Wastewater Using UF/NF/RO Membranes for Water Reuse Application. *Membranes* **2020**, *10*, 37. [[CrossRef](#)] [[PubMed](#)]
23. Ambre, H.P.; Saner, A.B.; Aher, P.D. Comparison of Life Cycle Cost Analysis for Water Treatment Plant by Net Present Value method and Equivalent Annual Cost Method. *Int. J. Mod. Trends Eng. Res.* **2016**, *3*, 421–425.
24. Leyman, P.; Van Driessche, N.; Vanhoucke, M.; De Causmaecker, P. The impact of solution representations on heuristic net present value optimization in discrete time/cost trade-off project scheduling with multiple cash flow and payment models. *Comput. Oper. Res.* **2019**, *103*, 184–197. [[CrossRef](#)]
25. Xing, C.-H.; Tardieu, E.; Qian, Y.; Wen, X.-H. Ultrafiltration membrane bioreactor for urban wastewater reclamation. *J. Membr. Sci.* **2000**, *177*, 73–82. [[CrossRef](#)]
26. Fan, J.; Hu, H.; Zhang, Y.; Zhu, L. Biological Phosphorus Removal Combined with Ferrous Chemical Phosphorus Removal. *Adv. Mater. Res.* **2014**, *955–959*, 3339–3342. [[CrossRef](#)]
27. Wu, Y.; Zhang, Z.; He, P.; Ren, H.; Wei, N.; Zhang, F.; Cheng, H.; Wang, Q. Membrane fouling in a hybrid process of enhanced coagulation at high coagulant dosage and cross-flow ultrafiltration for deinking wastewater tertiary treatment. *J. Clean. Prod.* **2019**, *230*, 1027–1035. [[CrossRef](#)]
28. Ao, L.; Liu, W.; Zhang, M.; Wang, X. Analysis of effect of particles on cake layer compressibility during ultrafiltration of upflow biological activated carbon effluent. *Sci. Total Environ.* **2018**, *619*, 232–238. [[CrossRef](#)]
29. Dogan, E.C.; Yasar, A.; Sen, U.; Aydinler, C. Water recovery from treated urban wastewater by ultrafiltration and reverse osmosis for landscape irrigation. *Urban Water J.* **2016**, *13*, 553–568. [[CrossRef](#)]
30. Maurer, M. Specific net present value an improved method for assessing modularisation costs in water services with growing demand. *Water Res.* **2009**, *43*, 2121–2130. [[CrossRef](#)]



31. Ahmad, T.; Guria, C.; Mandal, A. A review of oily wastewater treatment using ultrafiltration membrane: A parametric study to enhance the membrane performance. *J. Water Process Eng.* **2020**, *36*, 101289. [[CrossRef](#)]
32. Falsanisi, D.; Liberti, L.; Notarnicola, M. Ultrafiltration (UF) Pilot Plant for Municipal Wastewater Reuse in Agriculture: Impact of the Operation Mode on Process Performance. *Water* **2010**, *2*, 872–885. [[CrossRef](#)]
33. Huang, H.; Lee, N.; Young, T.; Gary, A.; Lozier, J.C.; Jacangelo, J.G. Natural organic matter fouling of low-pressure, hollow-fiber membranes: Effects of NOM source and hydrodynamic conditions. *Water Res.* **2007**, *41*, 3823–3832. [[CrossRef](#)] [[PubMed](#)]
34. Howe, K.J.; Clark, M.M. Fouling of microfiltration and ultrafiltration membranes by natural waters. *Environ. Sci. Technol.* **2002**, *36*, 3571–3576. [[CrossRef](#)] [[PubMed](#)]
35. Yin, N.; Zhong, Z.; Xing, W. Ceramic membrane fouling and cleaning in ultrafiltration of desulfurization wastewater. *Desalination* **2013**, *319*, 92–98. [[CrossRef](#)]
36. Bourgeois, K.N.; Darby, J.L.; Tchobanoglous, G. Ultrafiltration of wastewater: Effects of particles, mode of operation, and backwash effectiveness. *Water Res.* **2001**, *35*, 77–90. [[CrossRef](#)]
37. Cabassud, C.; Laborie, S.; Lainé, J.M. How slug flow can enhance the ultrafiltration flux in organic hollow fibres. *J. Memb. Sci.* **1997**, *128*, 93–101. [[CrossRef](#)]
38. Benito, A.; Garcia, G.; Gonzalez-Olmos, R. Fouling reduction by UV-based pretreatment in hollow fiber ultrafiltration membranes for urban wastewater reuse. *J. Membr. Sci.* **2017**, *536*, 141–147. [[CrossRef](#)]
39. Wang, Z.; Fan, Z.; Xie, L.; Wang, S. Study of integrated membrane system for the treatment of wastewater from cooling towers. *Desalination* **2006**, *191*, 117–124. [[CrossRef](#)]
40. Huttinger, A.; Dreibelbis, R.; Roha, K.; Ngabo, F.; Kayigamba, F.; Mfura, L.; Moe, C. Evaluation of Membrane Ultrafiltration and Residual Chlorination as a Decentralized Water Treatment Strategy for Ten Rural Healthcare Facilities in Rwanda. *Int. J. Environ. Res. Public Health.* **2015**, *12*, 13602–13623. [[CrossRef](#)]
41. Ren, H.-J.; Lin, W.-Z.; Gao, L.-X.; Shi, C.-L.; Kong, X.-J. Discussion on Evaluation System of Ultrafiltration Membrane System for Municipal Sewage Treatment. *China Water Wastewater* **2016**, *32*, 30–33.



© 2020 by the authors. Licensee MDPI, Basel, Switzerland. This article is an open access article distributed under the terms and conditions of the Creative Commons Attribution (CC BY) license (<http://creativecommons.org/licenses/by/4.0/>).

Review

# Diffusion Dialysis for Acid Recovery from Acidic Waste Solutions: Anion Exchange Membranes and Technology Integration

Chengyi Zhang, Wen Zhang \*  and Yuxin Wang

State Key Laboratory of Chemical Engineering, Tianjin Key Laboratory of Membrane Science & Desalination Technology, and School of Chemical Engineering and Technology, Tianjin University, Tianjin 300350, China; zhangqqzhang@tju.edu.cn (C.Z.); yxwang@tju.edu.cn (Y.W.)

\* Correspondence: zhang\_wen@tju.edu.cn

Received: 5 July 2020; Accepted: 27 July 2020; Published: 29 July 2020



**Abstract:** Inorganic acids are commonly used in mining, metallurgical, metal-processing, and nuclear-fuel-reprocessing industries in various processes, such as leaching, etching, electroplating, and metal-refining. Large amounts of spent acidic liquids containing toxic metal ion complexes are produced during these operations, which pose a serious hazard to the living and non-living environment. Developing economic and eco-friendly regeneration approaches to recover acid and valuable metals from these industrial effluents has focused the interest of the research community. Diffusion dialysis (DD) using anion exchange membranes (AEMs) driven by an activity gradient is considered an effective technology with a low energy consumption and little environmental contamination. In addition, the properties of AEMs have an important effect on the DD process. Hence, this paper gives a critical review of the properties of AEMs, including their acid permeability, membrane stability, and acid selectivity during the DD process for acid recovery. Furthermore, the DD processes using AEMs integrated with various technologies, such as pressure, an electric field, or continuous operation are discussed to enhance its potential for industrial applications. Finally, some directions are provided for the further development of AEMs in DD for acid recovery from acidic waste solutions.

**Keywords:** diffusion dialysis; anion exchange membrane; acid recovery

---

## 1. Introduction

It is well known that large amounts of inorganic acids are widely used in several processes of mining, metallurgical, metal-processing, and nuclear-fuel-reprocessing industries, including pickling, cleaning, leaching, etching, electroplating, and metal-refining and so on. Just for the stainless steel pickling process, it is estimated that at least 0.65 million tons of acidic waste solution is produced in China each year [1]. Dumping this waste into the environment could corrode metal pipes, contaminate the water and soil, and pose severe risks to the health of humans and animals (Figure 1). Accordingly, recovering acid from acidic waste solutions not only saves resources but also protects the environment [2]. Developing efficient and eco-friendly regeneration approaches to recover acid from these industrial effluents has attracted substantial attention and has significant ecological and economic implications.

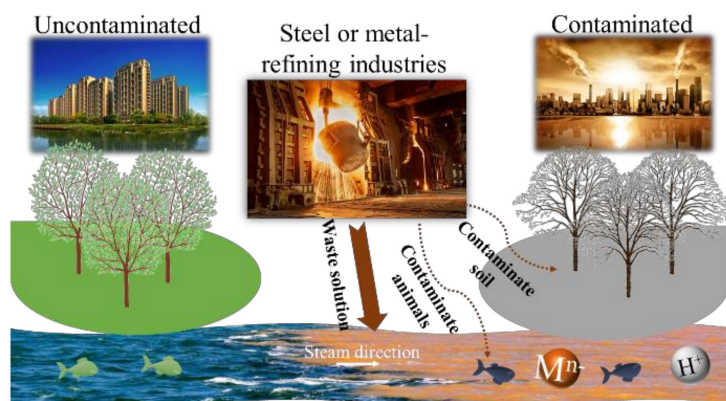


Figure 1. The schematic diagram for the influence from acid waste solutions.

To date, many methods for recovering acid from acidic waste solutions, such as crystallization [3,4], solvent extraction [5–7], ion exchange resin [8–10], and membrane technology [11–13], have been explored. These methods are summarized including their advantages and disadvantages for acid recovery in Table 1. In the current industrial practices, fluidized bed process or spray roasting is applied to recover HCl from spent pickling solutions. However, the main disadvantage is the high operational cost and high consumption of fresh water and energy [14]. While in some small hot-dip galvanizing plants, precipitation or neutralization process is applied to recover acid. This process is easy and there is no complex installation, but it needs plenty of chemicals and the cost of storage of the sludge is high [15]. Membrane technology is considered to be a simple, effective, and environmentally friendly method to recover acids [16]. This is because the equipment for acid recovery using membrane technology is compact and simple, the effective area of membrane is large and controllable, and there is no by-product produced during the acid recovery process. As one such membrane technology, diffusion dialysis (DD) using anion exchange membranes (AEMs) has been used industrially since 1984 [17]. Compared to other technologies, DD using AEMs for acid recovery has the following significant advantages [16]:

1. Low energy consumption owing to the spontaneity of the process driven by an activity gradient;
2. Low installation costs, simple operation, and maintenance;
3. High product quality due to the high selectivity of AEMs for acids;
4. Environmentally friendliness because of no extra postprocessing and chemical agents.

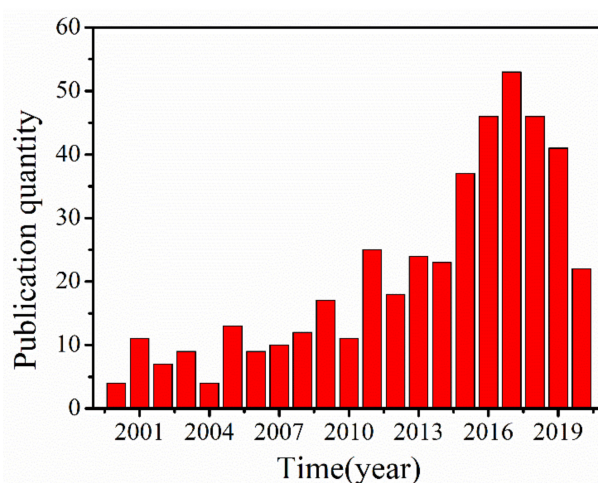
Table 1. A summary of methods for acid recovery.

Methods	Description	Advantages	Disadvantages
Crystallization [3,4]	The solubility of saline, such as FeCl <sub>2</sub> or AlCl <sub>3</sub> , in the waste solutions reduces at low temperature, resulting in crystallization and separation.	Less investment in equipment simple to install	Long production period Low processing capacity High energy cost
Solvent extraction [5–7]	Extraction agents are used to extract acid or metal ions selectively from waste solutions. Then, the acid or metal ions could be collected via back-extraction.	High yield and selectivity Pure product	Complicated operation Bad for environmental owing to the extraction agents.
Ion exchange resin [8–10]	Ion exchange materials are used to absorb acids or metal ions in the waste solution, and then the acids or metal ions could be desorbed from the solid phases.	High selectivity Simple to operation	High costs Low adsorption capacities
Membrane technology [13,18,19]	Membrane technologies contain the reverse osmosis process, electro dialysis and diffusion dialysis which correspond to pressure, an electric field or activity as driving forces, respectively. Acids are transported through membranes from feed side to the receiving side under the driving forces.	High efficiency Reliable Simple to install and scale up.	Limited processing capacities

The DD process was comprehensively applied in acid recovery by researchers, such as in the recovery of inorganic acid (sulfuric acid (H<sub>2</sub>SO<sub>4</sub>) [20], hydrochloric acid (HCl) [21] hydrofluoric acid (HF) [22,23], nitric acid (HNO<sub>3</sub>) [24]) and organic acid (carboxylic acids [25,26]). As the core component, anion exchange membranes (AEMs) which could influence the efficacy of the acid recovery play an important role during the DD process. AEMs as one kind of ion exchange membranes containing positively charge groups allow the migration of anions and repel cations. In fact, AEMs have already attracted much attention in various areas, such as desalination [27], alkaline fuel cells [28–30], wastewater treatment [31,32] and so on. At present, some commercial AEMs, including Selemion DSV (Asahi Glass, Tokyo, Japan), Neosepata AFX/N (Tokuyama Co., Tokyo, Japan) and DF120 (Shandong Tianwei Membrane Technology Co., Weifang, China) series are available for recovering acids. However, the acid permeabilities and selectivities of these commercial AEMs are limited [16]. In addition, the economic investment of DD system using AEMs for acid recovery is shown in Table 2. It can be seen that the DD system is high attractive economically. Recently, many efforts to improve the properties of the AEMs used in DD for acid recovery have been made over the years. Figure 2 shows the number of papers published on AEMs for acid recovery via DD from 2000. The number of published papers on this subject is small at the beginning of ten years. However, the number between 2015 and 2019 is approximately double of that between 2009 and 2015, which suggests that the acid recovery via DD began to attract researchers’ attention in the recent five years. This growth could be attributed to the rising environmental regulation and sustainable development issue.

**Table 2.** The economic investment of the DD system using AEMs for acid recovery [13,22,33,34].

Material	Price (\$)
Diffusion dialysis unit	170,000–1,350,000
Membranes replacement	15,000–300,000
Auxiliary (pump, circuit, valve, and tank)	150,000
Power, labor, and others	3000–5000
Total	338,000–1,805,000
Write-off (investment-recovery period): 4.8–26.4 months	



**Figure 2.** Chronology of diffusion dialysis using anion exchange membranes for acid recovery documents [35].

In 2011, Luo published a broad and systematic review of DD for inorganic acid, organic acid and alkali recovery, including the properties of the membranes, nature of the waste solutions and running conditions [16]. In the past decade, many studies on new materials, methods, and technologies for acid recovery via DD were published. Although reviews on acid recovery involving membrane technologies have been published recently, they focused on specific application scenarios, such as

acid recovery from acid mine drainage [36,37] and fatty acid recovery [38] or specific technologies, such as electromembrane technology [39] and reactive separation technology [40]. There are few comprehensive reviews that summarize the developments for the key component, AEMs, in detail. Hence, this review intends to bridge this gap and provide an overview of the AEMs for use in DD for acid recovery published in the past decade with a focus on the properties of AEMs, including the acid permeability, acid selectivity, trade-off effect and membrane stability. In addition, to further enhance mass transfer and improve the processing capacity, the integration of DD using AEMs with other technologies for acid recovery is also assessed.

## 2. Description of Acid Recovery Using AEMs

During DD, the ions in an acidic waste solution (the feed solution) migrate through the AEM to the other side, which is filled with deionized water (the receiving solution), driven by an activity gradient. Because of the presence of positively charged functional groups in the AEM, anions ( $\text{Cl}^-$ ,  $\text{SO}_4^{2-}$ ,  $\text{NO}_3^-$ , etc.) can freely migrate through the membrane, while most cations are blocked by the membrane owing to the Donnan criteria of co-ion rejection [41]. Notably,  $\text{H}^+$ , although positively charged, migrates more easily than other cations through the AEM due to its small size, low valence state and high mobility. Therefore,  $\text{H}^+$  can migrate by the dragging effect with the anions from the feed solution into the receiving solution to maintain the electrical neutrality of the solutions [42]. As a result, the acid could be collected on the receiving side, while metal ions could be retained on the feed side.

Two models are usually used to describe the migration of acids through AEMs during DD. The first model is the solution-diffusion model, as shown in Figure 3a. The migration of ions through the AEM involves three steps [43]: (1) The ions can interact with the membrane on the feed side via absorption, electrostatic interactions or other interactions. (2) These ions diffuse into the membrane along the activity gradient. (3) These ions divorce the membrane at the receiving side. In the solution-diffusion process, the anions easily migrate through the AEM. However, the crucial step in acid recovery is separating  $\text{H}^+$  and the metal ions. They can be separated over time due to the differences in their solubilities and diffusion rates in the membrane phase during the solution-diffusion process. The second model is the three-phase membrane model, as shown in Figure 3b. During the migration of ions through the AEM, the membrane can be divided into three regions [44,45]: a hydrophobic region, an active region and an interstitial region. The hydrophobic region mainly provides stability and integrity for the membrane. The active region is full of positively charged functional groups for the migration of anions. The interstitial region is considered the swollen region that permits migration of the cations due to the low resistance (such as low electrostatic repulsion) in this area. In this process, the exceptionally high mobility of  $\text{H}^+$  in the interstitial region and anions in the active region via the Grotthus mechanism results in efficient acid recovery.

Here, the dialysis coefficients of  $\text{H}^+$  ( $U_H$ ) and separation factor ( $S$ ) are used to describe the acid permeability and selectivity of AEMs in the acid recovery process. The  $U_H$  could be obtained following the equation,

$$U_H = \frac{M}{At\Delta C} \quad (1)$$

where  $M$  (mol) means the number of ions transported to the permeation solution,  $A$  ( $\text{m}^2$ ) is the effective area for dialysis,  $t$  (h) is the time for dialysis and  $\Delta C$  (mol/L) represents the logarithm average concentration of ions between the two compartments.

The equation of  $\Delta C$  (mol/L) is defined as follows,

$$\Delta C = \frac{C_f^0 - (C_f^t - C_d^t)}{\ln[C_f^0 / (C_f^t - C_d^t)]} \quad (2)$$

where  $C_f^0$  (mol/L) and  $C_f^t$  (mol/L) mean the concentration of ions in feed solution at initial and selected time, respectively and  $C_d^t$  (mol/L) means the concentration of ions in permeation solution at selected time.

The equation of the separation factor ( $S$ ) is as follow,

$$S = \frac{U_H}{U_M} \quad (3)$$

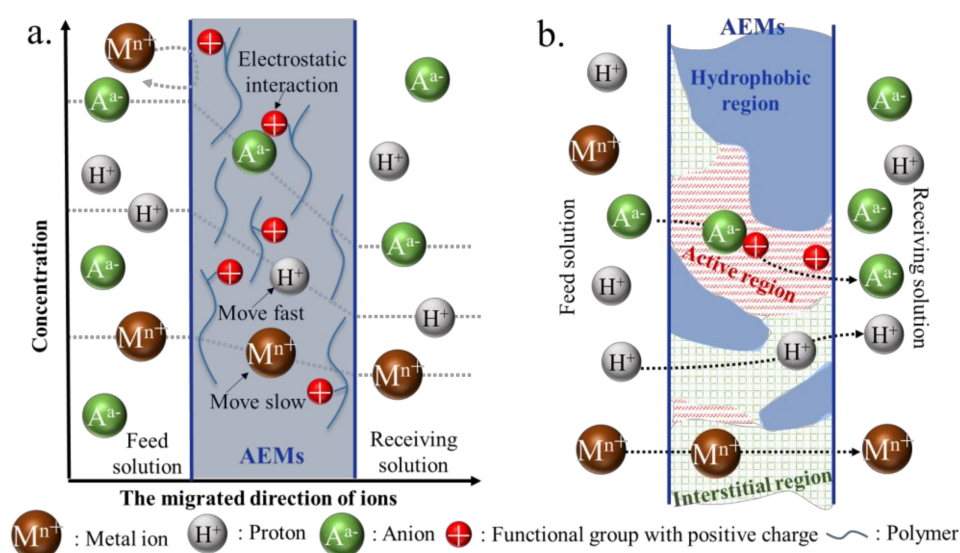


Figure 3. The solution-diffusion model (a) and the three-phase membrane model (b).

### 3. Acid Permeability

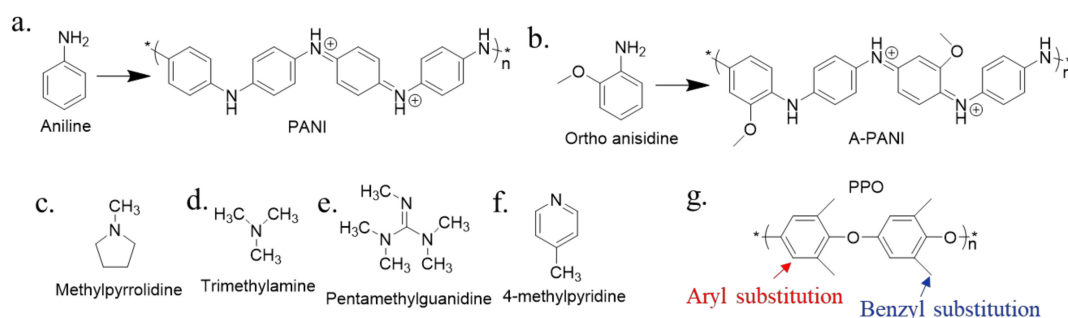
Acid permeability is an important factor in acid recovery. Both the kinds of functional groups in the AEM and the structure of the AEM influence its acid permeability.

#### 3.1. Alkaline Functional Groups for Permeability

To date, many AEMs based on a variety of polymer materials, including polyether sulfone [46], polysulfone (PSF) [47,48], brominated poly(2,6-dimethyl-1,4-phenylene oxide) (BPPO) [49,50] and polyvinyl alcohol (PVA) [32,44], have been prepared for acid recovery. These polymers do not only serve as the backbone of the membrane but also provide sites for functional group modification of the membrane. Incorporating alkaline functional groups, such as  $-NR_2H^+$ ,  $-NR_3^+$ ,  $-PR_3^+$  and so on, into polymer materials is a common method for synthesizing AEMs [51–55]. Overall, the alkaline functional groups, with different types, contents, and substitution sites, have different effects on the acid permeability.

Firstly, the different functional groups have different impacts on the acid permeability. On the one hand, the hydrophilic/hydrophobic characteristics of the membrane could be influenced by different groups, allowing the acid permeability to be tuned. Prajapati [56] prepared two kinds of AEMs using polypropylene (PP) as the substrate: a polyaniline (PANI, Figure 4a)-based AEM and a poly(o-anisidine) (A-PANI, Figure 4b, see Appendix A for the abbreviations of chemicals)-based AEM. The PANI-based AEM was prepared from aniline as the monomer, while the A-PANI-based AEM was prepared from ortho-anisidine as the monomer. The results showed that the acid dialysis coefficient of the A-PANI-based AEM is  $42 \times 10^{-3}$  m/h, which was higher than that of the PANI-based AEM ( $U_H = 32 \times 10^{-3}$  m/h). This is because the A-PANI-based AEM is more hydrophilic due to the higher hydrophilicity of the ortho-anisidine. On the other hand, the different groups have different alkalinity ( $pK_b$ ), corresponding to different association and dissociation properties with

hydroxyl ions, could also influence the acid permeability. Compared to the acid dialysis coefficient of the BPPO-based membrane modified by quaternary ammonium groups using trimethylamine ( $U_H = 13 \times 10^{-3}$  m/h) [57], that of the BPPO-based membrane modified with pyrrolidinium groups using methylpyrrolidine is  $49 \times 10^{-3}$  m/h [50]. The higher anion permeability was a result of the higher alkalinity of methylpyrrolidine ( $pK_b = 3.68$  at 25 °C, Figure 4c) [58,59] compared to trimethylamine (TMA,  $pK_b = 4.20$  at 25 °C, Figure 4d) [50], which facilitated the dissociation of anions from the ion exchange groups. Using an alkaline material with a lower  $pK_b$  to modify the membrane might result in a higher acid permeability due to its higher alkalinity. Pentamethylguanidine (PMG, Figure 4e) shows an extraordinarily high  $pK_b = 0.2$ , and Lin [60] used it as a modifier to prepare a guanidinium-based AEM. The obtained AEMs showed excellent hydroxide conductivity. Although it seems that the functional groups with high  $pK_b$  decrease the acid permeability, a different trend is seen when the  $pK_b$  is higher than 7. Khan [61] synthesized BPPO-based AEMs functionalized with 4-methylpyridine (MP, Figure 4f) with a  $pK_b$  of 8.02. Though its  $pK_b$  is much higher than that of methylpyrrolidine, the membranes functionalized with 4-methylpyridine (MP) showed an excellent acid permeability of  $66 \times 10^{-3}$  m/h, which is higher than that of the BPPO-based AEM modified with pyrrolidinium mentioned above [50]. This difference might be because MP is weakly acidic which might accelerate the migration of  $H^+$  [44].



**Figure 4.** The structure of (a) PANI, (b) A-PANI, (c) Methylpyrrolidine, (d) TMA, (e) PMG, (f) MP, (g) PPO [50,56,60,61].

Secondly, the degree of functionalization of the AEM can also influence its acid permeability. In Ji's work [62], both the ion exchange capacity and the water uptake increased with increasing the degree of quaternization, which improved the acid permeability. This phenomenon was also observed in acid recovery using the PVA-based membranes modified by multisilicon copolymers by Wu [63]. The results showed that the acid permeability increased from  $10 \times 10^{-3}$  to  $29 \times 10^{-3}$  m/h with the increasing content of multisilicon copolymer.

Thirdly, the different sites of functionalization have different influences on acid permeability. Xu [57] found that the  $H_2SO_4$  recovery rate using poly(2,6-dimethyl-1,4-phenylene oxide) (PPO)-based AEMs increased with increasing benzyl substitution but not aryl substitution, as shown in Figure 4g.

### 3.2. Acid-Alkali Functional Groups for Permeability

Considering the advantages of functional groups with weak acidity, polymer backbones were prepared with both alkaline and acidic functional groups to form acid-base ion pairs, which may facilitate acid permeability.

On the one hand, the acidic functional groups could improve the migration of  $H^+$  in the AEM due to electrostatic attractions [64,65]. Irfan [64] incorporated both quaternary nitrogen and  $-COOH$  groups into PPO to recover acid. In the membrane, the quaternary nitrogen permitted the migration of  $Cl^-$ , while the  $-COOH$  groups provided sites for the migration of  $H^+$ . The quaternary nitrogen allowed  $H^+$  to migrate passively, while the  $-COOH$  groups allowed active  $H^+$  migration. As a result, the acid permeability of this membrane was  $19 \times 10^{-3}$  m/h, which is slightly higher than that of quaternized PPO ( $U_H = 13 \times 10^{-3}$  m/h). In addition, a semi-interpenetrating network-based AEM was

synthesized by Cheng [65] from polyvinyl chloride (PVC), dimethylaminoethyl methacrylate (DMAM) and divinylbenzene (DVB) via polymerization and quaternization for HCl recovery. The presence of  $-\text{COOH}$  groups from DMAM could accelerate the migration of  $\text{H}^+$ , and as a result, the membrane exhibited high acid permeability ( $U_H = 40 \times 10^{-3}$  m/h).

On the other hand, the acid-alkali ion pair could form a hydrogen bonding network that enhances the migration of  $\text{H}^+$ . Polyvinyl alcohol (PVA) has been widely used as a polymer backbone to prepare AEMs with enhanced acid permeability due to its high content of  $-\text{OH}$  groups [66]. Mondal [32] prepared a PVA-based AEM mixed with quaternary aromatic amine groups from quaternary 4,4'-(1,1'-biphenyl-4,4'-diylidioxy)dianiline (QBAPB) for HCl recovery via DD. The presence of  $-\text{OH}$  groups in QBAPB and PVA allowed the formation of a hydrogen-bonded network, which accelerated the migration of  $\text{H}^+$ . Emmanuel [67] synthesized a PVA-based membrane modified with 1,4-diazabicyclo [2,2,2]octane (DABCO). The results showed that the membrane had good acid permeability ( $U_H = 45 \times 10^{-3}$  m/h). The hydrogen-bonded network constructed from the  $-\text{OH}$  groups of PVA and the N atoms of DABCO also enhanced the migration of  $\text{H}^+$ . In addition, Yadav [68] prepared a PSF-based membrane by incorporating neem leaves powder (NP) for acid recovery. The NP contained many functional groups, such as  $-\text{COOH}$  and  $-\text{OH}$ . These groups could form a hydrogen bond network, facilitating the migration of  $\text{H}^+$ .

### 3.3. Membrane Structure

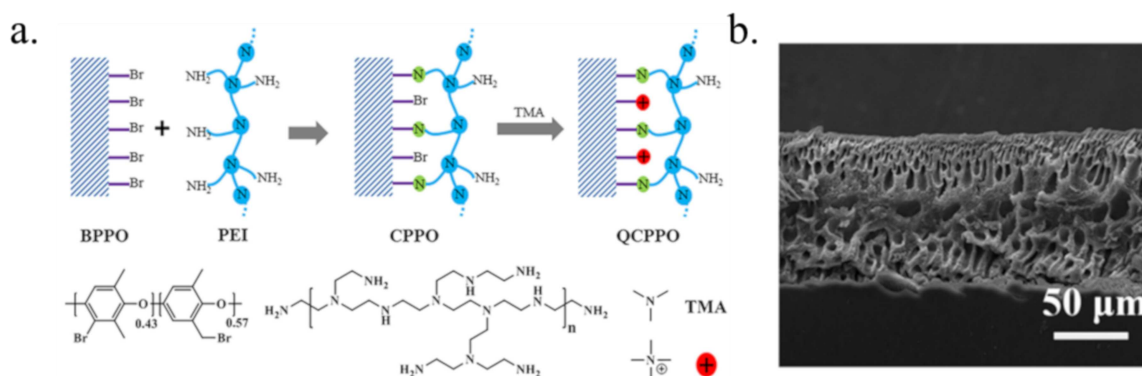
Considering the low ion migration resistance due to the presence of gaps in the membrane, preparing porous membranes is one strategy for improving acid permeability [69]. The pores can provide channels for ion migration with less resistance. Recently, in DD for acid recovery, porous membranes have also attracted much attention.

The first porous membrane is pore-filled AEMs, which are prepared by soaking a porous substrate into the monomer mixture followed by a radical polymerization process. As a result, a guest polyelectrolyte gel is introduced into the pores of a host polymer [70–72]. Chava [73] prepared a pore-filled AEM by filling the microporous substrate of polypropylene (PP) with organosiloxane-based organic-inorganic hybrid anion exchange microgels. The membrane showed a higher  $\text{HNO}_3$  permeability compared to the commercial Selemion membrane, which is a dense and aminated polysulfone membrane. This is because the PP-based pore-filled membrane had thin and dense layers at surfaces and a porous interior, which was effective for acid diffusion. In addition, Kim [74] prepared a pore-filled AEM using porous polyethylene (PE) as the substrate for  $\text{H}_2\text{SO}_4$  recovery from the  $\text{FeCl}_3\text{-H}_2\text{SO}_4$  solution. The acid permeability of this pore-filled AEM is almost triple as high as that of the dense membrane Neosepta-AFX which is aminated polystyrene-co-divinylbenzene.

The second porous membrane is an ultrafiltration membrane prepared by the phase-inversion method containing a thin surface layer and a microporous supporting substrate [75]. The polymers commonly used as substrates to prepare ultrafiltration membranes are PPO or PSF [47,76]. Lin [77] prepared a PPO-based ultrafiltration AEM modified with polyethyleneimine (PEI) and aminated with trimethylamine (TMA) shown in Figure 5a. There are plenty of pores which do not penetrate through the whole membrane but could accelerate the migration of acid (Figure 5b). Compared to the commercial DF-120 membrane, the optimal BPPO-based ultrafiltration membrane after modification and amination exhibited 6.4 times higher HCl permeability. Similarly, Sun and his coworkers [78] also prepared a PPO-based ultrafiltration AEM that contained  $-\text{COOH}$  and quaternary ammonium groups. Compared to the acid permeability of the dense PPO-based membrane bearing both quaternary nitrogen and  $-\text{COOH}$  groups ( $U_H = 5\text{--}19 \times 10^{-3}$  m/h) [64], this porous membrane exhibited a higher acid permeability ( $U_H = 20\text{--}25 \times 10^{-3}$  m/h). Asymmetrically porous AEMs based on PSF and modified with N,N,N',N'-tetramethyl-1,3-propanediamine (TMPDA) were prepared by Lin [47]. The membranes showed excellent acid permeability of  $65 \times 10^{-3}$  m/h, which was 6.6 times higher than that of the commercial DF-120 membrane. This was because this membrane possessed a supporting layer with an appropriate number of pores and a selective layer thickness of 0.5–0.6  $\mu\text{m}$ , which was notably thinner



than that of conventional compact membranes, resulting in reduced resistance in the migration of  $H^+$ . In addition, Jyothi [79] used the phase-inversion process to prepare a PSF-based porous membrane by incorporating different contents of eggshell membrane (ESM) power to recover HCl from  $FeCl_2$ -HCl solutions. The acid permeability of this membrane was approximately 5.55 times higher than that of the commercial DF-120 membrane due to the porous structures.



**Figure 5.** The preparation of the BPPO-based ultrafiltration membrane after modification and amination (a) and the cross section from SEM of the BPPO-based ultrafiltration membrane after modification and amination for 2 h (b) [77].

The third porous membrane is a kind of nanofiber AEM prepared by electrospinning and posttreatment. Pan [80] prepared novel nanofiber AEMs from a quaternized PPO/silicon dioxide hybrid material. The acid permeability of the nanofiber membrane prepared by electrospinning and posttreatment is 1.3 times that of the membrane prepared by the conventional casting method. The loose microscale structure of the membrane could facilitate acid permeability better than that of the compact membrane.

#### 4. Acid Selectivity

Excellent acid selectivity is a key factor for collecting high-quality acid products during DD so that they can be reused in the steel or metal refining industry. The type of functional groups and the size-sieving effect have main influence on improving acid selectivity in the DD process.

##### 4.1. Alkaline Functional Groups for Selectivity

The functional groups in the AEMs not only affect the acid permeability mentioned in Section 3.1 but also influence the acid selectivity during DD.

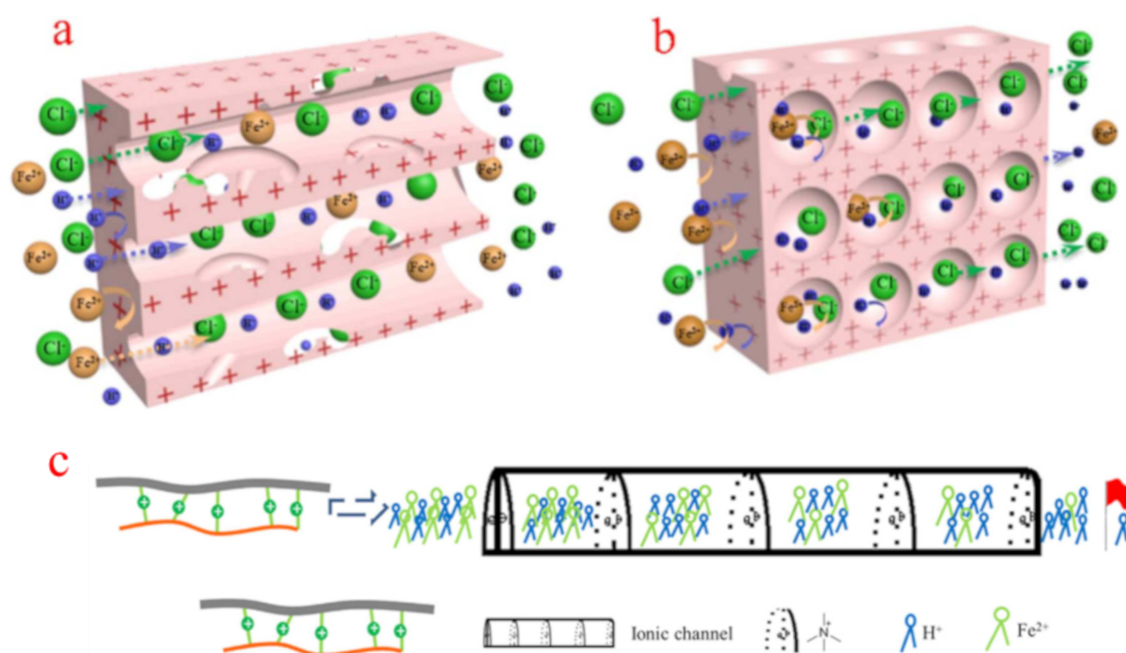
According to the mechanism of acid recovery using AEMs in the DD process, alkaline functional groups can allow anion migration and block cations due to their positive charge. However, the electrostatic repulsion between the groups and  $H^+$  is lower than that between the groups and metal ions owing to the small size, low valence state and high mobility of  $H^+$  [81]. Hence,  $H^+$  and metal ions can be effectively separated during DD.

Firstly, different alkaline functional groups show different electrostatic repulsions to cations, resulting in different acid selectivities. Pyridinium was used to modify the PVA-based AEM for HCl recovery from  $FeCl_2$ -HCl solutions [82]. In addition, Emmanuel prepared an imidazolium functionalized PVA-based AEM for acid recovery [83]. Compared to the acid selectivity of the PVA-based membrane functionalized by quaternary ammonium groups ( $S = 21$ ) [84], both the PVA-based AEM modified with pyridinium ( $S = 58$ ) and the PVA-based AEM modified with imidazolium ( $S = 53$ ) exhibited higher acid selectivities. Khan [61] also prepared a pyridinium functionalized PPO-based AEM to recover acid. The membrane showed an excellent acid selectivity of 78, which was higher than that of the commercial DF-120B membrane ( $S = 24$ ), which is a quaternized PPO-based membrane with

polyester as the substrate [49]. Pyridinium and imidazolium are promising functionalized materials for AEMs to improve acid selectivity during DD. In addition, Pyrrole has an excellent affinity for anions and repulsion for cations [74], and therefore the AEM modified by pyrrole might show a good acid selectivity. Kim [85] used pyrrole to modify surfaces of the commercial AEM, Neosepta-AFX. The acid selectivity of Neosepta-AFX modified by 5 vol.% pyrrole was almost twice higher than the original Neosepta-AFX.

Secondly, the density of the functional groups in the membrane can influence the acid selectivity. Cheng synthesized a series of PVA-based AEMs by grafting different contents of allyltrimethylammonium chloride with a large number of quaternary ammonium groups to recover HCl from FeCl<sub>2</sub>-HCl solutions [66]. The grafting ratio (GR) was correlated with the content of quaternary ammonium groups. The results showed that the acid selectivity improved with increasing GR in the range of 8–26%. A higher content of quaternary ammonium groups in the membrane resulted in stronger electrostatic repulsion of cations. Electrostatic repulsion has a greater influence on Fe<sup>2+</sup> migration than on H<sup>+</sup> migration. Hence, higher acid selectivity ( $S = 23$ ) was obtained at a higher GR (26%).

Thirdly, the morphology of the AEM could also influence the acid selectivity. Ge and coworkers [86] prepared PPO-based porous membranes with different pore structures functionalized with quaternary ammonium groups. The acid selectivity for the AEM with a sponge-like pore structure is eight times higher than that of the membrane with finger-like pore structures. Compared to the AEM with finger-like pores, the sponge-like pores were disconnected from each other in the AEM, leading to the formation of a multilayered barricade in the migration path of ions (Figure 6a,b). Ions need to pass through more functional groups in the AEM with sponge-like pores. Hence, the AEM with a sponge-like structure will possess better acid selectivity.



**Figure 6.** Plausible physical model of ions transferred in the finger-like (a) sponge-like structures during the DD process (b) and the separation of H<sup>+</sup> and Fe<sup>2+</sup> through the quaternary ammonium groups-based ionic channel (c) [86,87].

Finally, the position and arrangement of the functional groups can influence the acid selectivity. Xu [22,57] found that the acid selectivity increases to a greater extent with aryl substitution by quaternary ammonium groups than benzyl substitution with the same groups in the PPO-based membrane, as shown in Figure 4g. In addition, Ge [87] prepared a PPO-based AEM functionalized with quaternary ammonium groups arranged in a more linear manner. Briefly, the BPPO was crosslinked by multiamine oligomers, forming an ionic column area full of quaternary ammonium groups between the BPPO and the multiamine oligomer (Figure 6c). As a result, the high acid selectivity for an AEM was obtained (approximately  $S = 2074$ ), which is dramatically higher than that of commercial AEMs. Every quaternary ammonium group is an exclusion site, and the linearly arranged quaternary ammonium groups form a connective ionic channel to continuously separate  $H^+$  and metal ions.

#### 4.2. Acid-Alkali Functional Groups for Selectivity

Incorporating both acid and alkaline functional groups into the polymer backbones can also be used to enhance acid selectivity [88]. Polyelectrolyte complexes (PECs)/PVA membranes containing  $-N^+(CH_3)_3$  and  $-SO_3^-$  were prepared by Wang [44] for HCl recovery. On the one hand, the hydrogen bonding network from the  $-OH$  of the PVA could facilitate the migration of  $H^+$  better than the metal ions. On the other hand, the presence of acid groups in the membrane may lead to a charge neutralization microphase, which could improve the migration of cations with low resistance. However, the promotion of the migration of metal ions might be less obvious due to their larger size and higher valence compared to  $H^+$ . The results showed that the acid selectivity of this PECs/PVA membrane was in the range of 57–90, which was higher than that of the membrane without  $-SO_3^-$  ( $S = 40$ ).

#### 4.3. Size-Sieving Effect

The size-sieving effect is based on the different sizes of the metal ions and  $H^+$ . If the sizes of the pores in the membrane are between the sizes of the metal ions and  $H^+$ ,  $H^+$  can migrate through the pores, while the larger metal ions might be blocked by these pores. Sun [89] used the sieving effect of graphene oxide (GO) nanocapillaries to separate  $Fe^{3+}$  and  $H^+$ . The GO membrane showed a layered structure that could block ions with hydrated radius larger than 4.5 Å. Therefore,  $Fe^{3+}$ , which has a hydrated radius of 4.57 Å, could be confined by the GO membrane, while  $H^+$  could migrate via the hydrogen bonding network in the GO membrane with less resistance. As a result, the migration rate of  $H^+$  was two orders of magnitude larger than that of  $Fe^{3+}$ .

Obviously, the size-sieving effect influences the separation of  $H^+$  and the metal ions and is applied in many fields, such as the separation of monovalent and multivalent ions [90], desalination [91], and gas separation [92]. However, applications of the size-sieving effect in acid recovery are limited, and further investigations could focus on relevant materials, including carbon nitride, layered double hydroxide, metal organic frameworks, and covalent organic frameworks.

The acid permeabilities and selectivities for  $H^+$  over metal ions of the reported membranes are listed in Table 3. The porous membranes and the AEMs with acid-alkali functional groups exhibited a higher acid permeabilities (such as the BPPO-based AEM modified by PEI and TMA [77] and the PSF-based AEM [47]) or selectivities (such as the PPO-based AEM with quaternary nitrogen and  $-COOH$  groups [64] and the PECs/PVA AEM [44]). However, Table 3 shows that many membranes show a trade-off effect, which means that membranes with excellent acid permeability exhibit poor acid selectivity and vice versa. Hence, solving these problems will require further study.

**Table 3.** The comparison of the comparison of dialysis coefficient ( $U_H$ ) and selectivity ( $S$ ) for  $H^+$  over metal ions of the reported membranes at 25 °C.

Membrane	Structure	$U_H$ ( $10^{-3}$ m/h)	$S$	Simulated Solution System
Commercial Neosepta-AFX [85]	Dense	4	25	0.05 M $FeCl_3$ –2 M $H_2SO_4$
Commercial DF-120 [44]	Dense	4	19	0.25 M $FeCl_2$ –1.0 M HCl
Neosepta-AFX modified with 5 vol.% pyrrole [85]	Dense	4	48	0.05 M $FeCl_3$ –2 M $H_2SO_4$
BPPO-based AEM crosslinked with a multi-amine oligomer [87]	Dense	9	2074	0.59 M $FeSO_4$ –1.03 M $H_2SO_4$
The pore-filled AEM with PE and polypyrrole [74]	Porous	10–11	36–54	0.05 M $FeCl_3$ –2 M $H_2SO_4$
The quaternized BPPO AEM [57]	Dense	3–13	H/Fe: 40 H/Ti: 70	0.15 M $TiO_2$ –0.17 M $FeSO_4$ –0.25 M $H_2SO_4$
The PPO-based AEM with quaternized nitrogen and –COOH groups [64]	Dense	5–19	73–390	0.25 M $FeCl_2$ –1.0 M HCl
The PVA-based AEM modified by pyridinium [82]	Dense	17–25	31–58	0.25 M $FeCl_2$ –1.0 M HCl
The BPPO-based AEM with sponge-like pores [86]	porous	15–20 22–28	81–665 100–2033	0.21 M $FeCl_2$ –1 M HCl 0.46 M $AlCl_3$ –2.12 M HCl
The PECs/PVA AEM [44]	Dense	3–23	40–90	0.25 M $FeCl_2$ –1.0 M HCl
The PPO-based ultrafiltration AEM containing –COOH groups and quaternary ammonium [78]	Porous	20–25	28–46	0.25 M $FeCl_2$ –1.0 M HCl
The PVC-based AEM immobilized by DMAM and DVB [65]	Dense	12–40	36–61	0.18 M $FeCl_2$ –0.81 M HCl
The nanofiber AEM [80]	Porous	41	50	0.225 M $FeCl_2$ –1 M HCl
PANI-based AEM [56]	Porous	32	20	5% $FeCl_3$ –3.5 M HCl <sup>–</sup>
A-PANI-based AEM [56]	Porous	42	17	5% $FeCl_3$ –3.5 M HCl <sup>–</sup>
The PVA-based AEM modified by multisilicon copolymers [63]	Dense	10–43	22–39	0.12 M $FeCl_2$ –1 M HCl
The double quaternization PVA-based membrane [67]	Dense	30–45	21–32	0.25 M $FeCl_2$ –1.0 M HCl
ESM/PSF membrane [79]	Porous	10–46	33–93	0.125 M $FeCl_2$ –0.5 M HCl
NP/PSF membrane [68]	Porous	47	154	0.125 M $FeCl_2$ –0.5 M HCl
Imidazolium functionalized PVA-based AEM [83].	Dense	19–48	13–53	0.25 M $FeCl_2$ –1.0 M HCl
The BPPO-based AEM modified pyrrolidinium [50]	Dense	18–49	36–66	0.18 M $FeCl_2$ –0.81 M HCl
PVA-based AEMs by grafting different contents of allyltrimethylammonium chloride [66].	Dense	17–60	8–26	0.18 M $FeCl_2$ –0.81 M HCl
The PSF-based AEM [47]	Porous	65	34	0.2 M $FeCl_2$ –1 M HCl
The BPPO-based AEM modified MP [61]	Dense	11–66	25–78	0.25 M $FeCl_2$ –1 M HCl
The PPO-based ultrafiltration AEM modified by PEI and TMA [77]	Porous	56–70	11–21	0.2 M $FeCl_2$ –1 M HCl

## 5. Trade-Off Effects between Acid Permeability and Selectivity

Though many approaches were used to improve the properties of AEMs for acid recovery during DD, there are trade-off effects between these properties, which limits the application of these AEMs in industry [93]. The common trade-off effect is between acid permeability and selectivity [94]. Ji [62] prepared a series of PPO-based AEMs with quaternary tris(2-(2-methoxyethoxy)ethyl)amine (TDA). The water uptake of the membranes increased with increasing ion exchange capacity. As a result, these AEMs exhibited dialysis coefficients of  $H^+$  ranging from  $2 \times 10^{-3}$  to  $60 \times 10^{-3}$  m/h with increasing TDA in the membranes, while the acid selectivity dropped from 1682 to 19. It showed an extreme imbalance between acid permeability and selectivity. The same trade-off effect is also seen in porous AEMs where the pores could improve the acid permeability at the expense of the acid selectivity [77].

As mentioned above, the incorporation of acid functional groups could enhance both the acid permeability and selectivity, as stated in Parts 3.2 and 4.2, due to the formation of hydrogen bonding networks for the migration of  $H^+$ . In addition, acid functional groups, such as carboxylic acids, have a stronger affinity for high valent metal ions via electrostatic attractions, obstructing the migration of the metal ions in the AEM [95]. Ran [96] prepared an AEM by adding graphene oxide (GO) sheets with a high content of acid functional groups into imidazolium functionalized BPPO for HCl recovery from  $FeCl_2$ –HCl solutions. The GO sheets act as auxiliary phases, which are key to overcome the trade-off

effects. On the one hand, the GO sheets with high contents of  $-OH$  and  $-COOH$  groups could provide channels for the migration of  $H^+$ . On the other hand, the GO sheets could act as a barrier for  $Fe^{2+}$  due to the interactions between  $Fe^{2+}$  and those groups on the GO sheets. Hence, the membrane showed high acid permeability ( $U_H = 3 \times 10^{-2}$  m/h) and selectivity ( $S = 200$ ). In addition, although it was not mentioned in the paper, the GO sheets might obstruct the mobility of  $Fe^{2+}$  due to their large sizes and high valences to some extent.

Inspired by the above work, AEMs could be mixed with certain materials, such as metal organic frameworks or covalent organic frameworks, as both auxiliary materials for the migration of  $H^+$  and barriers for the mobility of metal ions to overcome the trade-off effects.

## 6. Membrane Stability

The excellent stability is another crucial parameter for application, as it determines the lifetime of the AEM [97]. Hence, researchers have made efforts to improve the stability of AEMs so that they can be used in DD for acid recovery for a long time.

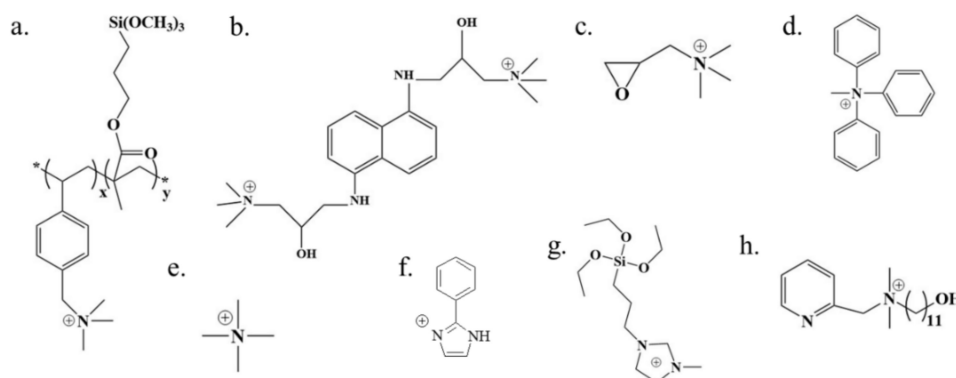
### 6.1. Types of Functional Groups

The types of functional groups can influence the stability of AEMs, such as the quaternary ammonium groups used in AEMs, which result in inferior thermal and chemical stability. Mao [98] studied erosion effect for the AEM containing quaternized PPO. The results showed that the structure of this membrane was damaged mainly through the loss of quaternary ammonium groups. To overcome this deficiency of the quaternary ammonium groups, researchers modified the quaternary ammonium groups or replaced it with other alkaline functional groups in the AEMs.

On the one hand, the presence of aromatic groups on the quaternary ammonium groups could increase their mechanical and thermal stability. Wu [99] used vinylbenzyl chloride (VBC) as the monomer to prepare a quaternary multialkoxo silicon copolymer poly(VBC-co- $\gamma$ -MPS) (Figure 7a), and then incorporated it into PVA to prepare a PVA-based AEM. Irfan [100] prepared a PVA-based AEM modified by quaternary 1,5-diaminonaphthalene (Q-DAN, Figure 7b). The presence of aromatic groups in poly(VBC-co- $\gamma$ -MPS) and Q-DAN enhanced the thermal and mechanical stabilities of the AEM. Compared to the PVA-based AEM modified with glycidyl trimethyl ammonium chloride (Figure 7c) with a thermal degradation temperature ( $T_d$ ) of 218 °C [84], the PVA-based AEM modified with poly(VBC-co- $\gamma$ -MPS) and Q-DAN showed higher thermal stabilities with  $T_d$  values of 270 °C and 280 °C, respectively. Khan [49] prepared a PPO-based porous membrane modified with quaternary aromatic amine groups (Figure 7d). Compared to the PPO-based porous membrane functionalized with quaternary ammonium groups (Figure 7e) without aromatic groups ( $T_d = 164.2$  °C) [78], the membrane exhibited a higher thermal stability (thermal degradation temperature ( $T_d = 179$  °C)). Besides, Khan [101] prepared a series of PPO-based AEMs modified by phenylimidazole groups (Figure 7f). The results showed that these AEMs exhibited excellent acid stability.

On the other hand, using other alkaline functional groups instead of the quaternary ammonium groups can be used to overcome the problem of poor stability. Emmanuel [83] used 1-methyl imidazole to synthesize an anion exchange silica precursor (AESP, Figure 7g) and then prepared PVA-based membranes modified by AESP. The prepared membrane from AESP and PVA has excellent physicochemical stabilities compared to those of the quaternary ammonium group-based AEMs due to the imidazole rings. Besides, the presence of heterocyclic aromatic amines could improve the chemical and thermal stabilities of the prepared AEMs because they are more chemically and thermally stable than aliphatic amines. Irfan [102] incorporated quaternary 1-hydroxy-N,N-dimethyl-N-(pyridine-2-ylmethyl) methanaminium (QUDAP, Figure 7h) into PVA to prepare an AEM for HCl recovery. The AEM showed good flexibility owing to the long alkyl chain in QUDAP, which could remain slightly relaxed in the membrane matrix. The results showed that the thermal stability of the AEMs increased as QUDAP increased. In addition, the alkylation of

hydrocarbons with long chains in heterocyclic aromatic amines could not only maintain stability but also enhance the flexibility of the membrane [82].

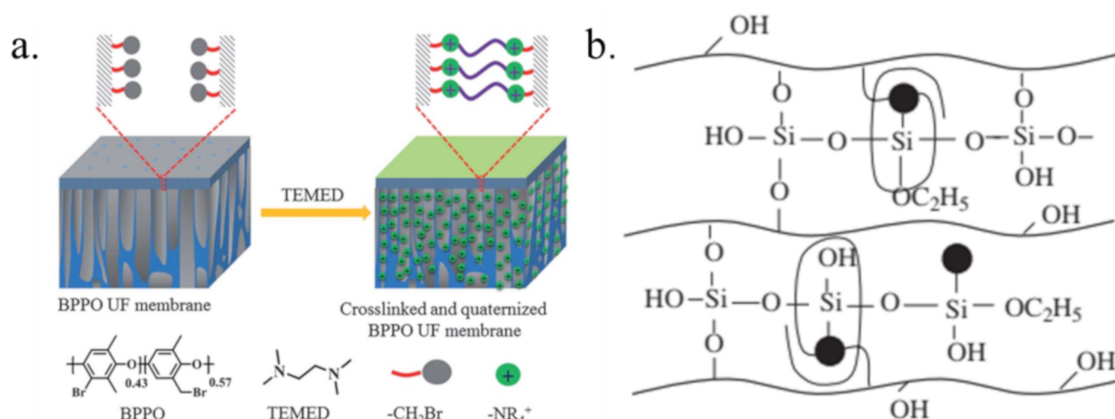


**Figure 7.** The structure of (a) quaternized poly(VBC-co- $\gamma$ -MPS), (b) Q-DAN, (c) glycidyl trimethyl ammonium chloride, (d) quaternary aromatic amine groups, (e) quaternary ammonium, (f) phenyl imidazole, (g) AESP (h) QUDAP [49,78,83,84,99–102].

### 6.2. Crosslinking and Incorporating Inorganic Components

The ion exchange capacity and water uptake could be enhanced as the functionalization degree increased, which might result in severe swelling behavior [103].

One effective strategy for solving this problem and improving membrane stability is crosslinking [104,105]. Wu [106] studied the properties of PVA-based AEMs crosslinked by different crosslinking agents, such as small alkoxy silanes (tetraethoxysilane (TEOS),  $\gamma$ -glycidoxypropyltrimethoxysilane (GPTMS), monophenyltriethoxysilane (EPh)) and copolymers (glycidylmethacrylate (GMA) and methacryloxypropyl trimethoxy silane (MPS)). As a result, the AEM crosslinked by poly(GMA-co-MPS) with multi-epoxy, alkoxy silicon ( $-\text{Si}(\text{OCH}_3)_3$ ) groups and long chains demonstrated outstanding tensile properties and high stabilities. Lin [107] prepared a porous BPPO ultrafiltration AEM crosslinked and quaternized by N,N,N',N'-tetramethylethylenediamine (TEMED), as shown in Figure 8a. The membrane showed no weight loss after immersion in hot acidic feed solution for 7 days and showed excellent thermal stability. In Wu's work [108], the quaternized PPO and PVA-based AEM was crosslinked with double crosslinking agents, including monophenyl triethoxysilane (EPh) and tetraethoxysilane (TEOS), for HCl recovery (Figure 8b). The swelling behavior was generally restrained, and the thermal stability of the membrane increased as the crosslinking degree between the organic and inorganic phases increased.



**Figure 8.** Schematic diagram of the preparation of crosslinked and quaternized BPPO ultrafiltration membrane (a) and the structure of quaternized poly(2,6-dimethyl-1,4-phenylene oxide) (QPPO) and PVA-based membrane (b) [107,108].

Although the AEMs with a high crosslinking degree show excellent stability, their compact structure, and the loss of functional groups due to crosslinking can reduce the acid permeability. Fortunately, there are other approaches used to improve stability, such as introducing inorganic materials into the membrane. Sharma [109] prepared PVA-based AEMs with different contents of functionalized graphene nanoribbons (f-GNRs) for HCl recovery from FeCl<sub>2</sub>-HCl solutions. The results showed that the membrane exhibited excellent stability and less swelling because f-GNR not only exhibited a high stability but could also be considered to be a filler for the polymer matrix and reduce its free volume, which resulted in a denser membrane. In addition, the acid permeabilities increased by the presence of f-GNRs in the AEMs and the dialysis coefficient is  $53 \times 10^{-3}$  m/h when the concentration of the f-GNR is 0.1 wt.%.

## 7. The Integration of Diffusion Dialysis with Other Technologies

The DD process still shows a limited processing capability for acid recovery due to the restriction of the equilibrium concentration. Hence, it is necessary to integrate diffusion dialysis with other technologies such as pressure, electric fields and continuous processes to overcome the limitation and improve the efficiency of the acid recovery [26,110,111].

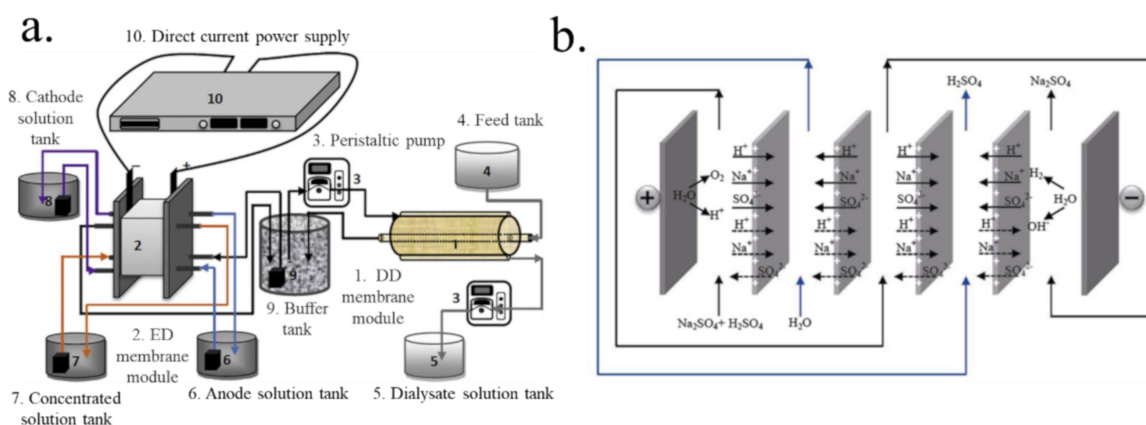
### 7.1. The Integration of Diffusion Dialysis with Pressure

In the DD process, the acid concentration achieved in the receiving solution is too low for reuse. Furthermore, water might be transported from the receiving side to the feed side due to the osmotic pressure difference between the sides, which reduces the concentration on the feed side, resulting in a driving force for the lower mass transport. Hence, using pressure as the auxiliary to drive the migration of acid in the DD process could achieve a higher acid concentration in the receiving side and prevent water osmosis [112]. Yun [113] used thermally cross-linked branched polyethyleneimine (b-PEI) with strong positive charges to coat the surface of a polyethersulfone (PES) nanofiltration membrane for the recovery of HCl from MgCl<sub>2</sub>, MgSO<sub>4</sub>, NaCl or Na<sub>2</sub>SO<sub>4</sub> solution. The results showed that the membrane exhibited excellent rejection of metal ions, especially Mg<sup>2+</sup> (95%) at 30 bars of pressure. Furthermore, the membrane showed good stability and could maintain selective acid permeability for a month. Zhang [114] proposed a pressure-concentration double-driven DD process to recover H<sub>2</sub>SO<sub>4</sub> from FeSO<sub>4</sub>-H<sub>2</sub>SO<sub>4</sub> solution using a commercial DF-120 membrane. As a result, the dialysis coefficient of H<sup>+</sup> increased from  $12 \times 10^{-4}$  to  $39 \times 10^{-4}$  m/h as the pressure ranged from 0 to 0.08 MPa, while the acid selectivity remained at an acceptable value ( $S \approx 65$ ). Moreover, the use of pressure could prevent osmosis from the receiving side to the feed side.

In summary, pressure-assisted DD uses an additional driving force to enhance the acid recovery performance in practical applications, especially for feed solutions with low acid concentrations.

### 7.2. The Integration of Diffusion Dialysis with an Electric Field

Using an electric field as an extra driving force in DD could overcome the disadvantage of DD. One method is integrating electrodialysis (ED) and DD to recover acid. As a common membrane technology-based ion exchange membrane, ED is widely used in the separation of ions driven by electrical fields [115–117]. Zhang [118] integrated DD and ED to recover HCl from simulated chemosynthesis aluminum foil wastewater, as shown in Figure 9a. The results showed that the integration of ED and DD was a more effective method to recover HCl than DD alone. This is because the integration could not only save water but also recover high purity HCl, which could be directly reused. In addition, Zhang [119] used a weak electric field as a secondary driving force in DD to improve the performance of H<sub>2</sub>SO<sub>4</sub> recovery from Na<sub>2</sub>SO<sub>4</sub>-H<sub>2</sub>SO<sub>4</sub> solutions using the DF-120 membrane (Figure 9b). There were one or many repeating AEMs in the weak-electric-field-assisted DD stack, which was different from the ED stack with cation-and-anion exchange membranes. In addition, the acid permeability in the weak-electric-field-assisted DD process was higher than that in DD alone, and the energy consumption was relatively low.



**Figure 9.** Flow chart of experimental apparatus (a). The schematic representation of the ED assisted DD stack (b) [118,119].

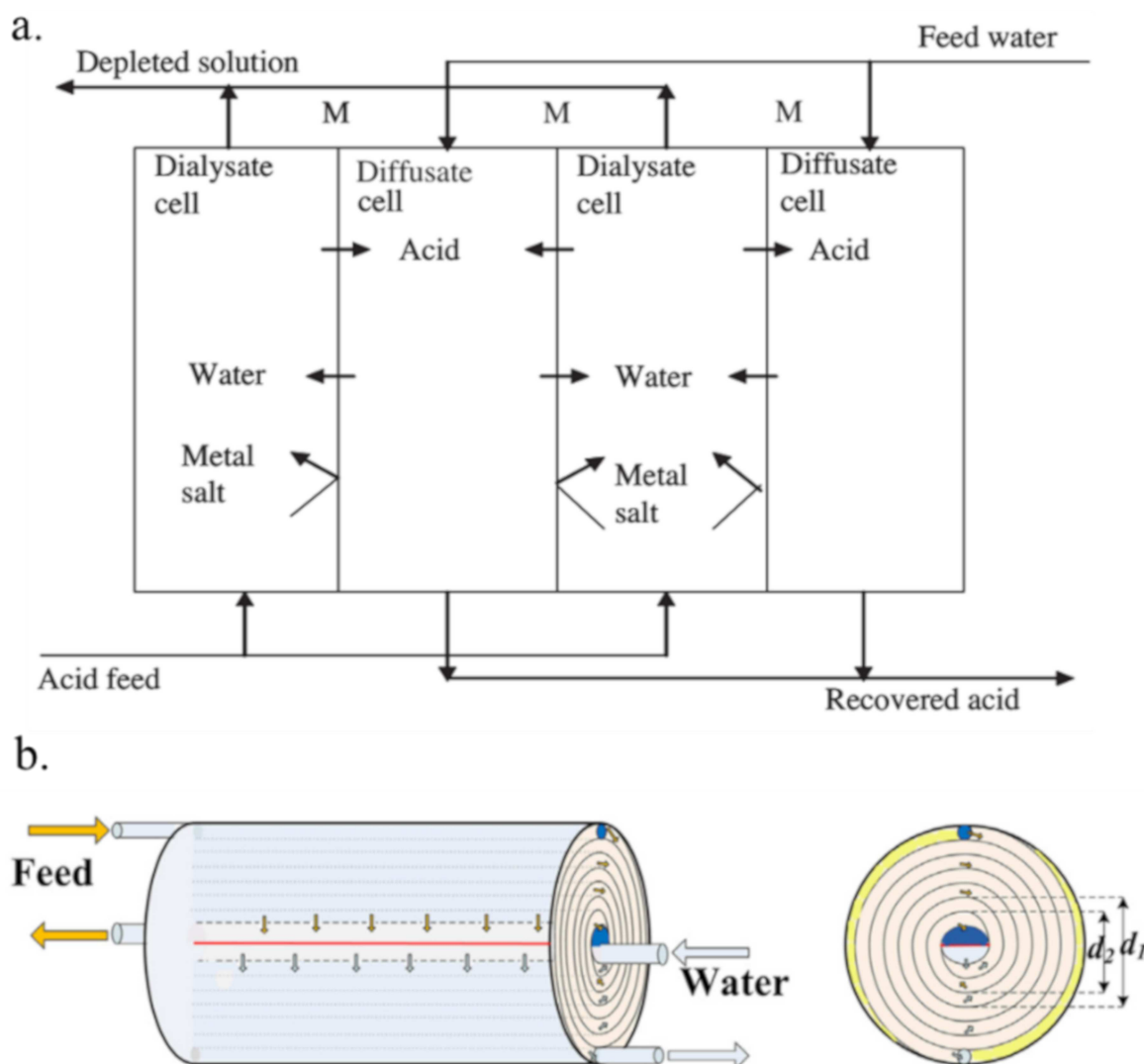
### 7.3. The Integration of Diffusion Dialysis with a Continuous Process

The reported acid recoveries using AEMs in DD were mainly obtained in a batch dialyzer. However, there is limited capacity for acid recovery in the batch dialyzer due to the limited membrane area for the migration of acid in practical applications [120]. Compared to the batch dialyzer, a continuous dialyzer for acid recovery exhibits various advantages, such as higher productivity, smaller sized dialysis equipment, lower costs and easier operation, and continuous processes could be appropriate for practical production [33,121,122].

The plate-and-frame diffusion dialysis (PFDD, Figure 10a) module is one kind of continuous dialyzers which is comprised of a series of flat membrane sheets to enhance the effective areas for acid recovery [123]. Li [124] recovered  $H_2SO_4$  from acid leaching solution (containing metal ions such as V, Al and Fe ions) using a PFDD module with the commercial DF-120 membrane. As a result, the recovery ratio of  $H_2SO_4$  and the rejection of V, Al and Fe ions reached 84 wt.%, 93 wt.%, 92 wt.%, and 85 wt.%, respectively, at a flow rate of  $2.1 \times 10^{-3} \text{ m}^3/\text{h m}^2$  and flow rate ratio of water to feed of 1.1–1.3 at 25 °C. The flow rate and water flow rate ratio are important parameters which influence the transport efficiency of acid diffusion process. Generally, with the increasing of the flow rate, the acid recovery efficiencies increase and get a maximum initially, and then decrease [123,124]. At a low flow rate of the feed solution, the processing capacity is low, and the water reverse osmosis phenomenon is enhanced due to the concentration polarization. However, a high flow rate is also not beneficial to the acid recovery efficiency, due to the short retention time for proton migration. In this situation, the time is not sufficient and only small parts of feed element could permeate the membrane, resulting in a decrease for the acid recovery ratio [125,126]. Hence, it is necessary to find an appropriate flow rate to get a high acid recovery ratio. For the flow rate ratio of water to feed, the acid recovery usually increases when the water flow rate ratio increases. However, this increase is not linear at higher water flow rate ratios because of the damage of the diffusion boundary layers between the membrane and the solution interface [21]. Besides, the metal ions rejection usually decreases at high water flow rate ratios [123]. Hence, it is also essential to optimize the water flow rate ratio to obtain a high efficiency recovery for acid using DD processes. Kim [123] also studied the recovery of  $H_3PO_4$  from a mixed acid solution (containing Al ions) using a PFDD module that contained four diffusate cells divided by three AEMs. In this work, 85 wt.%  $H_3PO_4$  could be recovered by DD, while 3.68 mg/kg of Al ions could leak into the diffusate cell. In addition, some mathematical models have been developed to describe the performance of continuous DD with AEMs for acid recovery. In Palatý's work [127], the recovery of  $H_2SO_4$  from a  $H_2SO_4$ - $Na_2SO_4$  mixture was studied in a two-cell counter current dialyzer equipped with a commercial Neosepta-AFN membrane at steady operation. Then, a rigorous mathematical



model was developed to describe both the convective transport in the cells and the transport of  $\text{H}_2\text{SO}_4$  and  $\text{Na}_2\text{SO}_4$  through the AEM and liquid films.

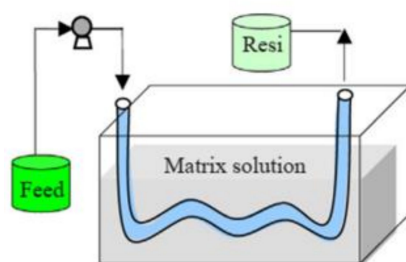


**Figure 10.** Scheme of Plate-and-frame diffusion dialysis (PFDD) module (a) and spiral wound diffusion dialysis (SWDD) module (b) [123,128].

However, the PFDD module has some disadvantages, including a complicated assembly process, bulky equipment, and limited mass transfer [128]. Another type of module, a spiral wound diffusion dialysis (SWDD, Figure 10b) module, which uses a long, flat membrane piece curled into a spiral together with partitions in the DD process for acid recovery. The SWDD module exhibits merits such as a smaller equipment size, relatively higher acid recovery and convenient transportation [128]. Zhang [126] recovered HCl from a HCl– $\text{AlCl}_3$  solution using a SWDD module with DF-120. Compared to the PFDD module, the SWDD module exhibited a relatively high acid recovery ratio (84.3 wt.%), low Al ion leakage ratio (less than 4 wt.%) and a similar time to reach equilibrium (3 h). However, the SWDD module is difficult to disassemble, check and replace due to the sealing of the two sides of the AEM with glue to prevent the leakage of the solution [129].

Hence, inspired by “blood vessels” from a biological perspective, another module comprising tubular AEMs immersed in the solution was designed for acid recovery in DD. The hollow-fiber AEM was synthesized from BPPO and 1-methyl-2-pyrrolidone (NMP) by Xu and then aminated by dimethylethanolamine (DMEA) and trimethylamine [130]. Considering that the hollow-fiber-type

dialyzers are more effective than the PFDD and SWDD modules, the hollow-fiber AEM could have broad applications. In Ye's work [129], a PVA-based tubular membrane was prepared to recover HCl in semicontinuous (Figure 11). The semicontinuous process was performed by immersing the membrane into the static matrix solution (water) and flowing the feed solution through the membrane. The semicontinuous process exhibited energy savings, easy operation, and a high feed capacity with a high acid recovery ratio of 71.1–75.5 wt.%. The recovered HCl concentration and acid recovery ratio in the continuous process were 1.27 mol/L and 65.2 wt.%, respectively, which could be on par with those in the PFDD process with recovered acid concentrations of 0.54–1.01 mol/L and recovery ratios of 29.2–80.9 wt.%. However, the new module with a tubular membrane has not been fully studied and has some drawbacks in its preparation, but it could provide a novel strategy for recovering acid in practical applications.



**Figure 11.** The schematic diagram for the static semi-continuous process using the PVA-based tubular membrane (“Resi” means residual liquor)[129].

## 8. Summary and Perspective

Diffusion dialysis (DD), which offers low energy consumption, easy operation and environmental friendliness, was comprehensively applied in the area of acid recovery from acidic waste solutions. An anion exchange membrane (AEM) for DD with excellent properties, including acid permeability, acid selectivity and membrane stability, is an important factor that determines the efficiency and processing capacity of the acid recovery. Substantial effort was devoted by researchers to developing three main methods to improve the properties of AEMs: functionalizing the membrane, changing the structure of the membrane, adding other materials and/or crosslinking. Besides, the works on diminishing the trade-off effects of AEMs between acid permeability and selectivity and integration DD using AEMs with other technologies were made for acid recovery. By reviewing the many reported works, we propose the following problems and directions for further improvements in AEMs: (1) Chemicals with high stability and alkalinity can be used as modifiers to prepare AEMs with improved acid recovery and stability. (2) Materials with a size-sieving effect could be introduced into AEMs to enhance acid selectivity. (3) Acidic functional groups, such as  $-\text{COOH}$  and  $-\text{HSO}_3$ , have an excellent effect on the acid recovery of AEMs and could even overcome trade-off effects. Further research should be conducted to broaden the kinds of acid-alkali ion pair functional groups used in AEMs. In addition, the mechanism and interactions during the migration of ions in the AEM should be clearly explained using calculations and simulations. Besides, integrating with various technologies, such as pressure, an electric field, and a continuous process, into DD processes could enhance its processing capacity, which enhances its potential for industrial applications. Furthermore, comprehensive optimization of the DD process using AEMs for acid recovery from acidic waste solutions should consider the operational costs, product quality and so on.

**Author Contributions:** C.Z.: Investigation, Writing—Original draft preparation; W.Z.: Conceptualization, Writing—Review & Editing, Investigation, Methodology, Supervision; Y.W.: Supervision. All authors have read and agreed to the published version of the manuscript.

**Funding:** This work was supported by the National Natural Science Foundation of China (11705126).

**Conflicts of Interest:** The authors declare that there is no conflict of interest.

## Appendix A. List of Abbreviations

A-PANI	Poly(o-anisidine)
b-PEI	Branched polyethyleneimine
BPPO	Brominated poly(2,6-dimethyl-1,4-phenylene oxide)
DABVO	1,4-diazabicyclo[2,2,2]octane
DMAM	Dimethylaminoethyl methacrylate
DMEA	Dimethylethanolamine
DVB	Divinylbenzene
GMA	Glycidylmethacrylate
GO	Graphene oxide
NMP	1-methyl-2-pyrrolidone
MPS	Methacryloxypropyl trimethoxy silane
PANI	Polyaniline
PE	Polyethylene
PEI	Polyethyleneimine
PES	Polyethersulfone
PFDD	Plate-and-frame diffusion dialysis
PP	Polypropylene
PPO	Poly(2,6-dimethyl-1,4-phenylene oxide)
PSF	Polysulfone
PVA	Polyvinyl alcohol
PVC	Polyvinyl chloride
QBAPB	4,4'-(1,1'-biphenyl-4,4'-diylldioxy)dianiline
Q-DAN	Quaternary 1,5-diaminonaphthalene
QUDAP	Quaternary 1-hydroxy-N,N-dimethyl-N-(pyridine-2-ylmethyl) methanaminium
SWDD	Spiral wound diffusion dialysis
TDA	Tris(2-(2-methoxyethoxy)ethyl)amine
TEMED	N,N,N',N'-tetramethylethylenediamine
TMPDA	N,N,N',N'-tetramethyl-1,3-propanediamine

## References

1. Yang, C.-C.; Pan, J.; Zhu, D.-Q.; Guo, Z.-Q.; Li, X.-M. Pyrometallurgical recycling of stainless steel pickling sludge: A review. *J. Iron Steel Res. Int.* **2019**, *26*, 547–557. [[CrossRef](#)]
2. Foureaux, A.F.S.; Moreira, V.R.; Lebron, Y.A.R.; Santos, L.V.S.; Amaral, M.C.S. Direct contact membrane distillation as an alternative to the conventional methods for value-added compounds recovery from acidic effluents: A review. *Sep. Purif. Technol.* **2020**, *236*, 116251. [[CrossRef](#)]
3. Hogle, B.P.; Shekhawat, D.; Nagarajan, K.; Jackson, J.E.; Miller, D.J. Formation and Recovery of Itaconic Acid from Aqueous Solutions of Citraconic Acid and Succinic Acid. *Ind. Eng. Chem. Res.* **2002**, *41*, 2069–2073. [[CrossRef](#)]
4. Lin, C.S.K.; Du, C.; Blaga, A.-C.; Cămăruț, M.; Webb, C.; Stevens, C.V.; Soetaert, W. Novel resin-based vacuum distillation-crystallisation method for recovery of succinic acid crystals from fermentation broths. *Green Chem.* **2010**, *12*, 666. [[CrossRef](#)]
5. Rasrendra, C.B.; Girisuta, B.; Bovenkamp, H.V.D.; Winkelman, J.G.M.; Leijenhors, E.; Venderbosch, R.; Windt, M.; Meier, D.; Heeres, H. Recovery of acetic acid from an aqueous pyrolysis oil phase by reactive extraction using tri-n-octylamine. *Chem. Eng. J.* **2011**, *176*, 244–252. [[CrossRef](#)]
6. Ijmker, H.; Gramblicka, M.; Kersten, S.; Ham, A.V.D.; Schuur, B. Acetic acid extraction from aqueous solutions using fatty acids. *Sep. Purif. Technol.* **2014**, *125*, 256–263. [[CrossRef](#)]
7. Shin, C.-H.; Kim, J.; Kim, H.-S.; Lee, H.-S.; Mohapatra, D.; Ahn, J.-W.; Ahn, J.-G.; Bae, W. Recovery of nitric acid from waste etching solution using solvent extraction. *J. Hazard. Mater.* **2009**, *163*, 729–734. [[CrossRef](#)]
8. Lin, S.H.; Kiang, C.D. Chromic acid recovery from waste acid solution by an ion exchange process: Equilibrium and column ion exchange modeling. *Chem. Eng. J.* **2003**, *92*, 193–199. [[CrossRef](#)]
9. Moldes, A.B.; Alonso, J.L.; Parajó, J.C. Resin selection and single-step production and recovery of lactic acid from pretreated wood. *Appl. Biochem. Biotechnol.* **2001**, *95*, 69–82. [[CrossRef](#)]

10. Nenov, V.; Dimitrova, N.; Dobrevsky, I. Recovery of sulphuric acid from waste aqueous solutions containing arsenic by ion exchange. *Hydrometallurgy* **1997**, *44*, 43–52. [[CrossRef](#)]
11. Agrawal, A.; Sahu, K.K. An overview of the recovery of acid from spent acidic solutions from steel and electroplating industries. *J. Hazard. Mater.* **2009**, *171*, 61–75. [[CrossRef](#)] [[PubMed](#)]
12. Tomaszewska, M. Recovery of hydrochloric acid from metal pickling solutions by membrane distillation. *Sep. Purif. Technol.* **2001**, *22*, 591–600. [[CrossRef](#)]
13. Jeong, J.; Kim, M.; Kim, B.; Kim, S.; Kim, W.; Lee, J. Recovery of H<sub>2</sub>SO<sub>4</sub> from waste acid solution by a diffusion dialysis method. *J. Hazard. Mater.* **2005**, *124*, 230–235. [[CrossRef](#)]
14. Regel-Rosocka, M. A review on methods of regeneration of spent pickling solutions from steel processing. *J. Hazard. Mater.* **2010**, *177*, 57–69. [[CrossRef](#)] [[PubMed](#)]
15. Stocks, C.; Wood, J.; Guy, S. Minimisation and recycling of spent acid wastes from galvanizing plants. *Resour. Conserv. Recycl.* **2005**, *44*, 153–166. [[CrossRef](#)]
16. Luo, J.; Wu, C.; Xu, T.; Wu, Y. Diffusion dialysis-concept, principle and applications. *J. Membr. Sci.* **2011**, *366*, 1–16. [[CrossRef](#)]
17. Kobuchi, Y.; Motomura, H.; Noma, Y.; Hanada, F. Application of ion exchange membranes to the recovery of acids by diffusion dialysis. *J. Membr. Sci.* **1986**, *27*, 173–179. [[CrossRef](#)]
18. Zaman, N.K.; Rohani, R.; Mohammad, A.W.; Isloor, A.M.; Jahim, J.M. Investigation of succinic acid recovery from aqueous solution and fermentation broth using polyimide nanofiltration membrane. *J. Environ. Chem. Eng.* **2020**, *8*, 101895. [[CrossRef](#)]
19. Sun, X.; Lu, H.; Wang, J. Recovery of citric acid from fermented liquid by bipolar membrane electro dialysis. *J. Clean. Prod.* **2017**, *143*, 250–256. [[CrossRef](#)]
20. Palatý, Z.; Žáková, A. Separation of H<sub>2</sub>SO<sub>4</sub> + ZnSO<sub>4</sub> mixture by diffusion dialysis. *Desalination* **2004**, *169*, 277–285. [[CrossRef](#)]
21. Palatý, Z.; Žáková, A. Separation of HCl + NiCl<sub>2</sub> Mixture by Diffusion Dialysis. *Sep. Sci. Technol.* **2007**, *42*, 1965–1983. [[CrossRef](#)]
22. Xu, T.; Yang, W. Industrial recovery of mixed acid (HF + HNO<sub>3</sub>) from the titanium spent leaching solutions by diffusion dialysis with a new series of anion exchange membranes. *J. Membr. Sci.* **2003**, *220*, 89–95. [[CrossRef](#)]
23. Palatý, Z.; Bendová, H. Permeability of a Fumasep-FAD Membrane for Selected Inorganic Acids. *Chem. Eng. Technol.* **2018**, *41*, 385–391. [[CrossRef](#)]
24. Lan, S.; Wen, X.; Zhu, Z.; Shao, F.; Zhu, C. Recycling of spent nitric acid solution from electro dialysis by diffusion dialysis. *Desalination* **2011**, *278*, 227–230. [[CrossRef](#)]
25. Narebska, A.; Staniszewski, M.; Narebska, A. Separation of Carboxylic Acids from Carboxylates by Diffusion Dialysis. *Sep. Sci. Technol.* **2008**, *43*, 490–501. [[CrossRef](#)]
26. Palatý, Z.; Stoček, P.; Bendová, H.; Prchal, P. Continuous dialysis of carboxylic acids: Solubility and diffusivity in Neosepta-AMH membranes. *Desalination* **2009**, *243*, 65–73. [[CrossRef](#)]
27. Khan, M.I.; Luque, R.; Akhtar, S.; Shaheen, A.; Mehmood, A.; Idress, S.; Buzdar, S.A.; Rehman, A.U. Design of Anion Exchange Membranes and Electro dialysis Studies for Water Desalination. *Materials* **2016**, *9*, 365. [[CrossRef](#)]
28. Kim, J.H.; Vinothkannan, M.; Kim, A.R.; Yoo, D.J. Anion dxchange membranes obtained from poly(arylene ether sulfone) block copolymers comprising hydrophilic and hydrophobic segments. *Polymers* **2020**, *12*, 325. [[CrossRef](#)]
29. Chu, J.Y.; Lee, K.H.; Kim, A.R.; Yoo, D.J. Improved electrochemical performance of composite anion exchange membranes for fuel cells through cross linking of the polymer chain with functionalized graphene oxide. *J. Membr. Sci.* **2020**, *611*, 118385. [[CrossRef](#)]
30. Chu, J.Y.; Lee, K.H.; Kim, A.R.; Yoo, D.J. Study on the Chemical Stabilities of Poly(arylene ether) Random Copolymers for Alkaline Fuel Cells: Effect of Main Chain Structures with Different Monomer Units. *ACS Sustain. Chem. Eng.* **2019**, *7*, 20077–20087. [[CrossRef](#)]
31. Khan, M.I.; Wu, L.; Hossain, M.; Pan, J.; Ran, J.; Mondal, A.N.; Xu, T. Preparation of diffusion dialysis membrane for acid recovery via a phase-inversion method. *Membr. Water Treat.* **2015**, *6*. [[CrossRef](#)]
32. Mondal, A.N.; Cheng, C.; Yao, Z.; Pan, J.; Hossain, M.; Khan, M.I.; Yang, Z.; Wu, L.; Xu, T. Novel quaternized aromatic amine based hybrid PVA membranes for acid recovery. *J. Membr. Sci.* **2015**, *490*, 29–37. [[CrossRef](#)]

33. Wei, C.; Li, X.; Deng, Z.; Fan, G.; Li, M.; Li, C. Recovery of H<sub>2</sub>SO<sub>4</sub> from an acid leach solution by diffusion dialysis. *J. Hazard. Mater.* **2010**, *176*, 226–230. [CrossRef] [PubMed]
34. Lin, S.H.; Lo, M.C. Recovery of sulfuric acid from waste aluminum surface processing solution by diffusion dialysis. *J. Hazard. Mater.* **1998**, *60*, 247–257. [CrossRef]
35. Web of Science. 2020. Available online: <http://apps.webofknowledge.com> (accessed on 23 July 2020).
36. Naidu, G.; Ryu, S.; Thiruvankatahari, R.; Choi, Y.; Jeong, S.; Vigneswaran, S. A critical review on remediation, reuse, and resource recovery from acid mine drainage. *Environ. Pollut.* **2019**, *247*, 1110–1124. [CrossRef] [PubMed]
37. Rezaie, B.; Anderson, A. Sustainable resolutions for environmental threat of the acid mine drainage. *Sci. Total. Environ.* **2020**, *717*, 137211. [CrossRef]
38. Aktij, S.A.; Zirehpour, A.; Mollahosseini, A.; Taherzadeh, M.; Tiraferri, A.; Rahimpour, A. Feasibility of membrane processes for the recovery and purification of bio-based volatile fatty acids: A comprehensive review. *J. Ind. Eng. Chem.* **2020**, *81*, 24–40. [CrossRef]
39. Handojo, L.; Wardani, A.K.; Regina, D.; Bella, C.; Kresnowati, M.T.A.P.; Wenten, I.G. Electro-membrane processes for organic acid recovery. *RSC Adv.* **2019**, *9*, 7854–7869. [CrossRef]
40. Talnikar, V.D.; Mahajan, Y.S. Recovery of acids from dilute streams: A review of process technologies. *Korean J. Chem. Eng.* **2014**, *31*, 1720–1731. [CrossRef]
41. Xu, T. Ion exchange membranes: State of their development and perspective. *J. Membr. Sci.* **2005**, *263*, 1–29. [CrossRef]
42. Xu, T.; Yang, W. Tuning the diffusion dialysis performance by surface cross-linking of PPO anion exchange membranes-simultaneous recovery of sulfuric acid and nickel from electrolysis spent liquor of relatively low acid concentration. *J. Hazard. Mater.* **2004**, *109*, 157–164.
43. Luo, J.; Wu, C.; Wu, Y.; Xu, T. Diffusion dialysis of hydrochloride acid at different temperatures using PPO-SiO<sub>2</sub> hybrid anion exchange membranes. *J. Membr. Sci.* **2010**, *347*, 240–249. [CrossRef]
44. Wang, C.; Wu, C.; Wu, Y.; Gu, J.; Xu, T. Polyelectrolyte complex/PVA membranes for diffusion dialysis. *J. Hazard. Mater.* **2013**, *261*, 114–122. [CrossRef] [PubMed]
45. Tugas, I.; Pourcelly, G.; Gavach, C. Electrotransport of protons and chloride ions in anion exchange membranes for the recovery of acids. Part I. Equilibrium properties. *J. Membr. Sci.* **1993**, *85*, 183–194. [CrossRef]
46. Ersoz, M.; Gugul, I.; Şahin, A. Transport of Acids through Polyether–Sulfone Anion-Exchange Membrane. *J. Colloid Interface Sci.* **2001**, *237*, 130–135. [CrossRef] [PubMed]
47. Lin, X.; Kim, S.; Zhu, D.M.; Shamsaei, E.; Xu, T.; Fang, X.; Wang, H. Preparation of porous diffusion dialysis membranes by functionalization of polysulfone for acid recovery. *J. Membr. Sci.* **2017**, *524*, 557–564. [CrossRef]
48. Mondal, P.; Samanta, N.S.; Kumar, A.; Purkait, M.K. Recovery of H<sub>2</sub>SO<sub>4</sub> from wastewater in the presence of NaCl and KHCO<sub>3</sub> through pH responsive polysulfone membrane: Optimization approach. *Polym. Test.* **2020**, *86*, 106463. [CrossRef]
49. Khan, M.I.; Mondal, A.N.; Cheng, C.; Pan, J.; Emmanuel, K.; Wu, L.; Xu, T. Porous BPPO-based membranes modified by aromatic amine for acid recovery. *Sep. Purif. Technol.* **2016**, *157*, 27–34. [CrossRef]
50. Khan, M.I.; Mondal, A.N.; Emmanuel, K.; Hossain, M.; Afsar, N.U.; Wu, L.; Xu, T. Preparation of Pyrrolidinium-Based Anion Exchange Membranes for Acid Recovery via Diffusion Dialysis. *Sep. Sci. Technol.* **2016**, *51*, 1881–1890. [CrossRef]
51. Yuan, Z.; Dai, Q.; Zhao, Y.; Lu, W.; Li, X.; Zhang, H. Polypyrrole modified porous poly(ether sulfone) membranes with high performance for vanadium flow batteries. *J. Mater. Chem. A* **2016**, *4*, 12955–12962. [CrossRef]
52. Zhao, Y.; Mai, Z.; Shen, P.; Ortega, E.; Shen, J.; Gao, C.; Van Der Bruggen, B. Nanofiber Based Organic Solvent Anion Exchange Membranes for Selective Separation of Monovalent anions. *ACS Appl. Mater. Interfaces* **2020**, *12*, 7539–7547. [CrossRef]
53. Zhang, X.; Fan, C.; Yao, N.; Zhang, P.; Hong, T.; Xu, C.; Cheng, J. Quaternary Ti<sub>3</sub>C<sub>2</sub>T<sub>x</sub> enhanced ionic conduction in quaternized polysulfone membrane for alkaline anion exchange membrane fuel cells. *J. Membr. Sci.* **2018**, *563*, 882–887. [CrossRef]
54. Zhang, W.; Liu, Y.; Jackson, A.C.; Savage, A.M.; Ertem, S.P.; Tsai, T.-H.; Seifert, S.; Beyer, F.L.; Liberatore, M.W.; Herring, A.M.; et al. Achieving Continuous Anion Transport Domains Using Block Copolymers Containing Phosphonium Cations. *Macromolecules* **2016**, *49*, 4714–4722. [CrossRef]

55. Cho, H.; Krieg, H.M.; Kerres, J.A. Performances of Anion-Exchange Blend Membranes on Vanadium Redox Flow Batteries. *Membranes* **2019**, *9*, 31. [[CrossRef](#)] [[PubMed](#)]
56. Prajapati, P.K.; Reddy, N.N.; Nimiwal, R.; Singh, P.S.; Adimurthy, S.; Nagarale, R. Polyaniline@porous polypropylene for efficient separation of acid by diffusion dialysis. *Sep. Purif. Technol.* **2020**, *233*, 115989. [[CrossRef](#)]
57. Xu, T.; Yang, W. Sulfuric acid recovery from titanium white (pigment) waste liquor using diffusion dialysis with a new series of anion exchange membranes-static runs. *J. Membr. Sci.* **2001**, *183*, 193–200.
58. Gu, F.; Dong, H.; Li, Y.; Sun, Z.; Yan, F. Base Stable Pyrrolidinium Cations for Alkaline Anion Exchange Membrane Applications. *Macromolecules* **2014**, *47*, 6740–6747. [[CrossRef](#)]
59. Döbbelin, M.; Azcune, I.; Bedu, M.; De Luzuriaga, A.R.; Genua, A.; Jovanovski, V.; Cabañero, G.; Odriozola, I. Synthesis of Pyrrolidinium-Based Poly(ionic liquid) Electrolytes with Poly(ethylene glycol) Side Chains. *Chem. Mater.* **2012**, *24*, 1583–1590. [[CrossRef](#)]
60. Lin, X.; Wu, L.; Liu, Y.; Ong, A.L.; Poynton, S.; Varcoe, J.R.; Xu, T. Alkali resistant and conductive guanidinium-based anion-exchange membranes for alkaline polymer electrolyte fuel cells. *J. Power Sources* **2012**, *217*, 373–380. [[CrossRef](#)]
61. Khan, M.I.; Khraisheh, M.; Almomani, F. Fabrication and characterization of pyridinium functionalized anion exchange membranes for acid recovery. *Sci. Total. Environ.* **2019**, *686*, 90–96. [[CrossRef](#)]
62. Ji, W.; Wu, B.; Zhu, Y.; Irfan, M.; Afsar, N.U.; Ge, L.; Xu, T. Self-organized nanostructured anion exchange membranes for acid recovery. *Chem. Eng. J.* **2020**, *382*, 122838. [[CrossRef](#)]
63. Wu, Y.; Luo, J.; Yao, L.; Wu, C.; Mao, F.; Xu, T. PVA/SiO<sub>2</sub> anion exchange hybrid membranes from multisilicon copolymers with two types of molecular weights. *J. Membr. Sci.* **2012**, *399*, 16–27. [[CrossRef](#)]
64. Irfan, M.; Afsar, N.U.; Ge, L.; Xu, T. Investigation of key process parameters in acid recovery for diffusion dialysis using novel (MDMH-QPPO) anion exchange membranes. *J. Taiwan Inst. Chem. Eng.* **2018**, *93*, 405–413. [[CrossRef](#)]
65. Cheng, C.; Yang, Z.; He, Y.; Mondal, A.N.; Bakangura, E.; Xu, T. Diffusion dialysis membranes with semi-interpenetrating network for acid recovery. *J. Membr. Sci.* **2015**, *493*, 645–653. [[CrossRef](#)]
66. Cheng, C.; Li, P.; He, Y.; Hu, X.; Emmanuel, K. Branched Polyvinyl Alcohol Hybrid Membrane for Acid Recovery via Diffusion Dialysis. *Chem. Eng. Technol.* **2019**, *42*, 1180–1187. [[CrossRef](#)]
67. Emmanuel, K.; Cheng, C.; Erigene, B.; Mondal, A.N.; Afsar, N.U.; Khan, M.I.; Hossain, M.; Jiang, C.; Ge, L.; Wu, L.; et al. Novel synthetic route to prepare doubly quaternized anion exchange membranes for diffusion dialysis application. *Sep. Purif. Technol.* **2017**, *189*, 204–212. [[CrossRef](#)]
68. Yadav, S.; Soontarapa, K.; Jyothi, M.S.; Padaki, M.; Balakrishna, R.G.; Lai, J.-Y. Supplementing multi-functional groups to polysulfone membranes using Azadirachta indica leaves powder for effective and highly selective acid recovery. *J. Hazard. Mater.* **2019**, *369*, 1–8. [[CrossRef](#)]
69. González, M.I.; Alvarez, S.; Riera, F.A.; Alvarez, R. Lactic acid recovery from whey ultrafiltrate fermentation broths and artificial solutions by nanofiltration. *Desalination* **2008**, *228*, 84–96. [[CrossRef](#)]
70. Stachera, D.M.; Childs, R.F. Tuning the acid recovery performance of poly(4-vinylpyridine)-filled membranes by the introduction of hydrophobic groups. *J. Membr. Sci.* **2001**, *187*, 213–225. [[CrossRef](#)]
71. Stachera, D.M.; Childs, R.; Mika, A.; Dickson, J.M. Acid recovery using diffusion dialysis with poly(4-vinylpyridine)-filled microporous membranes. *J. Membr. Sci.* **1998**, *148*, 119–127. [[CrossRef](#)]
72. Prajapati, P.K.; Nimiwal, R.; Singh, P.S.; Nagarale, R. Polyaniline-co-epichlorohydrin nanoporous anion exchange membranes for diffusion dialysis. *Polymer* **2019**, *170*, 168–178. [[CrossRef](#)]
73. Chavan, V.; Agarwal, C.; Adya, V.; Pandey, A.K. Hybrid organic-inorganic anion-exchange pore-filled membranes for the recovery of nitric acid from highly acidic aqueous waste streams. *Water Res.* **2018**, *133*, 87–98. [[PubMed](#)]
74. Kim, D.-H.; Park, J.-H.; Seo, S.-J.; Park, J.-S.; Jung, S.P.; Kang, Y.S.; Choi, J.-H.; Kang, M.-S. Development of thin anion-exchange pore-filled membranes for high diffusion dialysis performance. *J. Membr. Sci.* **2013**, *447*, 80–86. [[CrossRef](#)]
75. Xiarchos, I.; Doulia, D.; Gekas, V.; Trägårdh, G. Polymeric Ultrafiltration Membranes and Surfactants. *Sep. Purif. Rev.* **2003**, *32*, 215–278. [[CrossRef](#)]
76. Tang, B.; Xu, T.; Gong, M.; Yang, W. A novel positively charged asymmetry membranes from poly(2,6-dimethyl-1,4-phenylene oxide) by benzyl bromination and in situ amination: Membrane preparation and characterization. *J. Membr. Sci.* **2005**, *248*, 119–125. [[CrossRef](#)]

77. Lin, X.; Shamsaei, E.; Kong, B.; Liu, J.Z.; Hu, Y.; Xu, T.; Wang, H. Porous diffusion dialysis membranes for rapid acid recovery. *J. Membr. Sci.* **2016**, *502*, 76–83. [[CrossRef](#)]
78. Sun, F.; Wu, C.; Wu, Y.; Xu, T. Porous BPPO-based membranes modified by multisilicon copolymer for application in diffusion dialysis. *J. Membr. Sci.* **2014**, *450*, 103–110.
79. Jyothi, M.; Yadav, S.; Balakrishna, G. Effective recovery of acids from egg waste incorporated PSf membranes: A step towards sustainable development. *J. Membr. Sci.* **2018**, *549*, 227–235. [[CrossRef](#)]
80. Pan, J.; He, Y.; Wu, L.; Jiang, C.; Wu, B.; Mondal, A.N.; Cheng, C.; Xu, T. Anion exchange membranes from hot-pressed electrospun QPPO–SiO<sub>2</sub> hybrid nanofibers for acid recovery. *J. Membr. Sci.* **2015**, *480*, 115–121. [[CrossRef](#)]
81. Dakashev, A.D.; Stancheva, K.A. Quantitative chemical analysis of electrolytes in aqueous solutions exploiting the Donnan dialysis process. *J. Anal. Chem.* **2008**, *63*, 69–74. [[CrossRef](#)]
82. Emmanuel, K.; Erigene, B.; Cheng, C.; Mondal, A.N.; Hossain, M.; Khan, M.I.; Afsar, N.U.; Ge, L.; Wu, L.; Xu, T. Facile synthesis of pyridinium functionalized anion exchange membranes for diffusion dialysis application. *Sep. Purif. Technol.* **2016**, *167*, 108–116. [[CrossRef](#)]
83. Emmanuel, K.; Cheng, C.; Ge, L.; Mondal, A.N.; Hossain, M.; Khan, M.I.; Afsar, N.U.; Liang, G.; Wu, L.; Xu, T. Imidazolium functionalized anion exchange membrane blended with PVA for acid recovery via diffusion dialysis process. *J. Membr. Sci.* **2016**, *497*, 209–215. [[CrossRef](#)]
84. Cheng, C.; Yang, Z.; Pan, J.; Tong, B.; Xu, T. Facile and cost effective PVA based hybrid membrane fabrication for acid recovery. *Sep. Purif. Technol.* **2014**, *136*, 250–257. [[CrossRef](#)]
85. Kim, D.-H.; Park, H.-S.; Seo, S.-J.; Park, J.-S.; Moon, S.-H.; Choi, Y.-W.; Jiong, Y.S.; Kim, N.H.; Kang, M.-S. Facile surface modification of anion-exchange membranes for improvement of diffusion dialysis performance. *J. Colloid Interface Sci.* **2014**, *416*, 19–24. [[CrossRef](#)] [[PubMed](#)]
86. Ge, L.; Mondal, A.N.; Liu, X.; Wu, B.; Yu, D.; Li, Q.; Miao, J.; Ge, Q.; Xu, T. Advanced charged porous membranes with ultrahigh selectivity and permeability for acid recovery. *J. Membr. Sci.* **2017**, *536*, 11–18. [[CrossRef](#)]
87. Ge, Q.; Ning, Y.; Wu, L.; Ge, L.; Liu, X.; Yang, Z.; Xu, T. Enhancing acid recovery efficiency by implementing oligomer ionic bridge in the membrane matrix. *J. Membr. Sci.* **2016**, *518*, 263–272. [[CrossRef](#)]
88. Luo, T.; Abdu, S.; Wessling, M. Selectivity of ion exchange membranes: A review. *J. Membr. Sci.* **2018**, *555*, 429–454. [[CrossRef](#)]
89. Sun, P.; Wang, K.; Wei, J.; Zhong, M.; Wu, D.; Zhu, H. Effective recovery of acids from iron-based electrolytes using graphene oxide membrane filters. *J. Mater. Chem. A* **2014**, *2*, 7734–7737. [[CrossRef](#)]
90. Zhang, H.; Hou, J.; Hu, Y.; Wang, P.; Ou, R.; Jiang, L.; Liu, J.Z.; Freeman, B.; Hill, A.J.; Wang, H. Ultrafast selective transport of alkali metal ions in metal organic frameworks with subnanometer pores. *Sci. Adv.* **2018**, *4*, 66. [[CrossRef](#)]
91. Huang, H.-H.; Joshi, R.; De Silva, K.K.H.; Badam, R.; Yoshimura, M.; De Silva, K. Fabrication of reduced graphene oxide membranes for water desalination. *J. Membr. Sci.* **2019**, *572*, 12–19. [[CrossRef](#)]
92. Liu, D.; Zhong, C. Understanding gas separation in metal–organic frameworks using computer modeling. *J. Mater. Chem.* **2010**, *20*, 10308. [[CrossRef](#)]
93. Peng, F.; Lu, L.; Sun, H.; Wang, Y.; Liu, J.; Jiang, Z. Hybrid Organic–Inorganic Membrane: Solving the Tradeoff between Permeability and Selectivity. *Chem. Mater.* **2005**, *17*, 6790–6796. [[CrossRef](#)]
94. Mondal, A.N.; Cheng, C.; Khan, M.I.; Hossain, M.; Emmanuel, K.; Ge, L.; Wu, B.; He, Y.; Ran, J.; Ge, X.; et al. Improved acid recovery performance by novel Poly(DMAEM-co- $\gamma$ -MPS) anion exchange membrane via diffusion dialysis. *J. Membr. Sci.* **2017**, *525*, 163–174. [[CrossRef](#)]
95. Wang, L.; Zhang, F.; Li, Z.; Liao, J.; Huang, Y.; Lei, Y.; Li, N. Mixed-charge poly(2,6-dimethyl-phenylene oxide)anion exchange membrane for diffusion dialysis in acid recovery. *J. Membr. Sci.* **2018**, *549*, 543–549. [[CrossRef](#)]
96. Ran, J.; Hu, M.; Yu, D.; He, Y.; Shehzad, M.A.; Wu, L.; Xu, T. Graphene oxide embedded “three-phase” membrane to beat “trade-off” in acid recovery. *J. Membr. Sci.* **2016**, *520*, 630–638. [[CrossRef](#)]
97. Cheng, J.; He, G.; Zhang, F. A mini-review on anion exchange membranes for fuel cell applications: Stability issue and addressing strategies. *Int. J. Hydrogen Energy* **2015**, *40*, 7348–7360. [[CrossRef](#)]
98. Mao, F.; Zhang, G.; Tong, J.; Xu, T.; Wu, Y. Anion exchange membranes used in diffusion dialysis for acid recovery from erosive and organic solutions. *Sep. Purif. Technol.* **2014**, *122*, 376–383. [[CrossRef](#)]

99. Wu, C.; Wu, Y.; Luo, J.; Xu, T.; Fu, Y. Anion exchange hybrid membranes from PVA and multi-alkoxy silicon copolymer tailored for diffusion dialysis process. *J. Membr. Sci.* **2010**, *356*, 96–104. [[CrossRef](#)]
100. Irfan, M.; Bakangura, E.; Afsar, N.U.; Xu, T.; Ran, J. Augmenting acid recovery from different systems by novel Q-DAN anion exchange membranes via diffusion dialysis. *Sep. Purif. Technol.* **2018**, *201*, 336–345. [[CrossRef](#)]
101. Khan, M.I.; Luque, R.; Prinsen, P.; Rehman, A.U.; Anjum, S.; Nawaz, M.; Shaheen, A.; Zafar, S.; Mustaqeem, M. BPPO-Based Anion Exchange Membranes for Acid Recovery via Diffusion Dialysis. *Materials* **2017**, *10*, 266. [[CrossRef](#)]
102. Irfan, M.; Afsar, N.U.; Bakangura, E.; Mondal, A.N.; Khan, M.I.; Emmanuel, K.; Yang, Z.; Wu, L.; Xu, T. Development of novel PVA-QUDAP based anion exchange membranes for diffusion dialysis and theoretical analysis therein. *Sep. Purif. Technol.* **2017**, *178*, 269–278. [[CrossRef](#)]
103. Liu, Y.; Wang, J. Preparation of anion exchange membrane by efficient functionalization of polysulfone for electro-dialysis. *J. Membr. Sci.* **2020**, *596*, 117591. [[CrossRef](#)]
104. Wang, L.; Liu, Y.; Wang, J. Crosslinked anion exchange membrane with improved membrane stability and conductivity for alkaline fuel cells. *J. Appl. Polym. Sci.* **2019**, *136*, 48169. [[CrossRef](#)]
105. Tuan, C.M.; Tinh, V.D.C.; Kim, D. Anion Exchange Membranes Prepared from Quaternized Polyepichlorohydrin Cross-Linked with 1-(3-aminopropyl)imidazole Grafted Poly(arylene ether ketone) for Enhancement of Toughness and Conductivity. *Membranes* **2020**, *10*, 138. [[CrossRef](#)] [[PubMed](#)]
106. Wu, Y.; Wu, C.; Li, Y.; Xu, T.; Fu, Y. PVA–silica anion-exchange hybrid membranes prepared through a copolymer crosslinking agent. *J. Membr. Sci.* **2010**, *350*, 322–332. [[CrossRef](#)]
107. Lin, X.; Shamsaei, E.; Kong, B.; Wang, H.; Liu, J.Z.; Xu, T. Fabrication of asymmetrical diffusion dialysis membranes for rapid acid recovery with high purity. *J. Mater. Chem. A* **2015**, *3*, 24000–24007. [[CrossRef](#)]
108. Wu, Y.; Luo, J.; Zhao, L.; Zhang, G.; Wu, C.; Xu, T. QPPO/PVA anion exchange hybrid membranes from double crosslinking agents for acid recovery. *J. Membr. Sci.* **2013**, *428*, 95–103. [[CrossRef](#)]
109. Sharma, P.P.; Yadav, V.; Rajput, A.; Kulshrestha, V. Poly (triethoxyvinylsilane-co-quaternaryvinylbenzylchloride)/fGMR based anion exchange membrane and its application towards salt and acid recovery. *J. Membr. Sci.* **2018**, *556*, 303–311. [[CrossRef](#)]
110. López, J.; Reig, M.; Gibert, O.; Cortina, J.-L. Increasing sustainability on the metallurgical industry by integration of membrane nanofiltration processes: Acid recovery. *Sep. Purif. Technol.* **2019**, *226*, 267–277. [[CrossRef](#)]
111. Zhang, X.; Li, C.; Ge, L.; Luo, J.; Xu, T. Recovery of acetic acid from simulated acetaldehyde wastewaters: Bipolar membrane electro-dialysis processes and membrane selection. *J. Membr. Sci.* **2011**, *379*, 184–190. [[CrossRef](#)]
112. Yun, T.; Chung, J.W.; Kwak, S.-Y. Recovery of sulfuric acid aqueous solution from copper-refining sulfuric acid wastewater using nanofiltration membrane process. *J. Environ. Manag.* **2018**, *223*, 652–657. [[CrossRef](#)]
113. Yun, T.; Kwak, S.-Y. Recovery of hydrochloric acid using positively-charged nanofiltration membrane with selective acid permeability and acid resistance. *J. Environ. Manag.* **2020**, *260*, 110001. [[CrossRef](#)]
114. Zhang, X.; Fan, M.; Li, W.; Wu, C.; Han, X.; Zhong, S.; Chen, Y. Application and modeling of pressure-concentration double-driven diffusion dialysis. *J. Membr. Sci.* **2020**, *595*, 117478. [[CrossRef](#)]
115. Ipekçi, D.; Kabay, N.; Bunani, S.; Altok, E.; Arda, M.; Yoshizuka, K.; Nishihama, S. Application of heterogeneous ion exchange membranes for simultaneous separation and recovery of lithium and boron from aqueous solution with bipolar membrane electro-dialysis (EDBM). *Desalination* **2020**, *479*, 114313. [[CrossRef](#)]
116. Jiang, C.; Wang, Q.; Li, Y.; Ge, L.; Xu, T. Water electro-transport with hydrated cations in electro-dialysis. *Desalination* **2015**, *365*, 204–212. [[CrossRef](#)]
117. Duan, X.; Wang, C.; Wang, T.; Xie, X.; Zhou, X.; Ye, Y. A polysulfone-based anion exchange membrane for phosphoric acid concentration and purification by electro-electro-dialysis. *J. Membr. Sci.* **2018**, *552*, 86–94. [[CrossRef](#)]
118. Zhang, X.; Li, C.; Wang, X.; Ge, L.; Xu, T. Recovery of hydrochloric acid from simulated chemosynthesis aluminum foils wastewater: An integration of diffusion dialysis and conventional electro-dialysis. *J. Membr. Sci.* **2012**, *409*, 257–263. [[CrossRef](#)]
119. Zhang, X.; Wang, X.; Li, C.; Feng, H.; Li, Q.; Ge, L.; Wang, G.; Xu, T. A preliminary study on electrically assisted diffusion dialysis. *Sep. Purif. Technol.* **2014**, *122*, 331–340. [[CrossRef](#)]



120. Palatý, Z.; Bendová, H. Transport of nitric acid through anion-exchange membrane in the presence of sodium nitrate. *J. Membr. Sci.* **2011**, *372*, 277–284. [[CrossRef](#)]
121. Carstensen, F.; Klement, T.; Büchs, J.; Melin, T.; Wessling, M. Continuous production and recovery of itaconic acid in a membrane bioreactor. *Bioresour. Technol.* **2013**, *137*, 179–187. [[CrossRef](#)]
122. Gueccia, R.; Aguirre, A.R.; Randazzo, S.; Cipollina, A.; Micale, G. Diffusion Dialysis for Separation of Hydrochloric Acid, Iron and Zinc Ions from Highly Concentrated Pickling Solutions. *Membranes* **2020**, *10*, 129. [[CrossRef](#)] [[PubMed](#)]
123. Kim, J.-Y.; Shin, C.-H.; Choi, H.; Bae, W. Recovery of phosphoric acid from mixed waste acids of semiconductor industry by diffusion dialysis and vacuum distillation. *Sep. Purif. Technol.* **2012**, *90*, 64–68. [[CrossRef](#)]
124. Li, W.; Zhang, Y.; Huang, J.; Zhu, X.; Wang, Y. Separation and recovery of sulfuric acid from acidic vanadium leaching solution by diffusion dialysis. *Sep. Purif. Technol.* **2012**, *96*, 44–49. [[CrossRef](#)]
125. Xu, J.; Fu, D.; Lu, S. The recovery of sulphuric acid from the waste anodic aluminum oxidation solution by diffusion dialysis. *Sep. Purif. Technol.* **2009**, *69*, 168–173. [[CrossRef](#)]
126. Zhang, X.; Li, C.; Wang, H.; Xu, T. Recovery of hydrochloric acid from simulated chemosynthesis aluminum foil wastewater by spiral wound diffusion dialysis (SWDD) membrane module. *J. Membr. Sci.* **2011**, *384*, 219–225. [[CrossRef](#)]
127. Palatý, Z.; Bendová, H. Continuous dialysis of sulphuric acid and sodium sulphate mixture. *J. Membr. Sci.* **2016**, *497*, 36–46. [[CrossRef](#)]
128. Luo, F.; Zhang, X.; Pan, J.; Mondal, A.N.; Feng, H.; Xu, T. Diffusion dialysis of sulfuric acid in spiral wound membrane modules: Effect of module number and connection mode. *Sep. Purif. Technol.* **2015**, *148*, 25–31. [[CrossRef](#)]
129. Ye, H.; Zou, L.; Wu, C.; Wu, Y. Tubular membrane used in continuous and semi-continuous diffusion dialysis. *Sep. Purif. Technol.* **2020**, *235*, 116147. [[CrossRef](#)]
130. Xu, T.; Liu, Z.; Huang, C.; Wu, Y.; Wu, L.; Yang, W. Preparation of a Novel Hollow-Fiber Anion-Exchange Membrane and Its Preliminary Performance in Diffusion Dialysis. *Ind. Eng. Chem. Res.* **2008**, *47*, 6204–6210. [[CrossRef](#)]



© 2020 by the authors. Licensee MDPI, Basel, Switzerland. This article is an open access article distributed under the terms and conditions of the Creative Commons Attribution (CC BY) license (<http://creativecommons.org/licenses/by/4.0/>).

Article

# Operating Conditions Optimization via the Taguchi Method to Remove Colloidal Substances from Recycled Paper and Cardboard Production Wastewater

Mayko Rannany S. Sousa, Jaime Lora-García, María-Fernanda López-Pérez \*,  
Asunción Santafé-Moros  and José M. Gozávez-Zafrilla 

Research Institute for Industrial, Radiophysical and Environmental Safety (ISIRYM) Universitat Politècnica de València (UPV), Plaza Ferrándiz y Carbonell s/n, 03801 Alcoy, Spain; maysanso@doctor.upv.es (M.R.S.S.); jlora@iqn.upv.es (J.L.-G.); assanmo@iqn.upv.es (A.S.-M.); jmgz@iqn.upv.es (J.M.G.-Z.)

\* Correspondence: malope1@iqn.upv.es; Tel.: +34-966-528-460

Received: 19 May 2020; Accepted: 22 July 2020; Published: 29 July 2020



**Abstract:** Optimization of the ultrafiltration (UF) process to remove colloidal substances from a paper mill's treated effluent was investigated in this study. The effects of four operating parameters in a UF system (transmembrane pressure (TMP), cross-flow velocity (CFV), temperature and molecular weight cut-off (MWCO)) on the average permeate flux ( $J_v$ ), organic matter chemical oxygen demand (COD) rejection rate and the cumulative flux decline (SFD), was investigated by robust experimental design using the Taguchi method. Analysis of variance (ANOVA) for an  $L_9$  orthogonal array were used to determine the significance of the individual factors, that is to say, to determine which factor has more and which less influence over the UF response variables. Analysis of the percentage contribution (P%) indicated that the TMP and MWCO have the greatest contribution to the average permeate flux and SFD. In the case of the COD rejection rate, the results showed that MWCO has the highest contribution followed by CFV. The Taguchi method and the utility concept were employed to optimize the multiple response variables. The optimal conditions were found to be 2.0 bar of transmembrane pressure, 1.041 m/s of the cross-flow velocity, 15 °C of the temperature, and 100 kDa MWCO. The validation experiments under the optimal conditions achieved  $J_v$ , COD rejection rate and SFD results of 81.15 L·m<sup>-2</sup>·h<sup>-1</sup>, 43.90% and 6.01, respectively. Additionally, SST and turbidity decreased by about 99% and 99.5%, respectively, and reduction in particle size from around 458–1281 nm to 12.71–24.36 nm was achieved. The field-emission scanning electron microscopy images under optimal conditions showed that membrane fouling takes place at the highest rate in the first 30 min of UF. The results demonstrate the validity of the approach of using the Taguchi method and utility concept to obtain the optimal membrane conditions for the wastewater treatment using a reduced number of experiments.

**Keywords:** paper mill treated effluent; ultrafiltration; optimization; fouling; DoE; Taguchi method

## 1. Introduction

The pulp and paper (P & P) industry is ranked as the world's third largest consumer of fresh water [1] and an important producer of wastewater with different organic and inorganic contaminants. Depending on the type of processes used in paper manufacture, the integration between production and environmental protection is one of the key topics in the paper industry.

According to the Confederation of European Paper Industries (CEPI) [2], Europe is the second largest producer of paper and paperboard with 22.7% (91.39 million tons) of world production,

making it one of the most important industries in the European economic sector. The paper industries hold an important place in Spanish economy, as Spain is one of the European leaders in paper recycling, with 84% of the raw materials used by the paper industry containing recovered paper [2]. However, we cannot forget that water is, also, an essential raw material for manufacturing paper and paperboard, and effluent treatment is a critical part of the process [3]. In order to minimize the amount of freshwater used and the volume of effluent discharged, the European Commission has described the best available techniques to be adopted by the P & P industry [4].

A number of conventional processes have previously been used to treat the different types of paper mill wastewater including coagulation and flocculation [5], adsorption [6,7], advanced oxidation [8,9] and membrane filtration [10–13]. It is important to mention that paper mills have their own wastewater treatment plants but some water treatment methods typically used for the P & P are not environmentally efficient: e.g.: coagulation/flocculation using inorganic coagulants create disposal problems and conventional aerobic processes have not been efficient in the removal of color or recalcitrant compounds [14,15]. This inadequacy can also make it impossible to reuse water in the papermaking process. Therefore, factories must improve their treatment plants to achieve the pollutant loadings permissible under current regulations and/or to reuse their process water.

Membrane separation technology has been attracting increasing attention as an alternative method for the post-treatment of paper mill wastewater. Some processing methods, such as nanofiltration, ultrafiltration (UF) and reverse osmosis, have recently been used in paper mills to purify secondary and tertiary effluents using external biological treatment [7,16–18]. Major advantages of membrane separation processes are their scalability, low installation costs and easiness of operation. However, their technical and economic liability must be carefully assessed for each specific process.

Ultrafiltration is an attractive process for paper mill wastewater treatment and it can be used as an advanced tertiary treatment to remove suspended solids and dissolved and colloidal substances (DCS) during the treatment of paper industry effluent in order to facilitate the reuse of the treated wastewater and reduce fresh water consumption [19,20]. What makes it so attractive is that most of the pollutants consist of high-molecular-weight compounds and these are easily removed by UF [10,21].

However, membrane fouling is still a limiting factor for the adoption and use of UF on a large scale in paper manufacturing applications. This fouling results in a sharp decline in permeate flux and, thus, changes in membranes selectivity [10,22,23]. Membrane fouling also increases the process cost due to repeated plant shutdowns to clean and wash the membranes [24]. Previous studies have shown that the main foulants of the membranes used for paper industry wastewater are DCS including fatty acids, resin acids, lignins and trace amounts of sterols, steryl esters and triglycerides [19,25]. Currently, this treatment technology can only be used to filter paperboard mill effluent that has been pre-treated and that still does not meet discharge standards [26].

Statistical experimental design incorporating design of experiments (DoE) techniques can be used to investigate the effects of all the possible interactions between the factors at one time, while undertaking the fewest possible experiments. A review of the literature revealed that an increasing number of studies are being conducted using DoE approaches in the membrane technology field to optimize operating conditions [10,27–32]. The DoE approaches for robust design include the Taguchi method that combines mathematical and statistical techniques to arrive at a special design of experiments with an orthogonal array (OA) to study multiple factors with a small number of experiments. This saves time and money by reducing the number of experiments required in the investigation [16]. It is worth mentioning that this approach is becoming popular because it is easy to adopt and applies an efficient method for optimizing the operating parameters.

This approach also allows studying the influence of each individual factor on the response variables, as well as on the effects of interactions between factors over the response variables, that is to say, all operational conditions varying simultaneously according to design array. This permits the factors that have the greatest and least influence to be determined, along with the optimal level for each factor in an OA [33]. In addition, in many UF approaches it is necessary to consider the application

of multiple response optimization, because the process performance is often evaluated using several quality characteristics (responses). In this case, the Taguchi method and utility concept are useful tools for optimizing operating parameters in multiple characteristics responses [34].

The statistical analysis of variance (ANOVA) can be used to provide information on whether the operating parameters (factors) are statistically significant or not, as well as to identify the influence of individual factors and establish the relationships between the factors and operating conditions. In this analysis, the *p*-value index is used to know which operating parameters have a significant effect on the response variables. This information is complemented with the F-test which helps to identify whether or not each factor is significant at the selected confidence level [35,36]. In this study, ANOVA was also used to analyze the experimental results.

The aim of this work was to determinate the effect of operating conditions such as transmembrane pressure (TMP), cross-flow velocity (CFV), temperature and molecular weight cut-off (MWCO) on the average permeate flux, chemical oxygen demand (COD) rejection rate and cumulative flux decline (SFD), in addition to determining the optimal conditions for the given sets of values and to find the best response variables by using Taguchi experimental design and the utility concept. The results of this study may be used as a guideline when operating UF systems under the best conditions in a wastewater treatment plant (WWTP) in a papermaking factory. The filtration results and analysis of the experimental data presented and discussed in this study were carried out by using ANOVA to find the significance of the controlling factors and optimized using the Taguchi method to find the optimal operating conditions. A standard L<sub>9</sub> orthogonal array was selected for experimental planning with four factors and three levels for each factor.

## 2. Materials and Methods

### 2.1. Paperboard Mill Treated Effluent Feedstock

The paperboard mill treated effluent (PMTE) used in this work came from a secondary clarifier effluent from a WWTP in a papermaking factory located in the south of the Valencian autonomous region in Spain. In order to prevent early membrane fouling, remove large suspended solids, and reduce initial turbidity and COD in the PMTE, the raw feed solution was pre-filtered by conventional filtration (low-pressure pump at around 1 bar) with a Cintropur® NW 50 filter element, and centrifugal propeller and filter cloths with a 5 µm nominal pore size. The significant characteristics of the PMTE samples are listed in Table 1.

**Table 1.** Average compositions of the ultrafiltration (UF) feed solution (prefiltered solution from a secondary clarifier effluent from a wastewater treatment plant (WWTP)).

Parameter	Units	Value
Suspended solids (TSS)	g·L <sup>-1</sup>	0.046 ± 0.01
Turbidity	NTU	3.21 ± 0.5
Conductivity	mS·cm <sup>-1</sup>	4.20 ± 1.0
COD	mg·L <sup>-1</sup>	146 ± 5.0
Total nitrogen	mg·L <sup>-1</sup>	0.8 ± 0.01
pH	–	8.30 ± 0.5

Pre-filtered by conventional filtration (pretreatment).

### 2.2. Membranes and Experimental Setup

This study used polyethersulfone (PES) membranes provided by Synder Filtration™ (Vacaville, CA, USA) with MWCO of 10, 50 and 100 kDa, denoted 10-ST, 50-MQ and 100-LY, respectively.

The experiments were performed in a typical UF pilot plant with a flat-sheet membrane module (Rhône-Poulenc, Lyon, France), that allowed working with two membranes with similar or different MWCO (depending on the experiment being carried out). The effective area for each membrane in

the module was 154.8 cm<sup>2</sup>. The details of the experimental set-up have been described previously by Sousa et al. [21]. The pilot plant had a data acquisition system (temperature, module input and output pressure) from LabVIEW® (National Instruments, Austin, TX, USA). The permeate was collected during the filtration in a beaker placed on an electronic balance connected to a computer in order to continuously register the weighting data. This data was then automatically logged every 30 s and subsequently used to calculate permeate flux through the membranes.

### 2.3. Analytical Methods

The PMTE used as the feed solution and the UF permeate samples were analyzed according to the methods described below. The suspended solids analyses were carried out in accordance with the standard methods [37]. Turbidity was measured using a Dinko 112 turbidimeter (ASTM D1889, Barcelona, Spain). Conductivity was measured using a WTW level 3 conductivity device (ASTM D1125–14, Weilheim in Oberbayern, Germany). COD and total nitrogen in the effluent were analyzed using a Merck photometer (Merck KGaA, Darmstadt, Germany) and a Merck TR-300 thermoreactor (Merck KGaA, Darmstadt, Germany) in accordance with the standard methods.

### 2.4. Field-Emission Scanning Electron Microscopy (FESEM)

Field-emission scanning electron microscopy (FESEM) measurements were used to provide information on the fouling that formed on the membranes. The surface and cross-section morphologies of the fresh and fouled membranes were observed by field-emission scanning electron microscope, (ZEISS ULTRA 55, Oxford Instruments, Berkshire, UK), operated with a voltage of 200 kV and an accelerating voltage of 0.02–5 kV. Before analysis, the dried membrane samples were attached to double-sided adhesive carbon tape on an aluminum holder, and subsequently coated with a thin layer of gold prior to analysis.

### 2.5. Experimental Procedure

#### 2.5.1. Membrane Characterization

Before the UF runs, permeability experiments were carried out to determine the intrinsic membrane resistance ( $R_m$ ). Distilled water was used as the feed solution and measurements were taken for 1.0, 1.5, 2.0, and 3.0 bar of transmembrane pressure (TMP) at 1.041 m/s and 22.5 °C, in total recirculation mode to generate a quasi-steady state. The characterization process was undertaken for an operation time of 2 h to stabilize the flux through the membrane during this time. Previously each membrane was worked under compaction conditions with pure water at 5 bar for 1 h, in order to obtain a stable membrane structure.  $R_m$  values were calculated using the resistance model (Equation (1)), where under this condition, there was no membrane fouling resistance ( $R_f$ ) [38]:

$$J_P = \frac{TMP}{\mu R_t} = \frac{TMP}{\mu (R_m + R_f)} \quad (1)$$

where  $J_P$  is the permeate flux,  $\mu$  is the viscosity of the permeate stream and  $R_t$  is the total membrane resistance.  $R_f$  can be understood as the result of the sum of the three main fouling mechanisms: (i) pore blockage resistance when colloids block the membrane pores, (ii) adsorption resistance as a result of foulant adsorption inside or over the membrane and, (iii) cake layer resistance as a consequence of the accumulation of particles on the membrane [35,39,40].

#### 2.5.2. Ultrafiltration Experiments

The UF experiments were performed in crossflow filtration mode. The studied parameters were varied in the following ranges: TMP (1.0–3.0 bar), CFV (0.463–1.041 m/s), MWCO (10–100 kDa) and

temperature (15–30 °C). These values were selected based on the operational limits of the experimental setup, industrial scale-up and economic considerations [21].

The evolution of permeate flux was gravimetrically measured at different time intervals according to Equation (2),

$$J_P = \frac{1}{A_m \rho} \frac{dm_p}{dt} \quad (2)$$

where  $A_m$  is the effective membrane area,  $m_p$  is the total mass of permeate,  $\rho$  is the water density, and  $t$  is the filtration time.

In order to keep the feed concentration constant, both the permeate and the retained streams were continuously recirculated to the feed tank.

To evaluate the UF performance in terms of permeability the average permeate flux was calculated by the following equation [41]:

$$\bar{J}_P = \frac{1}{t_M} \int_{t_1}^{t_M} J_P(t) \cdot dt \quad (3)$$

where  $J_P(t)$  is the permeate flux evolution over time determined by regression analysis on the experimental data,  $t_1$  is the initial time operation (first data collected), and  $t_M$  is 2 h.

To analyze the effect of the operating conditions on UF resistance, the cumulative flux decline (SFD) [41] was calculated from the following equation:

$$SFD = \sum_{i=1}^M \frac{J_P(0) - J_P(i)}{J_P(0)} \quad (4)$$

where  $M$  is the number of experimental data collected and,  $J_P(0)$  is the initial permeate flux measured at  $t_1$ .

This parameter gives information about how the flux declines over the duration of the experiment (not just the difference between the initial and final permeate flux). Therefore, the higher the *SFD* value, the faster and more noticeable is the flux decline, indicating that the membrane fouling is more severe.

The average flux decline index ( $\overline{FD}$ ) provides information on the decrease of feed permeate flux throughout the experiment estimated as follows:

$$\overline{FD} = \left[ \frac{1}{t_M} \int_{t_1}^{t_M} \frac{J_P(0) - J_P(t)}{J_P(0)} dt \right] \times 100 \quad (5)$$

To evaluate the UF efficiency in removing organic matter, the COD rejection rate was chosen as the response variable calculated as:

$$R(\%) = \left( 1 - \frac{C_p}{C_f} \right) \times 100 \quad (6)$$

where:  $C_p$  and  $C_f$  are the COD concentration in the permeate and feed, respectively.

## 2.6. Experimental Design Based on the Taguchi Method

An experimental design based on the Taguchi method was used to design the experiments. The Taguchi method applies fractional experimental designs, called orthogonal arrays (OA), to reduce the number of experiments required to determine the optimum conditions based on the results [29,30,42]. One of the important steps in the Taguchi approach is the appropriate selection of OAs, which depends on the number of control factors and their levels. The minimum number of experimental trails required in an OA is given by  $N_{min} = (L - 1) \cdot F + 1$ , where  $F$  and  $N$  are the number of factors and levels respectively [36,43].

As mentioned above, the four factors (parameters) chosen were the transmembrane pressure, the cross-flow velocity, the temperature and the MWCO of the membrane; and three response variables were analyzed: the average permeate flux, the COD rejection and the cumulative flux decline. The selected factors, their designated symbols and levels are presented in Table 2.

**Table 2.** Operating parameters and their levels.

Parameters	Labels	Levels		
		L <sub>1</sub>	L <sub>2</sub>	L <sub>3</sub>
TMP (bar)	A	1.0	2.0	3.0
CFV (m/s)	B	0.463	0.752	1.041
Temperature (°C)	C	15.0	22.5	30.0
MWCO (kDa)	D	10	50	100

MWCO = Molecular weight cut-off.

For an experimental design with four factors and three levels for each factor, an L<sub>9</sub> (3<sup>4</sup>) orthogonal array was selected. In this case, 27 runs were conducted (three repetitions at each trial condition). The design of the experiments planning matrix for the L<sub>9</sub> array [43] is shown in Table 3. The experiments were carried out in a randomized order. New membrane samples were preconditioned and used in the experimental runs (27 membrane samples). In this way, the lurking effect of possible irreversible fouling was avoided and the intrinsic variability of the membrane material is included in the replications.

**Table 3.** Experimental layout using L<sub>9</sub> (3<sup>4</sup>) orthogonal array in accordance with the Taguchi method.

Experimental Trial (*)	Levels			
	A	B	C	D
1	1	1	1	1
2	1	2	2	2
3	1	3	3	3
4	2	1	2	3
5	2	2	3	1
6	2	3	1	2
7	3	1	3	2
8	3	2	1	3
9	3	3	2	1

\* All experiments were carried out in a randomized run.

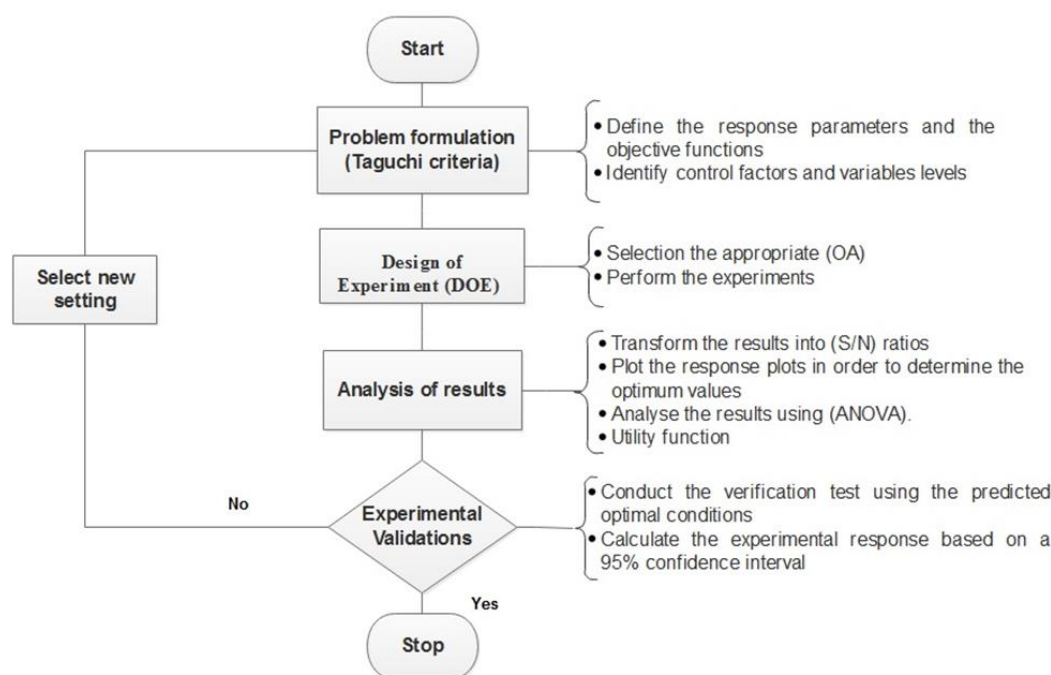
The aim of this DoE was to determine the operating parameters (factors) under which the average permeate flux and COD rejection rate achieve their maximum values, and the SFD achieved its minimum value. The Taguchi method uses a statistical measure of the process performance, called signal-to-noise ratio (S/N), which depends on the criterion for the response variable to be optimized. The S/N ratios are divided into three different categories and data sets, the larger-the-better, the smaller-the-better and the nominal-the-better [16,29]. In this study, the system was optimized when the average permeate flux and COD rejection rate were as large as possible (Equation (7)), and the SFD was as small as possible (Equation (8)):

$$\text{The larger – the – better (S/N)} = -10 \log \left( \frac{1}{n} \sum_{i=1}^n \frac{1}{Y_i^2} \right) \tag{7}$$

$$\text{The smaller – the – better (S/N)} = -10 \log \left( \frac{1}{n} \sum_{i=1}^n Y_i^2 \right) \tag{8}$$

where Y<sub>i</sub> the response variable at each experiment and n is the total number of repetitions in a trial.

The sequence of steps to be followed using the Taguchi method to optimize the UF process is shown in Figure 1.



**Figure 1.** Flow diagram of Taguchi method steps to optimize a UF process to remove dissolved and colloidal substances (DCS) from paperboard mill treated effluent [43,44].

Minitab Statistical and Statgraphics Centurion XVII Software were used to analyze the Taguchi experiments and optimize the operating conditions.

### 2.6.1. Utility Concept

The implementation of the utility concept in the Taguchi method helps to obtain the best combination of operating parameters to optimize multiple response S/N ratios (MRSN) simultaneously by differentiating the relative importance (weights) of various responses [34,45,46]. In this work, it is assumed that the overall utility is the sum of the responses of the individual utilities and it can be written as [34,47]:

$$U(x_1, x_2, \dots, x_n) = f [U_1(x_1), U_2(x_2), \dots, U_n(x_n)] \quad (9)$$

where  $U(x_1, x_2, \dots, x_n)$  is the overall utility of  $n$  response variables and  $U_i(x_i)$  is the utility index of  $i^{th}$  response.

The response variables can be attributed priorities depending upon the process goals to be achieved. The priorities can be adjusted by providing a weight to the individual utility index. Therefore, by assigning weights to the response variables, the overall utility function can be expressed as:

$$U(x_1, x_2, \dots, x_n) = \sum_{i=1}^n W_i U_i(x_i) \quad (10)$$

where  $W_i$  is the weight assigned to the  $i^{th}$  response variable.

It is worth noting that the assignment of weights is a purely subjective (empirical) step and depends on each experiment or process that will be carried out [48]. Therefore, in this paper, the analytic hierarchy process (AHP) method, developed by [49] was used to determine the associate weight criteria for each response variable in the multiple optimization required to calculate the overall utility index. The relative normalized weight  $W_i$  of each criterion is calculated using the AHP geometric mean



method  $GM_i$  on the rows in the pairwise comparison matrix,  $A ||a_{ij}||$  and it can be calculated from the follow equation [49]:

$$W_i = \frac{GM_i}{\sum_{i=1}^M GM_i} \tag{11}$$

where  $i, j = 1, 2, \dots, M$  and  $M$  is the number of factors in judgement matrix  $A$ .

$$a_{ij} = 1 \text{ for } i = j,$$

$$a_{ij} = 1/a_{ji} \text{ for } i \neq j.$$

In addition, the total sum of the weight for all the responses must be assigned to hold the following condition:

$$\sum_{i=1}^n W_i = 1 \tag{12}$$

For this study, as stated above, the objective was to maximize permeate flux and COD rejection rate, and minimize the SFD, simultaneously. From the utility concept, the MRSN of the overall utility value is given by Equation (13):

$$\mu_{MRSN} = W_{j_p} \mu_1 + W_{COD\_rejection} \mu_2 + W_{SFD} \mu_3 \tag{13}$$

where:

$$\mu_1 = -10 \log\left(\frac{1}{j_p^2}\right) \tag{14}$$

$$\mu_2 = -10 \log\left(\frac{1}{COD_{rejection}^2}\right) \tag{15}$$

$$\mu_3 = -10 \log(SFD^2) \tag{16}$$

$W_{j_p}$ ,  $W_{COD\_rejection}$ , and  $W_{SFD}$  are the weights assigned to the permeate flux, COD rejection rate and SFD.

It is worth mentioning that the utility function is of the higher-the-better type. If the composite measure (the overall utility) is maximized, the quality characteristics considered for the evaluation of utility will automatically be optimized (maximized or minimized) [44].

### 2.6.2. Optimal Performance Prediction

Once the optimal level of the operating conditions has been selected, it is possible to predict and verify the utility responses using the optimal parameters. The predicted response values under optimal conditions  $Y_{opt}$  can be calculated from Equation (17) [50,51]:

$$Y_{opt} = m + \sum_{j=1}^p [(m_{i,j}) - m] \tag{17}$$

where  $m$  is the overall mean value of  $\mu_{MRSN}$  over nine trials;  $m_{i,j}$  is the mean value of the quality response under optimal conditions; and  $p$  is the number of significant operating parameters that affect the UF process.

The 95% confidence interval for the confirmation experiments ( $CI_{CE}$ ) must be evaluated at the selected error level according to the following expression [43,50,51]:

$$CI_{CE} = \pm \sqrt{F_{\alpha}(1, f_e) \cdot MS_e \left( \frac{1}{n_{eff}} + \frac{1}{R} \right)} \tag{18}$$

where  $F_\alpha(1, f_e)$  is the F-ratio at a confidence level of  $(1 - \alpha)$  against a DOF equal to one and an error degree of freedom  $f_e$  and,  $n_{eff}$  is the effective sample size calculated as:

$$n_{eff} = \frac{N}{1 + (\text{DOF of all factors used to estimate the mean})} \tag{19}$$

where  $N$  is the number of experiments,  $R$  is the number of repetitions, and  $MS_e$  is the error variance.

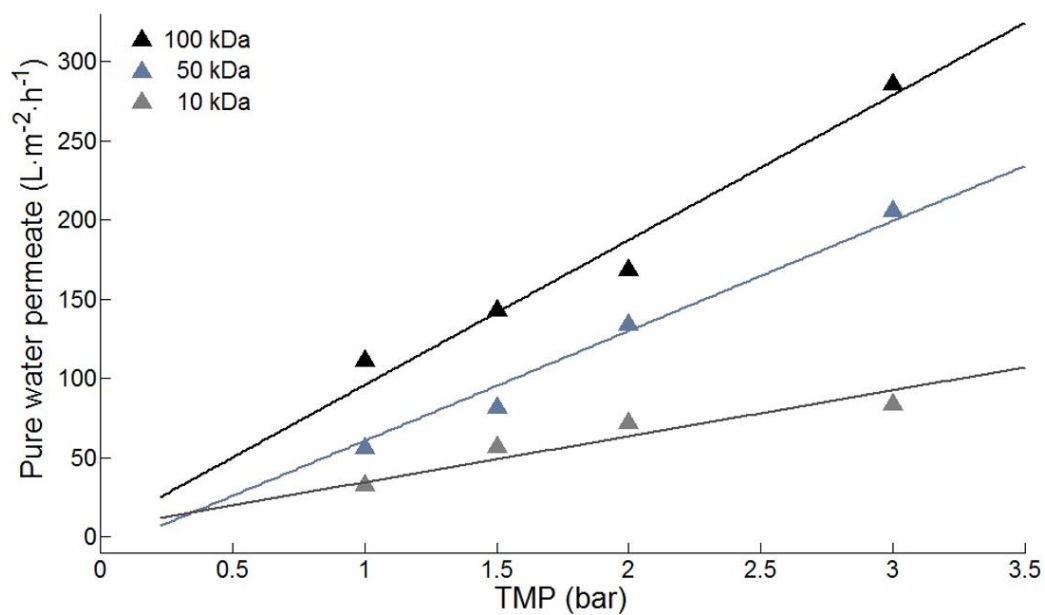
### 2.7. Analysis of Variance (ANOVA)

In order to determine the relative importance of the factors, ANOVA was employed by calculating the sum of squares ( $SS$ ), degrees of freedom ( $DOF$ ), mean of square ( $MS$ ), associated F-test of significance ( $F$ ) and percentage contribution ( $P\%$ ) [52].

## 3. Results and Discussions

### 3.1. Experimental Results

As previously mentioned, permeability tests were carried out prior to each Taguchi experiment with pure water as the feed, in order to determine the intrinsic resistance of the membrane for each membrane used, as illustrated in Figure 2.



**Figure 2.** Volumetric flux as a function of transmembrane pressure for polyethersulfone (PES) membranes of different MWCO ( $T = 22.5\text{ }^\circ\text{C}$ ).

The specific resistance values obtained from the permeability test for the membranes of 10, 50 and 100 kDa were  $3.46 \times 10^{12}$ ,  $4.56 \times 10^{12}$  and  $9.88 \times 10^{12}\text{ m}^{-1}$ , respectively.

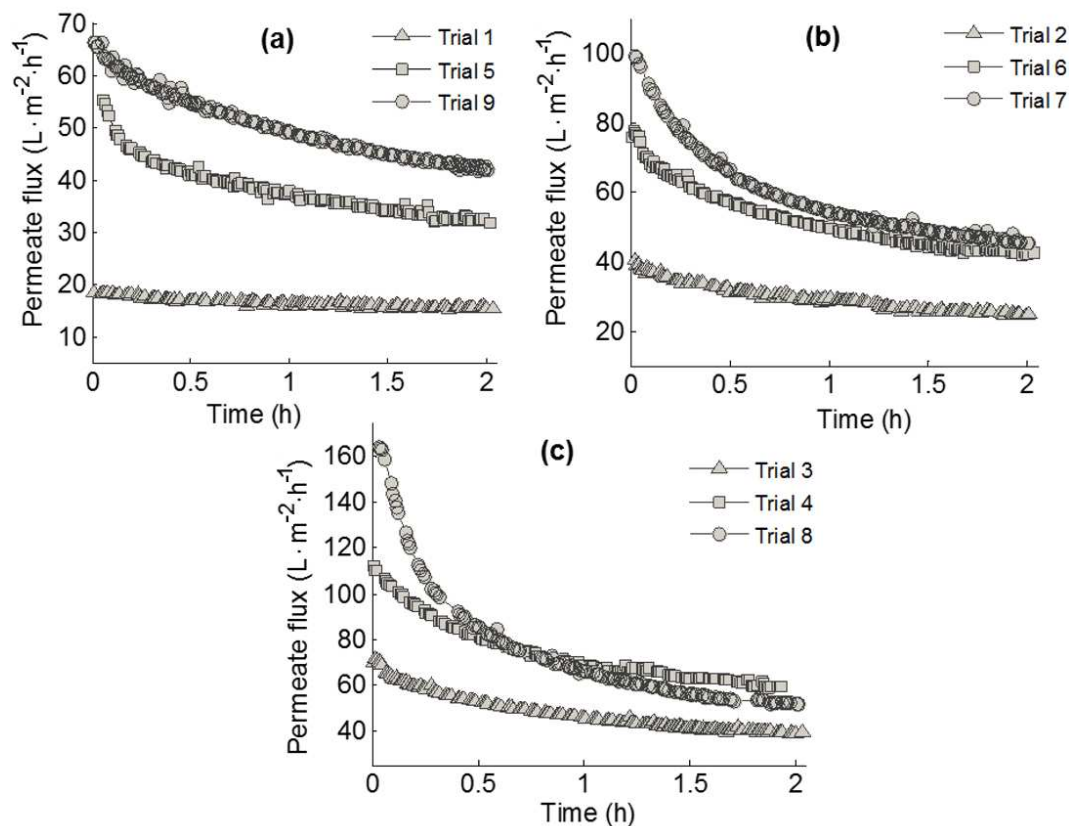
The values for the average permeate flux, COD rejection rate and the cumulative flux decline caused by membrane fouling for each trial experiment according to the Taguchi design are shown in Table 4. The highest average permeate flux was obtained in Trial 8 ( $\bar{J}_P = 95.16\text{ L}\cdot\text{m}^{-2}\cdot\text{h}^{-1}$ ) and the lowest value was obtained in Trial 1 ( $\bar{J}_P = 15.23\text{ L}^{-1}\cdot\text{h}^{-1}$ ). The corresponding average flux decline indices were respectively  $\overline{FD} = 44.87\%$  and a  $\overline{FD} = 14.0\%$ .

For some trials, significant differences on the results can be observed between replicates. The reason can be found in the inhomogeneous behavior between samples taken from the same sheet. The replication used in the experimental method aims to diminish the effect of the membrane variability on the response.

**Table 4.** Experimental responses of the Taguchi orthogonal array L<sub>9</sub> (34) for the three repetitions of each trial (R1, R2 and R3).

Trial n°	Factors (Parameters)				Responses								
	TMP (bar)	CFV (m/s)	T (°C)	MWCO (kDa)	$\bar{J}_p$ (L·m <sup>-2</sup> ·h <sup>-1</sup> )			COD Rejection (%)			SFD		
					R1	R2	R3	R1	R2	R3	R1	R2	R3
1	1.0	0.463	15.0	10	15.23	25.74	15.97	46.25	48.9	46.85	2.92	2.73	2.80
2	1.0	0.752	22.5	50	29.47	32.85	29.18	38.85	35.83	34.23	4.90	4.59	3.99
3	1.0	1.041	30.0	100	45.15	42.07	47.79	41.83	41.77	42.85	6.19	5.98	6.18
4	2.0	0.463	22.5	100	72.04	69.67	74.30	36.92	34.23	33.75	8.07	7.68	7.06
5	2.0	0.752	30.0	10	49.54	39.02	41.43	50.42	50.96	51.96	4.29	5.97	3.99
6	2.0	1.041	15.0	50	57.79	67.81	53.69	47.69	46.25	46.85	3.77	4.22	4.56
7	3.0	0.463	30.0	50	59.14	59.59	73.57	40.46	41.37	40.68	8.29	7.94	8.46
8	3.0	0.752	15.0	100	82.50	90.55	95.16	43.75	43.85	42.05	9.73	9.16	9.21
9	3.0	1.041	22.5	10	48.11	50.32	49.30	52.5	53.46	55.38	5.65	4.81	5.46

Figure 3 shows the evolution of the permeate average flux for all the trials carried out according the Taguchi design of Table 3. It can be seen that for the same MWCO, the permeate flux decreased with increasing TMP in all trials because of the membrane fouling. An increase in the TMP leads to higher accumulation of colloidal substances on the membrane surface and pore blocking. At the beginning of the process, flux declined very quickly, mainly for the trials corresponding to higher TMP and MWCO (Figure. 4c), possibly because of the membrane pores becoming blocked more rapidly by adsorption and the accumulation of colloidal substances. Afterwards, the permeate flux continued to decline due to the growth of a cake layer on the membrane surface, until the permeate flux reached a quasi-stationary state [53–56].



**Figure 3.** Evolution of the permeate flux through the operating time for each MWCO: (a) 10 kDa, (b) 50 kDa, and (c) 100 kDa (values are the average of the three replicates).

### 3.2. Taguchi Results

The corresponding S/N ratio (in dB) calculated for the response variables at each trial are listed in Table 5.

**Table 5.** Signal-to-noise results (mean ± standard deviation for the three repetitions at each trial).

Trial n°	S/N Ratio		
	$\bar{J}_p$	COD Rejection	SFD
1	24.88 ± 2.52	33.50 ± 0.25	−8.98 ± 0.28
2	29.65 ± 0.57	31.16 ± 0.56	−13.13 ± 0.94
3	33.03 ± 0.55	32.49 ± 0.12	−15.73 ± 0.16
4	37.14 ± 0.28	30.85 ± 0.42	−17.64 ± 0.59
5	32.60 ± 1.09	34.17 ± 0.13	−13.67 ± 1.86
6	35.41 ± 1.04	33.43 ± 0.14	−12.46 ± 0.82
7	36.01 ± 1.08	32.22 ± 0.10	−18.31 ± 0.28
8	39.01 ± 0.67	32.71 ± 0.20	−19.43 ± 0.29
9	33.84 ± 0.19	34.61 ± 0.24	−14.52 ± 0.74

In order to analyze the influence of each factor on the response variable, the S/N ratio for a single factor can be determined by averaging the S/N ratios at their levels. The range of the effect for each factor ( $\Delta s$ ) is calculated as the difference between the two readings, the higher the range, the stronger the effect of the factor, in other words, it shows which parameter has the greatest effect on the response.

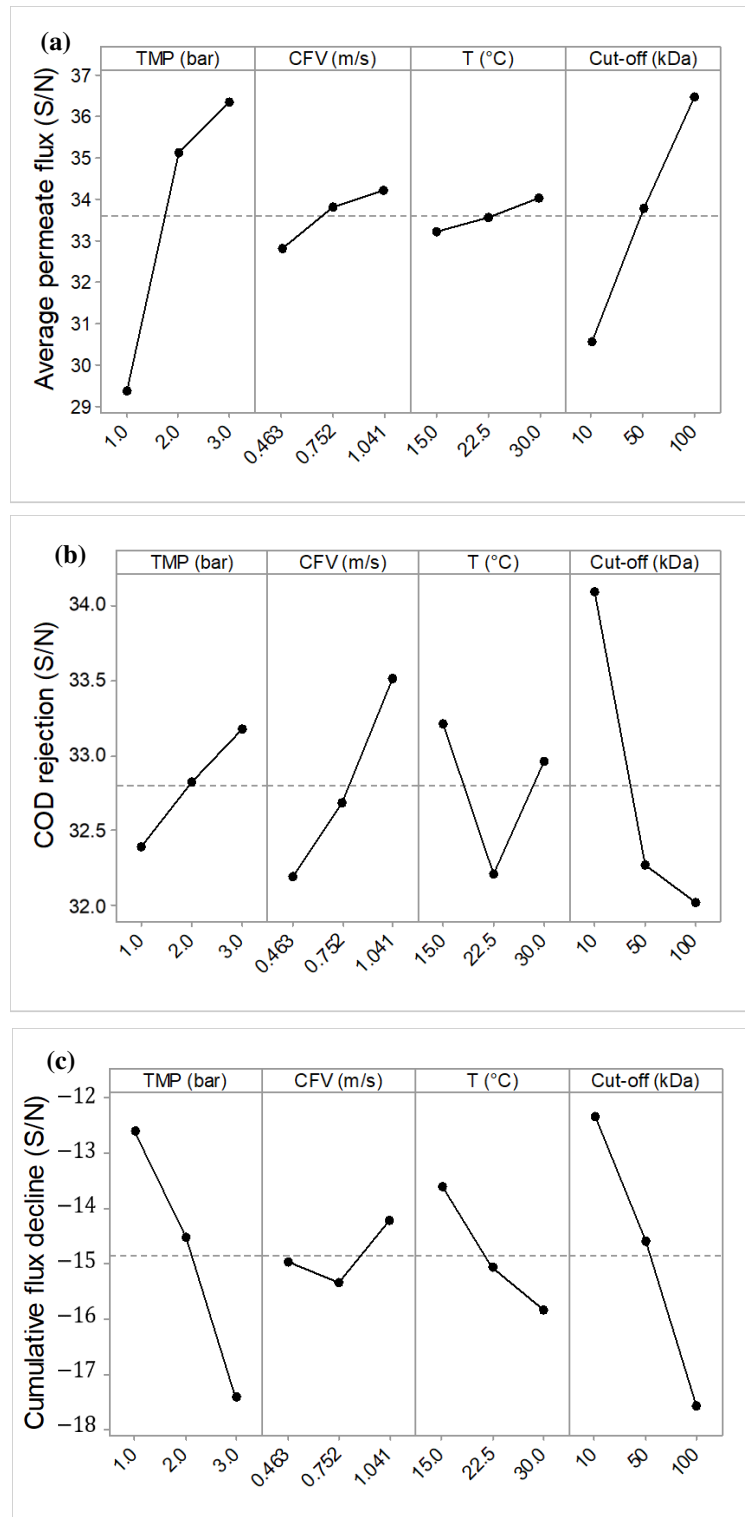
The mean S/N ratio curves for each factor are shown in Figure 4. It is worth mentioning that the peak points in these plots correspond to the optimal condition.

As can be seen in Figure 4, the variations ( $\Delta s$ ) around the mean S/N value were different for the different factors. TMP and membrane MWCO had the greatest effect on the average permeate flux as they have the steepest slope,  $\Delta s = 7.10$  and  $5.95$  respectively. CFV was the next one with a  $\Delta s = 1.42$ , and temperature had the lowest variation around the mean S/N value, with  $\Delta s = 0.78$ . In addition, from Table 5, the overall mean value was calculated as 33.59 (dB) from all the trial experiment results. It can be observed that the increase in  $\bar{J}_p$  was stronger when the TMP changes from 1.0 to 2.0 bar than when it changes over the range from 2.0 to 3.0 bar, this could be due to the effects of polarization and cake compaction on the membrane surface. For CFV, the slope of the line between the different levels is not the same (0.463–0.752 m/s is higher than at 0.752–1.041 m/s), but with a small variation around the  $\bar{J}_p$  value. Also, it can be seen for MWCO and temperature that the slopes from 10 to 100 kDa and 15 °C to 30 °C (respectively) are almost the same. Therefore, the maximum average permeate flux can be obtained for 3.0 bar, 100 kDa, 1.041 m/s CFV and high temperature (30 °C).

Under optimal COD rejection conditions, a positive and larger value of S/N is desired. In Figure 4b when comparing the S/N between different factors, it was shown that the most significant variation around the mean S/N ratios is observed for MWCO and CFV ( $\Delta s = 2.07$  and  $1.32$  respectively). Also, it can be seen that the S/N ratio increased with TMP and CFV and decreased with MWCO. Hence maximum COD removal occurred at higher TMP and CFV (3.0 bar and 1.041 m/s), and 10 kDa. It is worth mentioning that the DCS found in the PMTE are a mixture of high and low molecular weight organic and inorganic compounds, thus the contribution of the smaller particles gives lower rejection during high MWCO UF in membranes with 50 and 100 kDa MWCO.

Figure 4c shows that an increase in TMP, temperature and MWCO caused a decrease in the S/N ratio for SFD, that is to say, these factors intensified the membrane fouling effects. On the other hand, an increase in CFV induced an increase in the S/N ratio, this resulted in a decrease in the fouling effect. The highest variations around the mean S/N ratio were found for MWCO and TMP ( $\Delta s = 5.21$  and  $4.81$ ). Generally, the permeate flux increased with increasing MWCO and TMP. However, under these operating conditions, DCS in PMTE can easily pass through the membrane and blocking can be observed within the pores and on the membrane surface. In addition, the highest S/N ratio for the SFD

factor ( $-8.98 \pm 0.28$ ) was achieved in Trial 1, whereas the lowest S/N ratio ( $-19.43 \pm 0.29$ ) was obtained in Trial 8. The optimal conditions that minimized the SFD (lowest level of fouling) were obtained at the lowest TMP (1.0 bar), highest CFV (1.041 m/s), at temperature 15 °C and at the smallest MWCO (10 kDa).



**Figure 4.** Mean effect curves for S/N ratios for (a) the average permeate flux, (b) COD rejection rate, and (c) the cumulative flux decline (SFD).

### 3.3. ANOVA Results

A statistical analysis of variance (ANOVA) was carried out to quantitatively determine the effect of each factor on the UF process indicators, with the aim of estimating whether the process parameters are statistically significant or not on the results responses. The ANOVA results are shown in Table 6.

**Table 6.** Analysis of variance (ANOVA) results for average permeate flux, COD rejection, and SFD for each factor.

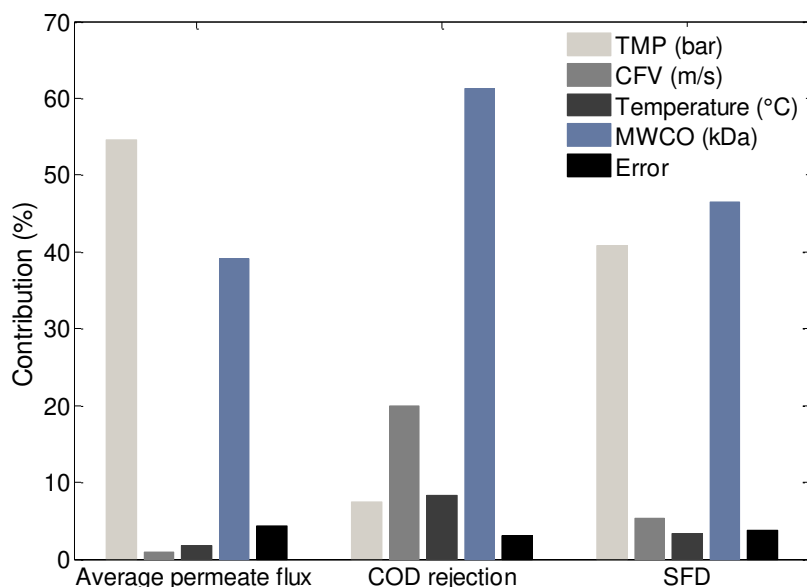
Responses	Factors	DOF	SS	MS	F-Value	p-Value
Average permeate flux	TMP (bar)	2	6357.68	3178.84	114.01	0.000
	CFV (m/s)	2	54.76	27.38	0.98	0.394
	Temperature (°C)	2	179.15	89.58	3.21	0.064
	MWCO (kDa)	2	4546.30	2273.15	81.52	0.000
	Error/others	18	501.90	27.88		
	Total	26	11,639.80			
COD rejection	TMP (bar)	2	73.55	36.78	21.70	0.000
	CFV (m/s)	2	198.21	99.11	58.47	0.00
	Temperature (°C)	2	82.58	41.29	24.36	0.00
	MWCO (kDa)	2	607.95	303.98	17.34	0.00
	Error/others	18	30.51	1.70		
	Total	26	992.79			
SFD	TMP (bar)	2	46.48	23.24	96.57	0.000
	CFV (m/s)	2	6.12	3.06	12.72	0.000
	Temperature (°C)	2	3.80	1.90	7.89	0.003
	MWCO (kDa)	2	52.95	26.47	110.00	0.000
	Error/others	18	4.33	0.24		
	Total	26	113.68			

In order to determine the qualitative significance of each factor on the responses, Fisher’s test (F-value) was employed in the ANOVA analysis. An F-value is defined as the ratio of variance due to the effect of a factor on the variance due to the inherent error in the system [57]. The F-value was compared to the critical F-value (Fcr) [52]. A calculated F-value lower than the Fcr-value means that the effect of that factor is not significant at the selected confidence level or/and it is not important in comparison with the error term. In this study, with four factors, three levels for each factor and three repetitions at each trial condition, the DOF for each factor is 2 and the DOF for the error is 18, so the Fcr-value at a confidence level of 95% is equal to 3.55. In accordance with the ANOVA table, for average permeation flux, the F-value for TMP and MWCO (114.1 and 81.52, respectively) are greater than the Fcr-value. This means that the variance of these factors is significant compared with the variance of error and they have a significant effect on the response. On the other hand, temperature and CFV had no meaningful qualitative effect on  $\bar{J}_p$ , as their F-values were less than the Fcr-value. Furthermore, COD rejection rate and SFD presented F-values for all factors greater than the Fcr-value which means that the effect of these factors is significant at the 95% confidence level and they have a meaningful qualitative effect on responses.

Another statistical tool that is helpful for qualitative evaluation in ANOVA is the p-value, which is used to indicate which factors had a significant effect on the responses. The smaller the p-value at an  $\alpha$  level of significance, the more significant is the corresponding factor [58,59]. In this study, based on p-values at the 95% confidence level ( $\alpha = 0.05$ ), all the factors had a statistically significant (p-value < 0.05) effect on the COD rejection rate and SFD. For  $\bar{J}_p$ , CFV and temperature had a p-value higher than 0.05, thus the effect may be regarded as insignificant and it can be ignored.

The use of the percentage contribution (P%) in ANOVA analysis is helpful for the quantitative evaluation of the factorial effects of the performance indicators. The percentage contributions P% of all factors on average permeate flux, COD rejection rate, and SFD are shown in Figure 5. TMP (P% = 54.62) was the most important factor on average permeate flux, as higher pressure resulted in higher permeate flux, according to Darcy’s law. MWCO (P% = 39.06) was the second most important factor, followed by temperature and CFV. For the COD rejection rate, the order of importance for the factors is as follows MWCO > CFV > temperature > TMP. In addition, MWCO and TMP (46.57% and 40.89%,

respectively) were the most significant parameters on membrane fouling resistance, followed by the CFV and temperature. TMP and MWCO were the most important factors for responses. Higher TMP and MWCO resulted in higher permeate flux. However, more intensive flux decline, due to membrane fouling, occurred at higher permeate flux.



**Figure 5.** ANOVA results for the percentage contribution of each factor to the response processes.

It is important to mention that the values reported due to error resulting from uncontrollable noises should be below 50% for the results to be reliable [28,29,60]. Therefore, it can be seen in Figure 5 that for average permeate flux, COD rejection rate and SFD, the error values are 4.31%, 3.07%, and 3.81%, respectively. This means that the error values for the experiment are not significant for the UF process.

### 3.4. Optimal Results Obtained from the Taguchi Method and Utility Concept

The aim of optimizing the process was to find the operating conditions that led to a maximum average permeate flux and COD rejection rate based on the levels that gave the highest S/N ratios for the factors (desirable values) and to minimize the SFD, that is, the levels that gave the smallest S/N ratios (adverse values).

#### 3.4.1. Analysis of Individual Response Optimization

After identifying the optimal operating conditions, the optimal responses were predicted individually using the Taguchi method and ANOVA. Table 7 shows the Taguchi prediction results for the optimal conditions for average permeate flux, COD rejection rate and SFD.

**Table 7.** Individual Taguchi predictions for average permeate flux, COD rejection rate and SFD.

Response Variables	Optimum Operating Conditions	Significant Factors	Predicted Optimal Responses	
			S/N Ratio (dB)	Value
$\bar{J}_p$	A3, B3, C3, D3	A, D	38.19	81.20 L·m <sup>-2</sup> ·h <sup>-1</sup>
COD Rejection	A3, B3, C1, D1	A, B, C, D	35.26	57.92%
SFD	A1, B3, C1, D1	A, B, C, D	-5.10	1.80

According to the Taguchi predictions, the average permeate flux at TMP 3.0 bar, CFV 0.752 m/s, at 22.5 °C and with a 100 kDa MWCO, achieves 81.20 L·m<sup>-2</sup>·h<sup>-1</sup>. The COD rejection rate predicted under optimal conditions indicates a 57.92% rejection, higher than any value obtained in the DoE combinations. For the SFD under optimal conditions estimated by the Taguchi method, the minimum

SFD predicted is approximately 1.80, equivalent to a  $\overline{FD}$  of 8.65%. Therefore, we can see that the values of the three response variables combined are far from those values obtained experimentally (see Table 4).

### 3.4.2. Analysis of Multi-Response Optimization

As mentioned above, in order to determine the weight for each response variable, a pairwise comparison matrix was compiled using the AHP method as presented in Table 8.

**Table 8.** Pairwise comparison matrix.

Response	$\mu_1$	$\mu_2$	$\mu_3$
$\mu_1$	1.0	5.0	2.0
$\mu_2$	1/5	1.0	1/4
$\mu_3$	1/2	4.0	1.0

Thus, the weights assigned to response variables were  $W_{JP} = 0.568$ ,  $W_{COD\text{ Rejection}} = 0.098$  and  $W_{SFD} = 0.334$ . The consistency ratio index (CR) is used to evaluate the consistency of AHP estimates. In this case, it was calculated as 0.021, which should be less than the allowed value of  $CR = 0.1$ , this means that the pairwise comparison matrix was considered acceptable.

The overall utility index for the  $\mu_{MRSN}$  was calculated using Equation (13) with values associated with the weights of each response, using the larger the better (S/N) and the results are presented in Table 9.

**Table 9.** Utility value based on UF responses ( $\bar{J}_P$ , COD rejection, SFD) for each repetition of the experiment.

Trial n°	Utility Value		
	R1	R2	R3
1	13.60	16.42	13.96
2	15.19	15.81	15.64
3	16.69	16.43	16.99
4	18.11	18.03	18.58
5	18.37	16.24	17.72
6	19.45	19.89	18.53
7	17.14	17.32	18.17
8	18.39	19.02	19.27
9	17.46	18.16	17.32

R1, R2 and R3 is the number of repetitions of the experiment.

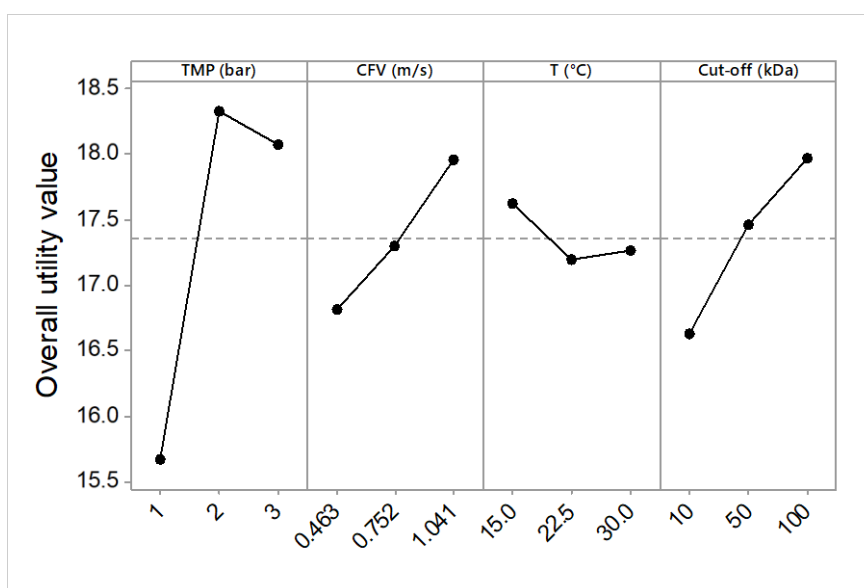
ANOVA analysis was also performed for the multiple response variables using the utility concept. From Table 10 it is clear that when F-value is compared with  $F_{cr}$  (3.55), TMP, MWCO and CFV had a qualitatively significant effect (at a confidence level of 95%) on MRSN. The percentage contributions extracted from the ANOVA table were also used to determine the significance of each operating parameter in the process. The P% values were arranged as follows:  $TMP > MWCO > CFV > Temperature$ . Therefore, according to the results, TMP and MWCO were the most important factors in optimizing the multi-response UF system.

The optimal operating conditions for the simultaneous response were obtained based on the criteria that both  $\bar{J}_P$  and COD rejection rate must be maximized and SFD should be minimized. The variation in the overall utility for the operating parameters at different levels is presented in Figure 6.



**Table 10.** ANOVA analysis results for multi-response UF (overall utility function).

Responses	Factors	DOF	SS	MS	F-value	p-value	P (%)
Utility concept	TMP (bar)	2	38.85	19.43	35.50	0.000	60.93
	CFV (m/s)	2	5.84	2.92	5.34	0.015	9.16
	Temperature (°C)	2	0.94	0.47	0.86	0.440	1.47
	MWCO (kDa)	2	8.28	4.14	7.57	0.004	12.99
	Error/others	18	9.85	0.55			15.45
	Total	26	63.76				100.00



**Figure 6.** Effect of operating parameters on mean utility value ( $\bar{J}_p$  COD rejection rate, SFD).

It is clear from Figure 6 that the optimal combination of operating conditions (maximum value of the overall utility) was found at the second level of transmembrane pressure (2.0 bar), the second level of cross-flow velocity (1.041 m/s), the first level of temperature (15 °C), and third level of MWCO (100 kDa).

Once the optimal levels had been selected the next step was to estimate the multi-response S/N ratio and predict the optimal values for the simultaneous optimization response, calculated using Equation (17) and presented in Table 11.

**Table 11.** Optimal conditions for multi-response UF predicted using the utility concept.

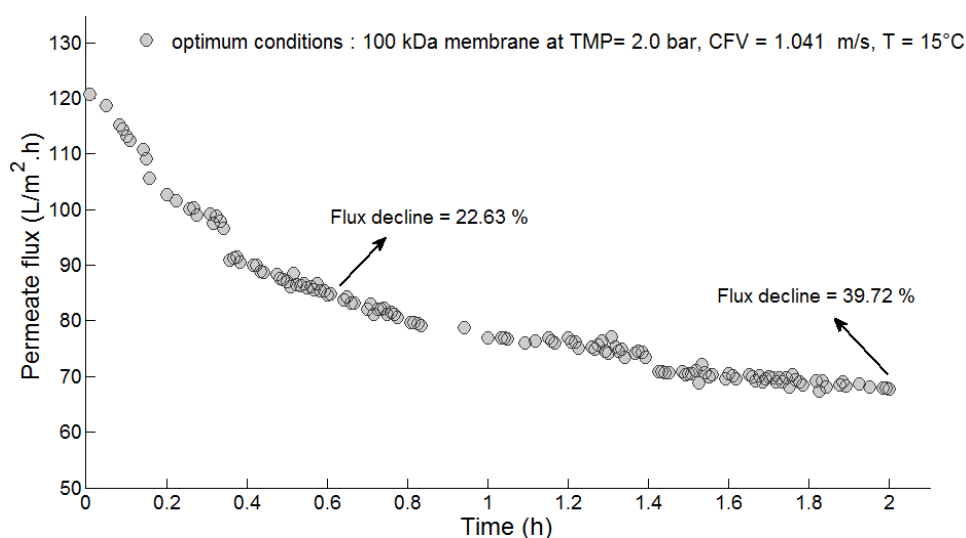
Method	Response	Optimal Conditions	Optimal Values
Multi-response	MRSN (dB)	A2 B3 C1 D3	19.82
	$\bar{J}_p$ (L·m <sup>-2</sup> ·h <sup>-1</sup> )		77.22
	COD (%)		45.69
	SFD/ $\overline{FD}$		6.24/30%

### 3.5. Confirmation Experiment under Optimal Conditions

After determining the optimal operating conditions for the overall utility value and the significance of factors, validation experiments (for multi-responses) were carried out at the optimal levels in order to validate the predicted UF responses suggested using the Taguchi method with utility concept [34,51].

The observed permeate flux results as a function of time under optimized conditions during the UF of PMTE are plotted in Figure 7. As described previously, the flux decline was mainly the result of two phenomena, pore blocking and cake layer formation, which mostly occurred in the first hour of the process [21,29]. During the first 30 min of the UF, the flux decreased by 22.63%. Furthermore,

immediately after pore blockage, the permeate flux continued to decline due to the formation and growth of a cake layer until the system approached the quasi-steady state. At the end of the process (after 2 h), the final permeate flux was about  $67.0 \text{ L}\cdot\text{m}^{-2}\cdot\text{h}^{-1}$  and flux decline was around 39.72%, which confirms that the membrane fouling took place with a higher rate in the first 30 min and at a slower rate when the system had achieved a steady state. Therefore, the observed experimental values of average permeate flux and cumulative flux decline were about  $81.15 \text{ L}\cdot\text{m}^{-2}\cdot\text{h}^{-1}$  and 6.01 (SFD equivalent to a  $\overline{FD}$  value of 28.96%).



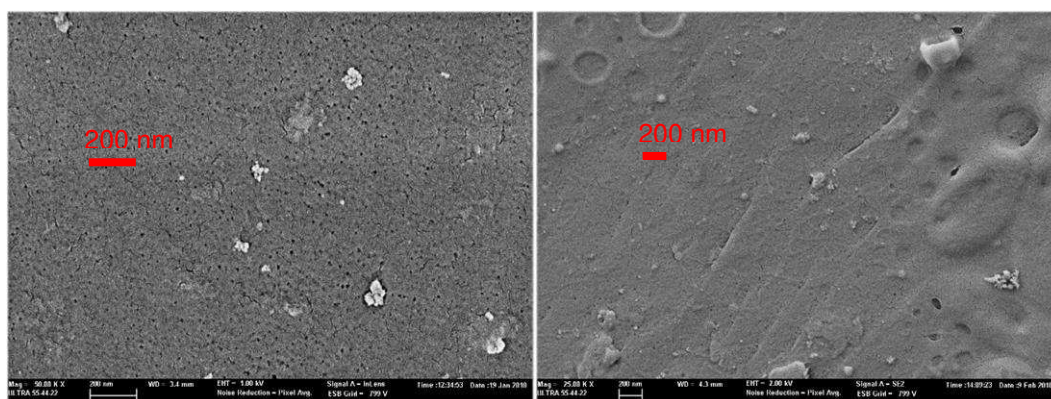
**Figure 7.** Permeate flux as a function of time under optimized conditions during UF of paper mill wastewater: PES 100 kDa membrane at TMP = 2.0 bar, CFV = 0.752 m/s and T = 15 °C.

The total resistance ( $R_t$ ) at the end of the 2-h experiment under optimal conditions was  $1.13 \times 10^{13} \text{ m}^{-1}$ , which is sum of the intrinsic membrane resistance ( $R_m = 3.40 \times 10^{12} \text{ m}^{-1}$ ) and fouling resistance ( $R_f = 7.91 \times 10^{12} \text{ m}^{-1}$ ).

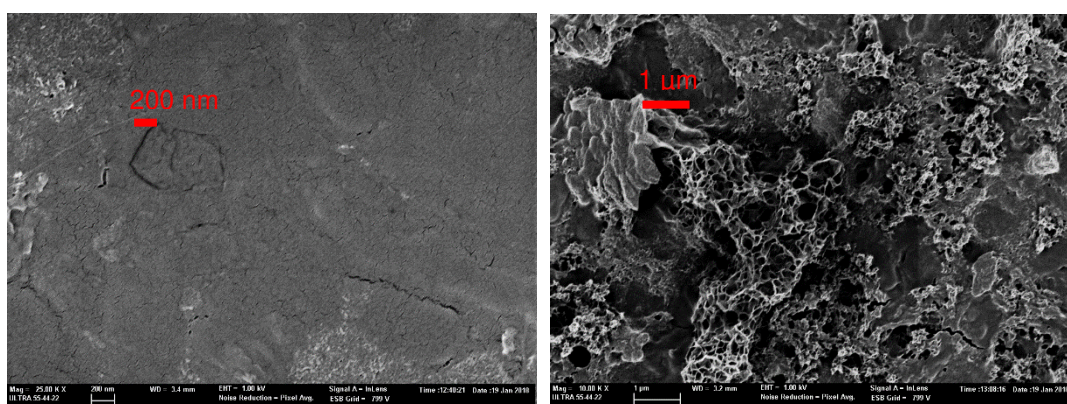
In addition, the membrane surface morphologies were observed by FESEM. Figure 8 shows the images of the membrane (PES 100 kDa) before and after the UF experiments were carried out. As can clearly be seen, before UF there is no blocking on the pores and no cake layer on the membrane surface. Figure 8b,c shows the surface of the membrane fouling after 30 min and after 2 h. In both cases, the images show the existence of pore blocking due to DCS adsorption within the membrane pores and sediments deposited on the surface (cake layer) acting to resist the UF [61]. Figure 8d shows the morphologies of the fouling sediments on the membrane.

Furthermore, it can be seen that the membrane was indeed fouled after 30 min filtration. However, the FESEM images of the membranes after filtration, at 2 h, were highly similar to the membranes after 30 min filtration. Therefore, it may be concluded that the permeate flux decline might result from the pore blocking as opposed to the formation and growth of the cake layer on the membrane.

Additionally, to verify the permeate applicability for paper mill reuse, the physical and chemical properties of the treated effluent obtained under optimal operational conditions (PES 100 kDa membrane at TMP = 2.0 bar, CFV = 0.752 m/s, and T = 15 °C) were compared with treated paper mil effluent used in this study as feed solution (Table 1). The results obtained for the physical-chemical parameters are given in Table 12. From the results obtained, all properties showed high retention efficiencies and proved the effectiveness of the UF under optimal conditions.



(a) (b).



(c) (d).

**Figure 8.** Field-emission scanning electron microscope (FESEM) image of fresh and fouled membranes (PES 100 kDa) at different operating times, (a) clean membrane surface, (b) membrane surface fouled after 30 min filtration, (c) at the end of the UF (2 h) with pore blocking and cake layer (d) membrane foulant sediments.

**Table 12.** Permeate quality (process performance) under optimum conditions, at the end of 2 h operating.

Parameter	UF Permeate Quality	Percent Removal (%)
TSS (g/L)	0.0002	99.57
Turbidity (NTU)	0.08	97.51
COD (mg/L)	81.8	43.90
Total nitrogen (mg/L)	0.53	33.75
particle size (nm)	12.76–24.36	–

The optimum predicted results at the 95% confidence interval calculated using Equation (18) and the observed experimental results for the response variables are given in Table 13.

The observed multi-response of the overall utility falls within the 95% confidence interval for the optimal range of the response variables. In addition, it is clearly observed that the deviation between predicted and experimental results is very small, which confirms that the Taguchi method and utility concept can be used to predict the multi-response UF for any parametric combination, while individual optimization don't got good predictions.

**Table 13.** Summary and comparison of experimental and predicted optimal conditions for PMTE.

Method	Response	Optimal Conditions	Optimal Values	95% CI <sub>CE</sub>	Confirmation Experiments	% Deviation
Multi-response	MRSN (dB)	A2 * B3 * C1 D3 *	19.78	18.54 ≤ MRSN ≤ 21.08	19.78	0.27
	$\bar{J}_p$ (L·m <sup>-2</sup> ·h <sup>-1</sup> )		77.22	68.16 ≤ $\bar{J}_p$ ≤ 86.28	81.15	4.84
	COD (%)		45.69	43.45 ≤ COD ≤ 47.92	43.90	4.07
	SFD		6.24	5.39 ≤ SFD ≤ 7.08	6.01	3.75

\* Significant at the 95% confidence interval.

#### 4. Conclusions

In this study, the Taguchi method, utility concept and ANOVA analysis were used as statistical tools to investigate the effects and significance of four operating parameters and to optimize the UF process with respect to average permeate flux, COD rejection rate and cumulative flux decline.

ANOVA was used to determine the most significant factors affecting the response variables. From the percentage contribution, the order of importance of each factor in maximum  $\bar{J}_p$  was TMP > MWCO > T > CFV; for maximum COD rejection rate it was MWCO > CFV > T > TMP; and to achieve the minimum SFD: MWCO > TMP > CFV > T.

The optimal UF operating parameters, based on the Taguchi method and utility concept, were found at TMP (2.0 bar), CFV (1.041 m/s), temperature (15 °C) and MWCO (100 kDa). Under these optimal conditions,  $\bar{J}_p$ , COD rejection rate and SFD resistance of 81.15 L·m<sup>-2</sup>·h<sup>-1</sup>, 43.90% and 6.01 (around and  $\bar{FD}$  value of 28.96 %), respectively, were obtained and they were within of the predicted range at the 95% confidence interval.

Measurements of turbidity, COD and particle size in the permeate showed a significant decrease 3.21 to 0.0002 NTU, 146 mg/L to 81.8 mg/L and 458–1281 nm to 12.71–24.36 nm, respectively, which confirms a substantial reduction in colloidal compounds. Therefore, it can be said that UF is suitable for removing dissolved and colloidal substances from wastewater effluents from recycled paperboard manufacturing.

Finally, we can say that the Taguchi method and utility allow membrane conditions for the P & P wastewater treatment to be optimized using a reduced number of experiments. The methodology used in this study could be used as a guideline for operating UF systems applied as a tertiary treatment for paperboard mill treated effluents under optimal conditions.

**Author Contributions:** Conceptualization, J.L.-G., M.-F.L.-P., M.R.S.S., A.S.-M. and J.M.G.-Z.; methodology, M.R.S.S., A.S.-M. and J.M.G.-Z.; software, M.R.S.S., A.S.-M. and J.M.G.-Z.; validation, J.L.-G., M.-F.L.-P., M.R.S.S., A.S.-M. and J.M.G.-Z.; formal analysis, J.L.-G., M.-F.L.-P., M.R.S.S., A.S.-M.; investigation, M.R.S.S. resources, M.R.S.S.; data curation, J.L.-G., M.-F.L.-P., M.R.S.S., A.S.-M. and J.M.G.-Z.; writing—original draft preparation, M.R.S.S.; writing—review and editing, M.-F.L.-P., M.R.S.S., A.S.-M. and J.M.G.-Z.; visualization, M.R.S.S., A.S.-M. and J.M.G.-Z.; supervision, J.L.-G. All authors have read and agreed to the published version of the manuscript.

**Funding:** This research received no external funding.

**Acknowledgments:** The authors of this work wish to gratefully acknowledge the assistance received from the UPV through its research program, and the Research Institute for Industrial, Radiophysical and Environmental Safety (ISIRYM).

**Conflicts of Interest:** The authors declare no conflicts of interest.

#### References

- Sevimli, M. Post-Treatment of Pulp and Paper Industry Wastewater by Advanced Oxidation Processes. *Ozone Sci. Eng. Ozone Sci. Eng.* **2005**, *27*, 37–43. [CrossRef]
- CEPI. Key Statistics Report 2017 | CEPI-CONFEDERATION OF EUROPEAN PAPER INDUSTRIES. Available online: <http://www.cepi.org/keystatistics2017> (accessed on 20 September 2018).
- Rajkumar, K. An Evaluation of Biological Approach for the Effluent Treatment of Paper Boards Industry-An Economic Perspective. *J. Bioremediation Biodegrad.* **2016**, *7*. [CrossRef]

4. Suhr, M.; Klein, G.; Kourti, I.; Gonzalo, M.R.; Santonja, G.G.; Roudier, S.; Sancho, L.D. Best Available Techniques (BAT) Reference Document for the Production of Pulp, Paper and Board. *Eur. Comm.* **2015**, *906*. [[CrossRef](#)]
5. Ahmad, A.; Wong, S.; Teng, T.; Zuhairi, A. Improvement of Alum and PACl Coagulation by Polyacrylamides (PAMs) for the Treatment of Pulp and Paper Mill Wastewater. *Chem. Eng. J.* **2008**, *137*, 510–517. [[CrossRef](#)]
6. Temmink, H.; Grolle, K. Tertiary Activated Carbon Treatment of Paper and Board Industry Wastewater. *Bioresour. Technol.* **2005**, *96*, 1683–1689. [[CrossRef](#)] [[PubMed](#)]
7. Zhang, Q.; Chuang, K.T. Adsorption of Organic Pollutants from Effluents of a Kraft Pulp Mill on Activated Carbon and Polymer Resin. *Adv. Environ. Res.* **2001**, *5*, 251–258. [[CrossRef](#)]
8. Catalkaya, E.C.; Kargi, F. Advanced Oxidation Treatment of Pulp Mill Effluent for TOC and Toxicity Removals. *J. Environ. Manag.* **2008**, *87*, 396–404. [[CrossRef](#)]
9. Pérez, M.; Torrades, F.; García-Hortal, J.A.; Domènech, X.; Peral, J. Removal of Organic Contaminants in Paper Pulp Treatment Effluents under Fenton and Photo-Fenton Conditions. *Appl. Catal. B Environ.* **2002**, *36*, 63–74. [[CrossRef](#)]
10. Gönder, Z.B.; Arayici, S.; Barlas, H. Treatment of Pulp and Paper Mill Wastewater Using Ultrafiltration Process: Optimization of the Fouling and Rejections. *Ind. Eng. Chem. Res.* **2012**, *51*, 6184–6195. [[CrossRef](#)]
11. Liua, G.; Liu, Y.; Shib, H.; Qianb, Y. Treatability of Kraft Spent Liquor by Microfiltration and Ultrafiltration. *Desalination* **2004**, *11*, 131–141. [[CrossRef](#)]
12. Nuortila-Jokinen, J.; Mänttari, M.; Huuhilo, T.; Kallioinen, M.; Nyström, M. Water Circuit Closure with Membrane Technology in the Pulp and Paper Industry. *Water Sci. Technol. A J. Int. Assoc. Water Pollut. Res.* **2004**, *50*, 217–227. [[CrossRef](#)]
13. Zaidi, A.; Buisson, H.; Sourirajan, S.; Wood, H. Ultra- and Nano-Filtration in Advanced Effluent Treatment Schemes for Pollution Control in the Pulp and Paper Industry. *Water Sci. Technol.* **1992**, *25*, 263–276. [[CrossRef](#)]
14. Toczyłowska-Mamińska, R. Limits and perspectives of pulp and paper industry wastewater treatment—A review. *Renew. Sustain. Energy Rev.* **2017**, *78*, 764–772. [[CrossRef](#)]
15. Kamali, M.; Khodaparast, Z. Review on recent developments on pulp and paper mill wastewater treatment. *Ecotoxicol. Environ. Saf.* **2015**, *114*, 326–342. [[CrossRef](#)]
16. Beril Gönder, Z.; Arayici, S.; Barlas, H. Advanced Treatment of Pulp and Paper Mill Wastewater by Nanofiltration Process: Effects of Operating Conditions on Membrane Fouling. *Sep. Purif. Technol.* **2011**, *76*, 292–302. [[CrossRef](#)]
17. Neves, L.C.; Souza, J.B.D. Pulp and paper mill effluent post-treatment using microfiltration and ultrafiltration membranes. *Cell. Chem. Technol.* **2017**, *51*, 579–588.
18. Shukla, S.K.; Kumar, V.; Van Doan, T.; Yoo, K.; Kim, Y.; Park, J. Combining activated sludge process with membrane separation to obtain recyclable quality water from paper mill effluent. *Clean Technol. Environ. Policy* **2015**, *17*, 781–788. [[CrossRef](#)]
19. Chen, C.; Mao, S.; Wang, J.; Bao, J.; Xu, H.; Su, W.; Dai, H. Application of Ultrafiltration in a Paper Mill: Process Water Reuse and Membrane Fouling Analysis. *BioResources* **2015**, *10*, 2376–2391. [[CrossRef](#)]
20. Krawczyk, H.; Oinonen, P.; Jönsson, A.-S. Combined Membrane Filtration and Enzymatic Treatment for Recovery of High Molecular Mass Hemicelluloses from Chemithermomechanical Pulp Process Water. *Chem. Eng. J.* **2013**, *225*, 292–299. [[CrossRef](#)]
21. Sousa, M.R.S.; Lora-Garcia, J.; López-Pérez, M.-F. Modelling Approach to an Ultrafiltration Process for the Removal of Dissolved and Colloidal Substances from Treated Wastewater for Reuse in Recycled Paper Manufacturing. *J. Water Process Eng.* **2018**, *21*, 96–106. [[CrossRef](#)]
22. Karthik, M.; Dhodapkar, R.; Manekar, P.; Aswale, P.; Nandy, T. Closing water loop in a paper mill section for water conservation and reuse. *Desalination* **2011**, *281*, 172–178. [[CrossRef](#)]
23. Mänttari, M.; Nuortila-Jokinen, J.; Nyström, M. Evaluation of Nanofiltration Membranes for Filtration of Paper Mill Total Effluent. *Filtr. Sep.* **1997**, *34*, 275–280. [[CrossRef](#)]
24. Cassano, A.; Conidi, C.; Drioli, E. Comparison of the Performance of UF Membranes in Olive Mill Wastewaters Treatment. *Water Res.* **2011**, *45*, 3197–3204. [[CrossRef](#)] [[PubMed](#)]
25. Puro, L.; Tanninen, J.; Nyström, M. Analyses of Organic Foulants in Membranes Fouled by Pulp and Paper Mill Effluent Using Solid-Liquid Extraction. *Desalination* **2002**, *143*, 1–9. [[CrossRef](#)]

26. Puro, L.; Kallioinen, M.; Mänttari, M.; Nyström, M. Evaluation of Behavior and Fouling Potential of Wood Extractives in Ultrafiltration of Pulp and Paper Mill Process Water. *J. Membr. Sci.* **2011**, *368*, 150–158. [[CrossRef](#)]
27. Hesampour, M.; Krzyzaniak, A.; Nyström, M. The Influence of Different Factors on the Stability and Ultrafiltration of Emulsified Oil in Water. *J. Membr. Sci.* **2008**, *325*, 199–208. [[CrossRef](#)]
28. Pourjafar, S.; Jahanshahi, M.; Rahimpour, A. Optimization of TiO<sub>2</sub> Modified Poly(Vinyl Alcohol) Thin Film Composite Nanofiltration Membranes Using Taguchi Method. *Desalination* **2013**, *315*, 107–114. [[CrossRef](#)]
29. Reyhani, A.; Sepehrinia, K.; Shahabadi, S.M.S.; Rekabdar, F.; Gheshlaghi, A. Optimization of Operating Conditions in Ultrafiltration Process for Produced Water Treatment via Taguchi Methodology. *Desalin. Water Treat.* **2015**, *54*, 2669–2680. [[CrossRef](#)]
30. Rezvanpour, A.; Roostaazad, R.; Hesampour, M.; Nyström, M.; Ghotbi, C. Effective Factors in the Treatment of Kerosene–Water Emulsion by Using UF Membranes. *J. Hazard. Mater.* **2009**, *161*, 1216–1224. [[CrossRef](#)]
31. Salahi, A.; Abbasi, M.; Mohammadi, T. Permeate Flux Decline during UF of Oily Wastewater: Experimental and Modeling. *Desalination* **2010**, *251*, 153–160. [[CrossRef](#)]
32. Salahi, A.; Mohammadi, T. Oily Wastewater Treatment by Ultrafiltration Using Taguchi Experimental Design. *Water Sci. Technol. Lond.* **2011**, *63*, 1476–1484. [[CrossRef](#)] [[PubMed](#)]
33. Ezzati, A.; Gorouhi, E.; Mohammadi, T. Separation of Water in Oil Emulsions Using Microfiltration. *Desalination* **2005**, *185*, 371–382. [[CrossRef](#)]
34. Kaladhar, M.; Subbaiah, K.V.; Rao, C.S.; Rao, K.N. Application of Taguchi Approach and Utility Concept in Solving the Multi-Objective Problem When Turning AISI 202 Austenitic Stainless Steel. *J. Eng. Sci. Technol. Rev.* **2011**, *4*, 55–61. [[CrossRef](#)]
35. Mohammadi, T.; Safavi, M.A. Application of Taguchi Method in Optimization of Desalination by Vacuum Membrane Distillation. *Desalination* **2009**, *249*, 83–89. [[CrossRef](#)]
36. Park, S. *Robust Design and Analysis for Quality Engineering*; Springer US: New York, NY, USA, 1996.
37. APHA. *Standard Methods for the Examination of Water and Wastewater*, 20th ed.; American Public Health Association: Washington, DC, USA, 1998.
38. Cheryan, M. *Ultrafiltration and Microfiltration Handbook*; CRC Press: Washington, DC, USA, 1998.
39. Khan, M.T.; Takizawa, S.; Lewandowski, Z.; Jones, W.L.; Camper, A.K.; Katayama, H.; Kurisu, F.; Ohgaki, S. Membrane Fouling Due to Dynamic Particle Size Changes in the Aerated Hybrid PAC–MF System. *J. Membr. Sci.* **2011**, *371*, 99–107. [[CrossRef](#)]
40. Rezaei, H.; Ashtiani, F.Z.; Fouladitajar, A. Fouling Behavior and Performance of Microfiltration Membranes for Whey Treatment in Steady and Unsteady-State Conditions. *Braz. J. Chem. Eng.* **2014**, *31*, 503–518. [[CrossRef](#)]
41. Cojocar, C.; Zakrzewska-Trznadel, G. Response Surface Modeling and Optimization of Copper Removal from Aqua Solutions Using Polymer Assisted Ultrafiltration. *J. Membr. Sci.* **2007**, *298*, 56–70. [[CrossRef](#)]
42. Idris, A.; Ismail, A.F.; Noordin, M.Y.; Shilton, S.J. Optimization of Cellulose Acetate Hollow Fiber Reverse Osmosis Membrane Production Using Taguchi Method. *J. Membr. Sci.* **2002**, *205*, 223–237. [[CrossRef](#)]
43. Phadke, M.S. *Quality Engineering Using Robust Design*; Prentice Hall: Englewood Cliffs, NJ, USA, 1989.
44. Roy, R.K. *A Primer on the Taguchi Method*; Society of Manufacturing Engineers: Southfield, MI, USA, 1990.
45. Barua, P.B.; Kumar, P.; Gaiindhar, J.L. Optimal Setting of Process Parameters for Multi-Characteristic Products Using Taguchi Design and Utility-Conceptan Approach. *Proc. ICAMIE Univ. Roorkee (India)* **1997**, *1997*, 839–842.
46. Goyal, S.; Singh Kandra, V.; Yadav, P. Experimental study of turning operation and optimization of MMR and surface roughness using Taguchi method. *Int. J. Innov. Res. Adv. Eng.* **2016**. [[CrossRef](#)]
47. Bunn, D.W. *Analysis for Optimal Decisions*; John Wiley & Sons: New York, NY, USA, 1982.
48. Kumar, Y.; Singh, H. Multi-Response Optimization in Dry Turning Process Using Taguchi’s Approach and Utility Concept. *Procedia Mater. Sci.* **2014**, *5*, 2142–2151. [[CrossRef](#)]
49. Saaty, T.L. *Analytic Hierarchy Process*; McGraw Hill Higher Education: New York, NY, USA, 1980.
50. Kansal, H.K.; Singh, S.; Kumar, P. Performance Parameters Optimization (Multi-Characteristics) of Powder Mixed Electric Discharge Machining (PMEDM) through Taguchi’s Method and Utility Concept. *Indian J. Eng. Mater. Sci.* **2006**, *29*, 81–94.
51. Ross, P.J. *Taguchi Techniques for Quality Engineering: Loss Function, Orthogonal Experiments, Parameter and Tolerance Design*; McGraw Hill Professional: Washington, DC, USA, 1996.

52. Montgomery, D.C. *Design and Analysis of Experiments*; John Wiley & Sons: Hoboken, NJ, USA, 2008.
53. Song, L. Flux Decline in Crossflow Microfiltration and Ultrafiltration: Mechanisms and Modeling of Membrane Fouling. *J. Membr. Sci.* **1998**, *139*, 183–200. [[CrossRef](#)]
54. Mulder, J. *Basic Principles of Membrane Technology*, 2nd ed.; Springer: Dordrecht, The Netherlands, 1996.
55. Xu, J.; Chang, C.-Y.; Gao, C. Performance of a Ceramic Ultrafiltration Membrane System in Pretreatment to Seawater Desalination. *Sep. Purif. Technol.* **2010**, *75*, 165–173. [[CrossRef](#)]
56. Seyed Shahabadi, S.M.; Reyhani, A. Optimization of Operating Conditions in Ultrafiltration Process for Produced Water Treatment via the Full Factorial Design Methodology. *Sep. Purif. Technol.* **2014**, *132*, 50–61. [[CrossRef](#)]
57. Ennil Köse, T. Agricultural Residue Anion Exchanger for Removal of Dye stuff from Wastewater Using Full Factorial Design. *Desalination* **2008**, *222*, 323–330. [[CrossRef](#)]
58. Cochran, W.G. *Experimental Designs*, 2nd ed.; WILEY: New York, NY, USA, 1992.
59. Myers, R.H.; Montgomery, D.C.; Anderson-Cook, C.M. *Response Surface Methodology: Process and Product Optimization Using Designed Experiments*, 4th ed.; Wiley: Hoboken, NJ, USA, 2016.
60. Gönder, Z.B.; Kaya, Y.; Vergili, I.; Barlas, H. Optimization of Filtration Conditions for CIP Wastewater Treatment by Nanofiltration Process Using Taguchi Approach. *Sep. Purif. Technol.* **2010**, *70*, 265–273. [[CrossRef](#)]
61. Reyhani, A.; Hemmati, M. Wastewater Treatment by Ultrafiltration System, Considering the Effects of Operating Conditions: Experimental and Modeling. *Desalin. Water Treat.* **2014**, *52*, 6282–6294. [[CrossRef](#)]



© 2020 by the authors. Licensee MDPI, Basel, Switzerland. This article is an open access article distributed under the terms and conditions of the Creative Commons Attribution (CC BY) license (<http://creativecommons.org/licenses/by/4.0/>).

Article

# A Simple Method to Identify the Dominant Fouling Mechanisms during Membrane Filtration Based on Piecewise Multiple Linear Regression

Hao Xu <sup>1,2</sup>, Kang Xiao <sup>1,3,\*</sup> , Jinlan Yu <sup>1</sup>, Bin Huang <sup>2</sup>, Xiaomao Wang <sup>4</sup>, Shuai Liang <sup>5</sup>, Chunhai Wei <sup>2,\*</sup> , Xianghua Wen <sup>4</sup> and Xia Huang <sup>4,6</sup>

<sup>1</sup> College of Resources and Environment, University of Chinese Academy of Sciences, Beijing 100049, China; xuhao9510@163.com (H.X.); yujinlan18@mails.ucas.ac.cn (J.Y.)

<sup>2</sup> School of Civil Engineering, Guangzhou University, Guangzhou 510006, China; huangbinstudy@163.com

<sup>3</sup> Center for Ocean Mega-Science, Chinese Academy of Sciences, Qingdao 266071, China

<sup>4</sup> State Key Joint Laboratory of Environment Simulation and Pollution Control, School of Environment, Tsinghua University, Beijing 100084, China; wangxiaomao@tsinghua.edu.cn (X.W.); xhwen@tsinghua.edu.cn (X.W.); xhuang@tsinghua.edu.cn (X.H.)

<sup>5</sup> College of Environmental Science and Engineering, Beijing Forestry University, Beijing 100083, China; shuai\_liang@bjfu.edu.cn

<sup>6</sup> Research and Application Center for Membrane Technology, School of Environment, Tsinghua University, Beijing 100084, China

\* Correspondence: kxiao@ucas.ac.cn (K.X.); weich@gzhu.edu.cn (C.W.)

Received: 8 July 2020; Accepted: 27 July 2020; Published: 29 July 2020



**Abstract:** Membrane fouling is a complicated issue in microfiltration and ultrafiltration. Clearly identifying the dominant fouling mechanisms during the filtration process is of great significance for the phased and targeted control of fouling. To this end, we propose a semi-empirical multiple linear regression model to describe flux decline, incorporating the five fouling mechanisms (the first and second kinds of standard blocking, complete blocking, intermediate blocking, and cake filtration) based on the additivity of the permeate volume contributed by different coexisting mechanisms. A piecewise fitting protocol was established to distinguish the fouling stages and find the significant mechanisms in each stage. This approach was applied to a case study of a microfiltration membrane filtering a model foulant solution composed of polysaccharide, protein, and humic substances, and the model fitting unequivocally revealed that the dominant fouling mechanism evolved in the sequence of initial adaptation, fast adsorption followed by slow adsorption inside the membrane pores, and the gradual growth of a cake/gel layer on the membrane surface. The results were in good agreement with the permeate properties (total organic carbon, ultraviolet absorbance, and fluorescence) during the filtration process. This modeling approach proves to be simple and reliable for identifying the main fouling mechanisms during membrane filtration with statistical confidence.

**Keywords:** fouling development model; filtration law; pore blocking; multiple linear regression; statistical test

## 1. Introduction

Membrane fouling is an obstinate problem in microfiltration (MF, see Appendix C for all the Abbreviations) and ultrafiltration (UF) for water and wastewater treatment [1–5]. Membrane fouling refers to the process of flux decline (or increase in hydraulic resistance) during filtration due to the deposition of suspended or soluble substances on the membrane surface, at the pore openings, or inside the pores. As a result, membrane fouling reduces the efficiency of filtration. Membrane fouling includes



organic fouling, inorganic fouling, and biofouling. Organic matter does not only cause organic fouling which is prevalent in MF and UF systems; it is also seriously involved in inorganic–organic combined fouling (such as impervious gel layers due to metal–organic complexation) and bio-organic fouling (such as biofilms stubborn against cleaning). Among organic foulants, polysaccharides, proteins, and humic acids are the most reported [6,7]. Upon removing the foulants from the membrane, frequent physical or chemical cleaning will increase energy consumption, shorten membrane life and increase operating costs. A realistic goal of fouling control is to preventively delay and mitigate fouling or to more efficiently remove the deposited foulants in a well phased and targeted manner [8–10]. To this end, it is of great significance to clearly identify the key mechanisms for the dynamic development of membrane fouling, from internal pore blockage to external cake build-up, using appropriate analytical or modeling approaches.

Classical filtration laws have been widely used to describe the fouling process. The classical filtration laws include four basic types of fouling, which can be expressed by a collective expression:

$$\frac{d^2t}{dV^2} = k\left(\frac{dt}{dV}\right)^N \text{ or equivalently, } \frac{dR}{dV} = kR^N \quad (1)$$

where  $t$  is filtration time,  $V$  is specific permeate volume,  $R$  is filtration resistance,  $k$  is a model coefficient, and the characteristic exponent  $N$  indicates fouling modes:  $N = 2, 1.5, 1,$  and  $0$  represent complete blocking (clogging at the pore opening), standard blocking (the first kind for instantaneous adsorption of foulant on the pore wall), intermediate blocking (random deposition on the membrane surface) and cake filtration (uniform growth of a cake or gel layer on the surface), respectively. Recently, the standard blocking law has been extended to include the second kind ( $N = 2.5$ ) for the case of slow adsorption (e.g., hydrophilic foulant on hydrophilic pore walls) compared to permeate advection through the pores [11]. Mathematical modeling plays an essential role in interpreting various fouling mechanisms and processes. Through model fitting using Equation (1), it is plausible that the characteristic exponent  $N$ , and, hence, the type of fouling mechanism can be determined.

However, the actual situation is often more complicated. First, a variety of mechanisms may coexist. Regarding this, researchers have developed combined models incorporating different fouling types. Many researchers have derived dually combined fouling models such as the cake-complete blocking, cake-intermediate blocking, cake-standard blocking, complete-standard blocking, and intermediate-standard blocking models [12–19]. Some have combined three or even four mechanisms to interpret fouling behavior. Duclos-Orsello et al. developed a flux decline model that combined three fouling mechanisms (standard blocking, complete blocking, and cake filtration) to describe the MF process of a bovine serum albumin solution [20]. Kim et al. combined all the four classical fouling modes into one mechanistic model to explain the effect of coexisting fouling mechanisms [21]. However, the forms of the combined models are often complex (the more combinations, the more complex), thus requiring nonlinear regression [22] and even genetic algorithms for the model fitting [21]. Second, the main mechanism may vary largely during the filtration process. However, a large number of researchers have used a fixed model to fit the whole process [23,24], and only a few have conducted piecewise fitting using multiple models [12,25,26]. The unreasonable setting of the time range or the number of time segments in the model fitting inevitably lead to deviations, such as the resultant autocorrelation of time series that has seldom been mentioned in previous fouling studies.

In the present study, we propose a simple and straightforward multiple linear regression model to describe the piecewise succession of five pore-blocking/cake-filtration fouling mechanisms during the full filtration process, based on the idea of the linear additivity of filtration volumes under different fouling mechanisms. The filtration curve (flux vs. volume) was fitted for each time segment, and the stepwise regression technique was used to screen out insignificant mechanisms and to identify the dominant mechanism in each time segment. The Durbin–Watson (DW) autocorrelation test was employed to justify the most reliable setting of the number and length of the time segments [27]. By using the proposed method, one can easily access the profile of fouling mechanisms during the

filtration process with statistical confidence. In comparison with the previous models, this method has the merits of the more complete inclusion of possible mechanisms, the more complete coverage of fouling stages, the more realistic handling of complex fouling caused by multiple foulants, and being statistically more rigorous. This method will help evaluate membrane potential, characterize foulant properties, and understand membrane–foulant interactions. MATLAB code is provided to support convenient usage of this method.

## 2. Model

The expression of the classical filtration laws, as shown in Equation (1), can be transformed to yield the flux vs. filtration volume relationship:

$$\frac{dJ}{dV} = -kJ^{2-N} \tag{2}$$

where  $J$  is the filtration flux ( $J = dV/dt$ ). The filtration curve can be described by five filtration models with  $N = 2.5, 2, 1.5, 1,$  and  $0$ , as shown schematically in Figure 1. By integrating Equation (2) on both sides, the  $J$ – $V$  relationships for these models are obtained as follows:

$$V - V_0 = \begin{cases} k_1(J_0^{0.5} - J^{0.5}) & \text{(1st - kind standard blocking, } N = 1.5) \\ k_2(J_0^{1.5} - J^{1.5}) & \text{(2nd - kind standard blocking, } N = 2.5) \\ k_3(J_0 - J) & \text{(complete blocking, } N = 2) \\ k_4(\ln J_0 - \ln J) & \text{(intermediate blocking, } N = 1) \\ k_5(J^{-1} - J_0^{-1}) & \text{(cake filtration, } N = 0) \end{cases} \tag{3}$$

where the subscript “0” refers to the initial state.

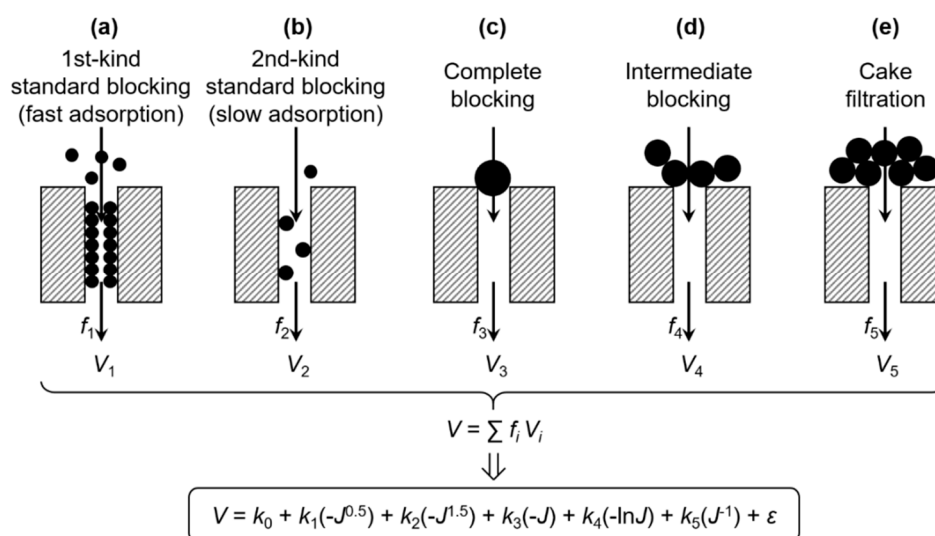
It is possible that different fouling mechanisms can simultaneously occur at different positions of the membrane. Assuming that  $f_i$  is the proportion of membrane area occupied by the  $i$ th mechanism and  $V_i$  is the resultant specific permeate volume, the contribution of various possible mechanisms to the total  $V$  can be expressed by  $V = \sum f_i V_i$  [28], as also illustrated in Figure 1. By substituting  $V_i$  using Equation (3), a comprehensive model of membrane fouling can thus be established in the form of:

$$V = \sum f_i V_i = k_0 + k_1(-J^{0.5}) + k_2(-J^{1.5}) + k_3(-J) + k_4(-\ln J) + k_5(J^{-1}) + \varepsilon \tag{4}$$

where  $V$  is the specific permeate volume of the whole membrane,  $J$  is the membrane flux of the whole membrane,  $k_0$  is a constant term, and  $k_1, k_2, k_3, k_4,$  and  $k_5$  are the coefficients of 1st kind of standard blocking (fast adsorption), the 2nd kind of standard blocking (slow adsorption), complete blocking, intermediate blocking, and cake filtration, respectively. Note that the original  $k_i$ 's in Equation (3) and the  $f_i$ 's were incorporated into the  $k_i$ 's in Equation (4). The error term,  $\varepsilon$ , encompasses errors due to the random error of  $V$  and  $J$ , the deviation of  $N$  (as a result of, e.g., non-uniformity of the pore structure [11,28,29] or polydispersity of the foulant particles [30]), the neglect of concentration polarization (a feedback effect on foulant mass transfer), and other fouling mechanisms [7,28,31], as well as possible interactive influences between different mechanisms (e.g., at adjacent areas of the membrane) that cause the nonlinearity of Equation (4).

Taking  $V$  as the dependent variable and the five  $J$ -derived terms as independent variables, Equation (4) can be used to fit the experimental  $J$ – $V$  data via least-squares regression. However, even though the multiple linear regression model takes account of all the five mechanisms, the fitting may still fail because the proportions ( $f_i$  or  $k_i$ ) of the mechanisms may change and the dominant mechanism(s) may shift during the filtration process. Therefore, a single regression model only holds in a time segment during which the mechanisms do not change significantly. In this context, it is more realistic to perform piecewise fitting into each time segment respectively, rather than fit the same model across the whole period. In each segment, the fitted result is validated by two criteria: (a) All

significant coefficients (any of  $k_1$ – $k_5$ ) should be positive, and (b) the autocorrelation of time series residuals should not be significant.



**Figure 1.** Scheme of the multiple linear regression model for membrane fouling.

The significance of the coefficients is judged by the *t*-test (by the convention that  $p < 0.05$  means significant), and a significantly positive  $k_i$  means that the *i*th mechanism is significant in this segment. The Durbin–Watson (DW) test is employed to judge the autocorrelation of time series residuals, i.e., the correlation between the regression residuals of two adjacent time points. In linear regression, it is always assumed that the residuals are independent (uncorrelated). If the assumption of independence is violated, the fitting results become problematic. For example, the positive correlation between error terms tends to amplify the value of coefficient, making the predicted variables appear important, even though they may, in fact, not be important. When fitting experimental data using Equation (4), autocorrelation arises from the unreasonable division of the time span when (a) the time segment is too long, which sacrifices the local accuracy of model fitting, or (b) the time segment is shorter than the segment used for flux calculation ( $J = \Delta V/\Delta t$ ), which causes periodic oscillation of the residuals. The autocorrelation is deemed to be significant when the *p* value of the DW test ( $p_{DW}$ ) is smaller than 0.05.

The protocol for optimizing the piecewise fitting is as follows: (a) evenly divide the filtration process  $V$  into  $n$  parts ( $n$  starts from 1), (b) conduct least-squares regression in the “stepwise” mode in each segment to automatically screen out insignificant  $k_i$ ’s, and check the DW test results for the remained significant  $k_i$ ’s, and (c) increase  $n$  and repeat the regression until the remained  $k_i$ ’s are all significantly positive and the DW test is not significant for all of the segments.

The MATLAB codes for raw data processing (to calculate  $J$ ,  $R$ , and  $dR/dV$  automatically from the original  $t$  and  $V$  data) and for the piecewise fitting are provided in Appendices A and B, respectively.

### 3. Experimental

#### 3.1. Membrane and Model Foulant Solution

Polyvinylidene fluoride (PVDF) flat-sheet membranes with a nominal pore size of 0.1  $\mu\text{m}$  (VVLP, Millipore, MA, USA) were employed in the fouling experiments. Prior to use, the membranes were rinsed and immersed in Milli-Q water for 24 h, and then they were kept in a salt background solution for 24 h to eliminate soluble impurities. The salt background solution consisted of 2 mM  $\text{CaCl}_2$ , 1 mM  $\text{MgCl}_2$ , 2 mM  $\text{NaHCO}_3$ , 12 mM  $\text{NaCl}$ , and 0.2 mM  $\text{Na}_2\text{SiO}_3$  in accordance with the salt background solution of the model foulant solution used in the fouling experiments.

The model foulant solution was comprised of 16 mg/L sodium alginate (SA) (MACKLIN, Shanghai, China), 8 mg/L humic acid (HA) (Aladdin, Shanghai, China), 4 mg/L bovine serum albumin (BSA) (Sigma-Aldrich, Saint Louis, MO, USA), and the aforementioned salt background. The polysaccharides/humics/proteins proportion was similar to that of membrane bioreactor supernatants in municipal wastewater treatment [32]. The solution was prepared by: (a) dissolving the organic foulant components in a 75% volume of Milli-Q water followed by 12 h of stirring, (b) adding the salts with the other 25% volume of Milli-Q water followed by another 12 h of stirring, and (c) filtering through a glass-fiber membrane (0.7 μm, GF/F, Whatman, Maidstone, UK) to remove undissolved coarse particles from the liquid.

### 3.2. Filtration Test

A dead-end filtration system was employed for the fouling development test at room temperature and constant pressure. The system consisted of a nitrogen cylinder, a pressure regulating valve, a liquid storage tank, a filtration cell (Amicon 8400, Millipore, MA, USA) with an effective filtration area of 41.8 cm<sup>2</sup> and a volume of 400 mL, an electronic balance (PL2002, Mettler Toledo, Zurich, Switzerland), and a computer, as shown in Figure 2. The fouling test was carried out in the procedure of: (a) pre-pressing the membrane under 5 kPa for 1 h to stabilize the deformation caused by pressure, (b) pre-filtering 200 mL of the salt background solution to measure the initial filtration resistance of the membrane, (c) pre-contacting the membrane with the model foulant solution at 5 kPa for 1 h without filtration to adapt the physicochemical state of the membrane to the solution, and (d) filtering the model foulant solution at 5 kPa with the water level in the filtration cell maintained at 200 mL (the water level was maintained via pressure balance and the net volume filtered was supplemented by the storage tank). The real-time filtration resistance  $R$  (m<sup>-1</sup>) was calculated according to Darcy’s law:

$$R = \frac{P}{\mu J} = \frac{P}{\mu} \left( \frac{\Delta V}{\Delta t} \right)^{-1} \quad (5)$$

where  $P$  is the trans-membrane pressure (Pa),  $\mu$  is the dynamic viscosity of the permeate (Pa s, approximately that of water) with the effect of temperature corrected, and  $J$  is the real-time filtration flux (m/s) calculated as  $\Delta V/\Delta t$ , where  $V$  is the specific permeate volume (m<sup>3</sup>/m<sup>2</sup>). For the calculation of  $J$ , the time increment  $\Delta t$  was found given a fixed  $\Delta V$  of 0.002 m<sup>3</sup>/m<sup>2</sup> (i.e., 0.2 cm<sup>3</sup>/cm<sup>2</sup>); see Appendix A for details.

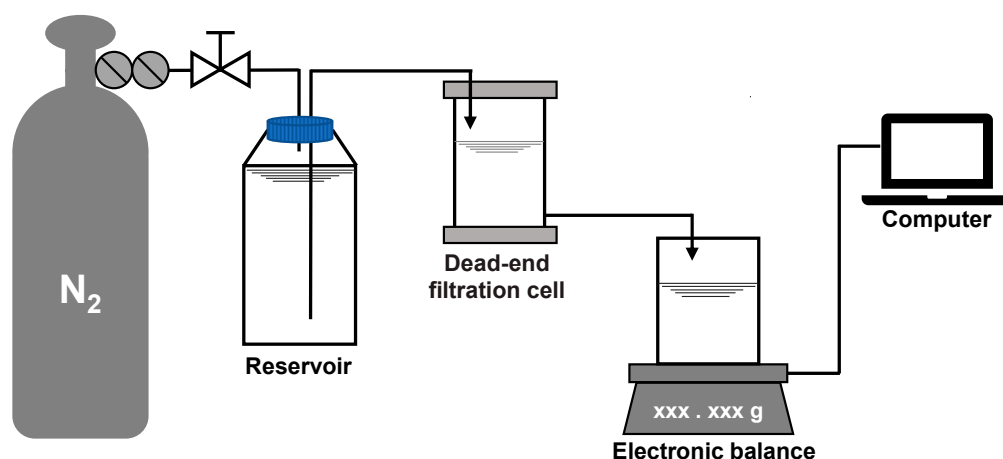


Figure 2. Layout of the dead-end filtration system.

### 3.3. Analytical Items

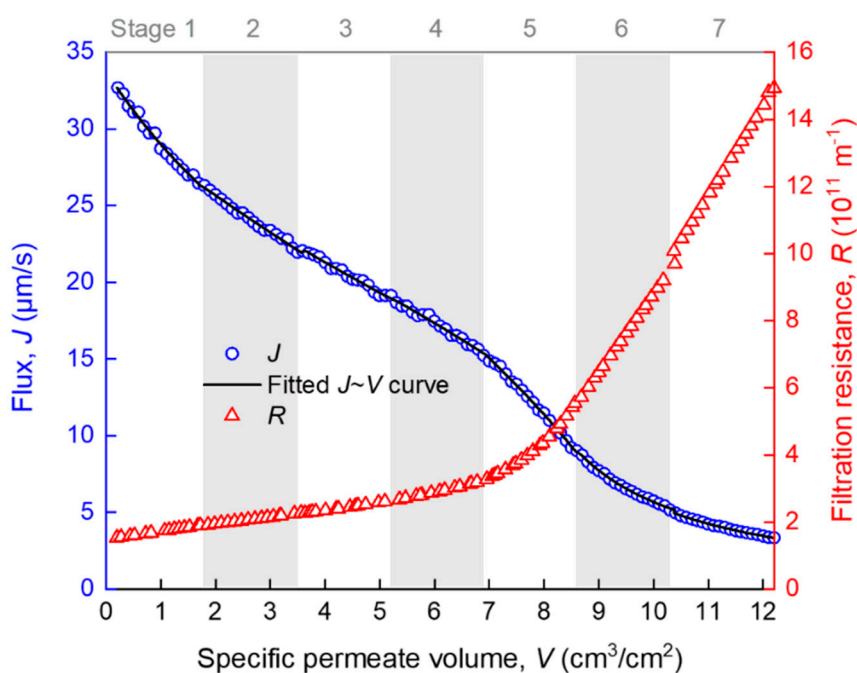
The total organic carbon (TOC) concentrations in the feed and permeate were determined using a TOC analyzer (Multi N/C 3100, Jena, Germany). The ultraviolet–visible (UV–Vis) absorbance of the

foulants was measured using a spectrophotometer (T3200, YOKE, Shanghai, China) with a scanning range of 200–500 nm. The fluorescence signals of the permeate were scanned using a fluorescence spectrophotometer (Cary Eclipse, Agilent, Palo Alto, CA, USA) in the 3D mode over the excitation wavelength range of  $E_x = 200\text{--}400$  nm and the emission wavelength range of  $E_m = 250\text{--}500$  nm. The obtained excitation–emission matrix (EEM) spectra were treated according to the following steps [33]: (a) subtracting pure water background, (b) removing Rayleigh and Raman scatterings, (c) correcting the inner-filter effect using UV–Vis absorbance, and (d) standardizing the fluorescence intensity (FI) into Raman units (R.U.) using the Raman signal of pure water as a reference.

#### 4. Results and Discussion

##### 4.1. Overview of Fouling Evolution

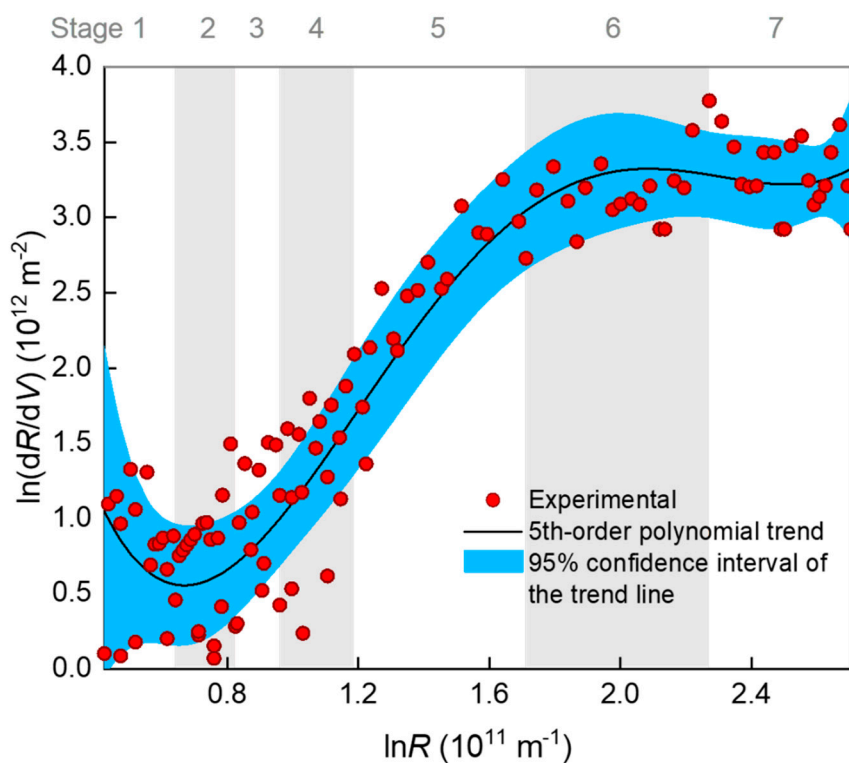
The development of membrane fouling can be reflected by the change of membrane flux ( $J$ ) and filtration resistance ( $R$ ) with specific permeate volume ( $V$ ).  $J$  and  $R$  were automatically calculated from the raw  $t$  and  $V$  data at an interval of  $\Delta V = 0.2 \text{ cm}^3/\text{cm}^2$ , using the homemade MATLAB function “VJR,” as given in Appendix A. As can be seen from Figure 3,  $R$  increased slowly when  $V$  was smaller than  $7 \text{ cm}^3/\text{cm}^2$ , and it increased rapidly thereafter. There are several turning points in the  $J$ – $V$  curve (such as those roughly around  $V = 2, 7$  and  $9 \text{ cm}^3/\text{cm}^2$ ), implying that there must have been more than one fouling mechanism over the whole process and the temporarily dominant mechanism was likely to change with  $V$ . However, it is difficult to accurately distinguish different fouling stages of the whole filtration process by only referring to the  $R$ – $V$  or  $J$ – $V$  curves. The further analysis of the  $R$ – $V$  or  $J$ – $V$  relationship is required. Note that the seven stages marked in Figure 3, as well as the fitted curve, were obtained by piecewise regression, as is described later in detail.



**Figure 3.** Variation of membrane flux and filtration resistance during the filtration process. Data are given as average from two repeated experiments with a relative error smaller than 4.4% (the error bars are thus omitted for simplicity of presentation). The R-squared values for the fitting in stages 1–7 were 0.983, 0.990, 0.985, 0.983, 0.996, 0.980, and 0.987, respectively.

A classical method for examining a fouling mechanism (e.g., blocking mode) is to plot the  $\ln(dR/dV)$ – $\ln R$  data and determine the slope of the curve as the characteristic  $N$  value (Equation (1)). In Figure 4,  $\ln(dR/dV)$  is shown to have decreased slightly at the very beginning of the filtration

(stage 1), increased almost linearly with  $\ln R$  in the middle stages of 2–5, and gradually reached a plateau after prolonged filtration (stages 6–7). Note that the so-termed seven stages were distinguished according to piecewise regression, as is introduced later. The plateau (i.e.,  $N = 0$ ) indicates that a cake or gel layer was eventually formed on the membrane surface. However, the large fluctuation of the data points rendered a large uncertainty of slope calculation. The fluctuation was very likely due to that the original  $V \sim t$  data that had been derived for many times to obtain  $dR/dV$ , and this concern has also been seriously raised by a number of researchers [12,31]. Considering that there were five possible mechanisms, we tentatively fitted the  $\ln(dR/dV) \sim \ln R$  data using a fifth-order polynomial trend line. Monte Carlo simulation based on the distribution of fitting residuals showed that the 95% confidence interval of the trend line was rather wide (Figure 4). Therefore, there was great uncertainty in judging the mechanisms with  $N$  value from the slope of the trend line, especially in the rising section. Alternatively, a better choice may have been fitting the  $J \sim V$  (or  $R \sim V$ ) rather than  $dR/dV \sim R$  data to reduce the uncertainty by using a piecewise fitting approach to deal with the changing mechanisms over the stages.

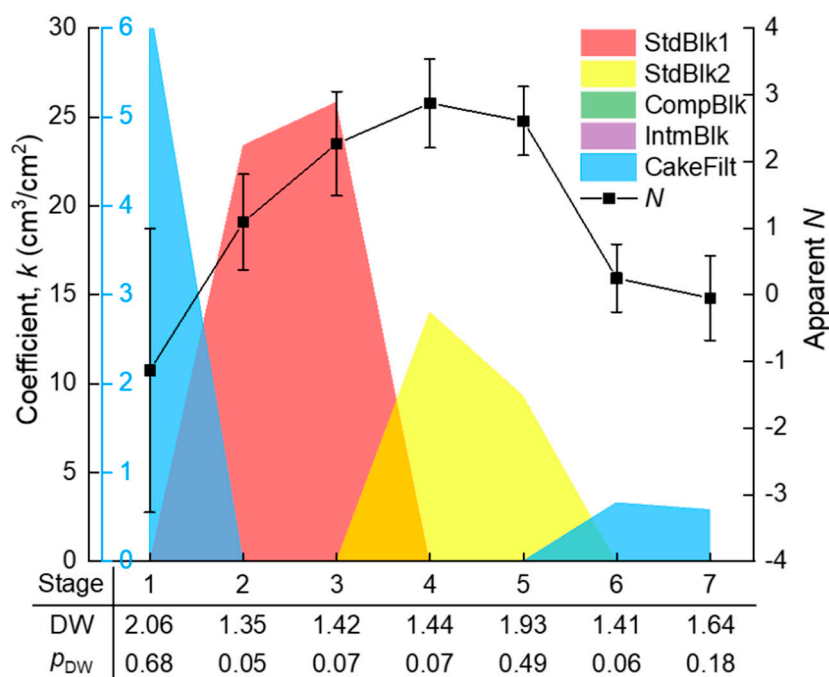


**Figure 4.** Relationship between  $dR/dV$  and  $R$  (filtration resistance) during the filtration process. The R-squared value of the 5th order polynomial fitting was 0.907. The 95% confidence interval of the 5th order polynomial trend line was produced using a 999-times Monte Carlo simulation based on the distribution of residuals.

#### 4.2. Piecewise Fitting Results

The whole filtration process ( $V \approx 12 \text{ cm}^3/\text{cm}^2$ ) was evenly divided into  $n$  segments ( $n = 1, 2, \dots$ ), and the segmented  $J \sim V$  data were subjected to piecewise fitting of the multiple linear model (Equation (4)) using the homemade MATLAB function “StepwiseModel,” as given in Appendix B. The appropriateness of the division was judged by a  $t$ -test for the significance of positive  $k_i$  coefficients and the DW test for the independence of the time series residuals. These tests were not successful until the segment number  $n$  increased to 7. The seven stages are marked in Figure 3, where it can be seen that the piecewise fitted  $J \sim V$  curve matched closely to the experimental data. As a consequence of the piecewise fitting, the significant  $k_i$  coefficients, as well as the DW test results along the seven stages,

are shown in Figure 5. The  $p_{DW}$  values were no smaller than 0.05, suggesting that the autocorrelations of residuals were tolerable. From the  $k_i$  coefficients, it is evident that the dominant fouling mechanism evolved in a sequence of: cake filtration (difficult to explain, possibly due to sudden change of hydraulic state at the beginning of filtration) (stage 1) → fast adsorption inside the membrane pores (stages 2–3) → slow adsorption inside the membrane pores (stages 4–5) → gradual growth of a cake layer on the membrane surface (stages 6–7).



**Figure 5.** The significant coefficients and the Durbin–Watson (DW) test results given by piecewise fitting of the filtration flux~specific permeate volume ( $J-V$ ) data in Figure 3, and the apparent  $N$  (fouling modes) values ( $\pm$  standard deviation) calculated from the  $\ln(dR/dV)-\ln R$  curve in Figure 4.

In comparison with the piecewise multiple linear regression results, the apparent  $N$  values were calculated using the conventional approach, i.e., from the slope of the  $\ln(dR/dV)-\ln R$  curve in Figure 4, with their standard deviations estimated via Monte Carlo simulation. The results are shown in Figure 5. It is obvious that the apparent  $N$  values exhibited great uncertainty due to the large fluctuation of the  $\ln(dR/dV)-\ln R$  data. The uncertainty made some of the  $N$  values deviate widely from the theoretical values. The deviation might have also been due to coexistence of multiple fouling mechanisms. For example, at the first kind of standard blocking-dominated stage 3, the apparent  $N$  of around 2 might have partly been due to coexistence of the emerging second kind of standard blocking; at the second kind of standard blocking-dominated stage 4, the apparent  $N$  of larger than 2.5 might have partly been due to the noncircularity of the actual membrane pores [11] or the acceleration of pore blocking efficiency when the adsorbed foulant concentration was approaching the gel point to form microgels in the pore channels. These uncertainties rendered the apparent  $N$  unreliable for identifying the main mechanism(s) during the filtration process. The apparent  $N$  value was sometimes even misleading; for instance, a value of 2 seemingly pointed to a single mechanism of complete blocking, whereas in fact it might have been a weighted average of two other mechanisms (e.g., first and second kinds of standard blocking with the true  $N$  values of 1.5 and 2.5, respectively).

In contrast to the apparent  $N$ , the piecewise multiple linear regression model could unequivocally identify the major mechanism(s) along the fouling stages with statistical confidence. The model was conservative in terms of the five known mechanisms, as it incorporated any uncertain factors (such as the aforementioned nonideality of membrane pores and fouling process) collectively into the error term

(Equation (4)). The relative importance (signal-to-noise ratio) of the main mechanism(s) compared to the error term was finally judged by statistical tests (*F*-test of the model or *t*-test of the coefficients). Therefore, this approach is considered to be more robust than the conventional apparent *N* approach.

#### 4.3. Interpreting the Transition of Major Mechanisms According to Foulant Composition

The modeling results were further evidenced by the consecutive measurements of the permeate properties during the filtration process. The TOC measured the total dissolved organic matter (DOM), UV absorbance at 254 nm ( $UV_{254}$ ) indicated the chromophoric portion of the DOM such as proteins and other unsaturated components [34,35], and the averaged fluorescence intensity at the emission wavelength range of 380–500 nm ( $FI_{380-500}$ ) mainly reflected the humic components of the DOM [33,36]. In Figure 6, the permeate TOC and  $UV_{254}$  both show a “Z”-shaped decreasing trend with the increase of *V*. At stages 5–6, the TOC dropped sharply, indicating that the overall rejection rate of organic foulants rose sharply due to the formation of a cake/gel layer on the membrane surface. At stage 7, the permeate TOC became stable at a low level of 2–3 mg/L, indicating full coverage and the steady growth of the cake/gel layer on the membrane surface. Correspondingly, the TOC rejection rate was below 10% at the pre-cake stages (stages 1–4), but it grew to over 60% at the cake/gel layer stage (stage 7). The cake/gel layer was mainly constructed of alginate since alginate was the major TOC contributor in the model foulant solution. The same trend of  $UV_{254}$  suggested that the chromophoric portion of the DOM (such as protein) also participated in the formation of the cake or gel layer. In contrast to the TOC and  $UV_{254}$ , the  $FI_{380-500}$  exhibited an “S”-shape increase during the filtration process, reflecting the gradual breakthrough of some small fluorescent molecules (such as some humic species) through the membrane and the cake/gel layer due to the equilibration of the dynamic adsorption [37,38]. The above showed that polysaccharide (alginate) and protein fouled the membrane mainly through forming a surface cake/gel layer (most likely polysaccharide formed the gel network and protein was trapped in it [7]), while small molecular humic substances successively underwent fast and slow adsorption, and they finally penetrated through the membrane and cake/gel layer. This is basically consistent with the understanding in the literature [39,40]. All the effluent properties were in good agreement with the model fitting results, which proves the rationality of the method proposed in this paper in identifying the main fouling mechanism during the membrane filtration process.

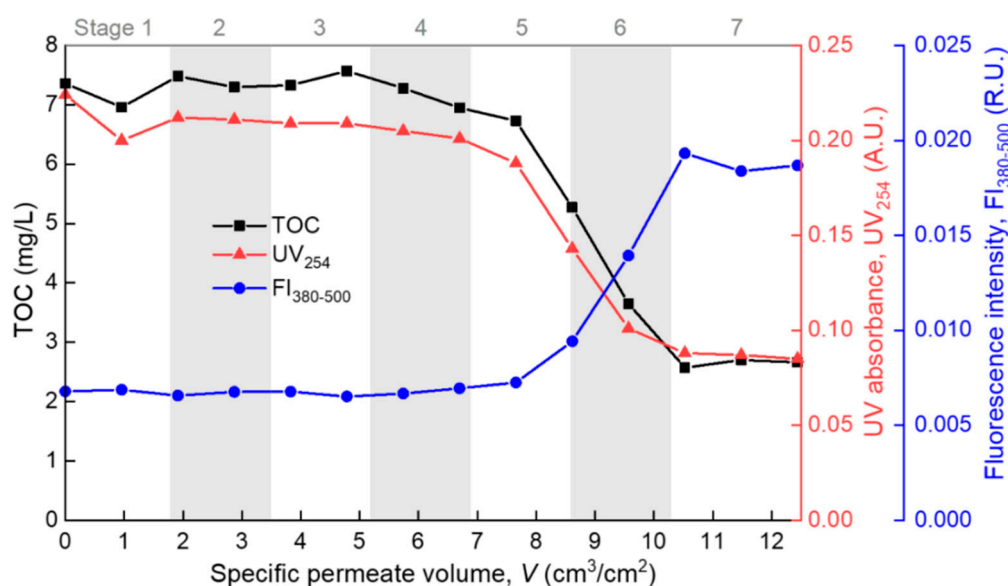


Figure 6. Permeate properties during the filtration process.

This comprehensive model, encompassing five mechanisms for pore blockage and cake filtration, should be widely applicable to various situations of dead-end filtration. For example, when the particle



size is much smaller than the pore size, standard blocking may be more dominant in the model. In the case of small particle size and weak hydrophobicity, the blockage may fall into the regime of the second kind of standard blocking, which is slow but lasts long. If the particle size is comparable to the pore size, complete blocking may rapidly occur. Moreover, the evolution to gel layer stage may be postponed or advanced given different hardness ion concentrations for metal–organic complexing gel layer formation. These situations are all within the scope of the comprehensive model.

## 5. Conclusions

In this paper, we proposed a semi-empirical multiple linear regression model that incorporates the five fouling mechanisms (first and second kinds of standard blocking, complete blocking, intermediate blocking, and cake filtration). MATLAB codes are provided for data processing and model fitting (“VJR” and “StepwiseModel” in the Appendices), which enable the optimal segmentation of the filtration process for the piecewise regression and refining of significant parameters with statistical tests. This provides a simple and rigorous method for identifying the main fouling mechanisms during the filtration process. In the case study of a Millipore MF membrane fouled by a model solution with polysaccharide, protein, and humic components, the model fitting results showed that the dominant fouling mechanism evolved in the order of: initial adaptation (stage1) → fast adsorption inside the membrane pores (stages 2–3) → slow adsorption inside the membrane pores (stages 4–5) → gradual growth of a cake/gel layer on the membrane surface (stages 6–7). The model fitting results were in good agreement with the permeate properties during the filtration process, which proves the rationality and effectiveness of this method in fouling mechanism study. It also provides a tool to assess membrane fouling potential, characterize foulant properties, and understand membrane–foulant interactions, all of which will profoundly support optimal selection of membrane and targeted pretreatment of foulant solution for efficient fouling control in industrial applications.

**Author Contributions:** Conceptualization, K.X., B.H., and C.W.; methodology, K.X., H.X., and J.Y.; software, K.X.; validation, K.X. and H.X.; formal analysis, K.X.; investigation, H.X. and J.Y.; resources, X.W. (Xianghua Wen) and X.H.; data curation, H.X.; writing—original draft preparation, H.X. and K.X.; writing—review and editing, X.W. (Xiaomao Wang) and S.L.; visualization, H.X. and K.X.; supervision, K.X., C.W., X.W. (Xiaomao Wang), and X.H.; project administration, K.X. and C.W.; funding acquisition, K.X., C.W., X.W. (Xianghua Wen), and X.H. All authors have read and agreed to the published version of the manuscript.

**Funding:** This work was supported by the Beijing Natural Science Foundation (No. L182044), the CAS Youth Innovation Promotion Association (No. 110500EA62), the Key Deployment Project of CAS Center for Ocean Mega-Science (No. COMS2019Q15), the 100-Talent Program of Guangzhou University (No. RQ2020103) and the Science and Technology Program of Guangzhou (No. 202002030150).

**Conflicts of Interest:** The authors declare no conflict of interest.

## Appendix A MATLAB Code for Automatically Calculating V, J, R and dR/dV from the Raw Data of Filtration

```
function [VJR_result] = VJR(tm)
% Input tm, of which the first column is filtration time (s), and the second column is effluent weight (g).
% Both time and weight should start from 0. The output Result = [T,V,J,R,dRdV] corresponds to filtration
% time (s), specific effluent volume (cm), flux (um/s), resistance (10^11 m^-1), and dR/dV (10^12 m^-2),
% respectively. The output Result is presented at a default V interval of 0.1 cm. You may change it to
% any value you like. The default membrane area is 41.8 cm^2, the default transmembrane pressure is
% 5 kPa, and the water density and viscosity are set as 1 g/cm^3 and 0.001 Pa.s. If different, please change
% them accordingly.
t = tm(:,1);% Filtration time in s;
m = tm(:,2);% Effluent mass in g;
v = m/41.8;% Specific volume per area in cm; the membrane area is 41.8 cm^2; the water density is
1 g/cm^3;
interval = 0.1;% Interval of specific volume in cm;
```

```

N = floor(max(v)/interval);
T = zeros(N,1);
V = zeros(N,1);
for k = 1:N
v1 = floor(v/k/interval);
v2 = 1-ceil(v1/N);
rn = sum(v2);
if (v(rn+1)-floor(v(rn+1)))<(ceil(v(rn))-v(rn));
rn = rn+1;
end
V (k) = v(rn);
T (k) = t(rn);
end
J = ([V;0;0]-[0;0;V])./([T;0;0]-[0;0;T]);
J = J(2:N)*1e4;% Filtration flux in um/s;
V = V(1:(N-1));
R = 5000/0.001./(J*1e-6)/1e11;% Filtration resistance in 10^11 m^-1; the trans-membrane pressure is 5 kPa;
the effluent viscosity is 0.001 Pa.s;
dRdV = ([R;0;0]-[0;0;R])./([V;0;0]-[0;0;V]);
dRdV = dRdV(3:(N-1))*10;% dR/dV in 10^12 m^-2;
R = R(2:(N-2));
J = J(2:(N-2));
V = V(2:(N-2));
T = T(2:(N-2));
VJR_result = [T,V,J,R,dRdV];
End

```

### Appendix B MATLAB Code for Piecewise Fitting of the Multiple Linear Model to the J~V Data

```

function [Vhat,StepwiseResults] = StepwiseModel(VJR_result,N_interval)
% By inputting the filtration data (as VJR_result) and the stage number (i.e., how many stages you
want to divide the whole process into), this function computes the coefficient of each blocking mode
in the model of:  $V = k_0 + k_1*(-J^{0.5}) + k_2*(-J^{1.5}) + k_3*(-J) + k_4*(-\log(J)) + k_5*(J^{-1})$ , using stepwise
regression. The terms of k1...k5 correspond to the blocking modes of 1st kind of standard blocking
(fast adsorption), 2nd kind of standard blocking (slow adsorption), complete blocking, intermediate
blocking, and cake filtration, respectively. The outputs include the stats of the regression (estimation of
the coefficients and standard error, R squared, and Durbin–Watson statistics for autocorrelation) and
the predicted V values.
V = VJR_result(:,2);% VJR_result is the output of the function VJR for pretreatment of the filtration data;
J = VJR_result(:,3);
J = J/J(1);% Normalized by dividing with the initial flux;
JJ = [-J.^0.5, -J.^1.5, -J, -log(J), J.^-1];
Int = round(length(V)/N_interval);
Vhat = V;
VN = zeros(N_interval,1);% Middle value of V in each stage;
R2 = zeros(N_interval,1);
DW = zeros(N_interval,1);% Durbin–Watson statistics;
pDW = zeros(N_interval,1);% p-value for DW test, <0.05 means significant autocorrelation between
sample points;
B = zeros(N_interval,5);% Coefficients of k1...k5;
SE = zeros(N_interval,5);% Standard error of k1...k5;

```

```

for i = 1:N_interval
lower = (i-1)*Int+1;
upper = min((i*Int),length(V));
y = V(lower:upper);
X = JJ(lower:upper,:);
[b,se,~,inmodel,stats] = stepwisefit(X,y);
B(i,:) = b'.*inmodel;
SE(i,:) = se'.*inmodel;
Vhat(lower:upper) = y - stats.yr;
R2(i) = 1 - stats.SSresid/stats.SStotal;
x = ones(upper-lower+1,1);
for j = 1:5
if inmodel(j)==1;
x = [x,X(:,j)];
end
end
[pDW(i),DW(i)]=dwtest(stats.yr,x);
VN(i) = mean(y);
end
StepwiseResults = [VN,B,R2,DW,pDW];
disp(' V k1 k2 k3 k4 k5 R2 DW p_DW')
disp(StepwiseResults)% Display the results for each stage;
StepwiseResults = [VN,B,SE,R2,DW,pDW];
end

```

### Appendix C Abbreviation List

BSA	Bovine serum albumin
DOM	Dissolved organic matter
DW	Durbin–Watson
EEM	Excitation–emission matrix
FI	Fluorescence intensity
HA	Humic acid
<i>J</i>	Filtration flux
<i>k</i>	Model coefficient (Equations (1)–(4))
MF	Microfiltration
<i>N</i>	Characteristic exponent
<i>n</i>	Number of segments of the filtration process
<i>P</i>	Trans-membrane pressure
<i>p</i> <sub>DW</sub>	<i>p</i> value of DW test
PVDF	Polyvinylidene fluoride
<i>R</i>	Filtration resistance
R.U.	Raman unit
SA	Sodium alginate
TOC	Total organic carbon
<i>t</i>	Filtration time
UF	Ultrafiltration
UV	Ultraviolet absorbance
<i>V</i>	Specific permeate volume
$\varepsilon$	Error term
$\mu$	Dynamic viscosity of the permeate

## References

1. Baker, R.W. *Membrane Technology and Applications*; John Wiley & Sons: New York, NY, USA, 2012. [[CrossRef](#)]
2. Shi, X.; Tal, G.; Hankins, N.P.; Gitis, V. Fouling and cleaning of ultrafiltration membranes: A review. *J. Water Process Eng.* **2014**, *1*, 121–138. [[CrossRef](#)]
3. Tong, T.; Carlson, K.; Robbins, C.A.; Zhang, Z.; Du, X. Membrane-based treatment of shale oil and gas wastewater: The current state of knowledge. *Front. Environ. Sci. Eng.* **2019**, *13*, 63. [[CrossRef](#)]
4. Obotey Ezugbe, E.; Rathilal, S. Membrane technologies in wastewater treatment: A review. *Membranes (Basel)* **2020**, *10*, 89. [[CrossRef](#)]
5. Yang, J.; Monnot, M.; Ercolei, L.; Moulin, P. Membrane-based processes used in municipal wastewater treatment for water reuse: state-of-the-art and performance analysis. *Membranes* **2020**, *10*, 131. [[CrossRef](#)] [[PubMed](#)]
6. Zularisam, A.W.; Ismail, A.F.; Salim, R. Behaviours of natural organic matter in membrane filtration for surface water treatment—A review. *Desalination* **2006**, *194*, 211–231. [[CrossRef](#)]
7. Xu, H.; Xiao, K.; Wang, X.; Liang, S.; Wei, C.; Wen, X.; Huang, X. Outlining the roles of membrane-foulant and foulant-foulant Interactions in organic fouling during microfiltration and ultrafiltration: A mini-review. *Front. Chem.* **2020**, *8*, 417. [[CrossRef](#)] [[PubMed](#)]
8. Meng, F.G.; Zhang, S.Q.; Oh, Y.; Zhou, Z.B.; Shin, H.S.; Chae, S.R. Fouling in membrane bioreactors: An updated review. *Water Res.* **2017**, *114*, 151–180. [[CrossRef](#)] [[PubMed](#)]
9. Wang, F.; Tarabara, V.V. Pore blocking mechanisms during early stages of membrane fouling by colloids. *J. Colloid Interface Sci.* **2008**, *328*, 464–469. [[CrossRef](#)]
10. Guo, W.S.; Ngo, H.H.; Li, J.X. A mini-review on membrane fouling. *Bioresour. Technol.* **2012**, *122*, 27–34. [[CrossRef](#)]
11. Xiao, K.; Mo, Y.; Sun, J.; Wang, M.; Liang, S.; Wang, X.; Huang, X.; Waite, T.D. An extended standard blocking filtration law for exploring membrane pore internal fouling due to rate-determining adsorption. *Sep. Purif. Technol.* **2019**, *212*, 974–979. [[CrossRef](#)]
12. Ho, C.; Zydney, A.L. A combined pore blockage and cake filtration model for protein fouling during microfiltration. *J. Colloid Interface Sci.* **2000**, *232*, 389–399. [[CrossRef](#)] [[PubMed](#)]
13. Huang, B.; Gu, H.; Xiao, K.; Qu, F.; Yu, H.; Wei, C. Fouling mechanisms analysis via combined fouling models for surface water ultrafiltration process. *Membranes (Basel)* **2020**, *10*, 149. [[CrossRef](#)] [[PubMed](#)]
14. Iritani, E.; Katagiri, N. Developments of blocking filtration model in membrane filtration. *KONA Powder Part. J.* **2016**, *33*, 179–202. [[CrossRef](#)]
15. Giglia, S.; Straeffer, G. Combined mechanism fouling model and method for optimization of series microfiltration performance. *J. Membr. Sci.* **2012**, *417*, 144–153. [[CrossRef](#)]
16. Kirschner, A.Y.; Cheng, Y.H.; Paul, D.R.; Field, R.W.; Freeman, B.D. Fouling mechanisms in constant flux crossflow ultrafiltration. *J. Membr. Sci.* **2019**, *574*, 65–75. [[CrossRef](#)]
17. Katsoufidou, K.; Yiantsios, S.G.; Karabelas, A.J. A study of ultrafiltration membrane fouling by humic acids and flux recovery by backwashing: experiments and modeling. *J. Membr. Sci.* **2005**, *266*, 40–50. [[CrossRef](#)]
18. Fernández, X.R.; Rosenthal, I.; Anlauf, H.; Nirschl, H. Experimental and analytical modeling of the filtration mechanisms of a paper stack candle filter. *Chem. Eng. Res. Des.* **2011**, *89*, 2776–2784. [[CrossRef](#)]
19. Nakamura, K.; Orime, T.; Matsumoto, K. Response of zeta potential to cake formation and pore blocking during the microfiltration of latex particles. *J. Membr. Sci.* **2012**, *401–402*, 274–281. [[CrossRef](#)]
20. Duclos Orsello, C.; Li, W.; Ho, C.C. A three mechanism model to describe fouling of microfiltration membranes. *J. Membr. Sci.* **2006**, *280*, 856–866. [[CrossRef](#)]
21. Kim, M.; Sankararao, B.; Lee, S.; Yoo, C. Prediction and identification of membrane fouling mechanism in a membrane bioreactor using a combined mechanistic model. *Ind. Eng. Chem. Res.* **2013**, *52*, 17198–17205. [[CrossRef](#)]
22. de Oliveira, R.C.; Docê, R.C.; de Barros, S.T.D. Clarification of passion fruit juice by microfiltration: analyses of operating parameters, study of membrane fouling and juice quality. *J. Food Eng.* **2012**, *111*, 432–439. [[CrossRef](#)]
23. Vela, M.C.V.; Blanco, S.Á.; García, J.L.; Rodríguez, E.B. Analysis of membrane pore blocking models applied to the ultrafiltration of PEG. *Sep. Purif. Technol.* **2008**, *62*, 489–498. [[CrossRef](#)]

24. Salahi, A.; Abbasi, M.; Mohammadi, T. Permeate flux decline during UF of oily wastewater: experimental and modeling. *Desalination* **2010**, *251*, 153–160. [[CrossRef](#)]
25. Kim, M.J.; Yoo, G.Y.; Yoo, C. Development of combined fouling model in a membrane bioreactor. *Asia-Pac. J. Chem. Eng.* **2011**, *6*, 423–432. [[CrossRef](#)]
26. Hou, L.; Wang, Z.; Song, P. A precise combined complete blocking and cake filtration model for describing the flux variation in membrane filtration process with BSA solution. *J. Membr. Sci.* **2017**, *542*, 186–194. [[CrossRef](#)]
27. Ofungwu, J. *Statistical Applications for Environmental Analysis and Risk Assessment*; John Wiley and Sons: Hoboken, NJ, USA, 2014. [[CrossRef](#)]
28. Tien, C.; Ramarao, B.V. Revisiting the laws of filtration: an assessment of their use in identifying particle retention mechanisms in filtration. *J. Membr. Sci.* **2011**, *383*, 17–25. [[CrossRef](#)]
29. Polyakov, Y.S.; Zydney, A.L. Ultrafiltration membrane performance: effects of pore blockage/constriction. *J. Membr. Sci.* **2013**, *434*, 106–120. [[CrossRef](#)]
30. Ramarao, B.V.; Tien, C. Approximate analysis of fine-particle retention in the cake filtration of suspensions. *Ind. Eng. Chem. Res.* **2005**, *44*, 1424–1432. [[CrossRef](#)]
31. Tien, C.; Ramarao, B.V.; Yasarla, R. A blocking model of membrane filtration. *Chem. Eng. Sci.* **2014**, *111*, 421–431. [[CrossRef](#)]
32. Shen, Y.; Xiao, K.; Liang, P.; Sun, J.; Sai, S.; Huang, X. Characterization of soluble microbial products in 10 large-scale membrane bioreactors for municipal wastewater treatment in China. *J. Membr. Sci.* **2012**, *415*, 336–345. [[CrossRef](#)]
33. Yu, J.; Xiao, K.; Xue, W.; Shen, Y.; Tan, J.; Liang, S.; Wang, Y.; Huang, X. Excitation-emission matrix (EEM) fluorescence spectroscopy for characterization of organic matter in membrane bioreactors: Principles, methods and applications. *Front. Environ. Sci. Eng.* **2020**, *14*, 31. [[CrossRef](#)]
34. Wu, Q.; Li, C.; Wang, W.; He, T.; Hu, H.; Du, Y.; Wang, T. Removal of fluorescence and ultraviolet absorbance of dissolved organic matter in reclaimed water by solar light. *J. Environ. Sci.* **2016**, *43*, 118–127. [[CrossRef](#)] [[PubMed](#)]
35. Arslanalaton, I.; Balcioglu, I.A. Biodegradability assessment of ozonated raw and biotreated pharmaceutical wastewater. *Arch. Environ. Contam. Toxicol.* **2002**, *43*, 425–431. [[CrossRef](#)] [[PubMed](#)]
36. Zhang, S.; Chen, X.W.; Ye, Q.H.; Zhang, Z.T.; Kong, S.F.; Cao, C.; Wang, J.J. Dissolved metal(loid) concentrations and their relations with chromophoric and fluorescent dissolved organic matter in an urban river in Shenzhen, South China. *Water* **2020**, *12*, 281. [[CrossRef](#)]
37. Jones, K.L.; O'Melia, C.R. Protein and humic acid adsorption onto hydrophilic membrane surfaces: effects of pH and ionic strength. *J. Membr. Sci.* **2000**, *165*, 31–46. [[CrossRef](#)]
38. Xiao, K.; Wang, X.; Huang, X.; Waite, T.D.; Wen, X. Analysis of polysaccharide, protein and humic acid retention by microfiltration membranes using Thomas' dynamic adsorption model. *J. Membr. Sci.* **2009**, *342*, 22–34. [[CrossRef](#)]
39. Yuan, W.; Kocic, A.; Zydney, A.L. Analysis of humic acid fouling during microfiltration using a pore blockage–cake filtration model. *J. Membr. Sci.* **2002**, *198*, 51–62. [[CrossRef](#)]
40. Sutzkover Gutman, I.; Hasson, D.; Semiat, R. Humic substances fouling in ultrafiltration processes. *Desalination* **2010**, *261*, 218–231. [[CrossRef](#)]



© 2020 by the authors. Licensee MDPI, Basel, Switzerland. This article is an open access article distributed under the terms and conditions of the Creative Commons Attribution (CC BY) license (<http://creativecommons.org/licenses/by/4.0/>).

Article

# Tuning the Surface Structure of Polyamide Membranes Using Porous Carbon Nitride Nanoparticles for High-Performance Seawater Desalination

Zongyao Zhou <sup>†</sup>, Xiang Li <sup>†</sup>, Digambar B. Shinde , Guan Sheng, Dongwei Lu, Peipei Li and Zhiping Lai <sup>\* </sup>

Advanced Membranes and Porous Materials Center, Division of Physical Science and Engineering, King Abdullah University of Science and Technology (KAUST), Thuwal 23955-6900, Saudi Arabia; Zongyao.zhou@kaust.edu.sa (Z.Z.); Xiang.li@kaust.edu.sa (X.L.); Digambar.Shinde@kaust.edu.sa (D.B.S.); Guan.sheng@kaust.edu.sa (G.S.); dongwei.lu@kaust.edu.sa (D.L.); peipei.li@kaust.edu.sa (P.L.)

\* Correspondence: zhiping.lai@kaust.edu.sa

<sup>†</sup> These authors contribute equally.

Received: 17 June 2020; Accepted: 22 July 2020; Published: 24 July 2020



**Abstract:** Enhancing the water flux while maintaining the high salt rejection of existing reverse osmosis membranes remains a considerable challenge. Herein, we report the use of a porous carbon nitride ( $C_3N_4$ ) nanoparticle to potentially improve both the water flux and salt rejection of the state-of-the-art polyamide (PA) thin film composite (TFC) membranes. The organic–organic covalent bonds endowed  $C_3N_4$  with great compatibility with the PA layer, which positively influenced the customization of interfacial polymerization (IP). Benefitting from the positive effects of  $C_3N_4$ , a more hydrophilic, more crumpled thin film nanocomposite (TFN) membrane with a larger surface area, and an increased cross-linking degree of PA layer was achieved. Moreover, the uniform porous structure of the  $C_3N_4$  embedded in the “ridge” sections of the PA layer potentially provided additional water channels. All these factors combined provided unprecedented performance for seawater desalination among all the PA-TFC membranes reported thus far. The water permeance of the optimized TFN membrane is 2.1-folds higher than that of the pristine PA-TFC membrane, while the NaCl rejection increased to 99.5% from 98.0%. Our method provided a promising way to improve the performance of the state-of-art PA-TFC membranes in seawater desalination.

**Keywords:** polyamide membrane; carbon nitride; seawater desalination; mixed matrix membranes; thin film composite

## 1. Introduction

Water scarcity is a global issue currently affecting about two-thirds of the world’s population [1]. Over the last half century, reverse osmosis (RO) has been demonstrated as an affordable approach to producing drinking water from seawater [2]. This is mainly owing to the successful development of the start-of-the-art RO membrane: a polyamide thin-film composite (PA-TFC) membrane consisting of a thin and highly cross-linked PA selective layer atop a strong and porous support layer [3–8]. However, similar to that of other types of membranes, further improvement in the PA-TFC membrane performance has been limited by the upper limit of the trade-off between permeability versus selectivity [8].

An effective approach to overcoming this limit is based on the concept of mixed matrix membranes. Hoek et al. demonstrated for the first time that by embedding zeolite 4A nanoparticles into the PA layer during interfacial polymerization (IP), the resultant thin film nanocomposite (TFN) membrane exhibited approximately a 50% improvement in water flux without considerable decline in salt rejection [9]. Since then, many other porous materials, such as zeolitic imidazolate frameworks [10–12],

metal–organic frameworks [13], covalent organic frameworks [14], porous aromatic frameworks [15], and hyper-cross-linked polymers [16], have been extensively studied [17–21]. It is generally believed that these porous materials provide faster transport pathways for water and thus improve the membrane flux. However, there are several challenges in this approach. Firstly, the state-of-the-art PA-TFC membrane is approximately 100 nm thick [2,22]. To synthesize such small nanoparticles is costly and time-consuming. Secondly, it is difficult to increase the particle loading as this may cause particle agglomeration and render the membrane brittle. Lastly, many of these materials are unstable in water, which has raised concerns pertaining to their long-term stability.

Another approach to improving the membrane performance is to optimize the membrane surface structure. The PA layer of a PA-TFC membrane is typically prepared in situ via IP between a diamine and an acyl chloride dissolved in water and an organic solvent, respectively. The organic solvent is immiscible in water. Thus, upon contact, the two species diffuse from each solution to the phase boundary and react there to form a thin film. The reaction is fast, highly exothermic, and typically occurs in an uncontrolled manner; hence, the resultant membrane structure is extremely sensitive to local conditions. One notable feature is the formation of a rough “ridge-and-valley” surface morphology, which is generally attributed to the inhomogeneous release of reaction heat [22–24]. The ridge-and-valley structure is very important for membrane performance because it can increase the membrane surface area [25,26]. Many innovative ideas have been developed to control the membrane surface structure by tuning the process of IP. Zhang et al. reported the formation of Turing patterns to increase the surface area and thus the membrane flux [27]. Jin et al. used a nanostructure-mediated IP process to increase the ridge-and-valley structure [26]. Livingston et al. introduced a sacrificial layer to tune the PA structure [23]. Several other publications have reported the use of a sublayer made of cellulose nanofibers [28], tannic acid/Fe<sup>3+</sup> nanoscaffold [29], or carbon nanotubes [22,30] to optimize the process of IP. However, although these membranes demonstrate an improved water flux, their NaCl rejection values are generally low. Therefore, these membranes are good for nanofiltration but not suitable for seawater desalination as the latter requires a NaCl rejection value of more than 98.4% to reduce the seawater salinity to a potable level via a one-stage RO process.

Here, we report, for the first time, the use of the highly crystalline carbon nitride (C<sub>3</sub>N<sub>4</sub>) to tune the surface structure of PA membranes to enhance their performance in seawater desalination. As a graphene-analogue material, C<sub>3</sub>N<sub>4</sub> has a 2D layered structure possessing uniform nanopores with a pore size of 3.11 Å, which is big enough to allow water molecules (kinetic diameter 2.65 Å) to pass through [31]. It has outstanding thermal and chemical stabilities, and is very stable in water and organic solvents [32–34]. Its synthesis is easy and inexpensive [35]. C<sub>3</sub>N<sub>4</sub> has abundant amino ending groups, which render it hydrophilic and chemically very compatible with the PA layer. It was determined that embedding the C<sub>3</sub>N<sub>4</sub> nanoparticles into the PA layer during the IP process could significantly enlarge the ridge-and-valley surface structure. This effect, as well as the additional transport pathway for water, substantially improved the water permeance of the membrane to  $3.2 \pm 0.2 \text{ Lm}^{-2}\cdot\text{h}^{-1}/\text{bar}$  (LMH/bar) and endowed it with an excellent NaCl rejection of 99.5%, which surpassed the performances of most TFN membranes reported to date.

## 2. Materials and Methods

### 2.1. Chemicals

Polysulfone (PSf, Ultrason<sup>®</sup> S 3010) was purchased from BASF (Frankfurt, Germany). N,N'-dimethylformamide, n-methyl-2-pyrrolidone (NMP), m-phenylenediamine (MPD), trimesoyl chloride (TMC), n-hexane, and melamine were all supplied by Sigma-Aldrich (St. Louis, MO, USA). Non-woven fabric was purchased from Sojitz (Osaka, Japan). NaCl was purchased from VWR Chemicals (Leuven, Belgium). All chemicals were used as received.

## 2.2. Synthesis of $C_3N_4$ Nanoparticles

$C_3N_4$  was prepared according to the literature [36]. Melamine powder was placed in an alumina crucible and first heated to 400 °C at a heating rate of 4.4 °C/min in an Ar atmosphere. The temperature was maintained at 400 °C for 90 min, and then raised to 600 °C at the same heating rate, held for another 120 min, and then cooled naturally to room temperature. The final product was collected in a yellow powder form (Figure S1).

## 2.3. Preparation of $C_3N_4$ Aqueous Suspension

A total of 30 mg of  $C_3N_4$  powder was dispersed in 20 mL of deionized (DI) water using a probe ultrasonicator operated at 160 W and 25 °C for 5 h. The undispersed  $C_3N_4$  powder was removed via centrifugation at 3000 rpm for 15 min. The supernatant solution was sonicated for another 2 h using an ultrasonic cleaner at 70 W and stored at room temperature for subsequent use as a stock solution (Figure S1). The particle concentration in the stock solution was approximately 0.6 mg/mL.

## 2.4. Preparation of PSf Porous Supports

A PSf ultrafiltration membrane was used as the support layer to prepare the TFC membrane. It was home-made using a previously reported method of non-solvent-induced phase separation [37]. A total of 12 g of PSf was first dried in a vacuum oven overnight at 90 °C and then dissolved in 88 g of NMP to form a homogenous casting solution. The casting solution was placed still for 12 h to remove air bubbles, and then cast on the surface of a non-woven fabric in a closed chamber using a casting knife with a gap of 200  $\mu$ m. Prior to the casting, the non-woven fabric was wetted with NMP. The relative humidity (RH) and temperature of the casting chamber were maintained at 40%  $\pm$  5% RH and 25  $\pm$  5 °C, respectively. The film obtained was immersed immediately into a room-temperature DI water bath and kept there for 12 h to remove most of the solvent. The film was stored at 4 °C for further use. The scanning electron microscopy (SEM) and atomic force microscopy (AFM) images, and the pure water flux of the PSf substrate prepared are shown in the Supporting Information (Figures S2–S4).

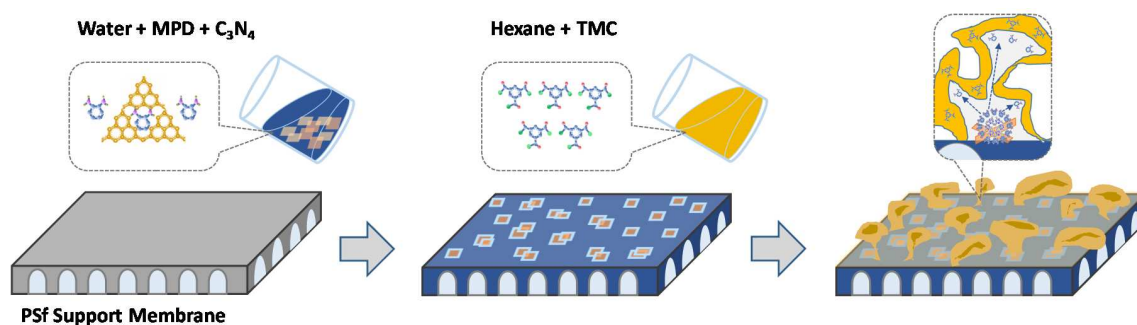
## 2.5. IP to Prepare PA-TFC Membrane

The process of IP was conducted according to our previous protocol [38]. The PSf support was first immersed in an MPD aqueous solution (3.4 wt.%) for 2 min and then withdrawn to naturally drain the MPD solution for 2 min. The excess MPD solution on the support surface was removed using a rubber roller. The TMC solution in hexane (0.15 wt.%) was then poured onto the support surface and reacted for 1 min. Afterwards, the excess TMC solution was removed and the membrane was cured in a hot water bath at 95 °C for 1 min. The final membrane was stored at 4 °C in DI water for further use (Figure S5).

## 2.6. IP to Prepare $C_3N_4$ TFN Membrane

The  $C_3N_4$  stock solution was diluted to concentrations of 0.04 ( $C_3N_4$ -4), 0.08 ( $C_3N_4$ -8), and 0.12 ( $C_3N_4$ -12) mg/mL. Next, MPD was added to the solutions to attain a concentration of 3.4 wt.%. The concentration of the TMC solution was 0.15 wt.%. The remaining steps were identical to those in the preparation of the PA-TFC membrane via IP, as illustrated in Scheme 1.





**Scheme 1.** Schematic illustration of the fabrication of thin film composite (TFC) and thin film nanocomposite (TFN) membranes.

### 2.7. Characterization

A high-resolution transmission electron microscopy (HRTEM, FEI Titan, Hillsboro, OR, USA) instrument was operated at 80 kV to obtain the TEM images. The TEM samples were prepared according to our previously reported procedure [22]. The SEM images were obtained using a Magellan XHR instrument (Hillsboro, OR, USA). The SEM samples of the back surface of the PA layer were prepared according to our previous report [22]. All the SEM samples were sputter-coated with 1 nm thick Ir. The dynamic light scattering (DLS) was measured using a Delsa Nano C system (Beckman Coulter, San Diego, CA, USA). The powder X-ray diffraction (PXRD) pattern was collected using a Bruker D8 Advance X-ray powder diffractometer (Karlsruhe, Germany). A Micromeritics ASAP 2420 analyzer (Norcross, GA, USA) was employed to record the N<sub>2</sub> adsorption isotherms at 77 K. The solid-state nuclear magnetic resonance (NMR) data were obtained using a Bruker Advance 400 WB spectrometer (Karlsruhe, Germany). Atomic force microscopy (Bruker, Dimension Icon, Karlsruhe, Germany) was used to investigate the membrane surface roughness in the tapping mode. X-ray photoelectron spectroscopy (XPS, Amicus Kratos Analytical, ESCA 3400, Kratos, UK) was employed to measure the elemental composition of the PA layer. The water contact angles (WCAs) were measured using the sessile drop method on a drop shape analyzer (Kruss, DSA100, Hamburg, Germany) at room temperature.

### 2.8. Evaluation of RO Desalination Performance

The water permeance and NaCl rejection of the TFC and TFN membranes were measured using a custom-designed RO permeation cell [10]. After 1.5 h of pre-compaction, the membranes were tested at 15.5 bar and 2000 ppm of NaCl feed solution at 25 °C. The water permeance,  $J_w$  (LMH/bar), was calculated using Equation (1).

$$J_w = \frac{V}{A \times t \times \Delta P} \quad (1)$$

where  $V$  (L) is the permeate volume collected in a certain period of time,  $t$  (h), based on the filtration area,  $A$  (m<sup>2</sup>), and transmembrane pressure drop,  $\Delta P$  (bar).

The NaCl rejection,  $R$  (%), was calculated using Equation (2).

$$R = 1 - \frac{C_{permeate}}{C_{feed}} \times 100\% \quad (2)$$

where  $C_{permeate}$  and  $C_{feed}$  are the concentrations of the permeate and feed solutions, respectively.

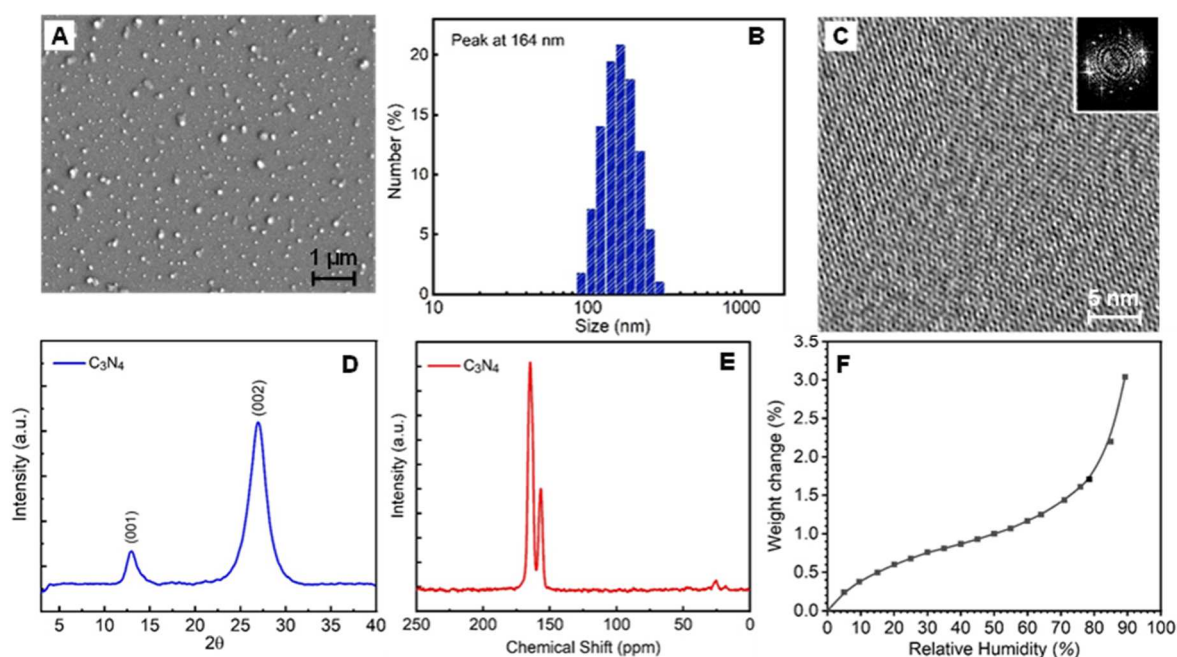
The salt permeability,  $B$  (LMH), was calculated using Equation (3).

$$B = J_w \times \Delta P \times \frac{1 - R}{R} \quad (3)$$

All the membranes were tested on at least three samples, and the average values were obtained.

### 3. Results and Discussion

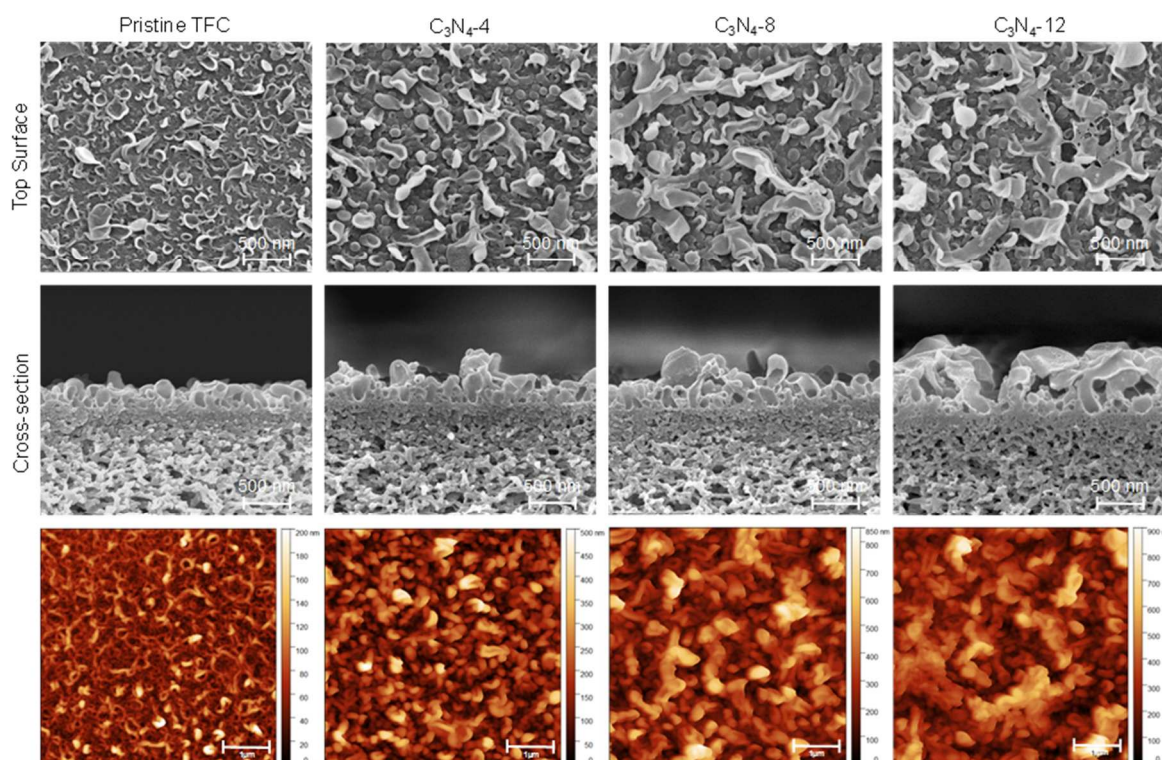
Figure 1A,B show the SEM image and DLS size analysis of the  $C_3N_4$  nanoparticles, respectively. The average particle size was around  $164 \pm 30$  nm. The HRTEM image in Figure 1C clearly shows the highly crystalline structure and regular pores, although the selective area electron diffraction displayed in the inset of Figure 1C indicates that the area studied was not a single layer. The high crystallinity was further confirmed by the PXRD pattern in Figure 1D, which contained two characteristic peaks at  $13.1^\circ$  and  $27.5^\circ$ . The PXRD pattern matched well with the reported graphitic  $C_3N_4$  pattern [39,40]. Two apparent resonances ( $\delta = 164$  ppm and  $\delta = 156$  ppm) were detected in the  $^{13}C$  cross polarization-magic angle spinning (CP-MAS) spectrum, which were owing to the  $sp^2$  carbon atoms, as shown in Figure 1E [41]. All these results are in good agreement with the reported results [42], validating that a highly crystalline graphitic  $C_3N_4$  was successfully synthesized. The  $N_2$  physisorption isotherm in Figure S6 indicates a very low Brunauer–Emmett–Teller (BET) surface area of  $21.5$   $m^2/g$ . This is because the molecular size of  $N_2$  ( $3.64$  Å) was greater than the pore size of  $C_3N_4$ . Figure 1F presents the water vapor adsorption isotherm at room temperature and indicates that  $C_3N_4$  was relatively hydrophilic. The water uptake at 90% RH was approximately 3 wt.%, which is approximately 15 times higher than that of the reported ZIF-8 nanoparticles [10].



**Figure 1.** Characterization of  $C_3N_4$  nanoparticles: (A) SEM image, (B) particle size distribution of  $C_3N_4$  nanoparticles dispersed in aqueous solution, (C) typical high-resolution transmission electron microscopy (HRTEM) image with the inset showing a fast Fourier transform of the electron diffraction pattern, (D) powder X-ray diffraction (PXRD) spectra, (E)  $^{13}C$  CP-MAS spectrum, and (F) water vapor adsorption isotherm at room temperature.

Figure 2 shows the morphologies of the PA-TFC and the  $C_3N_4$  TFN membranes at different  $C_3N_4$  concentrations, as listed in Table 1. The surface morphologies of all membranes showed the ridge-and-valley feature, but the feature size increased notably with the concentration of  $C_3N_4$ . The cross-section additionally showed that the height of the PA layer increased with the loading rate of  $C_3N_4$ . The surface roughness ( $Ra$ ) was measured via AFM. The  $Ra$  of the pristine PA-TFC membrane was  $20.2 \pm 5.6$  nm whereas that of  $C_3N_4$ -12 was  $89.7 \pm 5.6$  nm, representing a considerable increase of four-fold (Table 1). The surface area ratio (SAR), which is defined as the ratio of the total surface area to the projected surface area, increased from  $1.4 \pm 0.1$  for the pristine membrane to  $2.3 \pm 0.1$  for

the C<sub>3</sub>N<sub>4</sub>-12 membrane (Table 1). The higher SAR implies a larger specific surface area for transport, which is beneficial to achieving higher water permeation [26].



**Figure 2.** SEM and atomic force microscopy (AFM) images of pristine TFC and TFN membranes with different amounts of C<sub>3</sub>N<sub>4</sub> nanoparticles.

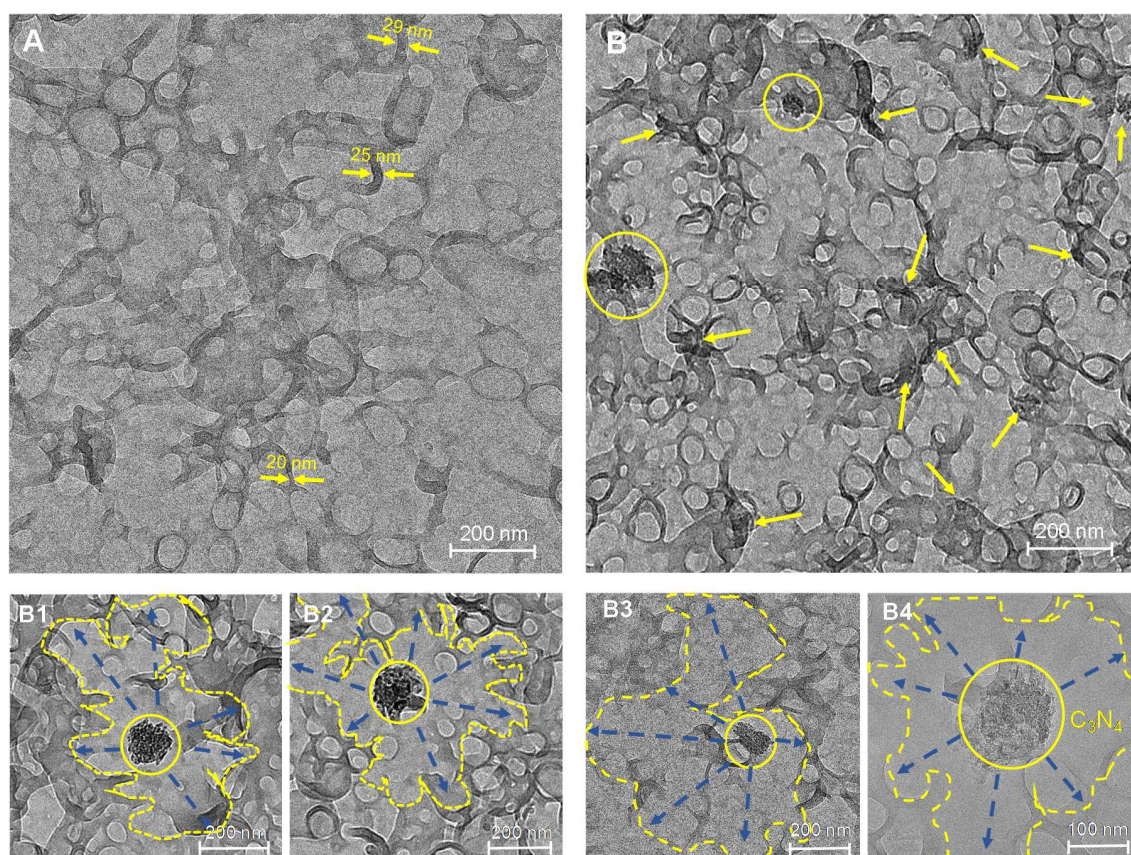
**Table 1.** Properties of the polyamide (PA) layer with various amounts of C<sub>3</sub>N<sub>4</sub> nanoparticles.

Membrane	C <sub>3</sub> N <sub>4</sub> Concentration [mg/mL]	SAR	Ra [nm]	Height [nm]	CLD [%]	WCA [°]
Pristine	0	1.4 ± 0.1	20.2 ± 5.6	260 ± 14	43.75	69 ± 11
C <sub>3</sub> N <sub>4</sub> -4	0.04	1.7 ± 0.1	45.3 ± 6.2	380 ± 10	53.45	58 ± 7
C <sub>3</sub> N <sub>4</sub> -8	0.08	2.1 ± 0.2	69.0 ± 6.1	505 ± 17	56.81	53 ± 8
C <sub>3</sub> N <sub>4</sub> -12	0.12	2.3 ± 0.1	89.7 ± 8.4	650 ± 25	60.09	45 ± 9

As shown in Figure S7 and Table S1, the O/N ratio of the membrane surface decreased from 1.46 to 1.31 as the concentration of the C<sub>3</sub>N<sub>4</sub> nanoparticles increased (Table 1). This can be attributed to two factors: (1) the increase in N resulting from the loading of the nanoparticles into the PA layer; (2) the higher apparent cross-linking degree (CLD) of the PA layer under the effects of the C<sub>3</sub>N<sub>4</sub> nanoparticles on the process of IP. It is well-known that increasing the CLD will increase the salt rejection [22,43,44]. On the other hand, the uniform nanopores of C<sub>3</sub>N<sub>4</sub> are also expected to give high salt rejection. Thus, in both cases it is beneficial to the membrane salt rejection, which explains the experimental observation where the NaCl rejection improved as the concentration of C<sub>3</sub>N<sub>4</sub> nanoparticles increased in the order of pristine TFC < C<sub>3</sub>N<sub>4</sub>-4 < C<sub>3</sub>N<sub>4</sub>-8. Interestingly, the result is different from that reported for TFN membranes with incorporated ZIFs [10,11] or zeolites [45,46]. Those traditional TFN membranes exhibited lower CLDs of the PA layers and lower salt rejection following the addition of the organic/hybrid nanomaterials. Therefore, we tentatively confirmed that, compared with zeolite or other inorganic nanoparticles, the C<sub>3</sub>N<sub>4</sub> nanoparticles in the present study have better compatibility with the polymer network structure and a much more positive influence on the customization of the IP. Furthermore, the C<sub>3</sub>N<sub>4</sub> nanoparticles did not compete with MPD or TMC, whereas some

nanoparticles modified with active groups [47], interfered with the IP and decreased the CLD of the PA layer, resulting in the loss of salt rejection. The WCA of the PA-TFC membrane was approximately  $69 \pm 11^\circ$ . It decreased with the increase in the concentration of  $C_3N_4$  (Table 1) and reached  $45 \pm 9^\circ$  for the  $C_3N_4$ -12 membrane. The hydrophilic nature of  $C_3N_4$  and the rougher surface should be the two possible reasons for these characteristic results.

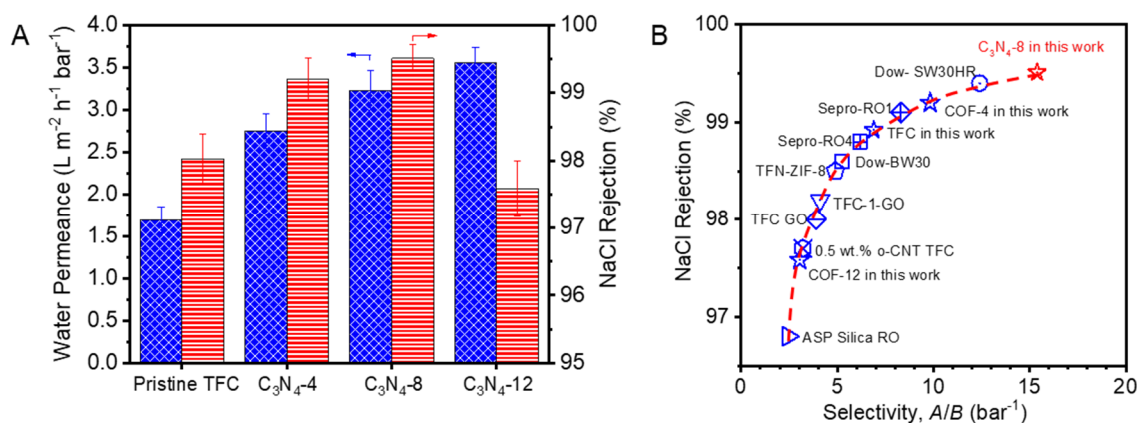
To understand the function of  $C_3N_4$ , the pristine PA-TFC and  $C_3N_4$ -8 membranes were studied in detail via TEM, as shown in Figure 3. In the PA-TFC membrane, the PA layer exhibited a hollow ridge-and-valley structure with a layer thickness of approximately 20–30 nm (Figure 3A), which was similar to that observed in our previous studies [22] and in the literature [23,48]. In the TFN membrane, the layer thickness was similar, but the ridge-and-valley structure was much larger than that of the PA-TFC membrane. A possible mechanism is proposed as follows. Interestingly, it was found that small  $C_3N_4$  particles were clearly embedded into the PA layer, as indicated by the yellow arrows, but the bigger  $C_3N_4$  nanoparticles (approximately over 150 nm) always sat in the middle of the ridge-and-valley structure, as shown in Figure 3B1–B4. A possible mechanism is proposed as follows. The large and hydrophilic  $C_3N_4$  nanoparticles can trap more MPD solution, as demonstrated by the vapor adsorption isotherm in Figure 1F. It forms a heterogenous reaction zone. The heat generated from the IP reaction further promotes the reaction and breaks the interfacial stability [22,23], thus leading to a larger ridge-and-valley feature. In the case of smaller particles, the influence on the reaction is weak, and thus they are embedded into the PA layer.



**Figure 3.** TEM images of (A) pristine PA without  $C_3N_4$ , and (B, B1, B2, B3, and B4) PA with  $C_3N_4$ . The yellow circles indicate large  $C_3N_4$  nanoparticles and the arrows indicate small nanoparticles.

The RO desalination performance is shown in Figure 4 and Table S2. The PA-TFC membrane exhibited a water permeance of  $1.7 \pm 0.2$  LMH/bar with a NaCl rejection of  $98.0\% \pm 0.4\%$ , which were similar to those reported in the literature under the same testing conditions [17,49–52]. The permeance of the TFN membranes increased with the loading rate of  $C_3N_4$ . The rejection increased for the  $C_3N_4$ -4

and  $C_3N_4$ -8 membranes too but declined for the  $C_3N_4$ -12 membrane. For the optimal  $C_3N_4$ -8 membrane, the water permeance reached  $3.6 \pm 0.2$  LMH/bar and the rejection increased to  $99.5\% \pm 0.2\%$ , which is 2.1-folds higher than the permeance of the PA-TFC membrane. Obviously, the enlarged ridge-and-valley structure contributed to the higher water permeance, but its contribution was approximately 1.6-folds according to the SAR. The remaining part was possibly owing to the additional channels provided by the  $C_3N_4$  nanoparticles embedded in the PA layer. The higher salt rejections of the  $C_3N_4$ -4 and  $C_3N_4$ -8 membranes were because of their higher CLD, as shown in Table 1. However, further increasing the particle loading caused particle agglomeration and defects as shown in Figure S8. Thus, the salt rejection declined.



**Figure 4.** (A) Water permeance and NaCl rejection of pristine TFC and TFN membranes, and (B) reverse osmosis (RO) performance towards NaCl rejection and selectivity from the present study and the literature. (References are listed in Table S3.).

The long-term flux of the prepared TFC and TFN membranes was measured to assess their stability during compaction incurred by high-pressure compression. As shown in Figure S9, the normalized steady-state permeance of the membranes approached 0.75–0.80, which is consistent with the literature reported values [49]. There is no significant difference in terms of the steady-state permeance between the pristine TFC membrane and the TFN membranes with various loadings of  $C_3N_4$  particles. Thus, the initial reduction in water permeance should be attributed mainly to the compaction of the PSf supports. The  $C_3N_4$ -8 membrane showed high salt rejection over 99.5% after 48 h testing, which indicated that  $C_3N_4$  particles have good compatibility with the PA layer and the resulting TFN membranes have sufficient stability in seawater desalination applications. The performance of the  $C_3N_4$ -8 membrane was compared with those of other reported TFN systems on the basis of the coefficient ( $J_w/B$ ), as shown in Figure 4B [10,49,50,53,54]. The  $C_3N_4$ -8 membrane showed an unprecedented  $J_w/B$  value of up to 15.4, which is superior to that of not only state-of-the-art commercial RO membranes, such as Dow<sup>®</sup> BW30 and Dow<sup>®</sup> SW30HR, but also other reported TFN membranes.

#### 4. Conclusions

In conclusion, we demonstrated that the highly crystalline  $C_3N_4$  could not only provide a faster transport pathway but also effectively tune the structure of PA by tailoring the process of IP to enhance both the water flux and salt rejection. It was found that the crystalline  $C_3N_4$  was hydrophilic, containing regular pores that could adsorb a significant amount of water. The organic–organic covalent bonds endowed  $C_3N_4$  with great compatibility with the PA layer, which positively influenced the customization of IP. With the increasing loading rate of  $C_3N_4$ , the size of the “ridge-and-valley” surface structure, the surface area ratio, and the surface hydrophilicity all increased compared to the pristine PA-TFC membrane. Moreover, the cross-linking degree (CLD) also increased with  $C_3N_4$  loading rate, which was different from other nanoparticle filler systems. As a result, both the membrane flux and salt

rejection were improved. Under the optimal conditions (C<sub>3</sub>N<sub>4</sub>-8), the water permeance was 2.1-folds higher than that of the pristine TFC membrane, while the NaCl rejection increased to 99.5% from 98.0%. Our method thus provided a promising way to improve the performance of the state-of-art PA-TFC membranes in seawater desalination.

**Supplementary Materials:** The following are available online at <http://www.mdpi.com/2077-0375/10/8/163/s1>, Figure S1: Optical photographs of C<sub>3</sub>N<sub>4</sub> powders and the aqueous solution, Figure S2: SEM images of the prepared PSf substrate, Figure S3: AFM image of the prepared PSf substrate, Figure S4: Pure water flux of the prepared PSf substrate, Figure S5: Optical photographs of the prepared pristine TFC and TFN membranes, Figure S6: N<sub>2</sub> adsorption isotherm (G), and pore size distribution (G inset) of the prepared C<sub>3</sub>N<sub>4</sub>, Figure S7: O/N ration of PA layer fabricated with various amounts C<sub>3</sub>N<sub>4</sub> nanosheets. The degree of cross-linking was calculated by  $\frac{X}{X+Y} \times 100\%$ , where X and Y were calculated from the following equations, 3X + 4Y = O1s and 3X + 2Y = N1s, Figure S8: SEM images of C<sub>3</sub>N<sub>4</sub> deposition on PSf support and surface coverage of the deposited particles on supports, as measured by *Image J* software, Figure S9: Normalized water permeance under long-term operation, Table S1: Elementary composition of PA layer with various C<sub>3</sub>N<sub>4</sub> amount, Table S2: *J<sub>w</sub>*, *B* and *R* of TFC and TFN membranes, Table S3: Comparison of the *A*, *B* and *R* of TFC and TFN membranes reported in references and in this work.

**Author Contributions:** Conceptualization, Z.Z. and Z.L.; methodology, Z.Z. and X.L.; validation, Z.Z. and Z.L.; formal analysis, Z.Z. and X.L.; investigation, Z.Z., D.B.S., G.S., D.L. and P.L.; resources, Z.L.; data curation, Z.Z., X.L., D.B.S., G.S., D.L. and P.L.; writing—original draft preparation, Z.Z.; writing—review and editing, Z.L.; visualization, Z.Z.; supervision, Z.L.; project administration, Z.L.; funding acquisition, Z.L. All authors have read and agreed to the published version of the manuscript.

**Funding:** This research was funded by King Abdullah University of Science and Technology, Saudi Arabia, under the competitive research grant URF/1/3435-01.

**Conflicts of Interest:** The authors declare no conflict of interest.

## References

- Mekonnen, M.M.; Hoekstra, A.Y. Four billion people facing severe water scarcity. *Sci. Adv.* **2016**, *2*, e1500323. [[CrossRef](#)] [[PubMed](#)]
- Hoover, L.A.; Phillip, W.A.; Tiraferri, A.; Yip, N.Y.; Elimelech, M. Forward with osmosis: Emerging applications for greater sustainability. *Environ. Sci. Technol.* **2011**, *45*, 9824–9830. [[CrossRef](#)]
- Kim, B.; Gwak, G.; Hong, S. Review on methodology for determining forward osmosis (FO) membrane characteristics: Water permeability (A), solute permeability (B), and structural parameter (S). *Desalination* **2017**, *422*, 5–16. [[CrossRef](#)]
- Klaysom, C.; Cath, T.Y.; Depuydt, T.; Vankelecom, I.F. Forward and pressure retarded osmosis: Potential solutions for global challenges in energy and water supply. *Chem. Soc. Rev.* **2013**, *42*, 6959–6989. [[CrossRef](#)] [[PubMed](#)]
- Shaffer, D.L.; Werber, J.R.; Jaramillo, H.; Lin, S.; Elimelech, M. Forward osmosis: Where are we now? *Desalination* **2015**, *356*, 271–284. [[CrossRef](#)]
- Choi, W.; Gu, J.-E.; Park, S.-H.; Kim, S.; Bang, J.; Baek, K.-Y.; Park, B.; Lee, J.S.; Chan, E.P.; Lee, J.-H. Tailor-Made Polyamide Membranes for Water Desalination. *ACS Nano* **2015**, *9*, 345–355. [[CrossRef](#)]
- Chowdhury, M.R.; Steffes, J.; Huey, B.D.; McCutcheon, J.R. 3D printed polyamide membranes for desalination. *Science* **2018**, *361*, 682–686. [[CrossRef](#)]
- Geise, G.M.; Park, H.B.; Sagle, A.C.; Freeman, B.D.; McGrath, J.E. Water permeability and water/salt selectivity tradeoff in polymers for desalination. *J. Membr. Sci.* **2011**, *369*, 130–138. [[CrossRef](#)]
- Jeong, B.-H.; Hoek, E.M.; Yan, Y.; Subramani, A.; Huang, X.; Hurwitz, G.; Ghosh, A.K.; Jawor, A. Interfacial polymerization of thin film nanocomposites: A new concept for reverse osmosis membranes. *J. Membr. Sci.* **2007**, *294*, 1–7. [[CrossRef](#)]
- Duan, J.; Pan, Y.; Pacheco, F.; Litwiller, E.; Lai, Z.; Pinnau, I. High-performance polyamide thin-film-nanocomposite reverse osmosis membranes containing hydrophobic zeolitic imidazolate framework-8. *J. Membr. Sci.* **2015**, *476*, 303–310. [[CrossRef](#)]
- Wang, L.; Fang, M.; Liu, J.; He, J.; Deng, L.; Li, J.; Lei, J. The influence of dispersed phases on polyamide/ZIF-8 nanofiltration membranes for dye removal from water. *RSC Adv.* **2015**, *5*, 50942–50954. [[CrossRef](#)]

12. Wang, F.; Zheng, T.; Xiong, R.; Wang, P.; Ma, J. Strong improvement of reverse osmosis polyamide membrane performance by addition of ZIF-8 nanoparticles: Effect of particle size and dispersion in selective layer. *Chemosphere* **2019**, *233*, 524–531. [[CrossRef](#)] [[PubMed](#)]
13. Van Goethem, C.; Verbeke, R.; Pfanmöller, M.; Koschine, T.; Dickmann, M.; Timpel-Lindner, T.; Egger, W.; Bals, S.; Vankelecom, I.F. The role of MOFs in thin-film nanocomposite (TFN) membranes. *J. Membr. Sci.* **2018**, *563*, 938–948. [[CrossRef](#)]
14. Li, C.; Li, S.; Tian, L.; Zhang, J.; Su, B.; Hu, M.Z. Covalent organic frameworks (COFs)-incorporated thin film nanocomposite (TFN) membranes for high-flux organic solvent nanofiltration (OSN). *J. Membr. Sci.* **2019**, *572*, 520–531. [[CrossRef](#)]
15. Wu, S.; Li, M.; Phan, H.; Wang, D.; Heng, T.S.; Ding, J.; Lu, Z.; Wu, J. Toward two-dimensional pi-conjugated covalent organic radical frameworks. *Angew. Chem. Int. Ed.* **2018**, *57*, 8007–8011. [[CrossRef](#)]
16. Lau, W.J.; Gray, S.; Matsuura, T.; Emadzadeh, D.; Chen, J.P.; Ismail, A.F. A review on polyamide thin film nanocomposite (TFN) membranes: History, applications, challenges and approaches. *Water Res.* **2015**, *80*, 306–324. [[CrossRef](#)]
17. Duan, J.; Litwiller, E.; Pinnau, I. Preparation and water desalination properties of POSS-polyamide nanocomposite reverse osmosis membranes. *J. Membr. Sci.* **2015**, *473*, 157–164. [[CrossRef](#)]
18. Dong, H.; Zhao, L.; Zhang, L.; Chen, H.; Gao, C.; Ho, W.W. High-flux reverse osmosis membranes incorporated with NaY zeolite nanoparticles for brackish water desalination. *J. Membr. Sci.* **2015**, *476*, 373–383. [[CrossRef](#)]
19. Guo, F.; Servi, A.; Liu, A.; Gleason, K.K.; Rutledge, G.C. Desalination by membrane distillation using electrospun polyamide fiber membranes with surface fluorination by chemical vapor deposition. *ACS Appl. Mater. Interfaces* **2015**, *7*, 8225–8232. [[CrossRef](#)] [[PubMed](#)]
20. Ma, D.; Peh, S.B.; Han, G.; Chen, S.B. Thin-film nanocomposite (TFN) membranes incorporated with super-hydrophilic metal–organic framework (MOF) UiO-66: Toward enhancement of water flux and salt rejection. *ACS Appl. Mater. Interfaces* **2017**, *9*, 7523–7534. [[CrossRef](#)]
21. Gupta, K.M.; Zhang, K.; Jiang, J. Water desalination through zeolitic imidazolate framework membranes: Significant role of functional groups. *Langmuir* **2015**, *31*, 13230–13237. [[CrossRef](#)]
22. Zhou, Z.; Hu, Y.; Boo, C.; Liu, Z.; Li, J.; Deng, L.; An, X. High-Performance Thin-Film Composite Membrane with an Ultrathin Spray-Coated Carbon Nanotube Interlayer. *Environ. Sci. Technol. Lett.* **2018**, *5*, 243–248. [[CrossRef](#)]
23. Santanu, K.; Jiang, Z.; Livingston, A.G. Sub-10 nm polyamide nanofilms with ultrafast solvent transport for molecular separation. *Science* **2015**, *348*, 1347–1351.
24. Ma, X.-H.; Yao, Z.-K.; Yang, Z.; Guo, H.; Xu, Z.-L.; Tang, C.Y.; Elimelech, M. Nanofoaming of Polyamide Desalination Membranes To Tune Permeability and Selectivity. *Environ. Sci. Technol. Lett.* **2018**, *5*, 123–130. [[CrossRef](#)]
25. Pacheco, F.; Pinnau, I.; Reinhard, M.; Leckie, J. Characterization of isolated polyamide thin films of RO and NF membranes using novel TEM techniques. *J. Membr. Sci.* **2010**, *358*, 51–59. [[CrossRef](#)]
26. Wang, Z.; Wang, Z.; Lin, S.; Jin, H.; Gao, S.; Zhu, Y.; Jin, J. Nanoparticle-templated nanofiltration membranes for ultrahigh performance desalination. *Nat. Commun.* **2018**, *9*, 1–9. [[CrossRef](#)]
27. Tan, Z.; Chen, S.; Peng, X.; Zhang, L.; Gao, C. Polyamide membranes with nanoscale Turing structures for water purification. *Science* **2018**, *360*, 518–521. [[CrossRef](#)]
28. Wang, J.-J.; Yang, H.-C.; Wu, M.-B.; Zhang, X.; Xu, Z.-K. Nanofiltration membranes with cellulose nanocrystals as an interlayer for unprecedented performance. *J. Mater. Chem. A* **2017**, *5*, 16289–16295. [[CrossRef](#)]
29. Yang, Z.; Zhou, Z.W.; Guo, H.; Yao, Z.; Ma, X.H.; Song, X.; Feng, S.P.; Tang, C.Y. Tannic acid/Fe<sup>3+</sup> nanoscaffold for Interfacial polymerization: Toward enhanced nanofiltration performance. *Environ. Sci. Technol.* **2018**, *52*, 9341–9349. [[CrossRef](#)]
30. Zhu, Y.; Xie, W.; Gao, S.; Zhang, F.; Zhang, W.; Liu, Z.; Jin, J. Single-Walled Carbon Nanotube Film Supported Nanofiltration Membrane with a Nearly 10 nm Thick Polyamide Selective Layer for High-Flux and High-Rejection Desalination. *Small* **2016**, *12*, 5034–5041. [[CrossRef](#)]
31. Cao, K.; Jiang, Z.; Zhang, X.; Zhang, Y.; Zhao, J.; Xing, R.; Yang, S.; Gao, C.; Pan, F. Highly water-selective hybrid membrane by incorporating g-C<sub>3</sub>N<sub>4</sub> nanosheets into polymer matrix. *J. Membr. Sci.* **2015**, *490*, 72–83. [[CrossRef](#)]

32. Ye, W.; Liu, H.; Lin, F.; Lin, J.; Zhao, S.; Yang, S.; Hou, J.; Zhou, S.; Van der Bruggen, B. High-flux nanofiltration membranes tailored by bio-inspired co-deposition of hydrophilic g-C<sub>3</sub>N<sub>4</sub> nanosheets for enhanced selectivity towards organics and salts. *Environ. Sci. Nano* **2019**, *6*, 2958–2967. [[CrossRef](#)]
33. Zhang, X.; Xie, X.; Wang, H.; Zhang, J.; Pan, B.; Xie, Y. Enhanced photoresponsive ultrathin graphitic-phase C<sub>3</sub>N<sub>4</sub> nanosheets for bioimaging. *J. Am. Chem. Soc.* **2013**, *135*, 18–21. [[CrossRef](#)]
34. She, X.; Xu, H.; Xu, Y.; Yan, J.; Xia, J.; Xu, L.; Song, Y.; Jiang, Y.; Zhang, Q.; Li, H. Exfoliated graphene-like carbon nitride in organic solvents: Enhanced photocatalytic activity and highly selective and sensitive sensor for the detection of trace amounts of Cu<sup>2+</sup>. *J. Mater. Chem. A* **2014**, *2*, 2563–2570. [[CrossRef](#)]
35. Wang, Y.; Wang, X.; Antonietti, M. Polymeric graphitic carbon nitride as a heterogeneous organocatalyst: From photochemistry to multipurpose catalysis to sustainable chemistry. *Angew. Chem. Int. Ed.* **2012**, *51*, 68–89. [[CrossRef](#)] [[PubMed](#)]
36. Kale, V.S.; Sim, U.; Yang, J.; Jin, K.; Chae, S.I.; Chang, W.J.; Sinha, A.K.; Ha, H.; Hwang, C.C.; An, J.; et al. Sulfur-Modified Graphitic Carbon Nitride Nanostructures as an Efficient Electrocatalyst for Water Oxidation. *Small* **2017**, *13*, 1603893. [[CrossRef](#)] [[PubMed](#)]
37. Liu, Z.; An, X.; Dong, C.; Zheng, S.; Mi, B.; Hu, Y. Modification of thin film composite polyamide membranes with 3D hyperbranched polyglycerol for simultaneous improvement in their filtration performance and antifouling properties. *J. Mater. Chem. A* **2017**, *5*, 23190–23197. [[CrossRef](#)]
38. Zhou, Z.; Lu, D.; Li, X.; Rehman, L.M.; Roy, A.; Lai, Z. Fabrication of highly permeable polyamide membranes with large “leaf-like” surface nanostructures on inorganic supports for organic solvent nanofiltration. *J. Membr. Sci.* **2020**, *601*, 117932. [[CrossRef](#)]
39. Bellardita, M.; García-López, E.I.; Marci, G.; Krivtsov, I.; García, J.R.; Palmisano, L. Selective photocatalytic oxidation of aromatic alcohols in water by using P-doped g-C<sub>3</sub>N<sub>4</sub>. *Appl. Catal. B* **2018**, *220*, 222–233. [[CrossRef](#)]
40. Xue, J.; Ma, S.; Zhou, Y.; Zhang, Z.; He, M. Facile photochemical synthesis of Au/Pt/g-C<sub>3</sub>N<sub>4</sub> with plasmon-enhanced photocatalytic activity for antibiotic degradation. *ACS Appl. Mater. Interfaces* **2015**, *7*, 9630–9637. [[CrossRef](#)]
41. Gao, H.; Yan, S.; Wang, J.; Zou, Z. Ion coordination significantly enhances the photocatalytic activity of graphitic-phase carbon nitride. *Dalton Trans.* **2014**, *43*, 8178–8183. [[CrossRef](#)]
42. Zou, X.; Silva, R.; Goswami, A.; Asefa, T. Cu-doped carbon nitride: Bio-inspired synthesis of H<sub>2</sub>-evolving electrocatalysts using graphitic carbon nitride (g-C<sub>3</sub>N<sub>4</sub>) as a host material. *Appl. Surf. Sci.* **2015**, *357*, 221–228. [[CrossRef](#)]
43. Ghosh, A.K.; Hoek, E.M. Impacts of support membrane structure and chemistry on polyamide–polysulfone interfacial composite membranes. *J. Membr. Sci.* **2009**, *336*, 140–148. [[CrossRef](#)]
44. Huang, L.; McCutcheon, J.R. Impact of support layer pore size on performance of thin film composite membranes for forward osmosis. *J. Membr. Sci.* **2015**, *483*, 25–33. [[CrossRef](#)]
45. Huang, H.; Qu, X.; Dong, H.; Zhang, L.; Chen, H. Role of NaA zeolites in the interfacial polymerization process towards a polyamide nanocomposite reverse osmosis membrane. *RSC Adv.* **2013**, *3*, 8203–8207. [[CrossRef](#)]
46. Lind, M.L.; Eumine Suk, D.; Nguyen, T.-V.; Hoek, E.M. Tailoring the structure of thin film nanocomposite membranes to achieve seawater RO membrane performance. *Environ. Sci. Technol.* **2010**, *44*, 8230–8235. [[CrossRef](#)]
47. Xue, S.-M.; Xu, Z.-L.; Tang, Y.-J.; Ji, C.-H. Polypiperazine-amide nanofiltration membrane modified by different functionalized multiwalled carbon nanotubes (MWCNTs). *ACS Appl. Mater. Interfaces* **2016**, *8*, 19135–19144. [[CrossRef](#)] [[PubMed](#)]
48. Yan, H.; Miao, X.; Xu, J.; Pan, G.; Zhang, Y.; Shi, Y.; Guo, M.; Liu, Y. The porous structure of the fully-aromatic polyamide film in reverse osmosis membranes. *J. Membr. Sci.* **2015**, *475*, 504–510. [[CrossRef](#)]
49. Lee, J.; Wang, R.; Bae, T.-H. High-performance reverse osmosis membranes fabricated on highly porous microstructured supports. *Desalination* **2018**, *436*, 48–55. [[CrossRef](#)]
50. Ali, M.E.; Wang, L.; Wang, X.; Feng, X. Thin film composite membranes embedded with graphene oxide for water desalination. *Desalination* **2016**, *386*, 67–76. [[CrossRef](#)]
51. Chong, C.; Lau, W.; Yusof, N.; Lai, G.; Othman, N.; Matsuura, T.; Ismail, A. Studies on the properties of RO membranes for salt and boron removal: Influence of thermal treatment methods and rinsing treatments. *Desalination* **2018**, *428*, 218–226. [[CrossRef](#)]



52. Kotp, Y.H.; Shebl, Y.A.; El-Deab, M.S.; El-Anadouli, B.E.; Shawky, H.A. Performance enhancement of PA-TFC RO membrane by using magnesium silicate nanoparticles. *J. Inorg. Organomet. Polym. Mater.* **2017**, *27*, 201–214. [[CrossRef](#)]
53. Lee, J.; Jang, J.H.; Chae, H.-R.; Lee, S.H.; Lee, C.-H.; Park, P.-K.; Won, Y.-J.; Kim, I.-C. A facile route to enhance the water flux of a thin-film composite reverse osmosis membrane: Incorporating thickness-controlled graphene oxide into a highly porous support layer. *J. Mater. Chem. A* **2015**, *3*, 22053–22060. [[CrossRef](#)]
54. Li, Q.; Yu, H.; Wu, F.; Song, J.; Pan, X.; Zhang, M. Fabrication of semi-aromatic polyamide/spherical mesoporous silica nanocomposite reverse osmosis membrane with superior permeability. *Appl. Surf. Sci.* **2016**, *363*, 338–345. [[CrossRef](#)]



© 2020 by the authors. Licensee MDPI, Basel, Switzerland. This article is an open access article distributed under the terms and conditions of the Creative Commons Attribution (CC BY) license (<http://creativecommons.org/licenses/by/4.0/>).

Article

# Fouling Mechanisms Analysis via Combined Fouling Models for Surface Water Ultrafiltration Process

Bin Huang <sup>1,2</sup>, Hangkun Gu <sup>1,2</sup>, Kang Xiao <sup>3</sup> , Fangshu Qu <sup>1,2</sup>, Huarong Yu <sup>1,2</sup>  
and Chunhai Wei <sup>1,2,\*</sup> 

<sup>1</sup> Department of Municipal Engineering, School of Civil Engineering, Guangzhou University, Guangzhou 510006, China; huangbinstudy@163.com (B.H.); ghk455818213@163.com (H.G.); qufs@gzhu.edu.cn (F.Q.); huarongyu@gmail.com (H.Y.)

<sup>2</sup> Key Laboratory for Water Quality and Conservation of the Pearl River Delta, Ministry of Education, Guangzhou 510006, China

<sup>3</sup> College of Resources and Environment, University of Chinese Academy of Sciences, Beijing 100049, China; kxiao@ucas.ac.cn

\* Correspondence: weich@gzhu.edu.cn; Tel.: +86-20-3936-6656

Received: 23 June 2020; Accepted: 8 July 2020; Published: 10 July 2020



**Abstract:** Membrane fouling is still the bottleneck affecting the technical and economic performance of the ultrafiltration (UF) process for the surface water treatment. It is very important to accurately understand fouling mechanisms to effectively prevent and control UF fouling. The rejection performance and fouling mechanisms of the UF membrane for raw and coagulated surface water treatment were investigated under the cycle operation of constant-pressure dead-end filtration and backwash. There was no significant difference in the UF permeate quality of raw and coagulated surface water. Coagulation mainly removed substances causing turbidity in raw surface water (including most suspended particles and a few organic colloids) and thus mitigated UF fouling effectively. Backwash showed limited fouling removal. For the UF process of both raw and coagulated surface water, the fittings using single models showed good linearity for multiple models mainly due to statistical illusions, while the fittings using combined models showed that only the combined complete blocking and cake layer model fitted well. The quantitative calculations showed that complete blocking was the main reason causing flux decline. Membrane fouling mechanism analysis based on combined models could provide theoretical supports to prevent and control UF fouling for surface water treatment.

**Keywords:** ultrafiltration; membrane fouling; fouling model; surface water; coagulation; backwash

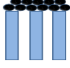


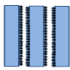


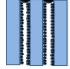
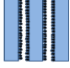
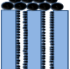
## 1. Introduction

The ultrafiltration (UF) membrane with a nominal pore size of 10–20 nm can reject suspended particles completely and colloids, bacteria and viruses efficiently, while keeping higher permeability than a tight UF membrane with a nominal pore size of a few nanometers, making it a promising advanced technology for drinking water production from conventional surface water resources (e.g., river, lake and reservoir). The rejection capability of UF membrane is generally not affected by the feed quality (e.g., turbidity) and operational conditions (e.g., pressure or flux), thus resulting in very stable and excellent permeate quality. UF membrane modules have also some advantages including the modular design and assembly, compact structure, small footprint and automatic operation. Therefore, the large-scale (up to 0.6 million m<sup>3</sup>/d) UF systems have been gradually implemented in conventional surface water treatment plants in recent years and more applications would be expected in the future based on the increasing demand for high quality drinking water and the decreasing

cost of UF technology [1]. However, membrane fouling is inevitably developed with the filtration time, which derives from the deposition on membrane surface and/or blocking membrane pores by suspended particles, colloids and microorganisms. Membrane fouling would increase the operational pressure under the constant-flux mode or decrease the membrane flux under the constant-pressure mode, increasing the maintenance cost of the UF process [2]. Therefore, it is of great significance to accurately understand membrane fouling mechanisms for the effective prevention and control of UF membrane fouling.

Several mathematical models have been developed to describe the mechanisms of pore blocking and cake layer fouling caused by the presence of contaminants during the filtration process [3]. Hermans and Bredée [4] initially proposed four classical single models (cake layer, intermediate blocking, standard blocking and complete blocking) for constant-pressure dead-end filtration based on the filter cloth tests. Then Grace [5] proposed the common differential equation, which unified the above-mentioned four classical single models via adjusting the values of two constants. Hermia [6] further improved the physical basis of the intermediate blocking model and deduced the linear expressions of four classical single models (shown in Table 1). Bowen et al. [7] and Cho et al. [8] subsequently introduced the single models into the field of microfiltration (MF) and UF. With the development of research on fouling models, Ho et al. [9] proposed a combined model describing the initial membrane pore blocking and the later cake layer. Furthermore, Bolton et al. [10] developed five combined models (complete blocking and cake layer, intermediate blocking and cake layer, standard blocking and cake layer, complete blocking and standard blocking, intermediate blocking and standard blocking) via combining two single models (shown in Table 1 for specific formula). The development of the above-mentioned models was mostly based on protein solution filtration tests.

**Table 1.** Membrane fouling models for the constant-pressure ultrafiltration (UF) process.

Model	Equation *	Characteristic Parameters	Schematic Diagram	References
Cake layer	$\frac{T}{(V/A)} = \frac{1}{J_0} + \frac{K_c}{2}(V/A)$	$K_c$ (s/m <sup>2</sup> )		[4,6]
Complete blocking	$\frac{d(V/A)}{dT} = J_0 - K_b(V/A)$	$K_b$ (s <sup>-1</sup> )		[4,6]
Intermediate blocking	$\frac{dT}{d(V/A)} = \frac{1}{J_0} + K_i T$	$K_i$ (m <sup>-1</sup> )		[4,6]
Standard blocking	$\frac{T}{(V/A)} = \frac{1}{J_0} + \frac{K_s}{2} T$	$K_s$ (m <sup>-1</sup> )		[4,6]
Complete blocking and Cake layer	$\frac{V}{A} = \frac{J_0}{K_b} \left( 1 - \exp\left( \frac{-K_b}{K_c J_0^2} \left( \sqrt{1 + 2K_c J_0^2 T} - 1 \right) \right) \right)$	$K_c$ (s/m <sup>2</sup> ), $K_b$ (s <sup>-1</sup> )		[10]
Intermediate blocking and Cake layer	$\frac{V}{A} = \frac{1}{K_i} \ln\left( 1 + \frac{K_i}{K_c J_0} \left( \sqrt{1 + 2K_c J_0^2 T} - 1 \right) \right)$	$K_c$ (s/m <sup>2</sup> ), $K_i$ (m <sup>-1</sup> )		[10]
Complete blocking and Standard blocking	$\frac{V}{A} = \frac{J_0}{K_b} \left( 1 - \exp\left( \frac{-2K_b T}{2 + K_s J_0 T} \right) \right)$	$K_b$ (s <sup>-1</sup> ), $K_s$ (m <sup>-1</sup> )		[10]
Intermediate blocking and Standard blocking	$\frac{V}{A} = \frac{1}{K_i} \ln\left( 1 + \frac{2K_i J_0 T}{2 + K_s J_0 T} \right)$	$K_i$ (m <sup>-1</sup> ), $K_s$ (m <sup>-1</sup> )		[10]
Standard blocking and Cake layer	$T = \frac{1}{K_s \left( \frac{V}{A} \right)^2 - 2} \left( \frac{K_s K_c \left( \frac{V}{A} \right)^3}{2} - K_c \left( \frac{V}{A} \right)^2 - \frac{2 \left( \frac{V}{A} \right)}{J_0} \right)$	$K_c$ (s/m <sup>2</sup> ), $K_s$ (m <sup>-1</sup> )		[10]

\*  $T$ —filtration time (s);  $V$ —permeate volume (m<sup>3</sup>);  $A$ —membrane area (m<sup>2</sup>);  $J_0$ —initial membrane flux (m/s).

The single models have been gradually applied in the water treatment field using MF/UF [11–14]. Schippers and Verdouw firstly proposed a modified fouling index (MFI) based on the cake layer model using 0.45  $\mu\text{m}$  MF membrane to characterize the particulate fouling potential of water samples [15], which became the theoretical basis of the standard methods for MFI measurement [16]. Jin et al. [17] conducted MFI measurements twice to eliminate the effects of membrane pore blocking and proposed the cake fouling index. Due to the ubiquitous colloids in natural water bodies (e.g., river, lake and sea), Boerlage et al. [18] employed UF membranes to develop the MFI-UF measurement to cover colloidal effects on fouling potential. Sim et al. [19] further proposed the cross-flow sampling MFI-UF measurement to cover the crossflow effects on fouling potential. However, there is little information available in the literature about the application of combined models for the UF membrane fouling analysis in the surface water treatment [20,21].

This study aimed to clarify UF membrane fouling mechanisms during both real raw and coagulated surface water filtration via mathematical model fitting including the above-mentioned single and combined fouling models, and investigate the performance and mechanisms of the coagulation pretreatment and backwash for UF membrane fouling control. The findings from this study would provide theoretical supports for the prevention and control of UF membrane fouling.

## 2. Materials and Methods

### 2.1. Raw Surface Water

The raw surface water was sampled from the landscape lake in the university town campus of Guangzhou University. The turbidity and dissolved organic carbon (DOC) of raw surface water were 33.8 NTU and 20.1 mg/L, respectively.

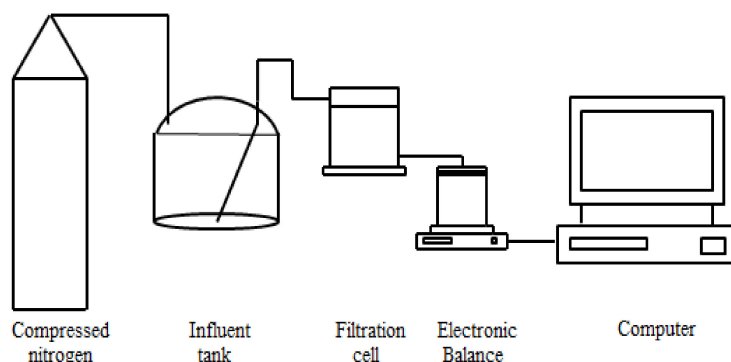
### 2.2. Coagulation Pretreatment

In this study, a coagulation device (model ZR4–6, Zhongrun, Shenzhen, China) was used to conduct the coagulation pretreatment of raw surface water.  $\text{FeCl}_3$  was selected as the coagulant. The coagulation sequence was coagulant spiking  $\rightarrow$  rapid stirring for 30 s at 500 r/min  $\rightarrow$  slow stirring for 300 s at 150 r/min  $\rightarrow$  slow stirring for 600 s at 100 r/min  $\rightarrow$  sedimentation for 15 min. The pH of raw surface water was 7.34 and no pH control was done for coagulation experiments. Turbidity removal under different  $\text{FeCl}_3$  dosage (1–20 mg/L) was firstly investigated. The turbidity of coagulated surface water showed a rapid decrease followed by a steady trend with the increase of  $\text{FeCl}_3$  dosage. The inflection point of the curve of turbidity vs.  $\text{FeCl}_3$  dosage was around 10 mg/L, which was selected as the optimum dosage considering turbidity removal and coagulant cost. Then, sufficient coagulated surface water samples were prepared under the optimum dosage for subsequent UF experiments. The turbidity and DOC of the coagulated surface water were 3.39 NTU and 17.5 mg/L, which were reduced by 90% and 13% compared with the raw surface water, respectively. This indicated that coagulation mainly removed suspended particles (i.e., the main turbidity substances) and a small part of organic colloids (characterized as DOC) in this study.

### 2.3. UF Experiments

A laboratory-scale constant-pressure dead-end filtration system (shown in Figure 1) was used for UF experiments in this study. Compressed nitrogen was used to pressurize the water sample in the stainless steel influent tank with an effective volume of 10 L into the filtration cell (Amicon 8400, Millipore, Burlington, MA, USA) for constant-pressure dead-end filtration. A flat-sheet UF membrane with a molecular weight cut-off of 150 kDa and material of polyvinylidene fluoride (Koch, Wilmington, NC, USA) was used. The mass of UF permeate was weighed by an electronic balance (ME4002E, Mettler Toledo, Greifensee, Switzerland) and sent to the computer for real time recording. Based on the measured temperature of the UF permeate, the density was determined, and thus the mass was further converted into volume. The instantaneous filtration rate was obtained by the numerical

differentiation between the UF permeate volume and filtration time, and thus the instantaneous membrane flux calculation and membrane fouling model fitting were carried out based on the effective UF membrane area.



**Figure 1.** Constant-pressure dead-end filtration system.

Before filtering surface water samples (raw surface water or coagulated surface water), pure water was filtered for 10 min under 100 kPa to record the pure water flux of the new membrane for pure membrane resistance calculation. Then, surface water was filtered for 1 h under 100 kPa. After filtration, the UF membrane was reversely placed in the filtration cell and backwashed with 5% of UF permeate under 150 kPa. After backwash, the UF membrane was placed in the normal direction and pure water was filtered for 10 min under 100 kPa again to record the membrane flux for residual resistance calculation after backwash. Thus, a complete cycle of filtration followed by backwash (total water yield 95%) was finished. A total of 5 cycles were conducted to simulate the real UF process for surface water treatment.

#### 2.4. Water Quality Analysis

Turbidity of all water samples was directly measured by a portable turbidity meter (WGZ-4000B, Xinrui, Shanghai, China). Raw and coagulated surface water samples were pre-filtered through a 0.45  $\mu\text{m}$  syringe filter to determine DOC by an organic carbon analyzer (TOC-L, Shimadzu, Kyoto, Japan). UF permeate samples were directly measured for DOC.

#### 2.5. Membrane Fouling Mechanism Analysis

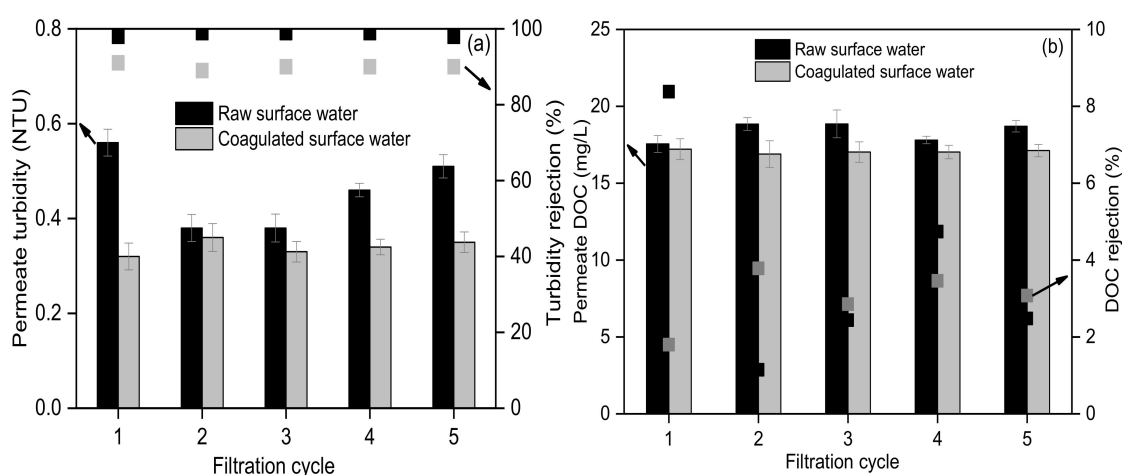
The single and combined fouling models for the constant-pressure UF process [4,6,10] was shown in Table 1. Origin 2018 software was used to fit the UF data of raw and coagulated surface water to the model equations in order to clarify the fouling mechanisms in this study. For single and combined membrane fouling models, linear and nonlinear fitting were performed respectively. The coefficient of determination  $R^2$  (i.e., the ratio of sum of squares for regression to the sum of squares for total,  $SSR/SST$ , with a value range of 0–1) characterizes the quality of the fitting results. On the basis of passing the parameter  $t$  test ( $<0.05$ ),  $R^2 > 0.95$  can be generally considered as a successful fitting, the closer to 1, the better the fitting.

### 3. Results and Discussion

#### 3.1. Rejection Performance by UF for the Surface Water Treatment

The turbidity and DOC of UF permeate for raw and coagulated surface water (shown in Figure 2) were 0.38–0.56 NTU and 17.5–20.1 mg/L, 0.32–0.36 NTU and 16.9–17.5 mg/L, respectively, showing slightly better UF permeate quality for the coagulated than raw surface water. This was mainly due to that most of the substances removed by coagulation (suspended particles and a small part of organic colloids) could be directly rejected by the UF membrane in this study, demonstrating the stable rejection

by the UF membrane. The rejection of turbidity and DOC by the UF membrane for raw and coagulated surface water was 98.3–98.9% and 85.3–90.6%, 1.1–8.4% and 1.8–3.8%, respectively, indicating that UF membrane achieved high turbidity rejection and low DOC rejection. Turbidity of surface water was generally composed of suspended particles and organic colloids (component of DOC). Based on the high turbidity rejection and low DOC rejection by UF membrane in this study, it could be preliminarily inferred that suspended particles were the main membrane foulants from the perspective of UF rejection.

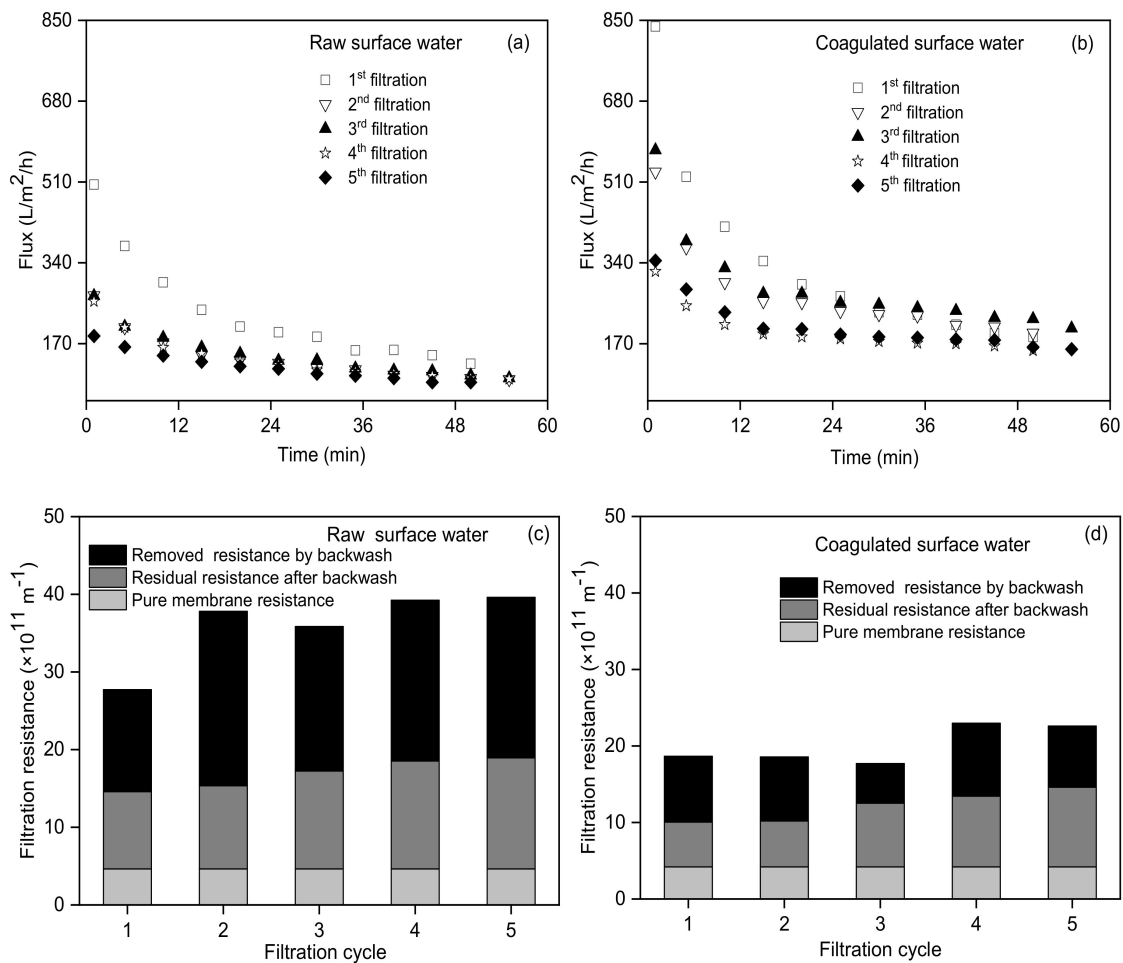


**Figure 2.** Rejection performance of turbidity (a) and dissolved organic carbon (DOC) (b) by UF membrane for the raw and coagulated surface water.

### 3.2. Membrane Fouling of UF for the Surface Water Treatment

The UF flux of the coagulated surface water during the first to fifth filtration cycle was significantly higher than that of raw surface water during the corresponding filtration cycle (shown in Figure 3a–b), indicating the significant UF fouling mitigation performance by coagulation. As a classical electrolyte coagulant, FeCl<sub>3</sub> used in this study can firstly neutralize the negatively charged colloids, then enhance these colloids aggregated into small particles, further making small particles aggregated into big particles via adsorption bridging, and finally enhance big particles settling from water. Thus, FeCl<sub>3</sub> coagulation could change the content and size of suspended particles and colloids in surface water [22,23], resulting in a 90% decrease of turbidity (mainly suspended particles) and 13% decrease of organic colloids (measured by DOC) after coagulation in this study. This further significantly reduced the fouling potential of coagulated surface water and thus UF membrane fouling. The initial UF flux (837 L/m<sup>2</sup>/h) of coagulated surface water during the first filtration cycle was slightly lower than the corresponding pure water flux (853 L/m<sup>2</sup>/h), which was derived from the simultaneous occurrence of fouling during the pressure regulation process (about 1 min) before the filtration test. The initial UF flux (504 L/m<sup>2</sup>/h) of the raw surface water during the first filtration cycle was significantly lower than the corresponding pure water flux (772 L/m<sup>2</sup>/h), which derived from the heavy fouling caused by the high turbidity of raw surface water (about 10 times of coagulated surface water) during the pressure regulation process before the filtration test. Park et al. also found that the higher the influent turbidity, the faster the membrane flux decreased [24]. Resistance distribution at the end of each filtration (shown in Figure 3c–d) indicated that the removed resistance by backwash accounted for 56.9–67.7% (average 60.6%) and 38.3–59.5% (average 50.1%) of the total fouling resistance developed during the UF process for the raw and coagulated surface water, respectively. The backwash performance was slightly better for the raw surface water than the coagulated surface water, which was mainly due to the higher fouling resistance for the raw surface water than the coagulated surface water. However, the residual resistance after backwash showed a gradual increase with the filtration cycle for both the raw and coagulated surface water, indicating the limited performance for fouling removal by the simple

backwash used in this study. This was similar to the findings from Jang et al. [25] that only backwash was less effective than the combined back and forward wash for UF membrane fouling control.

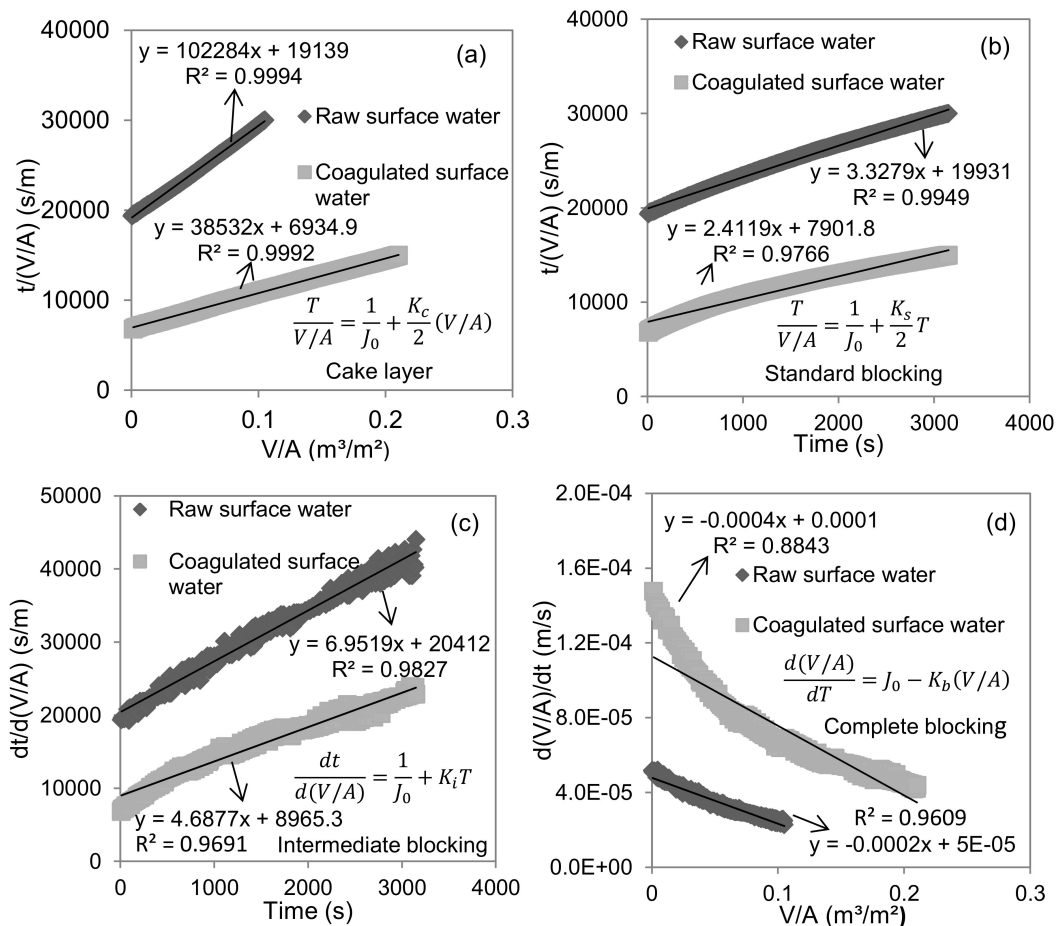


**Figure 3.** UF membrane fouling including a flux decline for the raw surface water (a) and coagulated surface water (b), and resistance distribution at the end of filtration for the raw surface water (c) and coagulated surface water (d).

### 3.3. Analysis of UF Membrane Fouling Mechanisms Based on Single Models

As a typical example, the fitting analysis of the second UF test for raw and coagulated surface water using single models was shown in Figure 4. The results of the other four UF tests were the same. All four single fouling models (cake layer, standard blocking, intermediate blocking and complete blocking) during the UF process of raw surface water showed good linear fitting ( $R^2 > 0.96$ ,  $t < 0.01$ ). Three single models (cake layer, standard blocking and intermediate blocking) during the UF process of the coagulated surface water also showed good linear fitting ( $R^2 > 0.96$ ,  $t < 0.01$ ). From a statistical point of view, this indicated that multiple fouling mechanisms occurred at the same time. The substances in the surface water had generally a wide size distribution (1 nm to 1 mm). The components significantly larger than the UF membrane pore size (mainly suspended particles and some large-size colloids) could form cake layer fouling, the components equivalent to the UF membrane pore size (mainly colloids) could form complete blocking and intermediate blocking fouling, and the components significantly smaller than the UF membrane pore size (mainly soluble substances and some small colloids) could form standard blocking fouling. Therefore, the four fouling mechanisms in the UF process of the surface water could occur simultaneously in theory. Wei and Amy [26] found the simultaneous occurrence of two fouling mechanisms during the UF process of the wastewater treatment plant

effluent. Corbaton et al. [27] found that single models did not characterize the membrane fouling mechanism. Li et al. [28] found multiple fouling mechanisms involved in the UF process of river water. Once the simultaneous occurrence of multiple fouling mechanisms, the single models may produce statistical illusions for the UF membrane fouling mechanism analysis, especially for the quantitative evaluation of the contribution of a single fouling mechanism. Thus, the applicability of single models should be further verified by the combined models.



**Figure 4.** Linear fitting of single models for the UF membrane fouling mechanisms analysis in terms of cake layer model fitting (a), standard blocking model fitting (b), intermediate blocking model fitting (c) and complete blocking model fitting (d).

### 3.4. Analysis of UF Membrane Fouling Mechanisms Based on Combined Models

Nonlinear fitting between the permeate volume  $V$  and filtration time  $T$  using combined models was conducted for the above-mentioned UF data (shown in Table 2). The combined standard blocking and cake layer model did not converge. The combined models of complete blocking and standard blocking, intermediate blocking and standard blocking and intermediate blocking and cake layer did not pass the parameter  $t$  test. Only the combined complete blocking and cake layer model fitted well ( $R^2$  was 0.9935 and 0.9948 for the UF process of the raw and coagulated surface water, respectively;  $t < 0.01$ , shown in Figure 5). Among the linear fitting results of four single models (shown in Table 2), the linearity of the complete blocking model for the UF process of the raw and coagulated surface water was the worst, while the linearity of the cake layer model and the standard blocking model was the best. Thus, it could be intuitively speculated that the combined standard blocking and cake layer model fitted the best among the combined models. However, the best-fitting combined model was the combined complete blocking and cake layer model in fact, indicating that single models might

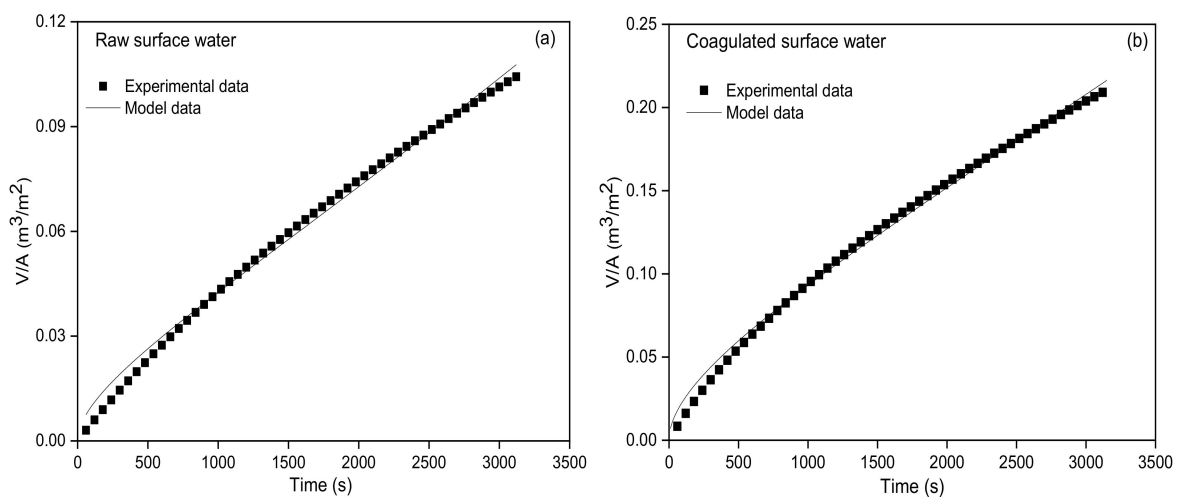


not be applicable when multiple fouling mechanisms occurred simultaneously. Due to the existence of colloids equivalent to UF membrane pore size and suspended particles much larger than the UF membrane pore size in surface water, the fouling mechanisms of complete blocking and the cake layer could occur simultaneously during the UF process of the surface water. Li et al. [28] also found the simultaneous occurrence of standard blocking (or intermediate blocking) and cake layer fouling during the UF process of flocculated but unsettled river water. Xing et al. [29] employed the hybrid adsorption/oxidation and the UF process for the algae-laden surface water treatment and found the simultaneous occurrence of multiple fouling mechanisms.

**Table 2.** Fitting results of combined and single models for the UF process of the surface water.

Model	Raw Surface Water		Coagulated Surface Water	
	Non-Linear/Linear Fitting R <sup>2</sup>	Characteristic Parameters	Non-Linear/Linear Fitting R <sup>2</sup>	Characteristic Parameters
Complete blocking and Cake layer	0.9935	$K_b = 1.12 \text{ s}^{-1}$ $K_c = 1.15 \times 10^6 \text{ s/m}^2$	0.9948	$K_b = 0.35 \text{ s}^{-1}$ $K_c = 1.94 \times 10^5 \text{ s/m}^2$
Intermediate blocking and Cake layer	0.9423	$K_i = 2.17 \times 10^{-6} \text{ m}^{-1} *$ $K_c = 5.90 \times 10^5 \text{ s/m}^2$	0.9908	$K_i = 2.83 \times 10^{-7} \text{ m}^{-1} *$ $K_c = 1.08 \times 10^5 \text{ s/m}^2$
Standard blocking and Cake layer	Fitting failed due to no convergence		Fitting failed due to no convergence	
Complete blocking and Standard blocking	0.6428	$K_b = 1.64 \times 10^{-5} \text{ s}^{-1} *$ $K_s = 22.90 \text{ m}^{-1} *$	0.9102	$K_b = 2.51 \times 10^{-6} \text{ s}^{-1} *$ $K_s = 28.15 \text{ m}^{-1} *$
Intermediate blocking and Standard blocking	0.7989	$K_i = 39.77 \text{ m}^{-1}$ $K_s = 1.77 \text{ m}^{-1} *$	0.9503	$K_i = 11.65 \text{ m}^{-1}$ $K_s = 0.84 \text{ m}^{-1} *$
Cake layer	0.9994	$K_c = 5.1 \times 10^4 \text{ s/m}^2$	0.9992	$K_c = 1.93 \times 10^4 \text{ s/m}^2$
Intermediate blocking	0.9827	$K_i = 6.95 \text{ m}^{-1}$	0.9691	$K_i = 4.69 \text{ m}^{-1}$
Complete blocking	0.9609	$K_b = 2 \times 10^{-4} \text{ s}^{-1}$	0.8843	$K_b = 4 \times 10^{-4} \text{ s}^{-1}$
Standard blocking	0.9949	$K_s = 1.66 \text{ m}^{-1}$	0.9766	$K_s = 1.21 \text{ m}^{-1}$

\* Failed the *t* test at the 0.05 significance level of the characteristic parameter, i.e., *t* > 0.05.



**Figure 5.** Graphic fitting of the combined complete blocking and cake layer model for the raw surface water (a) and coagulated surface water (b).

Since the combined model derives from two single models, the fitting parameters can be used to quantitatively evaluate the contribution of a single model to the combined model. According to the definition of fouling models, cake layer fouling increases the filtration resistance, resulting in a flux decline of  $\Delta J/J_0 = K_c J_0 V / (1 + K_c J_0 V) \approx K_c J_0 V$  (when *V* is small). When complete blocking fouling occurs, the blocked membrane pores lose filtration capacity, resulting in a flux decline of  $\Delta J/J_0 = (K_b/J_0)V$ . Therefore, the ratio of the above-mentioned two values of  $\Delta J/J_0$  (i.e.,  $K_c J_0 / (K_b/J_0)$ ) can be used to quantitatively evaluate the individual contribution of the cake layer and complete blocking

fouling to the decline in membrane flux. The ratio of  $K_c J_0 / (K_b / J_0)$  for the UF process of the raw and coagulated surface water was 0.052 and 0.027 (i.e., the percentage of complete blocking fouling for flux decline was 95.1% and 97.4%), respectively, indicating that complete blocking fouling was the main reason for the UF flux decline in this study. This seemed to be somewhat contradictory to the previous deduction from the analysis of water quality before and after UF that “from the perspective of UF rejection, suspended particles were the main membrane foulants”. The main reasons were the different fouling characteristics of the complete blocking formed by colloids and the cake layer formed by suspended particles as well as the different concentrations of colloids and suspended particles in the surface water. The blocked membrane pores lost the filtration capacity (i.e., the resistance was infinite) when complete blocking fouling occurred, while the resistance caused by cake layer fouling was finite. Therefore, the flux decline caused by complete blocking fouling formed by colloids would be higher than that caused by the cake layer formed by suspended particles with the same amount to colloids. Despite no direct measurement in this study, the concentration of suspended particles could be roughly estimated as 33.8 mg/L and 3.39 mg/L for the raw and coagulated surface water, respectively, according to the turbidity and the conversion factor between turbidity and standard SiO<sub>2</sub> concentration. The low-concentration suspended particles in surface water in this study were not enough to quickly form a uniform and dense cake layer, resulting in a low flux decline caused by cake layer fouling. Membrane pores were also not effectively covered by the cake layer and thus more colloids with equivalent size to membrane pores in the surface water could reach membrane surface and form complete blocking, resulting in a high flux decline. Bolton et al. [11] investigated the UF process of the bovine serum protein solution with a concentration of up to 2500 mg/L and found  $K_c J_0 / (K_b / J_0)$  of 28.3 (i.e., the cake layer and complete blocking fouling accounted for 96.6% and 3.4% of the flux decline, respectively), indicating that the dominant cake layer fouling occurred under high concentration conditions. Li et al. [28] investigated the UF process of flocculated but the unsettled river water and found the simultaneous occurrence of minor standard blocking (or intermediate blocking) and dominant cake layer fouling due to the existence of high-concentration flocs in flocculated but unsettled river water. It should be pointed out that if the property of the surface water and/or UF membrane (e.g., particle/pore size distribution) is changed, the fouling mechanism would also change because it is intrinsically dependent on the interactions between the surface water and UF membrane.

Table 3 lists the fitted characteristic parameter values,  $R^2$  and  $K_c J_0 / (K_b / J_0)$  of the combined complete blocking and cake layer model for the UF process of the raw and coagulated surface water. The  $K_c$  and  $K_b$  of raw surface water were higher than that of the coagulated surface water, showing a significant correlation with water quality. The concentration of suspended particles and organic colloids (measured as turbidity) in the raw surface water was higher than that of the coagulated surface water. During the UF process of the surface water in this study, suspended particles with a size larger than 0.45  $\mu\text{m}$  could form cake layer fouling, while some organic colloids with the same or close molecular weight cut-off (150 kDa) of the UF membrane could form complete blocking fouling. The  $K_c J_0 / (K_b / J_0)$  of the coagulated surface water was lower than that of the raw surface water, meaning that cake layer fouling accounted for a lower contribution to flux decline during the UF process of the coagulated surface water than the raw surface water. This reflected the performance of coagulation pretreatment to mainly remove suspended particles. In addition, the  $K_c J_0 / (K_b / J_0)$  (i.e., the contribution of cake layer fouling) of both the raw and coagulated surface water showed an upward trend with increasing filtration cycles, which might be related to foulants accumulation caused by the limited backwash performance.

**Table 3.** Fitting results of the combined complete blocking and cake layer model for the UF process of the surface water.

Filtration Cycle	Raw Surface Water			Coagulated Surface Water		
	Characteristic Parameter	R <sup>2</sup>	K <sub>c</sub> J <sub>0</sub> /(K <sub>b</sub> /J <sub>0</sub> )	Characteristic Parameter	R <sup>2</sup>	K <sub>c</sub> J <sub>0</sub> /(K <sub>b</sub> /J <sub>0</sub> )
1st	K <sub>b</sub> = 0.27 s <sup>-1</sup> K <sub>c</sub> = 1.78 × 10 <sup>5</sup> s/m <sup>2</sup>	0.9931	0.033	K <sub>b</sub> = 0.24 s <sup>-1</sup> K <sub>c</sub> = 9.70 × 10 <sup>4</sup> s/m <sup>2</sup>	0.9938	0.021
2nd	K <sub>b</sub> = 1.12 s <sup>-1</sup> K <sub>c</sub> = 1.15 × 10 <sup>6</sup> s/m <sup>2</sup>	0.9945	0.052	K <sub>b</sub> = 0.35 s <sup>-1</sup> K <sub>c</sub> = 1.94 × 10 <sup>5</sup> s/m <sup>2</sup>	0.9952	0.027
3rd	K <sub>b</sub> = 0.61 s <sup>-1</sup> K <sub>c</sub> = 5.55 × 10 <sup>5</sup> s/m <sup>2</sup>	0.9949	0.046	K <sub>b</sub> = 0.29 s <sup>-1</sup> K <sub>c</sub> = 1.55 × 10 <sup>5</sup> s/m <sup>2</sup>	0.9954	0.027
4th	K <sub>b</sub> = 0.71 s <sup>-1</sup> K <sub>c</sub> = 6.83 × 10 <sup>5</sup> s/m <sup>2</sup>	0.9948	0.049	K <sub>b</sub> = 0.56 s <sup>-1</sup> K <sub>c</sub> = 4.10 × 10 <sup>5</sup> s/m <sup>2</sup>	0.9953	0.037
5th	K <sub>b</sub> = 0.65 s <sup>-1</sup> K <sub>c</sub> = 6.37 × 10 <sup>5</sup> s/m <sup>2</sup>	0.9951	0.049	K <sub>b</sub> = 0.82 s <sup>-1</sup> K <sub>c</sub> = 4.93 × 10 <sup>5</sup> s/m <sup>2</sup>	0.9951	0.031

#### 4. Conclusions

This study investigated the rejection performance, membrane flux changes and membrane fouling mechanisms of the constant-pressure UF process of the raw and coagulated surface water. The average rejection of turbidity and DOC by the UF membrane for the raw and coagulated surface water was 98.6% and 89.1%, 3.8% and 3.0%, respectively. There was no significant difference in the UF permeate quality of the raw and coagulated surface water under the short-term filtration conditions in this study. Coagulation mainly removed turbidity substances (including most suspended particles and a small part of organic colloids) in the raw surface water, thereby significantly reducing UF membrane fouling. Simple backwash showed limited performance to remove membrane fouling. Linear fitting of single membrane fouling models to UF data showed good linearity ( $R^2 > 0.96$ ) of four models (cake layer, standard blocking, intermediate blocking and complete blocking) and three models (cake layer, standard blocking and intermediate blocking) for the raw and coagulated surface water, respectively, indicating statistically the simultaneous occurrence of multiple fouling mechanisms. Non-linear fitting of combined membrane fouling models showed firstly that only the combined complete blocking and cake layer model fitted well ( $R^2 > 0.99$ ), indicating that the single membrane fouling models produced statistical illusions and thus could not truly describe the UF process of the real surface water with the simultaneous occurrence of multiple fouling mechanisms. The quantitative calculation from the combined model showed for the first time that the complete blocking fouling formed by the colloids was the main reason for the decline of UF membrane flux (accounting for more than 95%). This study employed real raw and coagulated surface water and simulated the representative operation mode of the filtration-backwash cycle in the UF plant for the surface water treatment. The findings from this study would provide theoretical supports for the mechanism analysis and the control method of UF membrane fouling in surface water treatment plants.

**Author Contributions:** B.H. wrote the first draft of the manuscript. B.H. and H.G. conducted the experiments. K.X., F.Q. and H.Y. provided the suggestions during the study and reviewed the manuscript. C.W. got the funding and supervised this work. All authors have read and agreed to the published version of the manuscript.

**Funding:** This work was supported by the 100-Talent Program of Guangzhou University (No. RQ2020103) and the Science and Technology Program of Guangzhou (No. 202002030150).

**Conflicts of Interest:** The authors declare no conflict of interest.

#### References

1. Bei, E.; Wu, X.M.; Qiu, Y.; Chen, C.; Zhang, X.J. A Tale of Two Water Supplies in China: Finding Practical Solutions to Urban and Rural Water Supply Problems. *Acc. Chem. Res.* **2019**, *52*, 867–875. [[CrossRef](#)] [[PubMed](#)]

2. Gao, W.; Liang, H.; Ma, J.; Han, M.; Chen, Z.L.; Han, Z.S.; Li, G.B. Membrane fouling control in ultrafiltration technology for drinking water production: A review. *Desalination* **2011**, *272*, 1–8. [[CrossRef](#)]
3. Iritani, E. A Review on Modeling of Pore-Blocking Behaviors of Membranes During Pressurized Membrane Filtration. *Dry. Technol.* **2013**, *31*, 146–162. [[CrossRef](#)]
4. Hermans, P.H.; Brede'e, H.L. Principles of the mathematical treatment of constant-pressure filtration. *J. Soc. Chem. Ind.* **1936**, *55T*, 1–4.
5. Grace, H. Structure and performance of filter media. II. Performance of filter media in liquid service. *Aiche J.* **1956**, *2*, 316–336. [[CrossRef](#)]
6. Hermia, J. Constant pressure blocking filtration laws—application to power-law non-Newtonian fluids. *Inst. Chem. Eng.* **1982**, *60*, 183–187.
7. Bowen, W.R.; Hall, N.J. Properties of microfiltration membranes: Mechanisms of flux loss in the recovery of an enzyme. *Biotechnol. Bioeng.* **1995**, *46*, 28–35. [[CrossRef](#)] [[PubMed](#)]
8. Cho, J.; Amy, G.; Yoon, Y.; Sohn, J. Predictive models and factors affecting natural organic matter (NOM) rejection and flux decline in ultrafiltration (UF) membranes. *Desalination* **2002**, *142*, 245–255. [[CrossRef](#)]
9. Ho, C.C.; Zydney, A.L. A Combined Pore Blockage and Cake Filtration Model for Protein Fouling during Microfiltration. *J. Colloid Interface Sci.* **2000**, *232*, 389–399. [[CrossRef](#)]
10. Bolton, G.; LaCasse, D.; Kuriyel, R. Combined models of membrane fouling: Development and application to microfiltration and ultrafiltration of biological fluids. *J. Membr. Sci.* **2006**, *277*, 75–84. [[CrossRef](#)]
11. Huang, H.; Young, T.A.; Jacangelo, J.G. Unified Membrane Fouling Index for Low Pressure Membrane Filtration of Natural Waters: Principles and Methodology. *Environ. Sci. Technol.* **2008**, *42*, 714–720. [[CrossRef](#)] [[PubMed](#)]
12. Wei, C.H.; Laborie, S.; Ben Aim, R.; Amy, G. Full Utilization of Silt Density Index (SDI) Measurements for Seawater Pre-Treatment. *J. Membr. Sci.* **2012**, *405*, 212–218. [[CrossRef](#)]
13. Liu, B.; Qu, F.S.; Liang, H.; Bruggen, B.V.D.; Cheng, X.X.; Yu, H.R.; Xu, G.R.; Li, G.B. Microcystis aeruginosa-laden surface water treatment using ultrafiltration: Membrane fouling, cell integrity and algogenic organic matter removal. *Water Res.* **2017**, *112*, 83–92. [[CrossRef](#)] [[PubMed](#)]
14. Xiao, K.; Mo, Y.H.; Sun, J.Y.; Wang, J.; Wang, M.Y.; Liang, S.; Wang, X.M.; Wang, X.; Huang, X.; Waite, T.D. An extended standard blocking filtration law for exploring membrane pore internal fouling due to rate-determining adsorption. *Sep. Purif. Technol.* **2019**, *212*, 974–979. [[CrossRef](#)]
15. Schippers, J.; Verdouw, J. The modified fouling index, a method of determining the fouling characteristics of water. *Desalination* **1980**, *32*, 137–148. [[CrossRef](#)]
16. ASTM. *D8002-15, Standard Test. Method for Modified Fouling Index (MFI-0.45) of Water*; ASTM International: West Conshohocken, PA, USA, 2015.
17. Jin, Y.X.; Ju, Y.G.; Lee, H.; Hong, S. Fouling potential evaluation by cake fouling index: Theoretical development, measurements, and its implications for fouling mechanisms. *J. Membr. Sci.* **2015**, *490*, 57–64. [[CrossRef](#)]
18. Boerlage, S.F.E.; Kennedy, M.D.; Aniyee, M.P.; Abogream, E.M.; EI-Hodali, D.E.Y.; Tarawneh, Z.S.; Schippers, J.C. Modified Fouling Index ultrafiltration to compare pretreatment processes of reverse osmosis feedwater. *Desalination* **2000**, *131*, 201–214. [[CrossRef](#)]
19. Sim, L.N.; Ye, Y.; Chen, V.; Fane, A.G. Crossflow Sampler Modified Fouling Index Ultrafiltration (C FS-MFIUF)—An alternative Fouling Index. *J. Membr. Sci.* **2010**, *360*, 174–184. [[CrossRef](#)]
20. Liu, B.; Qu, F.S.; Yu, H.R.; Tian, J.; Chen, W.; Liang, H.; Li, G.B.; Bruggen, B.V.D. Membrane fouling and rejection of organics during algae-laden water treatment using ultrafiltration: A comparison between in-situ oxidation with Fe(II)/persulfate and ozone. *Environ. Sci. Technol.* **2018**, *52*, 765–774. [[CrossRef](#)]
21. Xu, C.H.; Gao, B.Y.; Cheng, D.D.; Yue, Q.Y. Evaluation of dynamic membrane formation and filtration models at constant pressure in a combined coagulation/dynamic membrane process in treating polluted river water. *Water Sci. Technol. Water Supply* **2013**, *13*, 286–293. [[CrossRef](#)]
22. Sun, J.; Hu, C.; Tong, T.; Zhao, K.; Qu, J.; Liu, H.; Elimelech, M. Performance and Mechanisms of Ultrafiltration Membrane Fouling Mitigation by Coupling Coagulation and Applied Electric Field in a Novel Electrocoagulation Membrane Reactor. *Environ. Sci. Technol.* **2017**, *51*, 8544–8551. [[CrossRef](#)]
23. Teng, J.; Chen, Y.; Ma, G.; Hong, H.; Sun, T.; Liao, B.Q.; Lin, H. Membrane fouling by alginate in polyaluminum chloride (PACl) coagulation/microfiltration process: Molecular insights. *Sep. Purif. Technol.* **2020**, 236. [[CrossRef](#)]

24. Park, W.; Jeong, S.H.; Im, S.J.; Jang, A. High turbidity water treatment by ceramic microfiltration membrane: Fouling identification and process optimization. *Environ. Technol. Innov.* **2020**, *17*, 1–10. [[CrossRef](#)]
25. Jang, H.; Charfi, A.; Lee, J.; Park, B.; Jang, J.; Kim, H.; Kim, J. Combined effect of periodic backwashing and forward flushing on fouling mitigation in a pressurized UF membrane process for high turbid surface water treatment. *Desalin. Water Treat.* **2018**, *101*, 24–30. [[CrossRef](#)]
26. Wei, C.H.; Amy, G. Membrane Fouling Potential of Secondary Effluent Organic Matter (EfOM) from Conventional Activated Sludge Process. *J. Membr. Sep. Technol.* **2012**, *1*, 129–136. [[CrossRef](#)]
27. Corbaton-Baguena, M.J.; Alvarez-Blanco, S.; Vincent-Vela, M.C. Fouling mechanisms of ultrafiltration membranes fouled with whey model solutions. *Desalination* **2015**, *360*, 87–96. [[CrossRef](#)]
28. Li, R.; Gao, B.; Wang, W.; Yue, Q.; Wang, Y. Floc properties and membrane fouling in coagulation/ultrafiltration process for the treatment of Xiaoqing River: The role of polymeric aluminum-polymer dual-coagulants. *Chemosphere* **2020**, 243. [[CrossRef](#)]
29. Xing, J.J.; Liang, H.; Xu, S.Q.; Chuah, C.J.; Luo, X.S.; Wang, T.Y. Organic matter removal and membrane fouling mitigation during algae-rich surface water treatment by powdered activated carbon adsorption pretreatment: Enhanced by UV and UV/chlorine oxidation. *Water Res.* **2019**, *159*, 283–293. [[CrossRef](#)]



© 2020 by the authors. Licensee MDPI, Basel, Switzerland. This article is an open access article distributed under the terms and conditions of the Creative Commons Attribution (CC BY) license (<http://creativecommons.org/licenses/by/4.0/>).

Article

# Fabrication of High-Performance Thin-Film Composite Nanofiltration Membrane by Dynamic Calcium-Carboxyl Intra-Bridging during Post-Treatment

Hongyi Han, Ruobin Dai and Zhiwei Wang \*

State Key Laboratory of Pollution Control and Resource Reuse, Shanghai Institute of Pollution Control and Ecological Security, School of Environmental Science and Engineering, Tongji University, Shanghai 200092, China; hanhy1219@163.com (H.H.); dairuobin@163.com (R.D.)

\* Correspondence: zwwang@tongji.edu.cn; Tel.: +86-21-65975669; Fax: +86-21-65980400

Received: 18 May 2020; Accepted: 26 June 2020; Published: 30 June 2020



**Abstract:** Widespread applications of nanofiltration (NF) and reverse osmosis (RO)-based processes for water purification and desalination call for high-performance thin-film composite (TFC) membranes. In this work, a novel and facile modification method was proposed to fabricate high-performance thin-film composite nanofiltration membrane by introducing  $\text{Ca}^{2+}$  in the heat post-treatment. The introduction of  $\text{Ca}^{2+}$  induced in situ  $\text{Ca}^{2+}$ -carboxyl intra-bridging, leading to the embedment of  $\text{Ca}^{2+}$  in the polyamide (PA) layer. This post modification enhanced the hydrophilicity and surface charge of NF membranes compared to the pristine membrane. More interestingly, the modified membrane had more nodules and exhibited rougher morphology. Such changes brought by the addition of  $\text{Ca}^{2+}$  enabled the significant increase of water permeability (increasing from  $17.9 \text{ L}\cdot\text{m}^{-2}\cdot\text{h}^{-1}\cdot\text{bar}^{-1}$  to  $29.8 \text{ L}\cdot\text{m}^{-2}\cdot\text{h}^{-1}\cdot\text{bar}^{-1}$ ) while maintaining a high selectivity ( $\text{Na}_2\text{SO}_4$  rejection rate of 98.0%). Furthermore, the intra-bridging between calcium and carboxyl imparted the NF membranes with evident antifouling properties, exhibiting milder permeability decline of 4.2% (compared to 16.7% of NF-control) during filtration of sodium alginate solution. The results highlight the potential of using  $\text{Ca}^{2+}$ -carboxyl intra-bridging post-treatment to fabricate high-performance TFC membranes for water purification and desalination.

**Keywords:** post-treatment; nanofiltration; calcium-carboxyl intra-bridging; water purification; desalination

## 1. Introduction

Water resources are distributed unevenly worldwide. As the rapidly increasing population and water consumption in many areas of the world, nearly one third of world's population live under water scarcity. Water purification and desalination can be an effective route to address the water shortage and crisis worldwide [1–4]. Membrane-based processes have attracted much attention due to their high efficiency for wastewater reclamation, desalination, and water purification [5,6]. Nanofiltration (NF) and reverse osmosis (RO)-based processes play a dominant role in water harvesting applications [7–9]. In these applications, thin-film composite (TFC) membranes have experienced the tremendous development for a few decades and each layer of TFC membrane can be independently controlled and optimized to achieve expected selectivity and permeability. The membranes hold the key to the performance and cost-effectiveness of the processes [10,11].

The structure of the commercial TFC polyamide (PA) membrane is typically composed of three layers [12], i.e., the bottom layer (nonwoven fabric) serving as mechanical support, the middle layer usually prepared by polyethersulfone (PES) or polysulfone (PSF) acting as porous substrate for

interfacial polymerization (IP) and the top PA selective layer about 10–200 nm thickness formed via IP process [13]. The IP process refers to a polymerization reaction that occurs at the interface of two different monomers dissolved in two immiscible solutions. The PA layer largely determines the permeability and selectivity, and therefore intensive efforts have been dedicated to regulating the IP process for fabricating a high-performance TFC membrane [14–16].

In a practical fabrication process, an immediate post-treatment was further applied after the IP reaction [17]. It has been reported that the post-treatment process induces further impacts on the structure and performance of TFC PA membranes. In general, the post-treatment can dynamically promote the cross-linking process between monomers, shrink pores of the substrate, increase the growth rate of polymer chains, and stabilize the structure of PA layer [18,19]. For instance, Maria et al. fabricated TFC PA membranes via IP followed by solvent activation, which resulted in the increase of flux [20]. Han et al. used different temperature and time in the post-treatment to improve rejection of NF membranes [21].

Based on the dynamic nature of the post-treatment process, we hypothesize that membrane modification could be incorporated directly into the post-treatment, thus enabling in situ modification for improving the membrane separation performance. There have been some studies relevant to introducing various ions into IP, for example, Hao et al. reported a fouling mitigation approach for forward osmosis (FO) and RO membranes via  $\text{Ca}^{2+}$  added during the IP process [22,23]. However, currently the ions have not been introduced into the post-treatment process.

Inspired by this, we proposed to use the intra-bridging between calcium and carboxyl groups in PA layer for modification of NF membrane during post-treatment, since calcium ion is capable of complexing with carboxyl groups [23]. During the post-treatment process, the intra-bridging might result in the embedment of  $\text{Ca}^{2+}$  into the PA layer, induce the change of physicochemical properties of membranes and thus enhance the separation performance. In this work, surface morphology, chemical composition, and separation properties of the modified membrane were systematically investigated, and the mechanisms in enhancing permeability and antifouling property were elucidated. The dynamic modification method in our work paves a new route to fabricate high-performance TFC membranes for water purification and desalination.

## 2. Materials and Methods

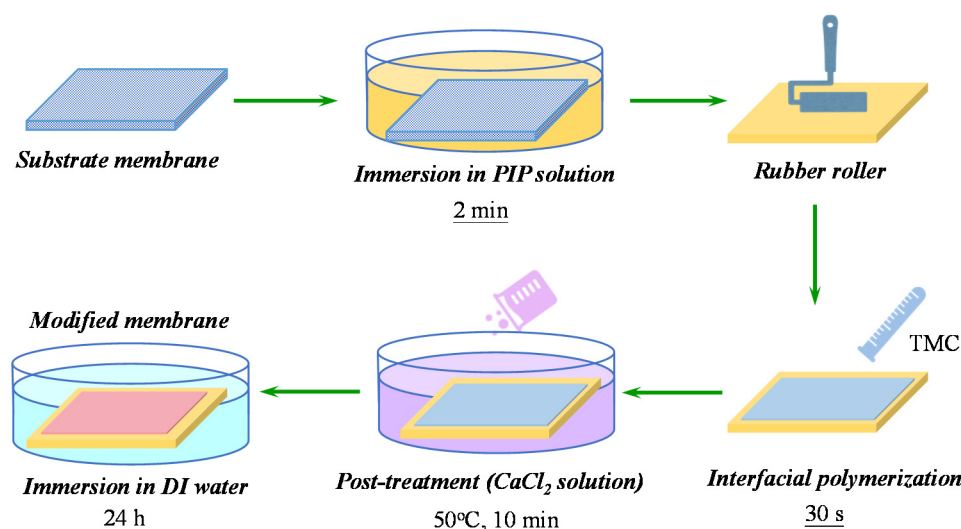
### 2.1. Materials

PES membrane (LX-300K, MWCO = 300 kDa), which was used as the substrate for forming PA layer, was provided by Synder Filtration. Piperazine (PIP, 99%), 1,3,5-benzenetricarbonyl trimesoyl chloride (TMC, 98%), and *n*-hexane used for IP process were purchased from Aladdin (Shanghai, China). Calcium chloride ( $\text{CaCl}_2$ , AR) from Macklin (Shanghai, China) was used in the post-treatment. Sodium sulfate ( $\text{Na}_2\text{SO}_4$ , AR) was used as the salt solute for NF tests. Sodium alginate (SA, AR) was adopted as organic model foulants for antifouling tests.

### 2.2. Membrane Fabrication

The NF membrane was prepared by a typical IP process followed by a dynamic calcium-carboxyl intra-bridging during post-treatment, which is shown in Figure 1. Prior to IP, the porous PES substrate was soaked into deionized water for at least 12 h before use. The PES substrate was removed from deionized water and dried by Kimberly tissue. Afterwards, the substrate was soaked in aqueous solution of PIP (1.0 wt%). After 2 min immersion, the residual PIP solution on the substrate was squeezed by a rubber roller. Then the *n*-hexane solution containing TMC (0.15 wt%) was poured onto the surface of PES substrate. After reaction for 30 s, the TMC/*n*-hexane solution was poured out and excess solution removed upon volatilization. Then the as-formed TFC PA membrane was transferred to 50 °C water bath which contains different concentration of  $\text{CaCl}_2$  (0, 10, 20, 40, and 80 g/100 mL). The membrane was cured in the water bath for 10 min. Finally, the prepared membranes were

thoroughly washed by DI water to remove any residual  $\text{CaCl}_2$  and further stored in DI water at  $4^\circ\text{C}$  before characterization and performance test. The resulting membranes were denoted as NF-control, NF-10, NF-20, NF-40, NF-80, respectively, based on the concentration of  $\text{CaCl}_2$  used in post-treatment.



**Figure 1.** Schematic of the fabrication process of thin-film composite nanofiltration (NF) membrane via dynamic calcium-carboxyl intra-bridging during post-treatment.

### 2.3. Membrane Characterization

The surface morphology of the composite nanofiltration membranes was observed by scanning electron microscope (SEM, Hitachi S-4800, Minato-Ku, Japan) with an acceleration voltage of 5.0 kV and platinum was sputtered on the surface to achieve the minimum conductivity for a valid SEM observation. An atomic force microscope (AFM, Veeco NanoScope MultiMode III, Santa Barbara, CA, USA) was used to detect the surface roughness of the polyamide selective layer in the peak force trapping mode. The surface elemental composition of the NF membrane was detected by X-ray photoelectron spectroscopy (XPS, PHI 5000C ESCA System, Lafayette, LA, USA) with the calibration using  $\text{C}1s = 284.6\text{ eV}$  as a reference [24]. Attenuated total reflectance Fourier transform infrared spectroscopy (ATR-FTIR, Nicolet 6700, Thermo Fisher Scientific Inc., Waltham, MA, USA) was used to analyze the chemical structures of membranes. The water contact angle of NF membranes was determined by a sessile drop method (OCA 15 Plus, Data Physics GmbH, Filderstadt, Germany). Zeta potential of all membranes was detected using a 1 mM KCl solution at  $\text{pH} = 7$  and 10 by a potentiometric analyzer (SurPASS 3, Anton Paar, Ashland, Virginia, USA). The salt concentrations of both the feed solution and permeate solution in NF performance test were determined by a conductivity meter (DDSJ-308F, INESA instrument, Shanghai, China). Membrane fouling was tested using sodium alginate (SA) as model organic foulants to represent polysaccharides. The applied pressure was adjusted to maintain an initial flux of  $228\text{ L}\cdot\text{m}^{-2}\cdot\text{h}^{-1}$  for all fouling experiments.

### 2.4. Nanofiltration Performance Tests

The NF performance of resulting membranes was characterized by measuring the pure water flux and salt rejection. Experiments were carried out in a cross-flow filtration cell with effective area of  $6.3\text{ cm}^2$  [24]. All NF performance tests were performed for three times. The concentration of  $\text{Na}_2\text{SO}_4$  solution, which was used to test the rejection rate, was 10 mmol/L. Each membrane was initially pre-compacted at 10 bar for 4 h, and then the pressure was adjusted to the operating pressure of 8 bar to



determine the NF performance. The water permeability (PWP) and salt rejection ( $R$ ) were determined by Equations (1) and (2), respectively.

$$\text{PWP} = \frac{\Delta V}{A \times t \times P} \quad (1)$$

where  $\Delta V$  (L) is the volume of permeate solution,  $A$  ( $\text{m}^2$ ) is the effective area of the PA NF membrane,  $t$  (h) is the testing time, and  $P$  is the operating pressure (bar).

$$R = \left(1 - \frac{C_p}{C_f}\right) \times 100\% \quad (2)$$

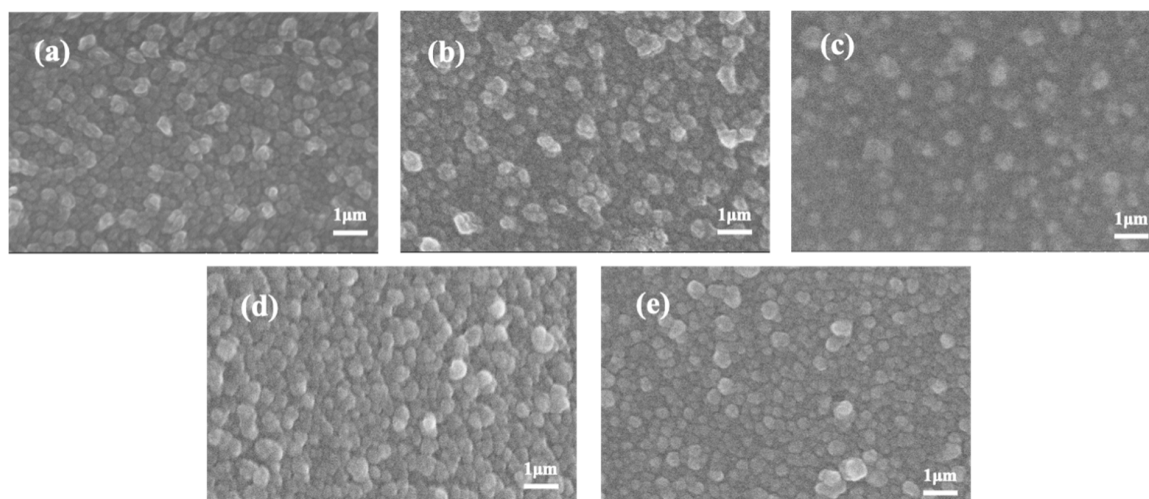
where  $C_f$  (mg/L) and  $C_p$  (mg/L) refer to the  $\text{Na}_2\text{SO}_4$  concentrations of the feed and permeate solutions, respectively.

### 3. Results and Discussion

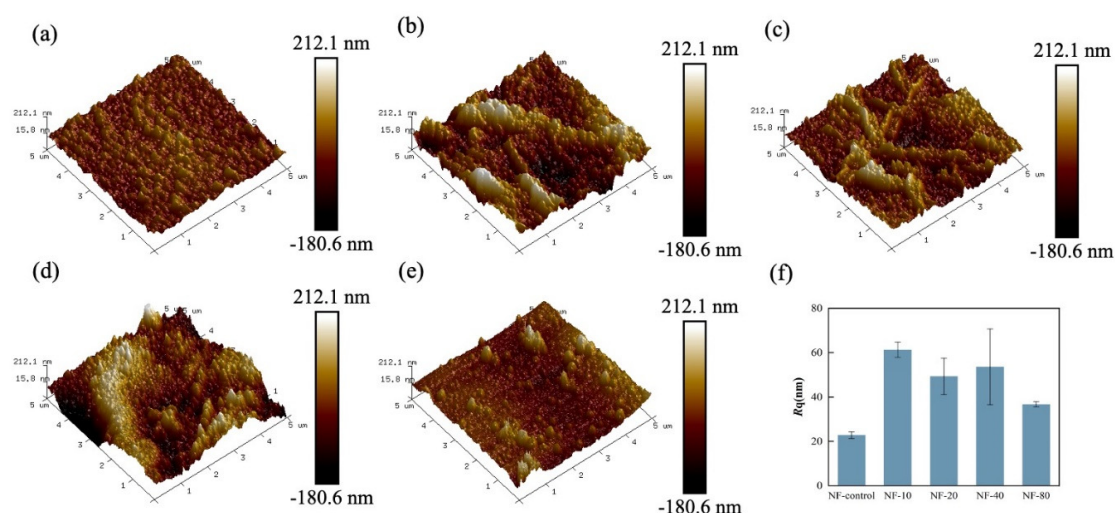
#### 3.1. Membrane Surface Morphology

Various NF membranes were synthesized via an IP process followed by the dynamic thermal post-treatment with addition of  $\text{CaCl}_2$ . The surface morphology and roughness of the resulting membranes were characterized by SEM and AFM, respectively. The surface morphology of NF membranes with different concentrations of  $\text{CaCl}_2$  added in water bath during post-treatment is shown in Figure 2. The images demonstrate that the PA selective layers had a nodular structure, which is the typical structure of PIP based PA layer [25,26]. Compared with the control NF membrane, the surface morphology of membranes upon dynamic post-treatment changed obviously with adding  $\text{Ca}^{2+}$ . It seems that the surface of NF-40 had the most significant nodular-structured morphology. With the increase of  $\text{CaCl}_2$  concentration used for dynamic post-treatment,  $\text{Ca}^{2+}$  in the surface of membrane would saturate as shown in the results of XPS. Therefore, the NF-40 possessed the most significant nodular-structured morphology, while the nodular structure of NF-80 was not obviously changed compared to those of NF-control and NF-10. After IP process of the NF membrane fabrication, there were some residual solutions of PIP/water and TMC/*n*-hexane during post-treatment. A possible intra-bridging [27] between calcium ions and carboxyl groups in PA matrix might account for the change in membrane surface morphologies. Moreover, heat-treatment could induce further cross-linking for membranes and removal of residual organic solvent [19,28]. The above-mentioned reasons explained why the structure of the modified membrane was different from the nascent membrane.

The AFM images revealing the surface morphology and the average surface roughness ( $R_q$ ) are shown in Figure 3. The NF-control membranes had the smoothest surface with  $R_q = 22.8$  nm. In contrast, the roughness of modified membranes sharply increased when calcium ions were added in the water bath. In post-treatment, with the further polycondensation reaction between two monomers, the surface morphology of the PA selective layer became rougher because of the formation of nodular structure promoted by calcium ions [18]. Residual solution continued to react during post-treatment and thus changed the degassing behavior which affected the morphology of the modified membrane [29]. However, the roughness of NF-80 decreased, which is consistent with the results of SEM (Figure 2) due to the decrease of the available calcium (the results of XPS). Furthermore, the complexation of calcium ions with the carboxyl groups of PA layer resulted in an unevenly distributed nodular morphology, contributing to the increase of surface roughness.



**Figure 2.** SEM characterization of thin-film composite NF membranes with different concentrations  $\text{CaCl}_2$  added in the post-treatment: (a) NF-control, (b) NF-10, (c) NF-20, (d) NF-40, (e) NF-80.



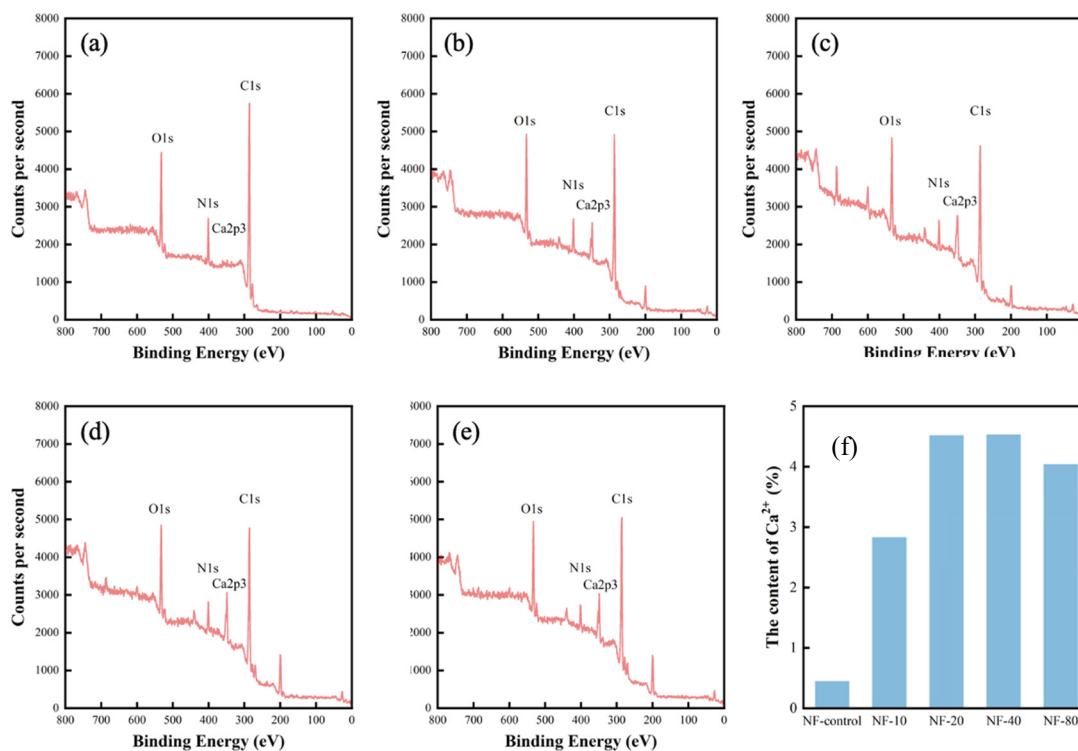
**Figure 3.** AFM micrographs of all resulting membranes: (a) NF-control, (b) NF-10, (c) NF-20, (d) NF-40, (e) NF-80; (f) the roughness of fabricated membranes.

### 3.2. Chemical Composition of Polyamide Layer

The element compositions (including carbon, nitrogen, oxygen, and calcium) of PA selective layer were detected by XPS. As shown in Figure 4, the main element compositions on the membrane surface were C1s, N1s, O1s, and Ca2p3 with peaks centered around 284, 399, 532, and 340 eV. It indicated that Ca content of membranes increased with the increase of  $\text{CaCl}_2$  concentration in the dynamic modification. The intensity of Ca2p3 peak reached the highest value (4.53%) for NF-40 membrane and then decreased slightly as shown in Table 1. This result suggests that the PA layer of resulting membrane had an saturated  $\text{Ca}^{2+}$  embedding due to the certain amount of residual carboxyl groups [30,31].

**Table 1.** Surface element composition of the resulting membranes.

Sample	Element Content (%)			
	C	N	O	Ca
NF-control	76.86	8.51	13.81	0.45
NF-10	71.16	6.79	15.96	2.83
NF-20	67.74	5.16	15.3	4.52
NF-40	67.1	6.35	15.86	4.53
NF-80	69.14	5.53	14.65	4.04



**Figure 4.** XPS spectra of the thin-film composite nanofiltration with different concentrations  $\text{CaCl}_2$  added in the post-treatment: (a) NF-control, (b) NF-10, (c) NF-20, (d) NF-40, (e) NF-80; (f) the element of  $\text{Ca}^{2+}$  for different membranes.

High-resolution oxygen (1s) XPS spectra of NF-control and NF-40 membranes was deconvoluted to further analyze chemical bonding of the PA layer. It showed that there were two peaks at 530.4 eV and 531.3 eV in Figure 5a, suggesting the presence of two types of oxygen in the PA layer of NF-control membrane [31]. The former peak represents carboxylic oxygen groups ( $\text{O}^*-\text{C}=\text{O}$ ) and the latter is ascribed to amide oxygen groups ( $\text{N}-\text{C}=\text{O}^*$ ). Compared with NF-control, another peak appeared at 532.6 eV in Figure 5b, which is associated with calcium species containing coordination bond ( $\text{C}-\text{O}^*-\text{Ca}$ ). The results provided strong evidence that the  $\text{Ca}^{2+}$  had been successfully incorporated into the selective layer. Furthermore, the ratio of  $\text{O}^*-\text{C}=\text{O}$  of NF-40 membrane decreased in comparison to that of NF-control membrane, due to possible competitive effect of  $\text{Ca}^{2+}$  bonding with carboxyl groups. Therefore, it can be inferred that  $\text{Ca}^{2+}$  was chemically bonded in the PA layer [30].

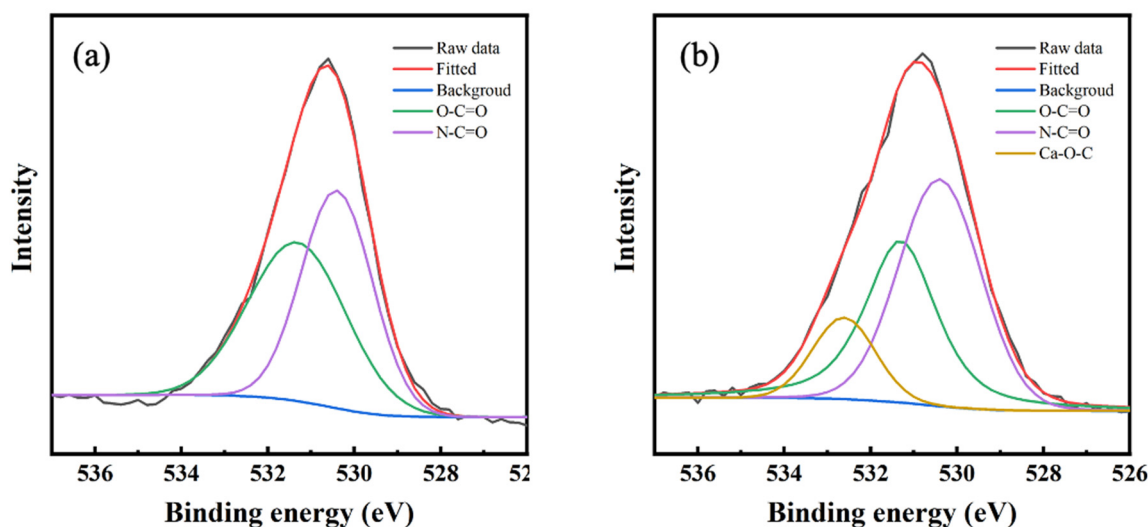


Figure 5. XPS spectra of oxygen 1s in high-resolution spectra: (a) NF-control; (b) NF-40.

In order to further confirm the complexation of  $\text{Ca}^{2+}$  with the carboxyl groups in PA selective layer, the FTIR spectra for resulting membranes were measured (Figure 6). Generally, the band of bending vibration of N-H (amide II peak) is located at  $1576\text{ cm}^{-1}$ , while the characteristic peak at  $1660\text{ cm}^{-1}$  is assigned to the stretching vibration of C=O (amide I peak), indicating the presence of functional groups of PA selective layer [32,33]. The spectra showed that the peak of C=O had a shift from  $1660\text{ cm}^{-1}$  to  $1655\text{ cm}^{-1}$ ,  $1648\text{ cm}^{-1}$ ,  $1645\text{ cm}^{-1}$ , and  $1645\text{ cm}^{-1}$  with the increase of  $\text{Ca}^{2+}$  concentrations, respectively. However, the characteristic peak of N-H had no shift in all groups. It implied that the shift of characteristic peak of C=O should be related to the complexation between  $\text{Ca}^{2+}$  and the carboxyl groups of PA selective layer.  $\text{CaCl}_2$  had a stronger electron-withdrawing effect on C=O than hydrogen bonding of N-H, which led to a shift of C=O band to a lower frequency [34,35]. In combination with the results of XPS, it further demonstrated that when the concentration of  $\text{Ca}^{2+}$  increased to an extent (NF-40 in this study), the complexation between  $\text{Ca}^{2+}$  and carboxyl groups reached saturation and further increase of  $\text{CaCl}_2$  concentration did not lead to the embedding of more  $\text{Ca}^{2+}$  in the PA selective layer.

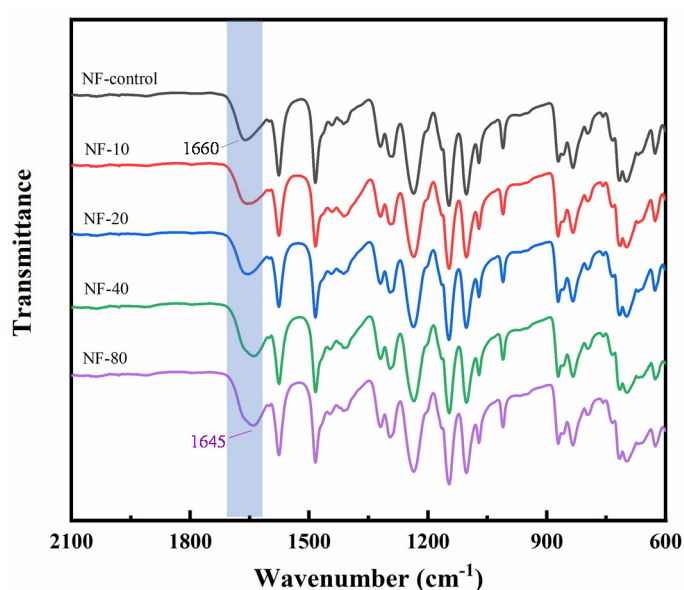
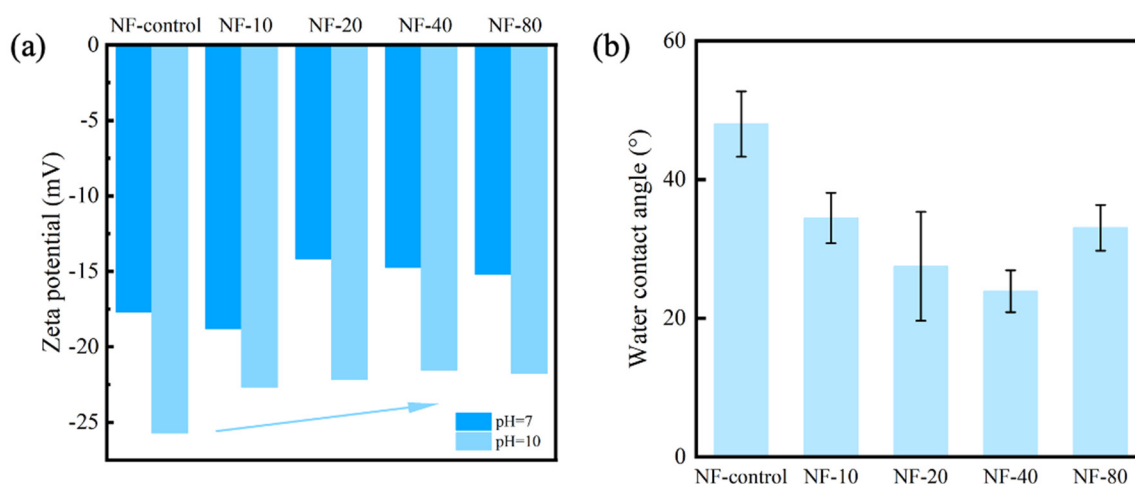


Figure 6. ATR-FTIR spectra of the thin-film composite NF with different concentrations  $\text{CaCl}_2$  added in the post-treatment.

### 3.3. Surface Charge and Hydrophilicity

The surface charge property of NF membrane is an important factor affecting rejection rate of charged solutes. Figure 7a shows the zeta potential of NF-control, NF-10, NF-20, NF-40, and NF-80 at different pH values (pH = 7 and pH = 10). In general, it shows that the PA selective layer was less negatively charged with the increase of concentration of  $\text{CaCl}_2$ . NF-control had the most negative zeta potential about  $-25.7$  mV (pH = 10), which was due to the deprotonated carboxyl group presenting negative charge (i.e., deprotonation of carboxylic acid groups) on the PA layer. NF-40 showed the least negative zeta potential around  $-21.5$  mV (pH = 10), attributed to the partial charge screening effect upon the complexation between  $\text{Ca}^{2+}$  and carboxyl groups. At pH = 7, NF-10 had the most negative zeta potential. Statistical analysis by SPSS showed that there was no significant difference of NF-control and NF-10, which indicated that the results of zeta potential at pH = 7 and 10 were generally consistent.



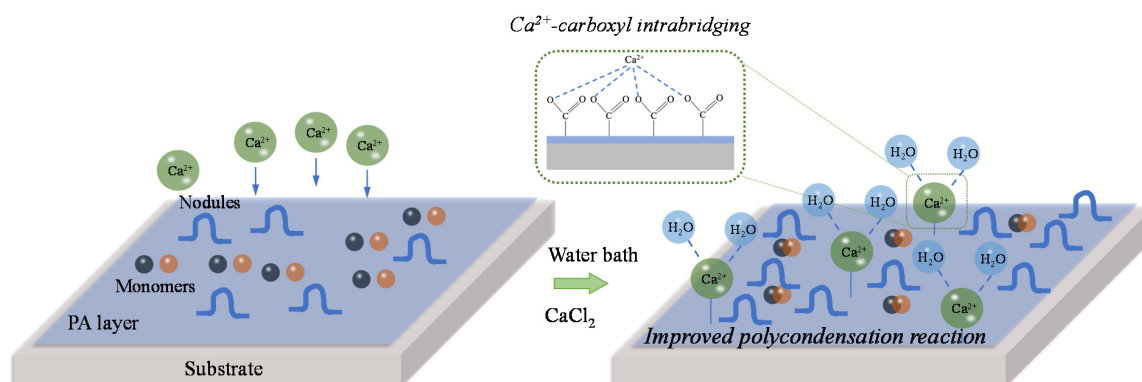
**Figure 7.** (a) Zeta potential of NF-control, NF-10, NF-20, NF-40, and NF-80; (b) Water contact of NF-control, NF-10, NF-20, NF-40, and NF-80.

The hydrophilicity of NF membrane was characterized by water contact angles via a sessile drop method. As shown in Figure 7b, the water contact angles dropped sharply and then increased. A hydrophilic surface can grant the membrane with antifouling performance [36,37]. The NF-control membrane had the largest water contact angle of  $48.0^\circ \pm 4.7^\circ$  and the lowest roughness. For comparison, the water contact angle of NF-40 was the lowest ( $23.9^\circ \pm 3.0^\circ$ ), indicative of the highest hydrophilicity. The dramatic changes in hydrophilicity was ascribed to a significant change of the physicochemical environment with  $\text{Ca}^{2+}$  addition (e.g., changing hydrogen bonding behavior and accommodating hydration water molecules by  $\text{Ca}^{2+}$ ) [23].

### 3.4. Mechanisms of Dynamic Modification Method

The possible mechanisms of dynamic modification are shown in Figure 8. Two main processes occur simultaneously in the post-treatment process based on  $\text{Ca}^{2+}$ -carboxyl intra-bridging involving the formation of  $\text{Ca}^{2+}$ -carboxyl chemical bonds and regulation of cross-linking by the presence of  $\text{Ca}^{2+}$ . In the presence of  $\text{Ca}^{2+}$ , the positively charged  $\text{Ca}^{2+}$  could easily complex with the negatively charged carboxyl groups in the PA matrix due to initial electrostatic interaction and further formation of coordination bonds (in the four-coordination or six-coordination) in the PA layer, which screened the negative surface charge of NF membrane [23]. Moreover, further polycondensation reaction between residual PIP and TMC would occur due to the increase of temperature, which could thermodynamically promote the reaction forward. It facilitated the formation of more nodules on the surface and incorporating of  $\text{Ca}^{2+}$  into PA matrix surrounded (or intra-bridged) by carboxyl groups. The intra-bridging made the surface of NF membrane more hydrophilic.  $\text{Ca}^{2+}$  may also interact with  $\text{H}_2\text{O}$  leading to the hydration of membrane, which can also improve the hydrophilicity. Furthermore,

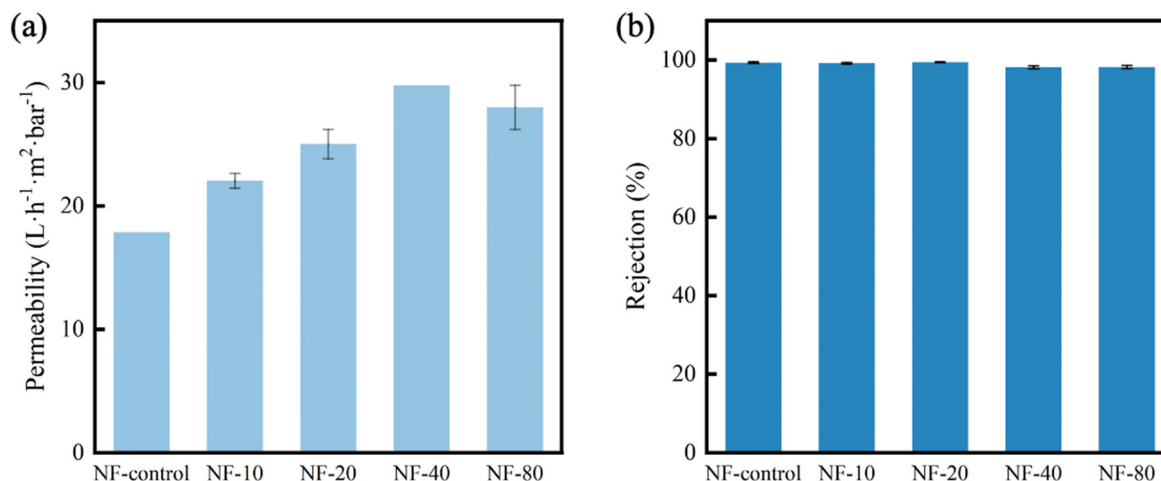
the complexation between  $\text{Ca}^{2+}$  and carboxyl groups avoided the exposure of carboxyl groups on the PA matrix, contributing the mitigation of membrane fouling.



**Figure 8.** Schematic of mechanisms for  $\text{Ca}^{2+}$ -carboxyl intra-bridging and modification during post-treatment.

### 3.5. Separation Performance of the Composite NF Membranes

Separation performance, including water permeability and  $\text{Na}_2\text{SO}_4$  rejection, were measured by crossflow filtration at the pressure of 8 bar, with the results shown in Figure 9. The NF-control membrane had the lowest permeability of  $17.86 \text{ L}\cdot\text{m}^{-2}\cdot\text{h}^{-1}\cdot\text{bar}^{-1}$ . In comparison, the membrane of NF-40 showed the highest permeability of  $29.76 \text{ L}\cdot\text{m}^{-2}\cdot\text{h}^{-1}\cdot\text{bar}^{-1}$ , which increased by 67% compared with that of NF-control membrane. The change in water permeability could be ascribed to the improved hydrophilicity and increased nodular structure of the modified PA selective layer.



**Figure 9.** The separation properties of membranes with different concentrations  $\text{CaCl}_2$  added in the post-treatment: (a) water permeability, (b)  $\text{Na}_2\text{SO}_4$  rejection.

Inorganic salt  $\text{Na}_2\text{SO}_4$  was applied to assess the solute rejection of the membrane. With the increase of water permeability, all the membranes still maintained almost the same salt rejection around 98%. Mechanisms governing the salt rejection of nanofiltration membrane typically include Donnan exclusion and steric hindrance [35]. As abovementioned (Figure 7), the zeta potentials showed that the surface charges of calcium contained membranes were higher than that of NF-control membrane, indicating a possible decreased electrostatic repulsion. Therefore, it can be inferred that intra-bridging between  $\text{CaCl}_2$  and carboxyl groups can narrow the pore size of NF membranes (which was evidenced by denser morphology of  $\text{CaCl}_2$  added membranes) with increased steric hindrance, which thus maintained the salt rejection rates. Note that the water permeability of calcium contained membranes

still increased when the steric hindrance increased, highlighting the positive role of the improved hydrophilicity and nodular structure induced by  $\text{Ca}^{2+}$ -carboxyl intra-bridging.

We further compared the performance of NF-40 with NF membranes in literature with different conditions of post-treatment in terms of water permeability and  $\text{Na}_2\text{SO}_4$  rejection, with the results listed in Table 2. The NF-40 membrane demonstrated better performance compared to those in literature, suggesting that dynamic modification using  $\text{Ca}^{2+}$  had great potential as a feasible post-treatment method to fabricate NF membranes with both high permeability and selectivity.

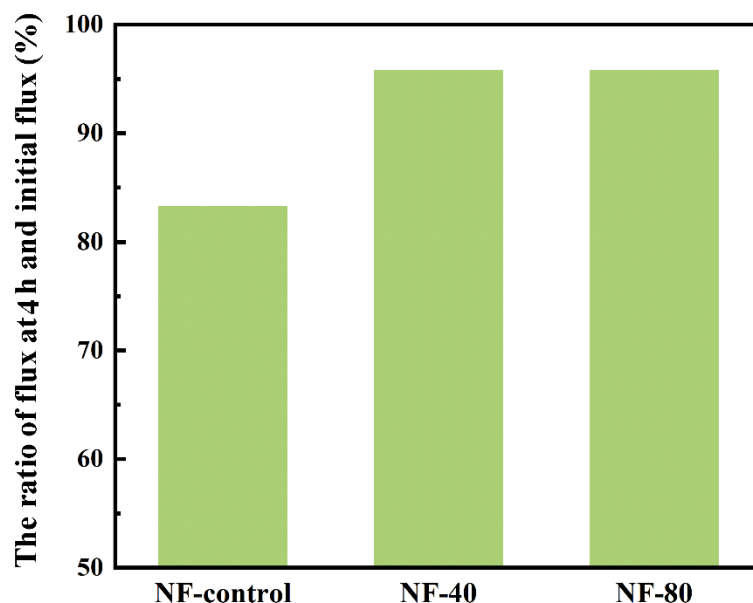
**Table 2.** The performance comparison of NF-40 with other NF membranes with various post-treatment methods.

Membrane	Operating Pressure (bar)	Post-Treatment	Water Permeability ( $\text{L}\cdot\text{m}^{-2}\cdot\text{h}^{-1}\cdot\text{bar}^{-1}$ )	$\text{Na}_2\text{SO}_4$ Rejection (%)	References
TFC-M3	13.8	thermal treatment	13.6	97.7	[17]
PA@A-0	6	heat curing	16.7	97.4	[28]
PA-16	6	organic solution	7.6	94.9	[25]
PEI/TMC	4	ethanol	9.5	56.0	[38]
MWCNT-OH	6	heat-treatment	6.9	97.6	[39]
NFM-5	6	heat-treatment	15.2	97.0	[40]
NF-90	5	alkali solution	15.8	-	[41]
TFNC-2	13	hot pressing	22.3	92.0	[42]
NF-40	8	adding $\text{Ca}^{2+}$	29.76	98.1	This work

### 3.6. Antifouling Performance

Figure 10 shows the changes of membrane flux for the NF-control, NF-40, and NF-80 with feeding solution containing 200 mg/L SA at the same initial flux after 4 h fouling test. The NF-40 and NF-80 membranes exhibited only slight water permeability decline of 4.2%, while the NF-control had a sharp decline of 16.7%. Typically, carboxyl groups on the selective layer provide potential bonding sites for foulants, thus accelerating the membrane fouling [43,44]. The complexation between  $\text{Ca}^{2+}$  and carboxyl groups enables the occupying of sites and effectively suppresses this fouling behavior. Additionally, the high hydrophilicity of the surface also contributes to the antifouling properties of NF-40 membrane [45].

Notably, the previous study showed that presence of  $\text{Ca}^{2+}$  in aqueous solution can accelerate the formation of gel network of foulants (e.g., SA) on membrane surface [46]. However, in this study, the intercalated  $\text{Ca}^{2+}$  performed antifouling performance which is surprisingly different from the role of  $\text{Ca}^{2+}$  in aqueous solution. It was ascribed that the intra-bridging of  $\text{Ca}^{2+}$  resulted in the shield of carboxyl groups and the increase of hydrophilicity, which reduced carboxyl-group-based foulant attachment on membrane surface. The intercalation of  $\text{Ca}^{2+}$  in PA matrix avoids its possible negative effects on membrane fouling (in the form of aqueous  $\text{Ca}^{2+}$ ).



**Figure 10.** The ratio of flux at 4 h and initial flux, containing NF-control, NF-40, and NF-80 membranes after 4 h fouling test using 200 mg/L sodium alginate.

#### 4. Conclusions

A “dynamic” modification based on  $\text{Ca}^{2+}$ -carboxyl intra-bridging method was successfully introduced during post-treatment to improve the membrane performance. The membrane roughness significantly increased when calcium ions were added. XPS and ATR-FTIR characterization demonstrated that  $\text{Ca}^{2+}$  was chemically embedded in the PA layer. Surface hydrophilicity and charge were also changed, due to the strong complexation between  $\text{Ca}^{2+}$  and carboxyl groups and the embedding of  $\text{Ca}^{2+}$  in the PA layer. It is noted that the NF-40 membrane had excellent water permeability compared with NF-control, maintaining a high  $\text{Na}_2\text{SO}_4$  rejection rate. Furthermore, the modified membranes showed antifouling performance. The changes of physicochemical properties are mainly associated with the formation of  $\text{Ca}^{2+}$ -carboxyl chemical bonds and regulation of cross-linking process by the presence of  $\text{Ca}^{2+}$ . This study highlights the importance of  $\text{Ca}^{2+}$ -carboxyl intra-bridging post-treatment during the fabrication, which provides a simple and easy-to-operate way for fabricating high performance of TFC NF membranes.

**Author Contributions:** Conceptualization, H.H. and R.D.; investigation, H.H. and R.D.; resources, H.H.; data curation, H.H.; writing—original draft preparation, H.H. and R.D.; writing—review and editing, Z.W., R.D. and H.H.; visualization, Z.W. and H.H.; supervision, Z.W.; funding acquisition, Z.W. All authors have read and agreed to the published version of the manuscript.

**Funding:** This work was supported by the National Science Foundation of China (grant number 51925806).

**Conflicts of Interest:** The authors declare no conflict of interest.

#### References

1. Pendergast, M.M.; Hoek, E.M. A review of water treatment membrane nanotechnologies. *Energy Environ. Sci.* **2011**, *4*, 1946. [[CrossRef](#)]
2. Kummu, M.; Ward, P.; De Moel, H.; Varis, O. Is physical water scarcity a new phenomenon? Global assessment of water shortage over the last two millennia. *Environ. Res. Lett.* **2010**, *5*, 034006. [[CrossRef](#)]
3. Wang, H.; Asefa, T.; Bracciano, D.; Adams, A.; Wanakule, N. Proactive water shortage mitigation integrating system optimization and input uncertainty. *J. Hydrol.* **2019**, *571*, 711–722. [[CrossRef](#)]
4. Li, X.; Jiang, W.; Duan, D. Spatio-temporal analysis of irrigation water use coefficients in China. *J. Environ. Manag.* **2020**, *262*, 110242. [[CrossRef](#)] [[PubMed](#)]



5. Lind, M.L.; Suk, D.E.; Nguyen, T.-V.; Hoek, E.M.V. Tailoring the Structure of Thin Film Nanocomposite Membranes to Achieve Seawater RO Membrane Performance. *Environ. Sci. Technol.* **2010**, *44*, 8230–8235. [[CrossRef](#)] [[PubMed](#)]
6. Subramanian, S.; Seeram, R. New directions in nanofiltration applications — Are nanofibers the right materials as membranes in desalination? *Desalination* **2013**, *308*, 198–208. [[CrossRef](#)]
7. Fang, W.; Shi, L.; Wang, R. Interfacially polymerized composite nanofiltration hollow fiber membranes for low-pressure water softening. *J. Membr. Sci.* **2013**, *430*, 129–139. [[CrossRef](#)]
8. Jhaveri, J.H.; Murthy, Z. A comprehensive review on anti-fouling nanocomposite membranes for pressure driven membrane separation processes. *Desalination* **2016**, *379*, 137–154. [[CrossRef](#)]
9. Vatanpour, V.; Madaeni, S.; Moradian, R.; Zinadini, S.; Astinchap, B. Fabrication and characterization of novel antifouling nanofiltration membrane prepared from oxidized multiwalled carbon nanotube/polyethersulfone nanocomposite. *J. Membr. Sci.* **2011**, *375*, 284–294. [[CrossRef](#)]
10. Lebrun, R.E.; Xu, Y. Dynamic Characterization of Nanofiltration and Reverse Osmosis Membranes. *Sep. Sci. Technol.* **1999**, *34*, 1629–1641. [[CrossRef](#)]
11. Lau, W.J.; Ismail, A.; Misdan, N.; Kassim, M. A recent progress in thin film composite membrane: A review. *Desalination* **2012**, *287*, 190–199. [[CrossRef](#)]
12. Xia, L.; McCutcheon, J.R. Understanding the influence of solvents on the intrinsic properties and performance of polyamide thin film composite membranes. *Sep. Purif. Technol.* **2020**, *238*, 116398. [[CrossRef](#)]
13. Tan, Z.; Chen, S.; Peng, X.; Zhang, L.; Gao, C. Polyamide membranes with nanoscale Turing structures for water purification. *Science* **2018**, *360*, 518–521. [[CrossRef](#)] [[PubMed](#)]
14. Wu, D.; Huang, Y.; Yu, S.; Lawless, D.; Feng, X. Thin film composite nanofiltration membranes assembled layer-by-layer via interfacial polymerization from polyethylenimine and trimesoyl chloride. *J. Membr. Sci.* **2014**, *472*, 141–153. [[CrossRef](#)]
15. Zhang, Y.; Su, Y.; Peng, J.; Zhao, X.; Liu, J.; Zhao, J.; Jiang, Z. Composite nanofiltration membranes prepared by interfacial polymerization with natural material tannic acid and trimesoyl chloride. *J. Membr. Sci.* **2013**, *429*, 235–242. [[CrossRef](#)]
16. Mansourpanah, Y.; Madaeni, S.; Rahimpour, A. Fabrication and development of interfacial polymerized thin-film composite nanofiltration membrane using different surfactants in organic phase; study of morphology and performance. *J. Membr. Sci.* **2009**, *343*, 219–228. [[CrossRef](#)]
17. Liu, B.; Wang, S.; Zhao, P.; Liang, H.; Zhang, W.; Crittenden, J. High-performance polyamide thin-film composite nanofiltration membrane: Role of thermal treatment. *Appl. Surf. Sci.* **2018**, *435*, 415–423. [[CrossRef](#)]
18. Mansourpanah, Y.; Madaeni, S.; Rahimpour, A.; Farhadian, A. The effect of non-contact heating (microwave irradiation) and contact heating (annealing process) on properties and performance of polyethersulfone nanofiltration membranes. *Appl. Surf. Sci.* **2009**, *255*, 8395–8402. [[CrossRef](#)]
19. Shi, M.; Yan, W.; Dong, C.; Liu, L.; Xie, S.; Gao, C. Solvent activation before heat-treatment for improving reverse osmosis membrane performance. *J. Membr. Sci.* **2020**, *595*, 117565. [[CrossRef](#)]
20. Solomon, M.F.J.; Bhole, Y.; Livingston, A.G. High flux membranes for organic solvent nanofiltration (OSN)—Interfacial polymerization with solvent activation. *J. Membr. Sci.* **2012**, *423*, 371–382. [[CrossRef](#)]
21. Han, R.; Zhang, S.; Hu, L.; Guan, S.; Jian, X. Preparation and characterization of thermally stable poly(piperazine amide)/PPBES composite nanofiltration membrane. *J. Membr. Sci.* **2011**, *370*, 91–96. [[CrossRef](#)]
22. Hao, X.; Gao, S.; Tian, J.; Wang, S.; Zhang, H.; Sun, Y.; Shi, W.; Cui, F. New insights into the organic fouling mechanism of an in situ Ca<sup>2+</sup> modified thin film composite forward osmosis membrane. *RSC Adv.* **2019**, *9*, 38227–38234. [[CrossRef](#)]
23. Hao, X.; Gao, S.; Tian, J.; Sun, Y.; Cui, F.; Tang, C.Y. Calcium-Carboxyl Intrabridging during Interfacial Polymerization: A Novel Strategy to Improve Antifouling Performance of Thin Film Composite Membranes. *Environ. Sci. Technol.* **2019**, *53*, 4371–4379. [[CrossRef](#)] [[PubMed](#)]
24. Dai, R.; Guo, H.; Tang, C.Y.; Chen, M.; Li, J.; Wang, Z. Hydrophilic Selective Nanochannels Created by Metal Organic Frameworks in Nanofiltration Membranes Enhance Rejection of Hydrophobic Endocrine-Disrupting Compounds. *Environ. Sci. Technol.* **2019**, *53*, 13776–13783. [[CrossRef](#)] [[PubMed](#)]

25. An, Q.; Li, F.; Ji, Y.; Chen, H. Influence of polyvinyl alcohol on the surface morphology, separation and anti-fouling performance of the composite polyamide nanofiltration membranes. *J. Membr. Sci.* **2011**, *367*, 158–165. [[CrossRef](#)]
26. Ang, M.B.M.Y.; Ji, Y.-L.; Huang, S.-H.; Tsai, H.-A.; Hung, W.-S.; Hu, C.-C.; Lee, K.-R.; Lai, J.-Y. Incorporation of carboxylic monoamines into thin-film composite polyamide membranes to enhance nanofiltration performance. *J. Membr. Sci.* **2017**, *539*, 52–64. [[CrossRef](#)]
27. Fan, X.; Dong, Y.; Su, Y.; Zhao, X.; Li, Y.; Liu, J.; Jiang, Z. Improved performance of composite nanofiltration membranes by adding calcium chloride in aqueous phase during interfacial polymerization process. *J. Membr. Sci.* **2014**, *452*, 90–96. [[CrossRef](#)]
28. Zhan, Z.-M.; Xu, Z.-L.; Zhu, K.-K.; Tang, Y.-J. How to understand the effects of heat curing conditions on the morphology and performance of polypiperazine-amide NF membrane. *J. Membr. Sci.* **2020**, *597*, 117640. [[CrossRef](#)]
29. Song, X.; Gan, B.; Yang, Z.; Tang, C.Y.; Gao, C. Confined nanobubbles shape the surface roughness structures of thin film composite polyamide desalination membranes. *J. Membr. Sci.* **2019**, *582*, 342–349. [[CrossRef](#)]
30. Dai, R.; Zhang, X.; Liu, M.; Wu, Z.; Wang, Z. Porous metal organic framework CuBDC nanosheet incorporated thin-film nanocomposite membrane for high-performance forward osmosis. *J. Membr. Sci.* **2019**, *573*, 46–54. [[CrossRef](#)]
31. Kwon, Y.-N.; Hong, S.; Choi, H.; Tak, T. Surface modification of a polyamide reverse osmosis membrane for chlorine resistance improvement. *J. Membr. Sci.* **2012**, *415*, 192–198. [[CrossRef](#)]
32. Tang, C.Y.; Kwon, Y.-N.; Leckie, J.O. Effect of membrane chemistry and coating layer on physiochemical properties of thin film composite polyamide RO and NF membranes: I. FTIR and XPS characterization of polyamide and coating layer chemistry. *Desalination* **2009**, *242*, 149–167. [[CrossRef](#)]
33. Zhao, H.; Qiu, S.; Wu, L.; Zhang, L.; Chen, H.; Gao, C. Improving the performance of polyamide reverse osmosis membrane by incorporation of modified multi-walled carbon nanotubes. *J. Membr. Sci.* **2014**, *450*, 249–256. [[CrossRef](#)]
34. Turturro, A.; Russo, S.; Antolinit, E.; Cirafici, S. Physical properties of anionic poly( $\epsilon$ -caprolactam) synthesized in the presence of calcium chloride. *Polymer* **1989**, *30*, 1099–1104. [[CrossRef](#)]
35. Yang, Z.; Yin, H.; Li, X.; Liu, Z.; Jia, Q. Study on dry spinning and structure of low mole ratio complex of calcium chloride-polyamide 6. *J. Appl. Polym. Sci.* **2010**. [[CrossRef](#)]
36. Liu, Y.-L.; Zhao, Y.-Y.; Wang, X.-M.; Wen, X.-H.; Huang, X.; Xie, Y.F. Effect of varying piperazine concentration and post-modification on prepared nanofiltration membranes in selectively rejecting organic micropollutants and salts. *J. Membr. Sci.* **2019**, *582*, 274–283. [[CrossRef](#)]
37. Zuo, X.; Chang, K.; Zhao, J.; Xie, Z.; Tang, H.; Li, B.; Chang, Z. Bubble-template-assisted synthesis of hollow fullerene-like MoS<sub>2</sub> nanocages as a lithium ion battery anode material. *J. Mater. Chem. A* **2016**, *4*, 51–58. [[CrossRef](#)]
38. Chiang, Y.-C.; Hsub, Y.-Z.; Ruaan, R.-C.; Chuang, C.-J.; Tung, K.-L. Nanofiltration membranes synthesized from hyperbranched polyethyleneimine. *J. Membr. Sci.* **2009**, *326*, 19–26. [[CrossRef](#)]
39. Xue, S.; Xu, Z.-L.; Tang, Y.-J.; Ji, C.-H. Polypiperazine-amide Nanofiltration Membrane Modified by Different Functionalized Multiwalled Carbon Nanotubes (MWCNTs). *ACS Appl. Mater. Interfaces* **2016**, *8*, 19135–19144. [[CrossRef](#)] [[PubMed](#)]
40. Zhang, Z.; Kang, G.; Yu, H.; Jin, Y.; Cao, Y. Fabrication of a highly permeable composite nanofiltration membrane via interfacial polymerization by adding a novel acyl chloride monomer with an anhydride group. *J. Membr. Sci.* **2019**, *570–571*, 403–409. [[CrossRef](#)]
41. Jun, B.-M.; Yoon, Y.; Park, C.M. Post-Treatment of Nanofiltration Polyamide Membrane through Alkali-Catalyzed Hydrolysis to Treat Dyes in Model Wastewater. *Water* **2019**, *11*, 1645. [[CrossRef](#)]
42. Kaur, S.; Barhate, R.; Sundarrajan, S.; Matsuura, T.; Ramakrishna, S. Hot pressing of electrospun membrane composite and its influence on separation performance on thin film composite nanofiltration membrane. *Desalination* **2011**, *279*, 201–209. [[CrossRef](#)]
43. Lu, X.; Chavez, L.H.A.; Castrillón, S.R.-V.; Ma, J.; Elimelech, M. Influence of Active Layer and Support Layer Surface Structures on Organic Fouling Propensity of Thin-Film Composite Forward Osmosis Membranes. *Environ. Sci. Technol.* **2015**, *49*, 1436–1444. [[CrossRef](#)] [[PubMed](#)]

44. Lu, X.; Castrillón, S.R.-V.; Shaffer, D.L.; Ma, J.; Elimelech, M. In Situ Surface Chemical Modification of Thin-Film Composite Forward Osmosis Membranes for Enhanced Organic Fouling Resistance. *Environ. Sci. Technol.* **2013**, *47*, 12219–12228. [[CrossRef](#)] [[PubMed](#)]
45. Van Oss, C.; Wu, W.; Docoslis, A.; Giese, R. The interfacial tensions with water and the Lewis acid–base surface tension parameters of polar organic liquids derived from their aqueous solubilities. *Colloids Surf. B Biointerfaces* **2001**, *20*, 87–91. [[CrossRef](#)]
46. SkjLk-Brek, G.; Grasdalen, H.; Smidsrod, O. Inhomogeneous Polysaccharide Ionic Gels. *Carbohydr. Polym.* **1989**, *10*, 31–54. [[CrossRef](#)]



© 2020 by the authors. Licensee MDPI, Basel, Switzerland. This article is an open access article distributed under the terms and conditions of the Creative Commons Attribution (CC BY) license (<http://creativecommons.org/licenses/by/4.0/>).

Article

# Behaviour of Aquaporin Forward Osmosis Flat Sheet Membranes during the Concentration of Calcium-Containing Liquids

Alibek Omir <sup>1,2</sup>, Aliya Satayeva <sup>2</sup>, Aigerim Chinakulova <sup>2,3</sup>, Arailym Kamal <sup>1</sup>, Jong Kim <sup>1</sup> , Vassilis J. Inglezakis <sup>2,4,5</sup>  and Elizabeth Arkhangelsky <sup>1,2,5,\*</sup>

<sup>1</sup> Department of Civil & Environmental Engineering, School of Engineering & Digital Sciences, Nazarbayev University, Nur-Sultan 010000, Kazakhstan; aomir@nu.edu.kz (A.O.); arailym.kamal@nu.edu.kz (A.K.); jong.kim@nu.edu.kz (J.K.)

<sup>2</sup> Environmental Science & Technology Group (ESTg), Nazarbayev University, Nur-Sultan 010000, Kazakhstan; aliya.satayeva@nu.edu.kz (A.S.); aigerim.chinakulova@gmail.com (A.C.); vasileios.inglezakis@nu.edu.kz (V.J.I.)

<sup>3</sup> National Laboratory Astana, Nazarbayev University, Nur-Sultan 010000, Kazakhstan

<sup>4</sup> Department of Chemical & Materials Engineering, School of Engineering & Digital Sciences, Nazarbayev University, Nur-Sultan 010000, Kazakhstan

<sup>5</sup> The Environment & Resource Efficiency Cluster (EREC), Nazarbayev University, Nur-Sultan 010000, Kazakhstan

\* Correspondence: yelyzaveta.arkhangelsky@nu.edu.kz; Tel.: +77-172709118

Received: 18 April 2020; Accepted: 13 May 2020; Published: 22 May 2020



**Abstract:** This study aims to examine the scaling and performance of flat sheet aquaporin FO membranes in the presence of calcium salts. Experiments showed that the application of calcium sulphate ( $\text{CaSO}_4$ ) resulted in an 8–78% decline in the water flux. An increase in the cross-flow velocity from 3 to 12 cm/s reduced the decline in the flux by 16%. The deposition of salt crystals on the membrane surface led to the alteration in the membrane's intrinsic properties. Microscopy, attenuated total reflection-Fourier transform infrared (ATR-FTIR) spectroscopy, and X-Ray fluorescence (XRF) analyses confirmed measurements of the zeta potential and contact angle. The use of a three-salt mixture yielded severe scaling as compared with the application of calcium sulphate dehydrate ( $\text{CaSO}_4 \times 2\text{H}_2\text{O}$ ), i.e., a result of two different crystallisation mechanisms. We found that the amount of sodium chloride (NaCl), saturation index, cross-flow velocity, and flow regime all play an important role in the scaling of aquaporin FO flat sheet membranes.

**Keywords:** aquaporin; forward osmosis (FO); membrane; scaling; calcium

## 1. Introduction

In the last decade, forward osmosis (FO) has attracted significant attention globally. FO is driven by osmotic pressure and, as a result, requires less energy than conventional pressure-driven membrane separation processes. In spite of this advantage, the industrial applications of the FO process are still limited. For example, FO is a component of the desalination process used at the Al Khaluf treatment plant in Oman, which has a capacity of 200 m<sup>3</sup>/day [1]. The plant uses FO to dilute the draw solution before it is desalinated by reverse osmosis. The diluted reverse osmosis feed decreases the desalination energy requirements by more than 20% [2]. Another example of an FO process industrial application is at the Statkraft prototype plant in Norway, which used river and seawater to generate power. Plant operation began in 2009 and terminated in 2014 due to the limited salinity gradient between river and seawater, as well as the membrane permeability [3]. Such a failure has led to the development of a new

type of filtration media, i.e., membranes with embedded aquaporin. Aquaporin is a specialised class of proteins, which facilitates water transport across a membrane in living organisms. The concept of FO with embedded aquaporin was first proposed in 2012 [4]. A limited number of early studies did not report detailed experimental results. For example, Nielsen [5] briefly presented a general strategy for biomimetic membranes. Several research groups have attempted to apply this approach; however, a conceptual demonstration has remained a challenge [6–9].

Although FO membranes are less susceptible to fouling, they still suffer from an accumulation of foulants. As aquaporin FO is a new technology, there are currently a limited number of studies focused on fouling. For example, Hey et al. [10] revealed that the pre-treatment of raw municipal wastewater affects the degree of fouling in biomimetic FO membranes. Li et al. [11] showed that the aquaporin FO membrane maintains a stable flux of approximately 5 L/m<sup>2</sup>-h (LMH) for 16 days, with the application of municipal secondary wastewater effluent. Song et al. [12] performed experiments on an FO-membrane distillation system, reporting that the application of dairy wastewater may impair the permeability of aquaporin FO membranes both gradually and sharply immediately after the application of the feed solution. Concentrations of fumaric acid, with an L-alanine draw solution, yielded a sharp decline in the flux within 4 h [13]. Xue et al. [14] bound TiO<sub>2</sub> nanoparticles to aquaporin FO membranes and detected an antifouling effect for an organic feed solution. Luo et al. [15] applied an aquaporin FO membrane in an osmotic membrane bioreactor, observing a gradual decline in the flux of synthetic wastewater. Singh et al. [16] analysed concentrations of molasses distillery wastewater with a biomimetic membrane, finding that the critical water flux and critical draw solution are below 4 LMH and 3 M (MgCl<sub>2</sub> × 6H<sub>2</sub>O), respectively. When Soler-Cabezas et al. [17] examined anaerobically digested sludge concentrations via aquaporin FO, they detected anomalous behaviours in the membrane after approximately 50 h of filtration before observing a sharp decrease and subsequent plateau in the water flux. Soler-Cabezas et al. [17] attributed such behaviour to the formation of a cake layer on the membrane surface. The aquaporin water channels were apparently blocked by precipitated salts or organic matter, which were later back-transported to the bulk solution with the recovery of the water flux. Kalafatakis et al. [18] applied the membranes to the fermentation of glycerol, detecting an approximately 90% decline in the water flux at a 5 cm/s cross-flow velocity over 15 h. Munshi et al. [19] investigated the dewatering of algae, observing that a NH<sub>4</sub>Cl draw solution is the best candidate for an improved water flux and low reverse salt flux, such that the increase in cross-flow velocity (2–11 cm/s) may enhance the permeate flux by 5–10%. From the works listed in this paragraph, it can be seen that all investigations were concentrating on organic fouling with a focus on the water flux and retention capability of the aquaporin FO membranes. Fouling mitigation or the efficiency of membrane cleaning methods were barely studied. Hence, research dedicated to other types of fouling with an emphasis on an understanding of its mechanisms, the influence of different parameters on the process productivity, the efficiency of the process and the membrane cleaning techniques are of high importance.

Previous studies focused on aquaporin activity have shown that there may be inhibited water transport through aquaporins. Preston et al. [20] and Barone et al. [21] found that mercury causes either a blockage or conformational change in the protein, which leads to inhibited water transport. Niemietz and Tyerman [22] tested aquaporins such as NOD 26, plasma membrane integral protein, and human aquaporin 1, observing that silver and gold, as AgNO<sub>3</sub>, silver sulfadiazine, or HAuCl<sub>4</sub>, can nearly fully inhibit water permeability. Other elements, such as cobalt, copper, cadmium, nickel, zinc, lanthanum, barium, lead, and platinum, may also significantly suppress the permeability of water through the protein channels. Martinez-Ballesta et al. [23] reported aquaporin closure triggered by cytosolic calcium and salt stress as an inhibitory mechanism at aquaporin level, and up-regulation of aquaporins by calcium at the whole plant level.

Calcium is one of the main constituents in sea and wastewater. During treatment, calcium concentrations may reach elevated levels. An exceedingly high solubility level leads to crystal formation and, as a result, membrane scaling, where the crystallisation mechanism can possibly have a drastic effect on membrane performance. For example, Shih et al. [24] reported that both bulk and

surface crystallisation controls the crystallisation of calcium sulphate ( $\text{CaSO}_4$ ) (i.e., a mix of calcium chloride ( $\text{CaCl}_2$ ), magnesium sulphate ( $\text{MgSO}_4$ ), and sodium sulphate ( $\text{Na}_2\text{SO}_4$ )). Lin and Cohen [25], Xie and Gray [26], and Shaffer et al. [27] reported that a surface crystallisation mechanism governs gypsum scaling on a polyamide membrane. However, bulk crystallisation mechanisms have been reported for cellulose acetate membranes [26,28]. Furthermore, previous studies have shown that bulk crystallisation has less of a negative effect on membrane performance than surface crystallisation.

Based on the authors' knowledge, this is the first systematic and controlled study on aquaporin FO membrane scaling. Aspects such as the influence of draw solution concentration on the process productivity, contribution of each salt to the degree of scaling, effect of saturation index, nature of calcium-containing liquid, cross-flow velocity, and direction of pumping were studied for the first time. We examined the effect that the crystallisation mechanism has on the water flux by applying (i) a mixture of sodium chloride ( $\text{NaCl}$ ),  $\text{CaCl}_2$ , and  $\text{Na}_2\text{SO}_4$  and (ii) calcium sulphate dihydrate ( $\text{CaSO}_4 \times 2\text{H}_2\text{O}$ ). Experiments were conducted in an active layer facing feed solution (AL-FS) configuration. The membranes were characterised before and after the scaling experiments.

## 2. Materials and Methods

### 2.1. Membrane and Chemicals

A commercially available aquaporin FO flat sheet membrane was used in this study. The membrane was a thin film composite with embedded protein in the active layer (Aquaporin A/S, Kongens Lyngby, Denmark). The membrane had a thickness of 110 microns, consisting of a polyamide active layer and polyethersulphone support.  $\text{NaCl}$ ,  $\text{CaCl}_2$ ,  $\text{Na}_2\text{SO}_4$ , and  $\text{CaSO}_4 \times 2\text{H}_2\text{O}$  were purchased from Sigma–Aldrich, St. Louis, MO, USA. Milli-Q water (Integral 15, Merck, Darmstadt, Germany) was used for the preparation of all solutions.

### 2.2. FO Experiment

The FO setup used in this study was described earlier and included two variable-speed peristaltic pumps (Cole-Parmer, Vernon Hills, IL, USA), membrane holder (Sterlitech, Kent, WA, USA), electronic balance (OHAUS, Parsippany, NJ, USA), and stirrer plate [29]. The membrane holder was aligned horizontally, the draw solution was placed on the balance, and the feed on the stirrer plate. The pumps were used to circulate the feed and draw side streams through the membrane holder with a channel depth of 2.3 mm and effective filtration area of  $4 \times 8.5 \text{ cm}^2$ . The feed and draw side streams were pumped at identical cross-flow velocities through both sides of the membrane. A spacer was used to support the membrane. The experiments were conducted at ambient temperature.

FO experiments were performed for 6 h.  $\text{NaCl}$  (1–5 M) was used as the draw solution. Tests with a 10 mM  $\text{NaCl}$  feed solution were performed to evaluate FO flux behaviour without the presence of scalants. To prepare the feed solutions with different  $\text{CaSO}_4$  saturation indices (SIs), varying salt concentrations were used. Table 1 lists the detailed compositions of the feed solutions used for the scaling experiments. Unless otherwise specified, the following reference conditions were applied to all scaling experiments: an AL–FS orientation; 12.5 cm/s cross-flow velocity; initial water flux of 13 LMH; and the feed and draw solutions were circulated counter-currently. A digital balance was used to record the water flux at predetermined time intervals. The water flux values were normalized to the initial water flux for the scaling experiments.

**Table 1.** Compositions of the feed solutions used in this study.

SI	Feed Solution (g/L)			
	NaCl	CaCl <sub>2</sub>	Na <sub>2</sub> SO <sub>4</sub>	CaSO <sub>4</sub> × 2H <sub>2</sub> O
<i>Multi-component feed</i>				
1.5	1.188	4.153	3.039	
2	1.493	5.22	3.82	
2.45	1.754	6.32	4.487	
3	2.138	7.475	5.469	
<i>Single-component feed</i>				
1.5				2.756
2				3.47
2.45				4.078

The experiments were replicated to ensure the reproducibility of results. The water flux profiles were plotted by taking the average values obtained from replicate FO experiments.

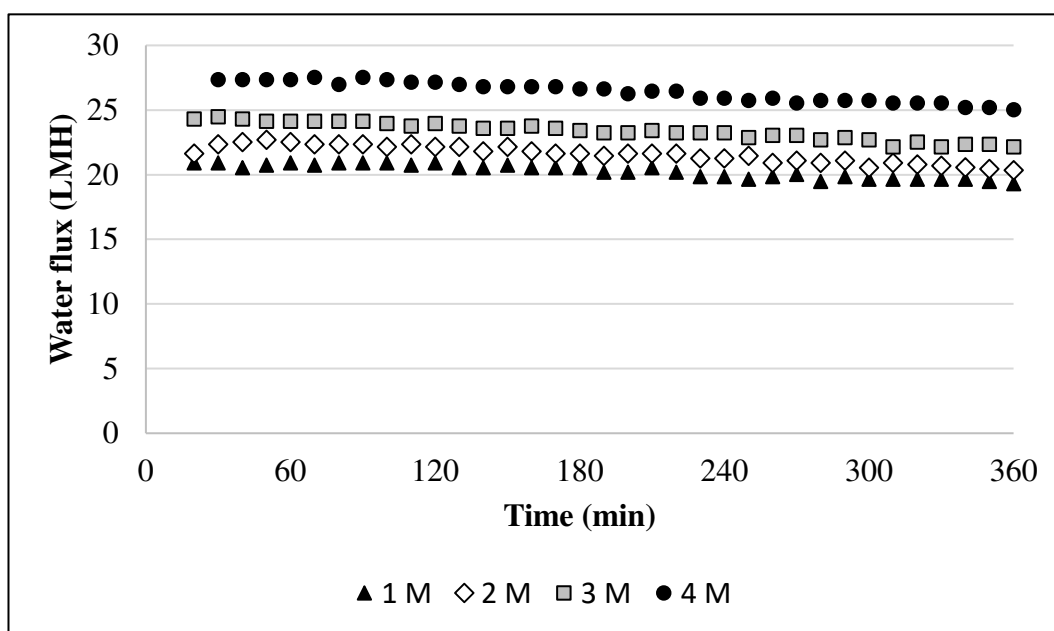
### 2.3. Membrane Characterisation Methods

Both pristine and scaled (SI 2.45) membranes were characterised. A SurPASS electrokinetic analyser (Anton Paar GmbH, Graz, Austria) was used to determine the zeta potential of the membrane. Here, 1, 10, and 100 mM potassium chloride (KCl) solutions were pumped through an adjustable gap sample holder. The streaming potential was detected via Ag/AgCl electrodes located at both ends of the sample. Measurements were performed at pH range of 2–11. The pH of the electrolyte was adjusted using either a 0.1 M KOH or HCl solution. Measurements of the contact angle were performed following the standard protocol: a drop of water was placed onto the membrane surface using a syringe and the air–water–surface contact angle was measured within 10 s [30]. The Leica DM 500 optical microscope (Leica Microsystems, Wetzlar, Germany) and an FESEM Auriga 50 scanning electron microscope (SEM) were used to characterise the membrane's surface morphology. Before SEM imaging, samples were coated with a layer of gold using a Q150T automatic sputter coater. Fourier transform infrared (FTIR) analysis was performed with a Cary 660 FTIR spectrometer (Agilent, Santa Clara, CA, USA), combined with an attenuated total reflectance (ATR) device. The ATR-FTIR analysis was used to study the chemical nature of both pristine and scaled membranes. An Axios mAX X-ray fluorescence (XRF) (Malvern Pananalytical, Malvern, U.K.) was used to determine the elemental composition of the membranes. All measurements were performed a minimum of three times.

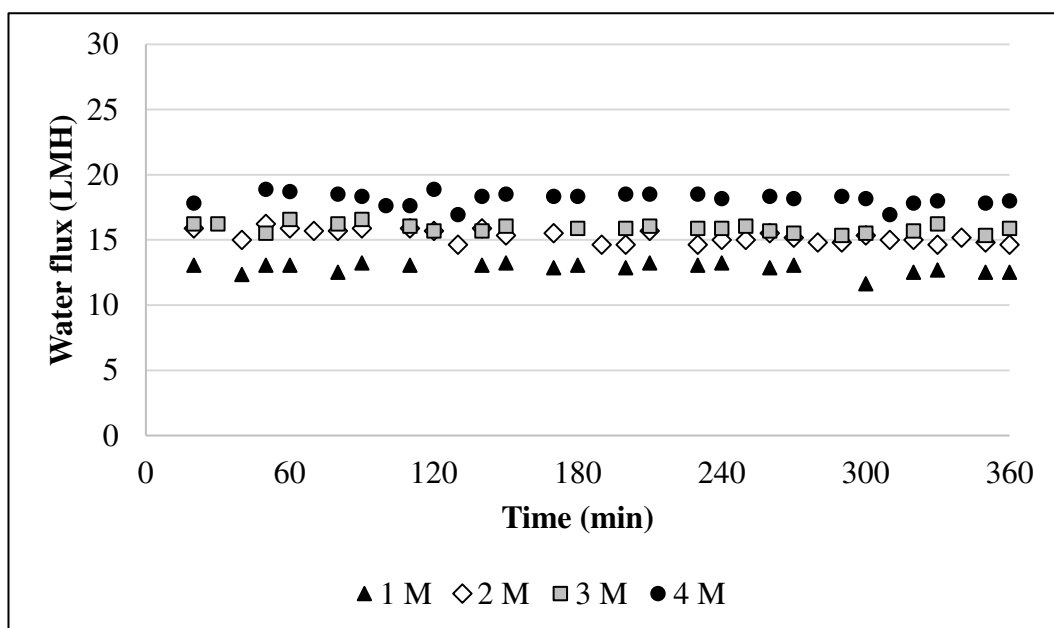
## 3. Results and Discussion

### 3.1. Performance of the Membrane without Scalants

To differentiate concentration-polarisation, dilution of the draw solution, and the scaling effect, the performance of the membrane was first examined without scalants. Figure 1 depicts the water flux as a function of the draw solution concentration in different orientations. The figure shows that, for identical draw solution concentrations, the water fluxes in the AL-FS were lower than those in the active layer facing draw solution (AL-DS) configuration. For example, for a 4 M draw solution, the water flux in the AL-FS was 1.5-fold lower than in the AL-DS (17.82 vs. 27.33 LMH). We did not observe a significantly higher decline in the water flux (Figure 2) for the AL-DS orientation.



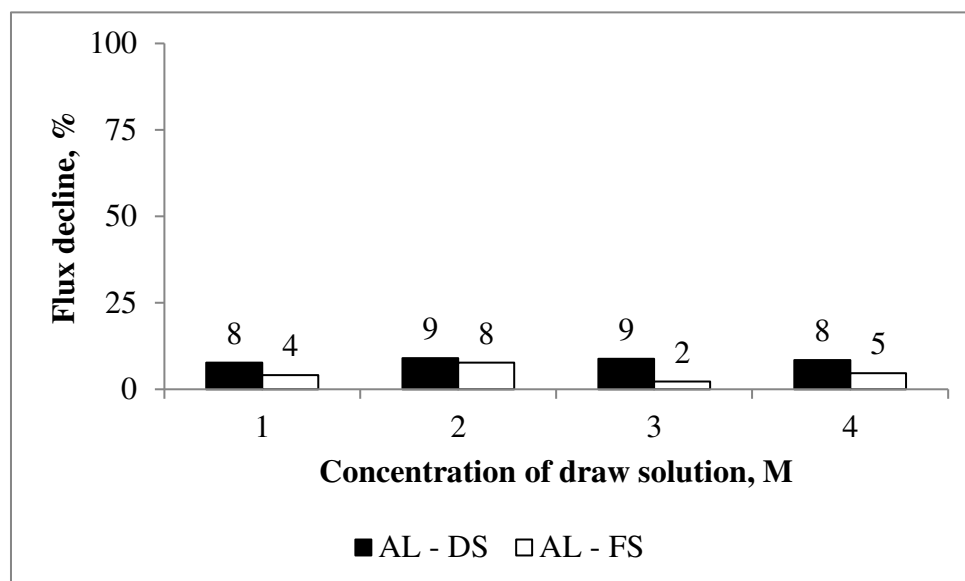
(a)



(b)

**Figure 1.** The water flux of the membrane in the absence of scalants: (a) active layer-facing draw solution (AL-DS) orientation; and (b) AL-feed solution (FS) orientation. Experimental conditions: concentrations of NaCl, CaCl<sub>2</sub>, and Na<sub>2</sub>SO<sub>4</sub> in the feed are 10, 0, and 0 mM, respectively; 12.5 cm/s cross-flow velocity; and the feed and draw solutions were circulated counter-currently.

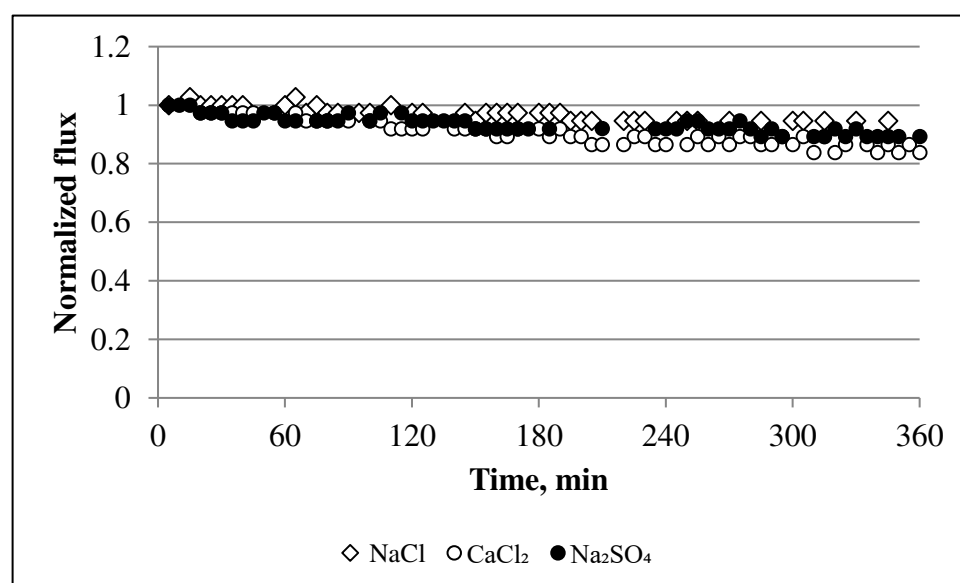




**Figure 2.** The decline in the flux observed for the baseline experiments. Experimental conditions: concentrations of NaCl, CaCl<sub>2</sub>, and Na<sub>2</sub>SO<sub>4</sub> in the feed are 10, 0, and 0 mM, respectively; 12.5 cm/s cross-flow velocity; and the feed and draw solutions were circulated counter-currently.

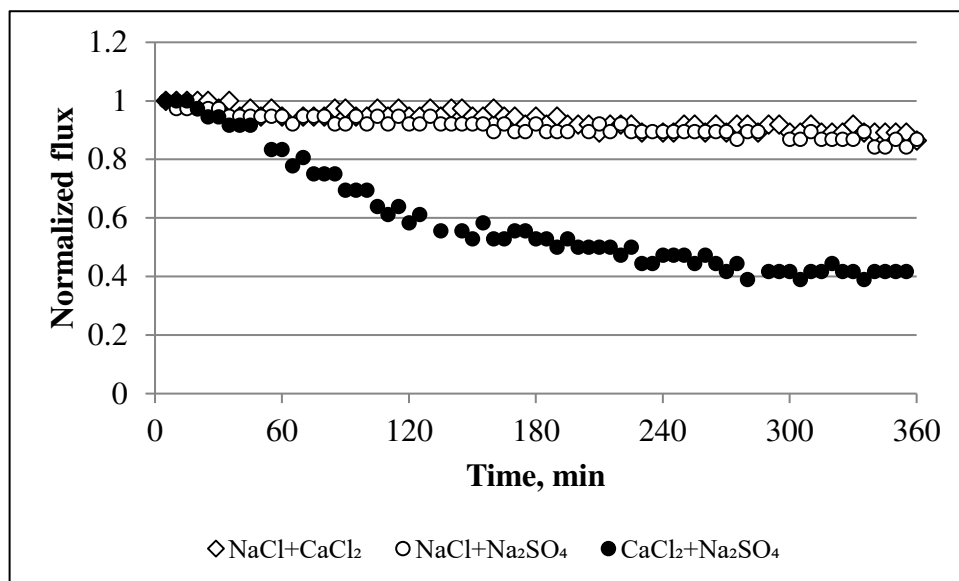
### 3.2. Membrane Behaviour in the Presence of Scaling Solutions

The investigation of scaling in the aquaporin FO flat sheet membranes began based on a study of the water fluxes for the single salts, i.e., NaCl, CaCl<sub>2</sub>, and Na<sub>2</sub>SO<sub>4</sub>. Figures 3a and 4a show the results obtained from these experiments. The application of single salts to the membrane resulted in a minor reduction in the flux. For example, the decline in the flux was 5%, 15%, and 11% for NaCl, CaCl<sub>2</sub>, and Na<sub>2</sub>SO<sub>4</sub>, respectively. When the salts were mixed to form binary solutions, the flux decreased by 13–14% for NaCl+CaCl<sub>2</sub> and NaCl + Na<sub>2</sub>SO<sub>4</sub> and 60% for CaCl<sub>2</sub> + Na<sub>2</sub>SO<sub>4</sub> (Figures 3b and 4a).



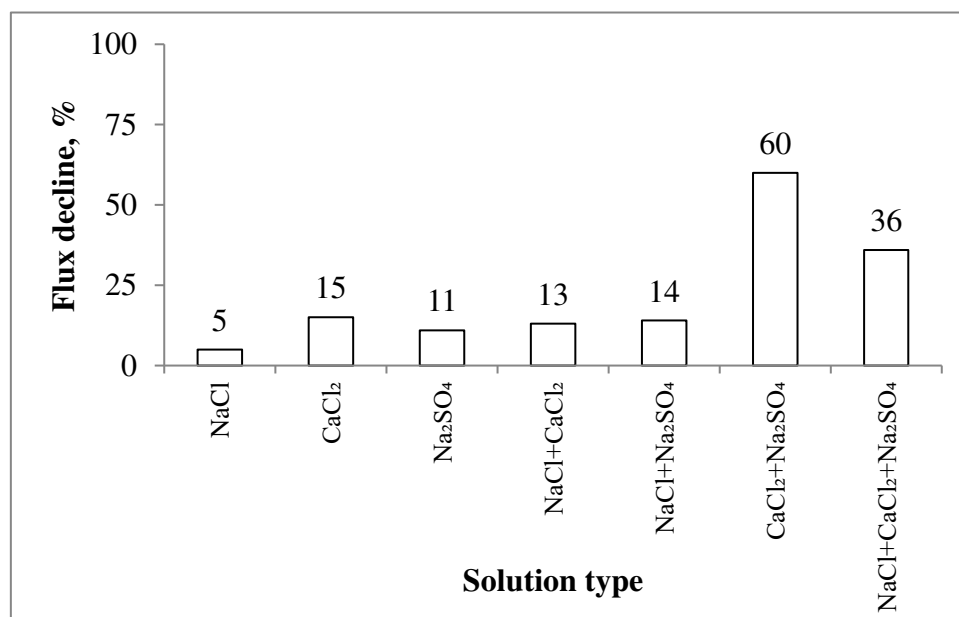
(a)

Figure 3. Cont.



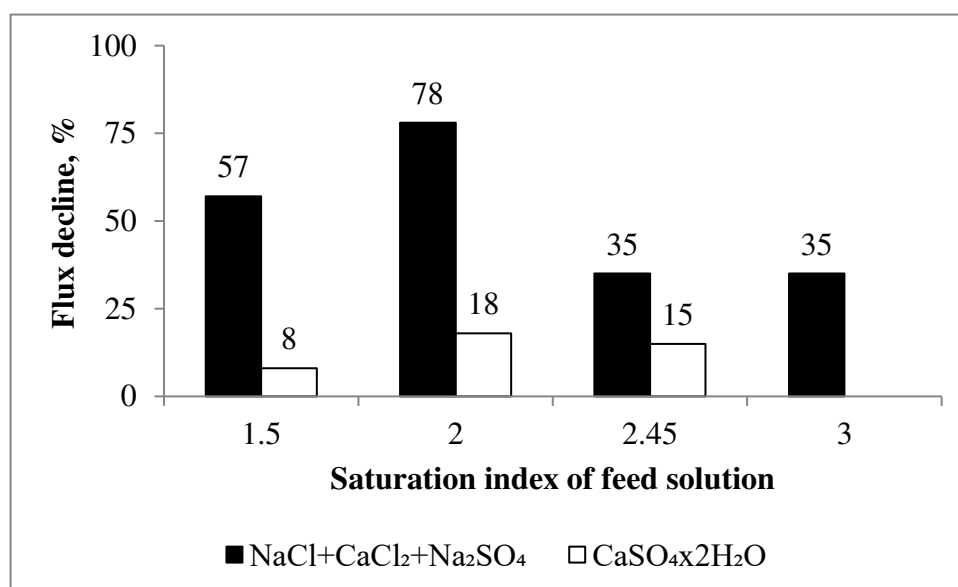
(b)

**Figure 3.** Normalized water flux profiles during the filtration of (a) single salt and (b) mix of two salts. Experimental conditions: concentrations of NaCl, CaCl<sub>2</sub>, and Na<sub>2</sub>SO<sub>4</sub> are 1.754, 6.132, and 4.487 g/L, respectively; 12.5 cm/s cross-flow velocity; the feed and draw solutions were circulated counter-currently; and an AL-FS orientation.



(a)

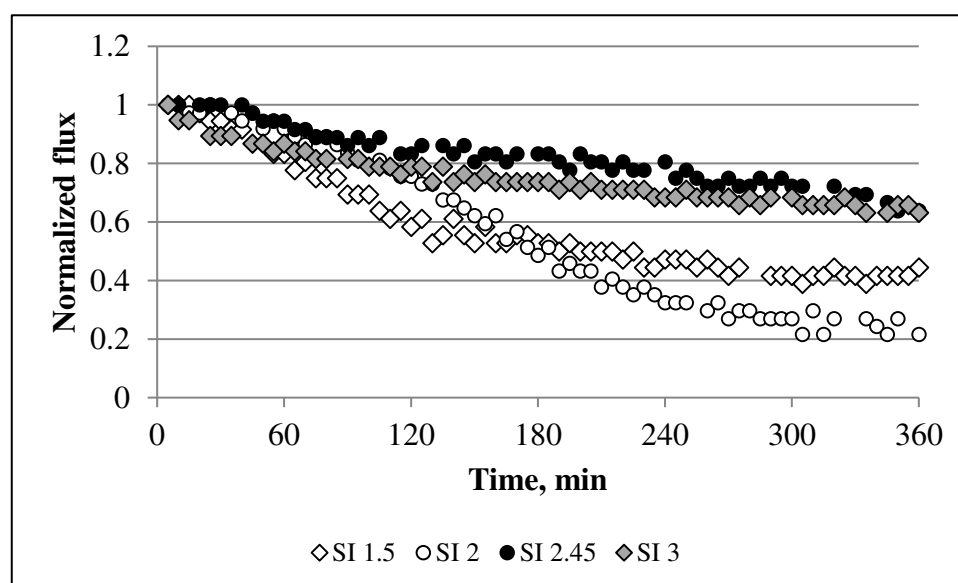
**Figure 4.** Cont.



(b)

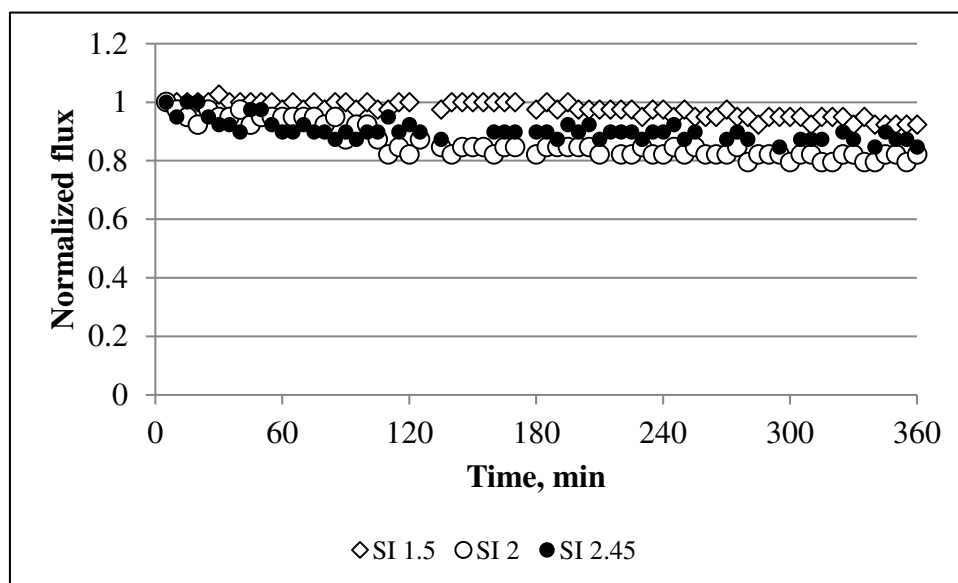
**Figure 4.** The decline in the flux observed for the scaling experiments: (a) single, binary, and ternary feed solutions; and (b) at different saturation indices for NaCl + CaCl<sub>2</sub> + Na<sub>2</sub>SO<sub>4</sub> and CaSO<sub>4</sub> × 2H<sub>2</sub>O. Experimental conditions: 12.5 cm/s cross-flow velocity; the feed and draw solutions were circulated counter-currently; and an AL-FS orientation.

Figures 4 and 5a show the water flux profiles for a mixture of three salts at different saturation indices. The largest decline in the water flux was observed for SIs of 1.5 and 2. The decrease in the water flux for these cases were 57% and 78%, respectively. An increase in SI of up to 2.45 and 3 suppressed the decline in the flux by up to 35%. The experiments performed with NaCl + CaCl<sub>2</sub> + Na<sub>2</sub>SO<sub>4</sub> were also compared with CaSO<sub>4</sub> × 2H<sub>2</sub>O (Figures 4b and 5b). The effect of CaSO<sub>4</sub> × 2H<sub>2</sub>O on membrane performance was less severe than that based on the mix of the three salts. All CaSO<sub>4</sub> × 2H<sub>2</sub>O SIs showed a range from 8–18% for a decline in the water flux.



(a)

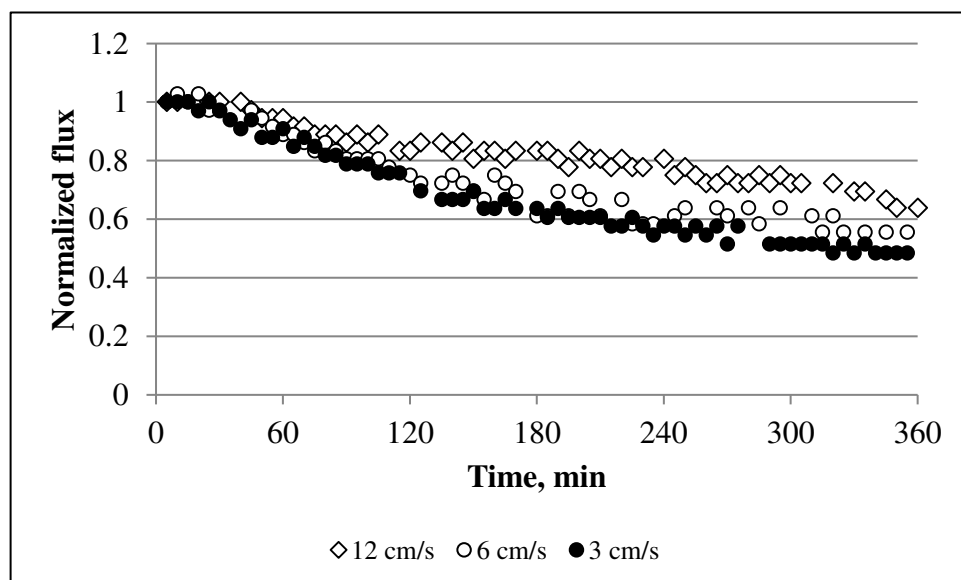
**Figure 5.** Cont.



(b)

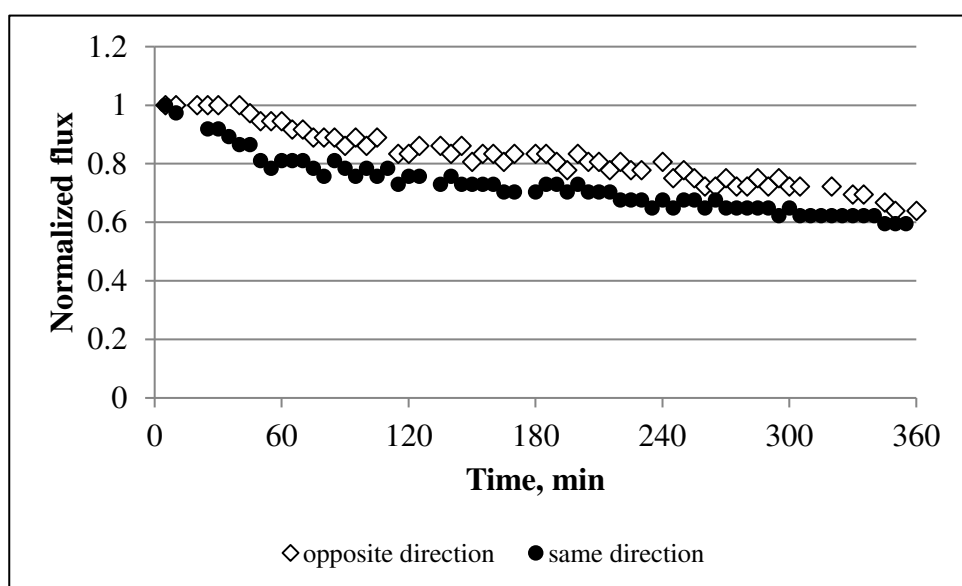
**Figure 5.** Normalized flux for: (a) NaCl + CaCl<sub>2</sub> + Na<sub>2</sub>SO<sub>4</sub>; and (b) CaSO<sub>4</sub> × 2H<sub>2</sub>O at different saturation indices (Table 1 lists the concentrations of the salts). Experimental conditions: 12.5 cm/s cross-flow velocity; the feed and draw solutions were circulated counter-currently; and an AL-FS orientation.

Figures 6a and 7a depict the influence that the cross-flow velocity has on membrane performance. A reduction in the cross-flow velocity from 12.5 to 3 cm/s intensifies the decline in the water flux, i.e., at 12.5, 6, and 3 cm/s the water flux at the end of experiment was equal to 64%, 55%, and 48%, respectively. Figures 7b and 8b show the effect of the feed and draw solution pumping direction. The membrane yielded a slightly higher average water flux in counter-current flow mode.



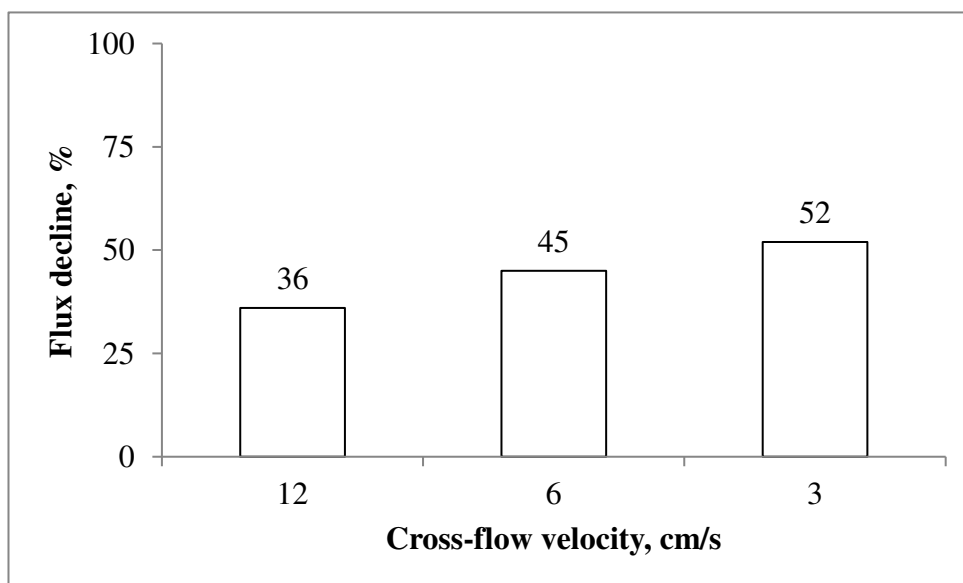
(a)

**Figure 6.** Cont.



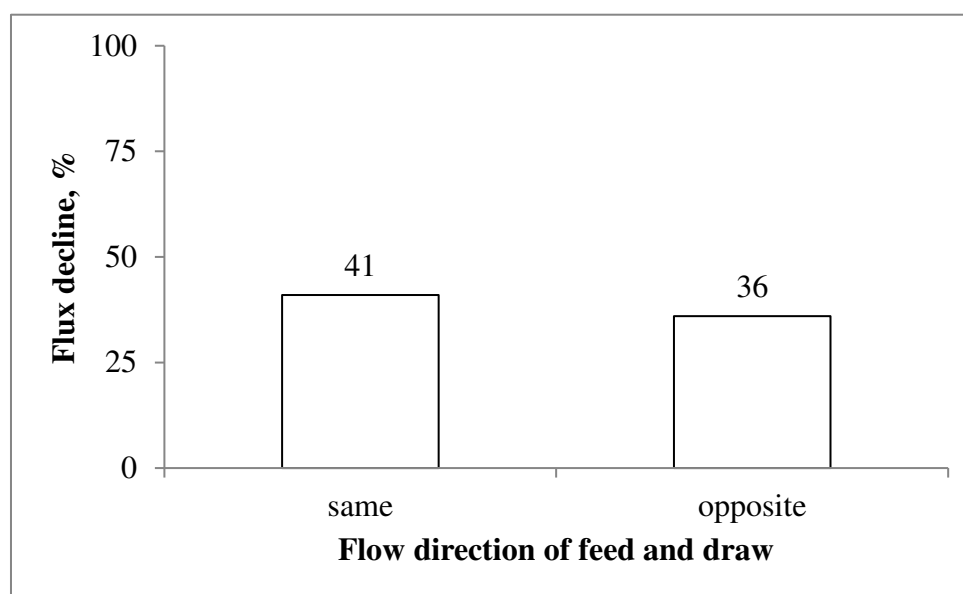
(b)

**Figure 6.** Effect of the: (a) cross-flow velocity; and (b) feed/draw solution pumping direction on the normalized flux. Experimental conditions: concentrations of NaCl, CaCl<sub>2</sub>, and Na<sub>2</sub>SO<sub>4</sub> are 1.754, 6.132, and 4.487 g/L, respectively; SI = 2.45; and an AL-FS orientation.



(a)

**Figure 7.** Cont.

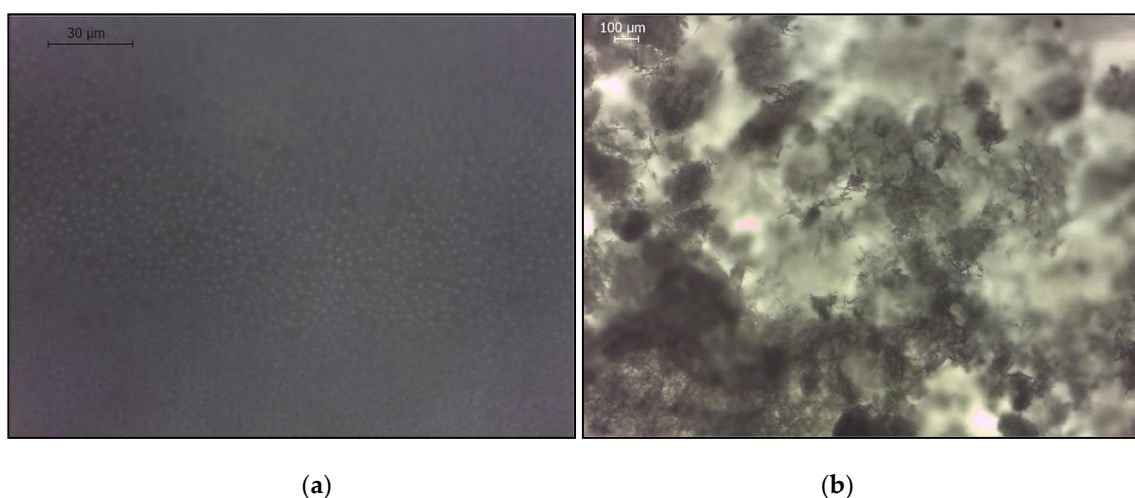


(b)

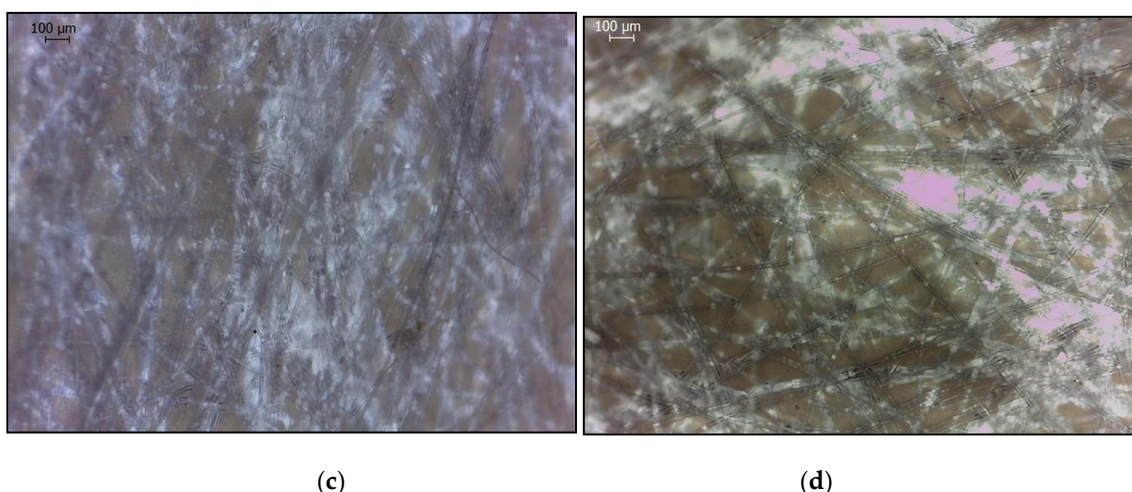
**Figure 7.** The decline in the flux observed for the scaling experiments: (a) effect of the cross-flow velocity; and (b) influence of the flow direction. Experimental conditions: concentrations of NaCl, CaCl<sub>2</sub>, and Na<sub>2</sub>SO<sub>4</sub> are 1.754, 6.132, and 4.487 g/L, respectively; SI = 2.45; and an AL-FS orientation.

### 3.3. Characterisation of the Pristine and Scaled Membranes

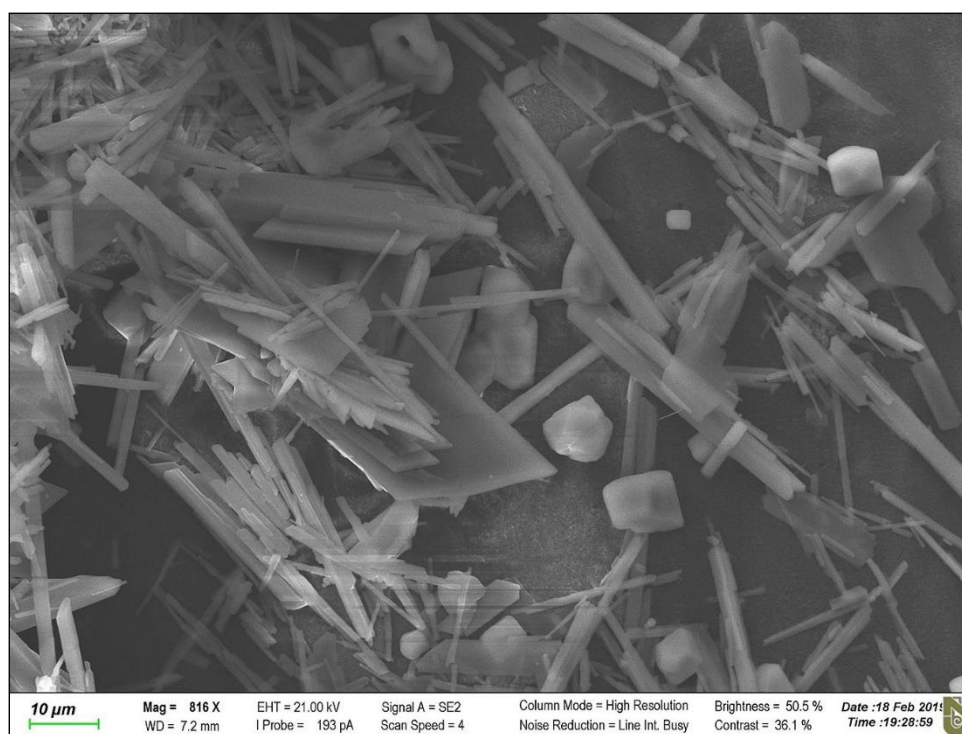
After the application of the SI 2.45 solution (mixture of three salts), the membrane was unevenly covered by crystals (based on a visual analysis). Figure 8 shows the scaled areas of the active layer and support layer after the FO experiment, comparing these areas with the intact membrane (based on an optical microscope analysis). We can observe that, after the FO experiment, the support layer had not changed, whereas certain parts of the active layer were fully covered by CaSO<sub>4</sub> crystals. Figure 9 shows that crystals, formed during the application of NaCl + CaCl<sub>2</sub> + Na<sub>2</sub>SO<sub>4</sub> (SI = 2.45), accumulated on the active layer of the membrane, and the crystal sizes were significantly larger than the membrane pore size [31].



**Figure 8.** Cont.



**Figure 8.** Optical microscope images of the membrane: (a) active layer before scaling; (b) active layer after scaling; (c) support layer before scaling; and (d) support layer after scaling. Scaling conditions: concentrations of NaCl, CaCl<sub>2</sub>, and Na<sub>2</sub>SO<sub>4</sub> are 1.754, 6.132, and 4.487 g/L, respectively; SI = 2.45; 12.5 cm/s cross-flow velocity; the feed and draw solutions were circulated counter-currently; and an AL-FS orientation.

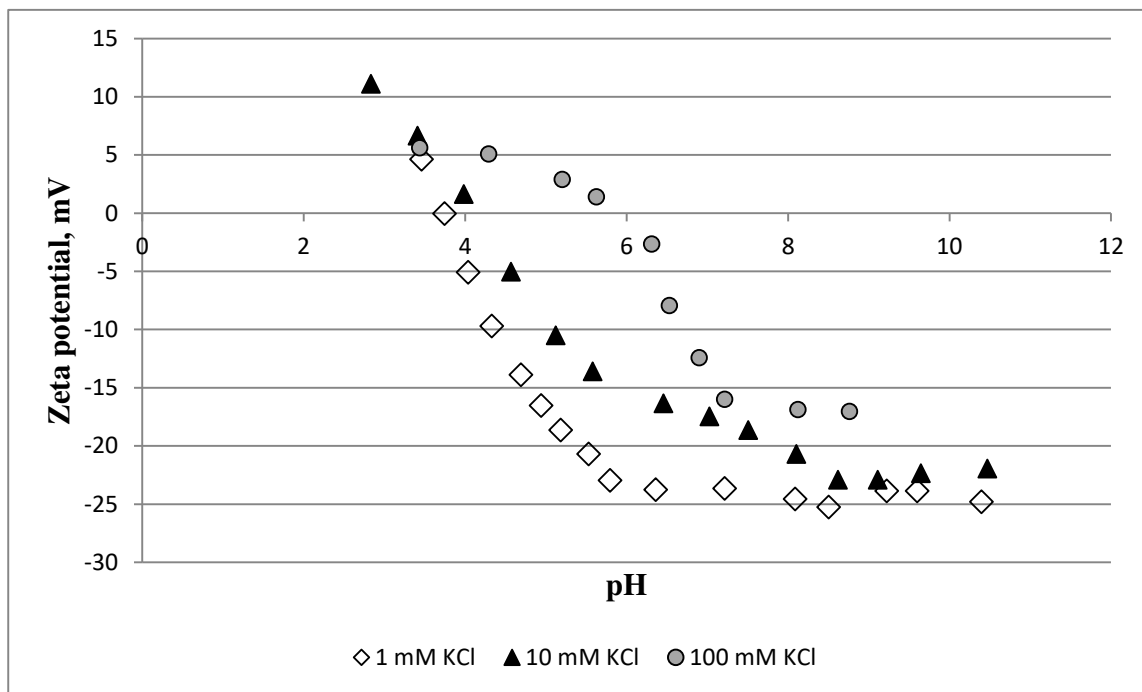


**Figure 9.** SEM image of the aquaporin FO membrane's active layer after the scaling experiment. Scaling conditions: concentrations of NaCl, CaCl<sub>2</sub>, and Na<sub>2</sub>SO<sub>4</sub> are 1.754, 6.132, and 4.487 g/L, respectively; SI = 2.45; 12.5 cm/s cross-flow velocity; the feed and draw solutions were circulated counter-currently; and an AL-FS orientation.

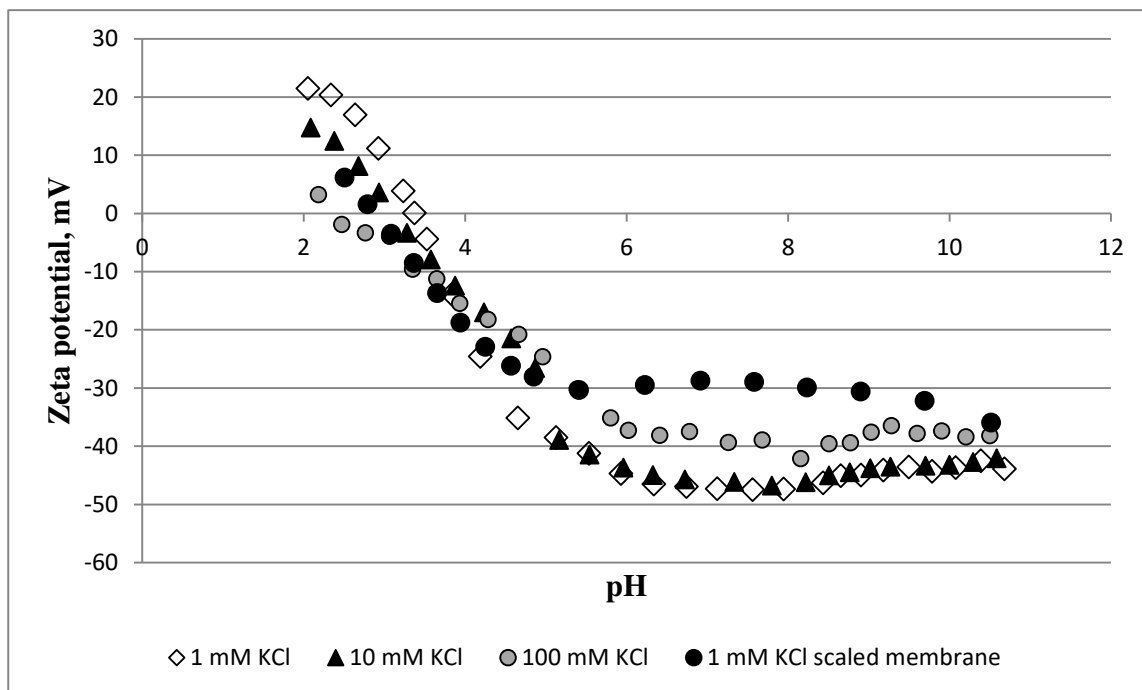
The hydrophobicity of the membrane was evaluated using the contact angle method. The contact angles of the active and support layers for the pristine membrane were 53° and 61°, respectively. These values suggest that both layers are hydrophilic, while the support layer is less hydrophilic than the active layer. When the membrane was exposed to the feed (three salts with SI = 2.45), there was a reduction in these values. The contact angle of the active layer was 41°, while the contact angle of the

support layer was 53°. These results indicate that the accumulation of substances on the membrane's surface leads to increased membrane hydrophilicity.

Figure 10 shows the zeta potential of the membrane for a pH range from 2–11.



(a)



(b)

**Figure 10.** The zeta potential of the membrane: (a) support layer; and (b) active layer at 1, 10, 100, and 1 mM KCl scaled membrane. Scaling conditions: concentrations of NaCl, CaCl<sub>2</sub>, and Na<sub>2</sub>SO<sub>4</sub> are 1.754, 6.132, and 4.487 g/L, respectively; SI = 2.45; 12.5 cm/s cross-flow velocity; the feed and draw solutions were circulated counter-currently; and an AL-FS orientation.



Comparing the intact active and support layers, we can observe that the former is characterised by more negative values. For example, from a pH of 4 to 11, the zeta potential of the active and support layers was equal to  $-24.6$  to  $-42.1$  mV and  $-5.1$  to  $-24.8$  mV (in a 1 mM KCl solution), respectively. The polyamide isoelectric point was detected at approximately a pH of 3 while polyethersulphone was detected between a pH of 4 and 6. The zeta potential of both the support and active layers is more positive at higher concentrations of KCl and lower pH values. The exposure of the membrane to the scaling solution ( $\text{NaCl} + \text{CaCl}_2 + \text{Na}_2\text{SO}_4$ ,  $\text{SI} = 2.45$ ) altered the membrane's charge, i.e., the active layer became more positive. In a 1 mM KCl solution, the scaled membrane showed a 2.5 to  $-35.9$  mV range in the zeta potential.

Table 2 lists the elemental compositions of the membrane from XRF analyses.

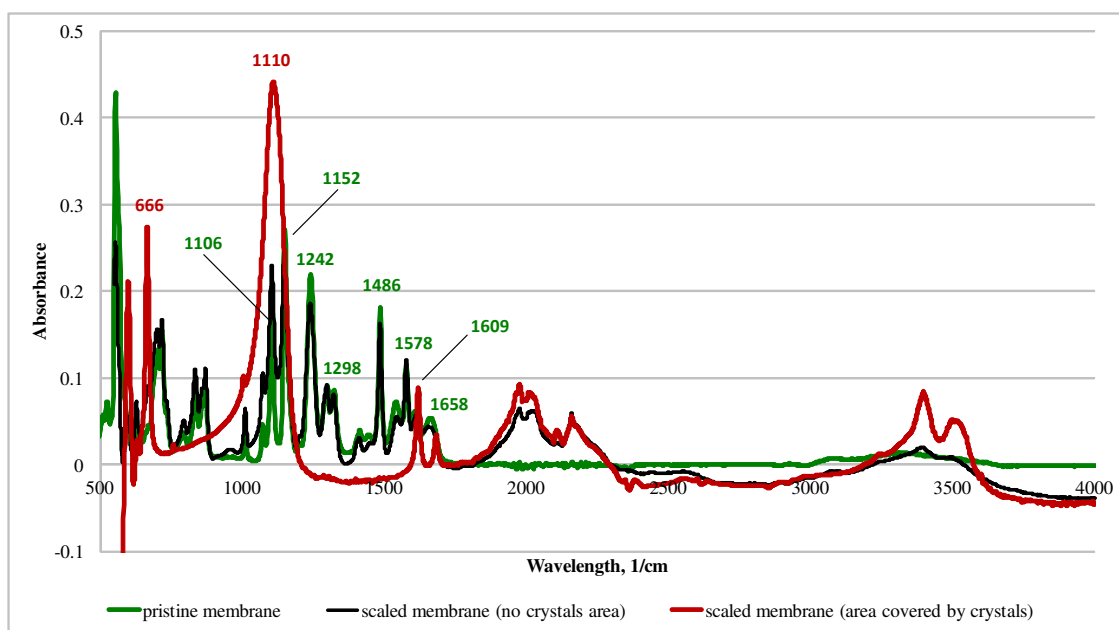
**Table 2.** XRF analyses of the intact and scaled aquaporin forward osmosis (FO) flat sheet membrane.

<i>Element</i>	<b>Concentrations (wt. %)</b>	
	<i>Intact</i>	<i>Scaled</i>
S	87.47	29.58
Cl	4.27	6.56
Ti	3.57	0.43
Ca	2.97	63.59
K	0.46	—
Fe	0.42	0.17
Si	0.15	—
Mg	0.13	0.09
Ni	0.10	0.05
Cu	0.07	—
Zn	0.03	—

Since the concentration of carbon, nitrogen, and oxygen could not be taken into account, Table 2 lists the normalized sum of the detected elements, i.e., 100% (the actual sum of the detected elements is 29%) [32]. Table 2 indicates that sulphur is the main elemental constituent in the virgin membrane (87%). The chlorine, titanium, and calcium contents ranged between 2% and 5%. Other elements, such as potassium, iron, silicon, magnesium, nickel, copper, and zinc, were also detected in the membrane, but their content was insignificant, i.e., less than 1%. XRF analysis of the scaled membrane indicates that the percentage of sulphur reduced to 30% while calcium increased to 64%. The concentration of chlorine increased by 2.3% and the amount of titanium, iron, magnesium, and nickel was less than 1%.

The pristine membrane is characterised by a polyamide characteristic peak at  $1578\text{ cm}^{-1}$  (C–N stretching, amide II),  $1609\text{ cm}^{-1}$  (–N–H), and  $1658\text{ cm}^{-1}$  (C=O stretching, amide I) [10]. For the polyethersulphone support, peaks were observed at  $1486\text{ cm}^{-1}$ ,  $1298\text{ cm}^{-1}$  ( $\text{SO}_2$ , asymmetric stretch),  $1242\text{ cm}^{-1}$  (aryl–O–aryl, C–O stretch),  $1152\text{ cm}^{-1}$  ( $\text{SO}_2$ , symmetric stretch), and  $1106\text{ cm}^{-1}$  (skeletal aliphatic C–C/aromatic hydrogen bending/rocking) [18]. Areas of the membrane where the crystals were not visually observed (after scaling) had similar spectra. In contrast, the membrane area that was covered by crystals exhibited different a spectrum, i.e., strong peaks were observed at  $1110\text{ cm}^{-1}$  and  $666\text{ cm}^{-1}$  (see the following section).

Figure 11 shows the ATR-FTIR spectra of the membranes.



**Figure 11.** ATR-FTIR spectra of the membranes. Scaling conditions: concentrations of NaCl, CaCl<sub>2</sub>, and Na<sub>2</sub>SO<sub>4</sub> are 1.754, 6.132, and 4.487 g/L, respectively; SI = 2.45; 12.5 cm/s cross-flow velocity; the feed and draw solutions were circulated counter-currently; and an AL-FS orientation.

### 3.4. Discussion

Fick's law states that the rate of transfer of molecules or atoms via diffusion through a unit area is proportional to the concentration gradient [33]. The baseline experiments show (Figure 1) that there was an initial increase in the water flux, which was not proportional to the concentration of the draw solution. For example, the initial water flux for the AL-DS was 27, 24, 22, and 21 LMH for NaCl concentrations of 4, 3, 2, and 1 M, respectively. In contrast, the AL-FS orientation had water fluxes of 18, 16, 16, and 13 LMH for identical concentrations to the draw solution. This behaviour can be attributed to the internal concentration polarisation (ICP) effect. Higher values of the water flux in the AL-DS orientation were due to a concentrative ICP effect, which is lower than a dilutive ICP effect (as was the case for the AL-FS orientation). Based on the results, we also observe that the flux was more stable in the AL-FS orientation. This is due to the low water flux and severe dilutive ICP effect in the AL-FS orientation. The internal ICP in the AL-DS orientation is a product of accumulation of ions inside of the membrane's support layer at the time of filtration. On the other hand, the internal ICP in the AL-FS configuration is arising from dilution of the draw solution by the permeate inside of the support layer. Both the internal ICP in the AL-DS and the AL-FS lead to a net driving force decrease. The water flux profiles obtained for the baseline experiments are similar to those reported for FO membranes without aquaporin [34].

By comparing the baselines with the scaling experiments, we observe that the reduction in the water flux was mainly caused by scaling, i.e., not due to the dilution of the draw solution. The dilution of the draw solution resulted in only a 2–8% decline in the water flux. Using the results obtained for the single salts (Figure 4a) and applying the additive flux concept, we can calculate the decline in the flux decline for a mix of two or three salts. For example, the calculated decline in the water flux decline for NaCl + CaCl<sub>2</sub> is 20%, 26% for CaCl<sub>2</sub> + Na<sub>2</sub>SO<sub>4</sub>, 16% for NaCl + Na<sub>2</sub>SO<sub>4</sub>, and 31% for three combined salts. The decline in the water flux caused by the NaCl solution was 5%. By comparing this result with the baseline experiments, the decline in the water flux from NaCl was only due to the dilution of the draw solution. Comparing the calculated additive flux values with the experimental data, we can observe that only one solution, i.e., CaCl<sub>2</sub> + Na<sub>2</sub>SO<sub>4</sub>, has a significant difference between the calculated and experimental values. The calculated value was 2.3-fold lower than the value obtained from the

experiments (26% vs. 60%). For the other solutions, this difference was minor, i.e., 13.5 vs. 20 LMH for NaCl + CaCl<sub>2</sub>, 13.5 vs. 16 LMH for NaCl + Na<sub>2</sub>SO<sub>4</sub>, and 35 vs. 31 LMH for the three salts. The NaCl + CaCl<sub>2</sub> + Na<sub>2</sub>SO<sub>4</sub> feed solution had a weaker decline in the flux than CaCl<sub>2</sub> + Na<sub>2</sub>SO<sub>4</sub> (35% vs. 60%). This is because, as NaCl was introduced into the feed, an increase in the ionic strength led to a reduction in the ionic activity of calcium and sulphate, which resulted in incremental solubility and a decrease in the saturation degree, otherwise known as the “salt in” effect [35]. This also explains the severe decline in the flux for SI = 1.5 and 2 as compared with the solutions at an SI of 2.45 and 3 (i.e., a higher concentration of NaCl increased the solubility). However, experiments performed with CaSO<sub>4</sub> × 2H<sub>2</sub>O were characterised by a negligible decline in the flux (for all saturation indices) compared with the NaCl + CaCl<sub>2</sub> + Na<sub>2</sub>SO<sub>4</sub> solution (Figure 4). This is because bulk crystallisation controls the scaling of CaSO<sub>4</sub> × 2H<sub>2</sub>O while surface crystallisation dominates the scaling of CaSO<sub>4</sub>. Surface crystallisation results in more a severe decline in the flux than bulk crystallisation [28].

The experiments performed at different cross-flow velocities show that membrane performance can be improved by an increase in the speed of the draw and feed solution pumping (Figure 6a). This indicates that a higher shear rate tends to mitigate scaling by hindering the deposition of the scalant on the membrane. These findings agree with previous studies [36]. However, a two-fold increase in the cross-flow velocity does not proportionally suppress scaling. For example, an increase in the cross-flow velocity from 3 to 6 cm/s mitigates water flux reductions by 13%, and by 20% for 6 and 12 cm/s. These results should be considered for further process optimisation and energy savings. The flat sheet aquaporin membrane used in this study also showed that the direction of pumping has a negligible effect on the membrane performance (Figure 6b). Improved membrane performance in a counter-current regime may be related to the net driving force, which is lower at the outlet point of the FO module in the co-current configuration [37,38].

A recent study [39] demonstrated that the water flux for an aquaporin FO membrane (Aquaporin A/S, Denmark) decreased from 20 to 15 LMH within 10 h of filtration. By comparing the results reported in Chun et al. [39] with data presented here, we can observe that similar SIs (i.e., 1.5 vs. 1.3) showed a 60 (current study) and 25% Chun et al. (Chun et al., 2018) decline in the water flux. Similar to this study, Chun et al. [39] performed FO experiments in the AL-FS orientation and counter-current mode, where NaCl was used as a draw solution for the scaling experiments. In contrast, the initial water flux and cross-flow velocity were 20 LMH and 9.5 cm/s (Chun et al., 2018), respectively. Such differences in experimental results can be explained by non-consistent characteristics of the membrane across batch production. This assumption may be supported by the current unavailability of aquaporin FO flat sheet membranes from Aquaporin A/S (Denmark).

The zeta potential, contact angle, microscopy, ATR-FTIR, and XRF analyses confirmed that the membrane was scaled during the FO experiments. The zeta potential measurements showed that the membrane charge increases with an increase in the KCl concentration. Elevated KCl concentrations led to a shrinking of the electric double layer, yielding a reduced zeta potential value. Changes in the membrane charge with the pH are due to the ionisation of carboxyl groups in the polyamide active layer (Figure 12), and a result of anion (Cl<sup>-</sup>) adsorption from the electrolyte to a polyethersulphone support [40].

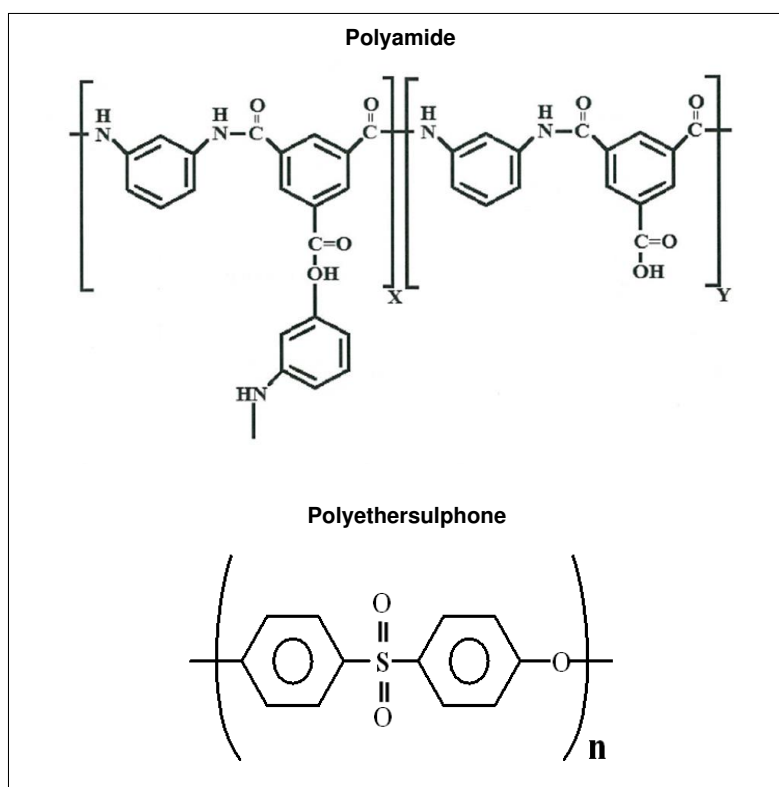


Figure 12. Chemical structure of the polymers.

The scaling layer on the membrane surface affected the charge of the active layer. For example, at a neutral pH, the membrane zeta potential increased from  $-47$  to  $-29$  mV. This is a result of the deposition of positively charged crystals [41]. Salt deposition on the membrane also elevated the hydrophilicity of both the active and support layers. This can be attributed to the presence of salt crystals that are hydrophilic in nature [42]. Here, 87% of the sulphur detected by XRF is from sulphur in the polyethersulphone support layer (Figure 12). When the scaling solution was applied to the membrane, calcium became a dominant element. Strong peaks observed at  $1110$  and  $666\text{ cm}^{-1}$  are the characteristic peaks in the sulphate [43,44].

#### 4. Conclusions

This study aimed to investigate the effect of calcium-containing salts on water transport through aquaporin channels and scaling in the aquaporin FO flat sheet membranes. The application of the scaling solutions resulted in the alteration in the membrane's intrinsic properties. Similar to other FO membranes, the membranes with embedded aquaporin are susceptible to concentration polarisation. The membrane's exposure to the feed solution containing only calcium ions ( $\text{CaCl}_2$  feed solution) resulted in a 15% decline in the water flux while a mix of the three salts led to a 35% reduction in the flux. This indicates that the decrease in the water flux occurred due to the membrane scaling, i.e., not the inhibition of the aquaporin channels. The highest degree of scaling was associated with the  $\text{SI} = 2$  feed solution, which is a result of the "salt out" effect. Our results suggest that bulk crystallisation mechanisms are more favourable for the aquaporin membranes. The process performance can be enhanced by the optimisation of both the feed- and process-related parameters, i.e., the pre-treatment of the feed solution, as well as the adjustment of the cross-flow velocity and flow regime.

**Author Contributions:** Conceptualization, E.A.; data curation, A.O., A.S., A.C. and A.K.; formal analysis, E.A.; funding acquisition, E.A.; investigation, A.O., A.S., A.C. and A.K.; methodology, E.A. and A.S.; project administration, E.A.; resources, E.A., V.J.I. and J.K.; supervision, E.A.; validation, E.A.; visualization, E.A.; writing,

E.A.; writing—review and editing, E.A., V.J.I. and J.K. All authors have read and agreed to the published version of the manuscript.

**Funding:** This study was supported by Nazarbayev University, grant number 110119FD4533.

**Acknowledgments:** The authors acknowledge funding support from Nazarbayev University.

**Conflicts of Interest:** The authors declare no conflict of interest.

## References

1. Lutchmiah, K.; Verliefde, A.R.D.; Roest, K.; Rietveld, L.C.; Cornelissen, E.R. Forward osmosis for application in wastewater treatment: A review. *Water Res.* **2014**, *58*, 179–197. [[CrossRef](#)]
2. Inglezakis, V.J.; Pouloupoulos, S.G.; Arkhangelsky, E.; Zorpas, A.A.; Menegaki, A.N. *Aquatic Environment*; Elsevier: Amsterdam, The Netherlands, 2016; ISBN 9780444627339.
3. Chung, T.S.; Luo, L.; Wan, C.F.; Cui, Y.; Amy, G. What is next for forward osmosis (FO) and pressure retarded osmosis (PRO). *Sep. Purif. Technol.* **2015**, *156*, 856–860. [[CrossRef](#)]
4. Wang, H.; Chung, T.S.; Tong, Y.W.; Jeyaseelan, K.; Armugam, A.; Chen, Z.; Hong, M.; Meier, W. Highly permeable and selective pore-spanning biomimetic membrane embedded with aquaporin Z. *Small* **2012**, *8*, 1185–1190. [[CrossRef](#)] [[PubMed](#)]
5. Nielsen, C.H. Biomimetic membranes for sensor and separation applications. *Anal. Bioanal. Chem.* **2009**, *395*, 697–718. [[CrossRef](#)] [[PubMed](#)]
6. Ibragimova, S.; Stibius, K.; Szewczykowski, P.; Perry, M.; Bohr, H.; Hélix-Nielsen, C. Hydrogels for in situ encapsulation of biomimetic membrane arrays. *Polym. Adv. Technol.* **2012**, *23*, 182–189. [[CrossRef](#)]
7. González-Pérez, A.; Stibius, K.B.; Vissing, T.; Nielsen, C.H.; Mouritsen, O.G. Biomimetic triblock copolymer membrane arrays: A stable template for functional membrane proteins. *Langmuir* **2009**, *25*, 10447–10450. [[CrossRef](#)] [[PubMed](#)]
8. Hansen, J.S.; Perry, M.; Vogel, J.; Vissing, T.; Hansen, C.R.; Geschke, O.; Emnéus, J.; Nielsen, C.H. Development of an automation technique for the establishment of functional lipid bilayer arrays. *J. Micromech. Microeng.* **2009**, *19*, 25014. [[CrossRef](#)]
9. Wang, H.; Chung, T.S.; Tong, Y.W.; Meier, W.; Chen, Z.; Hong, M.; Jeyaseelan, K.; Armugam, A. Preparation and characterization of pore-suspending biomimetic membranes embedded with Aquaporin Z on carboxylated polyethylene glycol polymer cushion. *Soft Matter* **2011**, *7*, 7274–7280. [[CrossRef](#)]
10. Hey, T.; Bajraktari, N.; Vogel, J.; Hélix Nielsen, C.; la Cour Jansen, J.; Jönsson, K. The effects of physicochemical wastewater treatment operations on forward osmosis. *Environ. Technol. (UK)* **2017**, *38*, 2130–2142. [[CrossRef](#)]
11. Li, Z.; Valladares Linares, R.; Bucs, S.; Fortunato, L.; Hélix-Nielsen, C.; Vrouwenvelder, J.S.; Ghaffour, N.; Leiknes, T.O.; Amy, G. Aquaporin based biomimetic membrane in forward osmosis: Chemical cleaning resistance and practical operation. *Desalination* **2017**, *420*, 208–215. [[CrossRef](#)]
12. Song, H.; Xie, F.; Chen, W.; Liu, J. FO/MD hybrid system for real dairy wastewater recycling. *Environ. Technol. (UK)* **2018**, *39*, 2411–2421. [[CrossRef](#)] [[PubMed](#)]
13. Hamad, M.J.A.; Chirwa, E.M.N. The viability of forward osmosis in the concentration of biologically produced fumaric acid using l-alanine as a draw solution. *Chem. Eng. Trans.* **2018**, *64*, 259–264.
14. Xue, W.; Sint, K.K.K.; Ratanatamskul, C.; Praserthdam, P.; Yamamoto, K. Binding TiO<sub>2</sub> nanoparticles to forward osmosis membranes: Via MEMO-PMMA-Br monomer chains for enhanced filtration and antifouling performance. *RSC Adv.* **2018**, *8*, 19024–19033. [[CrossRef](#)]
15. Luo, W.; Xie, M.; Song, X.; Guo, W.; Ngo, H.H.; Zhou, J.L.; Nghiem, L.D. Biomimetic aquaporin membranes for osmotic membrane bioreactors: Membrane performance and contaminant removal. *Bioresour. Technol.* **2018**, *249*, 62–68. [[CrossRef](#)]
16. Singh, N.; Petrinic, I.; Hélix-Nielsen, C.; Basu, S.; Balakrishnan, M. Concentrating molasses distillery wastewater using biomimetic forward osmosis (FO) membranes. *Water Res.* **2018**, *130*, 271–280. [[CrossRef](#)]
17. Soler-Cabezas, J.L.; Mendoza-Roca, J.A.; Vincent-Vela, M.C.; Luján-Facundo, M.J.; Pastor-Alcañiz, L. Simultaneous concentration of nutrients from anaerobically digested sludge centrate and pre-treatment of industrial effluents by forward osmosis. *Sep. Purif. Technol.* **2018**, *193*, 289–296. [[CrossRef](#)]

18. Kalafatakis, S.; Braekevelt, S.; Lymperatou, A.; Zarebska, A.; Hélix-Nielsen, C.; Lange, L.; Skiadas, I.V.; Gavala, H.N. Application of forward osmosis technology in crude glycerol fermentation biorefinery-potential and challenges. *Bioprocess Biosyst. Eng.* **2018**, *41*, 1089–1101. [[CrossRef](#)]
19. Munshi, F.M.; Church, J.; McLean, R.; Maier, N.; Sadmani, A.H.M.A.; Duranceau, S.J.; Lee, W.H. Dewatering algae using an aquaporin-based polyethersulfone forward osmosis membrane. *Sep. Purif. Technol.* **2018**, *204*, 154–161. [[CrossRef](#)]
20. Preston, G.M.; Jung, J.S.; Guggino, W.B.; Agre, P. The mercury-sensitive residue at cysteine 189 in the CHIP28 water channel. *J. Biol. Chem.* **1993**, *268*, 17–20.
21. Barone, L.M.; Mu, H.H.; Shih, C.J.; Kashlan, K.B.; Wasserman, B.P. Distinct biochemical and topological properties of the 31-and 27-kilodalton plasma membrane intrinsic protein subgroups from red beet. *Plant Physiol.* **1998**, *118*, 315–322. [[CrossRef](#)]
22. Niemietz, C.M.; Tyerman, S.D. New potent inhibitors of aquaporins: Silver and gold compounds inhibit aquaporins of plant and human origin. *FEBS Lett.* **2002**, *531*, 443–447. [[CrossRef](#)]
23. Martínez-Ballesta, M.C.; Cabañero, F.; Olmos, E.; Periago, P.M.; Maurel, C.; Carvajal, M. Two different effects of calcium on aquaporins in salinity-stressed pepper plants. *Planta* **2008**, *228*, 15–25. [[CrossRef](#)] [[PubMed](#)]
24. Shih, W.Y.; Rahardianto, A.; Lee, R.W.; Cohen, Y. Morphometric characterization of calcium sulfate dihydrate (gypsum) scale on reverse osmosis membranes. *J. Memb. Sci.* **2005**, *252*, 253–263. [[CrossRef](#)]
25. Lin, N.H.; Cohen, Y. QCM study of mineral surface crystallization on aromatic polyamide membrane surfaces. *J. Memb. Sci.* **2011**, *379*, 426–433. [[CrossRef](#)]
26. Xie, M.; Gray, S.R. Gypsum scaling in forward osmosis: Role of membrane surface chemistry. *J. Memb. Sci.* **2016**, *513*, 250–259. [[CrossRef](#)]
27. Shaffer, D.L.; Tousley, M.E.; Elimelech, M. Influence of polyamide membrane surface chemistry on gypsum scaling behavior. *J. Memb. Sci.* **2017**, *525*, 249–256. [[CrossRef](#)]
28. Mi, B.I.; Elimelech, M. Gypsum scaling and cleaning in forward osmosis: Measurements and mechanisms. *Environ. Sci. Technol.* **2010**, *44*, 2022–2028. [[CrossRef](#)]
29. Balkenov, A.; Anuarbek, A.; Satayeva, A.; Kim, J.; Inglezakis, V.; Arkhangelsky, E. Complex organic fouling and effect of silver nanoparticles on aquaporin forward osmosis membranes. *J. Water Process Eng.* **2020**, *34*, 101177. [[CrossRef](#)]
30. Wang, K.; Xu, L.; Li, K.; Liu, L.; Zhang, Y.; Wang, J. Development of polyaniline conductive membrane for electrically enhanced membrane fouling mitigation. *J. Memb. Sci.* **2019**, *570–571*, 371–379. [[CrossRef](#)]
31. Xia, L.; Andersen, M.F.; Hélix-Nielsen, C.; McCutcheon, J.R. Novel Commercial Aquaporin Flat-Sheet Membrane for Forward Osmosis. *Ind. Eng. Chem. Res.* **2017**, *56*, 11919–11925. [[CrossRef](#)]
32. Melián-Martel, N.; Sathwani, J.J.; Malamis, S.; Ochsenkühn-Petropoulou, M. Structural and chemical characterization of long-term reverse osmosis membrane fouling in a full scale desalination plant. *Desalination* **2012**, *305*, 44–53. [[CrossRef](#)]
33. Kaufmann, R.S. Fick's law. In *Geochemistry. Encyclopedia of Earth Science*; Marshall, C.P., Fairbridge, R.W., Eds.; Springer: Berlin/Heidelberg, Germany, 1999; p. 245. ISBN 978-0-412-75500-2.
34. Zou, S.; Gu, Y.; Xiao, D.; Tang, C.Y. The role of physical and chemical parameters on forward osmosis membrane fouling during algae separation. *J. Memb. Sci.* **2011**, *366*, 356–362. [[CrossRef](#)]
35. Sheikholeslami, R. Mixed salts-Scaling limits and propensity. *Desalination* **2003**, *154*, 117–127. [[CrossRef](#)]
36. Zhao, P.; Gao, B.; Yue, Q.; Liu, S.; Shon, H.K. Effect of high salinity on the performance of forward osmosis: Water flux, membrane scaling and removal efficiency. *Desalination* **2016**, *378*, 67–73. [[CrossRef](#)]
37. Majeed, T.; Phuntsho, S.; Sahebi, S.; Kim, J.E.; Yoon, J.K.; Kim, K.; Shon, H.K. Influence of the process parameters on hollow fiber-forward osmosis membrane performances. *Desalin. Water Treat.* **2015**, *54*, 817–828. [[CrossRef](#)]
38. Jung, D.H.; Lee, J.; Kim, D.Y.; Lee, Y.G.; Park, M.; Lee, S.; Yang, D.R.; Kim, J.H. Simulation of forward osmosis membrane process: Effect of membrane orientation and flow direction of feed and draw solutions. *Desalination* **2011**, *277*, 83–91. [[CrossRef](#)]
39. Chun, Y.; Qing, L.; Sun, G.; Bilad, M.R.; Fane, A.G.; Chong, T.H. Prototype aquaporin-based forward osmosis membrane: Filtration properties and fouling resistance. *Desalination* **2018**, *445*, 75–84. [[CrossRef](#)]
40. Zhao, Z.P.; Wang, Z.; Wang, S.C. Formation, charged characteristic and BSA adsorption behavior of carboxymethyl chitosan/PES composite MF membrane. *J. Memb. Sci.* **2003**, *217*, 151–158. [[CrossRef](#)]

41. Gehr, R.; Zhai, Z.A.; Finch, J.A.; Rao, S.R. Reduction of soluble mineral concentrations in CaSO<sub>4</sub> saturated water using a magnetic field. *Water Res.* **1995**, *29*, 933–940. [[CrossRef](#)]
42. Hancer, M.; Celik, M.S.; Miller, J.D. The significance of interfacial water structure in soluble salt flotation systems. *J. Colloid Interface Sci.* **2001**, *235*, 150–161. [[CrossRef](#)]
43. Genestar, C. Characterization of grounds used in canvas and sculpture. *Mater. Lett.* **2002**, *54*, 382–388. [[CrossRef](#)]
44. Ray, J.R.; Wong, W.; Jun, Y.S. Antiscalcing efficacy of CaCO<sub>3</sub> and CaSO<sub>4</sub> on polyethylene glycol (PEG)-modified reverse osmosis membranes in the presence of humic acid: Interplay of membrane surface properties and water chemistry. *Phys. Chem. Chem. Phys.* **2017**, *19*, 5647–5657. [[CrossRef](#)] [[PubMed](#)]



© 2020 by the authors. Licensee MDPI, Basel, Switzerland. This article is an open access article distributed under the terms and conditions of the Creative Commons Attribution (CC BY) license (<http://creativecommons.org/licenses/by/4.0/>).

MDPI  
St. Alban-Anlage 66  
4052 Basel  
Switzerland  
Tel. +41 61 683 77 34  
Fax +41 61 302 89 18  
[www.mdpi.com](http://www.mdpi.com)

*Membranes* Editorial Office  
E-mail: [membranes@mdpi.com](mailto:membranes@mdpi.com)  
[www.mdpi.com/journal/membranes](http://www.mdpi.com/journal/membranes)







MDPI  
St. Alban-Anlage 66  
4052 Basel  
Switzerland

Tel: +41 61 683 77 34  
Fax: +41 61 302 89 18

[www.mdpi.com](http://www.mdpi.com)



ISBN 978-3-0365-1988-3